THE UNIVERSITY OF QUEENSLAND

AUSTRALIA

Astronomical Forcing of Sub-Milankovitch Climate Oscillations during the Late Quaternary

Alison Marguerite Kelsey

Honours, Bachelor of Arts, Archaeology

Bachelor of Arts, Archaeology

Diploma of Information Technology, Software Development

A thesis submitted for the degree of Doctor of Philosophy at

The University of Queensland in 2017

School of Earth and Environmental Sciences

Abstract

A climate signal of ~1500-yr quasi-periodicity (e.g., Bond events) has been found from the Arctic to Antarctica, in palaeoclimatic data derived from a range of environmental proxy records. Solar and lunar forcing have individually been suggested as the cause of this millennial-scale signal, although some contend that it is little more than stochastic resonance within the climate system. Also debated is whether this climate signal is forced by the ocean-atmosphere dynamics of the North Atlantic or the tropical Pacific, as well as relevant climatic teleconnections. The cause of this cycle is elusive as no known solar cycle of this length exists, whilst forcing due to lunar gravitation has been dismissed as being too weak.

The most likely cause of any periodic climate signal is an astronomical one, as demonstrated in Milankovitch cycles. This thesis explores a potential astronomical cause of millennial- and centennial- scale periodicities and variability, based on a combination of solar and lunar forcing. Conceptual and trigonometric models, physical models of insolation, solar irradiance, and gravitation, and astronomical data were used in this exploration. Identified as a possible cause of the ~1500-yr climate cycle is precession. Precession changes the timing of Earth's seasons relative to our calendar and external reference points, such as the fixed stars and the closest point in Earth's orbit to the Sun (the perihelion). The primary actors in precession are the Sun and Moon through their gravitational influence on the rotating Earth. Significant climatic impacts of precession are seen in the ~21-ky Milankovitch precessional cycle, the result of two interacting precessional cycles: equinoctial (associated with the seasonal/tropical year) and apsidal (associated the perihelion and anomalistic year). This thesis investigates precession at a high-frequency scale, enabling a more detailed tracking of the moving seasons relative to the moving perihelion at sub-Milankovitch scales through-out the last 5,500 yrs.

This research found a statistically-significant, strong positive correlation between solar insolation reconstruction derived from Antarctic ^{10}Be ice-core data and a normalised, chronologically-anchored model of superimposed astronomical cycles that emulates the ~1500-yr climate cycle. Pronounced millennial-scale signals were observed in Earth-Moon distances and gravitation data. Maximum forcing occurs at perihelion, close to lunar perigee and Bond events occur at these points during the range of the astronomical data. Previously identified potential components of the ~1500-yr climate signal, *viz* the 209-yr Suess de Vries cycle and a 133-yr cycle, can be clearly seen in the astronomical and physical data. Modelled, high-frequency, perigee-perihelion interaction by this research reinforces these results, reproducing and explaining the variability of millennial-scale climate signals. Such variability is also supported through the movement relative to the tropical year, in conjunction with mapping of Metonic lunation and perihelion positions.

Supported by multiple lines of evidence, the results of this thesis suggest that the Sun and Moon act together through gravitation and insolation to produce millennial-, centennial-and decadal- scale climate signals through tidal forcing of Earth's atmosphere and ocean. Key mechanisms and components are precession, perihelion, perigee, lunation, and nutation (wobble of Earth's axis). Key inferences from these results are that astronomical forcing influences radiocarbon chronological variability, such as marine reservoir values, variability and time lag in radiocarbon data, and also suggest that the 209-yr SdV cycle is caused by combined solar and lunar forcing rather than previously inferred solar variability.

Declaration by author

This thesis is composed of my original work, and contains no material previously published or written by another person except where due reference has been made in the text. I have clearly stated the contribution by others to jointly-authored works that I have included in my thesis.

I have clearly stated the contribution of others to my thesis as a whole, including statistical assistance, survey design, data analysis, significant technical procedures, professional editorial advice, and any other original research work used or reported in my thesis. The content of my thesis is the result of work I have carried out since the commencement of my research higher degree candidature and does not include a substantial part of work that has been submitted to qualify for the award of any other degree or diploma in any university or other tertiary institution. I have clearly stated which parts of my thesis, if any, have been submitted to qualify for another award.

I acknowledge that an electronic copy of my thesis must be lodged with the University Library and, subject to the policy and procedures of The University of Queensland, the thesis be made available for research and study in accordance with the Copyright Act 1968 unless a period of embargo has been approved by the Dean of the Graduate School.

I acknowledge that copyright of all material contained in my thesis resides with the copyright holder(s) of that material. Where appropriate I have obtained copyright permission from the copyright holder to reproduce material in this thesis.

Publications during candidature:

KELSEY, A. M., MENK, F. W. & MOSS, P. T. 2015. An astronomical correspondence to the 1470-year cycle of abrupt climate change. *Clim. Past Discuss.,* 2015, 4895-4915.

Conference abstracts:

KELSEY, A.M. 2015. The astronomy of the 1,470yr climate cycle: extending the Milankovitch connection. *XIX INQUA-Congress,* G01-03, 2015, Nagoya, Japan.

KELSEY, A.M. 2015. Millennial Oscillations of the Late Quaternary and the Great Sandy Region of Southeast Queensland. *XIX INQUA-Congress,* P19-03, 2015, Nagoya, Japan.

KELSEY, A. M. 2016. The Milankovitch connection: astronomical forcing of millennial-scale climate signals. *AQUA Biennial Conference,* 2016, P2, Auckland, New Zealand.

Publications included in this thesis:

Nil

Contributions by others to the thesis:

The supervisory team Patrick Moss and Fred Menk assisted with technical support, revisions and editing of the thesis. Peter Kershaw, Cian Brinkmann, and Janet McCoy assisted with editing of the thesis.

Statement of parts of the thesis submitted to qualify for the award of another degree:

None.

Acknowledgements

I firstly wish to thank my supervisors, Patrick Moss and Fred Menk, for their time, guidance, support, and encouragement during the course of my thesis. I greatly appreciate the opportunities they afforded me in allowing me to take this journey of discovery.

To my family, and especially my children, Matthew Cole, Ross Cole, Cassie Robinson, Michael Kelsey, and Cian Brinkmann, thank-you from the bottom of my heart; your enduring patience, support and words of encouragement have made this achievement possible. My journey was plagued with obstacles, including breast cancer, broken bones, and multiple surgeries. Thank-you all for looking after me during those difficult times and helping me get across the finishing line, and feeding me when I forgot to eat, especially Cian and Matt Brinkmann, Cassie, Mick, and Anjuli Lansley. Cian, you were also a wonderful help in providing another set of eyes to edit my thesis. Although my parents, Max and Maureen Kelsey, are no longer of this world, I cannot forget them: to Mum and Dad I owe so much for encouraging and feeding my thirst for knowledge.

I wish to say very big thank-you to my friends, all of whom provided encouragement, support and friendship throughout the course of my PhD research. In particular, I'd like to thank Phil Stewart, Janet McCoy, and Peter Kershaw for their friendship. You were all there when I needed a friend. Phil, your friendship, sense of humour, and words of encouragement helped me when I felt discouraged. Thank-you to Peter and Janet for editing my thesis, and Peter for your advice.

I'd also like to thank Jamie Shulmeister, Lynda Petherick, Quan Hua, Jian-Xin Zhao, Patricia Gadd, and Matthew Fischer. Although our discussions were brief, you none-the-less provided guidance when I needed it.

Keywords:

Astronomy, Milankovitch precession, Bond events, ENSO, geochronology, cosmogenic isotopes, solar and lunar forcing

Australian and New Zealand Standard Research Classifications (ANZSRC):

ANZSRC code: 040605 Palaeoclimatology (33.33%)

ANZSRC code: 020199 Astronomical and Space Sciences not elsewhere classified (33.33%)

ANZSRC code: 040606 Quaternary Environments (33.33%)

Fields of Research (FoR) Classification:

FoR code: 0201 Astronomical and Space Sciences (50%)

FoR code: 0406 Physical Geography and Environmental Geoscience (50%)

Chapter Guide

List of Figures

List of Tables

Acronyms

AICC12	Antarctic Ice Core Chronology 2012
AMOC	Atlantic Meridional Overturning Circulation
AMS	Accelerator Mass Spectroscopy
BOM	Bureau of Meteorology
BP	Before present (1950)
CFA	Continuous flow analysis
CLIMAP	Climate: Long-range, Investigation, Mapping, and Prediction
CME	Coronal mass ejection
DO	Dansgaard-Oeschger
DWF	deep-water formation
ECM	Electrical component modelling
EDC3	EPICA Dome C chronological model
EDML	EPICA Dronning Maud Land chronological model
ENSO	El Niño Southern Oscillation
EPICA	European Project for Ice Coring in Antarctica
GICCO5	Greenland Ice Core Chronology 2005
GISP	Greenland Ice Sheet Project
GRIP	Greenland Ice Core Project
ICM	Ice flow model
IRD	ice-rafting debris
LIA	Little Ice Age
LMT	Local mean time
MIS	Marine Isotope Stage; see OIS
MDP	Magnetic dipole moment
MWP	Medieval Warm Period
NASA	National Aeronautics and Space Administration
NCP	North Celestial Pole
NGRIP	New Greenland Ice Core Project
NOAA	National Oceanic and Atmospheric Administration
NSI	North Stradbroke Island
OIS	Oxygen Isotope Stage

PDO	Pacific Decadal Oscillation
RA	Right ascension
RRA	First closest return of anomalistic year length to starting geographic longitude
RRS	First closest return of sidereal year length to starting geographic longitude
RRT	First closest return of tropical year length to starting geographic longitude
RWP	Roman Warm Period
SCP	South Celestial Pole
SdV	Suess de Vries
SFCP04	Shackleton Fairbanks GRIP chronological model
SO	Southern oscillation
SPECMAP	Spectral Mapping Project
SS09SEA	A GRIP chronological model
SST	Sea-surface temperature
TOA	Top of atmosphere
TSI	Total solar irradiance
calBP	Calibrated BP
WPWP	West Pacific Warm Pool

Glossary

Anomalistic month	The average of a lunar month measured from perigee to perigee.
Anomalistic year	Relative to the perihelion, this is the period of one Earth revolution around the Sun, equalling ~365.2596 days
Apsides	The plural form of apsis. This is the intersection of the semi-major axis with the elliptical orbit of a satellite at the perihelion and aphelion
Apsidal precession	See Precession of the apsides
Aphelion	In a solar orbit, this is the point furthest from the Sun. See also apsides.
Apogee	Furthest point in the lunar orbit to the Earth.
Astronomical meridian	A line connecting points of the same astronomical longitude.
Callipic cycle	76 yrs (calendar) or 75.9994 tropical years. Used in the intercalation of solar and lunar calendars.
Cambridge half-life	(of radiocarbon), equal to 5730±40yrs
Celestial equator	Extension of Earth's equator into space.
Celestial meridian	The celestial meridian is relative to the observer and is an astronomical meridian that passes through the zenith, nadir, and celestial poles. It is part of the Great Circle.
Circumpolar	Situated around the pole.
Declination	Measure of angular distance north or south of the celestial equator.
Draconic month	An average of the month measured relative to the Moon's ascending node.
Eccentricity	The difference (measured along the semi-major axis) of each of the foci to the centre of the ellipse
Ecliptic	Earth's orbital plane.
Equinoctial	Pertaining to the equinox
Equinox	Two points of intersection of the ecliptic with the celestial equator.
First point of Aries	See vernal equinox.
Great circle	An astronomical meridian that runs through the poles, nadir, and zenith.

Intercalation	Insertion into a calendar
Julian year	Mean solar year of 365.25 days, named after Julius Caesar.
Libby half-life	(Of radiocarbon), equal to 5568±30 yrs
Lunation	New Moon
Lunar nodes	Two points of intersection of the lunar orbital plane and the ecliptic, one ascending node (north node) and one descending node (south node).
Mean solar day	The time between two consecutive solar zeniths.
Metonic cycle	A cycle of lunations that returns to the same longitudinal degree once every 19 yrs. Discovered by Athenian astronomer, Meton in 432BC. Used in the intercalation of solar and lunar calendars.
Nadir	Opposite point of the zenith.
Milankovitch climatic precession	A climatic precession, resulting from the interaction between the precession of the apsides and the precession of the equinoxes.
Nutation	Nodding of the axis of rotation.
Obliquity	Tilt of Earth's axis to the ecliptic.
Perigee	Closest point in the lunar orbit to the Earth.
Perihelion	The closest point in the orbit to the Sun. See also apsides.
Precession of the apsides	The orbital precession of the semi-major axis.
Precession of the equinoxes	A ~26k y cycle that sees the Vernal Point move backwards along the ecliptic through the fixed stars of the sidereal zodiac, resulting in a slowly changing orientation of the north celestial pole.
Right Ascension	An angular measure of distance of the vernal equinox relative to the celestial equator.
Saros cycle	Saros cycle of eclipses, in which a solar eclipse returns to the same part of the heavens after 18.03yrs.
Semi-major axis	One half of the longest axis of an eclipse.
Semi-minor axis	One half of the shortest axis of an ellipse.
Sidereal day	The length of day measured relative to the vernal equinox.
Sidereal year	Measured relative to fixed stars, this is the period of one Earth revolution around the Sun, equalling ~365.2563 days.
Solar luminosity	A measure of the sun's power.

Sothic cycle	This is the cycle of 1461 yrs (Julian) created by the disparity between the lengths of the tropical year and the Egyptian calendar year.
Solar zenith	Occurs at noon (local time), when the Sun is at maximum altitude.
Solstice	One of two points marking the furthest northern and southern declinations of the Sun. The winter solstice is the shortest day of the year and the summer solstice is the longest day of the year.
Solstitial	Relating to the solstice
Sothic cycle	Cycle named after the star, Sirius. A cycle caused by the desynchronisation of the ancient Egyptian calendar from the seasonal year. Equal to 1461 Julian years.
Synodic month	Average measure of lunar month from one New Moon to the next.
Syzygy	Points of conjunction or opposition in the orbit of a satellite such as the Moon, i.e., New Moon and Full Moon.
Tropical year	Measured relative to the Vernal equinox, this is the period of one Earth revolution around the Sun, equalling ~365.2422 days.
Vernal equinox	The intersection of the celestial equator with the ecliptic, associated with the spring equinox. The vernal equinox occurs when the Sun moves from southern declination to northern declination.
Vernal point	See vernal equinox.
Zenith	The zenith is one of four main points defining the great circle of the celestial meridian, the others being the poles and the nadir. The zenith is located on this meridian directly overhead of the observer, and its opposite point is the nadir.

Chapter 1 - Introduction

1.1 Introduction

Central to questions on Holocene climate stability is an apparent ~1470±500-yr climate quasi-periodicity of abrupt climate change (deMenocal *et al.*, 2000; cf. Wolff *et al.,* 2010). This ~1500-yr climate oscillation was found to persist through the last glacial and Holocene periods (Bond *et al.,* 1997; Bond *et al*., 1999). Evidence for this quasi-periodicity appears in multiple sources from around the world, such as (Bond) ice-rafting debris (IRD) events in deep-sea sedimentary cores from the North Atlantic (Bond *et al.,* 1997); Dansgaard-Oeschger oscillations in atmospheric temperature found in the Greenland ^{18}O ice-core record of the lacial period (Bond *et al.,* 1997; Grootes and Stuiver, 1997; Johnsen *et al*., 1992; Dansgaard *et al*., 1993; Schulz, 2002; Wolff *et al.,* 2010); and cyclical climatic conditions precursory to increased El Niño/Southern Oscillation (ENSO) variability and intensity in the tropical Pacific at the millennial-scale [Figure 1.1] (Anderson *et al*., 2006; Gagan *et al*., 2004; Turney *et al.,* 2004; van Buren, 2001). The peaks in Figure 1.1 occur in high resolution peat humification data from Lynch's Crater, North Queensland (Turney *et al.,* 2004).

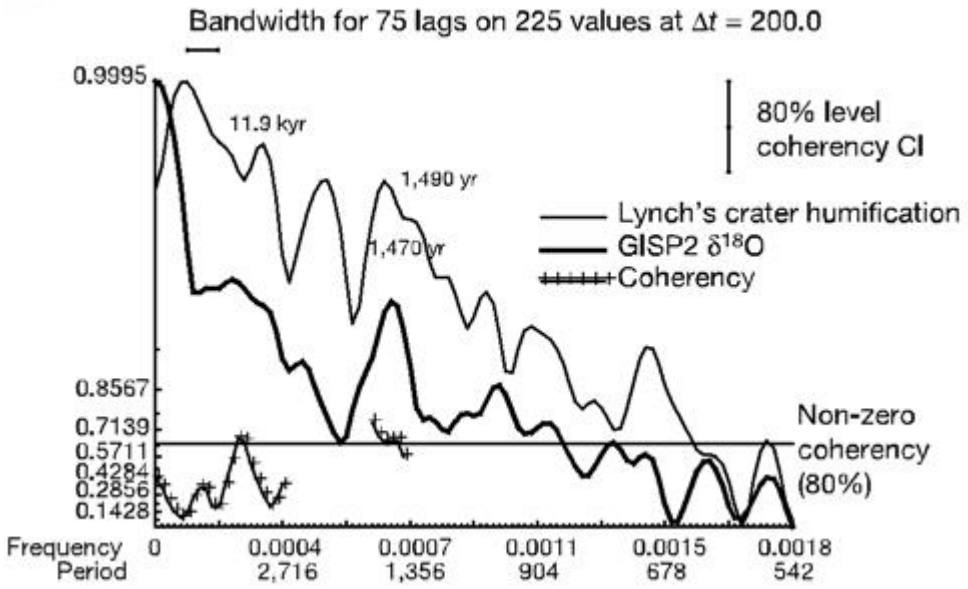

Figure 1.1: 1490-yr spectral peak. Results of spectral and cross-spectral analysis of Lynch's crater in North Queensland and the GISP2 ice-core records from Greenland (Turney *et al.,* 2004:308). These peaks are significant at the 95% confidence level.

Bond *et al.* (1999) identified the ~1500-yr quasi-periodic oscillation to which Dansgaard-Oeschger and Heinrich events appear to be tuned, meaning that the underlying Bond quasi-periodicity is a low amplitude signal that appears to be magnified at the times of Dansgaard-Oeschger and Heinrich events [Figure 1.2]. Dansgaard-Oeschger events occur at times of rapid warming at the transition

from cold stadial to warm interstadial (Schulz, 2002; cf. Cooper *et al.,* 2015; Wolff *et al.,* 2010), with events generally occurring at 1ky-12ky intervals, but more frequently during MIS3 at 1ky-5ky intervals (Schulz, 2002). However, the timing and number of Dansgaard-Oeschger events depends on the time-scale used (Wolff *et al.,* 2010) and how they are defined (Alley *et al.,* 2001; cf. Ditlevsen *et al.,* 2005). The largest IRD discharges occur with Heinrich events that occur at 11±1 ky intervals in response to precessional forcing (Bond *et al.,* 1999; Heinrich, 1988; Summerhayes, 2015). Heinrich events occurred more frequently in the last 32 ky [Figure 1.2]. Whilst Mayewski *et al.* (1997) estimated that Heinrich events occurred on ~6.1 ky periodicity, Bond *et al.* (1999) noted that this periodicity is not always coincident with Heinrich events in the GISP2 time series.

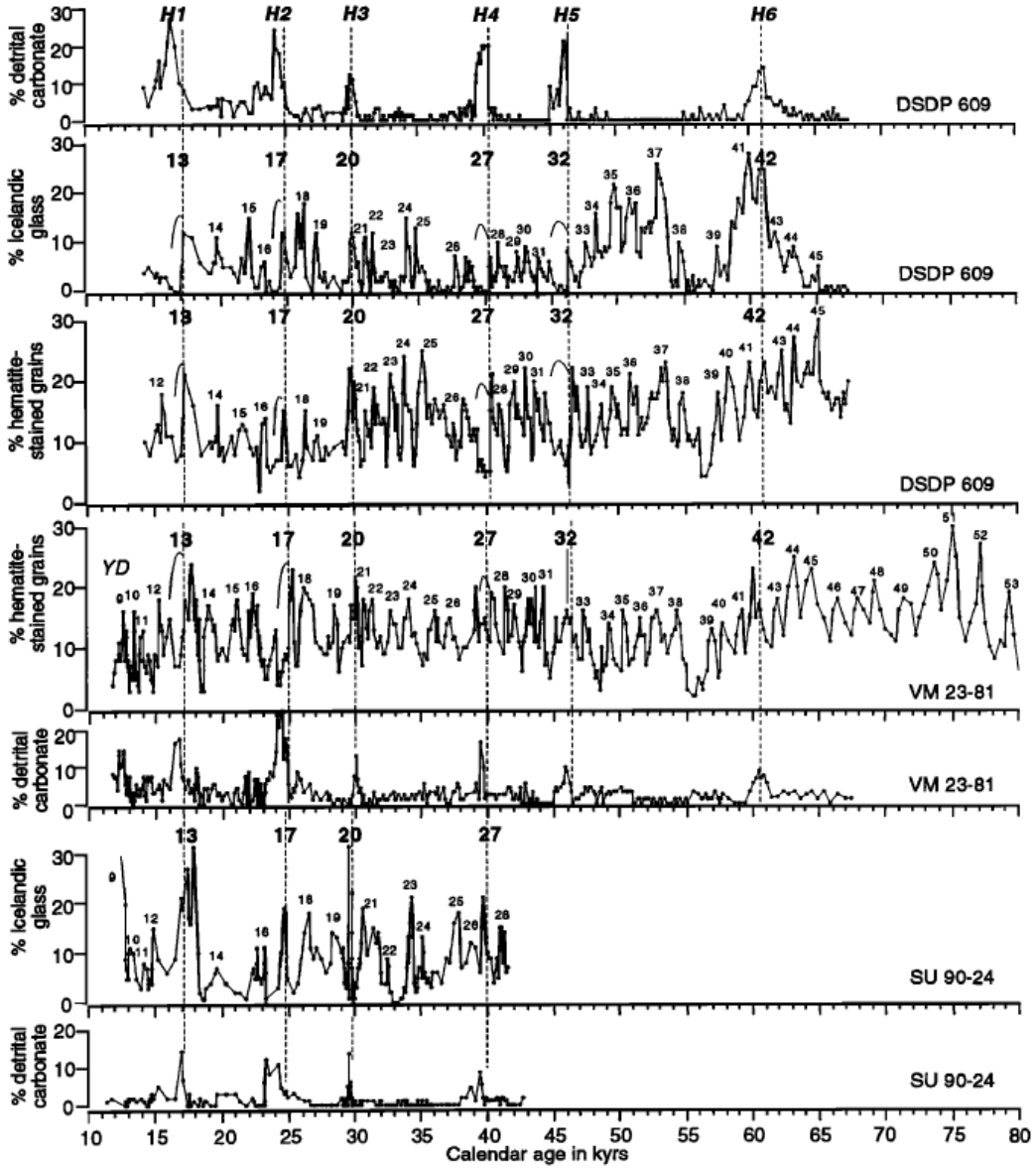

Figure 1.2: Timing of Heinrich and Bond events during the last glacial from three deep-sea sediment cores (DSDP 609, VM23-81, SU 90-24) (Bond *et al.,* 1999:42). Heinrich events are Marked (H1-H6), whilst the smaller numbered peaks of statistically-significant peaks are numbered, with the count starting at 0 for the Little Ice Age. These peaks of ice-rafted debris consist of detrital carbonate, stained and Icelandic glass.

Proposed causes of the ~1500-yr 'cycle', *viz* the thermohaline current and ENSO, were criticised as candidates for this role (Broecker, 2003). The deep-water formation/thermohaline scenario was seen as lacking a mechanism for rapid dispersal over the planet as the oceanic circulation system is sluggish. The tropical scenario was seen as lacking a locking mechanism and evidence that the tropical atmosphere-ocean is multi-modal in the first place, thereby enabling it to be locked (Broecker, 2003). To date no causal mechanism has been identified, although possible mechanisms may include amplification of both solar and gravitational forcing (Bond *et al.*, 2001; Braun *et al.,* 2005; Keeling and Whorf, 2000; Turney, 2008; Turney *et al.,* 2004; Wolff *et al.,* 2010). Bond *et al.* (2001) noticed correspondences to the ~1500 quasi-periodicity with solar irradiance variation. Despite debates as to the inability of small variations of solar output to influence abrupt climate change, Bond *et al.* (1999) concluded that Earth's climate system was extremely sensitive to weak variations in solar irradiance. Braun *et al.* (2005) proposed a model based on a combination of solar periodicities (viz, the Gleissberg and Suess de Vries cycles). Additionally, the very existence of the ~1500-yr 'cycle' has been challenged on the basis of a new Greenland ice-core chronological model (Wolff *et al.,* 2010) and statistical tests (Ditlevsen *et al.,* 2009). Wolff *et al.* (2010) consider the matter unresolved.

The physics of abrupt climate change is poorly understood (Banderas *et al*., 2015; Broecker, 2003, Ditlevsen *et al.,* 2009; Turney, 2008) and this factor likely contributes to these debates. Questions thus proliferate. Does this climate quasi-periodicity exist or are these climate events just random events that resonate throughout Earth's climate system? If it does exist, what is its cause? It follows then that the need to understand and identify the causal mechanism in sudden climate change is of primary importance (cf. Ditlevsen *et al.,* 2005; Hertzberg *et al.,* 2012). Improved understanding of millennial-scale oscillations and their potential climatic impacts is important for the production of more accurate climate models in the future, especially in the differentiation between anthropogenic and natural causes of climate change. Currently, the matter of global warming is at the forefront of societal and political concern.

As a natural component of climate change, the ~1500-yr quasi-periodicity contributes to climate variability irrespective of anthropogenic global warming, and consequently impacts on human lives. A key debate in archaeological circles is on determinism, which is the extent to which environment influences free-will and the consequent impact on humans (e.g., Berglund, 2003; Feynman and Ruzmaikin, 2007). Another associated issue is to whether the changes in the archaeological record are due to human impact or climate change (e.g., Parker *et al.,* 2002; Junk and Claussen, 2011). Whilst it is difficult to directly assess climatic impacts on society, environmental stress is clearly placed on societies by disruption to stable climatic conditions (van Buren, 2001). Numerous archaeological

researchers have noted the coincidence between times of abrupt climate change and likely impact on civilisations (e.g., Anderson *et al*., 2006; Feynman and Ruzmaikin, 2007; Manzanilla, 1997; Nunn, 2001).

Examples of concurrences with the 1500-yr quasi-periodicity include: the beginning of the Early Neolithic in NW Europe associated with the Elm decline (Parker *et al.,* 2002; Batchelor *et al.,* 2014); the establishment of early Egyptian civilisation (pre-dynastic), following the severe aridification of the Sahara (Manzanilla, 1997; Sereno *et al.,* 2008); the collapse of Egypt's Old Kingdom and Akkadian Empire in Mesopotamia, and Harrapan civilisation around 4.2kya (Feynman and Ruzmaikin, 2007; Possehl*,* 1993 cited in Manzanilla, 1997); the beginning of the Dark Age in the mid-6th century AD (Manzanilla, 1997); the demise of the Peruvian Moche civilisation that began with the collapse of the Moche capital (600AD) (van Buren, 2001); the beginning of Teotihuacan's decline around 550AD; and the expansion of Polynesian society in the Pacific (Anderson *et al*., 2006). The Medieval Warm Period (~900AD to ~1300AD) saw the colonisation of Easter Island and the Greenland Norse colonies (Diamond, 2005). The Little Ice Age (LIA) (~1300AD to ~1850AD) saw the disappearances of the Greenland Norse (Kintisch, 2016) and Polynesian culture on Easter Island (Diamond, 2005; cf. Gossen, 2011). In Europe, Asia, and North America temperatures were cooler, and civilisations had to contend with drought, harvest failures and plagues (McMichael, 2017). The impact of the LIA was also felt in Australia, where increased variability and intensity of climate due to ENSO was shown (Donders *et al.,* 2006; Moss *et al.,* 2013).

To better understand the future, it is first necessary to understand the past (cf. Blackford and Chambers, 1991; Blois *et al*., 2013). An important part of this process is the understanding that can be derived from consideration of Earth's position within its celestial neighbourhood and the potential of astronomical forcing of this signal. Circular or near circular orbits are essential to climate stability, and the evolution and maintenance of life, such as with Earth's near circular shaped orbit (Professor Michio Kaku , University of New York in Ward, 2012). Stability in climate has been seen as essential in the development of agriculture (Feynman and Ruzmaikin, 2007). Whilst Earth's orbit is near circular, it is slightly elliptical, with Earth-Sun distances currently varying by 5Mkm (million kilometres) annually between the closest point to the Sun at perihelion and furthest point from the Sun at aphelion. The magnitude of this ellipticity changes through time.

In this thesis, a theoretical approach is taken to developing an independent model not derived from the data. Could this ~1500-yr quasi-periodicity be caused by variations in Earth's orbital parameters that affect both gravitation and solar irradiance, in similar manner to the Milankovitch cycles? Could this quasi-periodicity be caused by a combination of periodicities involving the Sun? Just as the Milankovitch cycles of astronomical forcing, at scales of tens of thousands of years, have contributed

to the waxing and waning of the Ice Ages, could the ~1500-yr climate oscillation be astronomically forced? Schulz (2002) suggested that the possibility of astronomical forcing was possible given the long-term stability of orbital elements.

The similarity between the length of the Sothic cycle and the ~1470-yr climate cycle is potentially suggestive of an astronomical cause of this climate cycle. The Sothic cycle was caused by the desynchronisation of the ancient Egyptian calendar from the seasonal year (Lockyer, 1964), to which an inexact measure of the year and precession both contributed. Precession, which is caused by solar and lunar gravitational influences acting on the rotating Earth (Lowrie, 2007), causes the timing of Earth's seasons relative to astronomical and calendrical markers to change. These astronomical markers may be fixed stars such as Sirius, after which the Sothic cycle is named; or a marker within Earth's orbit such as the perihelion, which is not stationary; or with a calendar. Consequently, the theoretical position taken for this thesis is that precession, through Sun, Moon, and Earth interaction, produces the ~1500-yr oscillation and sub-harmonics, shaping the gravitational and solar irradiance impact on Earth's palaeoclimatic record and climate.

1.2 Scope and limitations

This research thesis only considers factors affecting Earth's orbit and hence changes in gravitation and solar irradiance and insolation, and does not undertake numerical climate modelling (as distinct from trigonometric modelling). This thesis examines whether short-term orbital forcing contributes to this ~1500-yr pattern of climate variability during the mid to late Holocene, which is the extent of the astronomical data used. Also examined are potential constituents of the ~1500-yr oscillation, such as the Suess de Vries (SdV) cycle, Gleissberg cycle (Braun *et al.,* 2005) and radiocarbon (^{14}C) signals of 57 yrs, 104 yrs, 131 yrs (Damon and Sonett, 1991; Stuiver and Braziunas, 1989). These cycles are also poorly understood, with the presumption of medium- to long-term cyclicity associated with solar variability resting on inferences (e.g., Abreu *et al.,* 2012; Chambers *et al.,* 2012; Damon and Sonett, 1991; cf. Hua *et al.,* 2015). As solar and lunar forcing are important considerations, short-term lunation and solar cycles will be scrutinised for their potential roles in ~1500-yr quasi-periodicity and related subharmonics. These cycles include the sunspot cycle, a 19-yr lunation cycle known as the Metonic cycle, and the anomalistic year (which is measured relative to the perihelion). A numerical overview of the relationships between the various constituent cycles of the ~1500-yr quasi-periodicity can be seen in Figure 1.3. This figure shows how these various cycles fit together and why they are of interest in the study of potential contributors to a quasi-periodic climate cycle.

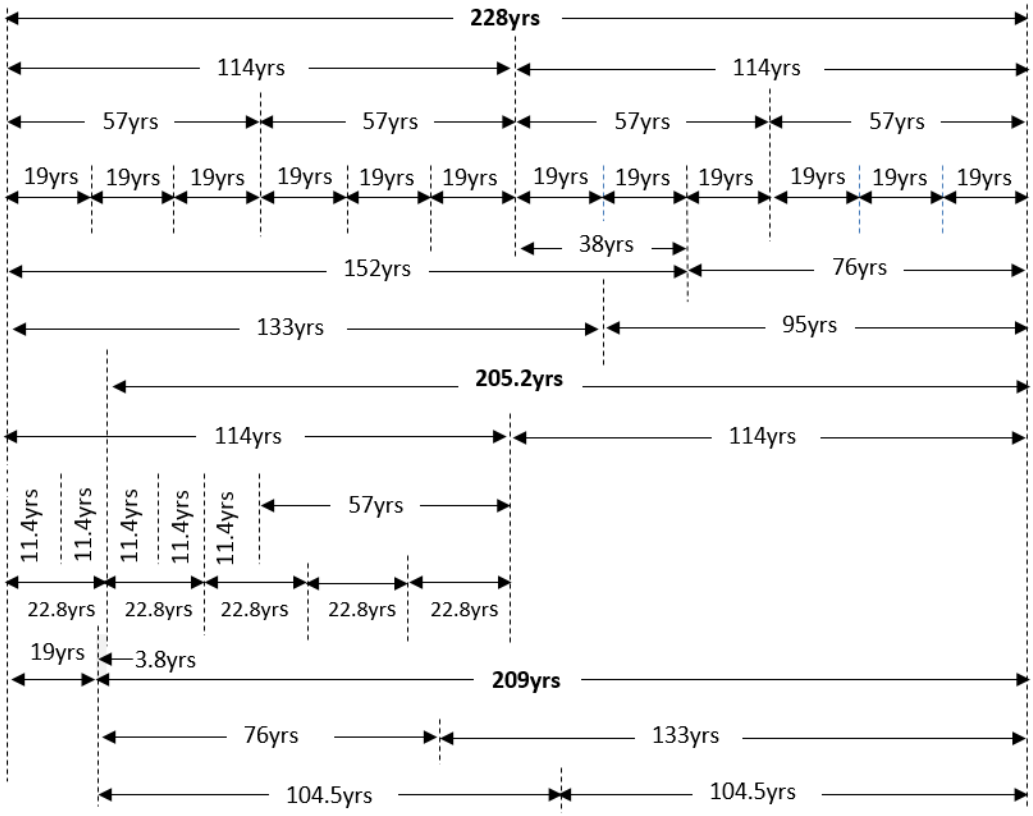

Figure 1.3: A schematic showing how the potential constituent cycles of the ~1500-yr quasi-periodicity. The Suess de Vries cycle in its various forms (206-yr, 209-yr, 228-yr); variants of the Gleissberg cycle (76-yr and 95-yr); harmonics of the 57-yr climate cycle; sunspot cycle (11.4-yr and 22.8-yr); the Metonic lunation cycle (19-yr); and radiocarbon signals which includes the SdV and Gleissberg cycles, and the 57-yr, ~104-yr, ~133-yr, ~152-yr cycles).

1.3 Research aims

This research aims to address these main questions:

1. Is the ~1500-yr quasi-periodicity recorded in palaeoclimatic archives real and explicable by astronomical forcing? If so, does the interaction of the Sun, Moon, and Earth produce these cycles?
2. How do the following cycles relate to the ~1470-yr quasi-periodicity and do they have an astronomical cause?
    - the Suess de Vries cycle (209 yrs)?
    - the Gleissberg cycle (70-100 yrs)?
    - radiocarbon signals of 104 yrs and 131 yrs?
    - a 57 yr signal in various climatic datasets

1.4 Thesis organisation

The following two chapters (2 and 3) review literature that provides the background to this study. Chapter Two explores the nature and history of the Milankovitch cycles, various millennial-scale climate signals at sub-Milankovitch scales, as well as decadal and centurial-scale harmonics of the

~1500-yr climate signal. Chapter Three places Earth's climate signals in the context of Earth's astrophysical characteristics and neighbourhood, whilst reviewing the cause of the Milankovitch precessional cycle and a brief, relevant history of chronometrics. The conceptual model for the astronomical cause of the ~1500-yr oscillation is developed in Chapter Four through trigonometric modelling and the exploration of astronomical data based on its principals. The physical models of insolation and gravity that are associated with this conceptual model and astronomical data are detailed in Chapter Five, along with results. Chapter Six introduces a revised and chronologically-anchored model, based on the astrophysical parameters hypothesised as causing the ~1500-yr signal and its harmonics, where it is statistically tested and results presented. Chapter Seven draws together the background chapters, and all the threads of these models and astronomical data together in a discussion of results. In Chapter Eight, the thesis is summarised, research aims and questions are addressed, and future directions in research are indicated, drawing this thesis to a conclusion.

Chapter 2 – The Climate Cycles

2.1 Introduction

The background for this research is a necessarily diverse one because of its multi-disciplinary nature, involving climate history, astronomy, chronology, and geochronology. An awareness of the nature of climate data and what it shows, will be placed into context of Earth's astronomical neighbourhood, without which patterns of climate change cannot be fully understood. This chapter focuses on the climate cycles and factors relevant to this research project, and will necessarily touch on factors of chronology and astronomy that are more fully explored in the next chapter. Also explored in this chapter will be potential contributing cycles to the ~1500-yr quasi-periodicity, as mentioned in the previous chapter.

The Milankovitch climate cycles were found to result from small shifts in Earth's orbital shape, direction and tilt of the axis, and timing of the seasons relative to its orbital position (Berger, 2009). The effects of small variations in Earth's orbital parameters and aspect have produced a succession of Ice Ages. Whilst Milankovitch cycles and their link to climate became a major paradigm in understanding Quaternary environmental change, there is a key debate about millennial scale climate variability and links to astronomical forcing. Because the Milankovitch cycles share common concepts with the theorised cause of the ~1500-yr quasi-periodicity of abrupt climate change, they provide an important prelude to understanding this oscillation and its potential astronomical causes

Understanding Earth's celestial neighbourhood is important to understanding these climate cycles. Whilst these matters are covered more fully in the next chapter, a brief overview sets the stage for discussion of millennial-scale climate oscillations. Earth's orbit is in a "Goldilocks" zone (Professor Michio Kaku , University of New York in Ward, 2012), positioned between Venus and Mars. If Earth shifted fractionally towards either one, it would become either a "snowball Earth" (Professor Michio Kaku , University of New York in Ward, 2012) or a greenhouse (Dr Michelle Thaller, Goddard Space Center in Ward, 2012). With the Sun as the major influence on climate, it is possible to understand this in terms of solar irradiance and its impact on internal planetary climate systems. Venus receives nearly twice the amount of solar irradiance as the Earth, because it is ~40 million kilometres closer to the Sun. Mars is ~60 million kilometres further from the Sun than Earth and correspondingly receives less than half of the solar irradiance Earth receives. By comparison Venus' atmosphere is comprised of 96.5% carbon dioxide (CO_2), while Earth's atmospheric CO_2 content is 0.0004%. Mars with virtually no atmosphere (<1% of Earth's) has a CO_2 level of 0.08%.

2.2 Climate cycles

2.2.1 The Milankovitch Cycles

Earth's velocity as it moves through its changing elliptical orbit, Earth's rotation as it spins on its wobbling axis, and the orientation and changing tilt of Earth's axis all have an influence on climate fluctuations, due to the proximity and orientation of Earth relative to the major source of heat, radiation, and gravitational force in our solar system – the Sun. The signals of these orbital-scale fluctuations, known as the Milankovitch cycles, have been found in climate data as fluctuations in glaciation cycles (Imbrie *et al.,* 1993). These glaciations have dominated Earth's climatic history during the last 1Ma (Berger, 2009). The Milankovitch theory is one of astronomically-induced climate change to account for Earth's glacial cycles. These cycles [Figure 2.1], which are superimposed on each other, consist of (1) eccentricity (2) obliquity of the ecliptic, and (3) the Milankovitch precessional cycle.

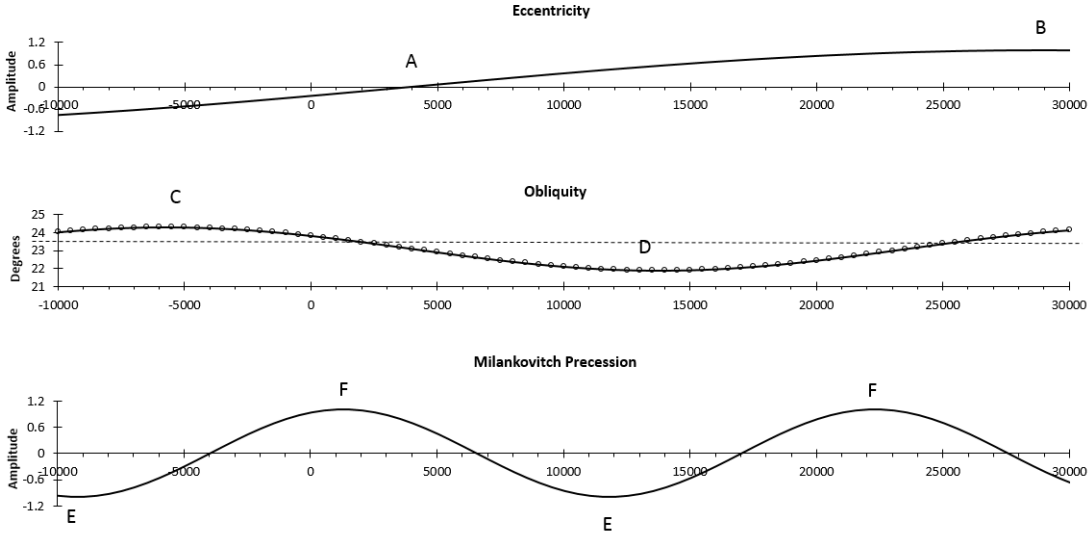

Figure 2.1: Depiction of Milankovitch cycles as sinusoids over a 40-ky period since 10,000BC. The representation here is based on anchor dates and cycle lengths approximations. In the top panel, maximum eccentricity occurs at B in about 27 ky from now; A is halfway through the extremes of the ~100-ky cycle. The middle panel is obliquity of the ecliptic, showing maximum tilt of the Earth's axis during the Holocene Climatic Optimum (c), and projected minimum tilt at D. The bottom panel shows the Milankovitch precessional cycle where E is the perihelion at June solstice and F is perihelion at December solstice.

The ~100-ky eccentricity period is based on the inconstant, slightly-elliptical shape of Earth's orbit that changes systematically over a period of ~100 ky, (Section 3.1.1.1). This signal in the palaeoclimatic record is global and is considered to be orbitally forced (Wolff *et al.,* 2010). Glacial cycles are thought to be forced by the extremities of eccentricity when Earth's orbit is most elliptical in shape. This diachronically unstable cycle is a superimposed pattern over a primary ~400-ky cyclical pattern of eccentricity [Figure 2.2] (Berger, 2009; Imbrie *et al.,* 1993). The obliquity cycle varies by two degrees over a period of ~41 ky and is due to changes of tilt in the Earth's axis, where

colder periods are associated with minimum axial tilt (Section 3.1.1.2). The Milankovitch precessional cycle results from the combination of the ~26-ky (equinoctial precession) cycle and the ~110-ky apsidal precession (Sections 3.1.1.3-3.1.1.5), with a mean periodicity of ~21 ky, producing variants of 19 ky and 23 ky (Berger, 2009). These two precessional movements may be thought of as two axes that are interacting as they rotate in opposite directions: the solstitial axis, based on the June and December solstice, and the apsidal axis, based on the closest and furthest points in Earth's orbit (respectively the perihelion and aphelion). Consequently, when the June solstice is conjunct the aphelion then the December solstice is conjunct the perihelion and *vice versa*, resulting in a covariance of insolation between the two hemispheres (Huybers and Denton, 2008). Although Milankovitch inferred a ~5-ky lag between summer insolation forcing of ice sheets (Ruddiman, 2004), there is a great deal of debate as to which hemisphere was more influential and which solstice forced the northern glacial advances (see following).

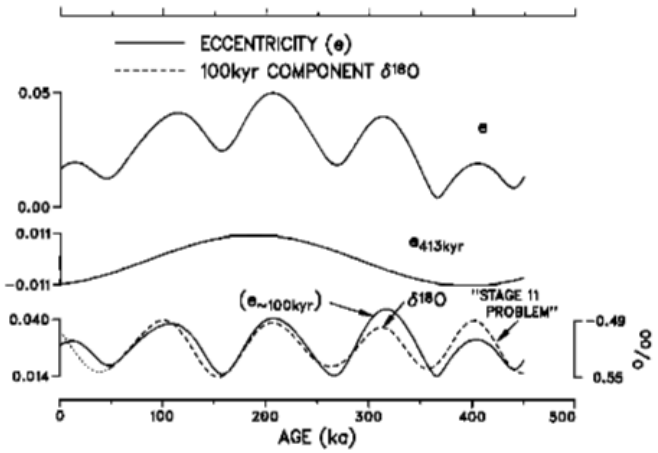

Figure 2.2: The 100-ky eccentricity (e) cycle superimposed on a 413-ky periodicity (Imbrie *et al.*, 1993:703). By removing the 413-ky signal (middle panel), the residual signal of ~100 ky remains. Averaging out this remaining signal is consistent with the 100-ky oxygen isotope record but leads it in this schematic by 13 deg. (bottom panel). Additionally, during OIS stage 11, the amplitude of the signal differs between the eccentricity and oxygen isotope signals on the basis of amplitude.

Sir John Herschel (1832) was the first to propose a general astronomical theory of climate change relative to Earth's geological history based on Earth's eccentricity and obliquity (Imbrie and Imbrie, 1979; cf. Croll, 1864): these factors were explained in terms of fluctuations to the amount of solar energy received by Earth and in the distribution of that energy over the Earth's surface. The first theory of an ice age was proposed by Louis Agassiz (1838) during a time when it had been suggested that Earth's astronomical environment influenced climate change (Imbrie and Imbrie, 1979; Summerhayes, 2015). Sir William Lyell had approached him with the notion that some astronomical factor could be influencing the waxing and waning of glaciers, based on the proposition that the precession of the equinoxes could cause interhemispheric fluctuations in solar heat and light (Lyell, 1830; Imbrie and Imbrie, 1979). Agassiz (1840) then produced geomorphological evidence of a significant glaciation in Earth's past.

In 1842 Joseph Adhémar, a mathematician, first proposed an astronomical theory for the ice ages based on the elliptical shape of Earth's orbit and the changing seasons relative to that orbit due to the wobble of Earth's axis (Adhémar, 1842). This wobble of Earth's axis, known as the precession of the

equinoxes, results in a 26-ky cycle that was investigated and explained by the French mathematician, Jean le Rond d'Alembert in 1754 (Imbrie and Imbrie, 1979). Adhémar postulated that that the changing lengths of seasons and daylight hours as a result of this cycle caused an ice age (Imbrie and Imbrie, 1979). However, Adhémar's theory was flawed as it had not taken into consideration the changing shape of Earth's orbit (Imbrie and Imbrie, 1979). Urbain Leverrier, a French astronomer, had determined that the shape of Earth's elliptical orbit varies over a 100-ky cycle (Croll, 1864; Imbrie and Imbrie, 1979). Consequently, James Croll believed Adhémar was wrong in the belief that the differing lengths of the seasons caused the ice age (Imbrie and Imbrie, 1979).

Croll (1864), being aware of the changing eccentricity of the Earth's orbit over a 100-ky cycle through the work of Adhémar (Imbrie and Imbrie, 1979), postulated that this was the cause of the ice ages. *Contra* Leverrier's findings that eccentricity did not affect Earth's annual heat influx from the Sun (Imbrie and Imbrie, 1979), Croll (1864) showed that seasonal radiation intensity did vary and was affected by orbital eccentricity. He determined that winter played an important role in influencing the glacial onset, using a theory of positive feedback through the accumulation of snow. He also realised that the ~22-ky precessional cycle must play a role, depending upon whether winter occurred at perihelion or aphelion. Croll theorised that alternating ice ages occur in the northern or southern hemispheres based upon the association between the winter solstice and aphelion, coupled with extreme orbital eccentricity. He further hypothesised that an ice age was more likely to occur when Earth's axial tilt was not at its steepest, when the polar regions receive less direct solar radiation (Croll, 1875). Although there was geological evidence supporting Croll's theory, it did not explain all the facts and was undermined by the end of the last ice age and its timing. At the time, geologists had determined that the glacial period had ended between 10-15 kya, whereas Croll's theory had estimated at least 80 kya (Dana, 1894 cited in Imbrie and Imbrie, 1979).

Following Croll, Milutin Milankovitch formulated a climate model using mathematical predictions (Imbrie and Imbrie, 1979). He used three orbital parameters to investigate solar radiation distribution over the Earth's surface: orbital eccentricity, obliquity of the ecliptic, and precession. Milankovitch's investigation was based on Newton's prior work on radiation and the heating capacity of the Sun, which was dependent on the distance from the Sun and the obliquity of the solar rays. Consulting with climatologist Wladimir Köppen, he constructed radiation curves for sensitive latitudes (55°N, 60°N, 65°N) (Milankovitch, 1941 cited in Imbrie and Imbrie, 1979), arriving at the conclusion that, *contra* Croll, it was the summer that was more important than the winter in determining the effects of the annual snow budget on glaciation. This reasoning prioritised the capacity of summer insolation to melt glaciers over the level of radiation received at winter. His complete radiation curves revealed how astronomical cycles influenced the pattern of incoming radiation. The obliquity of the ecliptic

over ~41 ky had a larger influence at the poles; and the precessional influence of ~22 ky had a bigger impact in equatorial regions based upon the distance from the Sun (Imbrie and Imbrie, 1979; cf. Loutre *et al.,* 2004).

In Europe, evidence from research by two geologists, Penck and Bruckner (1909), was used to support the Milankovitch theory. Köppen and Wegener (1924) had tested the Penck and Bruckner data against Milankovitch radiation curves, and found a good match despite some discrepancies in radiation minima. Consequently, support for the Milankovitch theory gained momentum (Imbrie and Imbrie, 1979). However, objections to the Milankovitch theory were based on Milankovitch's sole consideration of radiation, rather than other factors being taken into account such as the roles of atmosphere and oceans in heat distribution (Imbrie and Imbrie, 1979). Despite being widely accepted during the 1930s and 1940s, the advent of radiocarbon dating in the 1950s undermined the Milankovitch theory (Imbrie and Imbrie, 1979). This was related to an issue of projected radiation minima at 25 kya that proved to be a warm period, during which peat had formed in both the U.S. and Europe.

However, oxygen isotope ratios indicative of sea-surface temperature (SST) from deep ocean cores were found to correspond well with Milankovitch radiation curves (Emiliani, 1955; Imbrie and Imbrie, 1979). Emiliani's findings were at odds on a number of fronts. Questions arose whether the match between Milankovitch radiation curves and the Emiliani isotopic curves was mere coincidence, and on the accuracy of his time scale (Ericson *et al.,* 1961 cited in Imbrie and Imbrie, 1979). Also, Ericson *et al.,* (1961), contended that the isotope ratios reflected ice volumes rather than sea temperature, and upheld his own general chronological classification based on the presence/absence of temperature-sensitive foraminifera. However, statistical analysis by John Imbrie, using a multi-factor method, was able to separate temperature from other environmental factors affecting the foraminifera (Imbrie and Imbrie, 1979), with findings supported by a comparative study by Broecker and van Donk (1970). These findings reinforced those of Emiliani despite the fact that important environmental factors had been ignored, namely sea-salt levels, resulting in an exaggeration of Emiliani's estimated temperature change at the beginning of each ice age (Imbrie and Imbrie, 1979). Further support came from Shackleton (1969), which demonstrated a connection between ice volumes and isotopic variation. These Oxygen Isotope Stages (OIS or MIS, where the latter is Marine Isotope Stage) consequently reflected changing global ice volume rather than sea temperature through the ratio of ^{18}O:^{16}O, as the lighter isotope is extracted from seawater and stored in ice during the ice ages (Imbrie and Imbrie, 1979).

The advent of new radiometric dating measures (e.g., thorium dating), coupled with evidence from sea level changes from coral terraces, eventually led to a Milankovitch theory revival in 1968

(Broecker *et al.,* 1968). The importance of the precessional sequence, which is stronger at lower latitudes, had been underestimated by Milankovitch, and adjustments to calculations (Imbrie and Imbrie, 1979) could thus explain key maximum sea level points at ~82 kya, ~105 kya, ~125 kya (Broecker *et al.,* 1968). This evidence came from raised coral terraces in Australia, the Caribbean, Florida, Hawaii, New Guinea, and Tahiti (Bard *et al.,* 1996; Broecker and Thurber, 1965; Chappell, 1974), which had formed by accretion due to sea-level change associated with the waxing and waning of ice sheets. However, measurements from a longer time sequence were needed (to establish the astronomical theory of climate change) than was available through corals (Imbrie and Imbrie, 1979). This was to come from deep-sea sedimentary cores (Shackleton and Opdyke, 1973). The coupling of new techniques in geomagnetic dating and Emiliani's oxygen isotope classification (OIS) of climate paved the way [Figure 2.3] (Chappell, 1973, 1974; Shackleton and Opdyke, 1973).

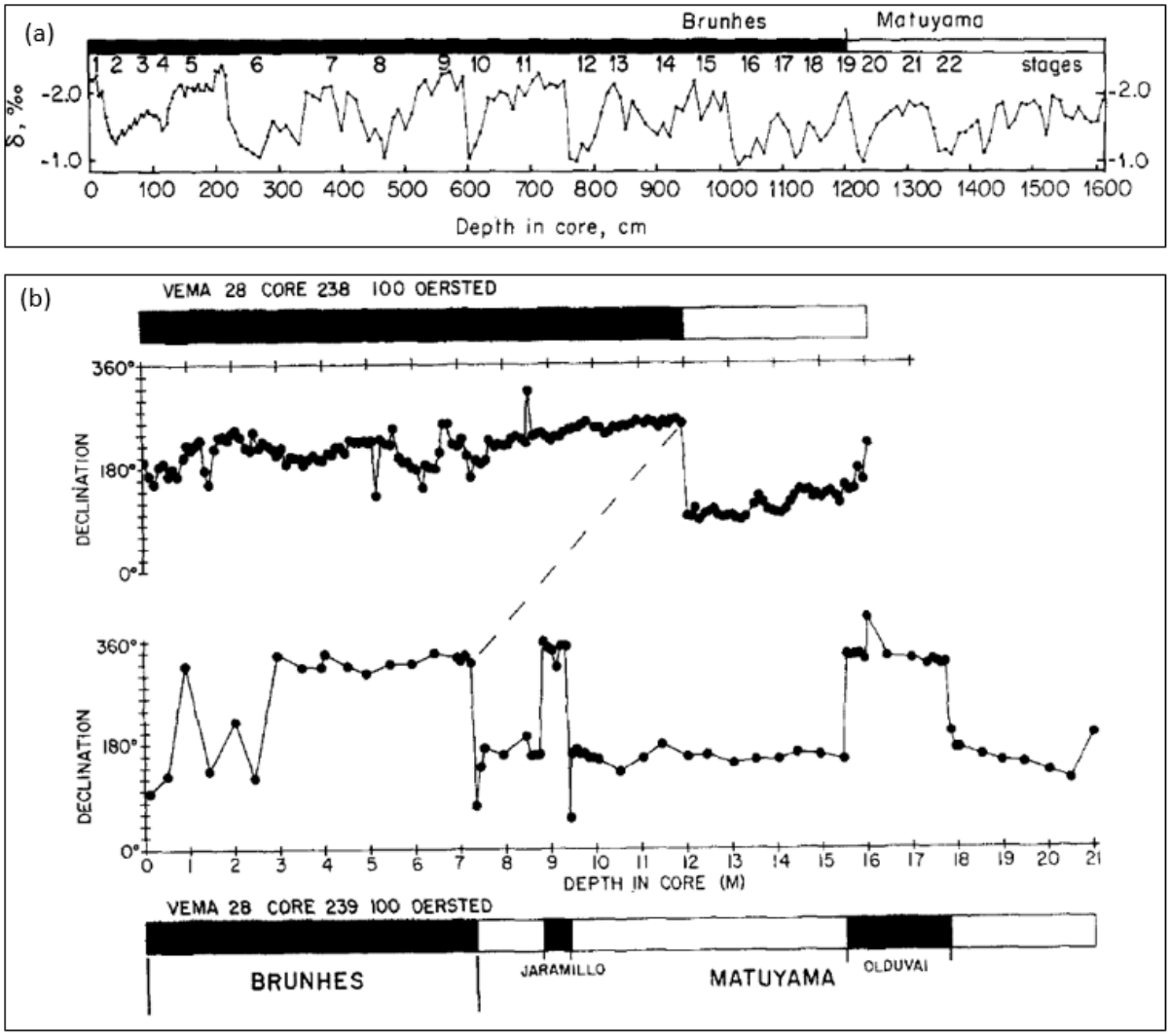

Figure 2.3: Magnetic stratigraphy in West Pacific Cores (from Shackleton and Opdyke, 1973:41). The bottom panel shows magnetic stratigraphy from two Pacific Ocean cores (VE28-238, VE28-239) taken from the Solomon Plateau at ~160ºE and slightly north of the equator (~1ºN, ~3ºN). One of these two cores (VE28-238) is featured in the top panel alongside the Emiliani oxygen isotope scheme. The Brunhes-Matuyama geomagnetic reversal is clearly seen in both cores, whilst VE28-239 also shows other geomagnetic reversals.

Penck and Bruckner had previously incorrectly determined the length of the Pleistocene Epoch to be 650-ky long (Imbrie and Imbrie, 1979). However, the Pleistocene Epoch was much longer at 1.5Ma. Following this determination, geomagnetic reversals in the palaeoclimatic record confirmed a 100-ky cycle (Imbrie and Imbrie, 1979; Shackleton and Opdyke, 1973). Kukla's ground-breaking work in 1968 investigated patterns of loess (wind-blown sediment) and found five geomagnetic reversals in his investigation of a Czechoslovakian quarry, through which he was able to date the length of the main Ice Age cycle (Kukla and Koĉí, 1972). Indicated within the stratigraphic markers, investigated by Kukla, was a pattern of gradual cooling followed by abrupt warming. Broecker and van Donk (1970) used the Brunhes-Matuyama geomagnetic boundary to determine the length of the major isotopic cycle in an ocean-bed core from the Caribbean Sea, confirming both orbital forcing of these patterns and Emiliani's isotopic scheme. Similarly, using deep-sea cores from the southern hemisphere, Hays *et al.* (1976) observed the 100ky-, 42ky-, and ~21ky- peaks of the Milankovitch cycles and concluded that the Ice Ages were attributable to Earth's orbital geometry; also confirming Emiliani's MIS stages (1-13). Furthermore, the discovery of Gulf Stream patterns associated with the Ice Ages by Ruddiman and McIntyre (1981) independently confirmed the existence of the 100-ky cycle. Kukla and Mesolella investigated whether the 100-ky cycle was attributable to orbital eccentricity by modification of the Milankovitch concept, which had been based on the faulty Penck and Bruckner Pleistocene time-scale (Imbrie and Imbrie, 1979). Despite a convergence in agreement on the primary cause of this cycle as being orbitally forced, Kukla and Mesolella differed on the primary season responsible: winter or summer (Imbrie and Imbrie, 1979). However, they agreed that precession controlled the intensity of radiation in any given season.

Spearheaded by James Hays in the early seventies, a multidisciplinary task force, CLIMAP (Climate: Long-range, Investigation, Mapping, and Prediction), was formed to establish a universal stratigraphy using a geomagnetic timescale. Emiliani's scheme of oxygen isotopic stages enabled such an investigation if a long enough core could be found (Imbrie and Imbrie, 1979). Nineteen geomagnetic stages were established by Shackleton using a suitable core from the west Pacific, with the top seventeen matching Emiliani's isotopic scheme (Shackleton and Opdyke, 1973). The 19th OIS coincided with the Brunhes-Matuyama epochs interface ~780 kya (Shackleton and Opdyke, 1973; cf. Zhou and Shackleton, 1999).

Using spectral analysis, Emiliani's isotopic stratigraphic scheme was tested first by van den Heuval (Imbrie and Imbrie, 1979). However, Imbrie and Shackleton believed that van den Heuval's initial results were flawed because they were based on a defunct chronology. They subsequently reanalysed Emiliani's results that were orbitally tuned to the 100-ky CLIMAP time-scale. Orbital tuning is the "wiggle matching of ice core records to insolation time series" (Lemieux-Dudon *et al.,* 2010; cf.

Martinson *et al.,* 1987). Using cores with a high sedimentation rate from the Southern Indian Ocean and Antarctica, Shackleton and Imbrie were able to identify Milankovitch's predicted isotopic precessional and obliquity signals at ~19 ky, ~24 ky, and ~43 ky through spectral analysis (Imbrie and Imbrie, 1979). The variants of the precessional signal (~23 ky and ~19 ky) were confirmed to correspond with precessional variations (Berger, 2009; Hays *et al*., 1976; Imbrie and Imbrie, 1979). In comparison, the temperature-sensitive radiolarian spectrum produced corresponding cycles of ~20 ky, ~23 ky, ~42 ky (Imbrie and Imbrie, 1979). Additionally, it was found that climatic changes between the northern and southern hemispheres were synchronised (Imbrie and Imbrie, 1979). Although lag times were as large as ~8 ky, it was consequently established that the Milankovitch obliquity and precessional cycles are linked with climate (Imbrie and Imbrie, 1979). The Milankovitch theory was confirmed.

However, from the early 1990s the Milankovitch theory faced a number of challenges (Summerhayes, 2015). Both Shackleton (2000) and Imbrie changed their minds, where a belief in indirect forcing based on CO_2 feedback replaced one in which solar insolation was directly responsible for the waxing and waning of northern ice sheets (Summerhayes, 2015). There were also problems with the 100-ky and 400-ky periods associated with the waxing and waning of northern ice sheets. Berger (2009:54) realised that "the 100-ky period attributed to eccentricity in palaeoclimatic records cannot by any means, be considered linearly related to the eccentricity". Part of the problem was that the numerically modelled 100-ky period weakened after 900ka instead of strengthening to match palaeoclimatic records, while the 400-ky period strengthened after 1Ma (Berger, 2009).

Another part of the quandary was also an inability, on the basis of the 100-ky cycle, to explain the long interglacial MIS11, which occurred ~400 kya [Figure 2.2] (Berger and Wefer, 2013; Imbrie *et al.,* 1993). Whilst some theoretical analysts were dismissive of the ability of small changes in insolation to affect the waxing and waning of the icesheets due to Earth's orbital variations, Berger (2009) argues that these models were questionable because of their simplistic nature. Paillard (2010) argues that due to the chaotic nature of the solar system, it is not possible to accurately compute orbital parameters in the deep past, with an exponential increase in errors through time. This, he explained, is due to the instability of the 100-ky eccentricity cycle with time due to the compounding effects of planetary orbits on Earth's eccentricity and the orientation of Earth's elliptical orbit (Paillard, 2010). Other numerical modelling of the 400 ky cycle lacks a correspondence in the climatic record, while the 100-ky cycle is not well replicated (Paillard, 2010). MIS11 exemplifies this problem, which lacks a strong amplitude modulation caused by eccentricity [Figure 2.2] (Paillard, 2010). Whilst eccentricity was at a minimum ~430 kya, MIS11 was a major glacial termination (Paillard, 2010).

Key arguments and counterarguments since the early nineties have been based on various models with premises often at odds with each other, such as those involving greenhouse gases (primarily CO_2); debates over which hemisphere caused the fluctuations in ice sheets; how the changes were transmitted between hemispheres (atmospheric versus oceanic mechanisms); and, explanations for the 100-ky cycle for the waxing and waning of the Ice Ages (e.g., Summerhayes, 2015). The new SPECMAP (Spectral Mapping) in the 1990s abandoned the Milankovitch theory and forged a different chronometric model, with the theoretical position that CO_2 flux in the southern hemisphere directly forced northern ice sheets (Ruddiman, 2004). In the light of this new model, the 100-ky cycle was reinterpreted as being a forced response rather than the previously paced response, with "unspecified" internal climate dynamics driving the cycle (Ruddiman, 2004). Ruddiman pointed out a number of issues with this model, including contradictory trends in proxies used by SPECMAP.

With the advent of a new, Vostok (Antarctica) ice core chronology (Petit *et al.,* 1999) using cores V19-30 and V19-28, Shackleton (2000) argued that the 100-ky cycle resulted from forcing by atmospheric CO_2 because Vostok's air and deep-water temperatures were in phase with orbital eccentricity while ice volumes lagged behind these factors. Blunier and Brook (2001), using Greenland's GISP2 and the Byrd station's ice cores, demonstrated a link between methane (CH_4) and temperature, demonstrating a match between millennial-scale peaks in Antarctic warming and DO events in Greenland. Ruddiman (2004), readopting the Milankovitch forcing theory shared by CLIMAP, tuned the Vostok record to northern summer insolation using a CH_4 time scale, based on the position that this seasonal timing drives CH_4 concentrations via the Asian monsoon. In his recalibration of the time-scale, Ruddiman (2004) also shifted Imbrie *et al.*'s (1984) ^{18}O marine time scale by 1500 yrs to align it with uranium-series dates from coral reefs. Ruddiman also relies on the coincidence between the June solstice and perihelion conjunction ~11 kya and a CH_4 concentration in Greenland ice to support his argument, which returns support to the Milankovitch theory and the CLIMAP model (Ruddiman, 2004). Ruddiman's new time scale very closely aligns the 100-ky cycles of CO_2 and eccentricity, compared with the SPECMAP model that places CO_2 8 ky ahead of the eccentricity cycle.

Current understanding favours orbital forcing of the waxing and waning of the ice-sheets, with outgassing of CO_2 from the Southern Ocean catalysing the bipolar seesaw (Summerhayes, 2015). The bipolar seesaw theory sees one pole warming as the other cools (Broecker and Henderson, 1998). Clear phase correspondences have been established between Greenland and Antarctic temperatures (cold Dansgaard-Oeschger stages to warm Antarctic temperatures and *vice versa*) (EPICA community, 2006 cited in Wolff *et al.,* 2010). EPICA Dome C core showed that Antarctica warmed by as much as 3°C, with the peak of such warming corresponding with abrupt warming in Greenland

(Turney, 2008). At times of cold in Greenland, gradual warming occurred at the polar opposite; these cyclical patterns are persistent over millennia (Turney, 2008). Previously, it was thought that the bipolar seesaw was catalysed in the northern hemisphere (Broecker, 1998; Summerhayes, 2015) via the Atlantic Meridional Overturning Circulation (AMOC). AMOC is part of the thermohaline current (see below). A cause of this bipolar seesaw was suggested by Thomas Stocker, who thought the Southern Ocean played a crucial role (Turney, 2008). In this scenario, tropical warm water relocated south while the North Atlantic cooled, consequently leading to a shutdown of DWF. Additionally, realisation that warming began some 2 ky prior to the strengthening of AMOC changed the line of causality (WAIS divide project members 2013).

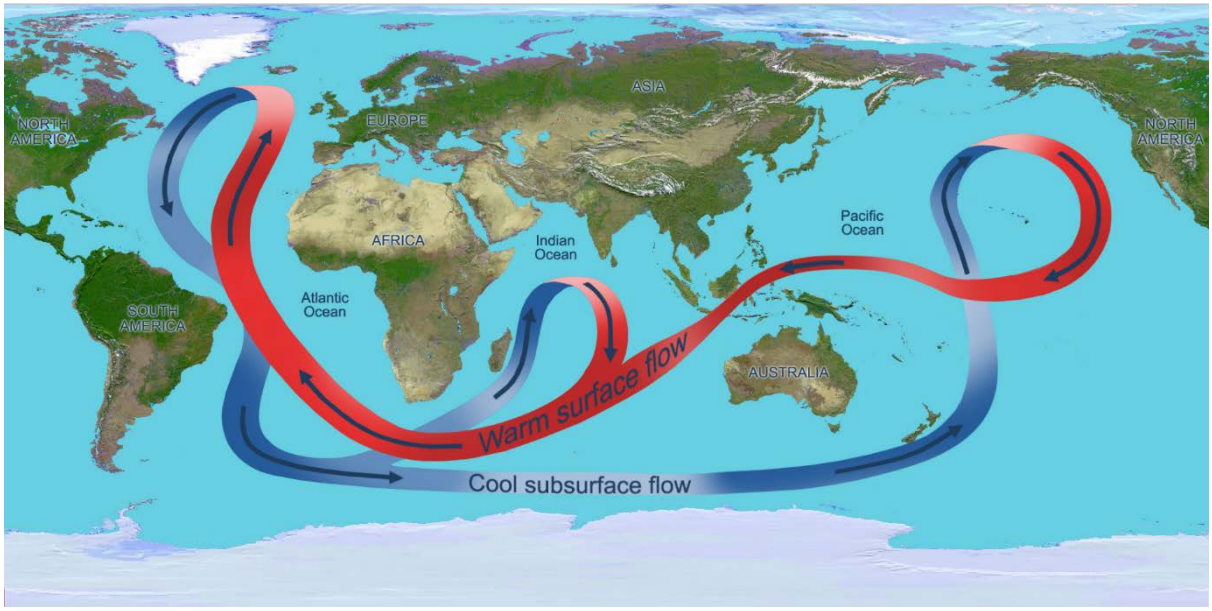

Figure 2.4: Depiction of the thermohaline current, which transports heat around the globe (NASA/JPL, 2010).

The thermohaline current [Figure 2.4], also known as the Meridional Overturning Circulation (Lorenzo *et al.*, 2008), is the major transporter of heat around the world (Toggweiler and Key, 2001). Wunsch (2010) suggests that the simple conveyor belt idea [Figure 2.4] is much more complex than often presented and that "only a tiny minority" has attempted to understand the underlying physics. The surface water of the thermohaline current carries heat polewards, where it cools at high latitudes and sinks to drive the deep-water component of this current towards equatorial regions (Summerhayes, 2015). Temperature and salinity are seen as key factors in driving the thermohaline current. As such, it is a major driver of climate and the carbon cycle, with the primary place of sequestration occurring in the colder high latitude regions (Toggweiler and Key, 2001; Wunsch, 2010) and ~70% of degassing associated with the tropical region (Volk and Liu, 1988; cf. Lorenzo *et al.,* 2008). However, "broad upwelling" occurs all over the world (Lorenzo *et al.,* 2008). This is because heat energy from solar radiation absorbed in seawater is considerable, despite being a small

fraction of total solar irradiance, and plays an important role in driving oceanic currents (Petterson, 1929; Toggweiler and Key, 2001). Wind-driven waters also contribute to upwelling (Toggweiler and Key, 2001; cf. van Buren, 2001).

Increases in subaerial volcanic activity by up to 600% over normal background levels also appear to have contributed to the increase in CO_2 levels coincident with the termination of the last glaciation (Huybers and Langmuir, 2009; Summerhayes, 2015). Positive feedback also occurs through methane release from tropical wetlands as temperatures increase (Ruddiman, 2003; Summerhayes, 2015). However, as Summerhayes (2015:346) pointed out, "there is not a one-to-one relationship between CO_2 and temperature at all times." CO_2 and temperature are linked (Summerhayes, 2015). Both are important to understanding the 100-ky cycle (cf. Paillard, 2010; Summerhayes, 2015). Temperature is dependent on insolation but is also influenced by feedback from CO_2 and other greenhouse gases such as CH_4 and water vapour; whilst CO_2 is dependent on temperature, which influences its absorption into and release from water. Regardless, patterns of CO_2, air and deep-water temperature, and orbital eccentricity are all in phase (Huybers and Denton, 2008; Pedro *et al.,* 2012; Shackleton, 2000; Summerhayes, 2015; *contra* Paillard, 2010). These synchronised patterns between CO_2 and temperature conform with the millennial-scale Dansgaard-Oeschger temperature cycle found in oxygen-isotope signatures of Greenland ice core records (Summerhayes, 2015; see following section).

2.2.2 The 1500-yr climate cycles

2.2.2.1 IRD events in the North Atlantic

Superimposed upon the Milankovitch cycles is a rapid, millennial-scale cycle of climate change, with oscillations of a mean value of ~1470±500 yrs during the Holocene and last glacial (Bond *et al.,* 1997; Bond *et al.,* 1999; Braun *et al.,* 2005; Schulz, 2002; Turney *et al.,* 2004; Wolff *et al.,* 2010) [Figure 2.5]. This quasi-periodic cycle is characterised by rapid warming, followed by gradual cooling (Alley, 2001; Johnsen *et al.,* 1992; Schulz, 2002; Turney, 2008). The ~1500-yr oscillation was found to be stable and appeared to be associated with

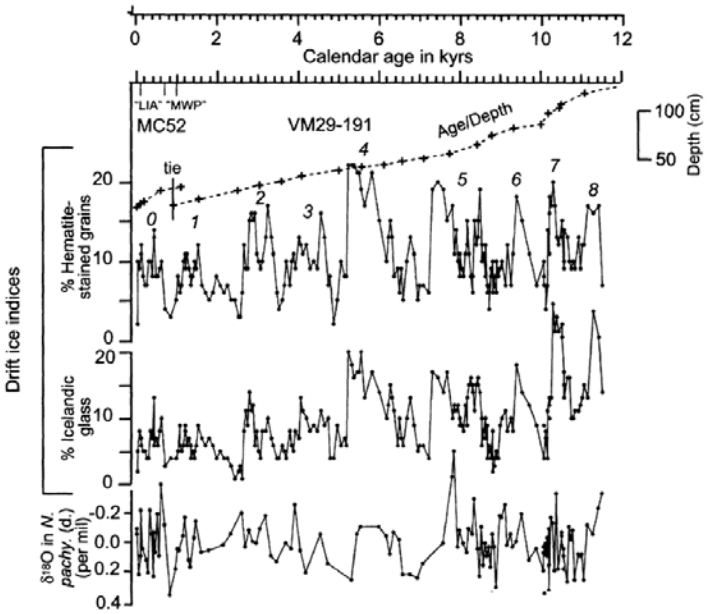

Figure 2.5: Bond events and timing from deep sea core VM29-191 during the past 12ky, numbered from 0 to 8 (extract from Bond *et al.,* 2001:2131). Variations in petrologic markers and planktic oxygen isotope record from drift ice are shown. This millennial-scale variation of the 1500-yr 'cycle' show modulation due to centennial-scale cycles.

Heinrich IRD events and transitions from cold to warm phases associated with the Dansgaard-Oeschger cycle (Bond *et al.,* 1997; Bond *et al.,* 1999; Bond *et al.,* 2001; Mayewski *et al.,* 1997; Schulz, 2002). Bond noted that these IRD events occurred 300-400 years ago and "1400, 2800, 4200, 5900, 8100, 9400, 10,300, 11,100 years ago" (Bond *et al.,* 1997:1257). Whilst the ~1500-yr quasi-periodicity is found in the last interglacial (Eemian) ~125 kya, the signals are best developed in the MIS3 (Marine Isotope Stage 3) interstadial, between ~25 kya and ~57 kya (Bond *et al.,* 1999). Wolff *et al.* (2010) note that Dansgaard-Oeschger 'cycles' are particularly weak during the MIS2 (15-25 kya) and MIS4 (60-70 kya) stadials. During the MIS3 there is no statistical difference between the Bond and Dansgaard-Oeschger 'cycles', with a mean of 1470±532 (1σ) yrs (Bond *et al*., 1999; cf. Schulz, 2002). Schulz (2002) found that Dansgaard-Oeschger events deviated by no more than ±20% from multiples of 1470 yrs.

Using cores of ocean sediments from the North Atlantic, Bond and colleagues (Bond *et al.,* 1997; Bond *et al.,* 1999) demonstrated that the Dansgaard-Oeschger events found in Greenland glacial, ice-core chronology and deep-sea sedimentary cores, continued into the Holocene as weakened Bond IRD events. The continuation of this cycle into the Holocene is not seen in the oxygen-isotope chronology of the Greenland ice cores, which had contributed to the viewpoint that the Holocene was climatically stable (Bond *et al.,* 1997; deMenocal, 2000). As sea-surface temperature cooling preceded IRD events, and calving events occurred in multiple ice-sheets, internal factors to ice-sheet collapse were dismissed as causal (Bond *et al.,* 1999). Instead, an ocean-atmosphere link through solar forcing was suggested as a combination of periodicities as no solar periodicities of that length exist (Bond *et al.*, 2001; cf. Braun *et al.,* 2005; Schulz, 2002). It was hypothesised that the discharge of ice associated with IRD events produced colder, less saline waters, affecting the thermohaline current triggering abrupt major climate change (Clement and Peterson, 2008).

The waxing and waning of northern-hemispheric ice sheets saw intrusive icebergs disperse up to a further 5˚ south into the North Atlantic Current during the Bond events, with implications for disrupting the thermohaline circulation and North Atlantic DWF as had been the case with Dansgaard-Oeschger events (Bond *et al.,* 1997). Apart from oxygen isotopes, temperature-sensitive foraminifera, and IRD as evidence for this ~1500-yr oscillation, geochemical signatures in the Summit Greenland Ice Core revealed increased atmospheric terrestrial dust and sea salt associated with glacial advances and the Dansgaard-Oeschger cycle (O'Brien *et al.,* 1995 cited in Bond *et al.,* 1997). Sea-salt spray in the ice cores was suggestively associated with increased storminess in the region during a weak Bond event, whilst peaks in terrigenous dust levels of potassium (K) were linked with increased windiness associated with extreme cold (Bond *et al.,* 1997).

At the last Bond event during the Little Ice Age (LIA) (1300-1850AD), Greenland snow showed increased peaks in sea-salt, which were attributed to an atmospheric condition known as an expanded polar vortex or an intensified meridional flow (Lamb 1977 cited in O'Brien *et al.,* 1995). The LIA saw glaciers advance in both hemispheres, accompanied by highly variable and enhanced atmospheric circulation (Gagan *et al.,* 2004). Lamb's hypothesis was supported by the increased sea salt in Greenland snow, coincident with the boreal winter during modern times (O'Brien *et al.,* 1995). Supportive evidence is found in modern Greenland records, which link peak sea salt in snow with winter at a time when meridional flow is intensified (Erickson *et al.,* 1986 cited in O'Brien *et al.,* 1995; Zhu and Newell, 1994 cited in O'Brien *et al.,* 1995).

Successful simulations of triggers in freshwater input into the North Atlantic used a coupled-climate model (CLIMBER-2) (Petoukhov *et al.* 2000). Whilst this simulation explained the mechanism, it did not explain the cause (Ganopolski and Rahmstorf, 2001 cited in Rahmstorf, 2003). Rahmstorf (2003) investigated the origin and stability of the 1500-yr cycle and concluded that Dansgaard-Oeschger events, rather than being a cycle, were instead paced by a regular cycle. Rahmstorf first developed an objective algorithm (where threshold was not critical) to identify Dansgaard-Oeschger cycle and examine its origin and variability in the layer-counted glacial portion of the GISP2 core (<51 ky). Layer-counting is more accurate than glaciological modelling (Rahmstorf, 2003). This algorithm detected all but one previously identified Dansgaard-Oeschger events (DO9, at ~40 kya), and also detected the Allerød event (at~12 kya), which was not previously classed as a Dansgaard-Oeschger event. By adjusting the algorithm's threshold, the DO9 event was detected, legitimising the inclusion of the Allerød event that is of the same magnitude.

Rahmstorf's algorithm was also applied to the GRIP ice core, which uses glaciological modelling throughout the glacial (Grootes *et al.*, 1993 cited in Rahmstorf, 2003). The same Dansgaard-Oeschger events were also found in this core, but their timing was not the same and the regularity was destroyed. Rahmstorf (2003) concluded that the layer-counted portion of GISP2 core used was more accurate than the same period in the modelled GRIP chronology for the same period. In the older portion of the GISP2 core, which was dated by correlation with Antarctica's Vostok ice core and is not layer-counted, no regularity in Dansgaard-Oeschger events was found. Rahmstorf (2003) attributed poor dating accuracy and resolution in this portion of the core.

Three types of timing error were also explored by Rahmstorf (2003): triggering, clock and dating errors. Triggering error caused by a strong noise role, would have led to large deviations in timing, but the data did not show this to be the case. Normally both clock and dating error are cumulative. However, Rahmstorf distinguished between cumulative and non-cumulative clock errors. Clock error showed a standard deviation of 12% (~181 yrs) with 95% confidence over 10,000 simulations of 23

cycles. Dating error in the layer-counted section of the core was determined to be <7% during the last 40 ky. Within a 95% confidence interval, 85% of Dansgaard-Oeschger events in the layer-counted portion of the GISP2 core fell within 10% of the timing of the expected event and the remainder within 20%. Rahmstorf (2003) stated that (i) these results suggest pacing by an external, regular 1470-yr orbital cycle such as orbital or solar forcing, and (ii) realistically, errors due to triggering and dating would contribute significantly to total deviations, whilst the clock error is much smaller than estimates.

The Milankovitch cycles have shown that Earth's climate patterns are shaped by small fluctuations in solar irradiance at orbital scales due to the orientation and proximity of Earth to the Sun. Although no known solar cycle of ~1500 yrs exists, suggestions have been made that the Sun may be responsible, due to a close correlation existing between drift ice in the North Atlantic and ^{14}C and ^{10}Be flux in deep sea cores (Bond *et al.,* 2001). Denton and Karlen (1973) suggested a link between variances in the solar constant and radiocarbon (^{14}C) fluctuations during their research on cyclical Holocene variability, linking ^{14}C fluctuations and glacial advances in Europe and North America. Heinrich (1988) suggested solar modulation of the climate as a factor in his model for Heinrich IRD events but qualified that it would need to accommodate locational sensitivity to filter the stronger pulses of ice-rafting. O'Brien *et al.* (1995) established a correlation between cold periods in GISP2 (Greenland Ice Sheet Project) (see below) and low solar output.

2.2.2.2 Millennial-scale ENSO events in the tropical Pacific

ENSO enables the atmospheric transport of heat and moisture from the tropics to extreme latitudes, providing global teleconnections (Clement and Peterson, 2008; Gagan et al., 2004; Turney *et al*., 2004). These teleconnections have been theorised as having the capacity to deposit snow and influence ice formation/dissolution (Turney et al., 2004). Whilst ENSO's cyclicity operates primarily at the interannual and decadal scales, millennial-scale ENSO variability has been seen as an alternative cause of the ~1500-yr cycle of abrupt climate change (Clement and Cane, 1999; Clement and Peterson, 2008; Gagan *et al.,* 2004; Moss *et al.,* 2011; Moss *et al.,* 2013; Stott *et al.,* 2002; Turney *et al.,* 2004; Turney and Palmer, 2004; Wang *et al.,* 2013). However, ENSO's role at this time scale is unclear (Rustic *et al.*, 2015).

ENSO's dynamic atmospheric-oceanic activity was proposed as an alternative cause of the millennial-scale climate cycle because associated convective systems dominate the planet's climate, utilising the extensive influence of the Hadley and Walker Circulations (Broecker 2003; Clement and Peterson, 2008). ENSO's association with the meridional poleward flow of heat, air and moisture from the tropics (Clement and Peterson, 2008; Gagan *et al.,* 2004; Turney *et al.,* 2004), was hypothesised as contributing to ice surge and sea ice formation through transported moisture and heat

in the ~1500-yr cycle (Turney *et al.,* 2004; cf. Gagan *et al.,* 2004). Solar forcing of ENSO at orbital scales is evident in climatic datasets based on the relative precessional positions of the equinox and perihelion (Gagan *et al.,* 2004; Turney *et al.,* 2004; cf. Vieira *et al.,* 2011). Evidence of forcing at this scale on both sides of the Pacific and in the Pacific, such as in Mexico (Marchitto *et al.,* 2010), Ecuador (Anderson *et al.,* 2006; Moy *et al.,* 2002), Peru (Manzanilla, 1997; van Buren, 2001), Australia (Turney *et al.,* 2004), Pacific islands (Anderson, 2006).

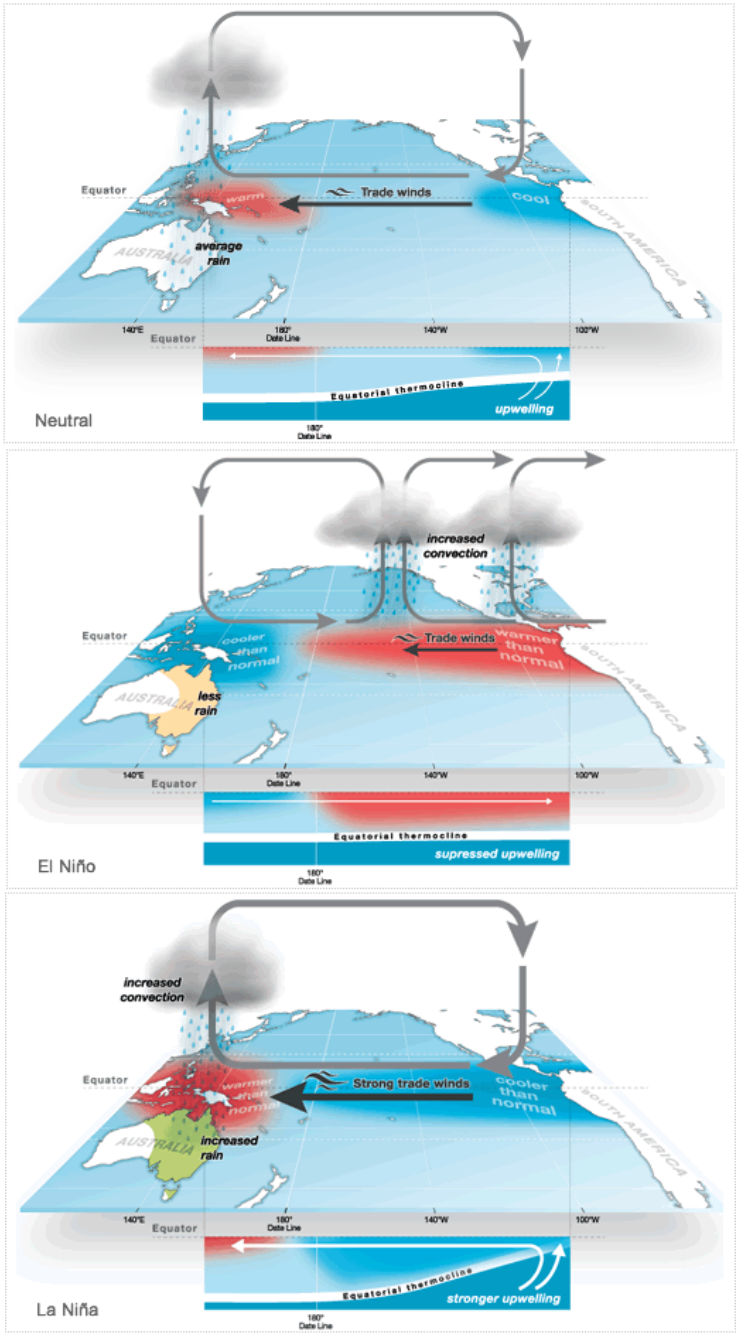

Figure 2.6: The different phases of ENSO, showing neutral conditions (top), El Niño conditions (middle), and La Niña conditions (bottom) (B.O.M. n.d.b).

ENSO is a phenomenon of atmospheric-oceanic interaction that manifests in the Pacific basin, with the atmospheric component being a Southern Oscillation (SO), and the oceanic, El Niño (Trenberth, 1997). Marine core evidence suggests that ENSO has been operational at least during the past 130 ky (Turney *et al.,* 2004), and is thought to have operated continuously at multiple time scales during the late Quaternary, achieving its modern climatology during the mid-Holocene (Turney and Hobbs, 2006; Moss *et al.,* 2011; Shulmeister and Lees, 1995). The term 'El Niño' originally referred to the annual occurrence of a southbound, weak, warm, oceanic current along the tropical South American coast in December. It currently refers to an anomalous warming extending from this coastal warming area across the eastern portion of the equatorial Pacific basin to the International Dateline (Trenberth, 1997). The mean interval between El Niño events is 3.8 yrs, with a strong periodicity of 38 yrs since 1800 AD (Quinn *et al.,* 1987 cited in van Buren, 2001). The SO component is a measure of the difference in atmospheric pressure between Tahiti, in the mid Pacific, and Darwin, NT, Australia, being indicative of the strength of developing El Niño and La Nina events (B.O.M. n.d.a.). Normally, warm, moist air rises in the equatorial west Pacific, promoted by warm SSTs, and is transported eastward via the Walker Circulation to the east equatorial Pacific, where it cools and descends into a region of cold oceanic upwelling (Laing and Evans, 2011) [Figure 2.6].

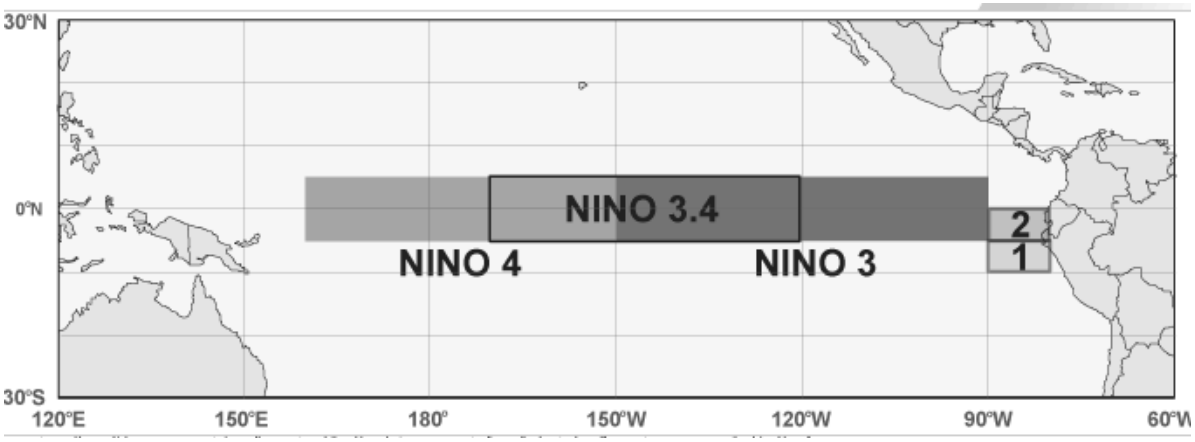

Figure 2.7: Regions covered by various indices of SST in connection with ENSO (B.O.M. n.d.c.).

However, during warm ENSO events (El Niño), the eastern and central equatorial Pacific heat up, disturbing the Walker Circulation, resulting in heavy rainfall in the central and eastern Pacific (B.O.M. n.d.b) [Figure 2.6]. Contemporaneously, in the western Pacific, dry conditions are experienced in association with cooler SSTs, resulting in drought in eastern Australia [Figure 2.6]. Intensification of heat over the western Pacific results in La Nina conditions (cool ENSO events) bringing warmer SSTs to the western Pacific, producing wetter than normal conditions and stronger trade winds (B.O.M. n.d.b). Concurrent to these conditions, in the eastern tropical Pacific drier than normal conditions are experienced, as well as stronger upwelling of cold water off the associated

south American coast (B.O.M. n.d.a). NINO3.4 [Figure 2.7], a newer SST index introduced by NOAA (National Oceanic and Atmospheric Administration), appears to be the key area for ENSO's coupled atmospheric-oceanic interactions (Trenberth, 1997).

The Hadley Circulation, a major convective unit in global circulation, is a poleward flow of air from the equatorial low-pressure belt to the subtropical high-pressure belt via the troposphere (Laing and Evans, 2011), and assists in extending ENSO's influence beyond the tropics (Gagan *et al.,* 2004; cf. Hou and Lindzen, 1992). The concentration of heat energy and its position has been shown to influence the intensity of the Hadley Circulation, with varying effects dependent upon whether this heat concentration occurs on the equator, or north or south of the equator; with implications that only small changes in heat distribution within the tropics may exert profound influences (Hou and Lindzen, 1992). Important regions of ocean-atmospheric interaction in ENSO cyclicity include the WPWP and the mid-Pacific (Gagan *et al.,* 2004; Moss *et al.,* 2013; Shulmeister *et al.,* 1999; Trenberth, 1997).

Correlated with Bond IRD and Dansgaard-Oeschger cycles (Section 2.2.2.1) is the ~1490-yr cycle in the Pacific associated with the onset of climatic conditions suitable for increased ENSO intensity and variability [Figure 1.1] (Turney *et al.,* 2004). ENSO, as a mechanism for global climate change, is seen as amplifying Milankovitch cycles (Clement and Cane, 1999). Evidence spanning the last 45 ky from Lynch's Crater, northern Queensland, Australia, supports an insolation-driven, ocean-atmosphere model of millennial-scale climate change associated with ENSO (Turney *et al.,* 2004).

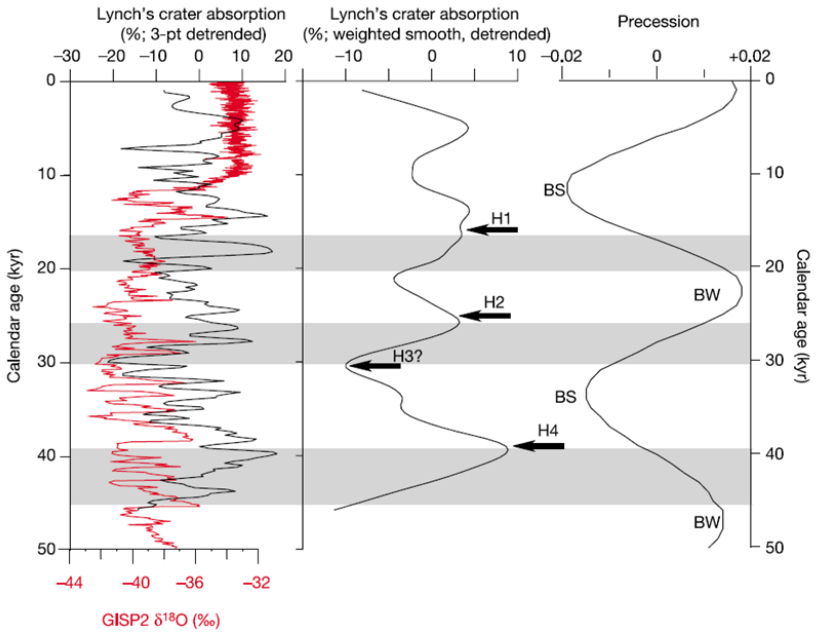

Figure 2.8: Diagram of humification results from Lynch's Crater compared to GISP2 $\delta^{18}O$ values, showing millennial, semi-precessional, and precessional influences (Turney *et al.,* 2004:309). BS/BW are indicative of whether the perihelion is in the boreal summer or winter (Turney *et al.,* 2004). A 15% weighted smooth to detrended absorption data was used to produce the 11.9-ky curve (Turney *et al.,* 2004). H1-H4 are Heinrich events (Turney *et al.,* 2004).

Spectral analysis of peat humification data from Lynch's Crater revealed two important frequencies: a semi-precessional periodicity of 11.9 ky and a millennial-scale cycle of ~1490 yrs [Figure 2.8] (Turney *et al.,* 2004). The semi-precessional cycle found in the Lynch's Crater record of drying events was linked to both ENSO variability and the Dansgaard-Oeschger-Bond-Heinrich cyclicity, in which the perihelion combination with the equinoxes and solstices over a ~21-ky Milankovitch precessional cycle plays a role (Turney *et al.,* 2004; cf. Heinrich, 1988). It was suggested that the perihelion 'timing' with the solstices and equinoxes on this precessional scale is associated with the strengthening and weakening of the equatorial seasonal cycle in the Pacific (Clement *et al.,* 2001). The perihelion/equinox combinations pointed to increased ENSO variability, and perihelion/solstice combinations of an ENSO shutdown (Turney *et al.,* 2004). Turney *et al.* (2004) further offer a potential explanation for teleconnections between ENSO and the North Atlantic: the warming of North America in a NW-SE transect during El Niño could result from increased SST in the Pacific that promotes an increased latitudinal gradient, melts an ice front, and causes a surge in ice.

A high resolution multi-proxy analysis of peat cores was undertaken, involving charcoal and palynological analyses, and spectral analysis of humification data (Turney *et al.,* 2004). Lynch's Crater revealed a millennial-scale cycle of dryness in the Pacific Ocean through evidence of altered precipitation associated with El Niño, the northward movement of the ITCZ, and disrupted trade winds (Turney *et al.,* 2004). Using cross-spectrum analysis, Turney *et al.* (2004) established a linear correlation between this millennial-scale climatic pattern and the ~1500-yr GISP2 ^{18}O signal (used in establishing the cyclicity of the Dansgaard-Oeschger-Heinrich-Bond events), within an 80% confidence interval [Figure 1.1]. They thereby demonstrated a phase correspondence between the two records, with increases in dryness at Lynch's crater and warm millennial-scale Dansgaard-Oeschger events in Greenland being linearly correlated. Turney *et al.* (2004:308) also found that the ~1490-yr periodicity found at Lynch's Crater matched the reported 1470-yr cyclicity for Holocene ENSO events in Ecuador by Moy *et al*. (2002), "within the error of the analysis".

ENSO has also been associated with the LIA through a variety of other evidence from the southern hemisphere (Anderson *et al.,* 2006*;* Gagan *et al.,* 2004; Rustic *et al.,* 2015; van Buren, 2001). Increased variability and intensity of climate due to ENSO is witnessed on North Stradbroke Island (NSI) and Fraser Island, and in other Australian records (Donders *et al.,* 2006; Moss *et al.,* 2013). In particular, on NSI further evidence of the LIA exists in association with shifting ENSO patterns during the last 1500 yrs (Moss *et al.,* 2011), as well as millennial-scale variability in vegetation linked to Heinrich events (Moss *et al.,* 2013). During the LIA, when glaciers advanced in both hemispheres, atmospheric circulation was highly variable and enhanced (Gagan *et al.,* 2004). There is also evidence that the Walker Circulation was significantly weaker as the Holocene began, but increased in strength for a while between 5000-3700 BP when the North Australian Monsoon increased in intensity and

ENSO assumed its modern climatology (Anderson *et al.,* 2006; Shulmeister, 1999; van Buren, 2001). Around 3 kya there was an abrupt increase in the magnitude of ENSO events (Gagan *et al.,* 2004).

Millennial-scale oscillations in palynological data, similar to Bond events, have been found in the Okanagan Highlands of British Columbia during the Early Eocene Climatic Optimum, which occurred 53-50Ma (Moss *et al.,* 2016). Darby *et al.* (2012) found a 1500-yr periodicity of the Arctic Oscillation in Holocene Arctic Ocean sediments using spectral analysis but dismissed solar forcing as a direct cause. These IRD sediments were carried from Russian shores to the Alaskan coast and only occur during strongly positive phases of Arctic Oscillation (Darby *et al.,* 2012). Compared with Steinhilber's (Steinhilber *et al.,* 2012) total solar irradiance (TSI) reconstruction from Greenland ice cores, there is no indication of direct solar forcing in the Holocene Arctic Oscillation records although some alternative studies show otherwise for shorter periods (Darby *et al.,* 2012). Consequently, this quasi-periodic cycle was seen as arising from internal climate circulations rather than external forcing (Clemens*,* 2005; Darby *et al.,* 2012). The periodicity found in Darby's study does not correlate with Bond events, which are also not regarded as arising from solar forcing at high latitudes (Darby *et al.,* 2012). However, the Bond IRD events correlate well with low-latitude solar forcing of ENSO at centennial and millennial scales (Marchitto *et al.,* 2010 cited in Derby *et al.,* 2012).

2.2.2.3 Potential causes of 1500-yr cycle

Individually, both solar and lunar forcing have been suggested as possible causes of the ~1500-yr oscillations of abrupt climate change, with two possible main causes: solar irradiance/insolation or gravitation. Gravitational forcing via changes to the thermohaline current has been discussed extensively in academic literature (e.g., Broecker, 2003; Munk *et al.,* 2002), whilst the argument for insolation is connected with millennial-scale oscillations of ENSO in the tropical Pacific. The influence of ENSO in the cause of this cycle was discussed in the previous section. In this section, both perspectives are discussed but with greater emphasis on gravitational forcing.

Any cyclicity to a climate signal is suggestive of external forcing, as with the Milankovitch cycles (cf. Capron *et al.,* 2010; Clemens, 2005; Davis and Brewer, 2011; Ditlevsen *et al.,* 2007; Hays *et al.,* 1976; Imbrie *et al.,* 1984). The Sun is clearly the primary driver of Earth's climate. Since Denton and Karlen (1973), ^{14}C fluctuations have been explained in terms of a stronger solar wind associated with increased sunspot activity (see Section 3.1.3), which reduces isotopic formations in the atmosphere caused by cosmic radiation (Blackman *et al.,* 2008; Palle *et al.,* 2004). This affects the patterning of climate signals in the palaeoclimatic record.

Previous modelling has suggested that the superposition of the ~209-yr SdV and ~88±11 yr Gleissberg solar cycles may be associated with the ~1500-yr climate cycle (Braun *et al.,* 2005; Damon

and Sonett, 1991). The SdV cyclical wiggles found in the radiocarbon calibration curve (Section 3.2.2) may be due to a modulation of cosmic rays by the solar wind (Damon and Sonett, 1991; Suess, 1986). For more details, see Sections 2.2.3 and 3.2.2. The Gleissberg cycle is a harmonic of the sunspot cycle (Damon and Sonett, 1991; Hathaway, 2010), and radioisotopic and temperature variations appear to be associated with the 11.4-yr sunspot cycle (Damon and Sonett, 1991; Eddy, 1976; cf. Williams, 2013a).

Tidal oceanic forcing has been proposed as an alternative to solar forcing as the cause of the ~1500-yr cycle (Keeling and Whorf, 2000). Based on the work of Pettersson (1930) that identified a 1800-1900-yr tidal cycle, Keeling and Whorf (2000) endeavoured to link a ~1800-yr tidal cycle with the ~1500-yr Bond IRD cycle. They hypothesised that the cause of the Bond IRD cycle was due to the same vertical lunar forcing mechanism proposed by Pettersson (1930), resulting in the mixing of oceanic layers, bringing colder waters to the sea surface. The Saros cycle of eclipses, which is a natural harmonic of the synodic, draconic and anomalistic months, was seen as important to this model. The Saros cycle sees a solar eclipse occurring in the same part of the heavens every ~18.03 yrs (~223 synodic months (New Moon to New Moon) or 6585.33 days). The synodic, draconic, and anomalistic months are respectively based on the New Moon, the monthly transit of the Moon through the north lunar node, and perigee. The north lunar node is where the Moon crosses the ecliptic on its northward journey, and perigee is the closest point in the lunar orbit to Earth. Their hypothesis was also based on observations of cyclical behaviour of SST that occurred on sub-harmonics of the Saros cycle of eclipses at 6 yrs and 9 yrs, with the 6-yr cycle unexpectedly being the dominant frequency. In their modelling, Keeling and Whorf (2000) used the three key parameters (lunar month types mentioned above) previously identified as important by Pettersson (1930). In order of importance, they identified syzygy, the lunar perigee, the lunar node, and perihelion as important influences. Lunar syzygy occurs at New Moon and Full Moon, and more precisely at eclipses.

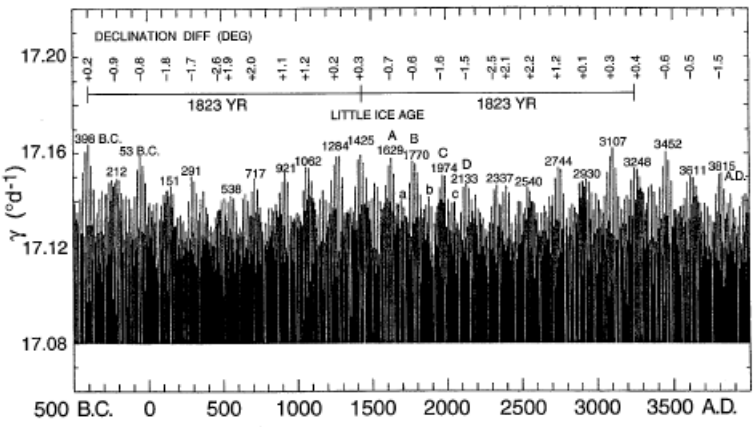

Figure 2.9: 1823-yr tidal cycle produced by the Moon at syzygy showing past and future computations of tide-raising forces (Keeling and Whorf, 2000:3815). Full Moon events are marked (A, B, C, D). Solar and lunar declination differences appear in the top graph.

Keeling and Whorf's (2000) numerical model reproduced the ~1800-yr tidal cycle [Figure 2.9] but also noted that the strength of this cycle varied in relation to proximity of the cycle to the perihelion. A ~5000-yr tidal cycle, which they identified with the Heinrich IRD cycle, was proposed as the result of variability in ~1800-yr signal that produced an amplitude modulation (with an average occurrence of 4650 yrs). The 1800-yr signal was amplified when syzygy, nodal cycle and perigee occurred close to the perihelion. On this basis, Keeling and Whorf (2000) concluded that the ~1500-yr cycle was caused by oceanic tidal forcing, despite not being able to explain the particular mechanism for the ~1500-yr cycle or the discrepancy between the lengths of the two cycles. A large gap also exists between the 5000-yr tidal cycle and Heinrich harmonics (cf. Keeling and Whorf, 2000).

There are several difficulties with the Keeling and Whorf (2000) model, including a lack of precision in correlating their model and tidal strength over longer periods with the Bond and Heinrich events, and problems associated with the Saros eclipse cycle. This is because the Saros eclipse cycle is incommensurate with the perigean cycle and an exact cyclical repetition cannot be expected (Cartwright, 1974; Munk *et al.,* 2002). The situation is complicated by the fact that each subsequent eclipse in each Saros cycle occurs 120° further west due to Earth's rotation or one third of Earth's rotation, at which time the eclipse location has further advanced by ~10° of celestial longitude relative to the fixed sidereal framework of stars and occurs ~10 days later beyond the 18-yr cycle. Their findings, which included the emphasis on a 6-yr harmonics in SST, can potentially be understood in terms of the Saros series eclipse interaction with Earth's rotation, each of which emphasise the one-third component in their respective cycles.

Similarly, the Saros cycle is problematic in investigating the cause of the ~1500-yr quasi-periodicity. This is because the Saros eclipse cycle is incommensurate with the tropical year due to the fact it overshoots the tropical year by ~10 days, whereas the Metonic lunation cycle occurs within a couple of hours of 19 yrs (Sections 3.1.4 and 3.2). Consequently, the Saros cycle's most precise return occurs after 1803 yrs (a harmonic of the 18.03-yr base Saros signal), which is significantly longer than the period investigated (cf. Bond *et al.,* 1997). Furthermore, the greatest gravitational force occurs at New Moon (not Full Moon) [Section 3.1.4], whereas Keeling and Whorf (2000) place equal importance on New and Full Moons.

Another issue with this model is that the greatest perigean tides currently occur at the equinoxes and not the perihelion (Cartwright, 1974), with the coincidence of perihelion to equinox determined only at Milankovitch precessional scales. Keeling and Whorf's gravitational-driven tidal research into the cause of the 1500-yr cycle was further discounted by proponents of insolation-driven ocean-atmosphere interaction (Munk *et al.,* 2002), who dismissed tidal forcing as being too weak to cause the ~1500-yr Bond cycle. Currently, two prominent theoretical camps exist on this matter: one

supportive of oceanic forcing driven by the thermohaline current in association with IRD events, and the other by atmospheric-oceanic interaction associated with millennial-scale ENSO variability (Broecker, 2003; Berger *et al.,* 2006; Munk *et al.,* 2002).

2.2.2.4 Ice core chronologies

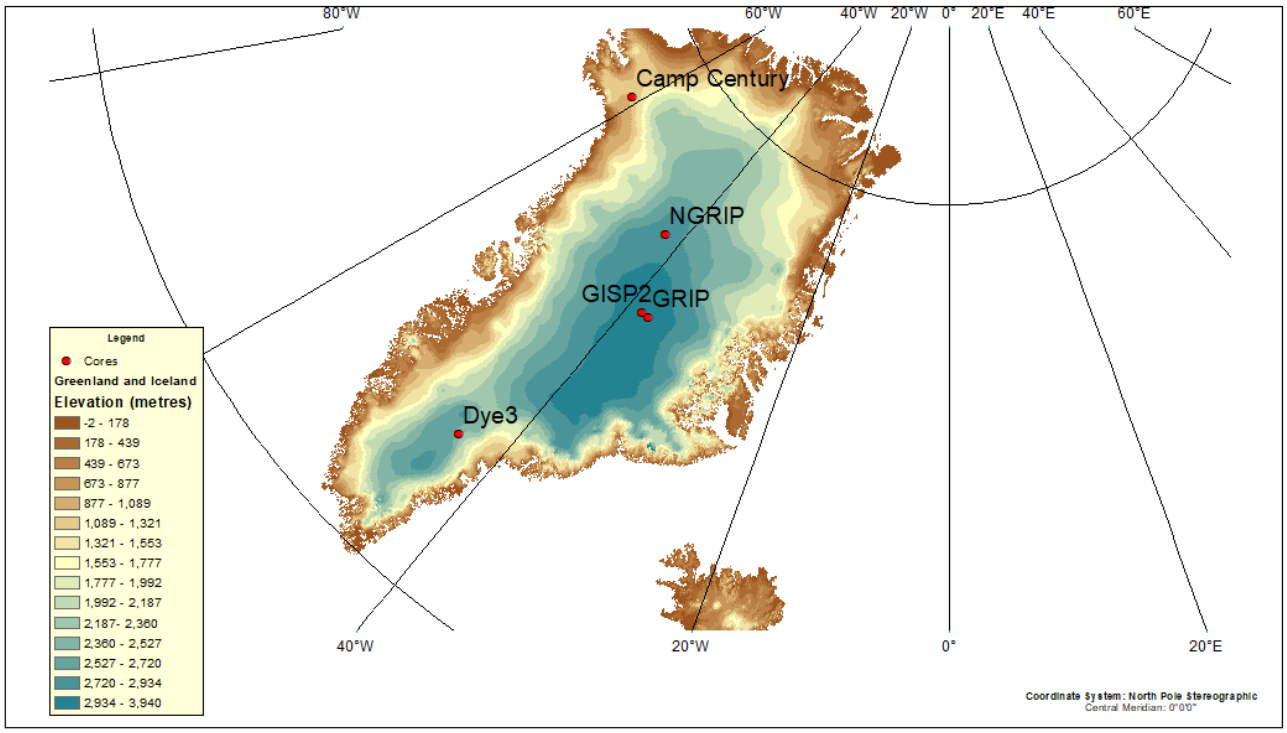

Figure 2.10: Locations of deep ice core drilling sites in Greenland. DEM sourced from Bamber (2001). A DEM is a digital elevation model.

Before delving into chronological issues and challenges to the periodicity of the ~1500-yr climate cycle (Section 2.2.2.5), it is necessary to first provide an overview of Arctic and Antarctic ice core research. The Greenland Ice Sheet Project (GISP) was a multinational effort to drill ice cores in Greenland [Figure 2.10], with the aim of investigating past climate change. The first ice-core drilled as part of this project over a ten-year period was at Dye3 in the early seventies, which was orbitally tuned via the SPECMAP stack derived from marine sediments (Bassinot, 1994; Lowe and Walker, 1997). The U.S. initiative, GISP2, followed with drilling at the Summit Camp. The Greenland Ice Core Project (GRIP), a European initiative, also drilled at the Summit. Subsequently, NGRIP was drilled at a new site in central Greenland, hitting bedrock in 2003, and has three different chronologies associated with it (SS09SEA, SFCP04, GICC05). Ice core chronologies are stratigraphically derived, based on layers within the ice-cores (Skinner, 2008) and assumed accumulation rates of ice (Damon and Sonett, 1991). Chronologies that are based on models, such as assumed accumulation rates, are hypothetical (cf. Skinner, 2008). Models need to be chronologically calibrated through reference to absolutely-dated reference points (see following). For methods and references used in construction of these different chronologies and differentiating layers see Table 2.1 on the next page.

Table 2.1: Greenland Ice Core Chronologies, showing reference models and methods used.

GICC05		
Period	**Reference model**	**Method used**
0-7.5ka	DYE3, GRIP, NGRIP	Layer counting of ^{18}O and deuterium isotopes
7.5ka - 14.8ka	GRIP, NGRIP	ECM; CFA
14.8ka - 41.8ka	GRIP, NGRIP	Annual counting and visual stratigraphic data; ECM and CFA
41.8ka - 60ka	NGRIP (10.3-41.8ka)	Annual layer counting
>60ka	SS09SEA	Spliced to SS09SEA model at 60ky.
NGRIP ss09sea		
to 105ka	GRIP ss09sea	Cross-dated to the GRIP core ss09sea chronology down to 105ky, using high resolution ice isotopic profiles, volcanic events
>105ka	Vostok	Dated based on methane and ^{18}O concentrations
General		Empirical ^{18}O accumulation relationship; ICM anchored at 11.5ka and 110ka
GRIP ss09sea		
0-7.5ka	DYE3	Volcanic acid fallout horizons; stratigraphic marker horizons
7.5ka - 14.8ka		Seasonal variations in micro-particles and several chemical species to establish annual layer chronology
>14.8ka		Glaciological modelling: ^{18}O relationship, ice accumulation rate, ICM
NGRIP SFCP04		
0-40ka	Marine core MD95-2042	^{14}C; calibrated to paired ^{14}C - ^{230}Ur pristine corals
>40ka	Hulu cave speleothems	key anchor points
GISP2		
0-50ka		Annual layer counting
50-110ka		^{18}O comparison to Greenland and other records
General		Absolutely dated back to 50ky
DYE3		
0-7ky		Absolutely calibrated

* Electrical component modelling (ECM); continuous flow analysis (CFA); ice flow model (ICM)

* Sources: Sources: (Andersen *et al.,* 2004; Dansgaard *et al.,* 1985; Hammer *et al.,* 1997; Johnsen *et al.,* 2001; Shackleton *et al.,* 2004; Southon, 2002; Svensson *et al.,* 2008; Wolff *et al.,* 2010; Yiou *et al.,* 1997)

Antarctic studies have enabled palaeoclimatology to reach further back into the past because of the extreme depths of some of its ice cores, with the most significant being derived from Vostok, European Project for Ice Coring in Antarctica (EPICA) Dome C, and Dome Fuji [Figure 2.11] (Summerhayes, 2015). The EPICA EDC3 chronology, the latest chronological model developed for Dome C, used radiometrically-dated age markers from various sources, including NGRIP, GRIP GICC05, Vostok, and EPICA (EDML) chronologies; speleothem records; volcanic ash layers; isotopic spikes in ^{10}Be with INTCAL radiocarbon calibration curve; and wiggle matching of ^{18}O and ^{10}Be records (Parrenin *et al.,* 2007). Its age scale was developed in three stages, using ice flow modelling, *a posteriori* matching to volcanic reference horizons and NGRIP GICC05 age scale in the youngest half of the core, and correction to ice-flow modelling due to flow irregularities in the oldest

part of the core (Parrenin *et al.,* 2007). Despite good agreement between EDC3, Vostok and Dome C, uncertainties in glaciological modelling result from "poorly known physical parameters" in ice flow models and other "non-identified sources" (Parrenin *et al.,* 2007). A more recent chronological model (AICC12) has been developed for four Antarctic ice cores (two EPICA cores (EDC and EDML), Vostok, and Talos Dome) using probabilistic modelling based on various background and age markers derived from Vostok, EDC, EDML, GICC05 (Veres *et al.,* 2013).

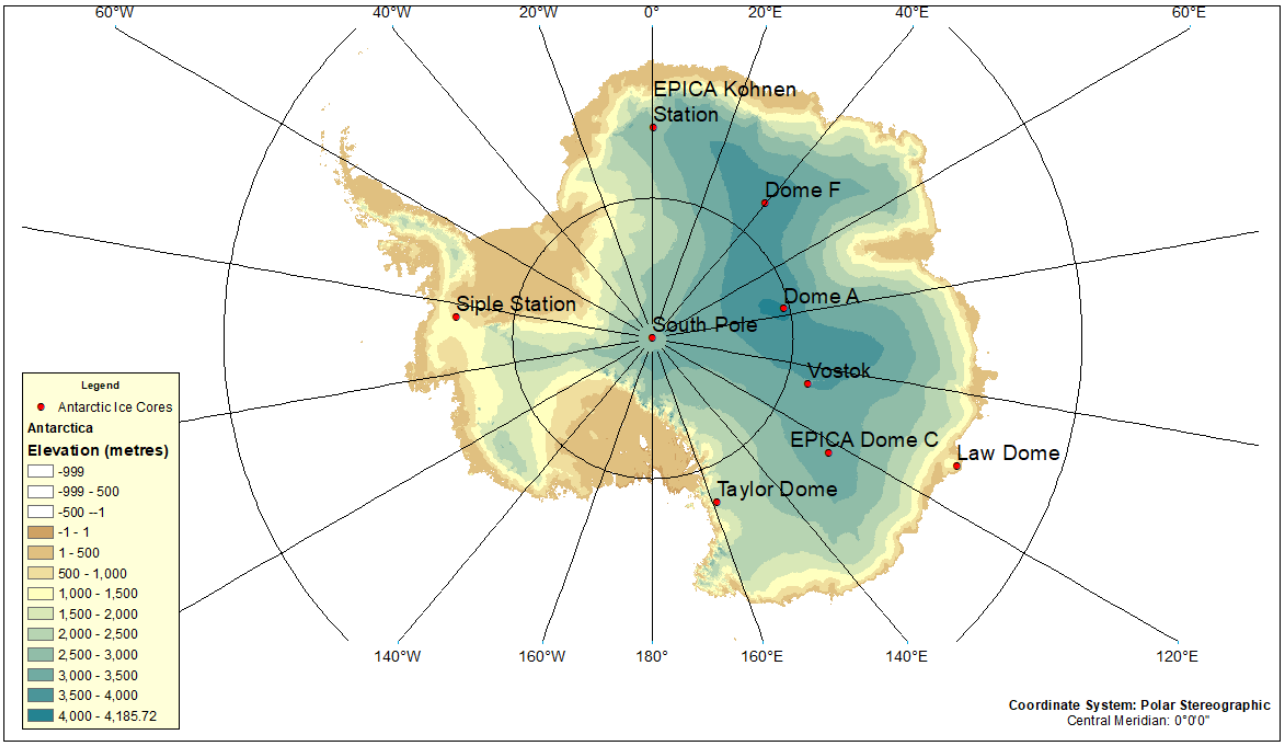

Figure 2.11: Map of Antarctica showing some key Antarctic ice cores. DEM sourced from Bamber *et al.,* 2009. A DEM is a digital elevation model.

In Greenland, ice core chronologies preceding the GISP2 chronology showed the ~1470-yr periodicity of the Dansgaard-Oeschger cycle (Dansgaard *et al.,* 1993; Johnsen *et al.,* 1992; Wolff *et al.,* 2010), but this signal was clearest in the GRIP and GISP2 chronologies [Figure 2.12], which showed distinct patterns of this cycle (Wolff *et al.,* 2010). However, the GISP2 chronology was questioned because of variances between it and the GRIP SS09SEA (SS09SEA) chronology (Clemens, 2005; Wolff *et al.,* 2010). Whilst the millennial signals in the GISP2 record are strongly featured in the 20-40 kya period, these signals are pervasive throughout the last 100 kya in the SS09SEA model (Clemens, 2005). Both the GISP2 and SS09SEA models show a ~1470-yr peak [Figure 2.12], although this is accompanied by spectral peaks at 1163 yrs and 1613 yrs in the SS09SEA model (Clemens, 2005). However, by tuning (wiggle-matching) the GISP2 record to the Hulu Cave speleothem record, the GISP2 record also showed similar spectral peaks in the millennial range (1190 yrs, 1490 yrs, 1667 yrs) to the SS09SEA model (Clemens, 2005). For more information on speleothem dating and issues involved see Section 3.2.3.

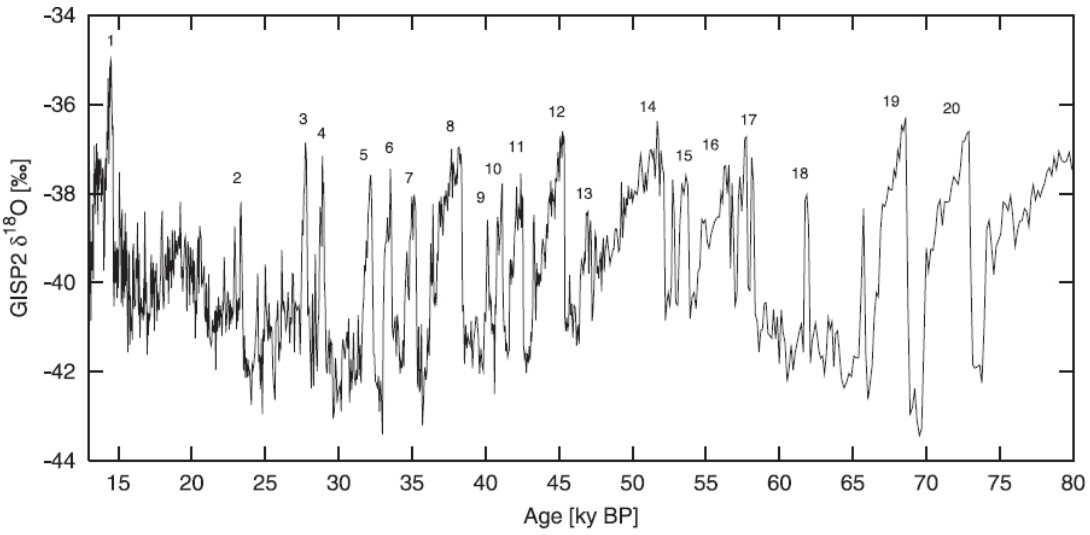

Figure 2.12: Dansgaard-Oeschger events in the ^{18}O record from Greenland's GISP2 ice-core (Grootes and Stuiver, 1997 cited in Schulz, 2002:2). Numerals above oxygen isotope maxima are classical Dansgaard-Oeschger events (Johnsen *et al.,* 1992 cited in Schulz, 2002; Dansgaard *et al.,*1993 cited in Schulz, 2002).

With the exception of the SFCP04 model, cores subsequent to GISP2 were referenced to previous ice core chronologies (Table 2.1). Given the reliance on previous models during the Holocene period, it is unsurprising that the composite GICC05 model agrees with the well-calibrated, detailed record since the termination of the last ice age (cf. Cooper *et al.,* 2015; Wolff *et al.,* 2010). Between the SS09SEA and GISP2 models there is good agreement at 30 kya but this diverges to a difference of 3 ky by 50 kya (Shackleton *et al.,* 2004). Around 40 kya, significant disagreement begins between these two records, stretching back to 110 kya (Clemens, 2005; Johnsen *et al.,* 2001; cf. Svensson *et al.,* 2008; Wolff *et al.,* 2010).

There is also "good agreement" between NGRIP's SS09SEA and GICC05 models in the past 60 ky, with a maximum discrepancy of 900 yrs (Svensson *et al.,* 2008). However, in the NGRIP GICC05 core there is an 800-yr uncertainty at ~40 ky, and "generally" better than 500 yrs throughout the intervening period (40-60 ky) based on modelling when compared to the "preferred" radiometric age from Hulu Cave's speleothem record (Ditlevsen *et al.,* 2007; Wolff *et al.,* 2010). At 60 kya, the GICC05 model is spliced to the SS09Sea model, reducing all ages by 705 yrs beyond this date to do so (Wolff *et al.,* 2010). At 60 ky the uncertainty in the GICC05 scale is 1300 yrs (Ditlevsen *et al.,* 2009). Alternatively, this uncertainty is expressed as a 4-7% in the GICC05 model during the last glacial (Parrenin *et al.,* 2007), whilst there is a ±2% uncertainty in the GISP2 model to 40 ky and 5-10% beyond 40 kya (Shackleton *et al.,* 2004). These uncertainties have not been helped by problems with glaciological modelling or distortion of layering near the base of cores (Johnsen *et al.,* 1992; Johnsen *et al.,* 2001; Lemieux-Dudon *et al.*, 2010; Meese *et al.,* 1997).

The SFCP04 ice core chronology is different from other Greenland ice core chronologies in that it is based on the absolutely-calibrated marine core from the Iberian Margin using high resolution AMS

^{14}C dating, the latter of which was calibrated using paired ^{14}C and uranium-series dating in pristine corals (Shackleton *et al.,* 2004; Skinner, 2008). The use of coral dating is preferable to speleothem dating because of the uncertainties and risks associated with the latter (see Section 3.2.3). The SFCP04 chronology was developed after a close coupling of temperature indicators in Greenland ice cores (GRIP and GISP2) and an Iberian Margin marine core (Shackleton *et al.,* 2004; Skinner, 2008; see also Vautravers and Shackleton, 2006; Martrat *et al.,* 2007). The implications were that "glaciological age-scales may not necessarily represent absolute calendar age-scales" (Skinner, 2008:297).

Back to 35 ky, the Iberian Margin dates on the SFCP04 scale agree with radiocarbon calibration datasets, including Bard's and Fairbank's coral datasets, as well as Hughen's speleothem-referenced, marine Cariaco dataset (Skinner, 2008). Between 30-40 kya there is a difference of 1.4 kya between SFCP04 and SS09SEA time scales (Shackleton *et al.,* 2004). Additionally, the SFCP04 chronology differs from the GICC05 chronology by up to 1200 yrs, with the latter being too young and missing layers (Skinner, 2008; cf. Cooper *et al.,* 2015). Similarly, the difference between the GICC05 chronology and radiocarbon-dated megafaunal transitions in Australia are out by up to 1000 yrs, due to cumulative counting errors in this Greenland ice core chronology (Cooper *et al.,* 2015).

Currently, there are multiple Greenland ice core chronologies, none of which agree with each other (Skinner, 2008), and the temporal variations between different ice core chronologies is as much as several thousand years (Veres *et al.,* 2013). Inaccuracies in the construction of chronologies can stem from a number of issues, including the chronological and glaciological models used, layer counting, and the temporal difference between dated tie points (Chiu *et al.,* 2007; cf. Hughen *et al.,* 2004; also see Chapter 3). For example, the Cariaco core (ODP1002) had an estimated calendar chronology based on correlation of visually-identified stratigraphy with GISP2 ^{18}O record (Chiu *et al.,* 2007). The application of various other Greenland ice core chronologies to this core altered the trends and amplitudes of the ^{14}C record. Inherited uncertainties have the potential of generating an artificial radiocarbon trend,

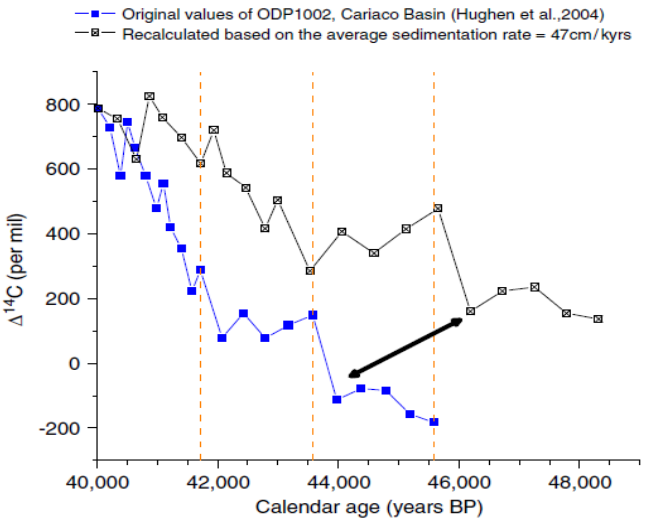

Figure 2.13: Impact on $\Delta^{14}C$ values of sedimentation rate changes in ODP1002 from the Cariaco Basin (Chiu *et al.,* 2007:25). The recalibration of dates changes the shape and amplitude of the signal in the direction of the black arrow. The original data (blue markers) are calibrated to ice-core chronology tie points and the recalibrated data to Fairbanks *et al.* (2005) coral-based calibration curve (grey markers). The three red-dashed lines are tie-points between the two records (ice-core and ODP1002), where changes in sedimentation rate are indicated in ice-core chronology.

resulting in distortions that affect the shape and amplitude of this record [Figure 2.13] (Chiu *et al.,* 2007). This figure shows the sensitivity of the ^{14}C record to these distortions, where chronological tie points in the ice-core were used to correlate the two cores. The use of different age-models consequently induces changes to the form of the record, which is constrained by these tie points.

Chronological issues specific to absolute dating using radioactive isotopes also need to be taken into consideration (Chiu *et al.,* 2007; see Section 3.2). Attempts to address these issues are ongoing such as the INTCAL calibration efforts that include the Fairbanks calibration curve (Chiu *et al.,* 2007; Fairbanks *et al.,* 2005), and the development of other glaciological chronologies such as the Greenland-Cariaco chronology that are tied to uranium-series dating using high quality coral records (Cooper *et al.,* 2015). To understand the potential causes of these discrepancies and the ability of these chronologies to assess the existence of the 1500-yr cycle, it is also important to understand how these chronologies are structured and factors affecting them (see Section 3.2).

Bard *et al.* (2007) highlighted several features with Greenland ice cores that do not occur in the Antarctic ice cores. Continental dust-transported ^{10}Be is one such issue (Bard *et al.,* 1997, 2007; Yiou *et al.,* 1997; Summerhayes, 2015; *contra* Muschler, 2007; see Section 3.2). The lack of consistency between different Greenland ice core peaks of ^{10}Be is cited as the cause of an anomalous fifth peak in these records between 950AD and 1800AD, whereas the South Pole ice-core record only shows four peaks (Bard *et al.,* 2007). Greenland's anomalous fifth peak is also at odds with radiocarbon calibration based on dendrochronological records (Bard *et al.,* 2007; see Chapter 3).

Greenland's abrupt climatic changes associated with the Dansgaard-Oeschger oscillation have an equivalent in Antarctic ice cores as Antarctic Isotopic Maxima [Figure 2.14], although temperature change is more gradual in the southern hemisphere (Veres *et al.,* 2013; cf. EPICA community, 2006). Greenland's GICC05 is a more recent composite glaciological age model (derived from Dye3, GRIP and NGRIP cores) than the GISP2 chronology (Svensson *et al.,* 2008; Veres *et al.,* 2013; Wolff *et al.,* 2010),

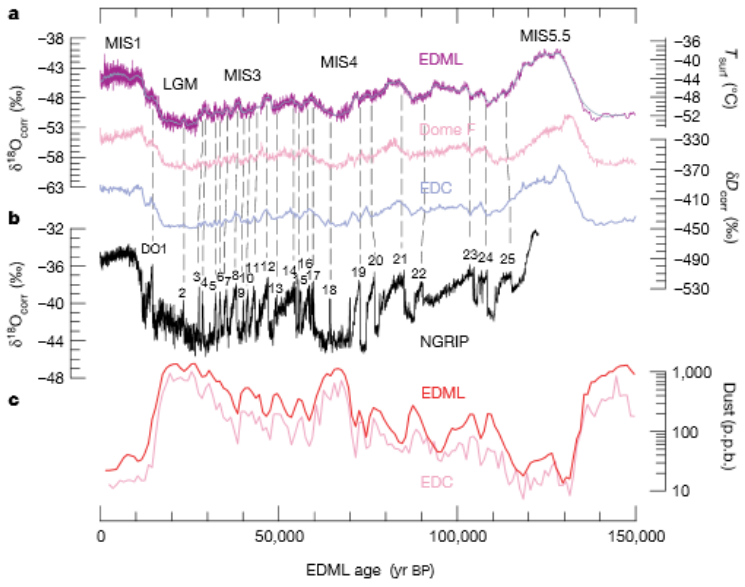

Figure 2.14: Synchronous millennial variations between Greenland and Antarctic ice core record of oxygen isotope flux (EPICA community, 2006:195). The various ice-cores are identified (EDML, Dome F, and EDC) from Antarctic (panel a) and NGRIP from Greenland (panel B). Panel C shows EDML's and EDC's mineral dust records. EDML and EDC are on the EDC3 time-scale, different to Dome F. Temperature scales are on the right (derived from the O18 record) and O18 scale is on the left.

with an "attempt at a fully layer-counted age scale and rests on a "strong assumption…that the annual pattern in observed signals persists, even under glacial conditions" (Wolff *et al.,* 2010:2830-2831). GICC05 alters the distinctive patterns of the Dansgaard-Oeschger cycle between tie points (Ditlevsen *et al.,* 2007). Between these radiometrically-dated tie points, incremental dating is used by counting layers. Whilst it has been suggested that "the GISP2 record prior to 40 ky BP becomes increasingly less trustworthy" (Wolf *et al.,* 2010) due to "substantial differences to the GISP2 dating prior to 40k-yr BP", the limit of radiocarbon dating (~50 kya) presents problems in resolving these questions due to poor resolution and increasing chronological and stratigraphic uncertainties (Clemens, 2005; cf. Cooper *et al.,* 2015; Stevens and Boney, 2013).

Fairbanks *et al.* (2005) have discussed problems with glaciological chronologies:

> "*Differences between the various Greenland ice core chronologies are due to age model assumptions, inherent subjectivity in discerning annual bands in ice or layered sediments in general, the fidelity of the proxies to record the annual signal, occasional wind erosion or scouring of some ice layers, and compacting and degrading signals deeper in the ice cores …"* (Fairbanks *et al.,*2005:1783).

In particular, missing and indistinct layers in varved sediments and ice core chronology can lead to accumulating errors, and "combining published radiocarbon calibration data" >12 kya "results in confusing and inaccurate calibration data" (Fairbanks *et al.,* 2005:1783). Developing a radiocarbon calibration curve using varved sediments correlated to "ice core proxies have compounded errors due to proxy interpretations, correlation errors, and large uncertainties in ice-core chronologies" (Fairbanks *et al.,* 2005:1783). There are means of error checking in coral dating that don't exist with glaciological models, such as overlapping with tree-ring chronology during the Holocene or using paired uranium-series dating beyond that time (Fairbanks *et al.,* 2005).

Given these issues, discrepancies seem to have much to do with how frequently these models have been calibrated to radiometrically-dated tie points, to what they have been calibrated, the level of certainty attached to visually-matched stratigraphic marker horizons between cores, and glaciological and age models used between tie points in different cores (cf. Clemens, 2005; Wunsch, 2010). Blaauw (2012) notes that given the dangers of tuning data from multiple proxy archives it is better for preference to be given to absolute dating over relative dating, although the expense of doing so is a major consideration in the construction of these chronologies.

2.2.2.5 Questioning the reality of the 1500-yr quasi-periodicity

Having provided the basis to the Milankovitch cycles, ~1500-yr quasi-periodicity, and glaciological chronologies, the necessary groundwork has been provided for examining questions on the reality of

the ~1500-yr quasi-periodicity. Whilst stochastic resonance is a possibility for explaining this quasi-periodicity, it is conceivable that a combination of astronomical forcing factors could also produce this climate signal. Part of the problem in understanding the Dansgaard-Oeschger cycle is that "detection of periodicity depends on the age scale used", the asymmetry of events, and small sub-sampling of datasets (Wolff *et al.,* 2010:2831). What has not been considered was a quasi-periodicity derived from multiple contributing periodicities. This thesis explores this latter unexplored option in relation to astronomical forcing.

Alley *et al.* (2001) suggested that the ~1500-yr peaks in the ^{18}O signatures from Greenland ice-cores could be potentially explained by stochastic resonance within the climate system, triggered by random freshwater flux into the North Atlantic, although stating that this did not constitute proof. Stochastic resonance produces a ripple effect through a system from a random event, growing weaker with each periodic return. Alley *et al.* (2001) supported the existence of the quasi-periodicity and believed that stochastic resonance model could be a contributor. They suggested that the stochastic resonance theory could be tested later. In relation to the number and timing of Dansgaard-Oeschger events,

> "*asymmetry in Dansgaard-Oeschger oscillations .... causes the times of coolings to depend upon the threshold to define a cooling, whereas times of warmings are less sensitive to the threshold chosen*" (Alley *et al.,* 2001:195).

Ditlevsen *et.al.,* (2009) dismissed this ~1500-yr quasi-periodicity as random, noise-driven, and potentially stochastic based on his redefinition of Dansgaard-Oeschger events. The redefinition process used by Ditlevsen *el al.,* (2005) used commonalities in the GRIP and NGRIP ice core records in an attempt to provide an objective definition (Ditlevsen *et al.,* 2007; Ditlevsen *et al.,* 2009). Consequently, new events were classified and one declassified (DO9). In a later test using the GISP2 record, the rejection of a strict periodicity could be achieved only by eliminating a Dansgaard-Oeschger event (DO9). This DO9 event occurred at about 40 kya [Figure 2.12], which was at the edge of the period tested in these studies (11-42 kya) (Ditlevsen *et al.,* 2007). With DO9 removed, the 1470-yr cycle was then "indistinguishable" from a random event (Ditlevsen *et al.,* 2007:129). Wolff *et al.* (2010) consider this matter to be unresolved.

A high band-pass filter was used to eliminate variations in the isotope record due to astronomical forcing at Milankovitch scales (Ditlevsen *et al.,* 2005; Ditlevsen *et al.,* 2007). The low band-pass filter was selected on shared commonalities between GRIP and NGRIP ice core records, which resulted in all signals of <30 yrs cyclicity being filtered out as background noise. This process excluded signals generated by the Sun and Moon considered in this PhD research (see Section 2.2.3 and Chapter 3). New thresholds in the isotope record were also established to identify Dansgaard-Oeschger events: one high and one low. An upper threshold was established through the use of

stochastic resonance models that assume the signal is random and not externally forced (Ditlevsen *et al.,* 2005).

In their analysis of this quasi-periodicity from the filtered record, Ditlevsen *et al.,* (2007) used three different model types (exponential distribution, periodic, and stochastic resonance), with assumptions of randomness for the exponential model, and a "perfect periodic signal" of 1470 yrs, for the periodic and stochastic resonance models. They then attempted to capture the variability of the 1470±500-yr quasi-periodicity using a standard deviation of ±100 yrs (Ditlevsen *et al.,* 2007). They concluded that the null hypothesis of no periodicity could not be rejected, and that there was "no long-term memory in the climate system or unknown 1470-yr periodic triggering of the climate shifts" (Ditlevsen *et al.,* 2007:134). On one hand Ditlevsen *et al.* (2007) state that statistical distribution of this quasi-periodicity "implies" that the climate system has a simple no-memory process. Thereafter, (Ditlevsen *et al.,* 2007; Ditlevsen *et al.,* 2009) this implication is specifically stated as "fact" (Ditlevsen *et al.,* 2009:446). Given the nature of the various ice-core records and chronologies (Section 2.2.2.4), which are complicated by chronometric uncertainties and disparities between various records, it is difficult to understand this transition from implication to fact. These Ditlevsen models were not designed to deal with quasi-periodicities, using only assumptions of randomness or perfect periodic beating.

Furthermore, the models used by Ditlevsen *et al.* (2007) have not considered the influence of some astronomical forcing factors on the timing signals. An example of this is chronometric complications (caused by precession), resulting from the inconstant rate of the March equinox movement relative to the changing shape of Earth's elliptical orbit. This factor must influence the length of the periodicity, which is exacerbated when the time-series is sub-sampled. Precession influences both the timing and strength of the climate signal due to the changing relationship between Earth's seasonal year and changing orbital shape. These matters are further discussed in Chapter Three. When considering astronomical cycles over very long periods, chronological precision is extremely important, especially because of these precessional influences (see Chapters 3-6). Despite the use of a perfect periodicity in their exponential model, the "waiting time" between Dansgaard-Oeschger events assumed by Ditlevsen *et al.* (2007) was 2800 yrs, which varies by 57.1 yrs to the definition supplied. The stochastic resonance model is also flawed in this instance, resting on a "precise periodicity" and approximations of "waiting time" (Ditlevsen *et al.,* 2007).

Given the prerequisite of the precision assumed for dating Dansgaard-Oeschger events in their modelling experiment (Ditlevsen *et al.,* 2007), any arguments based on this premise are undermined by the cycle's quasi-periodic nature and the fact that "all palaeoecological and palaeoclimatological data come with a degree of uncertainty" (Blaauw, 2012:38). The combination of periodicities suggested as the cause of the Bond and Dansgaard-Oeschger cycles (Bond *et al.,*1997) is unlikely to

result in a periodicity of a precise length, particularly if multiple factors are involved. Ditlevsen *et al.,* (2005) acknowledged a similar point, citing Paillard and Labyerie (1994) as "only simplified models with few degrees of freedom exhibit strict cyclic behaviour". Clemens (2005) emphasises the importance of accurate chronologies, noticing that millennial-band frequencies are sensitive to small changes in the modelled centennial-scale patterns on which they are based.

Other issues with the aforementioned Ditlevsen papers include the use of a monotonic function and assumptions about the Gaussian form of dates based on strict periodicity (Ditlevsen *et al.,* 2007). What has not been taken into account is the fact that the radiocarbon calibration curve is not a monotonic function and the derived distribution of calendar dates for the data from radiocarbon dating "is no longer Gaussian, nor is mathematically definable" (Bowman, 1990:46). For example, variations in the radiocarbon curve caused by the 209-yr SdV cycle result in a radiocarbon date that can equate to more than one calendar date (cf. Bowman, 1990). Calendar dates should be regarded as a range of equally likely dates, not as a central term with an error margin (Bowman, 1990; cf. Dincauze, 2000).

To place the Ditlevsen's dismissal of the 1500-yr quasi-periodicity as a real phenomenon in context, Alley *et al.* (2001:196) states that "No finite data sequence ever uniquely defines the process that produced it." This is in keeping with the notions that the use of empirically-derived models risk arguments of circularity being levelled against them (cf. Henshilwood *et al.*, 2003; Popper, 1972). The testing and development of such models requires a good understanding of the data in order to compensate for problems associated with the use of statistics on non-linear and non-stationary geographic data, the nature of which violates statistical assumptions (Longley *et al.,* 2011; Mitchell, 1999; Schulz, 2002). If the cause of the quasi-periodicity is not known or understood, this makes the job even more difficult. This is a problem acknowledged by Ditlevsen *et al.* (2009:446): "Dansgaard-Oeschger (DO) events of rapid climate shifts in the glacial climate observed in the Greenland ice cores are still not well understood."

Referencing Ditlevsen *et al.* (2007) and Clemens (2005), Obrochta *et al.* (2012:25) dismiss the 1470-yr quasi-periodicity stating that the signal is "absent from other Greenland ice cores". The Ditlevsen arguments have already been discussed. In contrast to Obrochta *et al.*'s (2012) claims that the 1470-yr cycle is absent from Greenland ice cores, Clemens (2005) reports (i) a bifurcation of the signal into 1163-yr and 1613-yr peaks in the GRIP spectrum, and (ii) spectral peaks in GISP2 (tuned to the Hulu Cave record) of 1190, 1490, and 1667 years (see Section 2.2.2.4). Additionally, Clemens' (2005) historical perspective of this cycle highlighted that it was evident throughout the last 100 ky years in the GRIP SS09 model, and strong in the 20-40ky period in GISP2. These two chronologies agree well

where layers are counted, but differ significantly between 40-80 kya when "age models are based on independent glaciological flow models" (Clemens, 2005:522).

Whereas the GISP2 chronology is layer counted to ~51 kya (Rahmstorf, 2003), based on visual stratigraphic layers, and sometimes refined using laser scattering, oxygen isotope chronology, and electrical conductivity (Alley *et al.,* 1997; see also Table 2.1), GICC05 is based on NGRIP records between 10-42 kya (Svensson *et al.* 2006), the SS09SEA model beyond 60 kya (after reducing the SS09SEA scale by 705 yrs at 60 kya) (Svensson *et al.* 2006; Wolff *et al.,* 2010), and annual layer counting (42-60 kya) (Svensson *et al.* 2006). The NGRIP chronology is based on the GRIP SS09SEA model (Svensson *et al.* 2006), which is an ice-flow model that factors in the ^{18}O:^{16}O relationship (Rasmussen *et al.,* 2008), and with which the GICC05 model agrees well (Wolff *et al.,* 2010). However, whilst the 1470-yr quasi-periodicity is evident in a number of Greenland ice cores over the past 120 ky (e.g., Rahmstorf, 2003), the GICC05 modelling alters the patterns of the Dansgaard-Oeschger cycle between its tie-points (Ditlevsen *et al.,* 2007). Whilst the 1470-yr cycles are best developed in MIS3 using the GISP2 Meese/Sowers model (Bond *et al.,* 1999), Obrochta *et al.* (2012) found that they were best developed during MIS4, which is based on the SS09SEA glaciological model.

Apart from the aforementioned arguments raised by Obrochta *et al.* (2012) to dismiss the existence of a 1500-yr cycle, they frequently reinforced their argument with the point that no solar cycle of that length exists. However, Bond *et al.* (2001) found coherency of IRD events in various North Atlantic deep-sea cores with cosmogenic nuclide production, specifically ^{10}Be and ^{14}C (Bond *et al*., 2001), and matched these events to other records from around the world during the Holocene, including (i) ^{18}O fluctuations in a well-dated-stalagmite core from Oman, (ii) advances of Scandinavian glaciers linked to dendrochronological ^{14}C variations, (iii) and evidence of abrupt climate change from other sources of atmospheric, lacustrine, and oceanic variations. Obrochta *et al.* (2012) argued that the coherency was not at 1500 yrs, but at 500, 1000, and 2000 yrs, ignoring Clemens' (2005) finding of spectral peaks in GRIP and GISP records close to the 1500-yr mark and within the variability of this quasi-periodicity.

These conclusions by Obrochta *et al.* (2012) were based on a reinterpretation of the last 70ky North Atlantic record, using only one of numerous deep-sea cores (Site 609) previously used by Bond *et al.* (1999, 2001). Previously, VM23-81 and Site 609 were extended by Bond further back in the glacial (beyond 26 kya) by transferring the GISP2 timescale to the foraminiferal record in these cores using tie points, and interpolating between these records. Bond also used radiocarbon ages from VM23-81 to construct a calendar age model for core SU90-24 that also enabled it to be extended further back

into the glacial. In contrast, Obrochta *et al.* (2012) updated the existing chronology on Site 609, using the latest marine calibration, extended it back to 31 kya BP using additional radiocarbon dates, and superimposed NGRIP's GICC05 model further back in time. Whilst Obrochta *et al.* (2012) imply that the whole of the GISP2 core is inferior to the NGRIP core due to thinning, this is not accurately reported (cf. Svensson *et al.,* 2006; also see Section 2.2.2.4). There is generally a good match between GICC05 and GISP2 until 40kya (Svensson *et al.,* 2007), with layer thinning occurring during the early MIS3 in the GISP2 ice core (Svensson *et al.* 2006). Ice layers are thin or absent during extreme cold (Svensson *et al.* 2006), which is also problematic for GICC05 (along with resolution) during the glacial (Anderson *et al.*, 2006).

Obrochta *et al.*'s (2012) conclusions fall short of effectively dismissing the 1500-yr quasi-periodicity. Firstly, their citation of Clemens (2005) and Braun *et al.* (2005) was selective, and potential modification of solar forcing using heterodynes (Clemens, 2005) or combination tones (Braun *et al.*, 2005) was effectively overlooked in their conclusion. This oversight occurred despite a statistically significant coherence between cosmogenic nuclide evidence with centennial- and millennial-scale IRD events (Bond *et al.,* 2001). Furthermore, their mathematical averaging argument that the 1500-yr cycle results from "1000 and 2000-year forcing, similar to variability of inferred solar proxies" (Obrochta et al., 2012:32) provides no real solution as no known solar cycle exists at either 1000-yrs or 2000-yr intervals, and the longest known solar cycle is ~11.4 mean years (Hathaway, 2010; also see Section 3.1.3). The question still remains as to the cause of the apparent millennial-scale variability of proxies for solar variability (*viz*, cosmogenic nuclides) and associated climate cycles. Finally, non-existence is not scientifically provable (cf. Popper, 1972).

2.2.3 Other related climate cycles

Numerous radiocarbon cycles observed in palaeoclimatic records are also seen in other isotopic records, such as historical records of sunspot and auroral activity and palaeomagnetic records (e.g., Damon and Sonett, 1991; Braun *et al.*, 2005; Raspopov *et al.,* 2000; Raspopov *et al.,*2011; Vasiliev and Dergachev, 2002). For example, Figures 2.15 and 2.16, and Table 2.2 show some of these signals in spectral peaks from radiocarbon data, such the Hallstadt cycle (~2.3 ky), the SdV cycle (~208 yrs), Gleissberg cycle (70-100 yrs), and cycles of ~57 yrs and multiples thereof, and ~131 yrs, and ~105 yrs. Other cycles mentioned in this chapter are also included in this table. Those cycles relating to the semi-precession and precession can also be seen and include 11.3-ky, 23.7-ky, 22.4-ky, and 19.2-ky cycles. In order of prominence in the radiocarbon record, these signals are the 11.3-ky, the Hallstadt, SdV cycle, Gleissberg cycle, and the ~11-yr Schwabe sunspot cycles (Damon and Sonett, 1991). Radiocarbon flux and causes are discussed in Section 3.2.2.

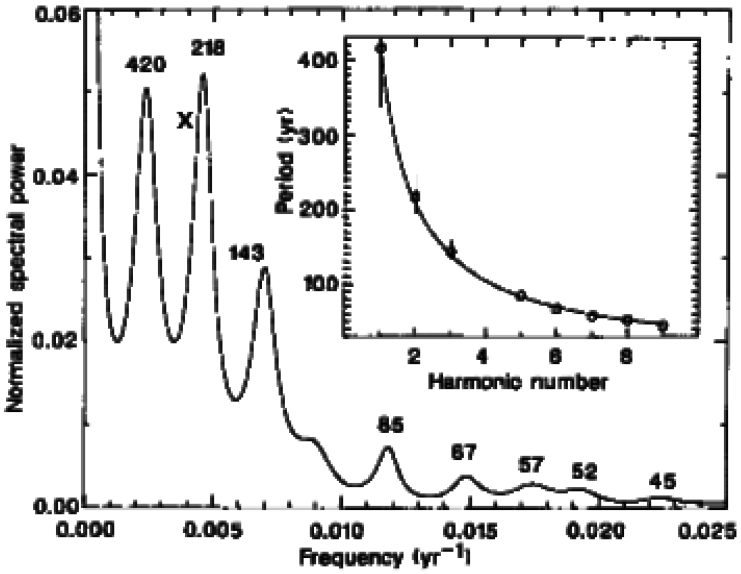

Figure 2.15: MEM power spectrum (AR=20) of ^{14}C carbon production rate (Q) from Stuiver and Braziunas (1989:406). The insert shows the expected harmonics for a fundamental frequency of 1/420 yr-1. Observed periods were plotted in the inset, with vertical bars being 1σ. Error bars smaller than the symbol size are not shown.

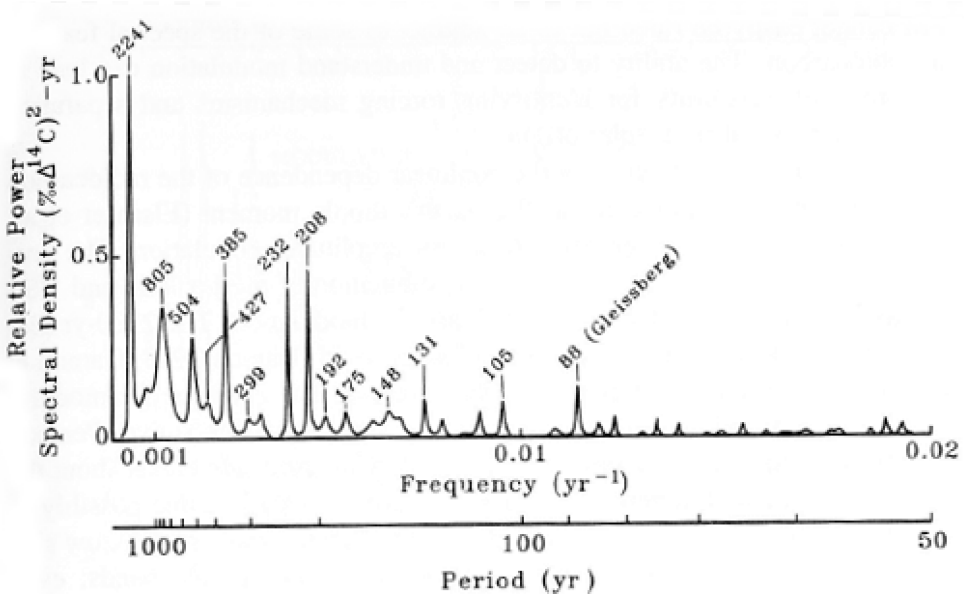

Figure 2.16: Spectral analysis of Stuiver and Pearson Belfast and Seattle data (Damon and Sonett, 1991:371) using maximum entropy power spectrum. This data came from dendrochronologically-dated wood used on radiocarbon calibration. Prominent spectral peaks associated with various cycles can be seen, including the SdV (208 yrs) and variants (232, 192, 175), and Hallstadt (2241) cycles.

Table 2.2: ^{14}C data from La Jolla (a) and Campito Mountain bristlecone pine (b) (Sonett and Suess 1984:142) for the periods 3405BC-AD1885. This table shows the frequencies, periods, and period resolution of some of the major lines in ^{14}C and bristlecone pine ring growth spectra.

Frequency (yr^{-1})		Period T (yr)	T-ΔT	T+ΔT
a	0.0004	2,500	1700	4740
	0.0014	714	629	826
	0.0047	213	205	222
	0.0087	115	113	118
	0.0096	104	102	106
	0.0114	88	86	89
b	0.0007	1430	1125	1957
	0.0015	667	592	763
	0.0048	208	200	217
	0.0088	114	111	116
	0.0103	97	95	99
	0.0122	82	81	82

The Hallstadt cycle equivalent in the Earth's palaeomagnetic record is an ~2.4-ky quasi-periodicity that has been attributed to directional components and westward drift of the nondipole field (Damon and Sonett, 1991; Lowrie, 2007). This westward drift is thought to be due to the "rotation of the outer layers of the core relative to the lower mantle" (Lowrie, 2007:314). Palaeomagnetic flux is found in geological material, and is strongest in rocks and soils containing ferromagnetic elements. Modern measurements come from land-based and satellite-based magnetometers. This ~2.3-ky cycle also appears in reconstructed sunspot numbers (Xapsos and Burke, 2009). For a more extensive list of these cycles, please see Table 2.3 on the next page.

Dendrochronological data shows evidence of sunspot cyclicity (Schwabe, Hale), and Gleissberg, and Bruckner (30-35 yrs) cycles (Branch *et al.,* 2005; Henry, 1927; Raspopov *et al.,* 2011). The Hale, Gleissberg, SdV, and Hallstadt cycles are found in the Greenland and Antarctic ice cores, whilst the 18.6-yr lunar nodal cycle associated with nutation also shows in tidal sedimentation patterns and air-pressure (Oost *et al.,*1993; Raspopov *et al.,* 2011; Stuiver *et al.,* 1995). Both the Gleissberg and SdV cycles are harmonics of the sunspot cycle, with a mean length of 11.4 yrs (NASA).

Sunspot minima were initially associated with the coldest parts of the LIA (Damon and Sonett, 1991; Eddy, 1976; Stuiver, 1961, 1965; Stuiver and Quay, 1980; Summerhayes, 2015). It is now evident that the waxing and waning of solar activity during the 11-yr sunspot cycle corresponds to fluxes in radiation levels in Earth's upper atmosphere, affecting upper atmospheric heat and density (Hathaway, 2010). Climatic associations with sunspot activity include the strength of cyclogenesis, land air and sea surface temperatures, sea-level atmospheric pressure, equatorial wind patterns, the

intensity of zonal flow (Bard *et al.,* 1997; Davis and Brewer, 2011; Friis-Christensen and Lassen, 1991; Kelly, 1977; Labitzke and Loon, 1988; Reid, 1987; Tinsley, 1994).

Table 2.3: Table of cycles. Palaeoclimatic and modern climatic cycles and their associations.

Cycle	Length (Mean)	Range/Variants	Multiples/Association	Records
3.8 yr				El Nino periodicity in NINO3.4; SST
18.6 yr				Lunar nodal cycle; tidal sedimentation; air-pressure
19 yr			Metonic lunation cycle 38 yrs; 57 yrs; 494 yrs	^{10}Be spectral peak in Holocene ice; air pressure; air temperature; precipitation data; PDO
57 yr	57 yrs		114 yrs, 228 yrs	Radiocarbon; PDO; North Atlantic Oscillation; global air temperature; length of day
104 yr	104 yrs		208 yrs, 416 yrs	Radiocarbon
131 yr	131 yrs			Radiocarbon; ice-cores; tropical Atlantic cyclones; ocean sediments; Nile water levels; auroral records; fire and drought cycles in China, Spain and Indonesia; arctic atmospheric oscillation; solar insolation; periodic variation in the interhemispheric offset of radiocarbon ages;
Bruckner	32.5 yrs	30-35 yrs		dendrochronology;
Bond	1470±532 yrs			Radiocarbon
Cartwright sedimentation	~493 yrs			Radiocarbon; tidal sediments
Dansgaard-Oeschger	1ky-12ky		Occurs at multiples of 1470 yrs	Ice-cores, deep-sea sedimentary cores
ENSO (millennial scale)	~1490 yrs			Peat humification data; radiocarbon
Gleissberg		70 yrs -100 yrs	77 yr; 88 yr	Radiocarbon; dendrochronology; ice-cores; harmonic of sunspot cycle
Hale	22.8 yr		57 yrs; sunspot cycle	Sunspot data (TSI, radio flux, magnetic, flares/CMEs, galactic cosmic ray flux); dendrochronology; ice-cores; strength of cyclogenesis; land air; SST; sea-level pressure; atmospheric pressure; equatorial wind patterns; the intensity of zonal flow
Hallstadt	~2.3ky			Radiocarbon; Palaeomagnetic; reconstructed sunspot numbers; ice-cores
Heinrich events	11±1ky		Occurs at multiples of 1470 yrs	Ice-cores, deep-sea sedimentary cores
~100ky				Mathematical; oxygen isotopes from deep-sea sediment cores; uranium-series dating coral terraces; geomagnetic dating
			Milankovitch (obliquity)	
~41ky				Mathematical; oxygen isotopes from deep-sea sediment cores; uranium-series dating coral terraces; geomagnetic dating
			Milankovitch (eccentricity)	
~21ky	~19ky, ~23ky	~11.5ky half cycle	Milankovitch precession	Mathematical; oxygen isotopes from deep-sea sediment cores; uranium-series dating coral terraces; geomagnetic dating; radiocarbon
Schwabe	11.4 yrs		Sunspot cycle	Sunspot data (TSI, radio flux, magnetic, flares/CMEs, galactic cosmic ray flux); dendrochronology; strength of cyclogenesis; land air; SST; sea-level pressure; atmospheric pressure; equatorial wind patterns; the intensity of zonal flow
Suess de Vries	~208 yrs	171-235 yrs		Radiocarbon; ice-cores; harmonic of sunspot cycle; dendrochronology; glacier variations; ice core chronologies; monsoon intensity changes

An ~130-yr climate signal is also evident from spectral analysis of climatic data (Damon and Sonett, 1991) and could potentially be a component of the ~1470-yr climate 'cycle'. A ~131-yr periodicity can be seen in ^{14}C spectral analysis [Figure 2.16] (Damon and Linick, 1986), and is also the value of the periodic variation in the interhemispheric offset of radiocarbon ages (Hogg *et al.,* 2013). A 133-yr periodicity is evident in climatic datasets such as tropical Atlantic cyclones [Figure 2.17], ocean sediments, and Nile water (Cohen and Sweetser, 1975; Yousef, 2000), as well as in auroral records (Attolini *et al.,* 1990; Damon and Sonett, 1991; Siscoe, 1980; Stuiver and Braziunas, 1998); fire and drought cycles in China, Spain and Indonesia (Biagioni *et al.,* 2015; Vázquez *et al.,* 2015; Xue *et al.,* 2008); and Arctic and Antarctic ice core chronologies (Yiou *et al.,* 1997). The signal in the Chinese fire data is at 90% confidence interval and the Indonesian data at 95%. Additionally, significant solar forcing at the ~130-yr scale is found in both the solar insolation and arctic atmospheric oscillation records (Darby *et al.,* 2012).

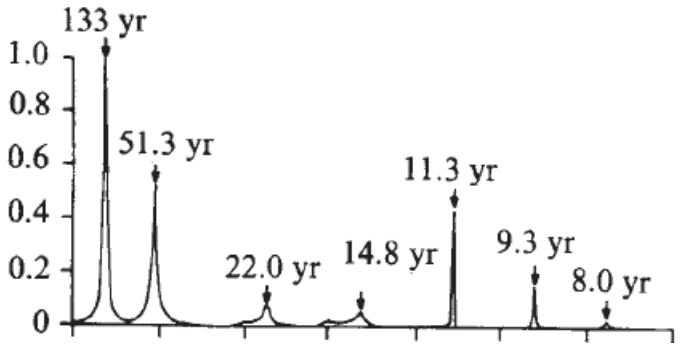

Figure 2.17: MEM spectral analysis showing an increased number of cyclones at 133 yrs (Cohen and Sweetser, 1975:296). Sunspot cycle frequencies can also be seen (11.3 and 22 yrs).

The 133-yr cycle is also a harmonic of a ~19-yr cycle, the latter of which is found as a prominent ^{10}Be spectral peak in Holocene ice (Yiou *et al.,* 1997); U.S. temperature peaks (Currie, 1993); air pressure and air temperature (O'Brien and Currie, 1993); rainfall data in Australia and South Africa (Vines, 2008); and volcanic eruptions [Figure 2.18] (Hamilton, 1973), with which there is significant correlation (Chappell, 1973). In the ^{14}C spectrum, a 19-yr lag time exists between minimum and maximum production (Damon and Sonett, 1991). The importance of the 19-yr cycle as a function of astronomical forcing is explored further in Chapters 3-7. Also, a harmonic of the 19-yr cycle is a 57-yr climate cycle that appears as nonstationary patterns of precipitation, SST, sea level peaks, and

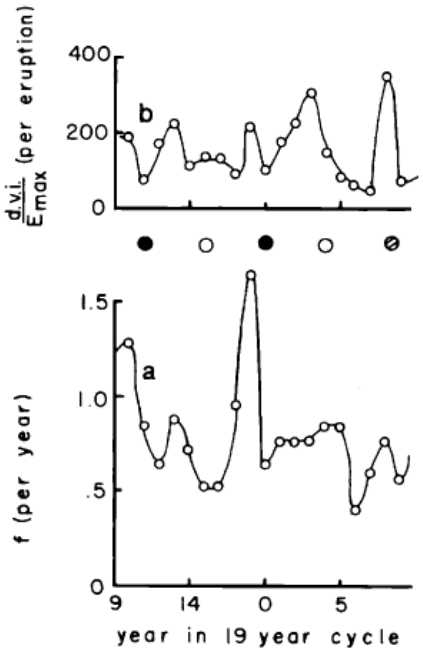

Figure 2.18: 19-yr eruption and tide cycle associated with synodic months and associations with solstices (Hamilton, 1973:115). New moons (black-filled circles) and full moons (empty circle) within 1.5 days of winter solstice are shown. The hatched circle shows a new moon at 1.5-3days distant from the winter solstice. Most eruptions occurred when (i) the New Moon and lunar perigee cycles were in phase or (ii) 180◦ out of phase. Of 68 eruptions studied, 42% occurred within 1 week of (i), while 34% occurred within 1 week of (ii).

geomagnetic cycles (Chambers *et al.,* 2012; Edvardsson *et al.,* 2011; Morner, 2013; Stuiver and Quay, 1980). This 57-yr cycle has been established as statistically significant in the analysis of radioisotopic data using spectral analysis [Figure 2.15] (Stuiver and Braziunas, 1989). In historical records, a 57-yr cycle has been associated with cyclical precipitation levels in Australia, Britain and Egypt, based on southern lunar declinations (Keele, 1910). A ~60-yr cycle has also been identified in the length of day (Mazarella, 2008), North Atlantic Oscillation (Mazarella and Scarfetta, 2012), and global air temperature (Mazarella, 2008). Another harmonic of the 19-yr cycle is a ~493-yr cycle of tidal sedimentation known as the Cartwright cycle (cf. Munk *et al.,* 2002).

A cycle thought to be a modulation of the cosmic radiation by the solar wind is the ~209-yr SdV cycle, which is yet another harmonic of the 19-yr cycle. This ~209-yr cycle has repeatedly been established as being statistically significant by a succession of researchers [Figures 2.14 and 2.15] (e.g., Suess, 1969; Stuiver and Braziunas, 1989). It is evident in the radiocarbon record over at least the past 50 kya (Muschler *et al.,* 2004; Summerhayes, 2015), and is a cycle of cold/warm temperature fluctuations that has been found in dendrochronological records, glacier variations, ice core chronologies, monsoon intensity changes, and other climate-linked processes (Breitenmoser *et al.,* 2012; see also Clemens, 2005)**.** A ~225-yr "mysterious" companion spectral peak of the SdV cycle is also found in palaeoclimatic datasets (Damon and Peristykh, 2004:243). A 104-yr overtone of the SdV cycle (Damon and Peristykh, 2004) appears as a spectral peak in the radiocarbon record, *viz* 104 x 2 = 208 (Damon and Sonett, 1991).

2.3 Chapter summary

Bond IRD events occurred during the Holocene, a time during which high-resolution radiocarbon calibration has been achieved using tree-ring chronology. These IRD events were seen by Bond as a lower amplitude signal that underlay the last glacial's Dansgaard-Oeschger and Heinrich events (Bond *et al.,* 1999). Millennial-scale climate events are also seen in palaeoclimatic datasets from other parts of the world, caused by changing patterns of ENSO intensity and variability, emanating from climatic processes that originated in the tropical Pacific Ocean. Whilst it has been difficult in the past to precisely correlate solar variability to the ~1500-yr quasi-periodicity, with respective correlation coefficients of 0.44 and 0.56 for ^{14}C and ^{10}Be (Summerhayes, 2015), a complete understanding of solar variability and radiocarbon chronological variability is still lacking (Abreu *et al.,* 2012; Damon and Sonett, 1991; see Section 3.2).

Whilst there is good agreement between various ice cores during the last 40 kya, the further we move into deep time the more problematic becomes the measurement of time using the relative chronologies of different glaciological models (cf. Capron, 2010; Fairbanks *et al.,* 2005). Skinner (2008) rightly points out that these models may be considered hypotheses, as the glaciological models are heavily

reliant upon modelling beyond the range of radiocarbon dating and layer counting (Clemens, 2005). Wunsch (2010:1965) reminds us that "models are incomplete representations" of the real world, for which they should never be mistaken. Additionally, the character, timing, and number of these Dansgaard-Oeschger events changed depending upon how these events were defined, and the glaciological model used. However, efforts to address some of these issues by calibrating glaciological chronologies to paired uranium-carbon dating are ongoing, as are those using varved chronologies. Other chronological factors are also involved and are discussed more fully over the coming chapters.

Given the discrepancies between the various age models and large age uncertainties beyond the range of radiocarbon dating, it seems premature to dismiss the ~1500-yr climate quasi-periodicity as a real phenomenon, particularly in light of the difficulties involved in statistically analysing nonlinear, nonstationary data. If the ~1500-yr quasi-periodicity is indeed a composite signal, the exercise of filtering it from records will not result in the removal of Dansgaard-Oeschger events (cf. Wunsch, 2000 cited in Ditlevsen *et al.,* 2007). The results of such an attempt do not imply that the signal is attributable to stochastic resonance. What is clearly needed is an independent, conceptual model against which data can be tested (cf. Kelsey *et al.,* 2015). This process begins in the next chapter.

Two potential causes of the ~1500-yr cycle were identified based on solar irradiance/insolation and lunar gravitation. Both were seen as too small by theoretical analysts to affect the scale of climate change evidence in palaeoclimatic records, but these arguments are undermined by the simplistic models on which they were based (Section 2.2.1). Additionally, Earth's climate system has been shown to be sensitive to small changes in obliquity and eccentricity at Milankovitch scales, and modelled millennial-scale cycles were shown to be sensitive to small changes to underlying harmonics (Section 2.2.1). The argument for the gravitational cause of this quasi-periodicity was also undermined by the incommensurate nature of the variables used for the cycle being tested. Part of this has to do with issues of scale and chronology (Chapter 3), as well as the selection of an appropriate natural variable (Chapters 3, 4).

Whilst this chapter provided an overview of Earth's major long-term climate cycles, its primary purpose was to examine the ~1500-yr climate quasi-periodicity in context of other cyclical climate patterns that could potentially throw light on its character and causes. The Milankovitch cycles demonstrate the role of solar forcing on Earth's climate over vast expanses of time. The Milankovitch cycles, apart from just providing evidence of solar forcing at orbital scales, also provide insights into the characteristics and potential causes of the ~1500-yr quasi-periodicity. The decadal- and centurial-scale cycles have been included in discussion as harmonics of the ~1500-yr climate 'cycle'. These shorter cycles have particular relevance to this thesis in the justification of variables used in modelling

the ~1470-yr climate ‘cycle’ and in explaining the variances in cycle lengths (see Chapter 4 ff.). Importantly, the first step is to place these climate cycles in their astronomical and chronological contexts, which is the purpose of Chapter 3.

Chapter 3 – Earth in Context

> "No man is an island entire of itself; every man is a piece of the continent, a part of the main; if a clod be washed away by the sea, Europe is the less, as well as if a promontory were, as well as any manner of thy friends or of thine own were; any man's death diminishes me, because I am involved in mankind. And therefore never send to know for whom the bell tolls; it tolls for thee." (John Donne, *Meditation XVII,* 1624).

This chapter reviews aspects of astronomy and chronology relevant to this thesis. Just as "no man is an island" Earth is part of an interconnected celestial neighbourhood. To understand Earth's climate, it is essential to consider Earth's climate patterns and cycles within the framework of that neighbourhood, especially as cyclical signals in the climate record suggest astronomical forcing as discussed in Chapter Two.

This situation has been shown to be the case: with the Milankovitch cycles operating over very long timescales (in the order of tens of thousands of years); at very short scales (multi-decadal scale or less), links have been made with astrophysical forces such as sunspot activity. However, in medium-term cycles the situation is less certain. These cycles have been inferred to be solar cycles although no known solar cycle of these lengths exist (e.g., Damon and Sonett, 1991). Reliable direct observations of sunspot activity only extend back ~200 yrs (Damon and Sonett, 1991; Eddy, 1976; Stuiver and Quay, 1980). Consequently, solar variability for these medium-term cycles is inferred from radioisotopic datasets (Damon and Sonett, 1991; cf. Hathaway, 2010). Some researchers have attributed some of these cycles to gravitational forcing (see Chapter 2); to others a combination of unknown factors (Chapter 2); to others yet again, natural harmonics or internal (to Earth) climate variability (e.g., Clement and Cane, 1999; Ditlevsen *et al*., 2009). A profile of Earth's celestial neighbourhood is important in understanding these patterns that are found in Earth's physical record. It is by these patterns that we are able to measure deep time and build chronological profiles (see Section 3.2).

Apart from solar patterns of insolation, irradiance, and gravitational influence on climate evidenced through the Milankovitch cycles (Chapter 2), solar forcing also occurs at a shorter scale through solar variability associated with the sunspot cycle. The Moon also strongly influences conditions on Earth, not only through tides in association with the Sun, but also by contributing to fluctuations of Earth's rotation rate (over long, time scales) and the timing of Earth's perihelion. Earth's rotation, with which the Moon is closely linked, is responsible for the Coriolis effect that affects both wind and ocean currents (Lowrie, 2007). Solar and lunar tides have both been shown to influence atmospheric and

oceanic currents (see below). Together, the solar and lunar gravitational forces are the primary contributors to the wobbling Earth axis, also influencing the orientation of this axis.

The Sun and Moon are also used as calendrical markers and indicators of the seasons and the year. These markers are not stationary and have or appear to have orbital motion. Whilst we know that the Sun isn't moving around Earth, it appears this way because the Sun's apparent motion is a measure of Earth's orbit. We try to emulate the seasonal year in our calendar year using solar and lunar markers of interacting solar and lunar cycles through the use of lunations (times of New Moon). However, it is important to remember that the tropical (or seasonal) and calendar years are not the same thing. The tropical year is a natural phenomenon whilst the calendar year is an artificial construction that tries to emulate the tropical year in length. Unless the calendar is adjusted from time to time (see Section 3.2.1), the seasons and calendar become desynchronised. Partly this is due to the differences between the tropical and calendar years, and problems with measurement. However, the measurement process is complicated and climate is affected by the wobbling of Earth's axis that results in an effect known as the precession of the equinoxes (see Section 3.1.1.3). As this occurs, the relationship of Earth's seasons to the fixed stars, constellations, and perihelion (see below) change over a ~26-ky cycle. Because these astronomical markers on which our calendar are based have natural climatic associations (such as the solar year and lunations), if the calendar system used is finely tuned then precise cyclical returns should result in prominent climatic trends and physical indicators due to both gravitational and solar irradiance/insolation influences.

For these reasons, the history of calendar development is an important component of this study, and will also provide a basis for the conceptual model, described in Chapter Four, which is used to identify and explain the cause of centennial and millennial scale climate cycles. Not all calendars will be discussed, but the ancient Egyptian calendar that hinted at causes of the ~1470-yr climate cycle is integral to this discussion, as well as the Julian and Gregorian calendars (see Section 3.2.1). As we move backwards through time into prehistory, discussion of how we measure time over long periods using radioactive isotopes is extremely important as climate signals become distorted unless our calendar is extremely well-calibrated to the tropical year (Section 3.2). Of particular interest is radiocarbon (^{14}C), beryllium-10 (^{10}Be), and uranium-series dating. Some of these factors have already been discussed in the previous chapter. These discussions will be expanded in this chapter.

3.1 Earth's astronomical setting

3.1.1 The celestial neighbourhood

Within the Milky Way galaxy, our solar system is positioned on an edge of the Orion spur and sits a little above the galactic plane (in the northern galactic hemisphere) and is moving away from it [Figure 3.1]. From a geocentric perspective, the constellation of Orion sits on the outer edge of the

galaxy, whilst the galactic centre is slightly below the ecliptic (Earth's orbital plane) on the galactic equator, in the direction of Sagittarius and close to the edge of the constellation of Scorpio [Figure 3.2]. These two constellations are important markers against which changes caused by precession can be observed. Both Scorpio and Orion are clearly recognisable in the night sky, appearing to sit permanently at the juncture of the galactic equator and ecliptic [Figure 3.3]. Being in the direction of the galactic centre, Scorpio and Sagittarius are obviously in the densest part of the Milky Way and can be seen clearly at night, except in November, December and January while the Sun transits these constellations. Similarly, the constellation of Orion is clearly visible in night skies where the Milky Way stars are sparsest, losing visibility during May and June. This setting of stars forms a convenient reference framework. Whilst the stars we see at night appear to be fixed, over hundreds of thousands of years the appearance of these constellations is slowly changing. However, these changes are so small that we ignore them for the purpose of this research.

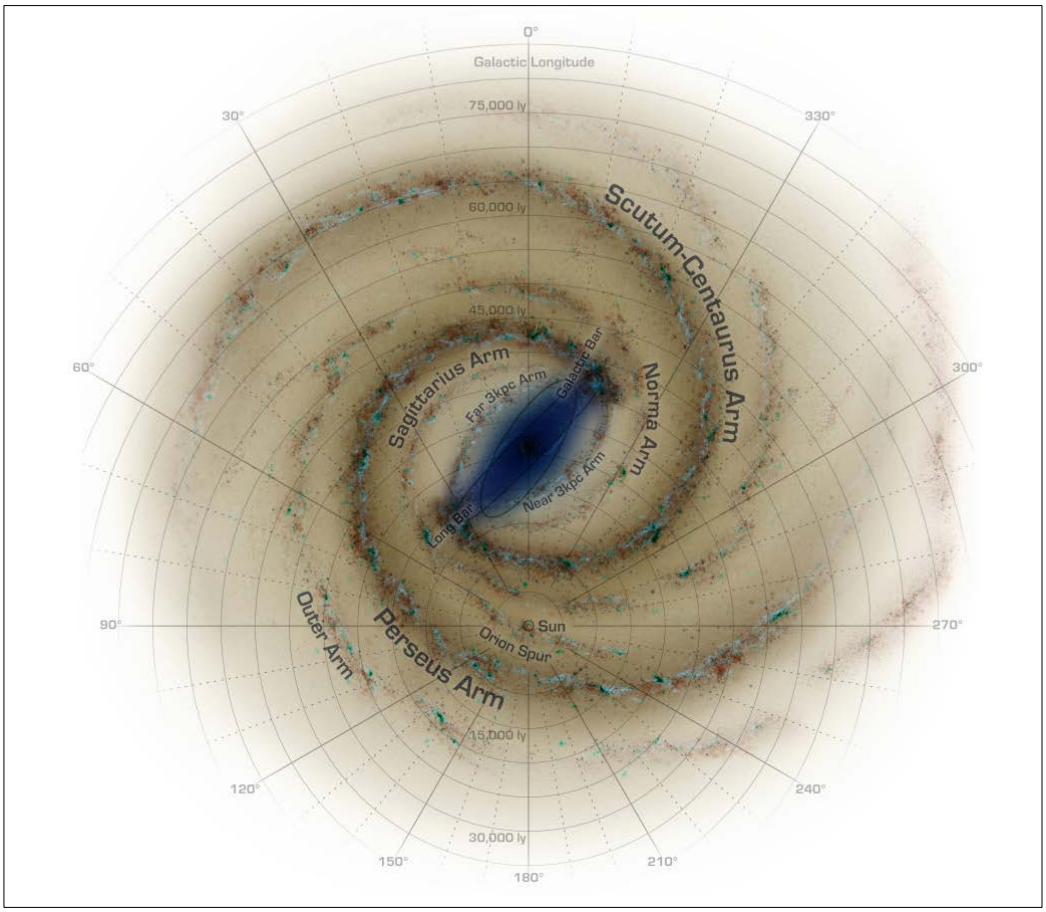

Figure 3.1: Recoloured image of the Milky Way Galaxy showing the position of our solar system in the Orion spur (NASA *et al.*, 2012).

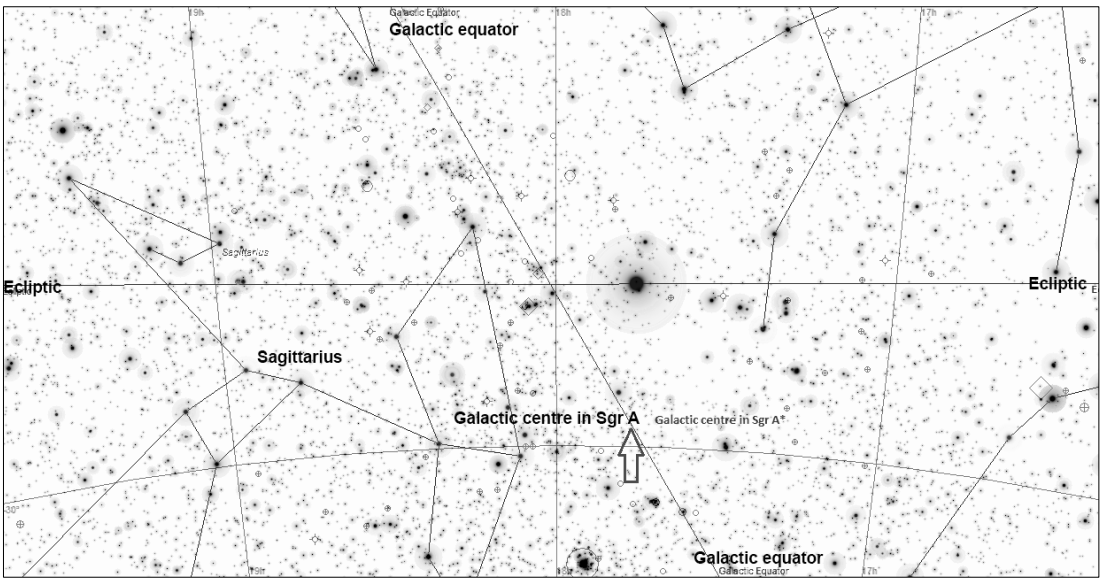

Figure 3.2: The galactic centre is positioned in early Sagittarius, slightly below the plane of the ecliptic. Developed using Skychart 3.5.1 software.

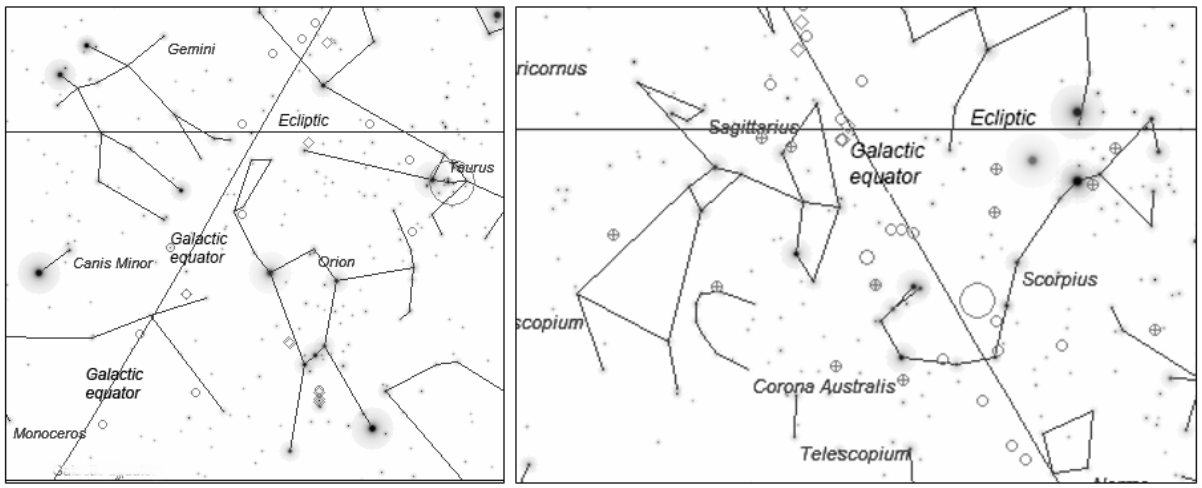

Figure 3.3: The constellation of Gemini, Orion, Taurus cluster around the junction of the ecliptic and galactic equator towards the galactic periphery (left). At the opposite junction of the galactic equator and the ecliptic, towards the galactic centre, sit the constellations of Sagittarius and Scorpio. Both Orion and Scorpio are easily identifiable in the night sky. Images were produced using Skychart 3.5.1 planetarium software.

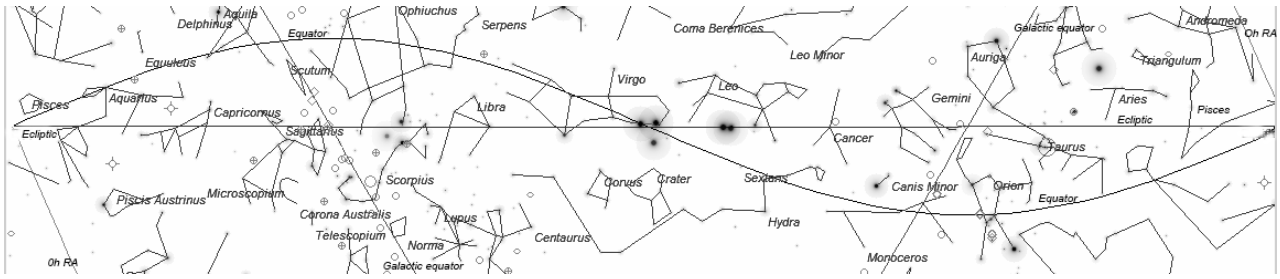

Figure 3.4: The ecliptic, which is the plane of the Earth's orbit or the apparent path of the Sun, runs through the middle of the zodiacal belt. It takes about one synodic month for the Sun to "travel" through each of these zodiacal constellations. The sinusoidal curve is the plane of Earth's Equator.

The time of year when we can see these constellations changes slowly over a 26-ky cycle due to the wobble of the Earth's axis, moving one degree every ~72 yrs (Lowrie, 2007). This cycle is known as the precession of the equinoxes (see Section 3.1.1.3) and the associated effect also causes the Earth's axis to point to a different pole star in different eras. These effects and others occur from the precession of the equinoxes because the stars we see at night are in one frame of reference (sidereal) while Earth is in non-stationary frame of reference (equinoctial) as it moves though it's orbit, and spins and wobbles on its axis. The visibility of constellations is primarily governed by the time of year, as the Sun's presence in close proximity to any particular constellation or star will render it invisible due to daylight. Clearly, this has a stronger influence on the stars banded around the ecliptic than on stars that are closer to the poles. The constellations through which the ecliptic runs comprise the zodiacal belt [Figure 3.4], whilst the stars close to the poles are called circumpolar. The size and location of this circumpolar region is dependent upon the geographical latitude of the observer. For each hemisphere, the circumpolar stars relative to each location never set, and at the poles themselves, the stars just appear to rotate around the pole, never rising or setting. The geographical regions where this occurs is determined by the tilt of Earth's axis (obliquity), which is currently at ~23.5°, also currently defining the Arctic and Antarctic circles at ~66.5° of geographical latitude. As Earth's obliquity changes, so does the location of the Arctic and Antarctic circles, which demark regions exposed to Earth's most extreme climate and seasonal differences due to very long, dark winters and summers without nights.

A third frame of reference is Earth's geographical coordinate system of latitude and longitude, based on Earth's rotation axis and equator. Just as the celestial equator is an extension of the Earth's equator into space, so each geographical longitude has a corresponding celestial meridian. It is by rotation (referenced to a meridian of longitude) that the length of the year is measured relative to external reference points [Figures 3.5 and 3.6]. The mean solar day is defined as the period between two consecutive solar zeniths, whilst the sidereal day is defined relative to the vernal point and is about 3.93 minutes shorter than the mean solar day [Figure 3.5]. The zenith location (which is a position directly overhead of an observer and peculiar to each location) is positioned on the great circle, which is an astronomical meridian that runs through the poles and the nadir [Figure 3.7]. The length of day is not constant and depends upon a number of factors, primarily the gravitational influence of the Sun and Moon. Correspondingly the days are longer than the mean at perihelion and shorter at aphelion. The perihelion and aphelion are respectively the closest and furthest points in Earth's orbit to the Sun, whilst the perigee and apogee are respectively the closest and furthest point in the lunar orbit to the Earth. The length of day is also growing longer very slowly as the Earth's rotation and Moon's angular momentum slow correspondingly due to tidal friction between the Earth and Moon (Lowrie, 2007).

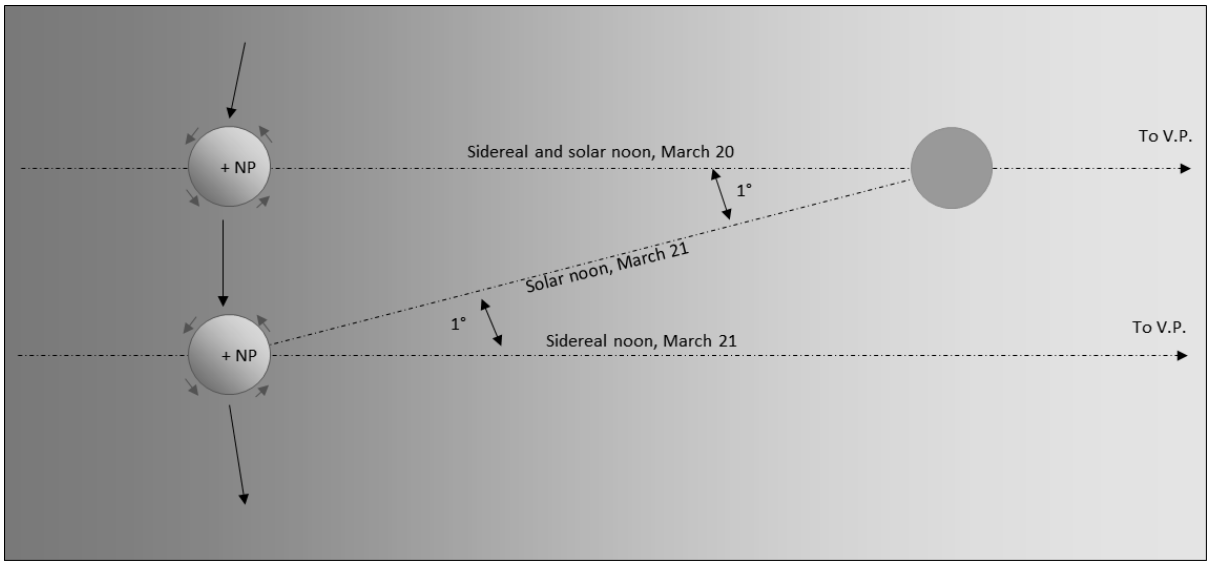

Figure 3.5: Schematic depicting the difference between the sidereal and solar year. The sidereal year is measured relative to the stars and the tropical or solar year is measured relative to the Sun at the vernal point (0hrs RA), which occurs around March 20/21 each year. NP=North Pole. VP=Vernal point. Adapted from Baker (1959).

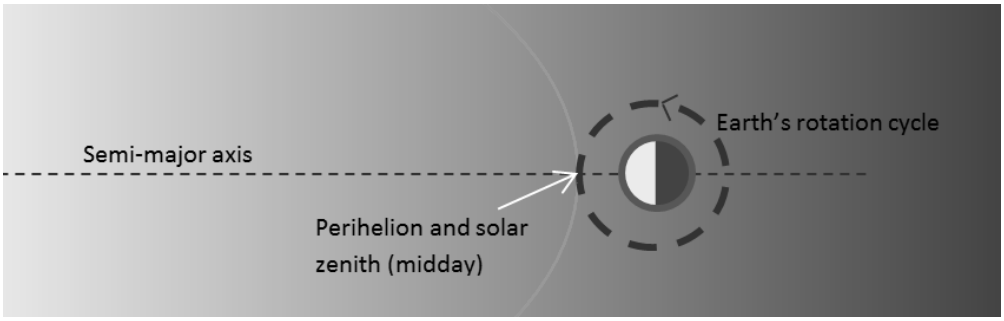

Figure 3.6: The anomalistic year is measured from perihelion to perihelion. This schematic shows the position of the solar zenith at perihelion, which occurs at noon LMT.

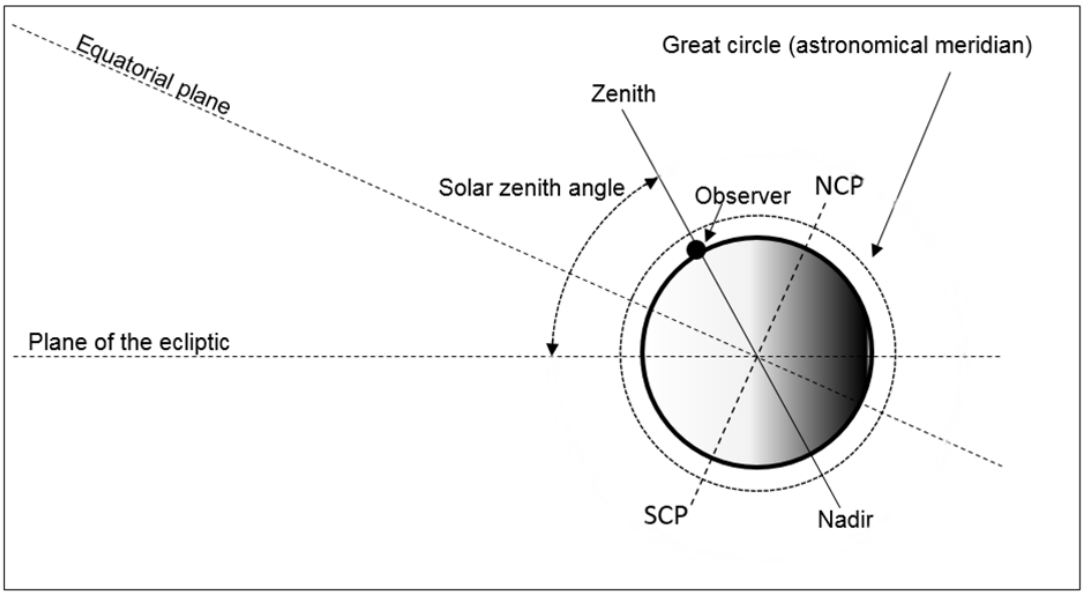

Figure 3.7: Schematic showing the relationship of an observer in the northern hemisphere to the zenith and nadir on the great circle. The solar zenith occurs at noon (local time) when the Sun reaches maximum altitude and is on the great circle relative to the observer. NCP=North celestial pole. SCP= South celestial pole.

All these factors contribute to changing insolation levels experienced at each location on Earth. Diurnal radiation is at its greatest when the sun has reached its maximum altitude on the great circle at solar zenith, whilst maximum heat lags behind by a number of hours. The maximum insolation derived from the length of daylight hours is greatest for each hemisphere at its summer solstice (December in the southern hemisphere and June in the northern hemisphere), and minimum during their respective winter solstices six months later. The extremes of polar climate are affected by Earth's changing obliquity, which is strongly influenced by the Moon's gravitational force (see Section 3.1.4). Precession of the equinoxes is a component of climatic precession known as Milankovitch precession, which is strongest at lower latitudes (Section 3.1.1.5). Earth's orbital eccentricity (Section 3.1.1.1) also influences levels of insolation, solar irradiance, and gravitation and hence climate.

3.1.1.1 Earth's orbit

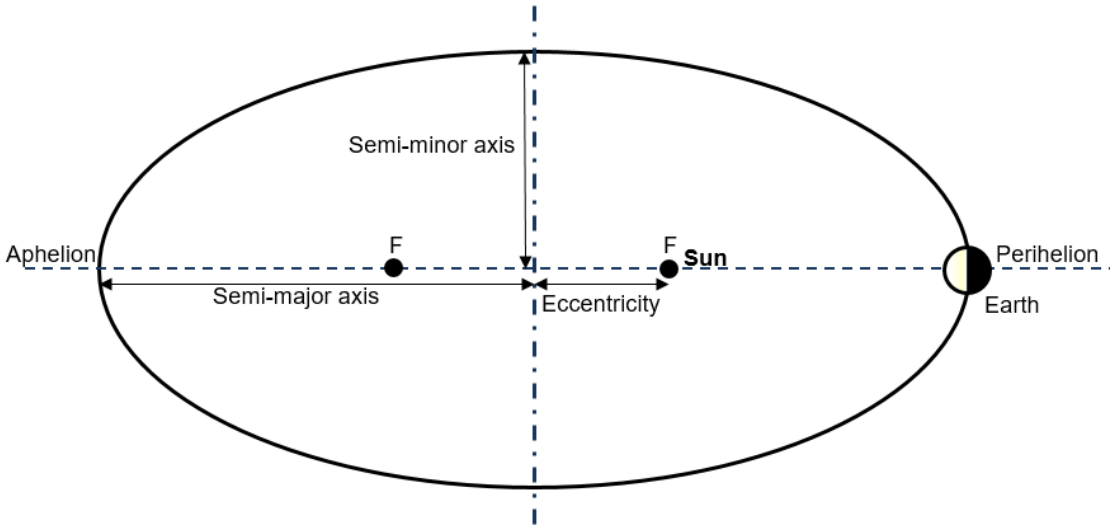

Figure 3.8: Exaggerated schematic of Earth's orbit, showing Earth at perihelion and the sun at one of two foci (F) of the ellipse. The semi-major axis is half the major axis and the semi-minor axis is half the minor axis. Eccentricity is measured along the semi-major axis.

As mentioned in Chapter Two, Earth's orbit is slightly elliptical and the degree of eccentricity varies over a period of about 100 ky, which is superimposed on a 400-ky cycle of eccentricity (Berger, 2009). Eccentricity is the difference (measured along the semi-major axis) of each of the foci to the centre of the ellipse [Figure 3.8], and varies throughout this cycle from near circular (~0.001) to more elliptical (~0.06) (Lowrie, 2007). The 100-ky cycle has been associated with the waxing and waning of the ice ages (Chapter 2) through changing insolation and solar irradiance levels. Earth's eccentricity is currently ~0.01675 (Williams, 2013a) and moving towards a near circular orbit in about 27 ky from now (Berger, 2009). As Earth travels through its orbit, its distance from the Sun changes and, as it does so, the intensity of solar radiation and gravitational forces varies according to the inverse square law. Earth's velocity through its orbital path is not constant, sweeping out equal areas in equal intervals of time (Kepler's 2nd law of planetary motion), thereby moving faster at perihelion and slower at aphelion. Conversely, lunar orbital speed increases at perihelion and slows

at aphelion (Gutzwiller, 1998). The current Sun-Earth distance at perihelion is ~147.09 x 10^6 km, and at aphelion is ~152.1 x 10^6 km, a variation of around 3%. The rate of precession (see below) depends upon the eccentricity and radius of the orbit (Greenberg, 1981). When Earth is at perihelion, it experiences maximum annual solar irradiance and an annual peak in spring tide (Berger, 1991; Lowrie, 2007; Thomson, 1997).

The annual variations in Earth's orbital velocity can also be readily seen in any ephemeris, showing an apparent faster motion of the Sun centred on the perihelion, which currently occurs annually around January 4, and is slowest around July 4 when Earth is at aphelion. Consequently, the intensity of solar irradiance and gravity is not evenly distributed throughout the year but is greatest at perihelion when the Earth is at the closest point in its orbit to the Sun. For these reasons, the measurement of time starting from either equinox will provided a distorted picture of time as the two halves are not equal in terms of precessional rate, as the Earth moves faster through the half year in which the perihelion is situated and slower in the alternate half containing the aphelion. These factors have implications for the measurement of time in palaeoclimatological studies (see Section 3.2) and makes statistical studies of millennial-scale climate cycles trickier (see Chapter 2), with cyclical lengths varying based on the position within the Milankovitch precessional cycle. It also has implications for the levels of solar irradiance and gravitational influences evident in the palaeoclimatic record, which cannot be normally distributed for the purposes of statistical analyses. These issues are also complicated by the fact that the perihelion itself is not stationary moving in a 110-ky cycle known as apsidal precession (Lowrie, 2007) [Figure 3.9] (see Section 3.1.1.4). Currently the perihelion is positioned in the direction of the galactic centre, separated from it by ~13° of arc.

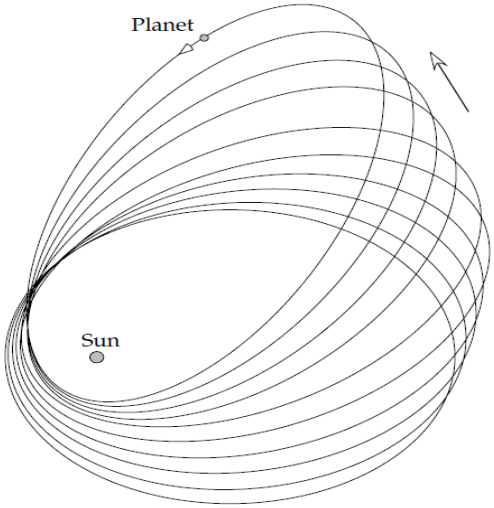

Figure 3.9: Exaggerated schematic of the cyclical 100-ky apsidal precession (Lowrie 2007:59).

3.1.1.2 Obliquity of the ecliptic

Milankovitch demonstrated through his radiation curves that the amount of solar insolation received by a particular geographic location is latitudinally dependent (Chapter 2). As the obliquity changes, so does Earth's orientation to incoming solar irradiance. The more extreme the obliquity, the greater the seasonal variation in temperature and contrast between summer and winter. Obliquity refers to the tilt of the Earth's axis with respect to the plane of the ecliptic, which fluctuates in cyclical

motion over ~41 ky, moving from 22.1° to 24.5° (Lowrie, 2007). This fluctuation arises because of torques imposed upon Earth's equatorial bulge by the Moon and planets such as Jupiter. The positions of the Tropics of Capricorn and Cancer accordingly vary throughout the 41-ky cycle as do the positions of the Arctic and Antarctic circles. Currently the obliquity is ~23.45°. Obliquity therefore affects the angle of incidence of incoming solar insolation [Figure 3.10], with the intensity of insolation being strongest when the Sun has attained greatest altitude on the celestial meridian. This is greatest when the Sun is at the zenith of an observer, which can only occur in the tropics. As the lunar orbital plane is inclined at ~5.145° to the ecliptic, the changing obliquity of Earth's axis also influences the extremes of lunar movement north and south of the equator [Figure 3.10] as well as the gravitational stresses associated with it, and associated wind and oceanic currents.

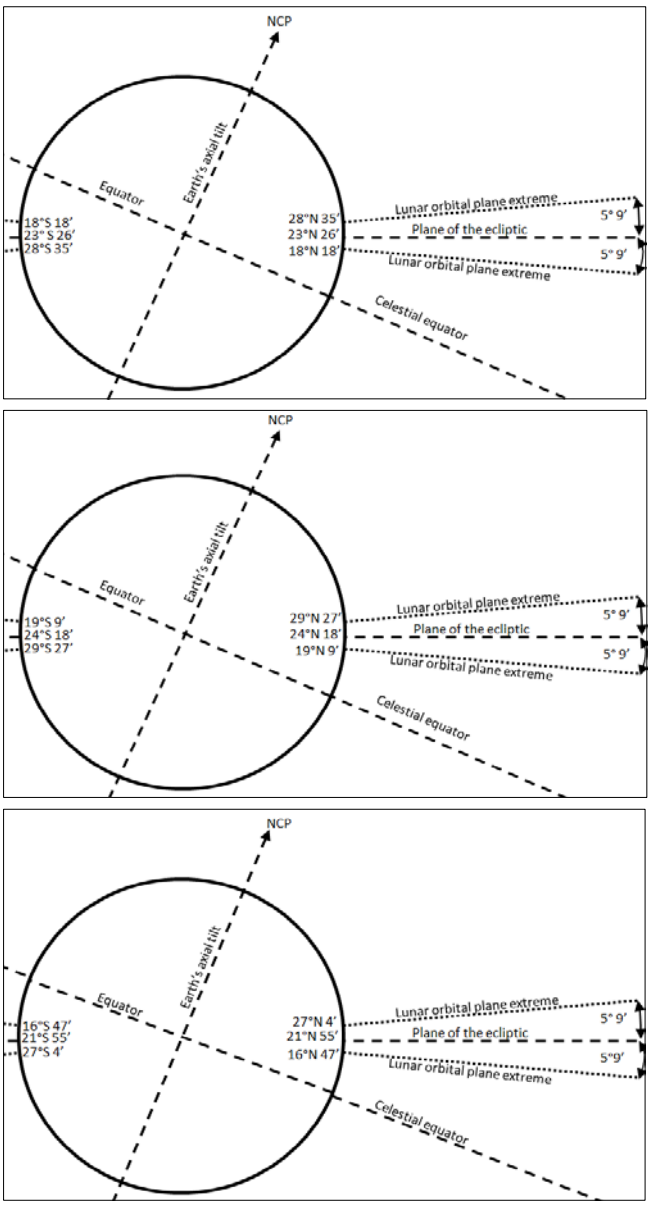

Figure 3.10: Obliquity of the ecliptic: current (top), maximum (middle), minimum (bottom). The changed relationships of the equator to the lunar orbital plane can also be seen. NCP= North celestial pole.

3.1.1.3 Precession of the Equinoxes

Over a ~26-ky cycle the constellations change in relation to the timing of the March equinox and consequently to Earth's seasons [Figures 3.11, 3.12]. The point from which the precession of the equinoxes is measured is known by a number of different names: vernal point, vernal equinox, March equinox, or first point of Aries (despite becoming disassociated from the beginning of the constellation of Aries due to the precessional effect). Whilst it has a number of different names, there is only one definition of this event: the vernal equinox occurs when the Sun moves from southern declination (measured with respect to the celestial equator) to northern declination, which occurs annually around March 21 at 0hrs right ascension (RA). The celestial equator is the extension of Earth's equator into space, and RA is an angular measure of distance of the vernal equinox relative to the celestial equator. A simplified graphical representation of a portion of equinoctial precessional can be seen in Figure 3.13.

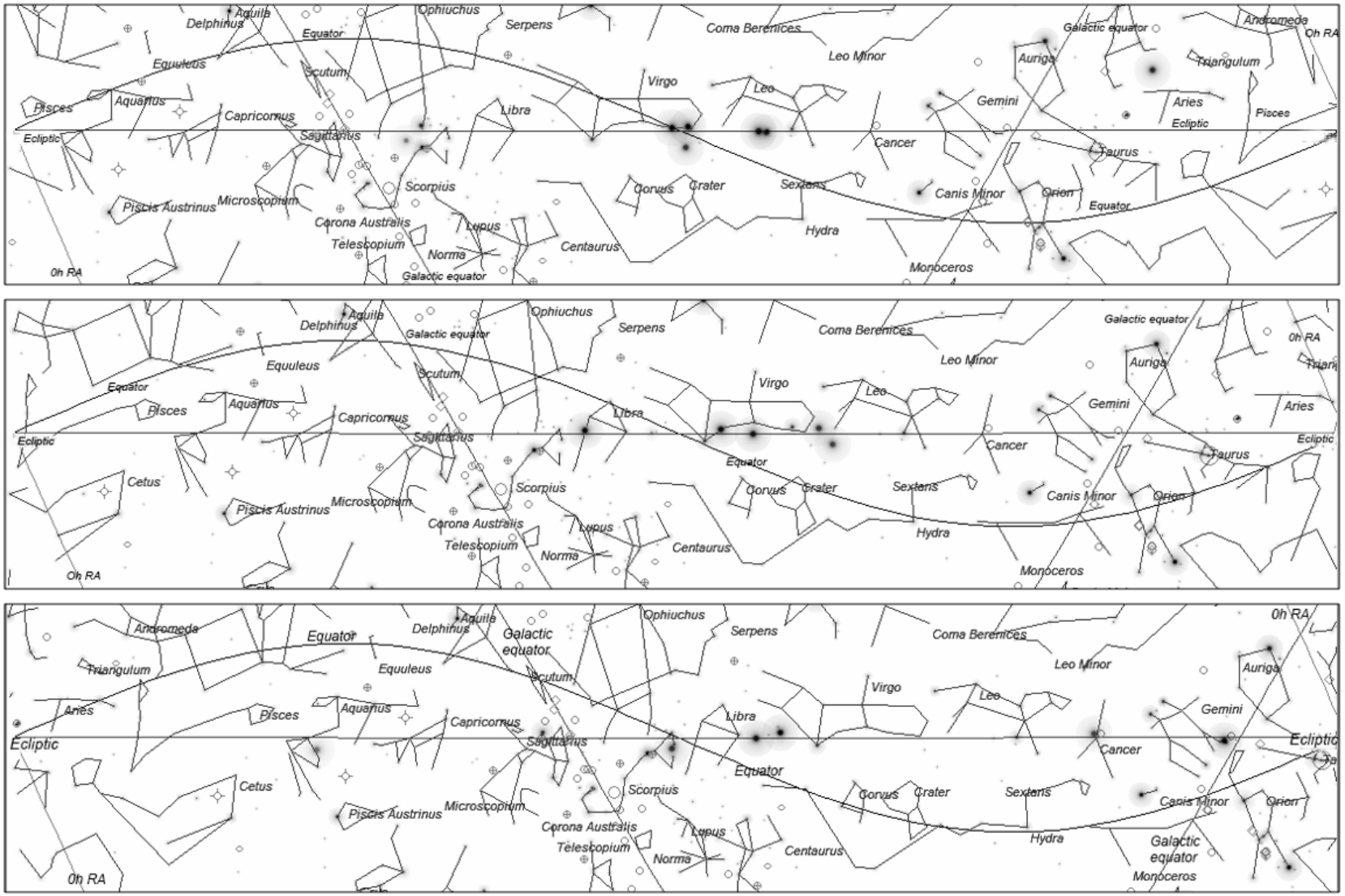

Figure 3.11: The visual effect of precession (part 1). The sinusoidal curve in these images is the celestial equator. The fixed wave form of this pattern appears to move along the ecliptic in this depiction, changing the relation of the seasons relative to the zodiacal belt. 0hr RA shows the position of the March equinox. The top panel is the current geocentric perspective of Earth's seasons to the stellar orientation. The middle panel is the perspective ~2.2 kya and the bottom panel 4.4 kya. The March equinox occurs when the Sun is in late Pisces (top), Aries (middle), Taurus (bottom). The constellations "appear" to be moving along the ecliptic. Image developed from planetarium software (Skychart 3.5.1).

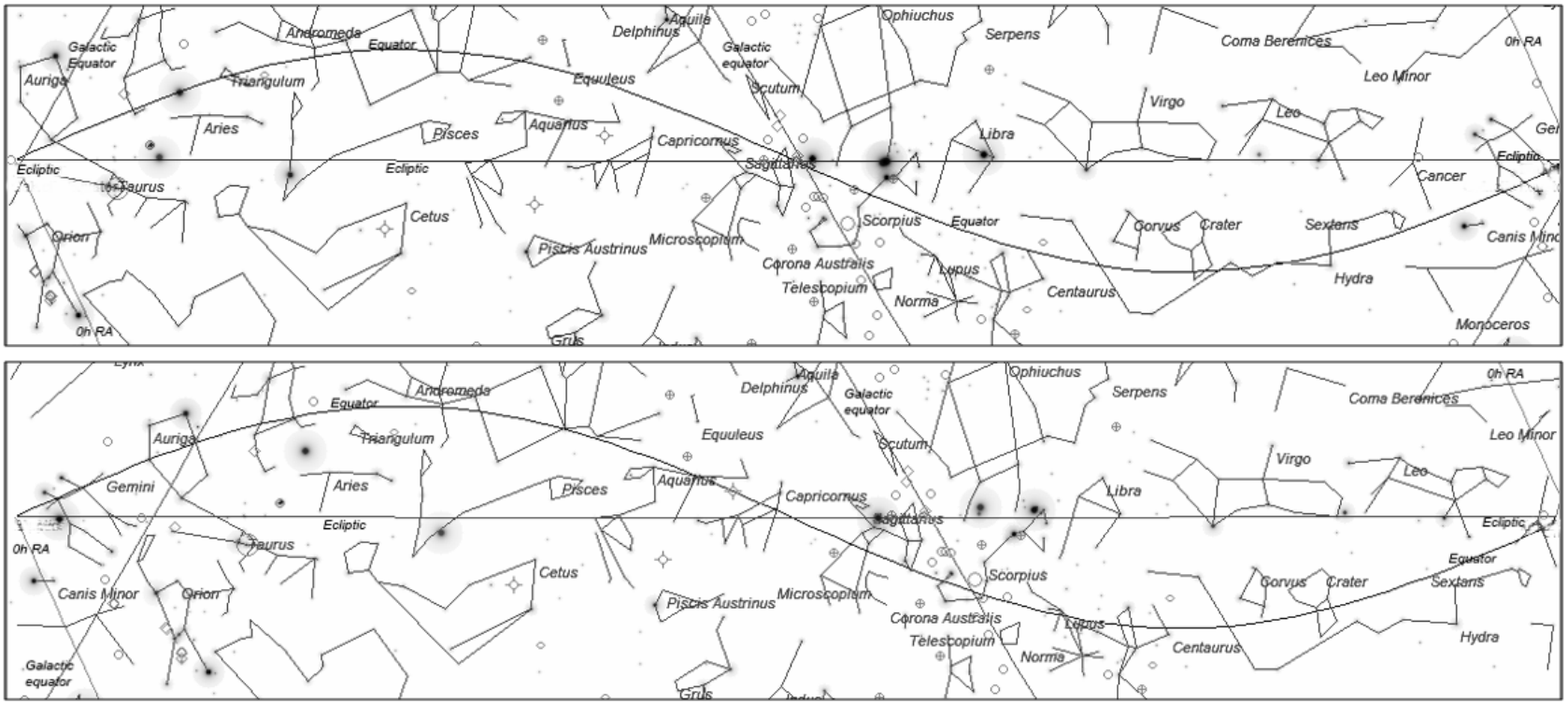

Figure 3.12: The visual effect of precession (part 2). The sinusoidal curve in these images is the celestial equator. The fixed wave form of this pattern appears to move along the ecliptic in this depiction, changing the relation of the seasons relative to the zodiacal belt. 0hr RA shows the position of the March equinox. The top panel is the geocentric perspective of Earth's seasons to the stellar orientation 6.6 kya and the bottom panel 8.8 kya. The March equinox occurred when the Sun was in Gemini (top) and Cancer (bottom). The constellations "appear" to be moving along the ecliptic. Image developed from planetarium software (Skychart 3.5.1).

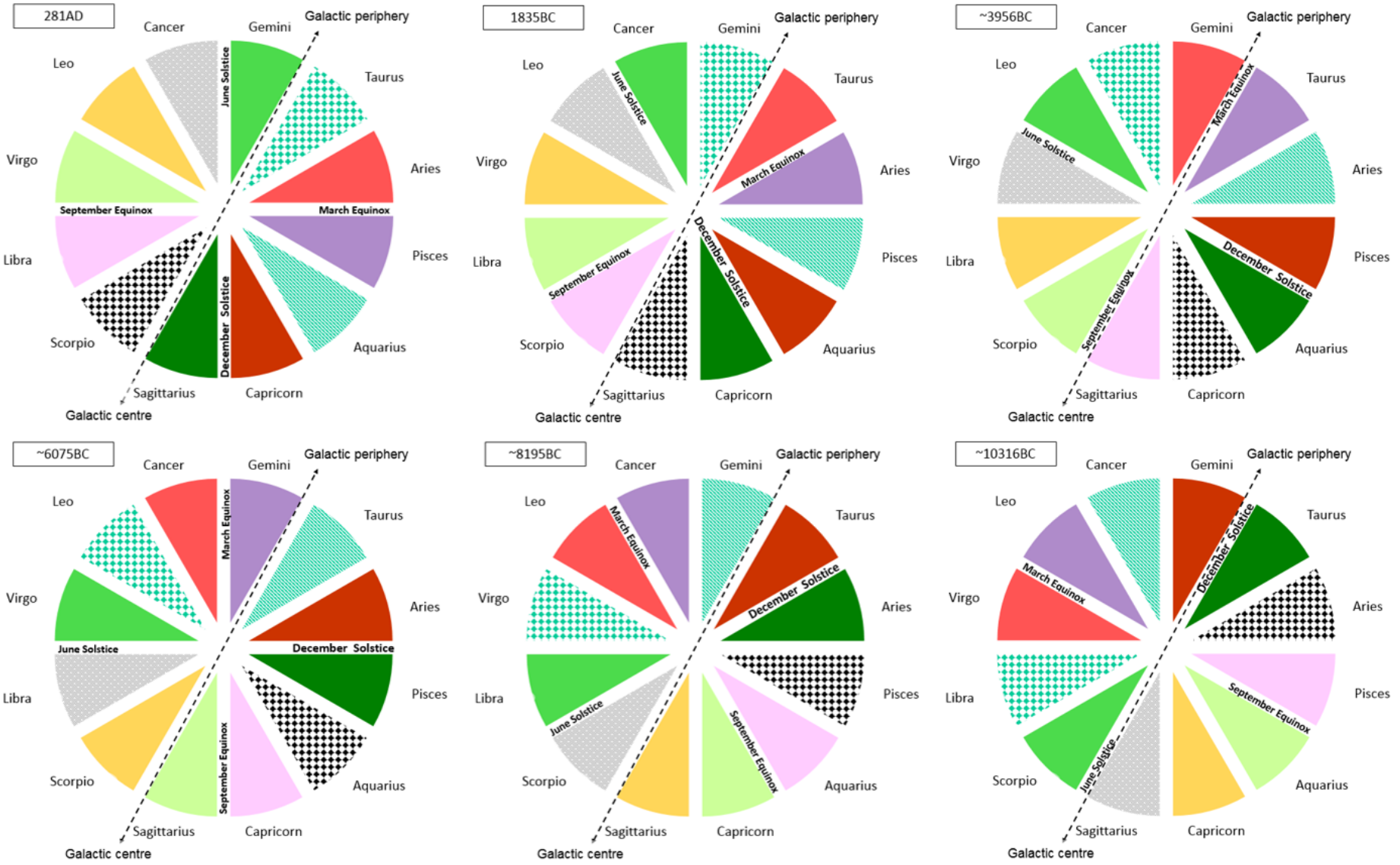

Figure 3.13: Schematic of the precession of the equinoxes relative to the sidereal framework, showing the changing relationship of the seasons to the zodiacal constellations.

The visual effect of precession [Figures 3.11, 3.12] is that in one era, the constellation Aries rises before dawn at the northern spring equinox in March and, in the next era more than 2 ky later, the adjacent constellation of Pisces will seem to have replaced it, and so on until a return to the starting point. Therefore, the monthly and seasonal relationships to the band of zodiacal constellations change. This proved perplexing as ancient astronomers struggled to measure the year precisely (see Section 3.2.1). The last time that the March equinox matched the beginning of the first zodiacal constellation, Aries, occurred ~280AD.

3.1.1.4 Apsidal precession and the perihelion

Along with the precession of the equinoxes, an important factor in Milankovitch precession is apsidal precession (see next section). The apsides are located on the major axis of Earth's orbit and are the perihelion and aphelion [Figure 3.8]. These apsides precess in an open-ended cycle [illustrated in Figure 3.9], moving in opposite direction to the equinoctial precession and in the same direction as the Sun's apparent path through the zodiacal constellations and Earth's rotational vector [Figure 3.14]. As discussed above, due to equinoctial precession the March equinox moves in retrograde motion along the ecliptic, travelling in the opposite direction of the Sun's apparent progress through the tropical year [Figures 3.11, 3.12, 3.14]. In other words, the March equinox moves backwards through the months.

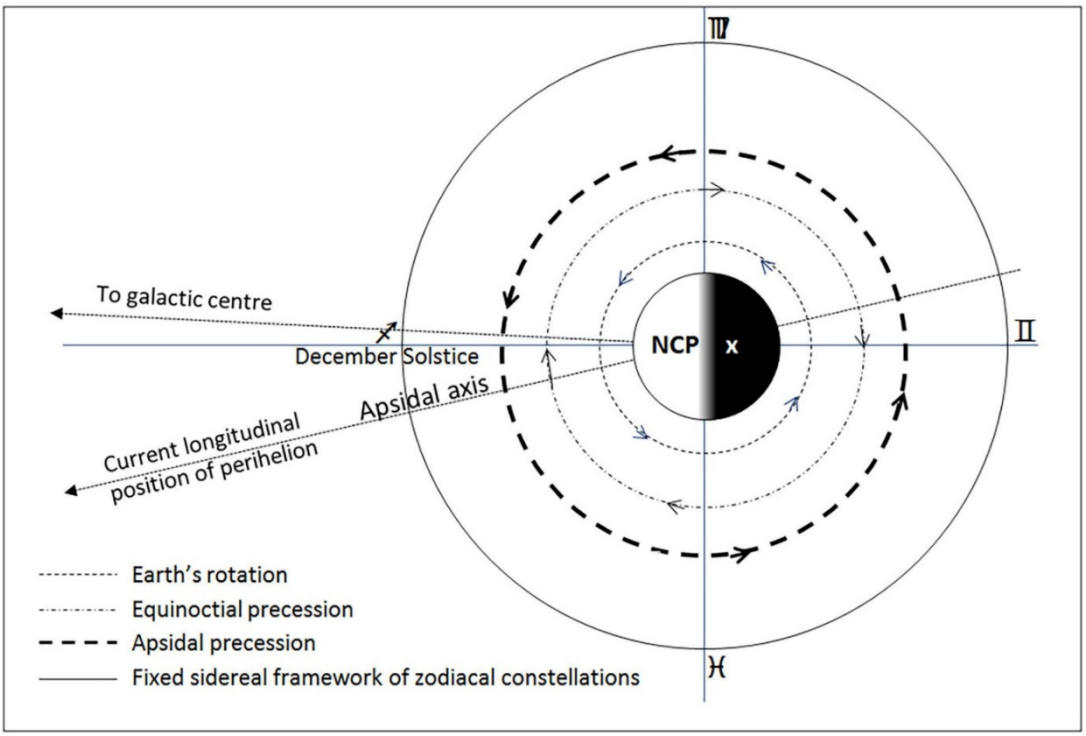

Figure 3.14: Schematic depicting the different vectors associated with equinoctial and apsidal precession. NCP= North celestial pole. Astronomical symbols for constellations, starting at top of circle and moving clockwise are Virgo, Gemini, Pisces, Sagittarius (NASA, 2016).

3.1.1.5 Understanding the Milankovitch cycles

As discussed in Chapter Two, the Milankovitch cycles account for prominent variations in solar irradiance received at the top of Earth's atmosphere. Earth's climate system is clearly driven at orbital scales of time by the eccentricity of Earth's orbit, obliquity, and precession. However, the ~21-ky Milankovitch precessional cycle, with its variants of ~19 ky and ~23 ky, is not the same as the ~26-ky precession of the equinoxes. The Milankovitch precessional cycle results from the interaction between Earth's ~110-ky apsidal and ~26-ky equinoctial precessions in which the relationship between the solstices and perihelion is continually changing (Berger, 1977; Imbrie and Imbrie, 1979; Imbrie *et al*., 1984). Figure 3.15 shows a schematic of these two precessional cycles, resulting in the Milankovitch climatic precessional cycle where the combination of two or more non-linear periodicities leads to amplitude modulations (cf. Damon and Sonett, 1991). The Milankovitch climatic precession can thus be seen as an interaction between the tropical year (i.e. time between solstices or equinoxes, and hence associated with the seasons) and the anomalistic year (time between perihelia) [Table 3.1]. Precession shapes the timing and patterning of irradiance and insolation patterns within the palaeoclimatic record, and is itself the result of multiple factors [Figure 3.16]. A simplified relationship between the seasons and perihelion as an expression of the Milankovitch precessional cycle is seen in Figure 3.17.

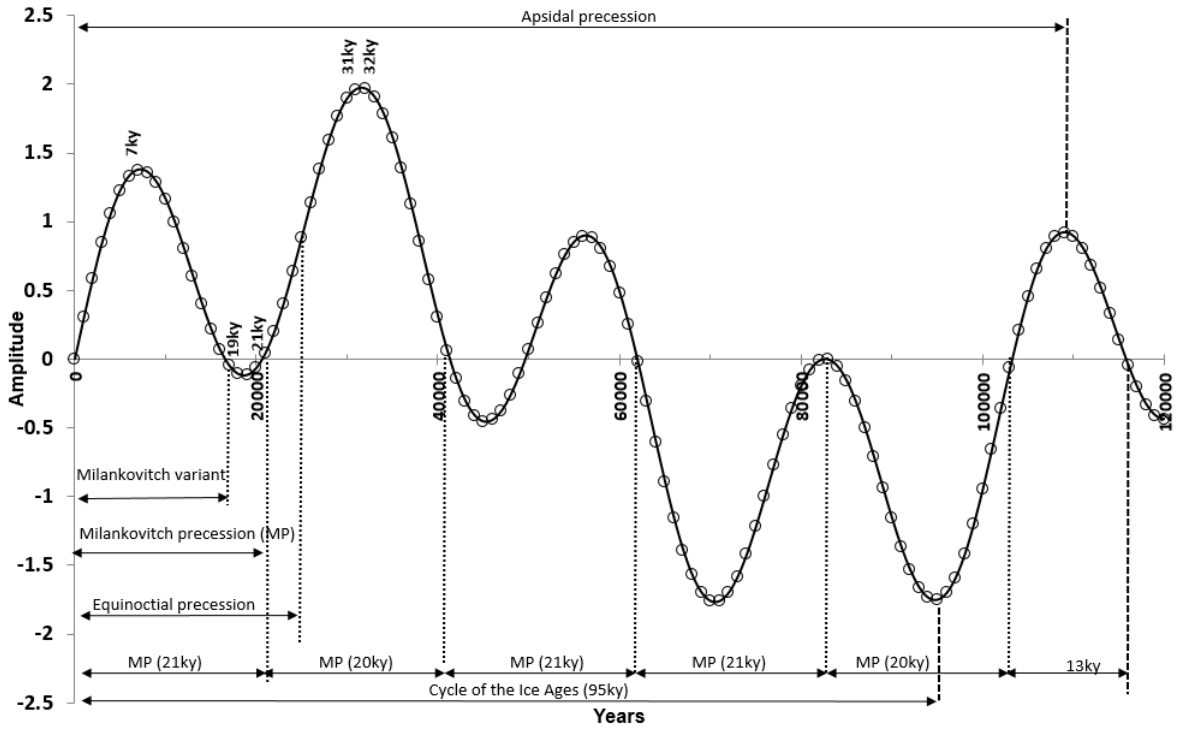

Figure 3.15: A schematic of graphed interaction of the apsidal and equinoctial precessions based on their superimposed sine curves, showing variations in amplitudes and variances in the length of the Milankovitch cycles as a function of their interaction. This schematic does not allow for variations due to changes in orbital velocity. The y-axis is a measurement of amplitude, MP= Milankovitch precessional period. The Milankovitch precessional cycle has a mean length of ~21 ky, with variants of ~19 ky and ~23 ky.

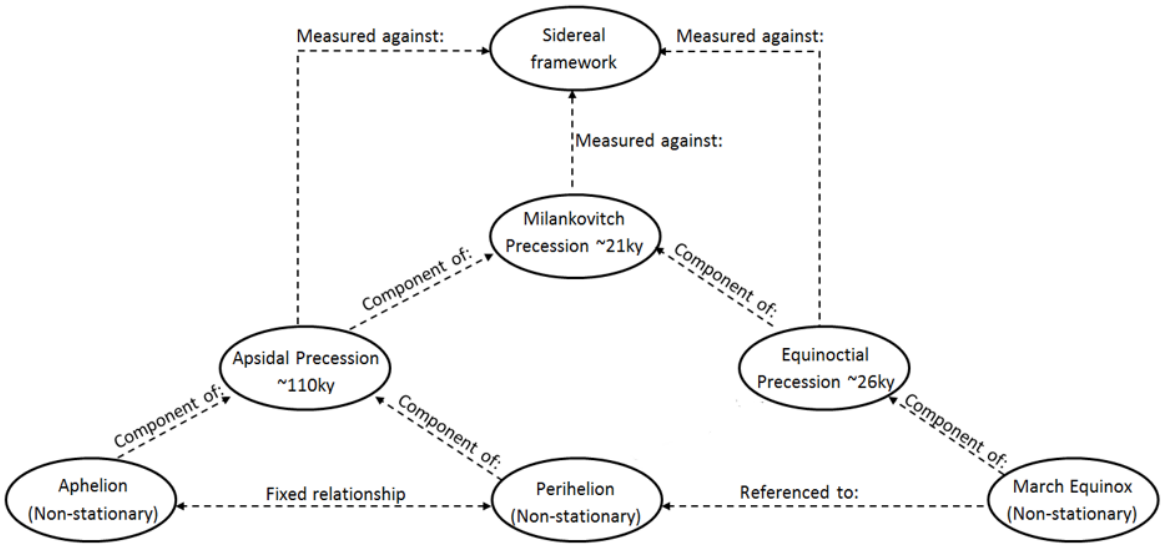

Figure 3.16: Schematic showing the multifactor contributions to the Milankovitch precessional cycle in context of the sidereal framework.

Table 3.1: Different year types. To complete the full year, Earth's rotation overshoots by ~a quarter of a daily rotation. The third column shows this residual in hours.

Year types	Length (days)	Residual Hrs
Anomalistic	365.2596	6.231264
Sidereal	365.2564	6.152641
Tropical	365.2422	5.812778
Julian	365.25	6.00
Gregorian	365.2425	5.82

The changing relationship between the perihelion and the tropical year therefore influences climatic variability at precession-type time scales. Proximity to the perihelion increases the intensity of solar irradiance and gravitational forces experienced by Earth, which is also influenced by the eccentricity of Earth's orbit (Berger, 1977). Equinoctial precession affects the timing of peak annual solar irradiance with respect to the seasons, the intensity of which is determined by the declination of the Sun (influenced by obliquity), and the amount of insolation received via daylight hours due to the season. The Milankovitch precessional signatures are found in isotopic and palaeomagnetic records, along with millennial-scale signals already discussed (Chapter 2), with obliquity signals stronger at the poles and precessional signals affecting all latitudes (Berger, 2009). Berger *et al.* (2006) also identified ~11-ky and ~5.5-ky precessional-related signals through mathematical modelling. This model considered the biannual occurrence of the Sun directly over the tropics at the equinoxes. The resulting interaction between the equinoctial and apsidal precessions is associated with different hemispheric impacts, which is consistent with the theory of a climatic bipolar seesaw that sees warming in the Antarctic with cooling in the Arctic and *vice versa* (Summerhayes, 2015; Chapter 2). As can be seen from Figure 3.15, it is also responsible for the differing intensities and duration of climate variation throughout the glaciological cycles.

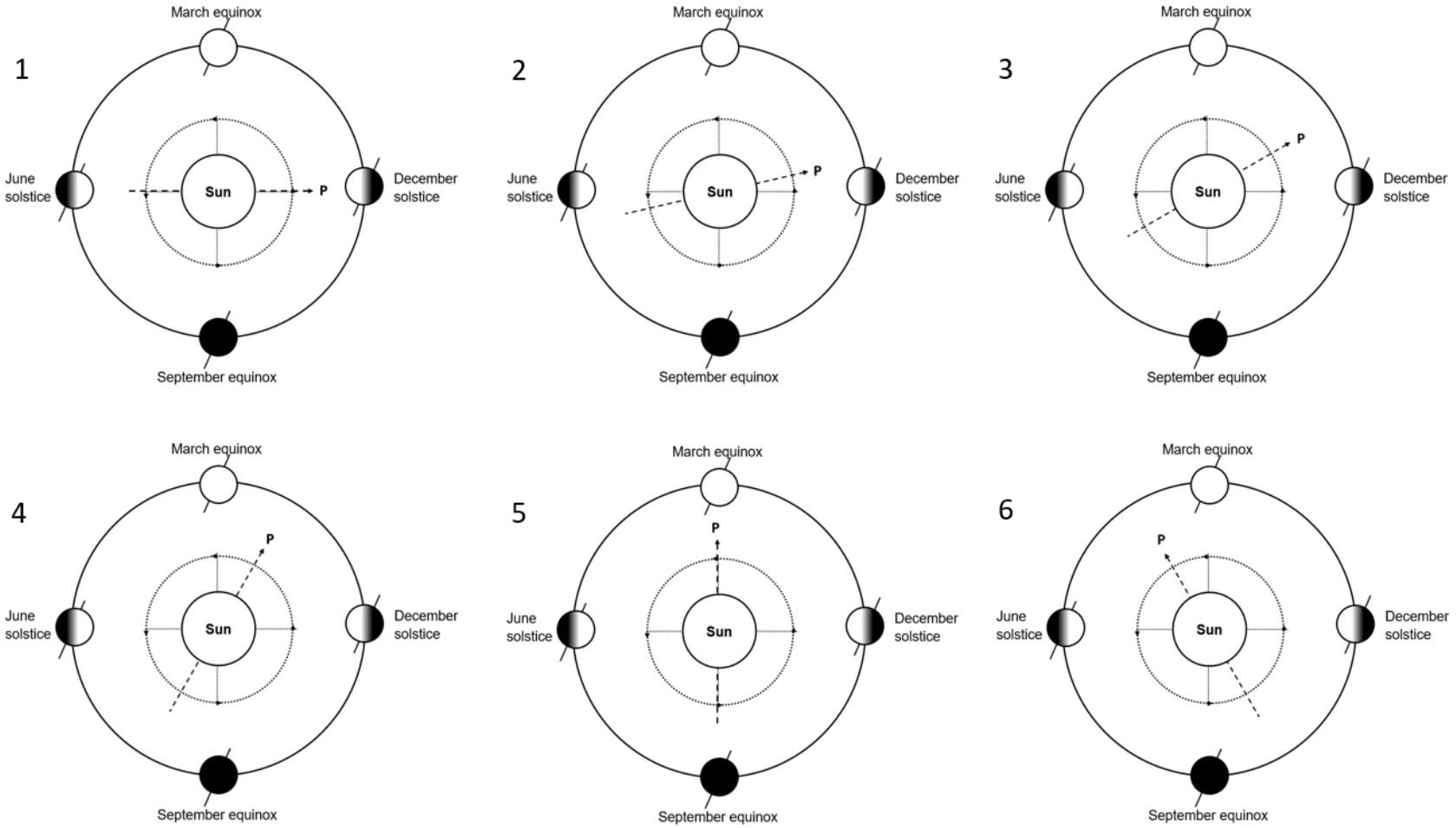

Figure 3.17: Simple schematic of Milankovitch precessional cycle showing the changing seasons and months relative to the perihelion over vast expanses of time. In this depiction, the seasonal clock is moving in an anti-clockwise motion as there is movement back through time. The mean interval for movement of 30°over a 21-ky cycle is ~1750 yrs.

3.1.2 Cosmic rays

Cosmic rays play an important role in the patterning of Earth's palaeoclimatic record. This radiation consists of streams of accelerated particles travelling at velocities close to the speed of light (Butt, 2009; Hathaway, 2010; NASA Astrophysics, 2013; Svensmark and Friis-Christensen, 1997). These particles consist mostly of hydrogen nuclei, but are also supplemented by electrons, positrons, and the nuclei of other elements (Butt, 2009; Comins and Kaufmann, 2008; Hathaway, 2010). Whilst their origins are still not clear and there is much that is unknown about them, we do know that the majority of cosmic rays are generated within the Milky Way galaxy (Hand, 2010).

These cosmic rays continually bombard Earth's atmosphere, producing radioactive isotopes that find their way into the palaeoclimatic record where they have been used in radiometric dating (Libby, 1960; Hathaway, 2010; see Section 3.2.2). When cosmic rays impact Earth's upper atmosphere, various radiogenic isotopes are produced, such as ^{14}C and ^{10}Be (Hathaway, 2010; Linick *et al*., 1989; Stuiver and Braziunas, 1989). Radiocarbon (^{14}C), which was the first of these isotopes to be used as a chronological tool, works its way through the biosphere via the carbon cycle, eventually being deposited in the palaeoclimatic record (Libby, 1960; Linick *et al*., 1989; Stuiver and Braziunas, 1989). The rate at which cosmic rays reach Earth is modulated by the interplanetary magnetic field (see following section). Whilst cosmic ray induced ionisation in Earth's atmosphere has been suggested to affect cloud formation and climate (Svensmark and Friis-Christensen, 1997), this assertion was disputed and not strongly supported (Laut, 2003; Vieira and da Silva, 2006). Svensmark *et al.* (2017) counterargued that ionisation substantially amplifies the small aerosol nucleation rate, lowering the potential loss of aerosols, and enhancing the survival of these aerosols to sizes essential for cloud formation. These assertions were demonstrated experimentally and theoretically.

3.1.3 Sunspots and the solar wind

The solar wind is a highly-energised stream of particles (Eddy, 1976; Stuiver and Quay, 1980; Hathaway, 2010; USGS, 2013) that produces an interplanetary magnetic field characterised by variable intensity (Lowrie, 2007). This solar wind is of lower energy than cosmic radiation (Butt, 2009). The solar wind modulates the cosmic ray flux, with the strength of the solar wind connected to both the strength of the Sun's magnetic field and solar luminosity (cf. Hathaway, 2010, Charbonneau, 2005), the latter of which is a measure of the Sun's power. Solar luminosity is weakly variable over the length of the ~11-yr sunspot cycle and therefore has an inferred connection to the sunspot cycle (Damon and Sonett, 1991). No such links are known to other cycles longer than this cycle (Damon and Sonett, 1991; Hathaway, 2010). Both sunspots and the solar wind are produced by fluctuations in the Sun's magnetic field. High solar magnetic activity is associated with solar flares, coronal mass ejections (CMEs), increased sunspots, and stronger solar wind, lowering radiocarbon production in Earth's atmosphere (Hathaway, 2010). Low solar activity is is associated with high-

speed solar wind streams emanating from coronal holes. Earth's atmosphere is significantly affected by the cyclical solar emissions associated with the sunspot cycle, with heating of the atmosphere associated with increasing atmospheric temperature and density (Hathway, 2010). At times of high solar activity, low energy cosmic rays (mostly protons) are more likely to be deflected by the interplanetary magnetic field, reducing the flux of the lower energy cosmic rays arriving at Earth.

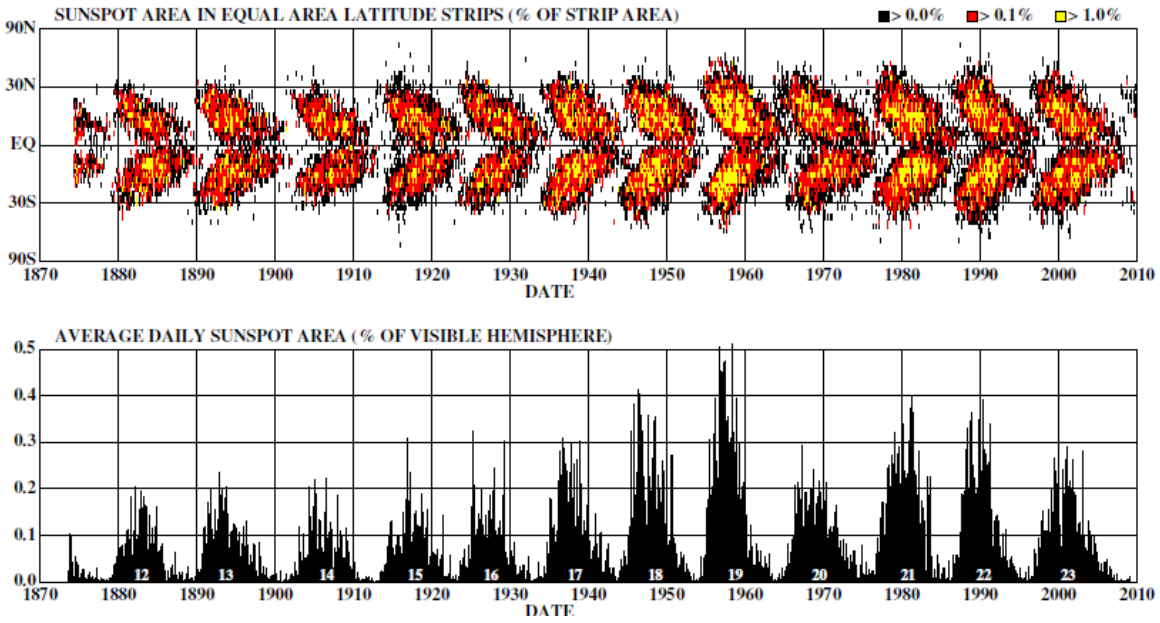

Figure 3.18: Sunspot activity does not occur randomly but forms butterfly patterns that are bounded by the 30° bands north and south of the solar equator (upper panel) (Hathaway, 2010:13). Sunspot numbers are shown as a function of time in the lower panel and are averages of daily sunspots since May 1874.

Sunspots are relatively cooler areas of the Sun's photosphere resulting from the Sun's differential rotation and its magnetic field, occurring in a semi-regular ~11.4-yr cycle (Schwabe cycle), during which numbers increase from minima to maxima and back again (Stuiver and Quay, 1980; USGS, 2013; Comins and Kaufmann, 2008; Hathaway, 2010). Their numbers and locations change during this cycle, moving from higher solar latitudes (~30˚N/S) toward the solar equator [Figure 3.18]. At the end of the 11.4-yr Schwabe cycle, the magnetic field polarity reverses, so that a complete sunspot cycle occurs every 22.8 yrs, called the Hale cycle. The polar fields reverse at sunspot maxima, and are at their strongest at sunspot minima (Babcock, 1959; Hathaway, 2010).

Earth's geomagnetic field deflects most cosmic rays and charged particles within the solar wind away from the Earth (Jordanova, 2017). At the interface of Earth's magnetic field and the interplanetary magnetic field are the Van Allen radiation belts. This is an area of magnetic reconnection where charged particles from the solar wind and Earth's atmosphere are accelerated to form the outer Van Allen radiation belts (Jordanova, 2017). The inner Van Allen radiation belts are created by ionisation of Earth's atmosphere by cosmic rays. Acceleration of particles (mostly electrons) in this region can be leaked through the magnetic field at the poles, where collisions with the atmosphere create aurorae (Jordanova, 2017). Whilst auroras occur constantly, the intensity of these displays is amplified by

magnetic storms that are triggered by CMEs and events linked to the solar cycle. Consequently, auroral records are important sources of information about historical sunspot activity (cf. Eddy, 1976).

Chapter Two reviewed evidence of the sunspot cycle in various climatic data. Following Suess' (1955) discovery of anthropogenic impact on atmospheric ^{14}C, the connection between colder climate and low sunspot activity was made based on minimal sunspot activity during the LIA. These efforts involved a number of researchers, including de Vries, Eddy, Stuiver, Quay, and Kocharov (Damon and Sonett, 1991; Eddy, 1976). However, the study of sunspots began much earlier. Towards the end of the LIA, Heinrich Schwabe's amateur interest in sunspot numbers over a short period in the early 19th century resulted in the discovery of a ~10-yr cycle between maxima (Eddy, 1976; cf. Hathaway, 2010). Stimulated by this finding, astronomer Rudolf Wolf extended the inquiry over a longer range by reviewing historical data, as well as organising an united European effort of observation by 1848 (Eddy, 1976; cf. Hathaway, 2010). Wolf's efforts also included standardising the recording of contemporary and future sunspot numbers (Eddy, 1976). In 1893 Walter Maunder, who continued Gustave Spörer's research following his death, noted that during a period of extreme cold in Europe and drought in NW America (1645-1715), no sunspots occurred. However, the issue is complex as ^{14}C fluctuations still occurred during the Maunder Minimum when sunspots were absent for a significant time (~70 yrs) (Damon and Sonett, 1991; Eddy, 1976; cf. Hathaway, 2010) Figure 3.19 shows the near absence of sunspot activity during the Maunder Minimum.

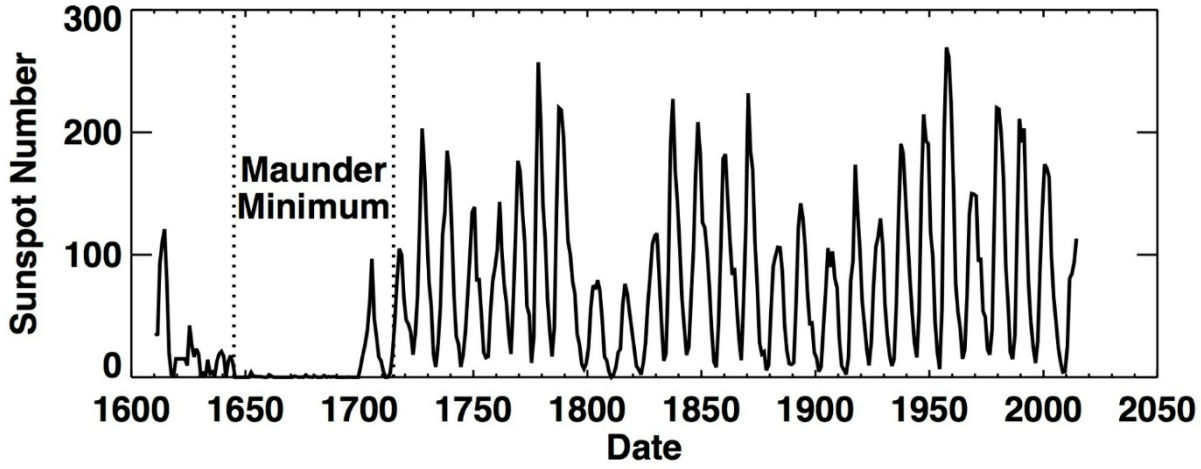

Figure 3.19: Sunspot activity since 1600AD, showing the Maunder Minimum (Hathaway, 2015).

In research to investigate long-term sunspot activity, records of historical sunspot observations in the Orient were important because they were more extensive than the patchy and inconsistent European records (Eddy, 1976). These oriental records, which stretch back to the 7th century AD, gave weight to the veracity of the European sightings and were able to identify increased sunspot activity and auroral activity during the Medieval Warm Period (~900-1310AD) (Damon and Sonett, 1991; de

Vries, 1958 cited in Eddy, 1976). Corresponding levels of global sightings of aurorae reinforced the connection between low solar output and sunspot activity during the LIA (Eddy, 1976).

3.1.4 The Moon, lunations and eclipses

The gravitational and climatic influence of the Moon is substantial. As discussed in Chapter 1, the development and maintenance of life requires stability such as circular orbits. However, the Moon is also a major contributor, stabilising the tilt of Earth's axis and consequently the seasons. Its effects on climate can be seen though the precession, as is the case with the Milankovitch precessional cycle. The Moon influences the timing of the perihelion; nutation and precession; it drives atmospheric and oceanic tides, and influences tidal heights; and, acts as a brake on Earth's rotation rate. As Earth rotates through the ellipsoidal-shaped tidal deformations created by the Moon, associated diurnal tides occur that are also influenced by Earth's obliquity (Lowrie, 2007). The obliquity influence causes the tides to be unequal at different latitudes, resulting in equal semi-diurnal tides at the equator, only one diurnal high tide at extreme latitudes, and unequal semi-diurnal tides between these two extremes [Figure 3.20]. Both the obliquity cycle and the lunar orbital plane influence the maximum latitudinal extent of these tides, with the Moon maximising or minimising the influence of obliquity because its plane is inclined at ~5° to the ecliptic [Figure 3.10]. Bond *et al.* (1997) found that icebergs drifted up to 5° further south into the North Atlantic Current at the time of Bond IRD events, disrupting the thermohaline current. Could there be an association between the inclination of the lunar orbital plane to the ecliptic and the extent of the IRD drift in Bond events? Apart from creating gravitational tidal deformations, the Moon is also tidally-deformed by both the Sun and Earth and its rotation is affected by solar gravitation (Lowrie, 2007). When Earth is at perihelion, lunar orbital velocity slows; at aphelion it increases (Gutzwiller, 1998). The vertical alignment of lunar orbital plane also straightens a little each synodic month as it "faces the Sun" (Gutzwiller, 1998:602).

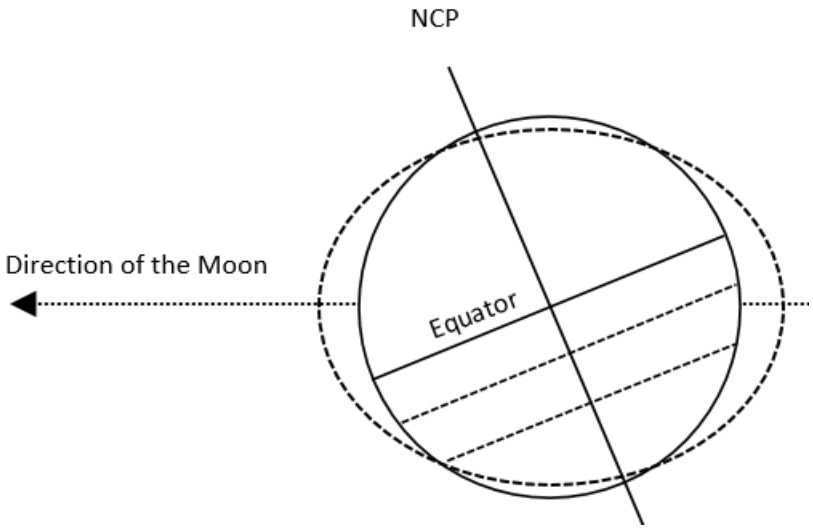

Figure 3.20: Depiction of the influence of the Moon and obliquity on Earth's diurnal/semi-diurnal tides. The dashed line shows the tidal distortion. NCP is North Celestial Pole. The different tidal heights and frequency can be seen at different latitudes.

The gravitational forces acting on Earth are strongest at New and Full Moon, being greatest at lunation. The closest of the Sun-Moon-Earth alignments result in eclipses at the lunar nodes,

enhancing gravitational forces on Earth. These nodes occur at the intersection of the lunar orbital plane and the ecliptic, rotating backwards with the lunar orbital plane through the zodiacal constellations over a period of ~18.63 yrs (Espenak, 2012a, 2012b). The north lunar node is the position where the Moon crosses the ecliptic on its northward journey. Whilst an association has been made between tidal cycles and lunar nodes, the gravitational potential of the lunar nodes is not fulfilled until the Moon is collocated with them, resulting in eclipses. For example, as discussed in Section 2.2.2.3, every 18 yrs 9-11 days the Saros cycle brings a solar eclipse to approximately the same part of the heavens as the previous eclipse (separated by ~10° celestial longitude from its previous position).

The Metonic cycle is equal to 19.0002 tropical years (18.9992 Julian years), i.e., ~2 hrs every 19 yrs, or one day over 228 yrs (O'Neil, 1975; cf. Munk *et al*., 2002), which is close to the mysterious 225-yr companion of the SdV cycle in radioisotopic spectral signals (Section 2.2.3). A more accurate integration between solar and lunar cycles is the 76-yr Callipic cycle, equivalent to 75.9994 tropical years, which was attributed to the ancient Greek astronomer, Kallippos, who was also investigating climatic phenomena in association with astronomical events (Bowen, 2013; Goldstein and Bowen, 1989). The Callippic cycle (which is used to integrate solar and lunar calendars) is a multiple of the Metonic cycle, with a reduction of one day over 76 yrs (Bowen, 2013). This cycle's length is close to the length of one of the spectral signals in climatic data identified as the Gleissberg cycle (cf. Damon and Linick, 1986; Hathaway, 2010; Morner, 2013). Through their respective periodicities, both the Metonic and sunspot cycles share a common ratio of 3:5 (with three Metonic cycles equal to five Schwabe cycles at 57 yrs). Because of this relationship, the Metonic and Schwabe cycles, are also numerically associated with 3.8 yrs, which is a common denominator between the 11.4-yr, 19-yr, and 57-yr cycles. The Metonic cycle is also numerically a factor in the lengths of another apparent solar cycle (SdV) of 209 yrs and the ~1470-yr to 1490-yr cycle (at 1482 yrs). The shared harmonics between the sunspot and Metonic cycle are suggestive of a common contributing factor, such as the impact of planetary orbits on both the heliomagnetic field, the lunar orbit, and Earth's axial rotation (cf. Abreu *et al*., 2012; Charbonneau, 2013; Lowrie, 2007; Morner, 2013).

Because of its close association with the length of the tropical year, the Metonic cycle is a better potential measure of Milankovitch precessional dynamics than the Saros cycle of eclipses. The incongruities in Keeling's and Whorf's (2002) research into the potential tidal forcing of millennial-scale cycles were due to the use of the Saros cycle of eclipses (Chapter 2). The Metonic cycle of lunations (19 yrs) identifies a return of the New Moon to the same calendar date and same celestial longitude (referenced to the ecliptic), within a couple of hours (cf. Goldstein and Bowen, 1989; Munk *et al*., 2002), and is helpful for integrating solar and lunar calendars (see Section 3.2). Being a New

Moon, the Metonic lunation is the exact time of peak gravitational forces acting on Earth's tides. When the Metonic lunation interacts with the lunar nodal position, an eclipse must occur and gravitational influences are heightened. As will be shown in Chapter Four, a previously undiscovered eclipse series is attached to the Metonic cycle of lunations making it suitable for inclusion in a conceptual model for the cause of millennial-scale climate cycles (Kelsey *et al*., 2015).

3.2 Chronologies

Measuring time is a tricky business because the astronomical markers on which our seasons and calendar are based are influenced by or have orbital motion, and time units do not fit neatly into each other. The mechanisms upon which our chronologies have depended through time are affected by gravitation, i.e., lunar motion, Earth's rotation and revolution. Regardless, the measurement of time has been essential to human survival because of human dependency on food, the supply of which is seasonal in nature. The Neolithic was the beginning of subsistence farming, leading to the development of civilisations, and was influenced by climate change and population pressure (Balter, 2007; Rosen, 2007; Twiss, 2007). The collapse of various civilisations has also been caused by natural climate change, such as the collapse of a number of numerous Bronze Age civilisations approximately 3.2 kya (Langgut *et al*., 2013; see Chapter 1).

In Mesopotamia and ancient Egypt, the development of calendars began more than 5,000 years ago, following the establishment of agriculturally-dependent civilisations (cf. Jespersen and Randolph, 1999; Turney, 2006). Sometime after 1200BC the oral traditions of the wandering Habiru were written down as the Pentateuch (first five books of the bible), where it is said that the stars were used for navigation and calendars (Genesis, 1:14; Hertz, 1981). Archaeological evidence and historical sources show that fixed stars and eclipses were important reference points, as was the Metonic lunation cycle (Bowler, 2009; Edmunds and Morgan, 2000; Sommerville, 2000). This cycle is named after Athenian astronomer, Meton, who first documented it in 432BC (Bengtson, 1968; O'Neil, 1975; Pritchett and Neugebauer, 1947). The 19-yr Metonic cycle was used to coordinate the political and religious calendars in Athens, and was supposed to be useless as it was shortly discarded by the Athenians (Pritchett and Neugebauer, 1947). However, since that time the Metonic cycle has also been extensively used as an intercalation tool in the construction of civilian and religious calendars, including the Chinese, Jewish and Christian calendars (de Jong, 2006; McGee, 1892; O'Neil, 1975; Pritchett and Neugebauer, 1947). The Callipic cycle mentioned above also played such a role.

From ancient Egypt to the modern measurement of deep time (*viz* geological time) using radioisotopes, an overview of selected key chronologies is important to grasp some of the issues involved in measuring time. This is important because measurements of time can become easily distorted, evidenced by the complexity and discontinuity of different chronologies through time that

are difficult to piece together into a continuous chronology (see following section; Section 2.2.2.4). These complexities, associated with physical processes (such as precession), contribute to difficulties in measuring time as experienced by the ancient Egyptians, the calibration of radiocarbon dating, and the uncertainties associated with deep time measurement (cf. Berger *et al*., 1989; see following section). Precession, Earth's rotation, and the eccentricity of Earth's orbit all play roles in these distortions of data because of Earth's non-uniform orbital velocity and rotation rate.

3.2.1 Difficulties with calendars

The tropical year on which the seasons are based is not the same as the calendar year (Julian or Gregorian). Nor is the sidereal year, which is measured relative to a star, the same as the tropical year on which our seasons are based (see Section 3.1.1; cf. Dincauze, 2000; Taylor and Bar Yosef, 2014). Consequently, our calendars get out of step with the seasons and stellar references unless they are adjusted from time to time (see Section 3.2.1.2; Dincauze, 2000). We understand the cause of this problem, which is partly due to precession of the equinoxes and the gravitational forces that cause the vernal point to move at inconstant rates in a backward motion against the stars. It is also partly due to disparities between natural and synthetic time units, *viz* our calendars are inaccurate and Earth's rotation rate is slowing changing due to the influence of the Moon (see Section 3.1.1; Dincauze, 2000). Not surprisingly, the ancient Egyptians were unaware of these precessional issues and the precise length of the day, with the result that their calendar slipped out of step with the seasons, producing a cycle of ~1460 yrs (Lockyer, 1964; O'Neil, 1975). The fact that there was a climate cycle of similar length is intriguing, prompting questions for this research as to whether the same factors that contributed to Egyptian chronological problems also caused the climate cycle of similar length.

3.2.1.1 The Sothic Cycle

From early Dynastic times, the ancient Egyptians were aware of the year as being approximately 365 days long (de Jong, 2006; Hornung *et al*., 2006; Krauss, 2006). Their calendar began at the summer solstice and consisted of three seasons, Akhet (Inundation), Proyet (Sowing and Growth), and Semut (Harvest) (Hornung *et al*., 2006; Krauss, 2006); and their year was comprised of 360 days plus five epagomenal days associated with the Osirian gods that were added at the end of the year (Hornung *et al*., 2006; Krauss, 2006). However, the discrepancy between their calendar year and the tropical year caused their cycle to get out of step with the seasons, resulting in a cycle of ~1460 yrs. The problem was compounded by the precession of the equinoxes as they measured the length of the year relative to the sidereal year.

The Sothic cycle of ancient Egyptian chronology is of interest to these discussions because it is of similar length to the ~1470-yr climate cycle and forms the basis of the conceptual model that will be developed in the next chapter. The star Sirius, known to the ancient Egyptians as Sopdet (Sothis),

rose heliacally (visible rising just before dawn) at the summer solstice in ancient Egypt, coincident with the flooding of the Nile (Lockyer, 1964; O'Neil, 1975). The last time that this occurred was in 3285BC (Lockyer, 1964) at the beginning of a significant period of global climatic change, which coincided with a sudden onset of increased ENSO variability and intensity in the Pacific (Turney and Hobbs, 2006; Vieira *et al*., 2011). This time also saw the start of drier conditions in the northern hemisphere associated with the Holocene's sub-boreal climatic period (Derricourt, 1971; Gagan *et al.,* 2004; Moss *et al.,* 2013; Vieira *et al.,* 2011). This time period is identified as a cold period associated with the Hallstadt cycle (Vasiliev and Dergachev, 2002), associated with complications in the radiocarbon calibration curve (van Geel *et al.*, 2014). These Hallstadt events are times of geomagnetic anomalies that disrupt the uniform production of ^{14}C, resulting in steep changes in the radiocarbon curve that are problematic for radiocarbon dating (Libby, 1980; cf. van Geel *et al.,* 2014). These climatic changes were of great concern to the ancient Egyptians during the Old Dynasty, evidenced in the "Prophecy of Nefer-Rohu" (cf. Pritchard, 1971).

Sirius' heliacal rising at the latitude of Memphis closely correlated with the length of the sidereal year (Lockyer, 1964; O'Neil, 1975) and, in the Old Kingdom of Egypt, this event marked the beginning of their calendar or civil year (Krauss, 2006; Hornung *et al*., 2006). However, because the ancient Egyptian calendar consisted of 365 days and the length of tropical year is ~365.24 days, their calendar became desynchronised from the seasons. The cycle produced is 1,460 Egyptian civil years or 1461 Julian years (Lockyer, 1964; cf. O'Neil, 1975; Williams, 2013b). This is the Sothic cycle. Confounding the ancient Egyptians in their quest for a functional calendar was the fact that the flooding of the Nile is a seasonal event tied to the tropical year and not to the sidereal year against which it was measured, with the sidereal measurement dependent upon Earth's rotation and the latitude of the observer (Kitchen, 1991). Their problem in determining the true length of the year was also compounded by a factor unknown to them: equinoctial precession (Lockyer, 1964). As a result of precession, Sirius gradually became disassociated with the summer solstice and could no longer be seen then as its light was submerged by sunlight at the summer solstice dawn.

3.2.1.2 Julian and Gregorian calendars

In 238BC, long before the Julian reform of the calendar, the Egyptians had tried and failed in the introduction of a calendar based on 365.25 days under the auspices of Ptolemy III Euergetes (Krauss, 2006). The early Roman calendar seems to have been originally a lunar-based one with a ten-month year, with a later adjustment around 700BC to a luni-solar calendar based on 12 synodic months (355 days) (O'Neil, 1975). In 46BC, with the aid of the Greek-Egyptian astronomer, Sosigenes, Julius Caesar reformed the Roman calendar which was at the time out of step with the seasons (O'Neil, 1975). Caesar introduced a year of 365 days, with the addition of a leap day in February in every

fourth year. The other extra days required to align the calendar year with the solar year were distributed throughout the various months of the year (intercalation), and it is essentially this calendar with which we are familiar today. He also adjusted the calendar by adding 90 days in an effort to align it with the solstices, such that they occurred on June 24 and December 25 of each year (O'Neil, 1975). These dates were associated with Roman solstice festivals.

Despite being an improvement on the 365-day calendar, the Julian calendar also began to slip out of step with the seasons because it over-estimated the length of the tropical year which is ~365.24 days long [Figure 3.21]. The difference between the tropical and the Julian years is only about 11 minutes. However, by 128 yrs, a difference of one day exists between the tropical and Julian years (Tompkins, 1978). By 325AD, the solstices and equinoxes were occurring about four days earlier such that the March equinox fell on March 21 (O'Neil, 1975). At this time, the first Council of Nicaea set this date as the time of the northern spring equinox (O'Neil, 1975). However, the calendar continued to slip out of step with the seasons until 1582AD when it was ten days out of alignment, such that the equinox fell on March 11. These issues did not go unnoticed over the intervening centuries, but it wasn't until the 16th century that action was taken. Advised by two astronomers, Lilius and Clavius, Pope Gregory XIII added ten days to the calendar in October 1582AD, which caused civilian riots because of their "stolen" ten days (Tompkins, 1978). Additional rules for calendar adjustment were introduced by Gregory XIII, affecting leap years that occurred in centurial years, with the result that the calendar was good for more than three millennia. Consequently, at the centurial scale only years divisible by 400 would be 366 days long, such that a leap year that would normally be due at 100, 200, and 300 years is only 365 days long.

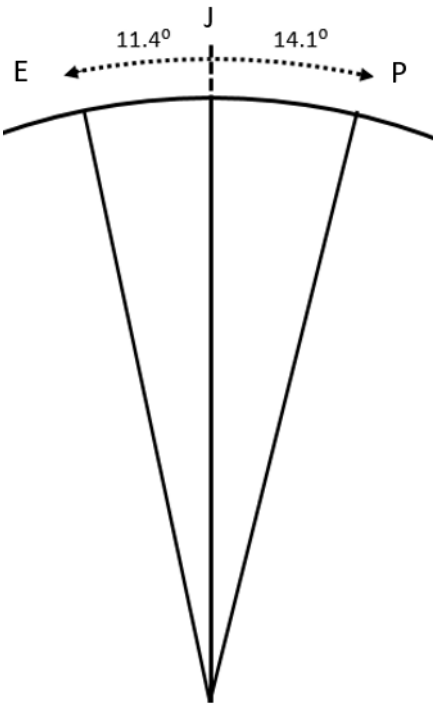

Figure 3.21: Schematic of the changing relationship between the Julian calendar, the tropical year (associated with the equinox), and the perihelion that is caused by precession. Over a 1461-yr period the equinox will move by 11.4° from the starting point in a 360° cycle. Similarly, the perihelion moves away from both the starting Julian date and the equinox. J= Julian date, E= equinox, P=perihelion.

The Gregorian calendar was not adopted immediately or uniformly throughout Europe due to religious factionalism (Turney, 2006). Its adoption was staggered, with the last European countries doing so in the 20th century (Turney, 2006). This situation resulted in a lengthy period of complicated and discontinuous chronologies. Similarly, calendars and the measurement of time have taken various forms and suffered from extensive discontinuities throughout human history, making it difficult for the construction of a cohesive historical timeline (see Kitchen, 1991; Taylor and Bar Yosef, 2014).

This situation did not help Libby in calibrating the radiocarbon curve based on the "Curve of Known Ages" (Libby, 1960, 1980; Taylor and Bar Yosef, 2014).

3.2.2 Radiocarbon chronological framework

The interplay between cosmic rays and magnetic fields shapes the isotopic imprint of cosmogenic nuclides in Earth's palaeoclimatic record, one of which is ^{14}C. The major magnetic influence is our Sun's heliomagnetic field, which is associated with sunspot activity, and it has also been postulated the solar dynamo may be influenced by its orbiting planets (Abreu *et al.,* 2012*;* Charbonneau, 2013). Playing a lesser role is Earth's geomagnetic field (Broecker, 2009; Damon and Linick, 1986; Damon and Sonett, 1991; Hathaway, 2010; Mauquoy *et al.,* 2004; O'Connell and Allen, 2004; Sternberg and Damon, 1983; Stuiver *et al.,* 1991). Earth's geomagnetic field has internal and external components that are demarcated by their distance from the Earth (Lowrie, 2007). The external component of Earth's magnetosphere interacts with the solar wind to form the outer Van Allen belts (discussed above). The internal component of Earth's geomagnetic field is powered by the geodynamics of Earth's molten core, an important part of which is the westward drift. This drift is thought to result from the relative rotation rates of the lower mantle to the outer layers of Earth's core (Lowrie, 2007). The wandering non-dipole component of Earth's geomagnetic field, mentioned in relation to the Hallstadt cycle of ~2.4 ky (Section 2.2.3), causes "high latitude maxima (to) pass over the north magnetic pole….in reversed polarity" every ~1.2 ky (Damon and Linick, 1986:266). This 2.4-ky cycle appears to be stationary and, as previously mentioned, is associated with modulations of atmospheric radiocarbon production (Damon and Linick, 1986) attributable to modulations of Earth's geomagnetic field (Broecker, 2009). Together the Sun's heliomagnetic field and Earth's geomagnetic field shape the production and patterning of radiocarbon and other cosmogenic isotopes found in Earth's climate records.

^{14}C is formed by secondary neutrons produced through extremely high-energy cosmic ray spallation of nitrogen (Damon and Linick, 1986; Libby, 1960; Hathaway, 2010; Taylor and Bar Yosef, 2014). ^{14}C works its way through the biosphere as part of the carbon cycle, initially through the photosynthesis of CO_2 by plants and thence to the rest of the food chain (Libby, 1960; Linick *et al.,* 1989; Taylor and Bar Yosef, 2014). Once an organism has died the intake of ^{14}C ceases and, using the half-life of radiocarbon and the ratio of ^{14}C to stable ^{12}C isotopes to which they decay, the age at the time of death of the organism can be established.

Initially the rate of ^{14}C production was thought to be constant but variations in production were eventually recognised, resulting from both anthropogenic and natural causes (Libby, 1960; see also Callaway, 2012; Damon and Sonett, 1991). Variations in radiocarbon levels were found to be influenced by a variety of causes. Around 70% of natural variability has been attributed to

heliomagnetic and geomagnetic activity, and the remainder to climate effects (Steinhilber *et al*., 2012). Anthropogenic causes include the Industrial Revolution, atomic bomb blasts, and the burning of fossil fuels (Libby, 1960; Damon and Sonett, 1991; Olsson, 2009; Suess, 1953, 1955; Taylor and Bar Yosef, 2014). Natural causes include changes in the strength and intensity of the geomagnetic dipole, astrophysical forcing, and changes in ocean circulation and global wind speeds (Blackwell and Buck, 2008; Damon and Sonett, 1991; Lal and Lingenfelter, 1991; Hathaway, 2010; Stuiver *et al.,* 1991; Tiwari and Rao, 1998; Suess, 1986; Taylor and Bar Yosef, 2014).

Contributing to variations in ^{14}C are rates of exchange with geochemical reservoirs, due to changes in climate and perhaps solar radiation (Damon and Sonett, 1991; cf. O'Connell and Allen, 2004; Hathaway, 2010), as well as exchanges between the atmosphere, hydrosphere and biosphere. For example, the rate of CO_2 absorption and release from the oceans is influenced by temperature, thereby affecting the ratios of atmospheric ^{14}C (Chapter 2). The largest reservoir of carbon is in the oceans through the dissolution of carbonaceous material, although carbon reservoirs are also found in rocks and soil (Dincauze, 2000; Taylor and Bar Yosef, 2014). However, ^{14}C is not distributed evenly through the oceans, with the deeper parts containing the oldest carbon (Blackwell and Buck, 2008; Dincauze, 2000; Taylor bar Yosef, 2014). Because of these factors, radiocarbon dating for marine organisms must be adjusted for a marine reservoir effect of ~400 yrs or more (Hughen *et al*., 2004; Taylor bar Yosef, 2014). The marine reservoir effect measures the adjustment for surface waters relative to the atmosphere; the Marine13 calibration curve for the period between ~14 ky and 50 ky uses the value of 405 yrs as the average global value (Taylor and Bar Yosef, 2014). There are other adjustments for location. For example, the southern hemisphere dates are ~40 yrs older than the northern hemisphere and therefore need to have an adjustment applied to the radiocarbon date (Hogg *et al.,* 2013). The richest source of terrestrial carbon is found in peat (Fairfax *et al.,* 2011; Linick *et al*., 1989; Loisel and Garneau, 2010), which is also suitable for uranium-series dating (Lowe and Walker, 1997; Schwarcz, 1989) and ^{10}Be dating (Wieder *et al*., 2010).

Radiocarbon can be used to date suitable material in archaeological and palaeoenvironmental contexts, and for this discovery William Libby won the Nobel prize in chemistry in 1960. Libby had originally used the "known" age of artefacts from ancient Egypt to test radiocarbon as a tool for dating (Bowman, 1990; Libby, 1960, 1980; Taylor and Bar Yosef, 2014). The premises of his research included the constancy of radiocarbon levels, rapid mixing and even global distribution of radiocarbon, as well as matching concentrations of radiocarbon between the biosphere and atmosphere (Dincauze, 2000). Other assumptions included the termination of the exchange of radiocarbon between the organism and the atmosphere upon its death, after which the amount of radiocarbon decreased based on its half-life (Taylor and Bar Yosef, 2014).

Contra Libby's assumption of constancy, dendrochronological research (tree-ring analysis) using samples of precisely known age revealed the fluctuating nature of the radiocarbon levels (Suess, 1986; cf. Bayliss, 2009). A dendrochronological calibration curve developed by Suess was based on bristlecone pine studies, and revealed two sinusoidal patterns: one short-term and the other long-term. The first of these patterns are the SdV wiggles (see below). The second of these patterns has a periodicity reported as either 9 ky or ~10-11 ky [Figure 3.22] (Suess 1969, 1986; cf. Damon and Linick, 1986; Taylor and Bar Yosef, 2014), and is of similar length to half the Milankovitch precessional cycle and spectral peaks found (Berger *et al.,* 2006; Hagelberg *et al.,* 1994; Weirauch *et al.,* 2008). At the time, Suess (1986) attributed this pattern to the changing magnetic dipole moment (MDP), but the issue was uncertain because of an imperfect relationship between the two.

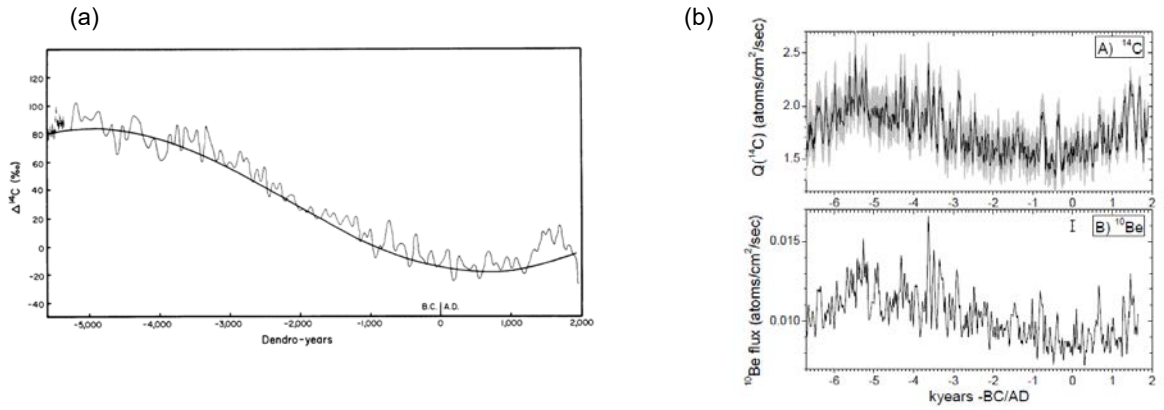

Figure 3.22: Radiocarbon calibration curves from Intcal98 (a) and Intcal09 (b). The sinusoidal form of the radiocarbon calibration curve and 200-yr SdV wiggles are evident in these diagrams from (a) Damon and Linick, 1986:268 and (b) Usoskin *et al.,* 2016. Panel (b)(top) is decadal ^{14}C flux (Roth and Joos, 2013 cited by Usoskin *et al.,* 2016:2) and (bottom) ^{10}Be flux in GRIP ice core (Yiou *et al.*, 1997 cited by Usoskin *et al.,* 2016). Grey area in top panel of (b) is 95% confidence interval. The period of the sinusoid is 11,300 yrs and is based on the Cambridge half-life of radiocarbon.

Damon and Linick (1986) found that a non-linear relationship existed between time-dependent ^{14}C production and the geomagnetic dipole using ^{14}C tree-ring data and ^{10}Be ice-core data from Camp Century, despite assertions otherwise from Beer and colleagues (1984). Stuiver *et al. (*1991) attributed most of the Holocene ^{14}C flux to geomagnetic and solar influence. The amplitude of ^{14}C fluctuations is influenced by the changing magnetic dipole, causing variations in the cosmic ray flux (Hathaway, 2010; Vasiliev and Dergachev, 2002). However, the issues involved are not well understood due to the lack of an underlying conceptual structure, and this is considered an important problem both to solar physics and understanding radiocarbon chronological variability (Abreu *et al*., 2012; Damon and Sonett, 1991; Taylor and Bar Yosef, 2014). Generally, global modulation of ^{14}C is inferred to have resulted from solar fluxes for short and medium-term cycles (Damon and Sonett, 1991; cf. Chiu *et al*., 2007; O'Connell and Allen, 2004). Although the hypothesis is not new (Charbonneau, 2013), recent modelling has suggested that the planetary orbits may perturb the solar dynamo and sunspot

activity, potentially explaining millennial and centennial-scale climate cycles in Earth's radioisotopic records (Abreu *et al*., 2012).

Superimposed on the long-term sinusoidal trend in Suess' (1986) dendrochronological calibration curve are short-term sinusoidal wiggles (SdV). These wiggles, now known as known as Suess or de Vries (SdV) wiggles (see Chapter 2), have a mean periodicity of 209 yrs and have been used in the construction of precise chronologies (e.g. Blaauw *et al*., 2003; cf. Bowman, 1990). The SdV wiggles were initially considered questionable and controversial, with their value questioned due to Libby's influential opinion that ocean-atmosphere exchange of CO_2 was extremely sluggish, and because they were statistically insignificant (Suess, 1986). However, these fluctuations were shown to be non-random (Suess, 1986) and to vary periodically (cf. Heinrich, 1988). With the link between patterns in tree rings and ^{14}C variations confirmed, wiggle matching is now important in matching floating pieces of chronology to a chronological framework (e.g., Blaauw *et al*., 2004; Olsson, 2009; Wieder *et al*., 2010).

These SdV wiggles extend back to the limit of radiocarbon dating (50-60 ky) (Bowman, 1990; Summerhayes, 2015; Taylor and Bar Yosef, 2014). Although sunspot records do not evidence the SdV cycle (Hathaway, 2010), the SdV wiggles have an inferred link to solar activity as it is a multiple of the sunspot cycle (Damon and Sonett, 1991; Suess, 1986; Vieira *et al.,* 2011; also see Chapter 2). An interesting aspect of these wiggles is that their amplitude was subdued between 2500BC and 1200BC [Figure 3.22], thought to be dampened by the impact of increased heliomagnetic intensity on Earth's geomagnetic dipole (Damon and Linick, 1986). These SdV wiggles vary in amplitude, with periods of strong amplitudes lasting up to a millennium before disappearing and eventually resurfacing again (Abreu *et al.,* 2012). Greatest amplitude of SdV signals tend to occur during periods of increased numbers of solar grand minima (Abreu *et al.,* 2012), and had the greatest amplitude when the terrestrial dipole moment was small (Damon and Sonett, 1991). However, these wiggles can also be problematic for radiocarbon dating, with radiocarbon age variations of 100-200 yrs when corresponding calendrical age variations are measured in decades (Bowman, 1990).

Using Irish oak and German oak, calibrations were first extended back to 11,857 calBP (Branch *et al.,* 2005; Stuiver *et al.,*1998). Radiocarbon calibration for periods older than this was then achieved using varved sediments and Greenland ice cores, with this calibration being less precise and accurate than dendrochronology (Fairbanks *et al*., 2005; see also Section 3.2.3). Oxygen-isotope chronology served as an age-equivalent marker in dendrochronology and radiocarbon dating (Lowe and Walker, 1997). Uranium-series dating on coral further extended this calibration back to 24,000 calBP, with an increasing difference observed between raw and calibrated ages (Stuiver *et al.,* 1998; cf. Mellars, 2006). Radiocarbon dating now extends back to its limit with a reasonably high degree of accuracy

using AMS and calibration to coral (e.g., Fairbanks *et al*., 2005); this is despite the trend of declining precision of age associated with the limit of half-life measurements, and the trending age difference between calibrated and uncalibrated dates (Blackwell and Buck, 2008; Linick *et al.,* 1989; Mellars, 2006).

Problems with radiocarbon dating back to ~14.6 ky have essentially been eliminated using dendrochronological calibration of radiocarbon and wiggle-matching (Hughen *et al*., 1998; Hughen *et al.,* 2004; Suess, 1986; Taylor and Bar Yosef, 2014), which is now used in conjunction with accelerator mass spectroscopy (AMS) to increase the accuracy of ^{14}C dating (Lowe and Walker, 1997; Pearson, 1986; Taylor and Bar Yosef, 2014). Beyond that date (the limit of dendrochronological calibration), the resolution of calibration datasets is not as high (Hughen *et al*., 2004). In fact, "non-dendrochronologically based calibration data sets provide significantly less precise offset correction data sets" (Taylor and Bar Yosef, 2014:54).

3.2.2.1 Problems with half-life, radiocarbon years, and calibrated years

Although Libby originally had used a radiocarbon half-life of 5720±47 yrs (Arnold and Libby, 1949), the value that came to be accepted and known as the Libby half-life was the experimentally derived value of 5568±30 yrs (Bowman, 1990; Chiu *et al*., 2007; Libby, 1960; Taylor and Bar Yosef, 2014). However, by 1962 the length of this half-life was challenged based on further experimentation and found to be 3% too young, with the "true" value deemed to be 5730±40 yrs called the Cambridge half-life (Bowman, 1990; Olsson, 2009; Taylor and Bar Yosef, 2014). At the Pullman Conference in 1965 (later upheld at other conferences since the early seventies), it was decided that, because of the large number of radiocarbon dates already published, the Libby half-life would continue to be used (Bowman, 1990; Chiu *et al*., 2007; Hughen *et al*., 1998; Olsson, 2009; Taylor and Bar Yosef, 2014). Providing that calibration tables used the same values as the half-life calculations, results would be legitimate (Bowman, 1990; Olsson, 2009; Taylor and Bar Yosef, 2014). The Libby half-life dates already calculated could easily be converted by multiplication using a factor of 1.03 (Bowman, 1990; Olsson, 2009; Dr. Quan Hua, 2016, personal communication, 11 July). In addition to the problem with the Libby half-life, there is also an unknown problem offset from calendar years (Bowman, 1990). However, half-lives are no longer used during the period to ~14.5 ky because of dendrochronological calibration (Taylor and Bar Yosef, 2014; Dr. Quan Hua, 2016, personal communication, 11 July). The calibrated radiocarbon dates through the range of dendrochronological calibration are quite good and the error is not cumulative (Dr. Quan Hua, 2016, personal communication, 11 July). However, the same is not true in the period beyond this, where the error is cumulative (Dr. Quan Hua, 2016, personal communication, 11 July).

This raises an important question on the different natures of radiocarbon years and calibrated years. Some confusion in terminology appears to exist in the literature on terminology, such as calendar years being confused with solar years or sidereal years, and incorrect terminology (e.g., Dincauze, 2000; Holdaway, 2006; Taylor and Bar Yosef, 2014). Whilst dendrochronological years represent the seasonal year through the usage of annual growth rings of trees (therefore correlating to the tropical year or solar year) (*contra* Dincauze, 2000; Holdaway, 2006), radiocarbon years are based on the calculations of the radiocarbon half-life. The length of this half-life obviously depends upon the type of year used to calculate it, i.e., Julian year, tropical year. Whilst the aim was to use the tropical year, the systemic error margins associated with the calculation of the Cambridge and Libby half-lives preclude the sort of accuracy required (cf. Bowman, 1990), thereby limiting the ability to account for precessional influences. This situation may contribute to the unknown problem offset from calendar years (cf. Bowman, 1990) and the trending age difference between calibrated and uncalibrated dates (cf. Blackwell and Buck, 2008; Linick *et al.,*1989; Mellars, 2006). An underestimation of the radiocarbon half-life has also been suggested as potentially producing the proportional offsets between calendar and radiocarbon ages (Chiu *et al*., 2007; see also Fairbanks *et al*., 2005). This may well be the case; however, the issue of the systemic error margin of the radiocarbon half-life does not allow precession to be factored into uncalibrated radiocarbon ages. The consequence is that these radiocarbon dates need to be calibrated, as has been achieved through dendrochronology and paired uranium-series coral dating.

These error margins may have important implications given that the current difference of approximately ~11 minutes between the Julian calendar year and tropical year results in a difference of one day in every ~128 yrs. This is the situation that occurs when using uncalibrated BP (see below) or b2k dates (ages relative to 2000AD) (cf. Wolff *et al.*, 2010). The precessional rate also changes throughout the cycle based on the distance from the Sun and Earth's orbital speed (Greenberg, 1981). These issues are particularly important in the range beyond dendrochronological dating, where errors are cumulative and dating is dependent upon glaciological and sediment profiles, modelling, distantly separated tie-points, and floating portions of paired uranium-series dating (see Section 3.2.3 and Chapter 2). Glaciological chronology cannot account for missing layers and relies heavily upon modelling to define annual layers as it delves deeper into the past (Fairbanks *et al*., 2005; also see Section 2.2.2.4).

Some of the problems associated with chronological disparities between calendar, radiocarbon, and BP years also led to the rejection of the simplistic conversion between AD/BC dates and BP in 1977 (Olsson, 2009; Taylor and Bar Yosef, 2014). Such a conversion cannot be simply derived by the subtraction of radiocarbon dates (BP value) from 1950. Whilst this practice gives an "approximation

to calendar years" (Dincauze, 2000:110), these errors are cumulative beyond continuous calibration, and may distort the appearance of time and cycles between distantly spaced tie points such as are used in glaciological modelling (see Section 2.2.2.4). This matter is also further complicated by the disparities between tropical and Julian years as a result of precession.

3.2.3 Uranium-series dating

A number of cosmogenic isotopes, such as ^{10}Be, ^{26}Al, ^{36}Cl, and radioactive isotopes from the uranium decay series, are used in archaeology, the geosciences, and palaeoenvironmental research to build chronological profiles and date contexts (Dincauze, 2000). The radioactive decay of Uranium 238 (^{238}U) produces a series of daughter products in which lead (Pb_{206}) is the final product. Uranium 234 (^{234}U), Thorium (^{230}Th), Radium, Radon, Protactinium, and Polonium form part of this radioactive decay chain, with different decay rates for each parent-daughter pair. For Uranium-Thorium dating that is used on corals, the limit of dating is 500,000 yrs and the minimum is just a few years (Lawrence Edwards *et al*., 1987; Schwarz, 1989). Measurements are quite precise at the younger end of this scale, whilst there are greater standard errors at the other extreme (Cobb *et al*., 2008; Schwarz, 1989). Uranium-series dating rests on a number of assumptions, including an uncontaminated closed system, known decay coefficients, and the ability to precisely measure the ratios of parent-daughter nuclides (Lowe and Walker, 1997; Schwarcz, 1989; Smart, 1991). A closed system is one in which there is no exchange of nuclides with the environment (Dincauze, 2000; Lowe and Walker, 1997; Schwarcz *et al*., 1989).

Speleothems (stalagmites and stalactites) and karst result from the deposition of water-borne carbonates and minerals in caves (Schwarcz, 1989). Clearly speleothems at the cave entrance are at greater risk from contamination by groundwater than those further removed from the cave entrance (Schwarcz, 1989). Whilst clean speleothems are closed systems, dirty speleothems are open systems because they are exposed to contaminated groundwater; molluscs, teeth, and bones are also examples of open systems (Dincauze, 2000; Lowe and Walker, 1997). Speleothems are also influenced by rainfall variations, and in extreme conditions may be missing annual layers. Whilst uncertainties associated with variable groundwater chemistry and the initial age of the bicarbonate are issues for the dating of speleothems (Fairbanks *et al*., 2005), they also offer potentially long records (cf. Fairbanks *et al*., 2005). Uranium-series dating of speleothems from Hulu Cave in China and Villiers Cave in France verified GISP2 dating from the end of dendrochronological dating to ~40 kya (Hughen *et al*., 2004). Uranium-series dating of Hulu cave records have also been used to investigate the length of millennial scale climate cycles (Section 2.2.2.4). These records are also the preferred dating for the GICC05 glaciological model (Section 2.2.2.4).

Coral is exceptionally good for paired uranium-series dating because it "behaves as a nearly ideal closed system" (Schwarcz, 1989:11), and because coral has multiple geochemical properties that enables it to be used for temperature and climate reconstruction (Bender *et al.*, 1989; Cobb *et al*., 2008; Lowe and Walker, 1997). Individual colonies of coral can live up to >200 yrs, although the average lifespan is ~100 yrs (Cobb *et al*., 2008). U_{234} is absorbed directly from seawater and deposited in carbonate secretions in annual growth rings on coral, along with other geochemical properties from its watery environment (Cobb, *et al*., 2008; Lawrence Edwards *et al.*, 1987). However, thorium is not soluble so that any remaining thorium in the closed system is the result of radioactive decay (Holdaway, 2006). Freshwater diagenesis, evidenced by secondary calcite or aragonite depositions, is a source of contamination (Chiu *et al*., 2007; Cobb *et al*., 2008; Fairbanks *et al*., 2006).

Uranium-series dating of uplifted coral terraces in Barbados and New Guinea have provided valuable climatological history, assisting in the establishment of timelines for interglacials, sea-level variations, and their connection with the Milankovitch cycles (Bender *et al*., 1979; Chappell, 1974; Lawrence Edwards *et al*., 1987; Lowe and Walker, 1997; Pickett *et al*., 1989; Schwarcz, 1989). The application of uranium-series dating to calibrating radiocarbon beyond the range of dendrochronological calibration was first explored by Bard *et al.* (1990a, 1990b), using paired uranium-thorium and radiocarbon dating from Barbados coral to allow direct comparison between the two chronometric methods. The uranium-series dates were in good agreement with dendrochronological calibration, while radiocarbon ages beyond the range of dendrochronology were increasingly too young (Bard *et al*., 1990b; Dincauze, 2000). Radiocarbon dating of foraminifera in a marine core from the Cariaco Basin in the Caribbean (Hughen *et al*., 1998), for the period between 8ka -14.5ka BP, agreed with the uranium-series calibrated chronologies developed by Bard and others (e.g., Bard *et al*., 1996; Lawrence Edwards *et al*., 1997), although was in disagreement with others (e.g., Goslar *et al*., 1995; Hajdas, 1993; Wohlfarth, 1996). The laminae from the Cariaco basin were previously shown to be in agreement with the GRIP ice core chronology during the last deglaciation (Hughen *et al*., 1998; cf. Johnsen *et al*., 1992). Comparisons with the GISP2 chronology were also in good agreement (Hughen *et al*., 1998).

The calibration of radiocarbon dating was also extended to 50 ky BP using deep-sea cores from the Cariaco Basin, the accuracy of which was confirmed using independent radiometric tests correlated to GISP2 (Hughen *et al*., 2004). However, Chiu *et al.* (2007) point out that the uncertainties of both radiocarbon and calendar ages are inherited by the Hughen *et al.* (2004) study. This is because these factors were derived from sources other than the Cariaco Basin cores, and relied upon an estimated chronology using visual stratigraphic comparisons and tie points from Greenland ice core models (Chiu *et al.,* 2007). The alternative calibration used uranium-series dating of coral, which was broadly

consistent with the Cariaco chronology to ~40 kya but differed beyond that range (Chiu *et al.,* 2007). The Chiu *et al*. (2007) study led to the suspicion that the radiocarbon half-life value needs to be revaluated. However, problems with calendar age measurement also need to be considered as discussed above.

3.2.4 ^{10}Be and the geomagnetic record

^{10}Be, like ^{14}C is, a cosmonuclide produced by spallation by cosmic rays in Earth's atmosphere and is modulated by the solar wind strength (Bard *et al*, 2000; Beer *et al*., 1984; Dincauze, 2000; Hathaway, 2010). ^{10}Be is used to establish chronologies through estimations of annual accumulation rates and for dating stratigraphic markers that serve as tie points between different cores (Yiou *et al*., 1997). Whilst radiocarbon is a global signal that is well-mixed after being absorbed into atmospheric CO_2, ^{10}Be expresses a regional signal that is latitude dependent and which is deposited within 1-2 yrs via precipitation (Bard *et al*., 1997). This ^{10}Be signal can be affected by local meteorological conditions and the deposition of continental dust-borne ^{10}Be, which distorts the local signal and interpretation of the record (Bard *et al*., 1997; Shulmeister, 2014, personal communication, April 10; Yiou *et al*., 1997). Radiocarbon takes longer to be deposited than ^{10}Be as it works its way into the biosphere and various reservoirs (Bard *et al*., 1997; Yiou *et al*., 1997). These different pathways into Earth's physical records explain why the ^{14}C signal lags the ^{10}Be signal by 10-20 yrs and why the two isotope records cannot be directly compared [Figure 3.24]. Consequently, Bard *et al*. (1997, 2000, 2007) converted the raw ^{10}Be record into a synthetic ^{14}C record using a 12-box numerical model to compare the two records, taking into consideration relevant various factors such as the geomagnetic influence on the deposition of ^{10}Be (Bard *et al*., 2007). This model is in agreement with both dendrochronologically calibrated radiocarbon data and the South Pole ^{10}Be data, showing a likely solar modulation of these signals [Figure 3.23] (Bard *et al*., 1997, 2000, 2007).

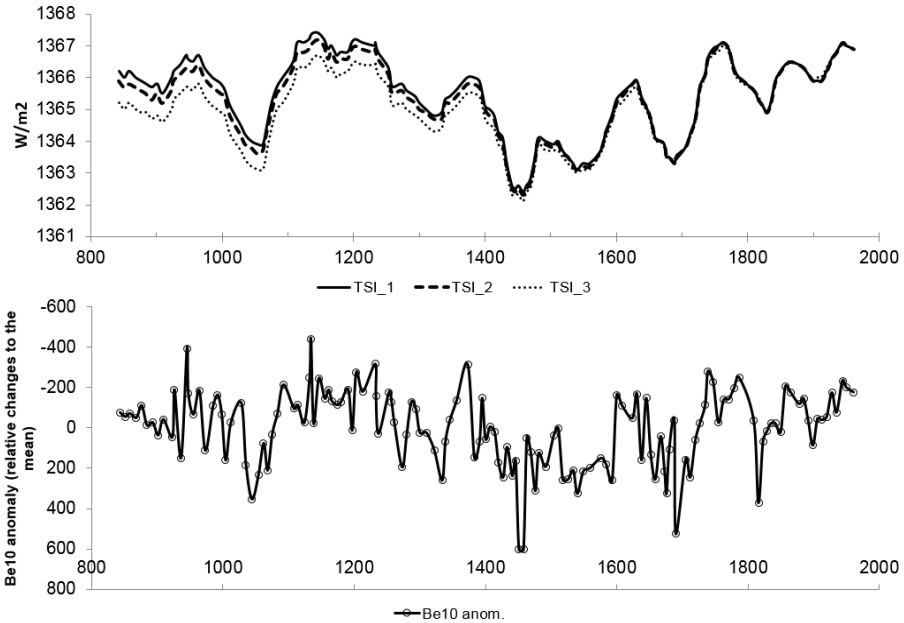

Figure 3.23: Total solar insolation (TSI) reconstruction (top) and ^{10}Be anomaly (bottom) from South Pole core (Bard *et al.,* 2003-2007). TSI_1 is is the original Bard *et al.* (2000) reconstruction, uncorrected for geomagnetic modulation; TSI_2 is corrected for geomagnetic modulation, with agreement between Bard *et al*., 2007, Korte and Constable 2005, Gubbins *et al.*, 2006; TSI_3 is corrected for geomagnetic modulation based on the superseded record of Yang *et al*., 2000 (Bard *et al.,* 2007).

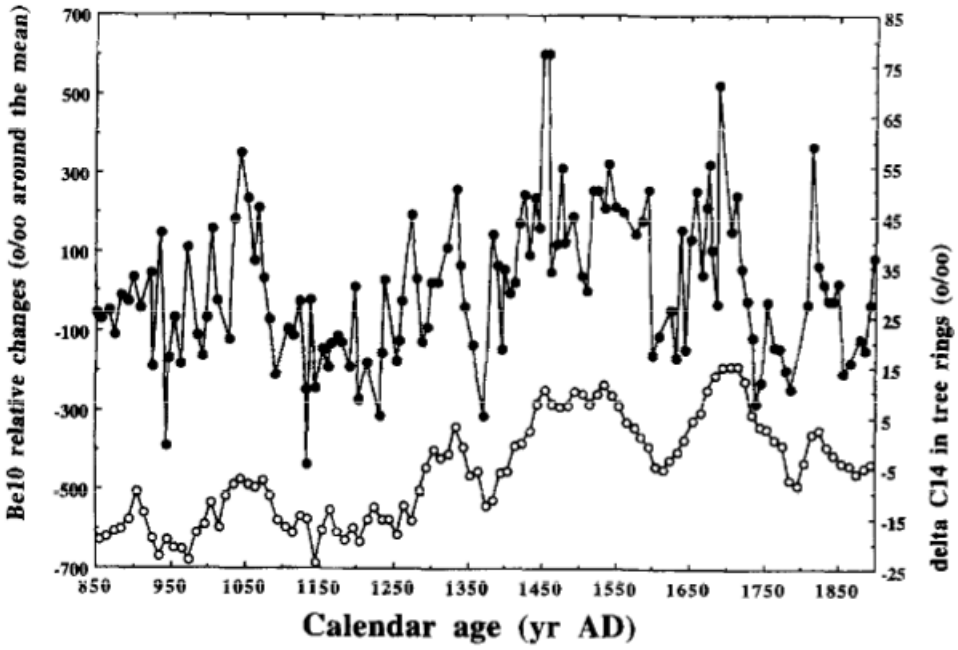

Figure 3.24: Bard *et al.* (1997:455) comparison of raw ^{10}Be record from the South Pole and dendrochronologically-calibrated radiocarbon record.

3.3 Chapter summary

This chapter placed Earth's climate cycles, discussed in Chapter Two, in context by reviewing Earth's chronology, celestial neighbourhood and position within it, and the astrophysical forces that shape Earth's climate. A list of cycle names mentioned in this chapter appears in Table 3.2. Our solar system is an interconnected and interactive system where gravitation, magnetism, and radiation influence the components of that system and shape climatic events on Earth and patterns within its palaeoclimatic datasets. The interplay between cosmic radiation and the solar wind imprints itself on these datasets through varying fluxes in cosmogenic isotopes, which is also filtered by Earth's geomagnetic field. The proximity and orientation of the Earth to the Sun (influenced by the axial tilt and time of year) influences the strength of gravitation and amount of insolation received. The changing shape of Earth's orbit and the tilt of Earth's axis is influenced by gravitational forces within our solar system, primarily by the Sun and Moon. As has already been established at Milankovitch scales, these variances in gravitational influence, solar irradiance, and insolation affect climate. Gravitation, through precession, affects our measurement and perception of time. In understanding these issues, it is possible to develop a conceptual model that will assist in explaining the causes of radiocarbon variability, the varying strength and cyclical lengths of quasi-periodic climate signals, and the patterns we see in the palaeoclimatic record. In

Table 3.2: Table of cycles mentioned in this chapter.

Cycle	Length
Apsidal precession	~110ky
Callipic cycle	~76 yrs
Equinoctial precession	~26ky
Hale (sunspot)	22.8 yrs
Lunar nodal cycle	18.6 yrs
Metonic lunation	19 yrs
Milankovitch eccentricity	~100ky
Milankovitch obliquity	~41ky
Milankovitch precessional	~21ky
Saros eclipse cycle	18 yrs 9-11 days
Schwabe (sunspot)	11.4 yrs

particular, the cause of millennial-scale climate cycles and the associated subharmonics are of particular importance. This is the topic of the next chapter.

Chapter 4 – Astronomical Correspondences

In the previous two chapters, the background to this study was presented, covering the Milankovitch cycles, and the ~1500-yr quasi-periodicity and associated subharmonics. These climate cycles were also placed in astrophysical and chronometric contexts in order to provide a better understanding of the nature of the millennial-scale cycles and their potential formation by astrophysical forcing. One of the primary objectives of this chapter is to elaborate on the conceptual model that may assist in explaining the cause of the ~1500-yr quasi-periodicity, its variability, and to contribute towards a better understanding of radiocarbon chronological variability. This is accompanied by associated trigonometric models and astronomical data. Results of the astronomical correspondences to climate signals based on these models and the astronomical data are also included.

Trigonometric models are developed to provide a means of exploring and understanding the potential of identified astronomical cycles in creating millennial-scale signals in the 1-2ky range, and also of their sub-harmonics. Correspondences do not constitute proof of causation, but the understanding obtained here assists in developing a chronologically-anchored trigonometric model that is statistically tested against data in Chapter Six. Before that testing begins, however, physical models of solar irradiance/insolation and gravitation need to be explored to expand on the understanding acquired here and place them in context (Chapter 5).

4.1 The conceptual model and justification of model variables

The background provided in the past two chapters is briefly reviewed and synthesised as part of the justification of the variables used in the trigonometric model presented here. In order to help clarify possible drivers of a ~1470-yr climate 'cycle', a conceptual model was developed that incorporates orbital forcing functions with similar time scales to numerical factors of the millennial-scale signal, and which may be linked to climatic variables (cf. Imbrie, 1985). Considered here as key players in this model are the Sun, Moon, tropical and anomalistic years, and sunspot variability. The superpositioning of these factors may produce important harmonics and sub-harmonics at millennial and centennial scale periods, which appear in the radiocarbon isotopic record.

The equinoctial precessional cycle, which is due to the gravitational influence of the Sun and Moon, is clearly an important consideration (cf. Lowrie, 2007). The Sun and Moon, therefore, contribute to the Milankovitch precessional cycle, which results from the interacting equinoctial and apsidal precessions. The extremes in Earth's orbit, the perihelion and aphelion, represent extremes in both solar irradiance and gravitation, both of which are influenced by the inverse square law [Figure 4.1]. The Earth-Sun distance annually varies by 3.4%, and there is a difference of ~6.6% in solar irradiance levels between these two orbital extremes. The extremes of gravitation experienced by Earth at

perihelion are enhanced at New and Full Moon, particularly the former as the greatest gravitational force is on the solar side of the Earth.

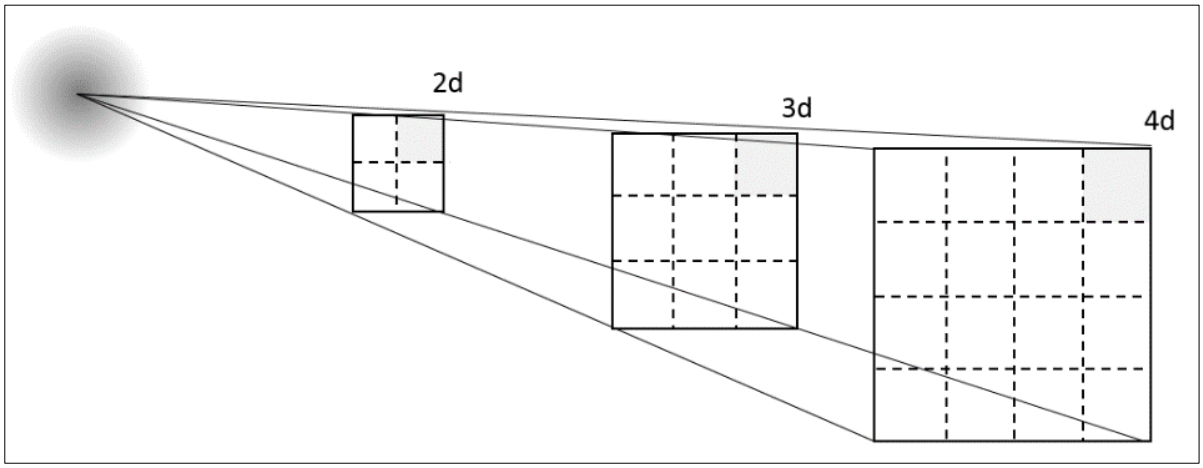

Figure 4.1: Schematic showing principle of Inverse Square Law, where 'd' is a constant value of distance from the source of energy. The further the distance from the energy source, the less the intensity, where intensity is inversely proportional to the distance squared. At twice the distance of 1d the intensity has decreased to 1/4, at 3d to 1/9, and so on.

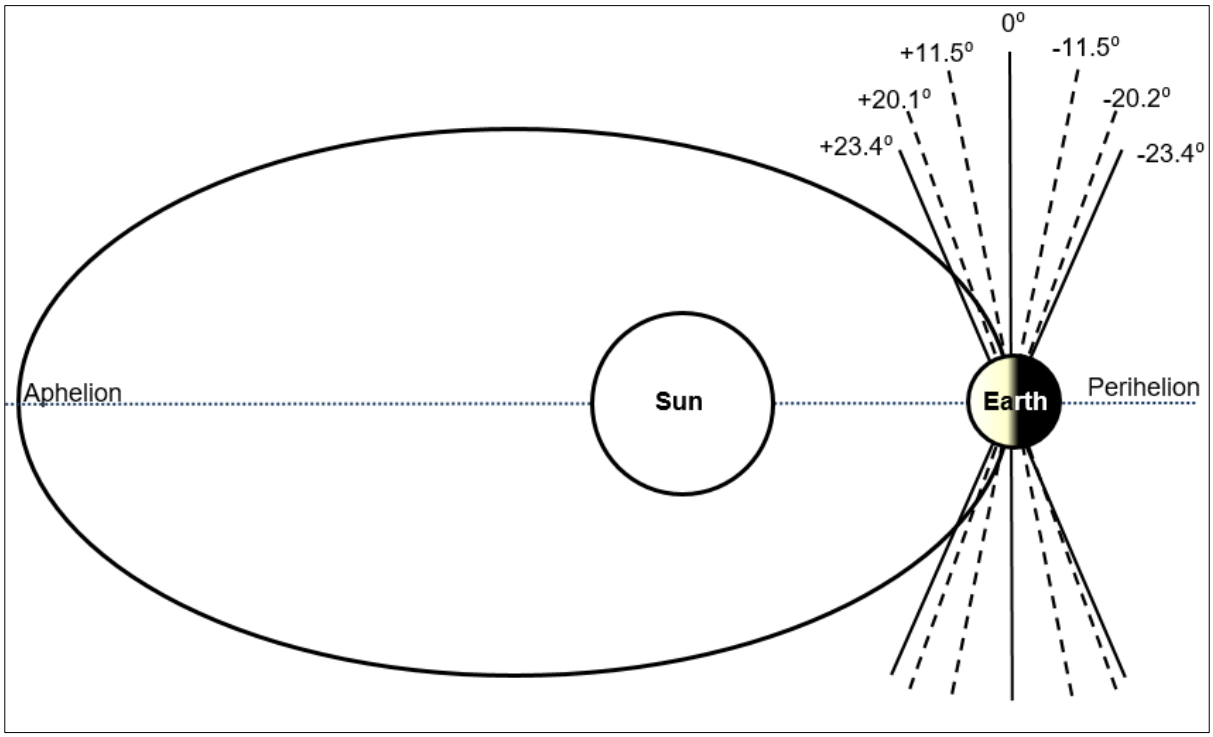

Figure 4.2: Schematic showing the changing solar declinations at perihelion, dependent upon the relationship between the apsides to the solstices and equinoxes. The declinations range from the extremes when the Sun is either on the Tropic of Cancer or Tropic of Capricorn at one or other of the solstices and zero at the equinoxes. The schematic contains values that show the solar declination at one monthly intervals. The southern hemisphere values are negative values. Values shown are for the current obliquity of the ecliptic.

Throughout the Milankovitch precessional cycle the orientation of Earth's axis will progressively vary in relation to the perihelion [Figure 4.2], thereby affecting levels of incoming solar radiation at perihelion. Consequently, the declinations of the Sun and Moon are thus dependent on the axial tilt and will also vary at perihelion. Declinations are measurements of angular distance from the celestial equator. The changing relationships between the solstices and apsides will thus result in the

moderation of insolation and gravitational forces impacting upon meteorological conditions on Earth, based on altered parameters for proximity and orientation to the Sun at particular times of the year.

Because the measurement of time involves Earth's rotation (see Chapter 3), whether it is the length of the day or year being measured, rotation must necessarily be incorporated in any model to serve as an interface to other interacting cycles. The celestial meridian, which is also associated with geographic longitude, is an obvious starting point for cyclical measurement; and to a certain extent also takes into account the need for regional sensitivity to be incorporated in any model of this nature (cf. Heinrich, 1988). The perihelion, upon which the anomalistic year is based, is also an important point as it is the time of maximum gravitation and solar irradiance, with its timing determined by the Moon (Section 3.1.4).

The Milankovitch precessional resulting from the separation between the solstice/equinox and the perihelion (and thus a measure of separation between the tropical and anomalistic years) is essential for examining trends at a higher-frequency scale. Firstly, the Metonic lunation could fulfil this role because it has the potential to capture diachronic precessional dynamics. The Metonic lunation cycle, which recurs at 19-yr (19.0002 tropical years or 18.9998 Julian years) intervals, is more closely coupled to the tropical year than the Saros cycle, which overshoots the year by ~10 days (Sections 3.1.4 and 3.2). The capacity for the Metonic lunations to act in this role is enhanced by the fact that the mean of the tropical and anomalistic years is equal to the length of the Julian year (365.2502 days compared to 365.25 days). The Metonic Moon's natural associations with the tropical, anomalistic, and Julian years, and its historical role as an intercalation tool between solar and lunar calendars (Section 3.2) make it an ideal chronological control.

This conceptual model and its implementation are different from previous attempts to explain the cause of this ~1470-yr 'cycle'. Firstly, the consideration of Earth's rotation relative to the anomalistic year is included as a measure of annual peak forcing associated with the perihelion, incorporating regional sensitivity. Secondly, the effect of solar and lunar declinations is included via astronomical data. Whilst the Saros cycle of eclipses and lunar nodal cyclicity have been extensively considered in prior research (e.g., Keeling and Whorf, 2000; Munk and Cartwright, 1966), I used the Metonic cycle of lunations within which I found a cyclical eclipse pattern (see below). This eclipse pattern automatically subsumes the lunar nodal cycle, as eclipses can only occur at the lunar nodes.

4.2 The trigonometric model

For the trigonometric model, I consider the superposition of mean values of three sets of interacting variables in the cause of the ~1470-yr 'cycle': (i) the ~11.4-yr Schwabe sunspot cycle; (ii) the Metonic cycle of lunations based on the current perihelion, and (iii) the anomalistic year, the time for Earth's

passage from perihelion to perihelion (365.2596 days). This last variable, in turn, determines the timing of Earth's rotation and revolution relative to the perihelion (RRA), i.e., the time for the perihelion to occur over the same geographic longitude on Earth. This model is not chronologically anchored, and no assumptions are made about the amplitude of individual variables. The point of osculation between the interacting variables [Figure 4.3] is based on the current Metonic lunation at perihelion, when the Sun is at solar zenith. This point represents maximum annual gravitational influences and solar irradiance relative to any given starting longitude on Earth. A fourth element (iv), the RRT (tropical year variable) is also included for the exploration of the superposition of the RRA and RRT, as representatives of the separation of the apsides from the solstices/equinoxes that occurs in Milankovitch cycles.

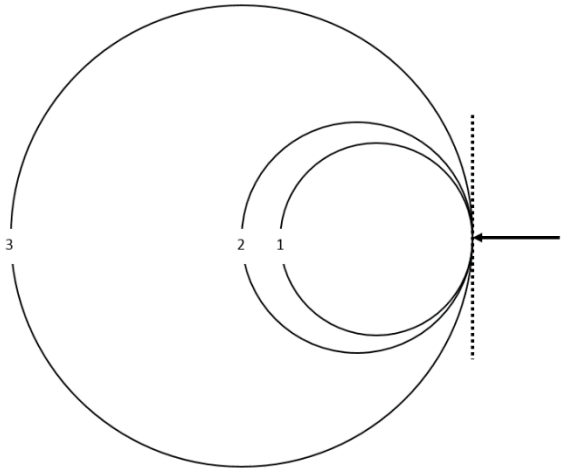

Figure 4.3: Point of osculation (indicated by arrow) of three separate cycles of different periodicities. The dotted line is at a tangent common to the three cycles. The point of osculation occurs at solar zenith at the Metonic-based perihelion.

Heinrich (1988) suggested that solar modulation of the climate needs to accommodate locational sensitivity to account for stronger instances of ice-rafting. The incorporation of locational sensitivity is represented in my conceptual and trigonometric models through the RRA timing, variable (iii) above. I assume that particular geographic regions are sensitive to astronomical forcing through periodic orientation to peak solar and lunar influences (via rotation and revolution), with geographic longitude delineating cyclic returns. These sensitive regions are visualised as key locations associated with ENSO phenomena, IRD events, deep-water formation and upwelling within the thermohaline current, with the inferred ability to influence atmospheric and oceanic circulation, heat distribution, and moisture transport. In effect, the RRA timing amplifies forcing at these locations. As with the ~18-yr Saros cycle (Sections 2.2.2.3), a relationship between the cyclical return to the same longitudinal position appears to be of relevance; *viz* the dominant sub-harmonic of 6 yrs in SST appears to be related to the longitudinal movement of the eclipse (each being one third of the total cycle, in terms of eclipse and rotation).

4.3 Method

4.3.1 Trigonometric model

Using the conceptual model outlined previously, a simple, trigonometric model was constructed using the values identified in (i), (ii), and (iii) above (Section 4.2) as the principal variables of this model. The values of these variables and others researched in preliminary modelling exercises are included in Table 4.1, and the values for the year types used in these calculations are identified in Table 4.2.

Along with charting the relationship of the anomalistic year (RRA) to a geographical longitude and full rotation of the Earth (*viz* 360° and one day), the tropical (RRT) and sidereal (RRS) years were also calculated [for sample see Tables A.1 to A.3, Appendix A]. The inclusion of the RRT and RRS also serve as chronological controls. This was achieved using the apparent angular advancement p.a. indicated in Table 4.2. For example, with a starting point of 0° for the tropical year, the Earth will have rotated 87.19° further west then the starting geographic longitude after one Julian year [Table 4.2]. Consequently, the timing of a full day and geographical longitude in relation to a tropical year will occur at ~128 yrs [Table 4.1; Figure B.1, Appendix B; Table A4, Appendix A]. This is the same value of 128 yrs where, due to precession, a difference of one day exists between the tropical year and Julian year (Section 3.2.1). These calculations are at annual resolution over a 5500-yr period. Where P=periodicity of the cycle and t=time elapsed (in years) since the start of the cycle, the scalable equation used for each trigonometric function was:

$$f(t) = \sin((2\pi t).P^{-1}).$$

Table 4.1: Modelled variables. RRA, RRT, and RRS respectively refer to values associated with the anomalistic, tropical, and sidereal years.

Variables	Period (yrs)
RRA	103.777501
RRT	128.1903
RRS	157.232
Hale sunspot cycle	22.8
Schwabe sunspot cycle	11.4
Metonic lunation cycle	19
Lunar nodal cycle	18.63
Base source of data: NASA (2011)	

Table 4.2: Values of year lengths. The apparent angular advancement is the value over and above 1 yr in degrees of geographic longitude, which is equivalent to approximately one quarter of a day. The values of these residuals are shown in days, hours, and apparent angular advancement.

Year type	Days	Residual (day)	Residual (Hrs)	Apparent angular advancement pa (◦)
Anomalistic (RRA)	365.259636	0.259636	6.231264	93.46896
Sidereal (RRS)	365.25636	0.25636004	6.152641	92.2896144
Tropical (RRT)	365.2421991	0.2421991	5.812778	87.191676
Gregorian	365.2425	0.2425	5.82	n/a
Julian	365.25	0.25	6	90
Base source of data: NASA (2011)				

For the RRA periodicity, the variable value used in this model is ~103.77 yrs, which is the first closest rotational return of Earth to <1° of the starting geographic longitude relative to a full year [Table 4.1; Figure 4.4]. Figure 4.4 shows the closest return of the RRA to the same geographic longitude occurs at 104 yrs (<1°), corresponding to the variable (iii). Such a period is found in radiocarbon spectral frequencies (Damon and Sonett, 1991; Sonett and Suess, 1984; Stuiver and Braziunas, 1989), and the 209-yr SdV cycle is a harmonic of this cycle. The precision of variable values is necessary for

calculating cyclical returns and resulting harmonics in this idealised model (cf. Berger *et al.,* 1989a). However, there are three prior returns to the starting geographic longitude [Figure 4.4], with the first occurring at 27 yrs (at 3.66° distant).

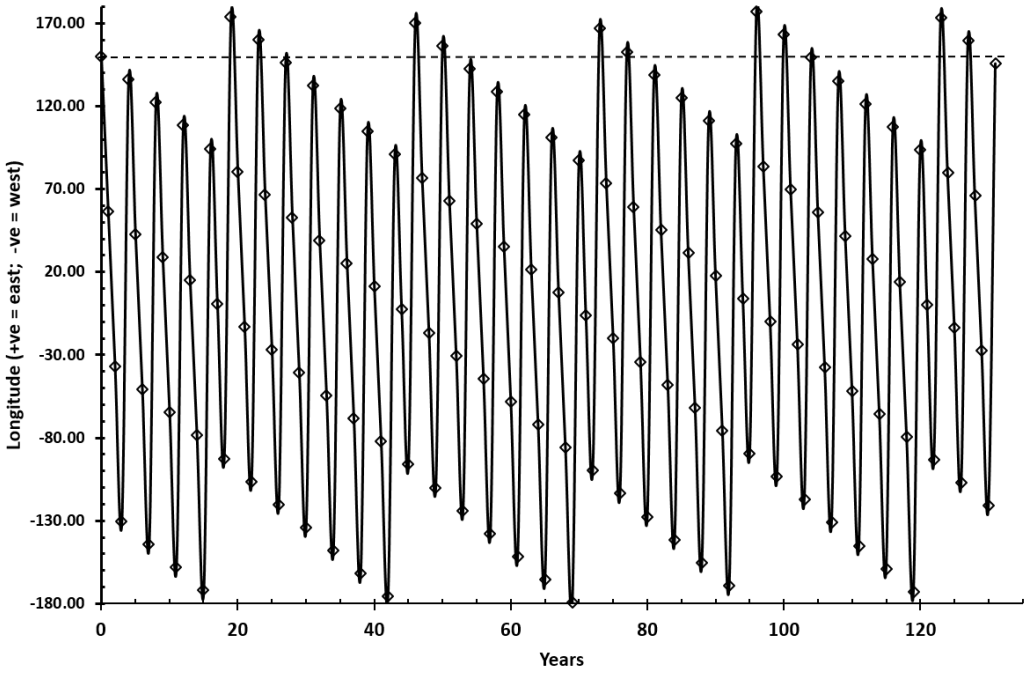

Figure 4.4: Earth's rotation-revolution relative to the perihelion in geographic context (associated with RRA). The starting longitude is 150°E and is indicated by the dashed horizontal black line. Consequent returns can be seen occurring along this line. Starting time is based on the solar zenith (local noon time)."

Exploratory data analysis, which mainly uses graphical techniques, was used to test underlying assumptions of the conceptual model and to gain insights into the interactive behaviour of these astronomical variables. Graphed interactive and combinations of the three primary variables were visually examined. Here "combination" is defined as the addition of the involved sine functions (which is the superposition of sine waves) whereas "interactive" is defined as an overlay of the separate sinusoidal forms in the one graph.

Differential calculus and graphed trigonometric functions were also used to examine periodicities for discontinuities and periodic returns of the three primary variables. The derivative is fundamental to differential calculus, expressing the instantaneous rate of change at any given point with reference to a variable. It is associated with limits and turning points, and equates to the slope of the tangent to a curve. Derivatives of trigonometric functions can be expressed in other trigonometric functions, and were used to identify discontinuities and key turning points in the graphed variables. Underlying tables, in which the calculations of annual changes in variables were made and stored as an Excel spreadsheet, were also manually scrutinised for cyclical returns.

All modelled activity of the three main variables were automatically cross-referenced to the extra variables (RRT, RRS, lunar nodal cycle, Hale sunspot cycle) by virtue of their position in the record for that year (i.e., a row data for the same year of the cycle) [Table A.1 in Appendix A]. Additionally,

as part of this exercise, 493-yr and 1868-yr periodicities evident as part of this trigonometric model were also filtered and chronologically ordered by RRA returns (≤1°), which were then sorted into series based on their relative proximity to the closest rotational return. RRA-RRT interaction and superposition were also graphed.

4.3.2 Astronomical data

The variable in (ii) above (the Metonic lunation) is represented for 5500 years (Section 4.5) at 19-yr intervals, generated using planetarium software: NOVA 2.13, (Hand, 1989-1994) and SkyChart III (DeBenedictis, 1993-2004). This is the Metonic cycle based on the lunation currently associated with the perihelion. Solar and lunar declinations and longitudes, right ascension, lunar nodal positions, and the obliquity of the ecliptic were recorded and referenced to Gregorian dates using Universal Time. Earth-Sun and Earth-Moon distances, and lunation type were also recorded for each record as were the variances of solar and lunar declinations from the ecliptic. NOVA provides data back to ~1221BC while SkyChart III provides the earlier results. For NOVA, the New Moon was calculated using an inbuilt function, while for SkyChart III the New Moon was determined by right ascension, longitude and declination for the Sun and Moon. For NOVA, the obliquity was automatically calculated by the program; for SkyChart III, the change in obliquity was calculated manually. Solar and lunar declinations in the resulting dataset were then graphed and visually scrutinised for periodicities. For a sample of this data, please see Appendix B.

4.4 Results

4.4.1 Solar and lunar declinations

Sinusoidal curves representing lunar and solar declinations, associated with the Metonic lunation series, presented in Figures 4.5, 4.6, 4.7 and 4.8, produce 209-yr and 228-yr harmonics (lunar declinations) [Figure 4.6], and a 133-yr cycle (solar declinations) [Figure 4.8]. For zoomed details of all graphed solar declinations see Appendix B. The lunar declination harmonics are the intervals between the Moon's position on the ecliptic and either the extreme northern and southern declinations within the data, viz the start of the four different phases of the sinusoidal curve. Four such periods result in one cycle of either 912 yrs (228 x 4) or 893 yrs ((228 x 3) + 209) [Figure 4.6].

A previously unreported series of total and annular solar eclipses occur as part of the Metonic lunation series at ~456±38-yr intervals [Figures 4.5 and 4.7]. Each set of Metonic eclipses predominantly has a range of 76 yrs and is comprised of Metonic eclipses that occur at 19-yr intervals [Figures 4.6 and 4.7]. Every eclipse within each series belongs to the same nodal series (i.e., north lunar node or south lunar node). The Metonic eclipses are only total when the Moon is at the south lunar node. As total eclipses can only occur when the Moon is at perigee, this Metonic series of eclipses naturally subsumes both the perigean cycle and lunar nodal cycle. This model therefore also captures enhanced gravitational forces that are associated with the lunar perigee cycle. As seen in Figure 4.5, three out

of four Bond events in the last 5500 yrs occurred in close proximity to these south nodal total eclipses in the Metonic eclipse series. The LIA produced the latest Bond IRD event (Bond *et al.*, 1999) and is coincident with a series of total south nodal eclipses.

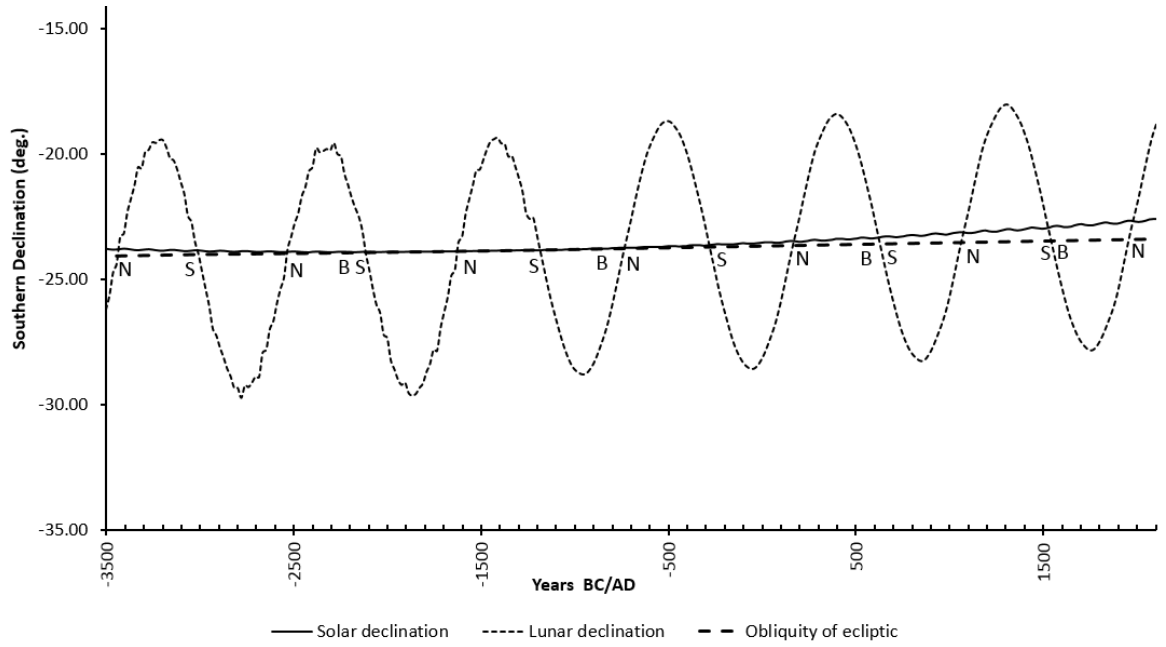

Figure 4.5: Solar and lunar declination associated with the Metonic lunation series attached to the current perihelion at 19-yr resolution. 'N' indicates the position of sets of north nodal eclipses and those marked by 'S' are sets of south nodal eclipses. Bond IRD events occurred close to Metonic lunation eclipses and are marked by 'B'; three of four Bond events occurred close to south nodal solar eclipses. Negative values on x-axis are BC.

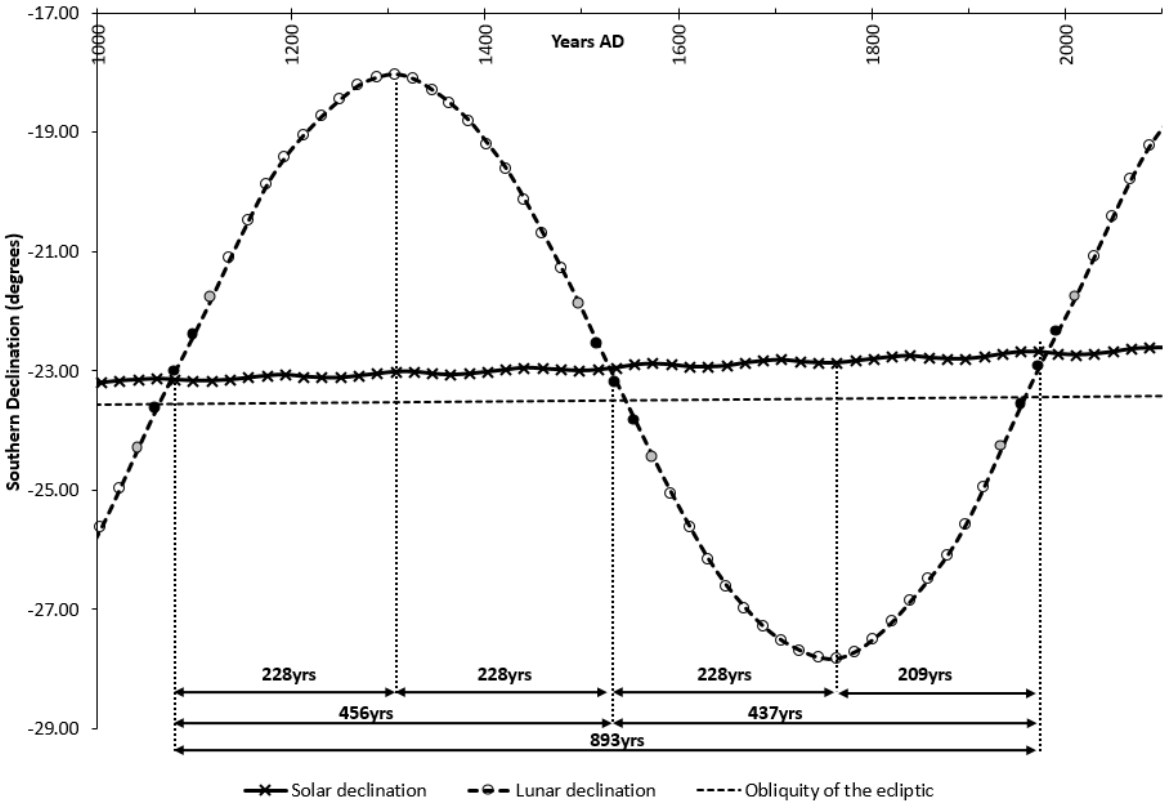

Figure 4.6: Lunar declinations since 1000AD showing one periodicity of a Metonic lunation series of 893 yrs, composed of four phases (three 228-yr periods and one 209-yr period). Black-filled markers are total or annular solar eclipses; grey-filled markers are partial solar eclipses.

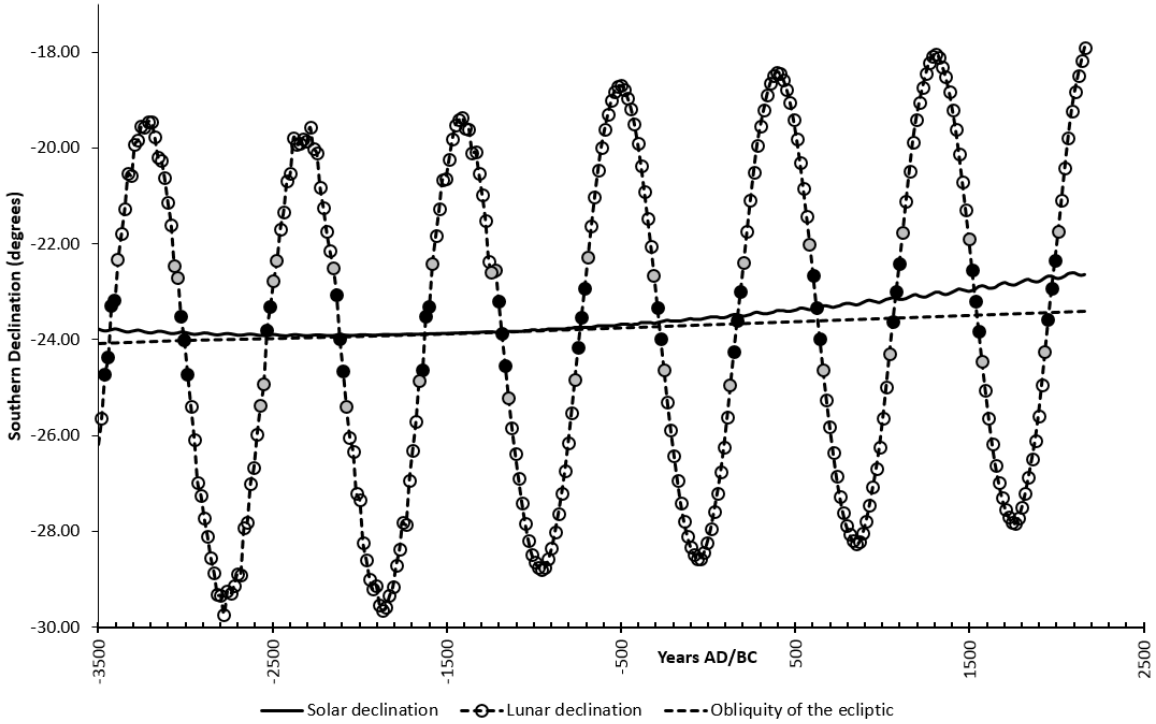

Figure 4.7: Solar and lunar declinations during the past 5500 yrs showing Metonic eclipse series at 456±38-yr intervals. Black-filled markers are total and annular solar eclipses; grey-filled markers are partial solar eclipses. As the solar declinations and Metonic lunations touch the maximum extent of the ecliptic (determined by the obliquity), the December solstice is reached, *viz* the Metonic lunations occur at the December solstice.

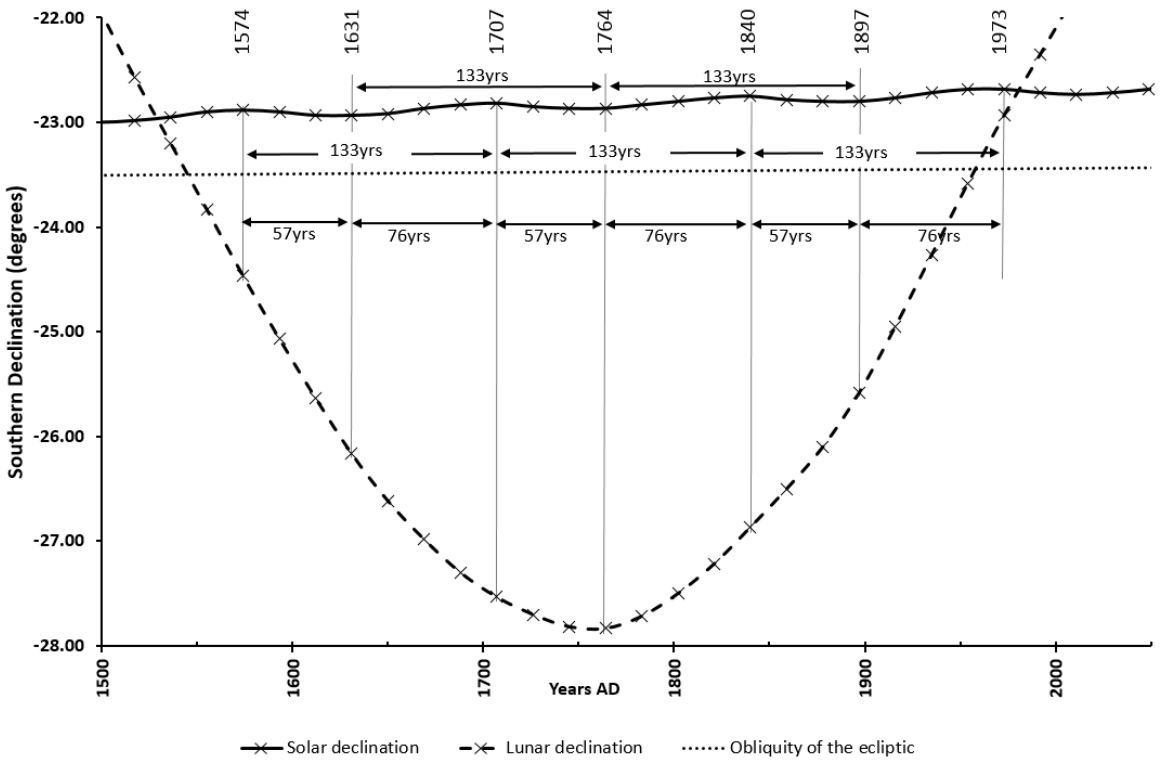

Figure 4.8: Solar declination cycle since 1500AD shows a periodicity spanning 133 yrs, comprised of 57-yr and 76-yr sub-periods.

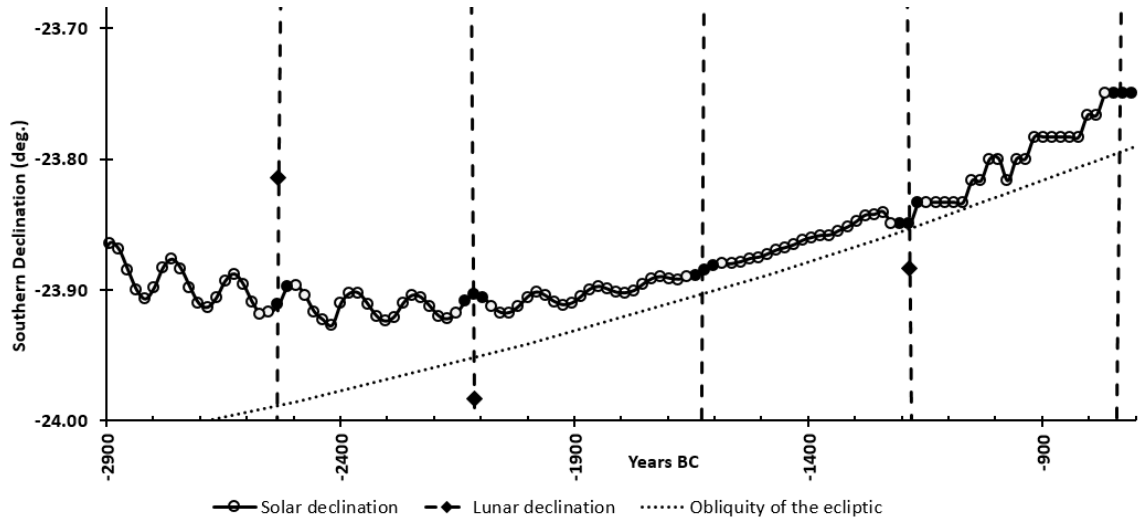

Figure 4.9: Zoom of solar declinations associated with the Metonic lunation series based on the current perihelion, showing the flattened declinations between ~1900BC and ~700BC. Black-filled markers are total or annular eclipses; grey-filled markers are partial solar eclipses. The dotted line shows the obliquity of the ecliptic. A Metonic eclipse occurs right on the ecliptic at the December solstice in 1183BC.

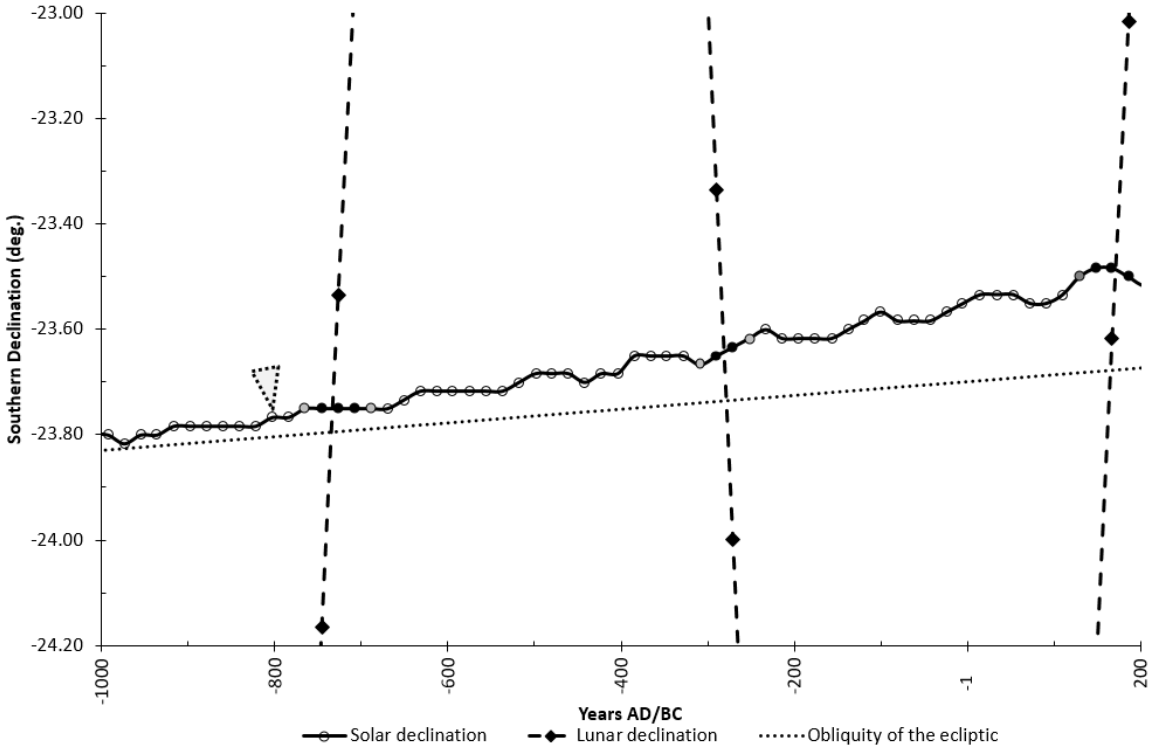

Figure 4.10: Zoom of solar declinations associated with the Metonic lunation series based on the current perihelion. Regaining sinusoidal form of solar declinations takes another ~700 yrs, during which there are extended periods of suppressed solar declination patterns. The further removed from the ecliptic, the greater the amplitude of the 133-yr solar declination cycle. Black-filled markers are total or annular eclipses; grey-filled markers are partial solar eclipses. The grey arrow is the approximate location of a Bond event.

The 133-yr solar declination cycle flattens out as the Metonic lunation approaches the December solstice conjunction, spanning a period of >1 ky [Figures 4.5, 4.7, and 4.9]. The solar declination pattern is smoother on the approach to the period of suppressed solar declinations [Figure 4.9] but the same is not the case after the period of suppressed declinations [Figures 4.9 and 4.10]. The solar declinations take ~700 yrs to resume their sinusoidal form [Figure 4.10].

4.4.2 Long-term periodic RRA returns

Table 4.3 lists RRA returns (where the RRA a measure of the anomalistic year) relative to the starting geographic longitude. Also listed for comparison are phase coincidences of these returns to harmonics of the SdV and Metonic cycles. The RRA periodicity is similar to known isotopic spectral peaks in palaeoclimatic records (Bond *et al.*, 1997; Bond *et al.*, 1999; Damon and Sonett, 1991; Stuiver and Braziunas, 1989), with the strongest of such signals associated with RRA returns to the same longitude (≤1.54°), phase-aligned to the sunspot and Metonic cycles (see Sections 2.2.3 and 4.5.5). The cycle with the most precise return to the starting longitude is 1868 years (0.017°). This is close to a multiple of the 18.63-yr lunar nodal cycle but has no correspondence to the sunspot and Metonic cycles. The third most precise RRA return (<0.2°) to the starting longitude is the 493-yr cycle and is associated with a Metonic return at 494 yrs, occurring in conjunction with a series of Metonic eclipses that occur at 456±38-yr intervals [Figures 4.5, 4.6 and 4.7]. This is the same length of the Cartwright tidal sedimentation cycle.

Table 4.3 RRA returns (<2°) to the same geographical longitude. Key spectral signals are highlighted in bold face, including the SdV cycle and variations of the ~1,470-yr cycle.

Period (yrs)	Cycle Return (°)	Precision (°)	Phase Alignment		
			Sunspot	Metonic	(yrs)
0	0	0			
1868	0.017	0.017			
1375	359.82	0.18			
493	**0.197**	**0.197**		x	**494**
2361	0.215	0.215	x		2360
882	359.623	0.377			
986	**0.395**	**0.395**		x	**988**
2257	359.443	0.557	x		2257
389	359.425	0.575	x		388
1479	**0.592**	**0.592**	x	x	**1482**
1764	359.245	0.755			
104	0.772	0.772	x		103
1972	0.789	0.789	x		1972
1271	359.048	0.952			
597	0.969	0.969			
2465	0.986	0.986			
778	358.851	1.149			
1090	1.166	1.166			
285	**358.654**	**1.346**	x	x	**285**
1583	1.364	1.363			
2153	358.608	1.392			
1660	358.472	1.526			
208	**1.544**	**1.542**	x	x	**209**
2076	1.561	1.561	x		2075
1167	358.276	1.724			
701	1.741	1.741			
2542	358.096	1.904			
674	358.079	1.921	x		673
1194	1.938	1.938			

The mean length of the ~1470-yr 'cycle' during the Holocene is 1374 yrs (Bond *et al.*, 1999). This is the second most precise return of the RRA (see in Table 4.3). It also has no correspondence to the

sunspot and Metonic cycles. However, the 1479-yr cycle (at 0.59°) [Table 4.3] is a harmonic of the 493-yr signal, amplifying a phase-aligned sunspot cycle; it is also the mean length of the climate signal during the early Glacial (32-75ka) (Bond *et al.*, 1999) and close to the mean length during the Glacial (1476 yrs between 15-65ka) (Bond *et al.*, 1999). In close proximity to the 1479-yr signal is a shared harmonic of both the 57-yr sunspot-Metonic cycle and tropical/anomalistic year separation rate (Sections 4.5.3 and 4.5.6) that also forms part of the 133-yr solar declination signal (Section 4.5.1).

4.4.3 Metonic and sunspot periodicity

The Metonic lunation and mean Schwabe sunspot cycles are harmonically related at periods of 57 yrs and multiples thereof (i.e., 114 yrs, 228 yrs, 456 yrs, 1482 yrs) [Figures 4.11 and 4.12], representing potential peaks/troughs of gravitational influence and temperature, with gravitational stresses greatest during solar eclipses. The 228-yr period is the length of one lunar declination phase, which is itself half of the Metonic eclipse period of 456±38 yrs and is also close to the SdV companion signal in radiocarbon data (Section 2.2.3).

The 57-yr cycle is also illustrated in geographic context in Figure 4.13, showing its nonstationary nature with respect to longitude, completing a 285-yr cycle when it returns to its starting geographic longitude (<1.5°). This 57-yr period is also a harmonic of interaction between the tropical and anomalistic years based on RRA and RRT sinusoidal interaction (Section 4.5.6), which migrates ~72° eastward every 57 yrs [Figure 4.13]. The characteristics of this interaction fit the profile of non-stationary ~57-yr cycles evidenced in climate data (Section 2.2.3). The 228-yr period is half the value of the Metonic eclipse period identified in astronomical data (Section 4.5.2) and one phase of the sinusoidal pattern of Metonic lunations.

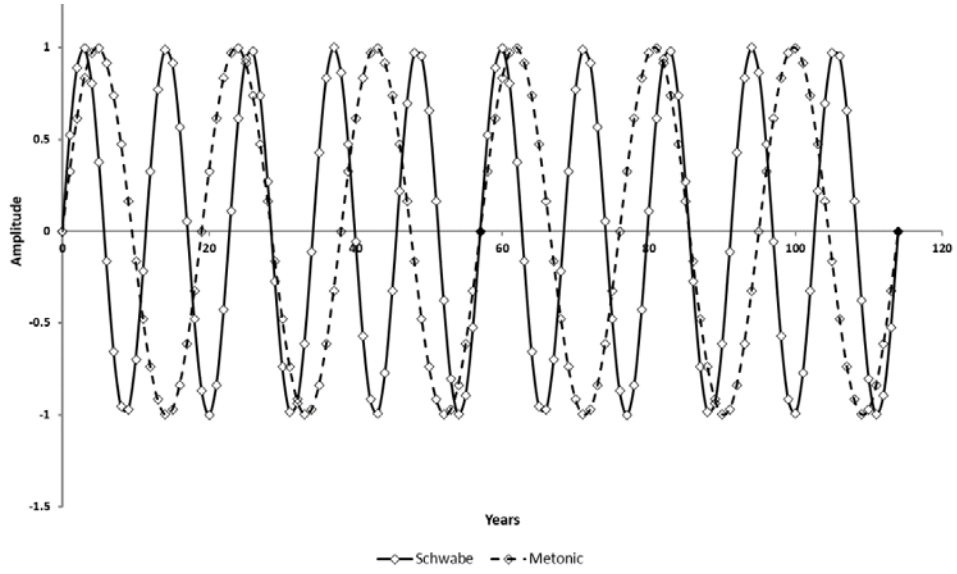

Figure 4.11: Modelled sinusoidal interaction of Schwabe sunspot cycle and Metonic lunation cycle. Common harmonics occur at 57 yrs and 114 yrs (marked by black-filled markers), and multiples thereof.

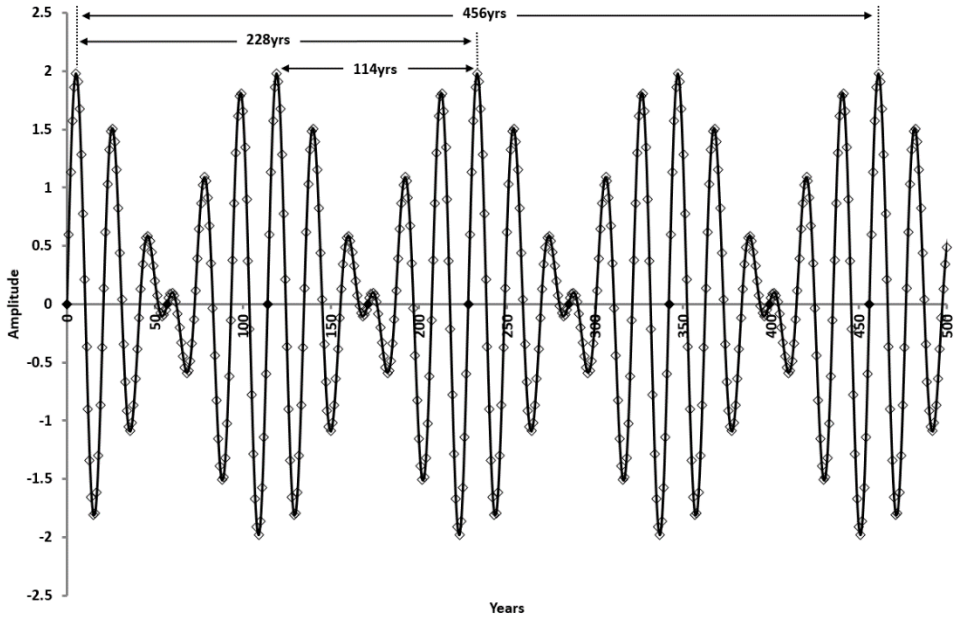

Figure 4.12: Modelled superposition of the mean Hale sunspot cycle and Metonic lunation cycle based on their sine values, showing 57-yr, 114-yr, 228-yr and 456-yr harmonics. The black-filled markers on the x-axis are each spaced 57 yrs apart, indicating a cyclical component of interaction between the Hale and Metonic cycles. The 114-yr frequency has been found in spectral data; the 228-yr period is associated with one lunar phase of the astronomical data; the 456-yr period is the periodicity of the cycle of Metonic eclipses found in astronomical data (Section 4.5.1).

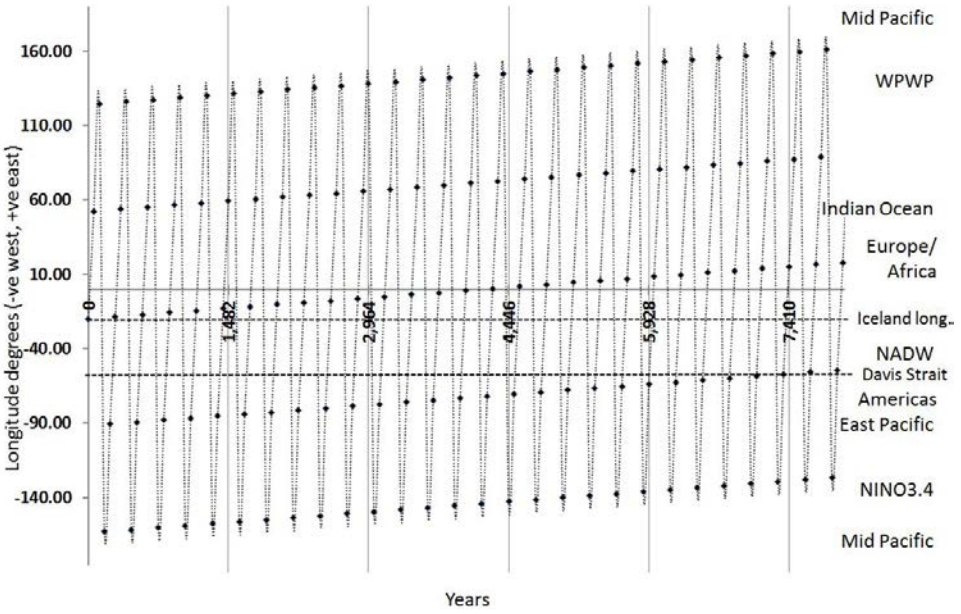

Figure 4.13: The 57-year Metonic-sunspot cycle in geographic context. Vertical axis represents geographic longitude and horizontal axis time in years, from an arbitrary start for 80 centuries. The regions listed on the right of the graph are associated with longitudinal positions indicated on the ordinate axis (y-axis). Time between points on the Metonic-sunspot track is 57 yrs, and time between points at the same longitude is 285 yrs. The 1,482-yr Metonic-sunspot period (solid vertical lines) is close to the RRA cycle of 1,479 yrs. The 285-yr and 1,482-yr periodicities are harmonics of the 57-yr non-stationary cycle.

4.4.4 Suess de Vries cycle

The SdV cycle is a cycle of warmer and cooler climatic conditions that have persisted during the past 50 ky (Sections 2.2.3 and 3.2.2). The 209 yr- and 228 yr-long phases of the lunar declination cycle are respectively the same lengths as the mean value of the SdV cycle and a companion cycle that is found in spectral analyses of climatic datasets. The superpositioning of the sunspot, Metonic and RRA cycles in the trigonometric model results in harmonics near 209 yrs and 91-95 yrs [Figure 4.14]. These respectively correspond to the SdV cycle and a variant of the Gleissberg cycle (Section 2.2.3). The SdV cycle [Figure 4.14a] matches the RRA return to ~1.54° longitude of the starting point [Table 4.3]. The RRA-Metonic return (209 yrs), based on interaction between the Moon and Earth's rotation relative to the anomalistic year, is closer to the SdV cycle than it is to the return based on interaction between the sunspot cycle and Earth's rotation (RRA) (~206 yrs) [Figure 4.14b].

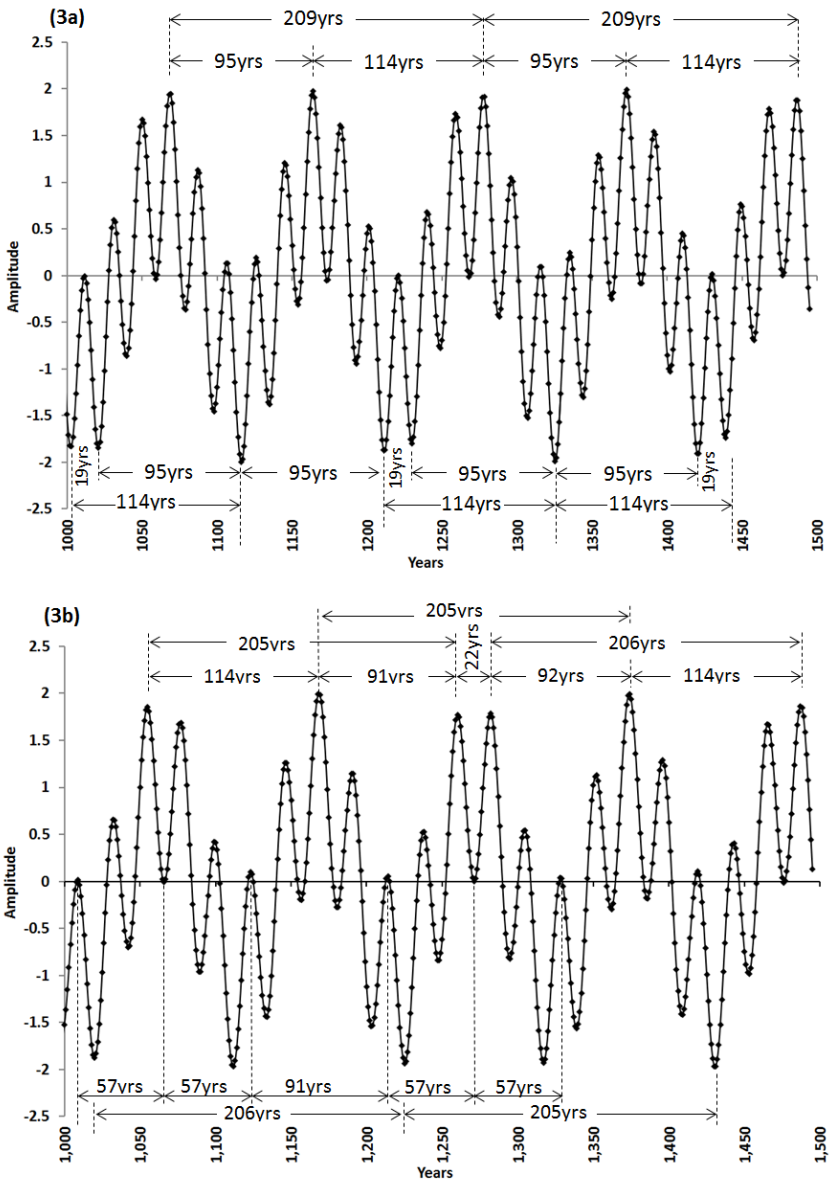

Figure 4.14: SdV and Gleissberg cycles. Combination of the RRA, Metonic and sunspot cycles reproduce the SdV and Gleissberg cycles; (a) Combined RRA and Metonic sinusoidal curves SdV (209 yrs) and Gleissberg (95 yrs); (b) Combined RRA and sunspot (Hale) sinusoidal curves: SdV (205-206 yrs) and Gleissberg (91 yrs).

The suppression of the SdV cycle (2600BC-1200BC) in the radiocarbon calibration curve [Figure 3.22] is coincident with the suppression of the 133-yr solar declination cycle found in astronomical data (due to the conjunction of the Metonic lunation with the December solstice) [Figures 4.9, 4.10. 4.15, and 4.16]. Greater variance of the solar declination movement is seen further removed from this

point, as shown in Figure 4.10 and 4.17. For higher resolution of the entire set of solar and lunar declination cycles see Appendix B.

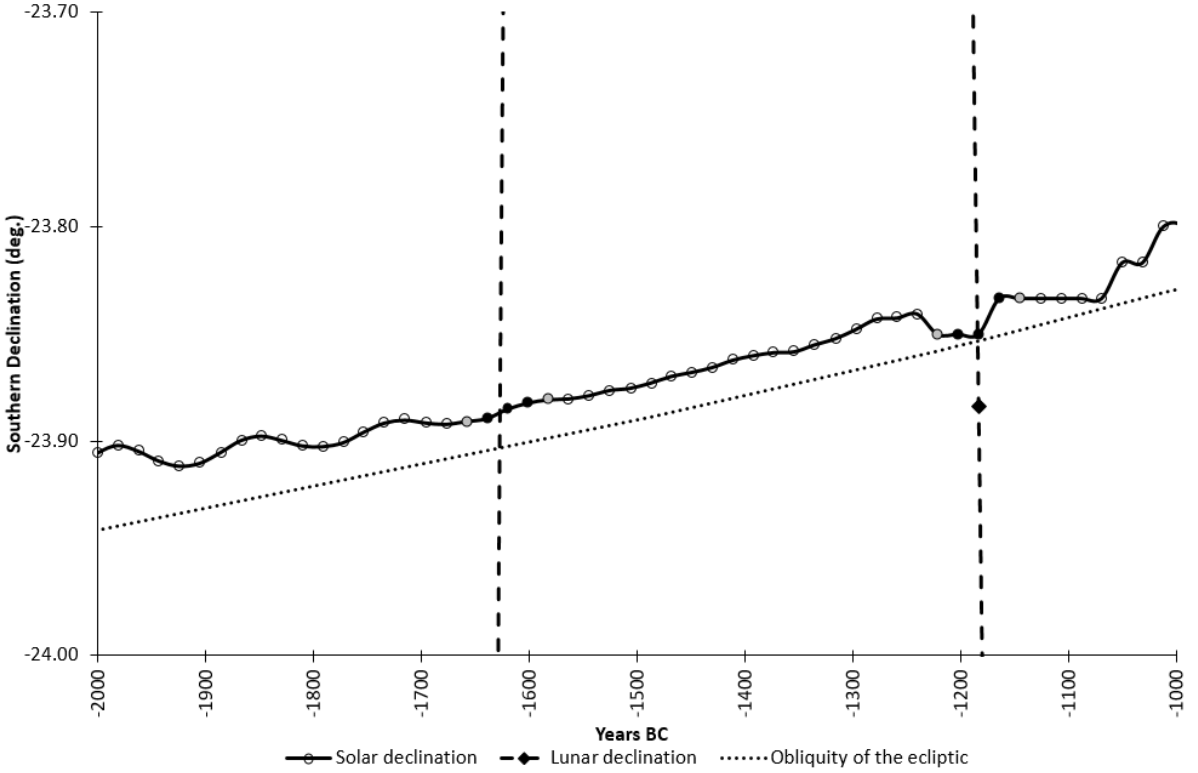

Figure 4.15: The astronomical data of solar declinations associated with the current perihelion-based Metonic cycle shows extensive flattening for the period coincident with suppressed SdV cycles. This effect occurs at the time of the Metonic lunation conjunction with the December solstice. Black -filled markers are total or annular solar eclipses and grey-filled markers are partial solar eclipses.

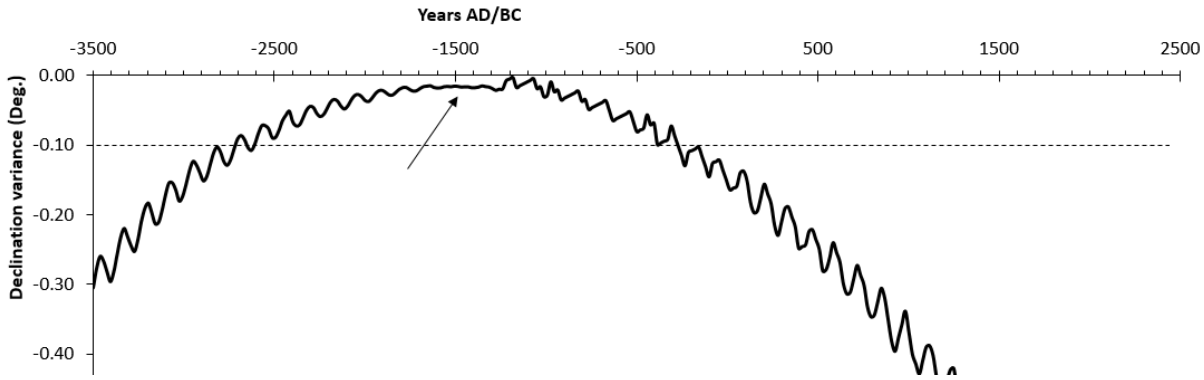

Figure 4.16: Solar declination variation from the ecliptic at the time of the Metonic lunation. Note constrained solar declination variance from the ecliptic during the period of the suppressed SdV cycles (marked by arrow), coincident with the conjunction of the December solstice and Metonic lunation. Negative values on x-axis are BC.

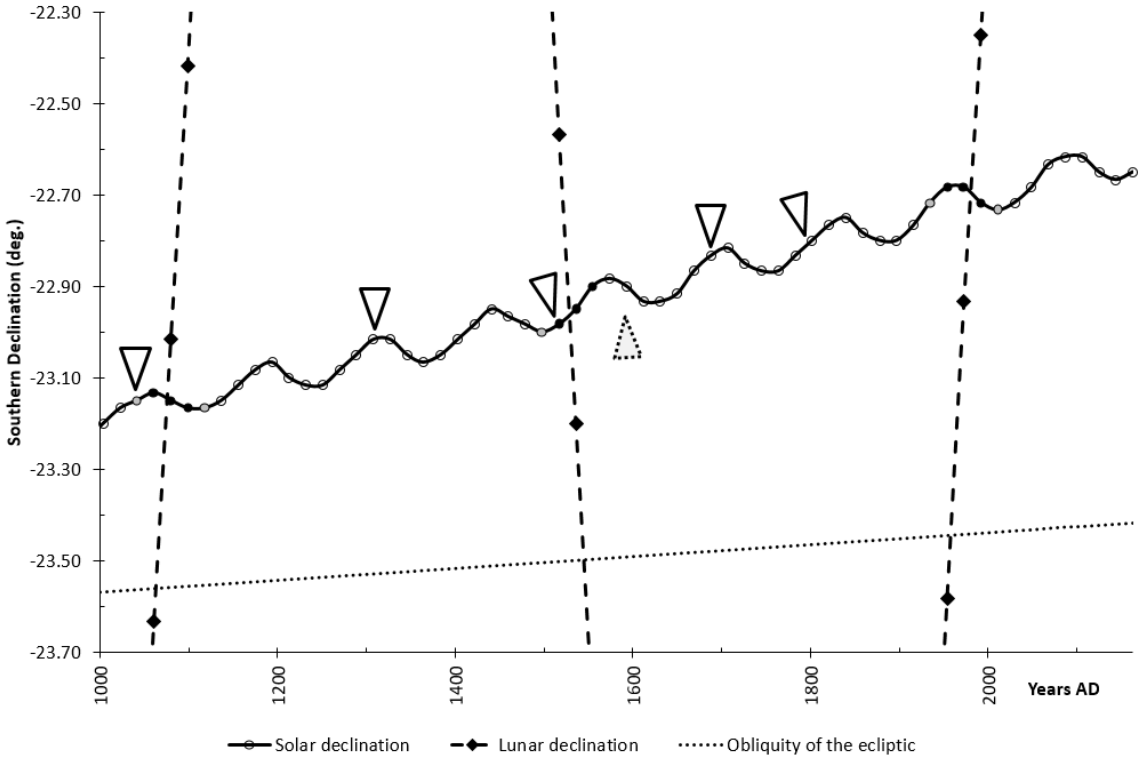

Figure 4.17: Solar declination cycles of 133 yrs since ~1000AD. Black-filled markers are total or annular eclipses and grey-filled markers are partial eclipses. Grey filled arrow approximates Bond event. Clear arrows in order from left to right show the Oort minimum, Wolf Minimum, Spörer Minimum, Maunder Minimum, Dalton Minimum. All these minima occur close to the northern peaks of the solar declination movement, with the exception of the Spörer Minimum (which has a split peak incorporating a Gleissberg cycle).

4.4.5 493-yr and Hallstadt cycles

The timing of the most precise RRA returns (<1°) are represented graphically in Figures 4.18 and 4.19. There are overlapping series of RRA returns at 493-yr intervals that move into phase as they approach and leave an exact RRA return. As these RRA series move away from an exact return, the Metonic lunation separates by an additional year at each ensuing harmonic, reducing the strength of the signal as that series moves out of range. At 493 yrs there is one-year separation from a Metonic lunation; at 1479 yrs the separation of the Metonic lunation is 3 yrs (occurring at 1482 yrs), which is also a harmonic of the mean sunspot cycle. On the third harmonic return of the 493-yr cycle (at 1482 yrs), the 57-yr cycle is superimposed (Section 4.5.3). Additionally, the period between precise RRA returns is 1868 yrs [Figures 4.18 and 4.19; Table 4.3]. A number of precise RRA returns (<1°) cluster around the ~2300-yr length of the Hallstadt cycle (cf. Damon and Sonett, 1991).

Figure 4.18 shows that there are generally three to four concurrent 493-yr RRA series that are within 1° of a longitudinal return, with a new series beginning every 1868 yrs [Figures 4.13 and 4.14]. The time taken for each series of 493 yrs to traverse a 1^0 range is a maximum of 2465 yrs, similar to the Hallstadt cycle found in both radioisotopic and geomagnetic data (Damon and Sonett, 1991; Raspopov *et al.*, 2011). Based on this cycle, at ~2300 yrs a phase shift appears to occur to realign the

RRA cycle to within a 1° return to the starting geographical longitude, shifting to a more closely-aligned 493-yr RRA series [Figures 4.18, 4.19].

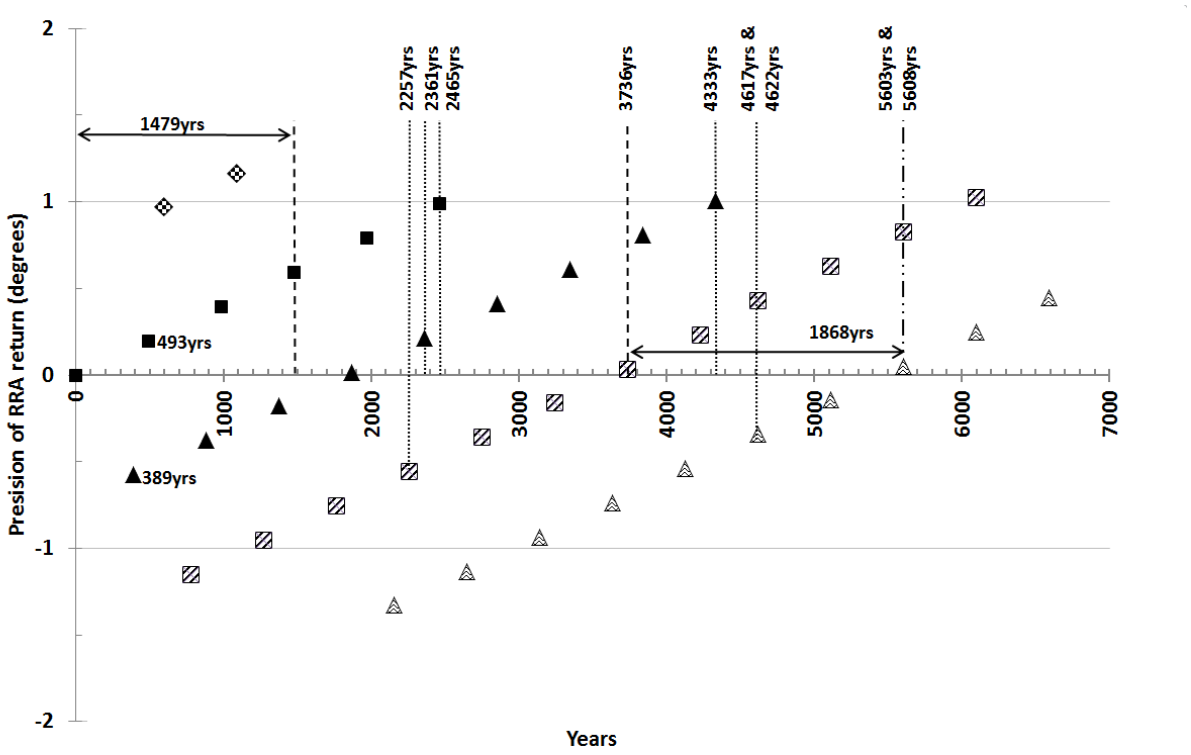

Figure 4.18: Series of RRA returns. The modelled RRA returns sorted by series based on their approach and departure from exact return points. The distance between each point in the series is 493 yrs, the third harmonic of which is 1479 yrs. A period of 1868 yrs occurs between the most precise returns. Clustering of RRA returns occurs in the Hallstadt range.

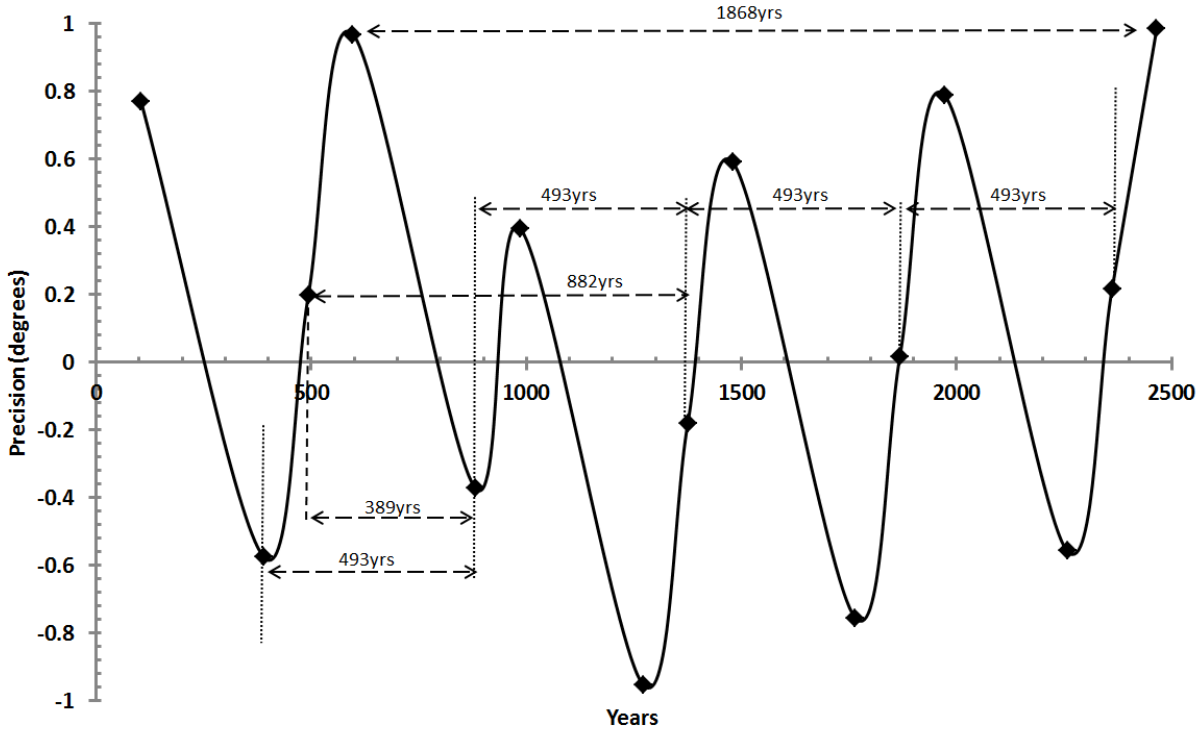

Figure 4.19: Sequential presentation of the 493-yr cycle. This figure shows the 493-yr cycle based on RRA returns for <1°, which is a base harmonic in the ~1470-yr cycle. The 389-yr harmonic is also found in radioisotopic spectral frequencies.

Table 4.4: Points of discontinuity in RRA using secant Θ (graphed in Figure 4.20). This table shows associations with Bond IRD cycles and other important frequencies. The angle or return is relative to starting geographic longitude, so that 180° is opposite in WPWP; 90°/270° are 90° distant; 0°/360° are return positions. Refer to IDS correspond with data points in Figure 4.20. IDs 1, 2, 3, 5, 12, 14, 21 are return to starting longitude.

ID	RRA harmonic (yrs)	Association	Angle (°)	Bond *et al.* (1999) ref.
1	26	First RRA at 27 yrs	3.66	
2	78	Gleissberg variant; Sunspot cycle; 3rd RRA return	358.59	
3	389	Solar spectral frequency	359.43	
4	441	Proximate to 3 Bond *et al.* (1999) cycle error margins	179.81	32-75ka; 64-79ka; 53-64ka
5	493	Cartwright cycle sedimentation cycle	0.20	
6	545	Proximate to Bond *et al.* (1999) cycle error margin	180.58	31-43ka
7	856	Double cycle error margin (Bond *et al.*,1999)	89.43	64-79ka
8	908	Within 4 yrs of lunar declination cycle	269.82	
9	960	2 x cycle error margin (Bond *et al.,* 1999)	90.20	53-64ka
10	1012	2 x cycle error margin; close RRT return (512 yrs)	270.59	0-79ka; 22-34ka; 1.5-12ka
11	1323	Bond IRD peak (within 5 yrs)	179.43	31-43ka
12	1375	Proximate to 3 Bond IRD peaks	359.82	1.5-12ka; 31-43ka; 43-55ka
13	1427	Bond IRD peak (within 16 yrs)	180.21	53-64ka
14	1479	Bond IRD peak (within 1 yr of *1; 3 yrs of *2)	0.59	32-75ka*1; 15-65ka*2; 13-24a
15	1531	Bond IRD peak (within 6 yrs)	180.98	12-32ka
16	1634	Bond IRD peak (within 3 yrs)	88.28	22-34ka
17	1790	Bond IRD (within 5 yrs); 2 x lunar declination cycle (within 3 yrs)	269.44	64-79ka
18	1842	Broad Bond IRD and sea sedimentation peak (Bond *et al.,* 1999)	89.82	
19	2257	Hallstadt length cycle	359.44	
20	2309	Hallstadt length cycle	179.83	
21	2361	Hallstadt length cycle	0.21	
22	2413	Hallstadt length cycle	180.60	

The RRA cycle also maps to all Bond IRD event variations during the last glacial and Holocene [Figure 4.20, Table 4.4], with error terms and variable lengths of the (Bond) 'cycle' that are explainable by the RRA and interacting periodicities of the model's variables [Table 4.4]. The location of the return positions of periodic components relative to each other, their position with respect to the Milankovitch precessional cycle, and the length of the sample period being tested are expected to influence these factors. This shows that the most precise RRA returns (those with the greatest amplitudes) are accompanied by a companion signal, with peaks being at starting longitude or separated by 180° (such as occurs with gravitational forcing at New Moon-Full Moon).

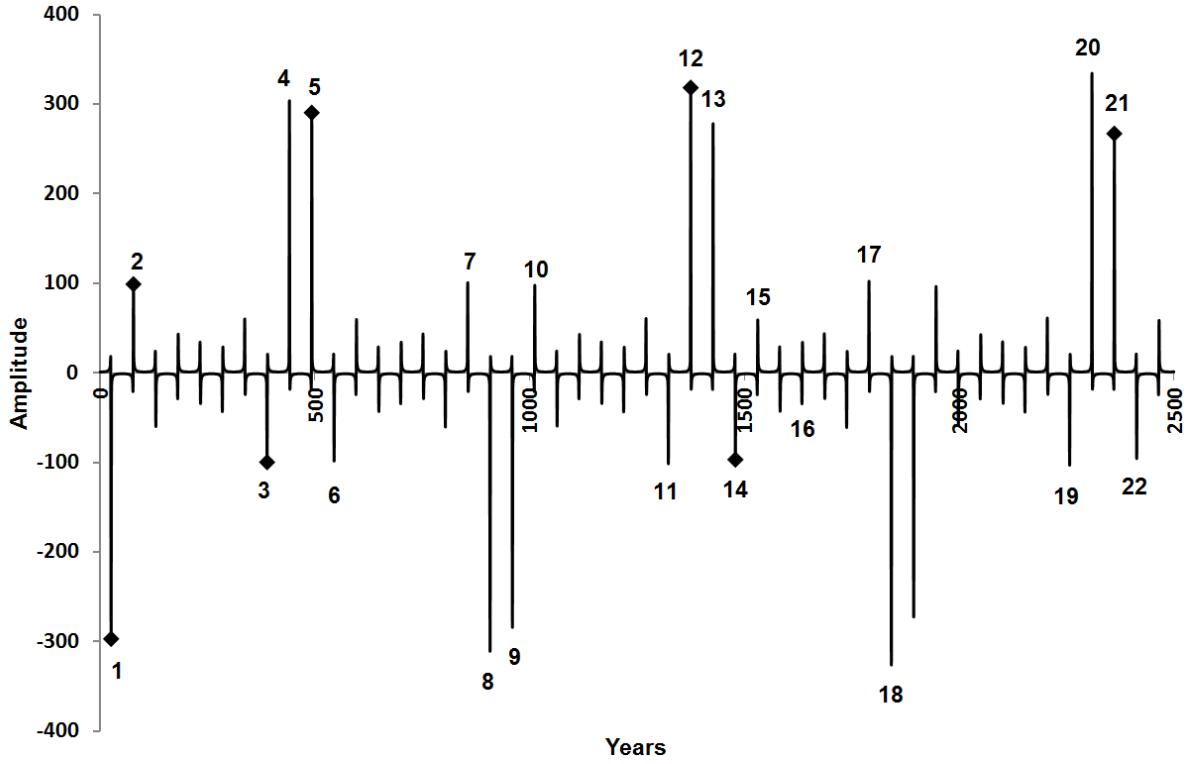

Figure 4.20: Discontinuities of RRA using secant function (the inverse trigonometric function of cos) to find points of discontinuity. These points are listed in Table 4.4. Those points marked by diamond markers (1, 2, 3, 5, 12, 14, 21) are returns to the same geographic location. IDs 4, 6, 11, 13, 15, 20, 22 are separated by 180° degrees from starting location, and IDS 7-10, 16-18 are located 90° from starting location (geographic longitude).

4.4.6 Results from RRA-RRT trigonometric modelling

The superposition of the anomalistic (RRA) and tropical (RRT) cycles through the addition of their sine values can be seen in Figures 4.21, 4.22, and 4.23. The overall interaction of the modelled RRT and RRA cycles produces a repetitive pattern that can be seen in Figure 4.21. Figures 4.22 and 4.23 zoom in on this interaction, where it can be seen that a ~57-yr period (half-cycle) is a component. This 57-yr period shares a common harmonic with both the Metonic lunation and Schwabe sunspot cycle (Sections 3.1.4). It is also the rate of precessional separation between the tropical and anomalistic years (one day in 57 yrs) ((365.2596-365.2422) x 57=0.9918). This 57-yr period is also

the same length as a non-stationary climate cycle, and a component of numerous other cycles. In the first few hundred years of this modelled activity [Figure 4.23] can be seen lengths associated with the SdV cycle (172 yrs, 228 yrs), and the marine reservoir figure for the open ocean (~400 yrs) (cf. Gagan *et al.,* 2004; Hua *et al.*, 2015).

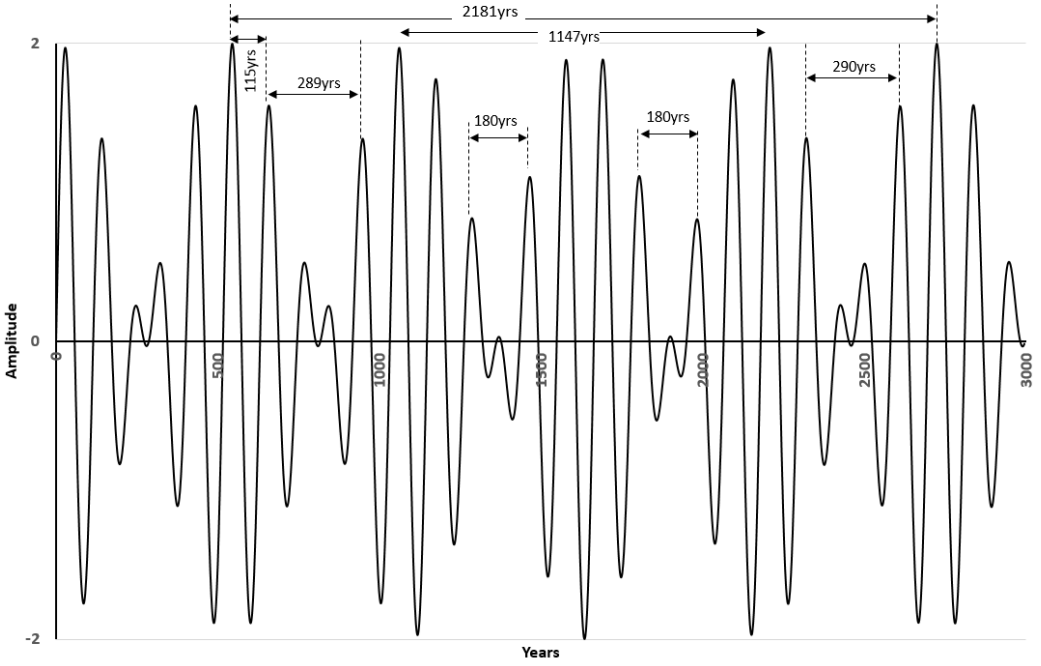

Figure 4.21: The superposition of the RRA and RRT cycles produces a repetitive pattern based on a fundamental periodicity of ~57 yrs [Figures 4.22 and 4.23].

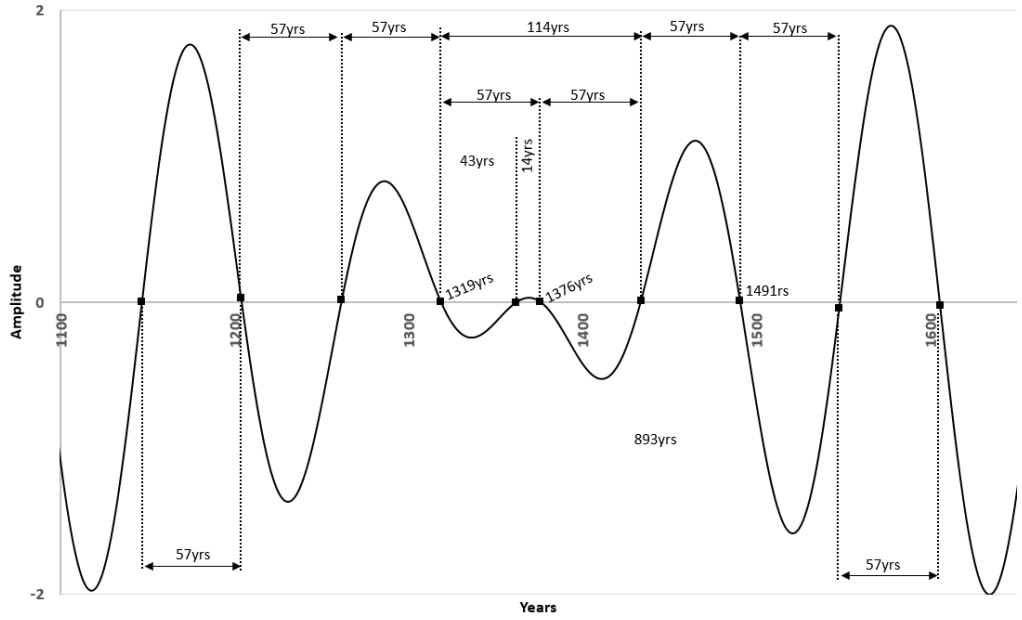

Figure 4.22: Zoomed view of the combined RRA and RRT sinusoidal curves, showing a repeating return (half-cycle) every 57 yrs. The 57-yr period is also found as a non-stationary climate cycle and in the sunspot-Metonic lunation cycle (Section 4.5.3). In this graph can also be seen the 1376-yr cycle that closely corresponds with the length of the Bond cycle during the Holocene.

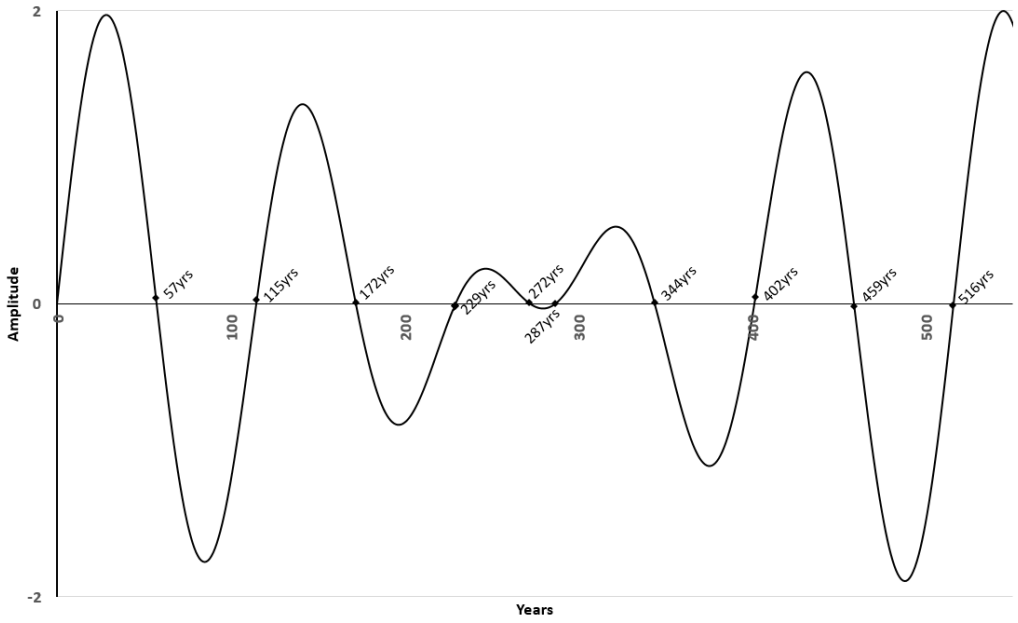

Figure 4.23: A zoomed view of the combined RRA-RRT sinusoidal curves showing a ~57-yr return period that is seen in other astronomical data (see above). Also seen here are variants of the SdV cycle (172 yrs, 229 yrs) and the marine reservoir value for the open ocean (~400 yrs) (cf. Hua *et al.*, 2015). The cyclical return of the 57-yr non-stationary climate cycle to the original starting longitude (285 yrs) is also close to one of these values (287 yrs).

4.5 Chapter summary

Here, I have shown that the superposition of Earth's rotation-revolution cycle (RRA), the Metonic cycle, and the sunspot cycle have the capacity to emulate the ~1470-yr climate cycle and associated harmonics. Primarily, the longer signals influence the general timing of these events, which are fine-tuned by the shorter Schwabe sunspot cycle. Associated physical mechanisms are gravitational and radiative forcing that could induce responses in Earth's internal climatic system. The harmonics produced by my astronomically-based modelled variables and discovered in my astronomical data appear as spectral frequencies in radioisotopic datasets with known climatic associations. Wobbles in solar and lunar declinations appear to match spectral frequencies in isotopic data and suggest that nutation and the orientation of the lunar orbital plane may affect Earth's solar irradiance and gravitational forcing at sub-Milankovitch frequencies, influencing climate and isotopic patterns. Previously the cause of such isotopic patterns was interpreted as inferred medium- to long-term cycles of solar variability (Damon and Sonett, 1991).

The combinations of variables used in these models are also capable of reproducing the SdV cycle and Gleissberg cycle (cf. Braun *et al.*, 2005), 493-yr and 131-yr RRA-Metonic cycles, and a 57-yr cycle. This also suggests that both the SdV and Hallstadt cycles are not physical process in their own right but result from the superposition of solar and lunar forcing, as seen in Figure 4.14. The Metonic lunation and mean sunspot cycles share multiple common harmonics (Section 4.5.3) with comparative cycles in palaeoclimatic records (cf. Chambers *et al.*, 2012; Edvardsson *et al.*, 2011; Stuiver and Braziunas, 1989).

Cycles or phases of 57 yrs and 133 yrs were also found in astronomical data. The 57-yr cycle is a sunspot-Metonic harmonic associated with a previously unreported 456±38-yr Metonic eclipse series (456=8x57), but is also associated with the separation rate between the tropical (RRT) and anomalistic (RRA) year cycles by one day in 57 yrs. The 57-yr cycle is a component of the lunar declination cycle (228=4x57), and a 1482-yr Metonic-sunspot cycle that is close to a return of the interacting RRA (1479-yr) and RRT (1474-yr) cycles. Each Metonic eclipse series usually includes 4-5 solar eclipses spanning a period of 57-76 yrs. The 76-yr cycle has been associated with the Gleissberg cycle by some sources (e.g., Hunten *et al.*, 1993) and is close to a multiple of the sunspot cycle. Additionally, the combination of the 57-yr and 76-yr cycles are factors in the 133-yr solar declination cycle [Figure 4.8].

Astronomical data for the last 5500 yrs, shown in Figure 4.5, indicates that Bond IRD events occurred close to the harmonic of ~1470±500-yr intervals, suggesting a possible causal relationship associated with both the perihelion (through the RRA metric) and the Metonic lunation through either gravitational forcing, solar irradiance/insolation, or a combination of both. These results also show that the RRA cycle return at 1479 yrs (a harmonic of the 493-yr RRA-Metonic harmonic) [Figures 4.18 and 4.19] is closely aligned with the Metonic-sunspot cycle at 1482 yrs (a multiple of the associated Metonic return of 494 yrs). By the RRA mechanism, the North Atlantic's IRD and Dansgaard-Oeschger cycles could be phase-locked to internal climate events and to millennial-scale climatic variability of ENSO phenomena in the Pacific. The RRA mechanism accounts for regional sensitivity required by Heinrich (1988) in order to filter stronger pulses of ice-rafting. The confluence of solar insolation extremes and peak gravitational, oceanic, and atmospheric tides has the capacity to catalyse both the thermohaline current and ENSO activity at millennial scales through their respective catalysts. Thee triggers include ice-sheet mechanics, oceanic and atmospheric currents, atmospheric temperatures, and SST.

Chapter 5 - Physical Models of Gravitation and Solar Flux/Insolation

In the previous chapter, a conceptual model for the cause of millennial-scale climate signals was developed which demonstrated orbital interactions between the Sun, Moon and Earth at periods similar to centennial- and millennial- scale climate variations. These astronomical features include a 456±38yr Metonic eclipse series, a 133-yr solar declination cycle, lunar declination periodicities of 209 yrs, 228 yrs, and 912 yrs, and cyclical Metonic-perihelion interaction of 209 yrs, 494 yrs, and 1482 yrs. In this chapter, physical calculations of gravitation, solar irradiance, and insolation are used to develop an understanding of the roles that the Sun and Moon may play in climate forcing at centennial and millennial scales. These calculations are based on the Metonic lunation data that was introduced in the last chapter. Additionally, the relationships of the Metonic lunation to the tropical year and the perihelion are explored in this chapter (Section 5.2), based on astronomical data provided in the last chapter. Examination of the Metonic lunation's relationships to both these factors also illustrates the Moon's role in precession and its potential capacity to contribute to chronological variability. To provide context to the impacts of gravitation, solar irradiance, and insolation on Earth's climate at these scales, the next section details relevant parameters related to Earth's orbit. Solar variability associated with sunspot activity is not considered in this chapter.

5.1 Background: the numbers of Earth's orbit

A general physical model of Earth's orbit is useful for providing a more detailed picture of the diachronic changes in solar irradiance and gravity than is generally available, and serves as a background to the physical models of irradiance and gravitation discussed in this chapter. NASA values (Williams, 2013a, 2013b) [Table 5.1] for Earth's current orbital parameters and established values for minimum, maximum and current eccentricities were used to calculate the lengths of the semi-major and semi-minor axes, perihelion and aphelion distances, length of orbital path, and velocities and distances travelled per day [Tables 5.2, 5.3, and 5.4]. These factors affect calculations of solar irradiance, gravity and rate of precession, and may influence the lengths and strengths of climate signals in the palaeoclimatic record. The average daily distance travelled and mean distance of Earth from the Sun occurs at 90^0 to the perihelion, which is currently in early April and October [Figure 5.1]. This does not always occur at the equinoxes, which happens only when either of the solstices is at perihelion.

Table 5.1: Table of values used in calculations (from NASA fact sheets for Earth and Sun) (Williams, 2013a, 2013b) and glossary (NASA, n.d.)

Gravitational constant (Nm^2/kg^2)	6.67E-11
Sun's effective temperature (photosphere) (ºK)	5,772
Solar irradiance at 1AU (W/m^2)	1,360.51
Mean Earth-Sun distance	1AU
Stefan Boltzmann constant (σ (W m−2 K−4))	5.67E-08
Surface area of Sun (photosphere) (m^2)	6.08E+18
Earth's radius (km)	6,380
Earth's radius (AU)	4.31E-05
Power (solar luminosity) (joules/sec)	3.83E+26
Solar mass (kg)	1.99E+30
Earth mass (kg)	5.97E+24
Lunar mass (kg)	7.35E+22
1AU (current) (km)	149,597,870.70

Table 5.2: Earth orbital parameters at different eccentricities (e) - calculated values. This table shows distances (km) for semi-major (a) and semi-minor (b) axes, perihelion and aphelion distances, and orbital length.

Eccentricity	e	a	b	Mean
Min	0.005	1.48E+08	1.48E+08	1.48E+08
Current	0.017	1.50E+08	1.50E+08	1.50E+08
Max	0.058	1.56E+08	1.55E+08	1.56E+08
	e	Perihelion	Aphelion	Orbit length
Min	0.005	1.47E+08	1.49E+08	9.29E+08
Current	0.017	1.47E+08	1.52E+08	9.40E+08
Max	0.058	1.47E+08	1.65E+08	9.77E+08

Table 5.3: Daily distances travelled by Earth - calculated values. Earth travels a maximum of ~61' per day at perihelion and a minimum of 58' daily at aphelion, which are the rates of apparent solar movement by longitude (ecliptic). This table shows the distances (km) travelled at these rates at different eccentricities, and also based on the average lengths of Julian and tropical years.

e	1º	61'	59'	58'	Julian	Tropical
Min	2.58E+06	2.62E+06	2.54E+06	2.49E+06	2.54E+06	2.54E+06
Now	2.61E+06	2.65E+06	2.57E+06	2.52E+06	2.57E+06	2.57E+06
Max	2.71E+06	2.76E+06	2.67E+06	2.62E+06	2.68E+06	2.68E+06

Table 5.4: Earth's velocity at minimum, maximum, and current eccentricity (e) - calculated values. These are based on the tropical and Julian years in km/hr, km/minute, and km/sec.

Velocities:	m/sec	
Eccentricity	Julian year	Tropical year
Min	29,442	29,443
Now	29,783	29,784
Max	30,969	30,969

Table 5.5: Solar irradiance and eccentricity - calculated values. This table shows irradiance at minimum, maximum and current eccentricity, and irradiance differences between the mean, and minimum and maximum irradiance (at aphelion and perihelion respectively), and the differences between irradiance levels.

Eccentricity		Irradiance differences (W/m2)				
		aphelion	perihelion	perihelion/aphelion	mean/apsides	% of mean
Min	0.005	1378.38	1406.23	27.85	13.92	2.00%
Current	0.017	1315.87	1407.06	91.19	45.60	6.70%
max	0.058	1122.26	1415.67	293.41	146.71	23.32%

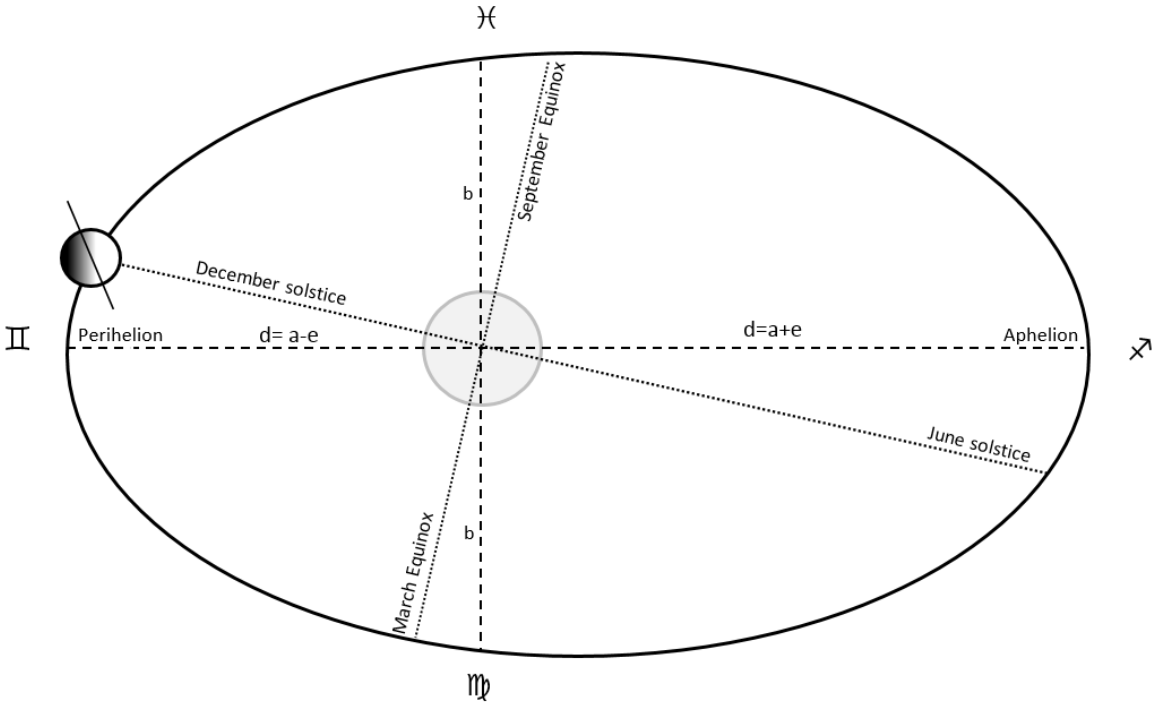

Figure 5.1: Schematic of Earth's orbit and current positions of equinoxes and solstices to perihelion and aphelion. The perihelion distance is the length of the semi-major axis (a) less the value of the eccentricity (e). The aphelion distance is the length of the semi-major axis plus the value of the eccentricity (e). The length of the semi-minor axis (b) is shown and is set at 90º to the semi-major axis. When Earth reaches the point at 90º to the apsides (perihelion and aphelion), the Sun's apparent motion (*viz* the Earth's) is moving at the mean of ~60'/day. Astronomical symbols for constellations, starting at the perihelion and moving clockwise are Gemini, Pisces, Sagittarius, Virgo (NASA, 2016). The galactic centre is at ~2º Sagittarius, the December solstice is at 4-5º Sagittarius, and current perihelion at 17-18º Sagittarius; In longitude (ecliptic), these values are respectively 267-268º, 270º, ~283º.

Based on Earth's orbital parameters, solar irradiance for different stages of the eccentricity cycle was also calculated [Table 5.5]. The calculations for irradiance were based on Earth's distance from the Sun (in metres), solar temperature in ^{0}K (T), and the Stefan Boltzmann constant (σ): using the formulae:

$$P = \sigma A T^4$$

and

$$I = P/A$$

where P is the power of the Sun, I its intensity, and A is the area of the solar photosphere. For the calculation of intensity, the area is based on Earth's distance from the Sun. The values for parameters

essential to these calculations are included in Table 5.1, along with other parameter values used in calculations for these physical models.

As can be seen [Table 5.5], solar irradiance does not vary much at perihelion through changes of eccentricity, with maximum eccentricity producing slightly higher irradiance than now. Whilst it might seem odd that more solar irradiance is produced at perihelion during maximum eccentricity, this situation is understandable because (i) the eccentricity is at its greatest then, and (ii) the perihelion distance is calculated by deducting the eccentricity from the mean length of the semi-major axis, whereas the aphelion distance is calculated by adding the eccentricity value to the mean length of the semi-major axis [Figure 5.1]. At aphelion, there is a substantial drop in solar irradiance and gravitational force due to the increased distance from the Sun and the application of the inverse square law. It can thus be seen that with varying eccentricity, the primary drop in solar irradiance and gravitational force occurs at aphelion.

In a simple model that does not consider atmospheric and oceanic influences, or greenhouse gases, basic calculations were performed for converting solar irradiance (W/m^2) to temperature (C^0) at Earth's surface during different eccentricities and at key times of the year. This model used Earth's average albedo (a) of 0.69, the calculated total solar irradiance (I) from Table 5.5, and the Stefan Boltzmann constant (σ):

$$T = \sqrt[4]{(I * a)/4\sigma) - 273.15}$$

Whilst this simple model gives the expected temperature, Earth is much warmer due to the influence of greenhouse gases. The purpose of this model is to show the variations in temperature due to orbital influences. The results for temperatures at perihelion and aphelion for current, minimum and maximum eccentricity can be seen in Table 5.6. In Table 5.7, temperature and solar irradiance differences can be seen between these orbital points at differing eccentricities. Whilst maximum solar irradiance and gravitational forces are experienced at perihelion, these values remain fairly constant through time and variations in eccentricity, with a solar irradiance range of 1406-1416 W/m^2. However, the aphelion values have an extreme range of 1122-1378 W/m^2 through varying eccentricities. Based on this simple model, it can be seen that at minimum eccentricity, which will be reached in ~27 ky from now (Berger, 2009), aphelion temperatures will be nearly 3^0C warmer than now, whilst at maximum eccentricity (~23 ky) during the LGM, aphelion temperatures were nearly 10^0 cooler than now [Table 5.7]. At maximum eccentricity, aphelion distances produce significantly colder conditions and weaker gravitational forcing. Consequently, during maximum eccentricity there are annual extreme variations of temperature between perihelion and aphelion, with a rapid transition in temperature between the two extremes of Earth's orbit. The positioning of the solstices and

equinoxes relative to these extremes of solar irradiance are significant; for example, substantially influencing potential maximum summer temperatures when the relevant solstice is conjunct the aphelion at maximum eccentricity.

Table 5.6: Temperatures (C°) calculated for minimum, maximum and current eccentricities (e) at perihelion, aphelion, and mean distance from Sun.

e	Perihelion	Mean	Aphelion
min	-17.40	-18.04	-18.68
current	-17.36	-19.46	-21.61
max	-16.97	-23.88	-31.42

Table 5.7: Solar irradiance at Earth's top of atmosphere (TOA) (W/m^2) and temperature differences (C°) between minimum, maximum, and current eccentricities at perihelion, aphelion, and mean distance.

Solar irradiance (TOA) (W/m2)						
	Mean		*Perihelion*		*Aphelion*	
Eccentricity	*Min*	*Current*	*Min*	*Current*	*Min*	*Current*
Current	30.84		-0.83		62.51	
Max	123.35	92.51	-9.44	-8.60	256.13	193.61
Temperature (°C)						
	Mean		*Perihelion*		*Aphelion*	
Eccentricity	*Min*	*Current*	*Min*	*Current*	*Min*	*Current*
Current	1.42		-0.04		2.94	
Max	5.85	4.42	-0.43	-0.39	12.75	9.81

5.2 Effects of the Metonic lunation and perihelion movements relative to the tropical year

The movement of the Metonic lunation and perihelion relative to each other and the tropical year were tracked and graphed [Figure 5.2]. This is necessary because the distances between the equinox/solstices and the perihelion change through the influence of the apsidal and equinoctial precessions, producing the Milankovitch precessional cycle. As the Metonic lunation is not precisely equal to the length of the tropical year, although very close at 18.99 tropical years, some movement of the Metonic lunation relative to the tropical year is to be expected. It is therefore helpful to have a visual aid in understanding this movement when interpreting data upon which it is based.

Astronomical data of Metonic lunations (based on the Metonic lunation currently associated with the perihelion from the previous chapter) was used to track these relationships. The longitudinal position of the perihelion was recorded using SkyChart III for quarter phases of the lunar declination cycle, which occurred at 209 yr-228 yr intervals (Section 4.4.1). This data was tabulated alongside the longitudinal positions of the Sun at the time of these Metonic lunations. For long-term tracking beyond the range of the Metonic lunation data, regression lines of best fit to the positions of the perihelion and Sun were determined and then projected into the past and future [Figures 5.3 and 5.4].

The solstices and equinoxes are associated with the y-axis of these two graphs, where 0° equals the March equinox, 90° equals June solstice, 180° equals the September equinox, and 270° equals the December solstice. Each 30º is roughly equal to a calendar month.

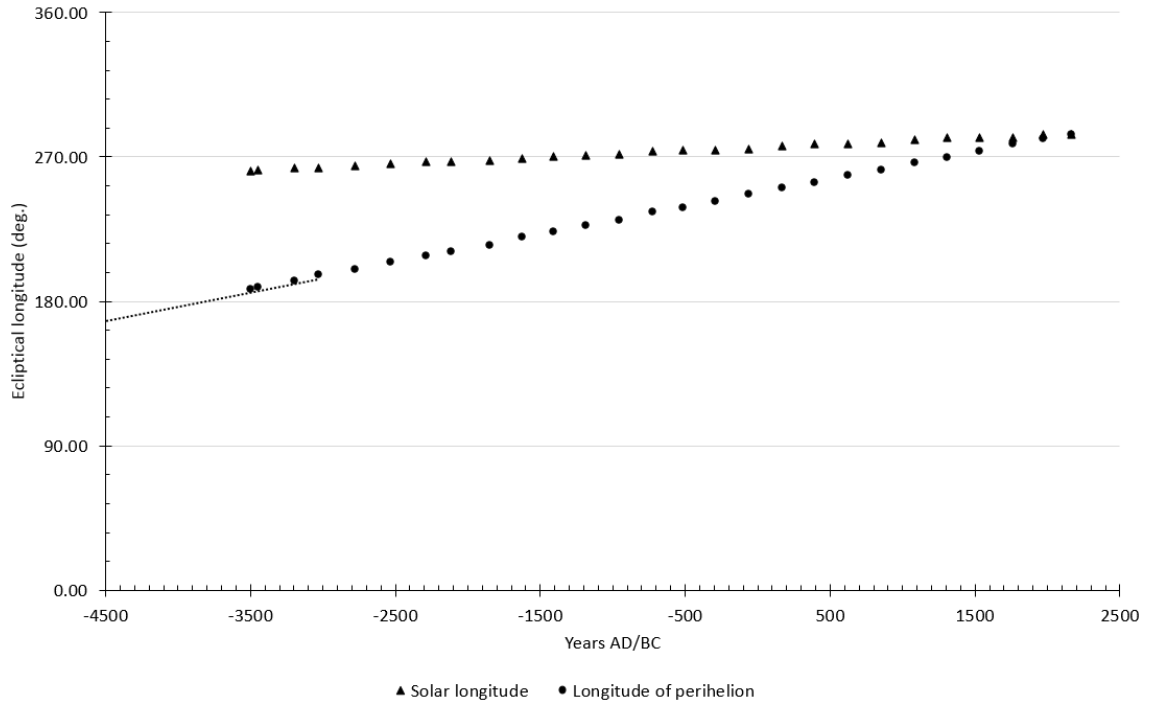

Figure 5.2*:* Longitudes of perihelion and Metonic lunation through time. This graph shows the relationship of the Metonic lunation and perihelion to the tropical year. Negative values on the x-axis are BC. Date of perihelion-December solstice conjunction from this graph is 1308AD. The trend line equations are: *y = 0.0171x + 247.53* (perihelion) and *y = 0.0041x + 275.89* (Metonic lunation).

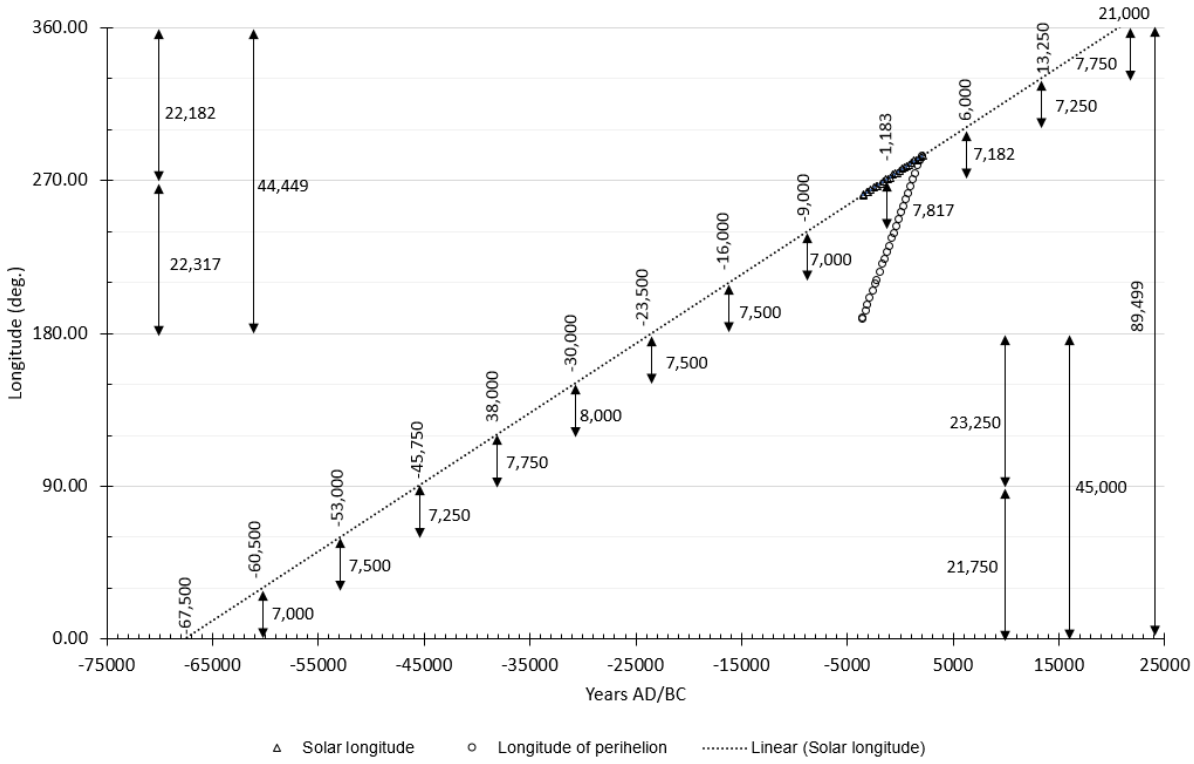

Figure 5.3: Map of Metonic lunation movement through time. The extension of the trend line of Metonic lunation data, reveals it takes the equivalent of the upper range of the Milankovitch cycle (~23 ky) to traverse the distance from equinox to solstice and vice versa. Negative values on the x-axis are BC. Line of best fit equation is: *y = 0.0041x + 275.89.*

The perihelion (line of circles), can be seen moving through the tropical year, reaching a conjunction with the December solstice in 1308AD at the end of the Medieval Warm Period, whilst the perihelion-Metonic conjunction is most exact at 2163AD [Figure 5.2]. The Metonic lunation series (based on the current perihelion) is at the December solstice (line of triangles) during the second millennium BC, and is most exact at ~1183BC. The Metonic lunation has been slowly moving away from the December solstice since 1183BC [Figure 5.2]. The perihelion-equinox conjunction occurs at ~3950BC, which can be seen by extending the trend line of perihelion movement. A full cycle of Metonic lunation movement relative to the tropical year produces a cycle of ~90 ky, with an average rate of movement per quarter (i.e., solstice to equinox) of ~23 ky [Figure 5.3]. The movement of the Metonic lunation (which is associated with the tropical year) through each 30° of longitude is not even, where 30° segments are approximately equal to one calendar month.

The time taken for the perihelion to traverse 360^0 of longitude, which is also the apparent annual path of the Sun during the tropical year mean, is ~21 ky [Figure 5.4]. The path of the perihelion through each 30^0 is not uniform and varies from ~1,700 yrs-1,800 yrs [Figure 5.4]. The movement through each quarter is also not uniform, ranging from approximately 4,958-5,292 years; similarly, each half is not consistent, producing two different values from equinox to solstice: 10,250 yrs and 10,450 yrs [Figure 5.4].

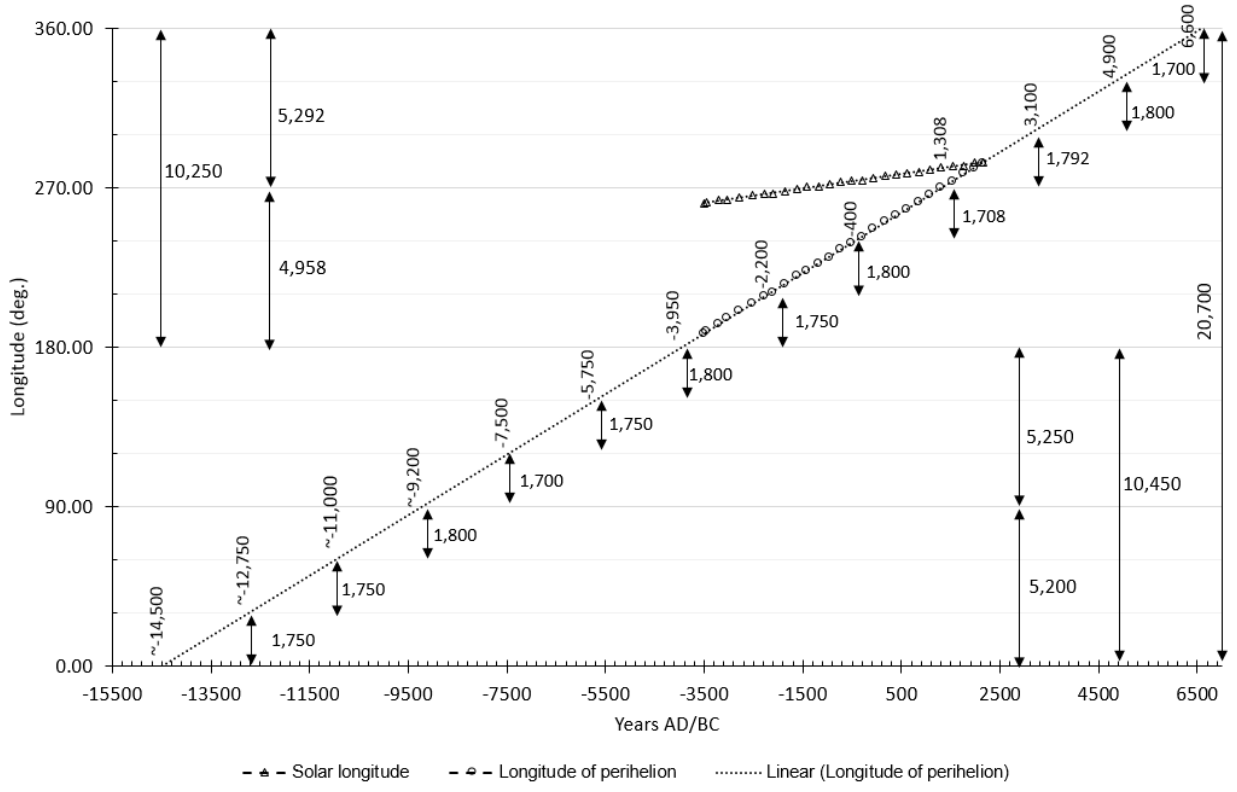

Figure 5.4: The movement of the perihelion relative to the tropical year. Negative values on the x-axis are BC. The movement of the perihelion through a full 360° of longitude (from 14,500BC to 6,600AD) is ~21 ky. Line of best fit equation is *y = 0.0171x + 247.53*

5.3 Gravitational model and results

The gravitational model is based on the Metonic lunation data from the previous chapter, which includes Earth-Moon and Earth-Sun distances at the time of the lunation. The gravitational constant appears in Table 5.1. Gravitational forces were calculated using the equation:

$$F = (Gm_1m_2)/r^2$$

where F is the gravitational force in newtons, G is the gravitational constant, and r is the distance between the centres of mass of the relevant two celestial bodies. Masses for the two objects being measured are m_1 and m_2: these masses are for pairs of the Sun and Earth, and the Earth and Moon. Distances and gravitational forces, individually and combined, were graphed for Earth's relationships with the Sun (Section 5.3.1) and Moon (Section 5.3.2) and appear below. For extract of data, see Table C.1 in Appendix C.

Additionally, the lunar perigee was also modelled relative to the anomalistic year. Results appear in Section 5.3.3. The relationship between the anomalistic year and perigee was established annually using the formula:

$$y = Y_c \times \frac{Y_a}{M_p}$$

where Y_c is the return number (in years), Y_a is the anomalistic year in decimal days, and M_p is the perigean month in days, and y is the number of perigean months in any particular year of that cycle, measured from the beginning of the cycle (Y_c=0). NASA's mean values (Williams, 2013a) were used in these calculations: perigee (27.554167 days), anomalistic years (365.2596 days). The residual of each full cycle was converted to degrees. These results were sorted by proximity to exact returns and then graphed (Section 5.3.3). For extract of data see Table C.2 in Appendix C.

5.3.1 Earth-Sun distance and gravitation

Overall, variations in the Sun-Earth distance produce related changes in gravitational force on Earth due to the Sun (ignoring other contributions) of around 0.06% during the mid to late Holocene, diminishing to negligible at modern times. The Earth-Sun distances [Figure 5.5] show a 133-yr cycle that flattens out as the perihelion and December solstice reach a conjunction around 1308AD (cf. Berger (2009) date of 1257AD). The combined gravitational influence of the Earth-Sun-Moon is depicted in this graph because calculations were based on Earth-Sun distances at New Moon. Figure 5.6 shows solar gravitational force peaks in modern times rather than during the Medieval Warm Period (MWP) because the data track the relationship of the Metonic lunation and perihelion as they move towards a precise conjunction in the near future. As with the 133-yr solar declination cycle in the previous chapter, a 133-yr cycle largely consists of 57-yr and 76-yr components, but variations of

95-yr and 38-yr components exist in both gravitation [Figures 5.7, 5.8, and 5.9] and distance. Additionally, during the last 600 yrs of the Roman Warm Period (~500BC-500AD), there is a flattening of the 133-yr cycle [Figure 5.8]. The modern peaks in gravitational force occur at closest approaches of the Earth to Sun at the times of Metonic lunations (1878, 1893, 1973, 2011) and can be clearly seen in Figure 5.9., along with a projected peak in 2106AD. The perihelion distance starts to plateau at the end of the Maunder Minimum and the start of the Industrial Revolution [Figure 5.9].

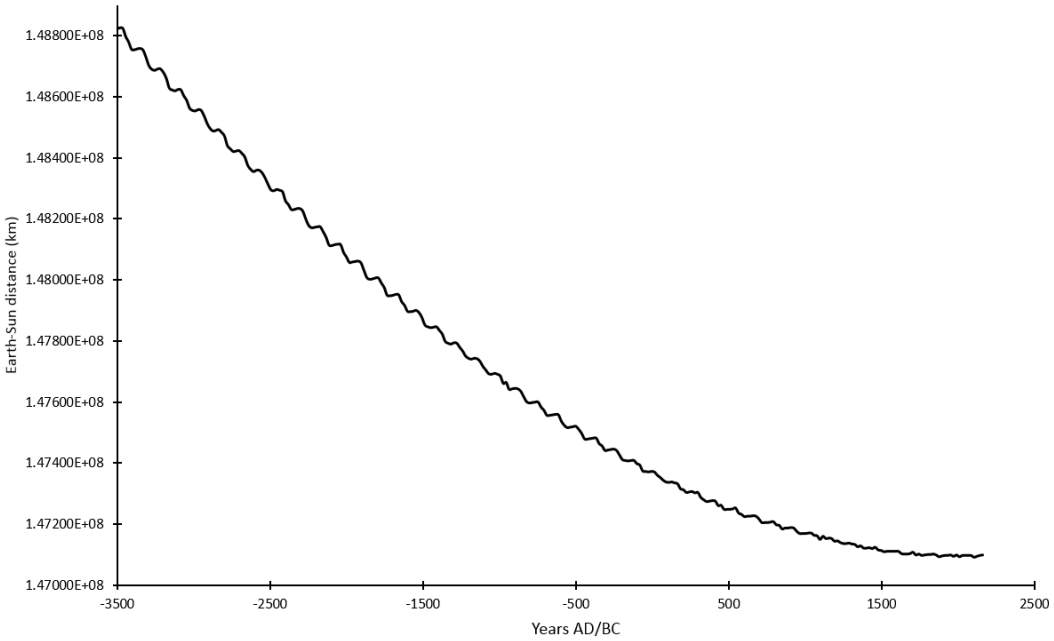

Figure 5.5: Earth-Sun distance at Metonic lunation (based on Metonic lunation series associated with the current perihelion). Negative values on the x-axis are BC.

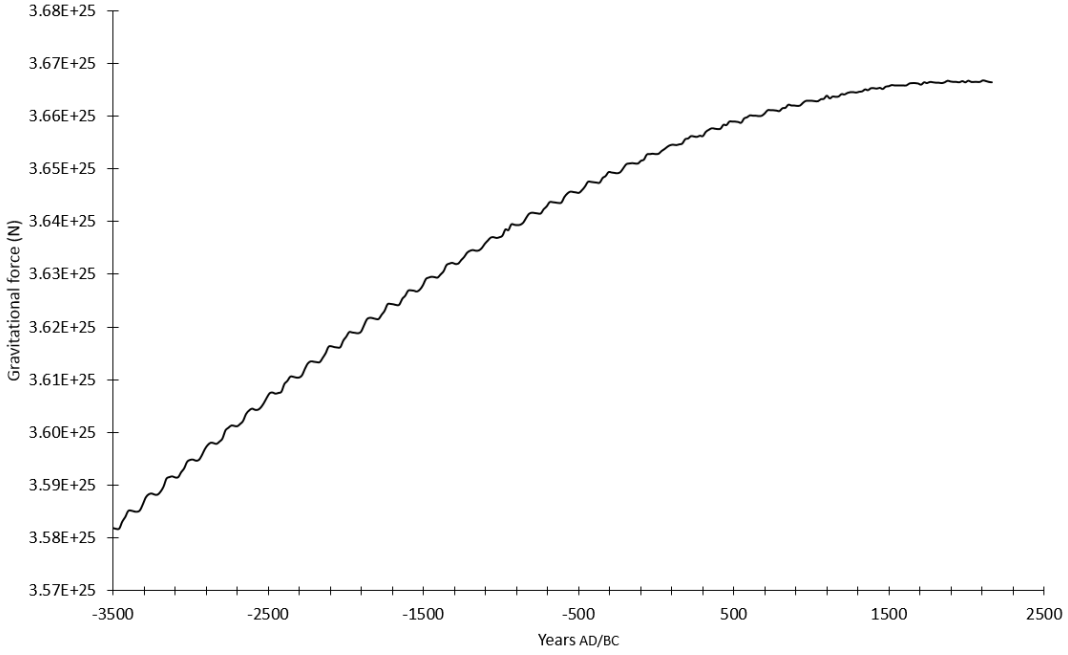

Figure 5.6: Gravitational force associated with Earth-Sun distance, based on Metonic lunation series associated with current perihelion. Negative values on the x-axis are BC.

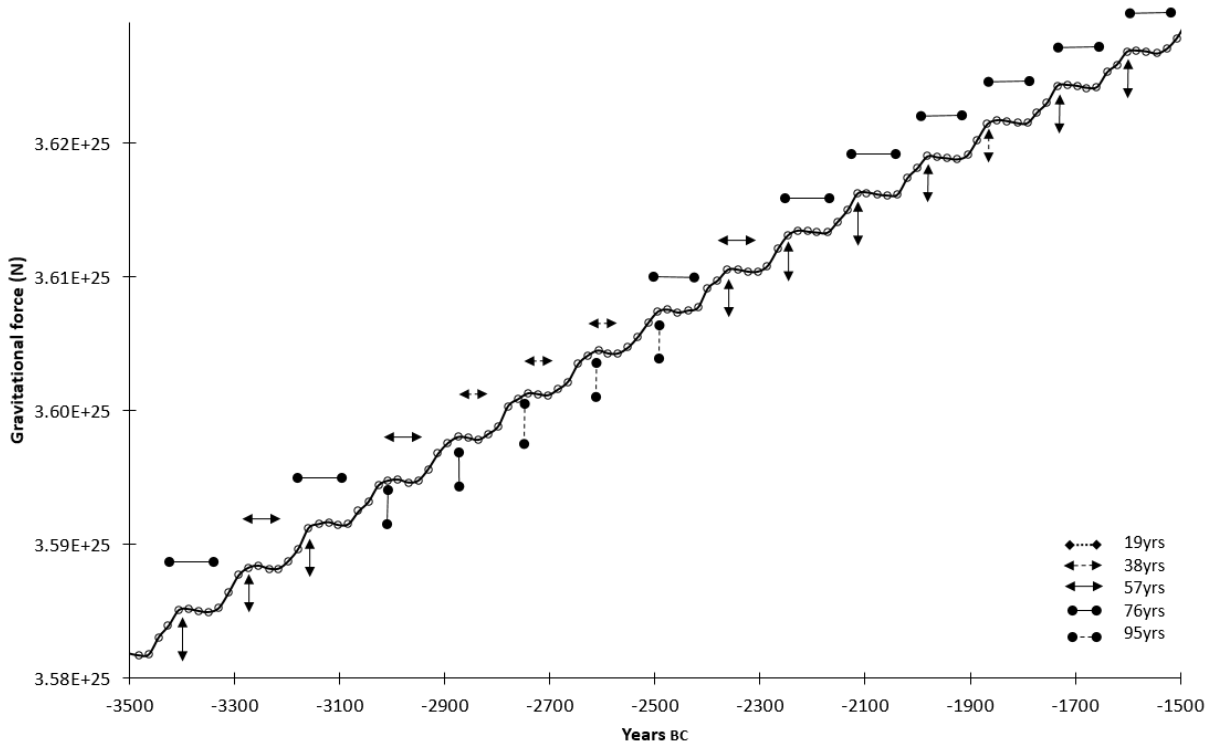

Figure 5.7: Fluctuations in gravitational force between Earth and Sun showing 133-yr cycle and their components, based on Metonic lunation data.

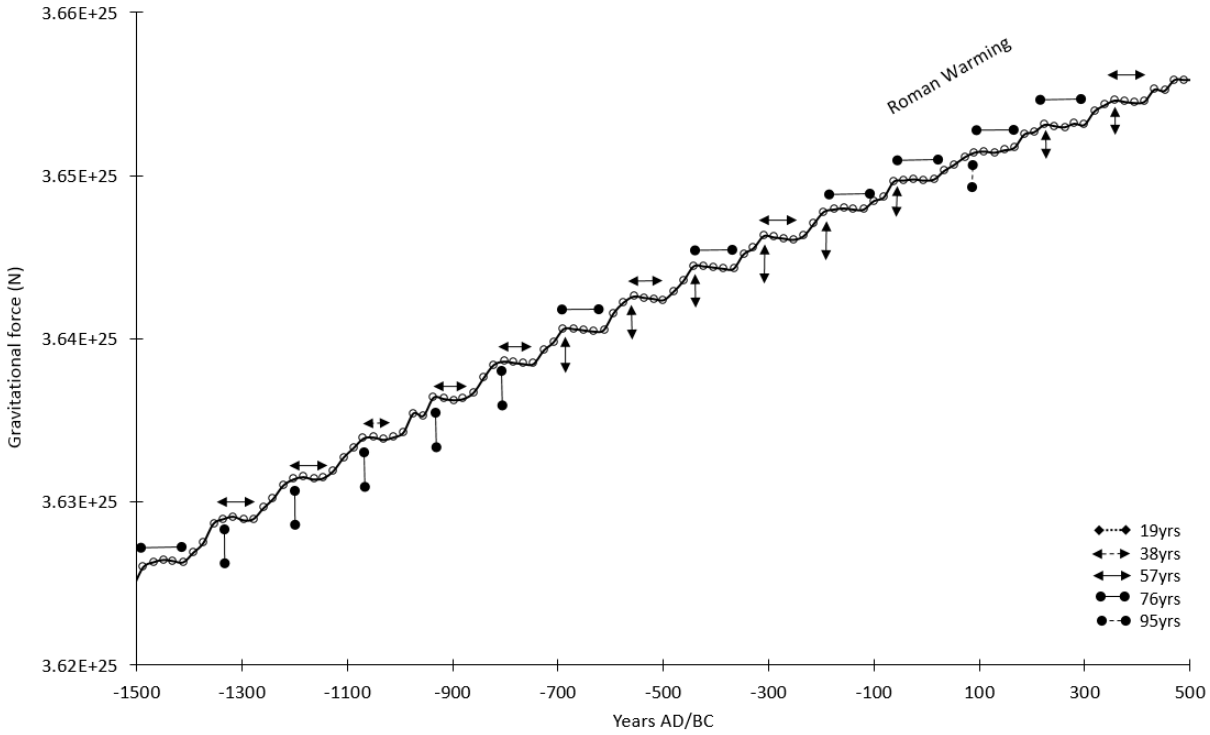

Figure 5.8: Fluctuations in gravitational force between Earth and Sun showing 133-yr cycle, based on Metonic lunation data. Notice slight flattening of the signal during the Roman warming. Negative values on the x-axis are BC.

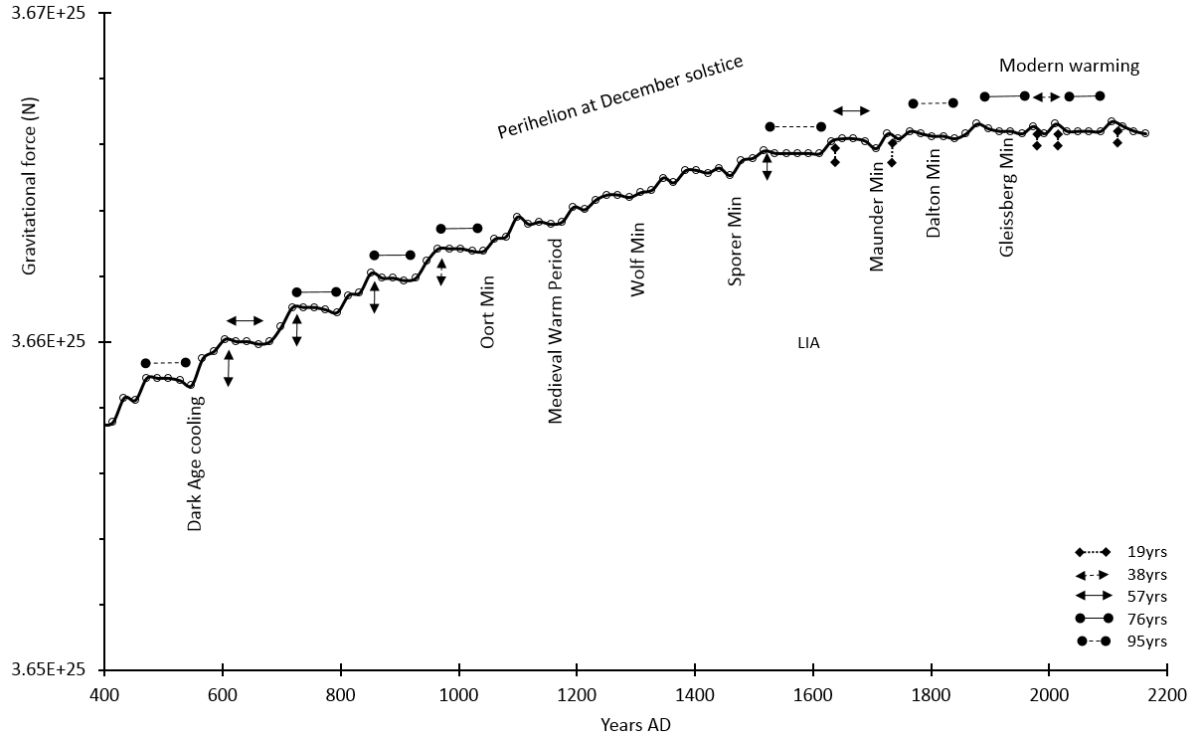

Figure 5.9: Fluctuations in gravitational force between Earth and Sun showing 133-yr cycle, based on Metonic lunation data. Notice flattening of the signal as perihelion and December solstice conjunction is reached and regular 133-yr cyclical pattern breaks down.

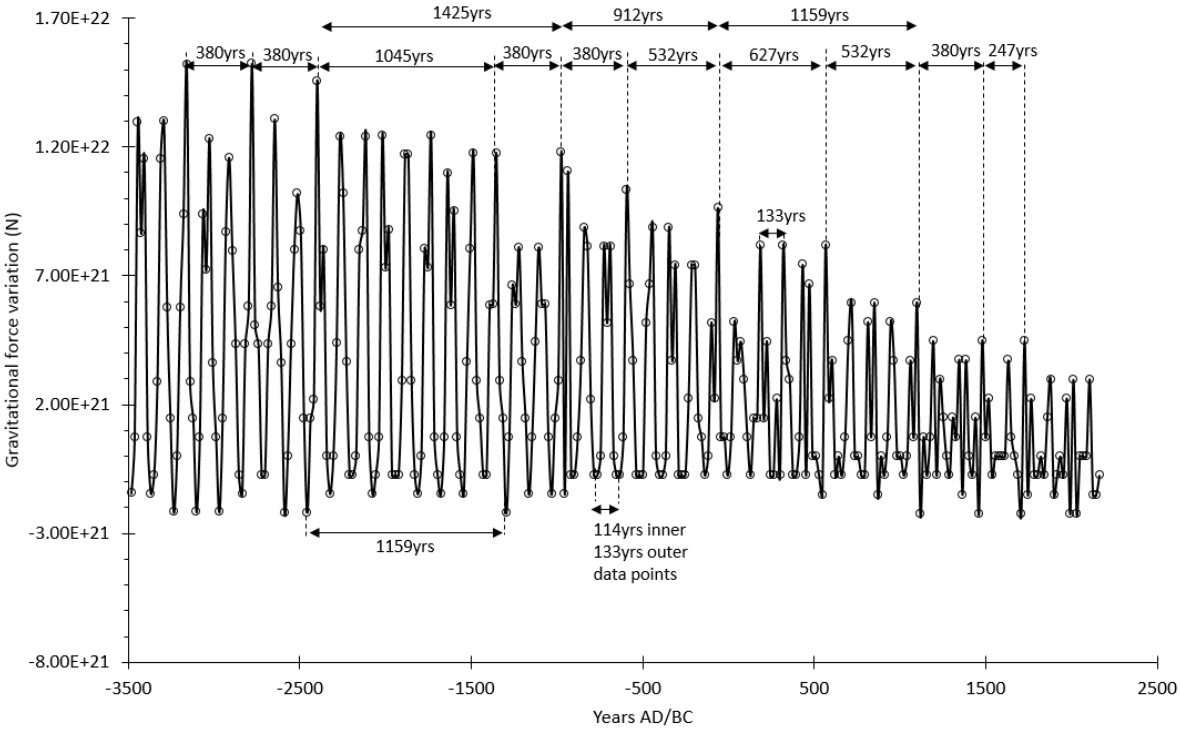

Figure 5.10: Gravitational variation due to Earth-Sun relationship, based on Metonic lunation data. Measurements of variation in gravitational force due to changed Earth-Sun distances are shown. A 133-yr cycle in gravitational force can be seen here. Negative values on the x-axis are BC.

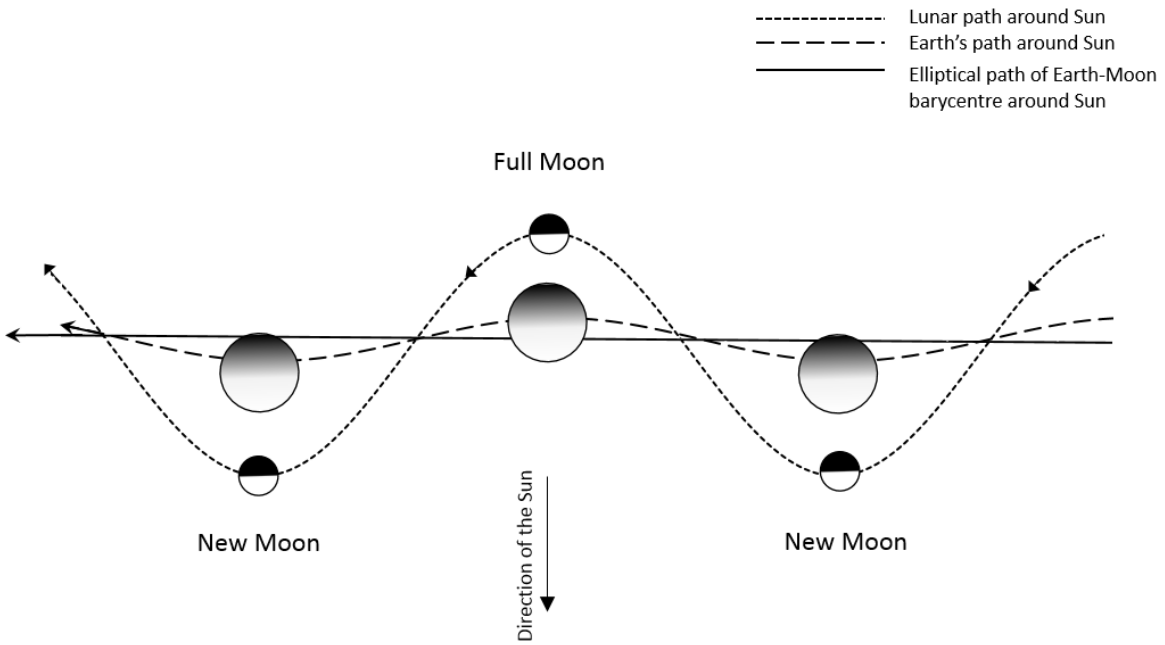

Figure 5.11: Schematic of Earth, Moon, and shared barycentre paths around the Sun. The distance of this barycentre is ~4641 km from Earth's centre and is dependent upon the Earth-Moon distance, and is constantly moving within the Earth as it rotates and interacts with the Moon.

Figure 5.10 quantifies the change in levels of gravitational force (based on Sun-Earth distances at the time of New Moon) between the times of each Metonic lunation. Patterns of quasi-periodic patterns at millennial- and centennial-scale can be seen. Movements in this graph towards the top of the y-axis shows Earth-Sun distance increasing, whilst reduced Earth-Sun distance is shown by drops in the y-value. Regular patterns towards greater Earth-Sun distances are 627 yrs, 380 yrs, 247 yrs [Figure 5.10], likely associated with the influence of the Moon (see below). A variable pattern of millennial-scale cycles also appears. During the time of suppressed SdV variability in radiocarbon data during the 2nd millennium BC (Sections 3.2.2), there is a sustained pattern of variability in Earth-Sun distances that may be explained by the Metonic lunation. This is because the Earth-Sun distance values in the astronomical data (produced by the planetarium software) occur at New Moon. During the Spörer Minimum (~1460AD-~1550AD) there is no variability in gravitational forces at the Metonic lunation for 76 yrs [Figure 5.10]. As the Metonic lunation moves towards conjunction with the perihelion, variation in gravitational forcing diminishes as Earth-Sun distances reduce.

The 133-yr cyclical pattern seen in the Earth-Sun distances can be attributed to the dance between the Earth and Moon on their orbital paths [Figure 5.11]. This figure shows that at each New Moon, the Earth is periodically closer to the Sun than at Full Moon. As the Metonic lunation and perihelion move closer together [Figures 5.2 and 5.5], solar gravitational forces acting on the Earth increase [Figures 5.6]. The step-like patterning of 133 yrs seen in Figures 5.6-5.9 is shaped by the sinusoidal patterns of the Earth-Moon dance illustrated in Figure 5.11. As the Moon journeys around the Earth,

and the Earth around the Sun, their paths create sinusoidal patterns around their common barycentre (Lowrie, 2007). The physical data show that during the 133-yr cycle, minimum distances between Earth and Moon (Section 5.3.2) correspond with minimum distances between Earth and Sun; they also share the timing of maximum distances. These distances influence both gravitational force and solar irradiance levels.

5.3.2 Earth-Moon distance and gravitation

Figures 5.12 and 5.13 show that the Earth-Moon distance and and gravitational force vary over a range of nearly 15% following a basic 133-yr pattern of variation. Also evident are additional millennial-scale patterns between extremes of relative perigee at the time of the Metonic lunation. The lengths of these intervals (based on minimum Earth-Sun distances and maximum gravitational force) progressively decrease as time progresses from past to present. The diminished length of these periods is coincident with the Metonic lunation moving closer to conjunction with the perihelion in modern times (see Section 5.2). A repetitive pattern of maximum Earth-Moon distance (912 yrs) occurs which is the same length as the lunar declination cycle [Figure 5.12], and is proximate to modelled perigee-perihelion conjunctions at 906 yrs and 910 yrs (Section 5.3.3). Corresponding peaks in gravitational force and the timing of these returns is seen in Figure 5.13.

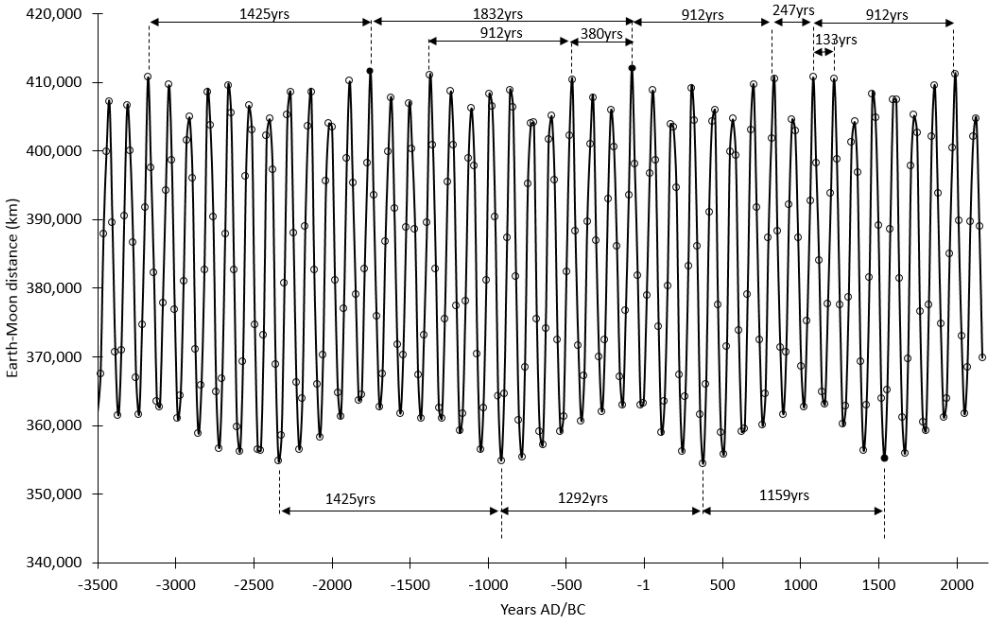

Figure 5.12: Earth-Moon distances based on Metonic data. A basic variability of 133 yrs can be seen. Millennial-scale cycles can also be seen and are most pronounced at perigee.

More distinctive cycles in gravitational force caused by perigee are evident in the data [Figure 5.13]. Extremes in gravitational force occur when the Earth is at the closest points to both the Sun and Moon [Figure 5.13], in close proximity to Metonic eclipses (Chapter 4). Bond IRD events coincide with

these extremes in gravitational forcing [Figure 5.13], when the Earth is at the closest points to both the Sun and Moon and in close proximity to Metonic eclipses (Chapter 4). The means of the Holocene gravitational variation based on increased Earth-Moon distances are 1375 yrs and 1482 yrs [Figure 5.14], with these values dependent upon the length of the period measured and the points from where they were measured. An ~1160-yr cycle in gravitational variation is also seen [Figure 5.14].

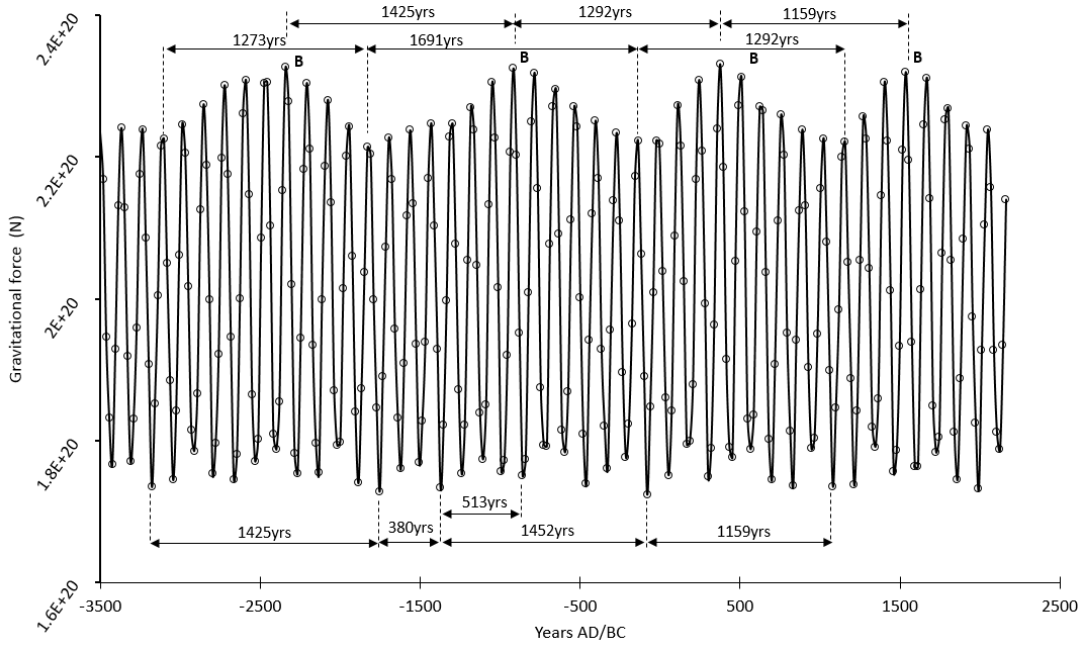

Figure 5.13: Earth-Moon gravity. The most prominent feature of Earth-Moon gravity is the millennial-scale quasi-periodicities that are most noticeable at perigee where maximum gravitational forces occur. B=approximate location of Bond event. Negative values on the x-axis are BC.

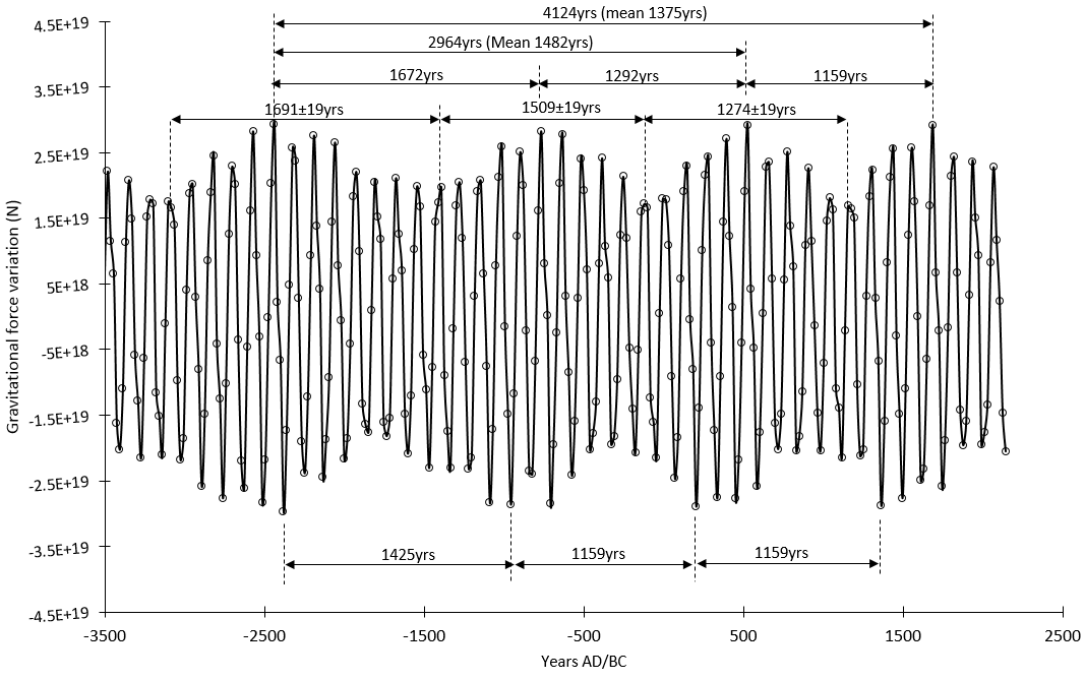

Figure 5.14: Quasi-periodicities of variation in Earth-Moon gravitational force. Negative values on the x-axis are BC.

5.3.3 Coincidences between lunar perigee and perihelion

Gravitational forces and solar irradiance models in this chapter are based on the astronomical data of Chapter Four. In this astronomical data, a series of Metonic lunation eclipses was discovered and occurs at 456±38 yrs intervals, with every second eclipse in this series being a south nodal eclipse. These south nodal eclipses subsume both the lunar nodal perigee cycles as total eclipses can only occur at perigee (Section 4.1.1). Gravitational maximums occur at perigee (Earth-Moon monthly cycle) and perihelion (Earth-Sun annual cycle), and a combination of both magnifies the gravitational force acting on the Earth. Understanding these interactions in relation to the Metonic eclipse series is important because the alignment of Earth-Moon-Sun along the ecliptic also maximises gravitational force. As such, the results here add understanding to the results in Sections 5.3.1, 5.3.2, and 5.4. The perigean-perihelion interaction was modelled to find the tightest conjunctions of perigean and perihelion cycles based on residuals relative to a cycle of 360° (see above). These results should show connections to the astronomical data that shows the Metonic series of eclipses. Figures 5.15 and 5.16 chart residual values of cyclical perigean returns relative to the perihelion.

Perigee sometimes occurs near the time of perihelion. A number of periodicities are apparent from the model, where 0° and 360° represent a complete cycle. Here the ordinate axis represents the nearness of coincidence in degrees longitude. The first most precise perigee-perihelion alignment occurs at 289 yrs [Figure 5.15], which is $<0.2^0$ distant from a precise conjunction of lunar perigee and perihelion. These perihelion-perigee conjunctions occur in series, with each point in that series separated by 289 yrs. Every 289 yrs a double occurrence of the perihelion-perigean cycle occurs, each separated by a four-year interval (i.e., 39 yrs and 43 yrs, then 328 yrs and 332 yrs). Each series runs diagonally across the graphs, showing that each return moves further away from a precise alignment [Figure 5.15], or approaches precision at the same rate [Figure 5.16]. An 82-yr interval return pattern can also be found in this data between sequential occurrences of the perigee-perihelion conjunctions, with the first return occurring within $\sim1.2^0$ of precision.

However, an even more precise perigean-perihelion return than the 289-yr event occurs at 2394 yrs [Figure 5.16], within 0.1^0 of precision, which is the same length as the Hallstadt cycle. This is close to the fourth closest RRA return, which charts the perihelion-geographical longitudinal return where maximum gravitational force is experienced along the length of the meridian of longitude (at solar zenith) [Table 4.3]. Close associations of the perigean-perihelion conjunction with the Metonic lunation also occur [Figure 5.17]. A 496-yr perigean-perihelion return occurs (<1.6°), which is proximate to the third closest RRA return [Table 4.3], occurs at a Metonic lunation and with a Metonic eclipse (Sections 4.4.2 and 4.4.5). However, only two Metonic-perigee-perihelion conjunctions occur in the 2500-yr period modelled: one at 43 yrs (<3.8°) and the other at 1484 yrs (4.2°) [Figure 5.17].

The first is not associated with a RRA return to geographic longitude but is associated with a Metonic lunation. The 1484-yr perigean-perihelion conjunction is close to both the 1482-yr sunspot-Metonic return and the modelled 1479-yr RRA return [Table 4.3], while the 43-yr perigean-perihelion conjunction is 5 yrs distant from the Metonic lunation at 38 yrs.

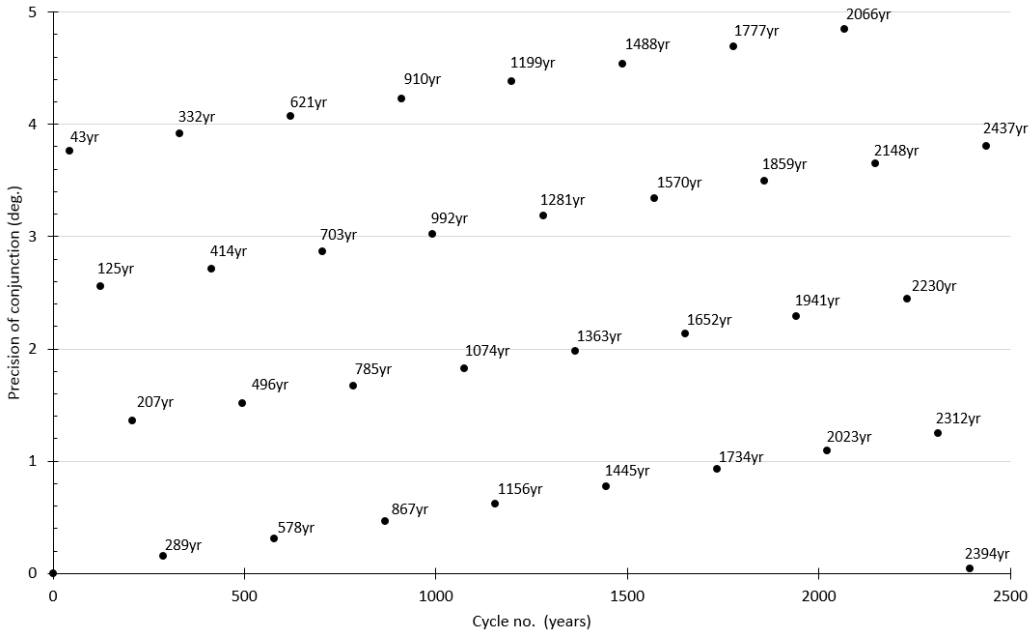

Figure 5.15: Precision of perihelion-perigee conjunction (part 1). Returns closest to 0º are closest returns in this graph, but also need to be considered in association with Figure 5.12. Grey boxes are associated with RRA returns (<1º), and boxed numbers with RRA returns (<1.5º).

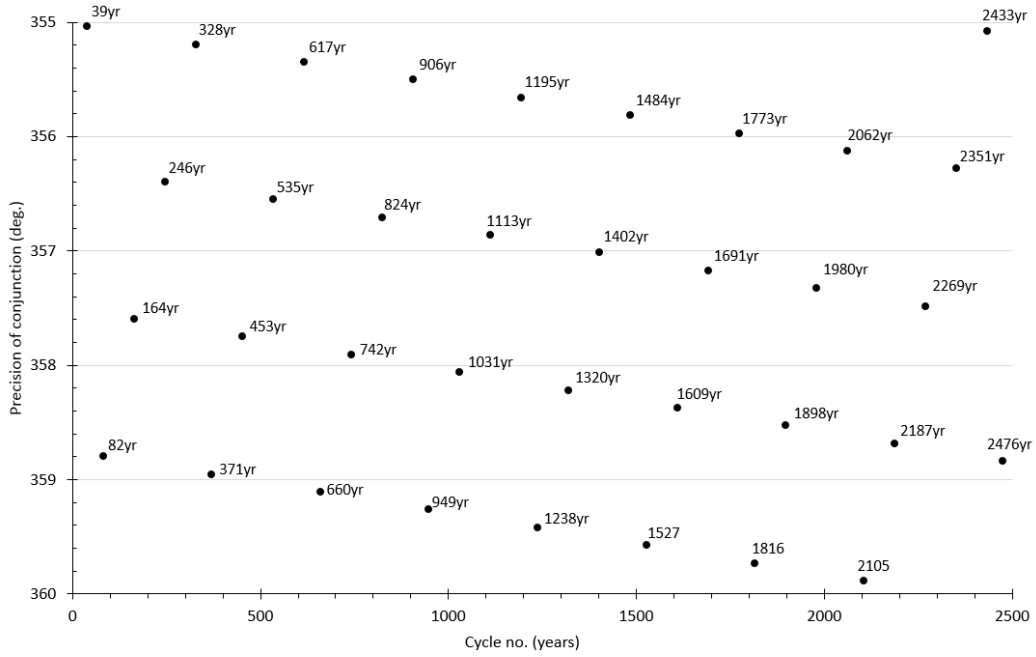

Figure 5.16: Precision of perihelion-perigee conjunction (part 2). Returns closest to 360º are closest returns in this graph, but also need to be considered in association with Figure 5.11. Grey boxes are associated with RRA returns (<1º), and boxed numbers with RRA returns (<1.5º).

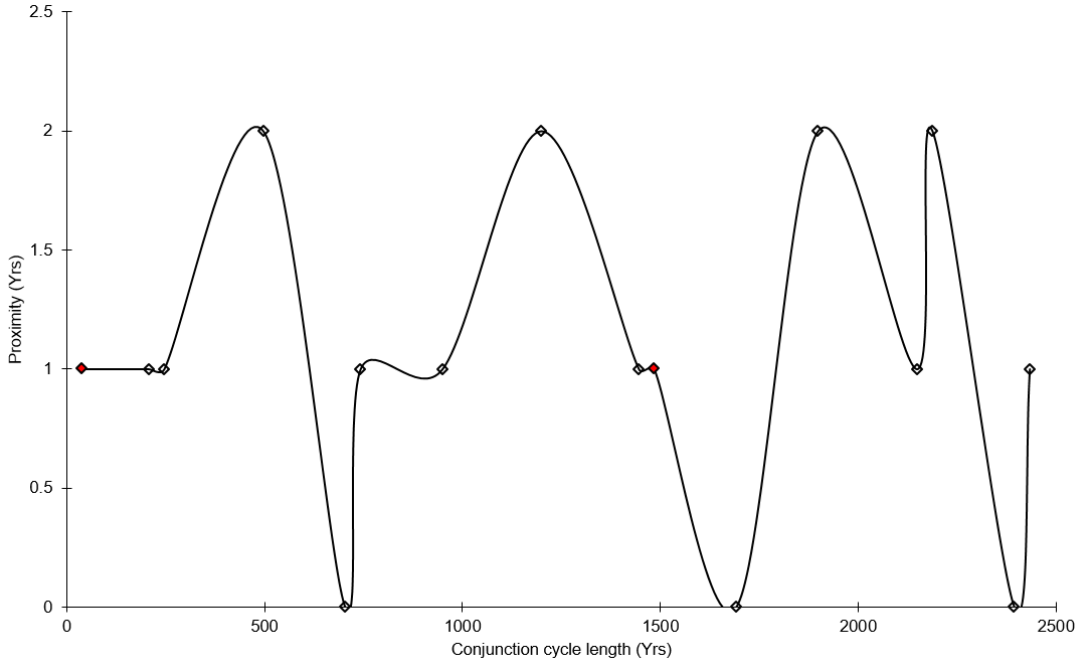

Figure 5.17: Perihelion-perigee conjunctions occurring with Metonic lunation (≤2 yrs). Modelled perigee-anomalistic year conjunction cycles occur with Metonic lunations.

5.4 Solar irradiance and insolation model and results

The Metonic lunation data from Chapter Four was used as the basis of this physical model. The measured Earth-Sun distance at the time of the Metonic lunation was used to calculate Earth's total solar irradiance for top of the atmosphere (TOA) at the time at the of the lunation, based on the formulae for power and intensity in Section 5.1. Calculations of insolation were also made for a number of latitudes using the solar zenith angle when the Sun is at maximum altitude: Tropics of Capricorn and Cancer, the Equator, and the Antarctic and Arctic Circles. The formula used was based on Lambert's Cosine Law (Liou, 2002):

$$y = S_M . cos\ \theta$$

where

$$cos\ \theta = sin\ \varphi . sin\ \delta + cos\ \varphi . cos\ \delta . cos\ h$$

and

$$S_M = \left(\frac{D_M}{D_A}\right)^2 * I$$

and where S_M is the solar flux at Earth's orbit at the time of the Metonic lunation (based on Sun-Earth distance), φ is the latitude of the Tropic of Capricorn, δ is the declination of the Sun, h is the hour angle at noon, D_M is the mean Earth-Sun distance, D_A is the actual Earth-Sun distance at the time of the Metonic lunation, and I is Earth's mean solar irradiance at current eccentricity. Cos θ is the same as the cosine of the solar zenith angle [Figure 3.7]. The value for S_M incorporates the moving perihelion relative to the tropical year through calculations of actual Earth-Sun distance relative to the mean Earth-Sun distance, based on the mean solar irradiance for Earth's current eccentricity (see

Table 5.1). Because of the relatively short period of this data compared to the eccentricity cycle, the mean solar irradiance for the current eccentricity is used in these calculations.

As with Earth-Sun gravitational forces and distances, Earth's peak annual solar irradiance increases as time progresses during the period of astronomical data [Figure 5.18]. The start of the Medieval Warm Period at ~900AD is nearing a once in ~21ky event: the December solstice conjunction with the perihelion in the late 13th century, and therefore maximum TOA solar irradiance (particularly for the southern hemisphere). Figure 5.19 zooms in on the last 1500 yrs of this data. In 1726AD, at the start of the Industrial Revolution and end of the Maunder Minimum [Figure 5.19], a threshold is reached as solar irradiance levels rise marginally above the calculated extremes of solar irradiance at perihelion seen in Table 5.5. These peaks of modern warming occur as the Metonic lunation forms a conjunction with the perihelion (Section 5.2), associated with shortened distance influence of the Metonic lunation at perihelion [Figure 5.2]. As with Earth-Sun distance, Earth-Moon distance, gravitation and solar declination, a 133-yr periodicity is present in the solar irradiance data. This is due to calculations of solar irradiance involving Earth-Sun distances, which contains this periodicity.

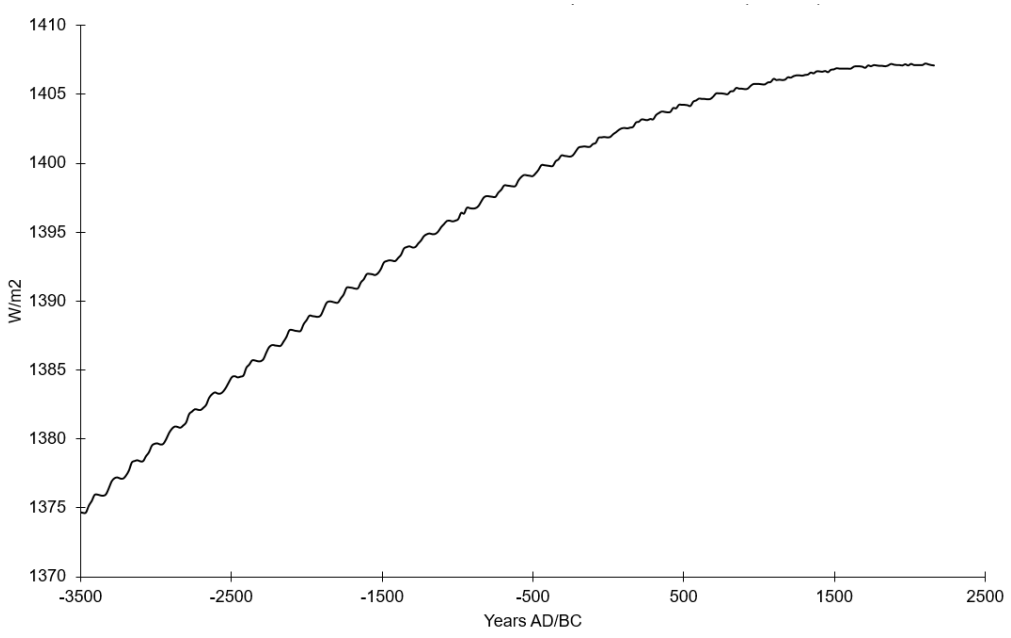

Figure 5.18: Solar flux (TOA) at the time of the Metonic lunation series based on the current perihelion and Earth-Sun distances. Negative values on the x-axis are BC.

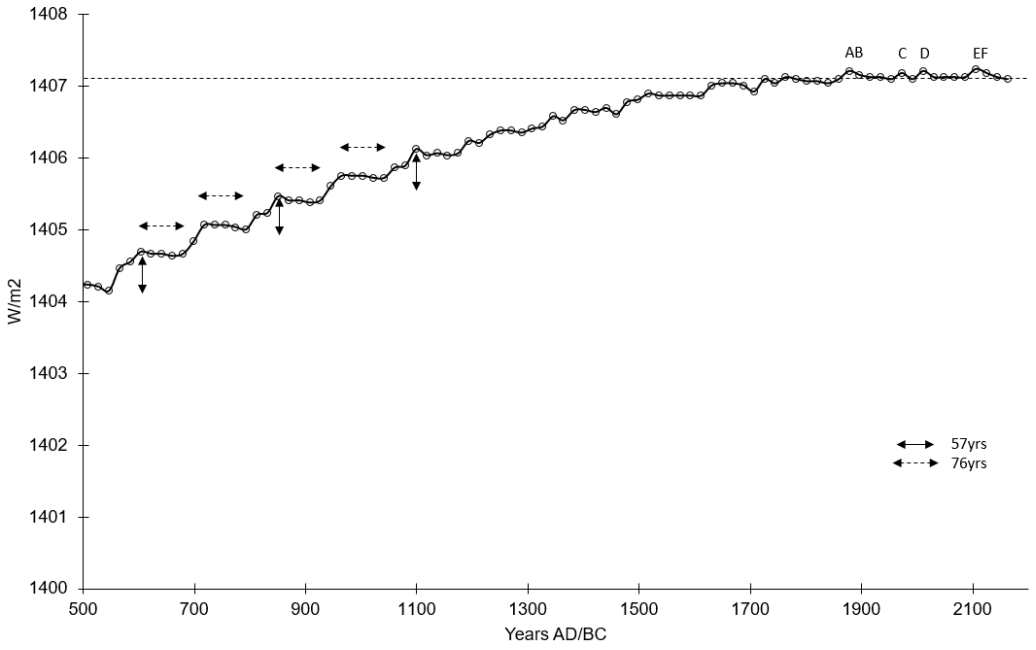

Figure 5.19: A zoom of solar flux (TOA) at the time of the Metonic lunation, based on Earth-Sun distances. Peak points marked in the diagram are A: 1878, B: 1897, C: 1973, D: 2011, E: 2106, F: 2125.

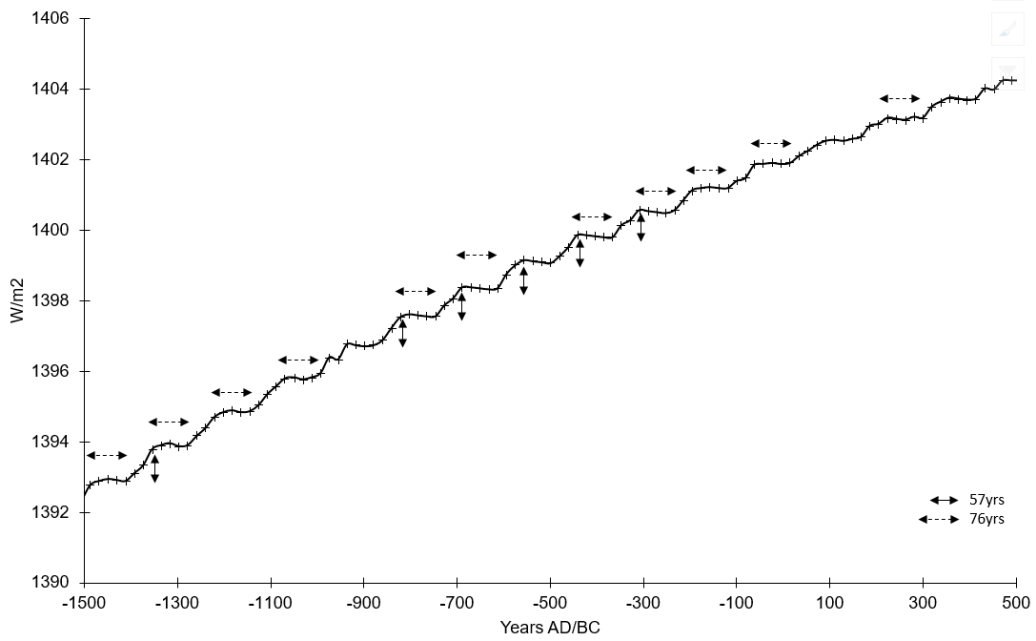

Figure 5.20: Solar irradiance at Metonic lunation between 1500BC and 1100AD, based on Earth-Sun distances. There is a flattening in the 133-yr cycle during the Roman Warm Period, occurring during 62BC and 300AD. Negative values on the x-axis are BC.

Corresponding with the modern peaks in gravitational force (due to closest approaches of the Earth to Sun at the Metonic lunation) are solar irradiance peaks (1878, 1897, 1973, 2011) that can be clearly seen [Figure 5.19], along with projected peaks in 2106AD and 2125AD. The timing of these peaks in TOA solar irradiance is due to minimal Earth-Sun distances at perihelion as solar irradiance calculations are based on Earth-Sun distances. Similarly, a flattening of the 133-yr periodicity

(diminished amplitude of wiggles) can be seen during the Roman Warm period and is noticeable between 62BC and 300AD [Figure 5.20].

Variation in TOA solar flux is seen in Figure 5.21, with the variation here based on Earth-Sun distances at the time of the Metonic lunation. Overall the range of variability reduces from a maximum of 0.7 W/m^2 in the third millennium BC to minimal during modern times, due to the influence of the December solstice/perihelion conjunction in the 13th century AD, and the closing gap between the perihelion and Metonic lunation [Figure 5.2]. Millennial- and centennial- scale patterns of variability can be seen. Reduced variability also occurs at times of Metonic solar eclipses, marked as E (north nodal) and ES (south nodal) in Figure 5.21. Total eclipses occur within the ES series of eclipses and are times of reduced Earth-Sun and Earth-Moon distances. As noted previously, the south nodal eclipses naturally subsume the perigean cycle. The more exact the eclipse, the greater the gravitational force pulling on the Earth towards the Sun. This accounts for reduced solar irradiance variability at the times of these eclipses seen in Figure 5.21. The precision of eclipses is seen in Figure 5.22, which shows the Metonic series of eclipses through the period of the astronomical data used in this study. Red markers show closest alignments by declination between the Sun and Moon; black markers are total or annular solar eclipses; grey markers are partial eclipses; blank markers are Metonic lunations. The most precise of these eclipses occurred in ~2115BC at the start of the Metonic lunation conjunction with the December solstice (see below); in 1183BC at the time of the exact Metonic lunation conjunction with the December solstice; and during the Dark Age cooling in 623AD.

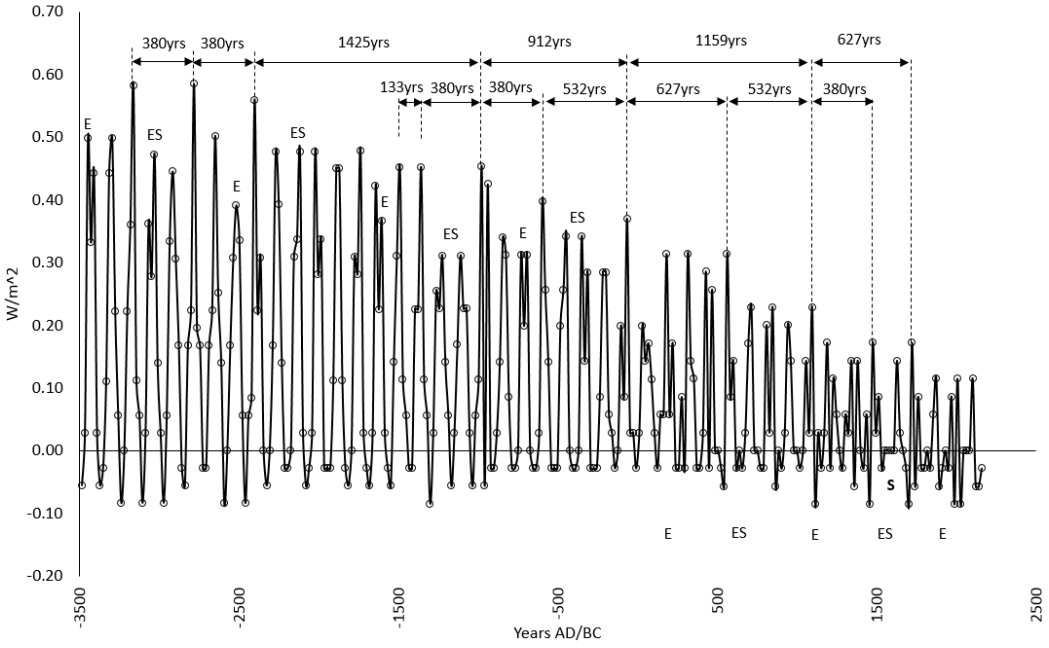

Figure 5.21: Variations in contribution of Earth-Sun distance only to TSI (rate of change between 19-yr intervals). Calculations based on TSI at current eccentricity. S=Spörer Minimum. E=positions of north nodal eclipses; ES=positions of south nodal eclipses. Measurements between prominent peaks in variation are shown. Negative values on the x-axis are BC.

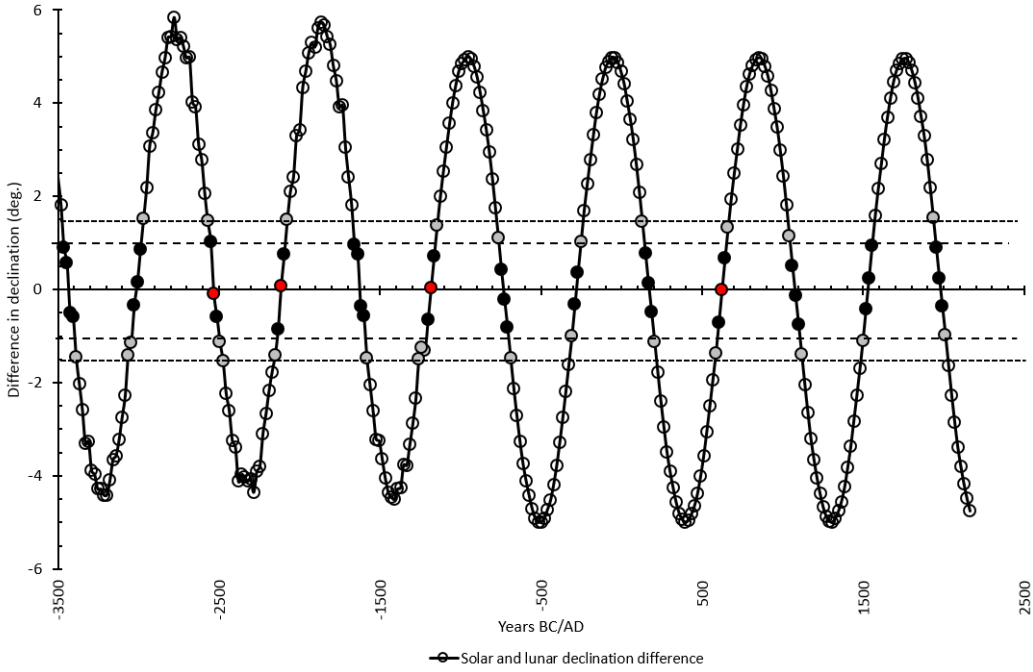

Figure 5.22: Metonic lunations and eclipses. Black and red filled markers are total and annual solar eclipses, grey-filled markers are partial eclipses; blank markers are lunations. The y-axis is a measure of difference in declination between the Sun and Moon.

The different variations in insolation based on latitude can be seen in Figures 5.24 - 5.28. The latitudinal variation in insolation also reflects the Earth-Sun distances seen in the gravitation model. These latitudinal responses behave differently, being moderate at the Tropic of Capricorn because of the small solar zenith angle during the period of the data. The graph for the Tropic of Capricorn [Figure 5.24] is very similar to that based on the Earth-Sun distance [Figure 5.21]. These different insolation response patterns are due to the obliquity of Earth's axis to incoming solar rays [Figure 5.23]. The largest variations occur at the Arctic Circle [Figure 5.25], with a maximum range of 2.05 W/m^2 (+1.23 W/m^2 to -0.82 W/m^2). However, large variations also occur at the Antarctic Circle [Figure 5.26], with a range of 1.54 W/m^2. All of these latitudinal insolation graphs (except for the Tropic of Capricorn) [Figures 5.25– 5.28] reach a minimum variation in the 1000 yrs centred on ~1500BC, which occurs at the time of the Metonic lunation conjunction with the December solstice. Antarctic and Arctic insolation graphs show increased variability since that time, whereas the graph for the Tropic of

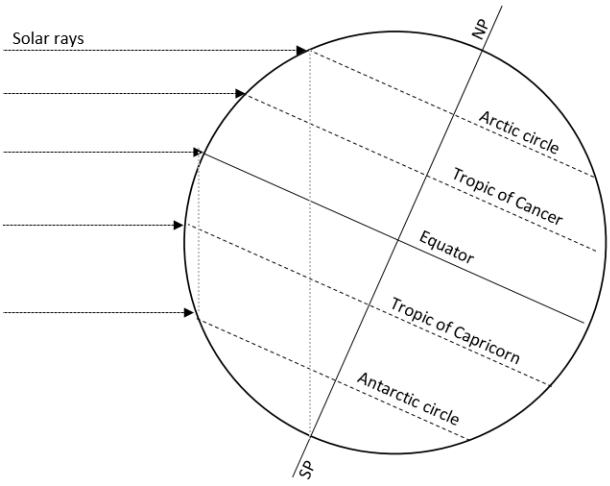

Figure 5.23: Obliquity of Earth's axis to solar rays.

Cancer [Figure 5.27] shows a more balanced distribution in variability around 1500BC (decreasing variability prior to 1500BC and increasing since then). Variability for the Tropic of Cancer also has a maximum range of 1.54 W/m^2. The graph for the Equator [Figure 5.28] shows a range in insolation levels of 1.11 W/m^2, but is smaller post-1500BC than pre-1500BC. The rate of change over each 19-yr period varies throughout time, and can be as little as 0 W/m^2. At the other extreme, for example, there is an increase of 1 W/m^2 between 1707AD and 1726AD (at the end of the Maunder Minimum) [Figure 5.26], whilst there is a drop of 1.23 W/m^2 at the Arctic Circle [Figure 5.25]. At the start of the Industrial revolution there was an increase of 0.91 W/m^2 [Figure 5.26] for the Antarctic Circle, whilst there was a corresponding increase at the Arctic Circle [Figure 5.25]. Periodicities of 133 yrs are dominant in these graphs, due to the same fluctuations in both Earth-Sun and Earth-Moon distances (Section 5.3) and solar declination cycles (Section 4.4.1).

Figure 5.29 shows insolation values for the Tropics of Capricorn and Cancer, Equator, Arctic and Antarctic Circles, and the South Pole. The tropical latitudes show marginal increases in insolation towards the present time. Arctic values also show marginal increases whilst Antarctic values show marginal decreases. The insolation values in this graph are influenced by the separation of the perihelion and December solstice. Increases in other values are due to the modern perihelion conjunction with the Metonic lunation. For the Arctic zone, the values rise above zero from the Roman Warm Period.

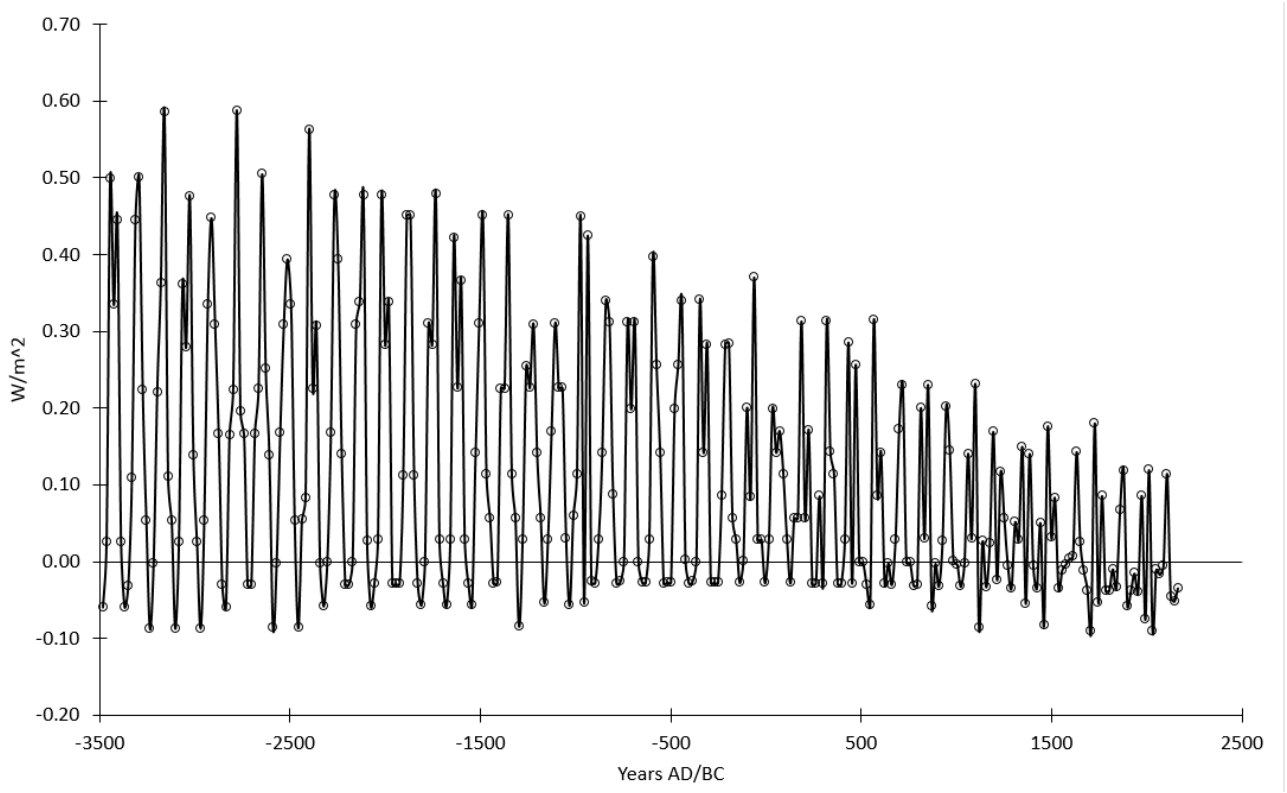

Figure 5.24: Insolation variability for the Tropic of Capricorn.

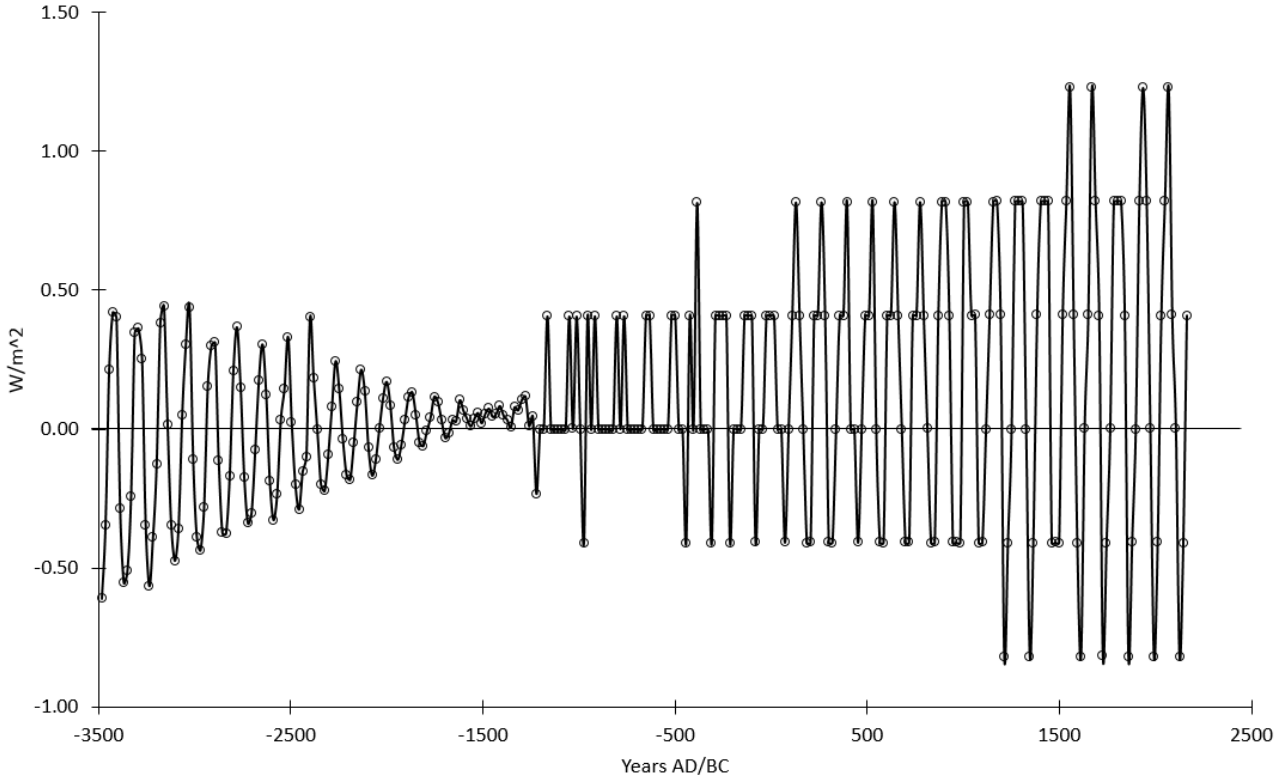

Figure 5.25: Insolation variability for the Arctic Circle.

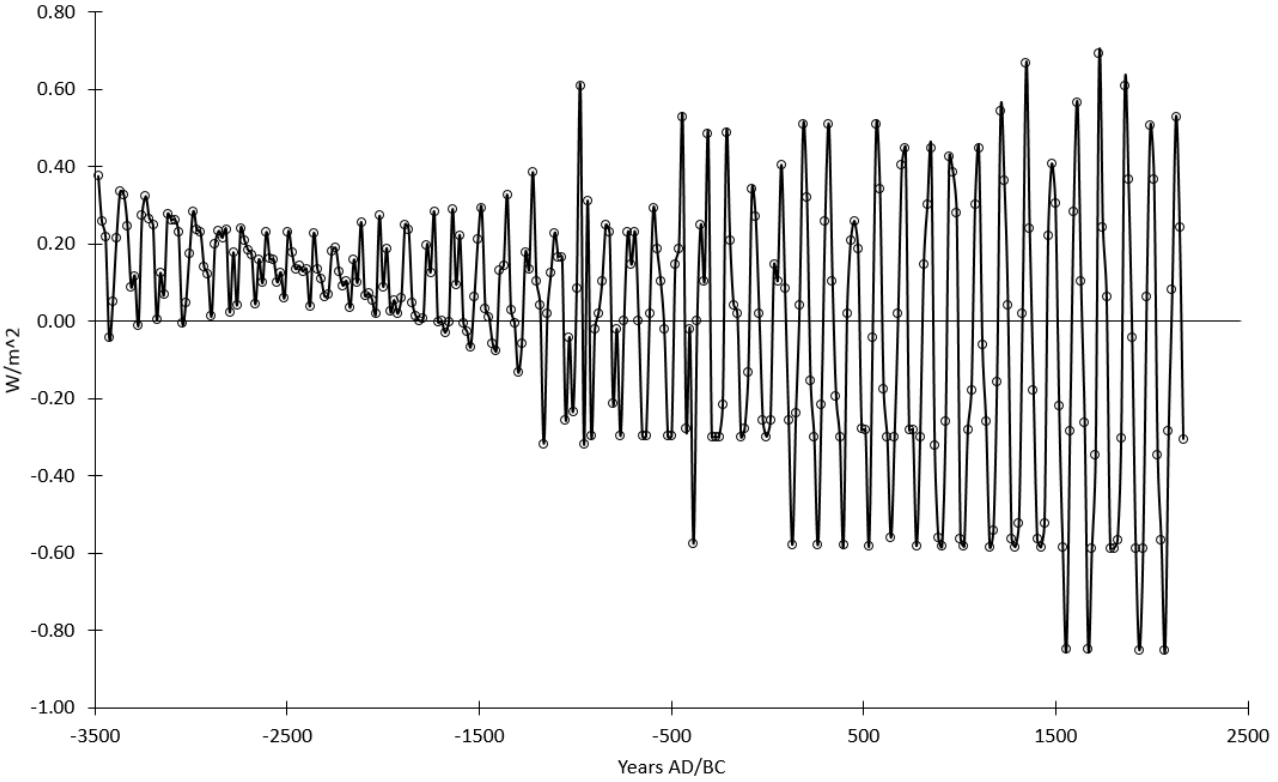

Figure 5.26: Insolation variability for the Antarctic Circle.

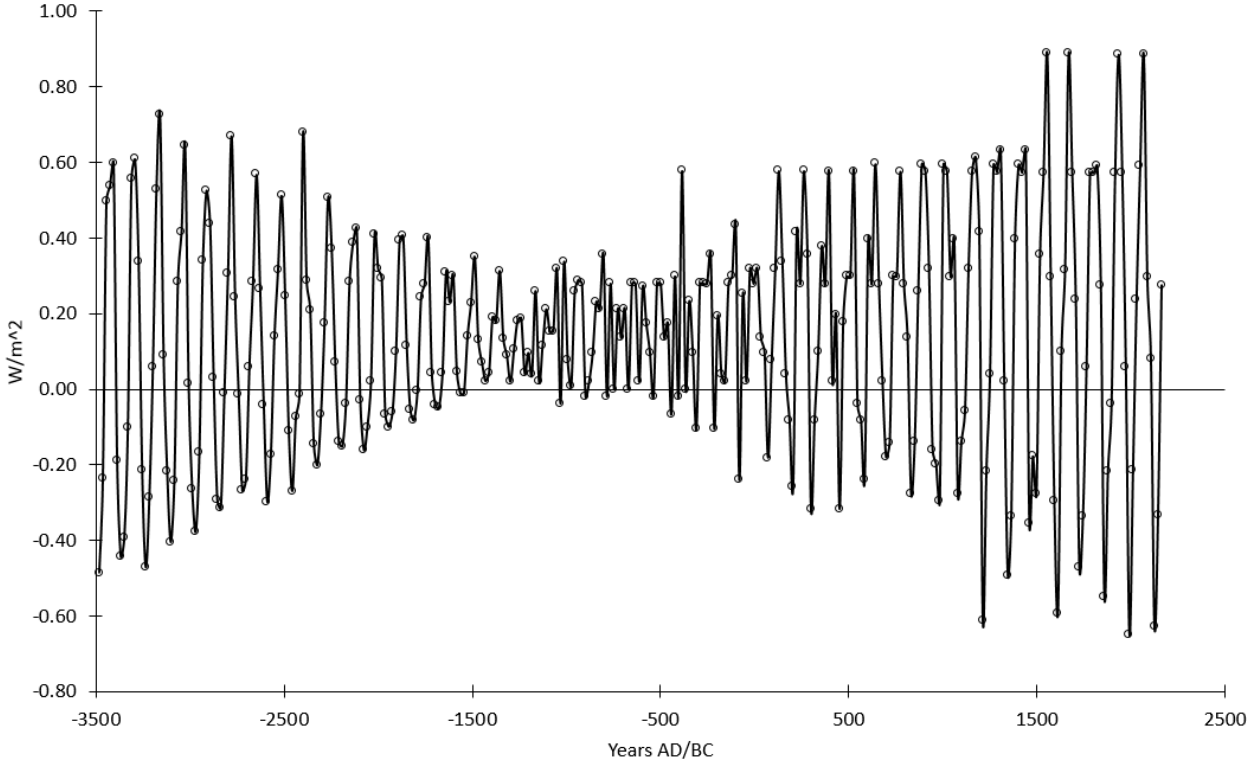

Figure 5.27: Insolation variability for the Tropic of Cancer.

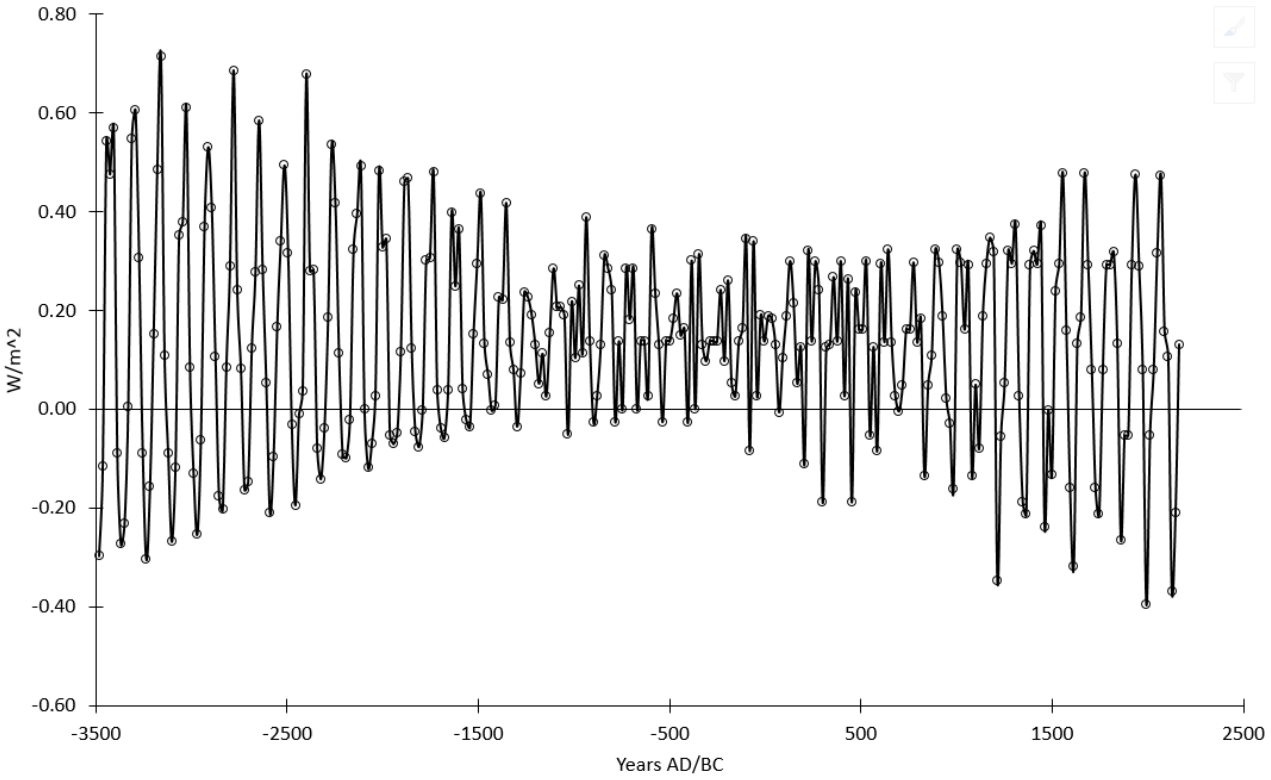

Figure 5.28: Insolation variability for the Equator.

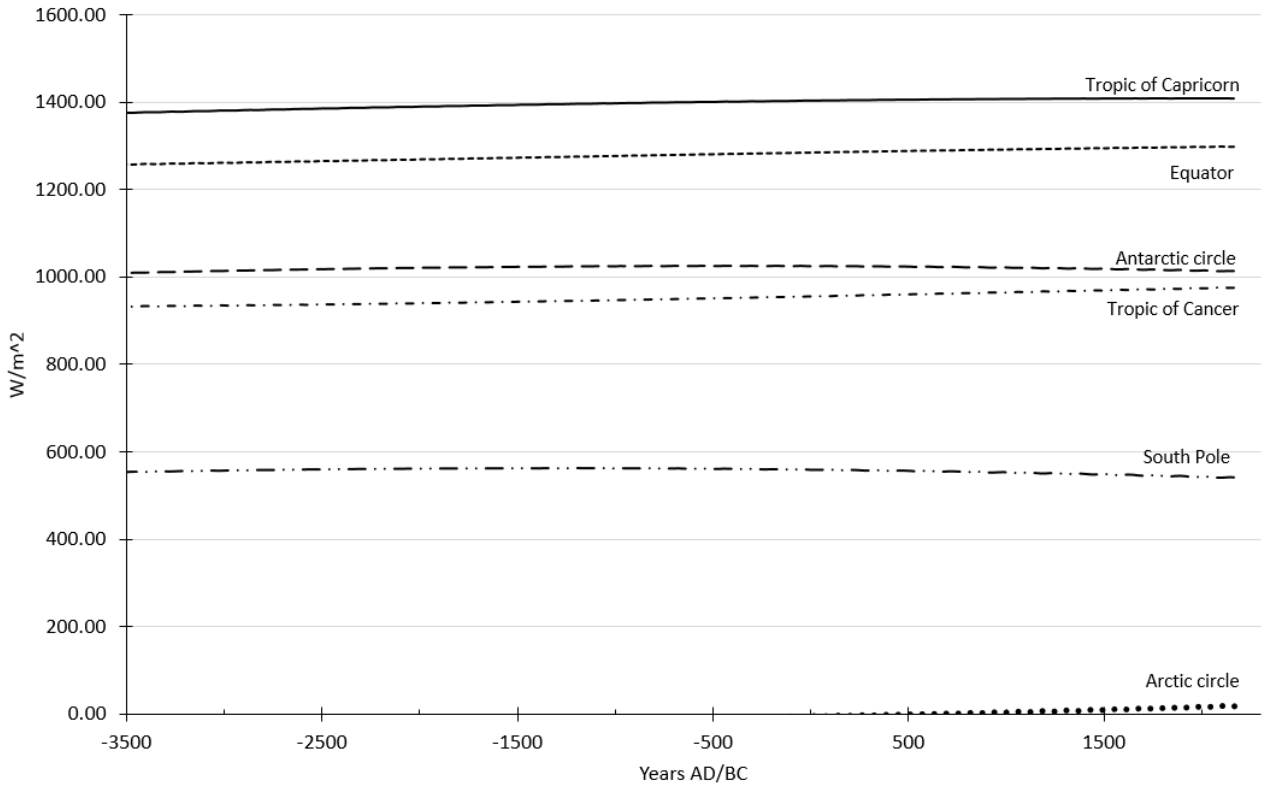

Figure 5.29: Insolation for the Equator, Tropics of Capricorn and Cancer, and the Arctic and Antarctic Circles.

5.5 Chapter summary

For the period of the astronomical data, an overall reduction in Earth-Sun distances and increase in gravitational force and TOA solar irradiance levels are shown. As the Earth-Sun distance measurements were taken at New Moon, the Earth-Sun distances and gravitational measurements included the gravitational influence of the Earth-Moon interaction. Gravitational force varied by ~0.06% due to Earth-Sun interaction during the range of the astronomical data. Gravitational flux due to Earth-Moon distances varied by ~15% during this same period. Based on Earth-Sun distances, variation in TOA solar irradiance was a maximum of 0.7% about 5.5 kya to minimal during modern times, corresponding to a range of 0.7W/m^2 when the solar zenith angle was zero. Insolation levels vary though time and are dependent upon latitude, with the most extreme variations of up to ~2 W/m^2 at the Arctic Circle during modern times. A dominant feature of these insolation patterns is an ~133-yr periodicity that can involve rapid fluctuations in insolation levels over periods as short as 19 yrs.

These factors are influenced by the forming perihelion-Metonic lunation conjunction that becomes exact in 2163AD (Section 5.2). At 5.5 kya, the perihelion occurred around September 24, reaching November 23 in 1183BC and December 21 in 1308AD. The perihelion currently occurs around January 4. Although the Metonic lunation is a proxy of the tropical year in this data, because of its close association with the length of the year (19.0002 tropical years, and 18.9998 Julian years), this astronomical data shows an impact of the moving Metonic lunation. The date of the Metonic lunation

has moved ~14 days from the December solstice since 1183BC, thereby affecting the overall patterning of the insolation data due to the changing day of year relative to the equinoxes and solstices. The impact of this influence can be seen in at the December solstice-perihelion conjunction in the mid-2nd millennium BC. At this point in time, a suppression of insolation variability occurred in all insolation graphs due to the relative reduction of the solar zenith angle during this period. The progression of the Metonic lunation and perihelion relative to the tropical year produced cycle lengths (~90 ky) similar to the Milankovitch eccentricity cycle (~95 ky) (cf. Berger *et al.,* 1993), Milankovitch precessional cycle (~21 ky, ~23 ky), Heinrich event harmonics (~6 ky), and variable lengths of millennial-scale cycles [Figures 5.3 and 5.4]. The physical effects of precession are due to the interaction of solar and lunar gravity.

In the Earth-Sun distance data, upon which gravitational and irradiance calculations are based, a suppression of these factors can be seen at times of the Roman Warm Period, Medieval Warm Period, and warming since the end of the LIA [Figures 5.19 and 5.20]. The Medieval Warm Period was the time of a ~21-ky conjunction of the perihelion with the December solstice, where the suppressed insolation and gravitational patterns are due to plateaus in the respective sinusoidal peaks of cyclical activity. As the Metonic lunation forms a conjunction with the perihelion in 2163AD, levels of irradiance and gravitational continue to rise marginally above this plateau due to reduced Earth-Sun and Earth-Moon distances associated with the perihelion and Metonic lunation conjunction [Figures 5.6 and 5.18]. Perigean-perihelion conjunctions and Metonic eclipses (Section 5.3.3) contribute to another reduction in variability due to the further minimisation of Earth-Sun distances. The pattern of millennial-scale variability was more pronounced in Earth-Moon distances and gravitational force (Section 5.3.2), with peak gravitational forces occurring at the time of maximum Earth-Moon gravitation. These peaks were also coincident with Bond IRD events, close to Metonic solar eclipses [Figure 5.13].

Earth-Sun distances, Earth-Moon distances, and the physical models of gravitation, TOA irradiance, and insolation all revealed patterns at millennial and centennial scales. Common to all these is a 133-yr cycle upon which the other centennial- and millennial-scale patterns are based. This 133-yr cycle is one in which there is a reduction in both Earth-Sun and Earth-Moon distances at the time of the Metonic New Moon that occurs every 19 yrs (Sections 5.3.1 and 5.3.2). The 133-yr cycle is also found in solar declination data (Section 4.4.1) and is associated with similar patterns in solar insolation and irradiance (Section 5.4). This 133-yr cycle generally involves 57-yr and 76-yr components [Figures 4.8, 5.27 and 5.28] in declination and TOA irradiance data. In the next chapter, a revised chronologically-anchored model of insolation, based in part on the 133-yr cycle, is explored,

providing further evidence of solar and lunar forcing of Earth's centennial- and millennial- scale climate patterns.

Chapter 6 – An Exercise in Wiggle Matching

In the previous two chapters, two important cycles stood out as potential contributors to the ~1500-yr signal: the 209-yr and 133-yr cyclicities. Modelling of the tropical year relationship with the perihelion, through the Metonic lunation and the RRA variables, highlights the roles that both these cycles played in terms of gravitational and solar forcing (Chapter 4). Both these astronomical cycles are associated with variations in gravitation and TOA solar irradiance based on cyclical variations in distance (Chapter 5). Both these cycles have equivalents in climate cycles (Section 2.2.3). The 133-yr cycle has a particularly strong impact on latitudinal insolation patterns and demarcates positions of reduced Earth-Sun distances at the time of the Metonic New Moon (Section 5.3.2). The 209-yr cycle is associated with the timing of the Metonic New Moon relative to the anomalistic year (through the RRA variable) and therefore proximity to the perihelion; it delineates cycles of Metonic New Moon interaction with the perihelion and its length varies over time due to precession. The timing of the New Moon with perihelion is associated with both reduced Earth-Sun and Earth Moon distances, and therefore also affects the level of solar irradiance reaching Earth. The 209-yr period and its companion 228-yr period appear in lunar declination data and have counterparts in the SdV cycle of warm-cool temperature cycles. The lunar gravitation associated with this 209-yr cycle also impacts on solar declination patterns, solar zenith angles and insolation through a reduction in the tilt of the Earth's axis at the time of the New Moon (cf. Gutzwiller, 1998).

This chapter examines in detail these two cycles as potential contributors to the ~1500-yr climate signal. The interaction of these two cycles is trigonometrically modelled, normalised, and chronologically anchored, before being wiggle-matched and statistically compared to total solar irradiance (TSI) reconstruction derived from Antarctic ice core ^{10}Be data (Bard *et al*., 1997, 2000, 2007). The model is also adjusted for precession and solar minima and maxima. These variations of the model are also statistically tested. This exercise shows that the null hypothesis, of no difference between the astronomical model's predicted pattern and the TSI reconstructions, cannot be dismissed.

6.1 A model of interacting 133-yr and 209-yr periodicities

Astronomical data based on the Metonic lunation series suggested a chronological link between the timing of Bond events and the timing of perihelion with relative perigee in close proximity to Metonic eclipses. This Metonic lunation series, based on the current perihelion, and the perihelion were chosen as proxies for the expression of Milankovitch precession at high-frequency scales (Chapter 4). Prominent cycles that were identified within this astronomical data were the 133-yr and 209-yr periodicities.

The superposition of the SdV and Gleissberg cycles was previously trigonometrically modelled and shown to emulate the ~1470-yr quasi-periodicity when compared to the CLIMBER-2 coupled climate system model (Braun *et al*., 2005). Both the SdV and Gleissberg cycles have been associated with inferred solar forcing derived from analysis of cosmogenic nuclide records (Braun *et al*., 2005). However, modelling of the interaction of the Metonic lunation and RRA has also demonstrated a capacity to reproduce the SdV signal, additionally showing the Gleissberg signal as an artefact of this interaction [Figure 4.14a]. Similarly, the relationship between sunspot activity and the perihelion (RRA) shows cycles at the length of the SdV cycle [Figure 4.14b], which delineates cycles of peak sunspot activity at perihelion. In Figure 4.14b, the Gleissberg cycle also appears as an artefact of interaction between the two components [Figure 4.14]. So, whilst the SdV cycle has been inferred to be the result of solar variability, despite not being evident in sunspot data (Hathaway, 2010), an alternative cause of variation in solar irradiance patterns is suggested by this modelling [Figure 4.14] and patterns in declination data (Section 4.4.1).

Whilst Braun *et al.* (2005) modelled the interaction of the Gleissberg and SdV cycles, here the 133-yr cycle and the 209-yr cycles are modelled. The 133-yr cycle is also a factor of the ~1470-yr quasi-periodicity when paired with the length of the variable sunspot cycle (*viz*, 11x133=1463; 11.1x133=1476.3; 11.2x133=1489.6; 11.3x133=1502.9; 11.4x133=1516.2). This cycle is prominent in the physical and astronomical data and is also linked to various climate cycles (Chapters 2, 5). An ~130-yr periodicity is also seen in the southern hemisphere radiocarbon calibration curve (Hogg *et al*., 2013).

6.1.1 Data

The data used for comparison to the model is the Bard *et al*. (2003-2007) TSI reconstruction based on Antarctic ice-core data from the South Pole of smoothed ^{10}Be record (Section 3.2.4 for further information). These data span ~1200 yrs from 843AD. The TSI reconstruction used a 12-box numerical model to convert ^{10}Be signals in ice-cores to a synthetic radiocarbon record (Bard *et al*., 1997, 2000, 2007). This reconstruction of TSI was found to strongly correlate with the dendrochronologically calibrated radiocarbon record (r=0.81), also showing no significant lag between the ^{10}Be and radiocarbon records [Figure 3.23]. Their study demonstrated the dominant solar role in shaping Earth's cosmonuclide record during the period of their study. Bard *et al*.'s (1997, 2000, 2007, 2003-2007) work is not explicit on whether precessional adjustments have been made to their chronology; the only indication is that the abscissa is in calendar years, which would suggest not. In their reconstructions (Bard *et al.,* 2007), three solar reconstructions are shown: TSI_1 is the original Bard *et al*. (2000) reconstruction, uncorrected for geomagnetic modulation (Section 3.2.4); TSI_2 is corrected for geomagnetic modulation, with agreement between Bard *et al*. (2007), Korte

and Constable (2005), and (Gubbins *et al*., 2006); TSI_3 is corrected for geomagnetic modulation based on the superseded record of Yang *et al*. (2000).

6.1.2 Method

Gravitational influences and solar insolation variances have already been demonstrated in association with the chosen proxies for the tropical and anomalistic years, *viz* perihelion and Metonic lunation (Chapter 5). These gravitational influences can most strongly be seen in millennial-scale periodicities associated with Bond events during the last 5500 yrs (Chapters 4, 5). Although there are only four Bond events during that time (Section 2.2.2.1), every event occurred near perigee-perihelion conjunctions and Metonic eclipses. These corresponded with minimal Earth-Sun and Earth-Moon distances (Chapter 5). Here, the theorised position associated with my conceptual model is statistically tested, based on the trigonometrically-modelled superpositioning of the 133-yr and 209-yr periodicities found in my astronomical data, expressed as an addition of their sines. This model was chronologically-anchored at the most exact alignment of this Metonic lunation series with the ecliptic, which occurred at 1183BC [Figure 4.9]. The amplitudes of each contributing signals are assumed to be the same as both astronomical cycles are associated with variations in solar irradiance based on changes in Earth-Sun distance. With t=time elapsed (in years) since the start of the cycle, the formula used to construct this model is:

$$f(t) = \sin\left((2\pi t).133^{-1}\right) + \ sin((2\pi t).209^{-1})$$

The model of the superimposed sinusoids was normalised (feature-scaled) to the data being tested, e.g., where 1 unit of amplitude of the model equated to 1 W/m^2 and the x-axis (where amplitude is 0) was equivalent to the mean TSI value used by the data (1365 W/m^2). This value is an estimation to cater for a number of factors, including annual variation in TSI during the year due to orbital eccentricity (±0.81W/m^2) (Vieira *et al.,* 2012; see also Tables D.4 to D.7 in Appendix D), and to account for drift in TSI due to precession (the variation in range of TSI shown in Figure 5.21 since 843AD is ~0.35W/m^2). These matters are discussed further and the sensitivity of this scale is also tested in Section 6.2.3. For S = 1365 W/m^2 where S (mean solar irradiance), which is the value used by Bard *et al.* (2007), the result for each value in the above equation was added to this mean TSI value in the normalisation process, such that:

$$f(t) = (\sin\left((2\pi t).133^{-1}\right) + \ sin((2\pi t).209^{-1}))+\text{S (W/m}^2\text{)}$$

Adjustments to the model were also made to account for total solar irradiance variations due to sunspot activity and the influence of precession. Each of these stages is depicted graphically in Section 6.2, and is accompanied by corresponding statistical results. Although the value for differences between sunspot minima and maxima is still debated, there is currently a consensus that

this value is ~0.12% (0.001) of total insolation, equivalent to ~1.6 W/m^2) (Friis Christensen and Lassen 1991; Kopp and Lean, 2011; Vieira *et al*., 2011; Wang *et al*., 2005). The values used in adjustments to this model are based on a value of 0.12% variance in TSI between recent solar minima and maxima. For further discussion on these matters see Section 6.2.3. Adjustments made on this basis are as follows: a general decrease in TSI by 0.12% was made to the model for both the Spörer Minimum (1455AD to 1550AD) and Maunder Minimum (1655AD-1715AD (cf. Eddy, 1976; Summerhayes, 2015). Additionally, the model values for TSI were increased by 0.12% during 1108AD-1300AD for the Medieval Warm Period (high sunspot activity and auroral sightings) (cf. (Eddy, 1976); and after 1835AD, for relatively high sunspot activity during modern times [cf. Figures 3.18 and 3.19] (cf. Gray *et al.,* 2010; Kopp and Lean, 2011).

Adjustments to the model were also made for precession. As the Julian year appears to be stationary, the date of the equinox moves backwards through the calendar year, increasing separation between it and the original calendar date with which it was associated, thereby "stretching" the length of the cycle. The rate of precessional separation between the Julian calendar year and tropical year is 1° for every 128.19 yrs (Table A.4). This is also the cyclical interaction between the starting geographic longitude and the tropical year (associated with RRT variable) that occurs every ~128 yrs [Figure B.1]. Over say 1463 yrs, the separation between the two interacting cycles (Julian calendar year and tropical year) is 11.41 yrs ($1463\ yrs \div 128.19\ yrs = 11.41\ yrs$). Therefore, the correction (1463 yrs + 11.4 yrs) is 1474.4 yrs. This correct value can be seen in Table A.3 (Appendix A) and Table 6.1, where the RRT variable associated with the tropical year shows a close return at 1474 yrs within 0.53° of precision. The previous RRT occurred 128 yrs earlier (at 1346 yrs) with a precision of 0°, whilst the following RRT return occurred 128 yrs later (at 1602 yrs) at 1.06° from a precise alignment [Table 6.1].

Table 6.1: Excerpt from trigonometric model showing the records for 1346 yrs, 1474 yrs, and 1602 yrs. These are times of close cyclical interaction between Earth's rotation and the tropical year, indicated by the RRT variable. Other modelled factors are shown in the records for these years, including those for the sidereal and anomalistic years, the sunspot cycle and lunar cycles.

Cycle No.	Rotation variables (degrees)		Schwabe			Hale		Metonic		Lunar node	
(yrs)	RRS	RRT	RRA	F	sin()	F	sin()	F	sin()	F	Sin ()
1346	21.82	0.00	169.22	118.07	0.43	59.04	0.22	70.84	-0.84	72.25	1.00
1474	314.89	0.53	253.25	129.30	0.95	64.65	-0.81	77.58	-0.48	79.12	0.68
1602	247.96	1.06	337.27	140.53	-0.16	70.26	1.00	84.32	0.92	85.99	-0.06

The chronologically anchored model of superimposed 209-yr and 133-yr cycles was tethered to 1183BC at the time of the December solstice-Metonic lunation conjunction, when there is a solar eclipse [Figure 4.9]. The Bard *et al.* (2003-2007) data begins at 843AD so, the model was brought into phase (or wiggle-matched – see Section 2.2.1) with the Bard data by adding 16 yrs (for precessional movement) to the modelled cycle length for the time difference between 1183BC and

843AD ($(1183 + 843 - 1) \div 128.19 = 15.80$). The model was further adjusted after 843AD by adding 1 yr every 128.19 yrs to the precessionally-adjusted model.

Statistical tests were used to compare the model of superimposed astronomical cycles and the TSI reconstructions of ^{10}Be data (Bard *et al*., 2003-2007). Non-stationary and non-linear data violates fundamental assumptions to inferential statistics, such as assumptions about independence (autocorrelation) and distribution (Urdan, 2010) and therefore presents problems for statistical analysis. However, non-parametric tests, such as the Pearson's X^2 goodness-of-fit test, are suitable for analysing non-linear and non-stationary data such as astronomical cycles and geographic data (Urdan, 2010). The X^2 test, is a test against the null hypothesis of observed versus expected or predicted values, which is one of no difference. Initially, the critical X^2 value (X^2_c) is determined using an identified α value (probability) and the degrees of freedom (df). The generally accepted α value is 5% or α=0.05, which was used here. If the X^2 statistic is greater than the X^2_c, then the null hypothesis of "no difference" between the expected and observed values is rejected (Urdan, 2010). If the X^2 statistic is less than the X^2_c, the null hypothesis is accepted. In these tests, $X^2_c = 168.61$ (df=140 and α=0.05). Regression analysis was also used.

Despite the violations of statistical assumptions in analysing non-stationary and non-linear data, compensations can be made if the nature of the data is understood Longley *et al.,* 2011; Mitchell, 1999; Schulz, 2002). In testing superimposed sinusoids of astronomically forced cycles against SST data (both of which are non-linear and non-stationary), Imbrie (1985) calculated the Pearson's correlation coefficient (r) to test the strength of the relationship between a model of superimposed sinusoids and the data. In the following tests upon the predictive model of superimposed sinusoids of astronomical cycles and the TSI reconstructions of ^{10}Be data, X^2 and r values were calculated at each stage of the model development. As with Imbrie (1985), the data and model were assumed to be stationary and independent, *contra* to the intrinsic natures of astronomical cycles and geographic data. Excerpts from these models appear in Appendix D. However, first, the unanchored model is explored.

6.2 Results of revised chronological model

6.2.1 Trigonometric model – unanchored

The numerical model shows that the interaction between the 209-yr and 133-yr cycles produce a periodicity of 1463 Julian years [Figure 6.1]. Corrected for precession this value is 1474.4 yrs (Section 6.1.2), which also approximates the time of a perigee cyclical alignment with the perihelion [Figure 6.2]. This value of 1474.4 yrs is also in accord with modelled RRT activity with a precise cyclical return to 0.53^0 of precision (Chapter 4, Table 6.1).

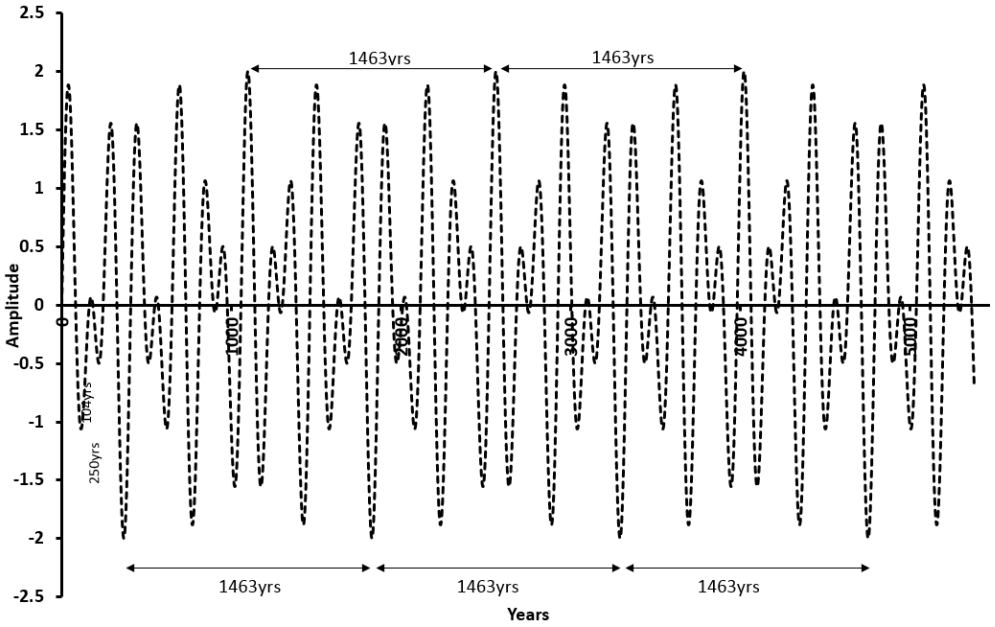

Figure 6.1: Modelled activity of the interaction between the 209-yr and 133-yr cycles at annual resolution. A regular 1463-yr cycle (Julian years) is formed.

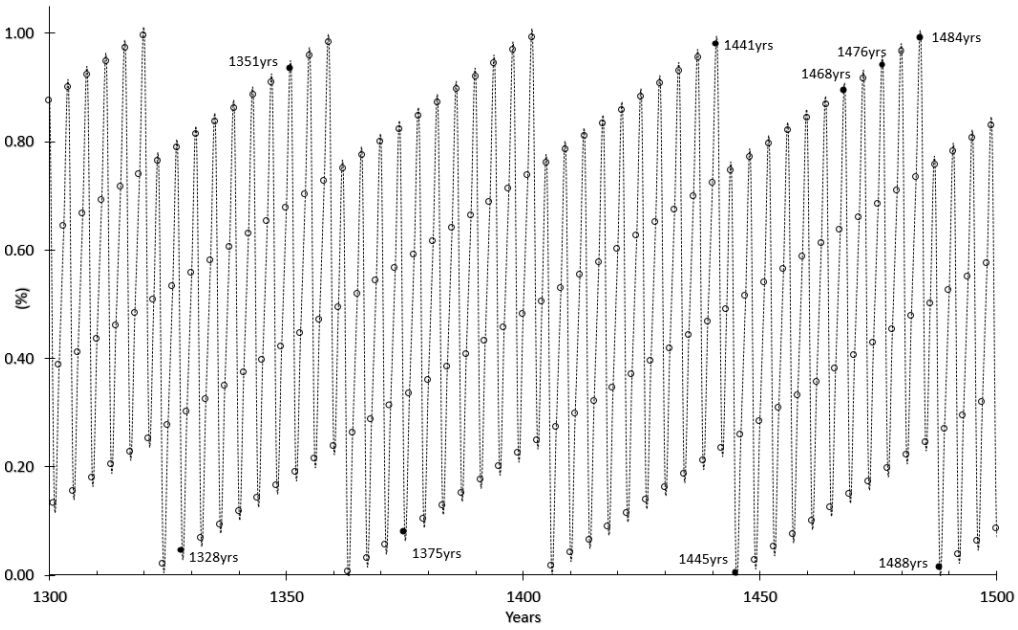

Figure 6.2: This graph shows the modelled relationship of the perigee to anomalistic year in terms of percentage of a whole cycle (range of 0 to 1) during 1300-1500 yrs of the cycle. Cyclical interaction occurs at points closest to 0 and 1. Black filled dots approximate Bond cycle lengths.

The same periodic activity is also shown but at resolutions of 19 yrs (associated with the Metonic lunation [Figure 6.3]; it is not seen in the 57-yr resolution, which is associated with sunspot-Metonic harmonic as well as the precessional separation rate between the tropical and anomalistic years [Figure 6.4]. However, the multiple of the 1463-yr cycle, viz 4,389 yrs is seen at the 57-yr resolution [Figure 6.4]. The cyclical pattern consistently repeats, with the 209-yr SdV cycle and variants most evident at the start and end of the cycle [Figure 6.3]. Similarly, in Figure 6.4, Metonic eclipse patterns merge with the model, repeating at 4,389-yr intervals (at the start and end of the cycle), indicated by the dotted line. These Metonic eclipse patterns are closely associated with the RRA returns at 493-

yrs [Table 4.3]. Other evident periodicities associated with the lunar declination cycle can be seen, i.e., 171 yrs, 228 yrs, 912 yrs. A major pattern between extremes of amplitude also produce a 399-yr cycle.

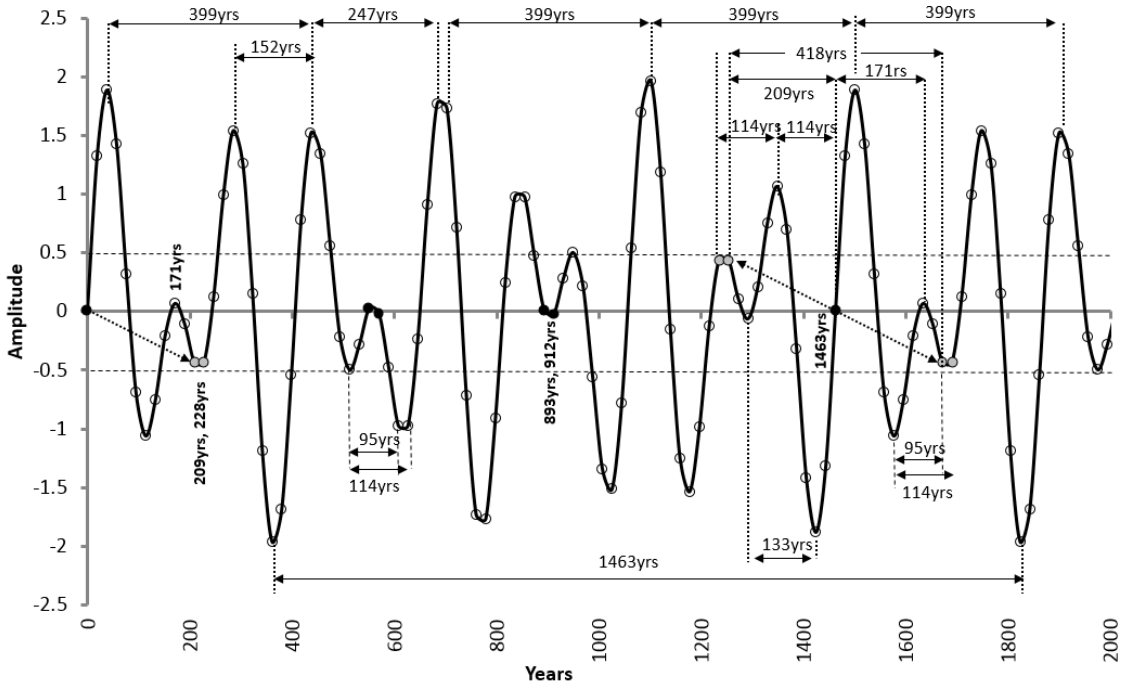

Figure 6.3: Modelled activity of the interaction between the 209-yr and 133-yr cycles at 19-yr resolution. The SdV patterns are marked by diagonal dotted arrows at the start and finish of the 1463-yr cycles.

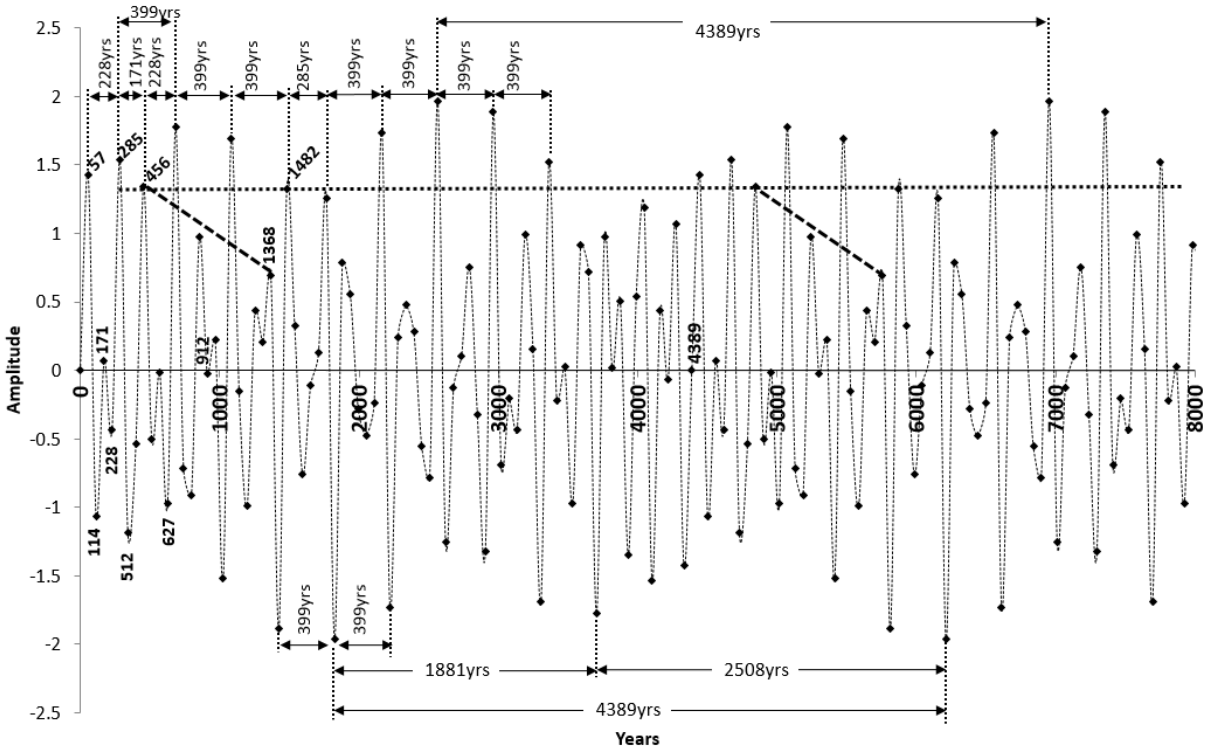

Figure 6.4: Astronomical links with the modelled activity of the 209-yr and 133-yr combined periodicities at 57-yr resolution. The dashed lines show a connection between Metonic eclipse occurrences and repetition of the same pattern.

6.2.2 Chronologically-anchored model of 209-yr and 133-yr interaction

Anchored at 1183BC, Figure 6.5 shows the precession-corrected, chronologically-anchored model of combined 209-yr and 133-yr climate periodicities in context of historical climatic periods. It matters little whether the model is anchored at 1183BC, or 1463 yrs later as the results are the same: a repeating pattern of 1463 Julian years is created that when precession corrected, is equivalent to a 1474-yr climate 'cycle'. Here it can be seen that extreme negative amplitudes of this cycle coincide with extremely cold periods, such as the Oort, Wolf, Spörer and Maunder Minimums and the beginning of a new Hallstadt period. The alternating historical periods of warm and cold tend to correspond with the greater number of negative amplitude peaks for cold periods and positive amplitude peaks for warm periods. As the Little Ice Age ended, the model indicates warming at the start of the Industrial Revolution.

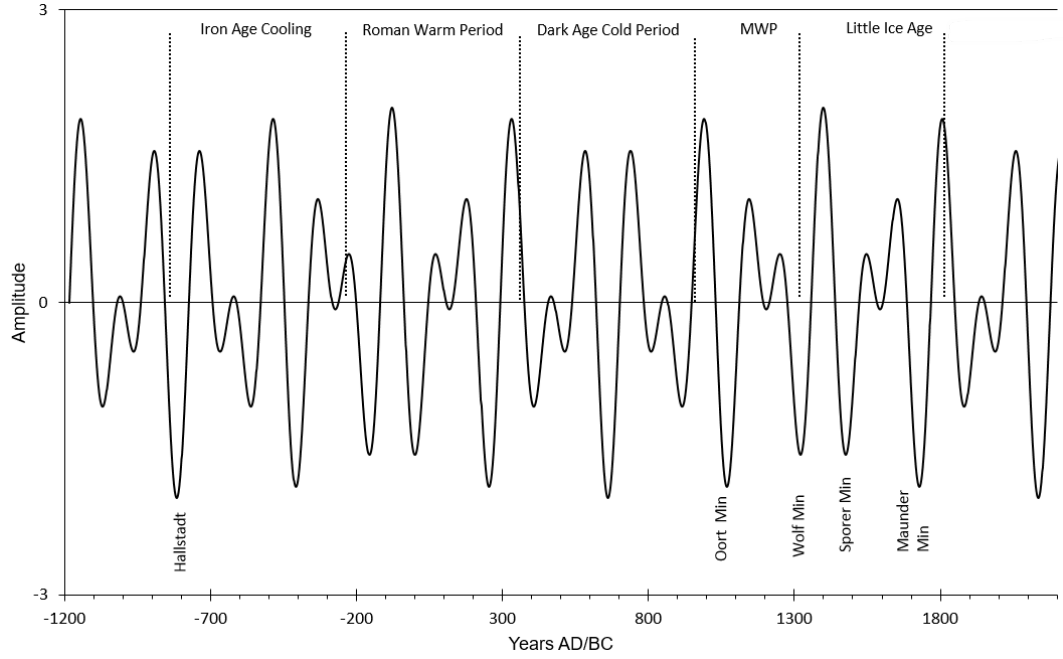

Figure 6.5: Chronologically-anchored model of combined 209-yr and 133-yr periodicities in historical context. This model is anchored at 1183BC and is precession corrected as described (Section 6.1.2). Some of the coldest periods during the last 5500 yrs are centred on extreme negative amplitude peaks.

6.2.2.1 Results: unadjusted model

There is a strong visual resemblance between the smoothed ^{10}Be record from the Bard *et al*. data (2003-2007) and the unadjusted trigonometric model [Figure 6.6], although the model appears to be slightly out of step with the ^{10}Be flux. In Figure 6.7, the normalised chronologically-anchored model can be seen with a strong visual resemblance to the TSI reconstruction based on the smoothed ^{10}Be record.

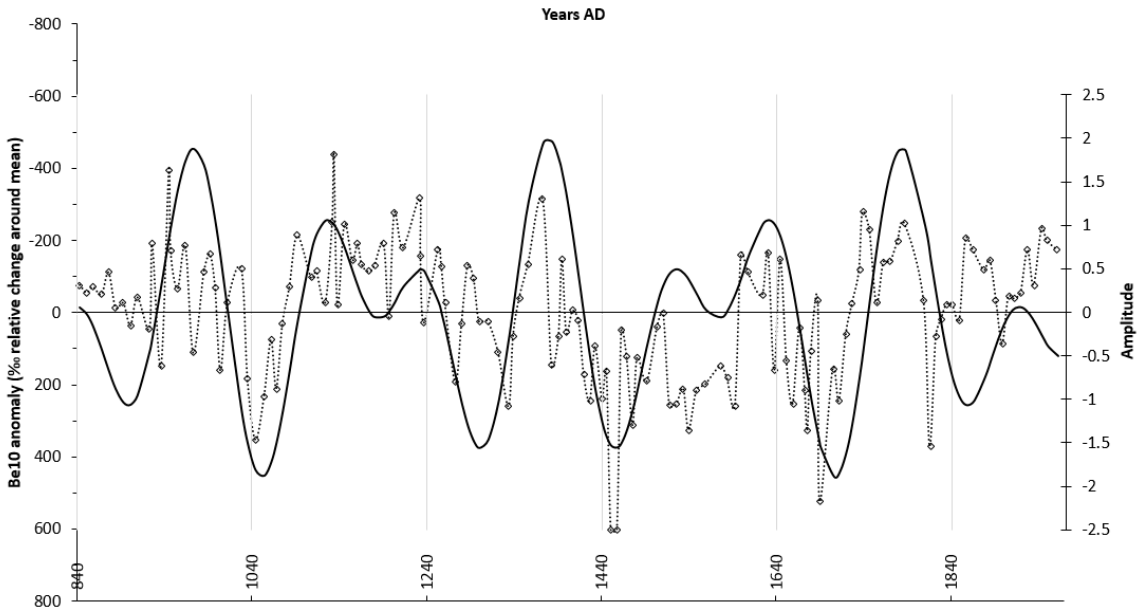

Figure 6.6: Chronologically anchored model visual comparison to Bard *et al.* (2007) smoothed ^{10}Be flux. The y-axis to the left is the scale of ^{10}Be flux, and the y-axis for the model is to the right and is measured in amplitude due to the superposition of the sines of the 133-yr and 209-yr cycles. The dotted line is the smoothed ^{10}Be flux and the solid line is the unadjusted trigonometric model. The model is noticeably out of step with the data at the end of the LIA and start of the Industrial revolution.

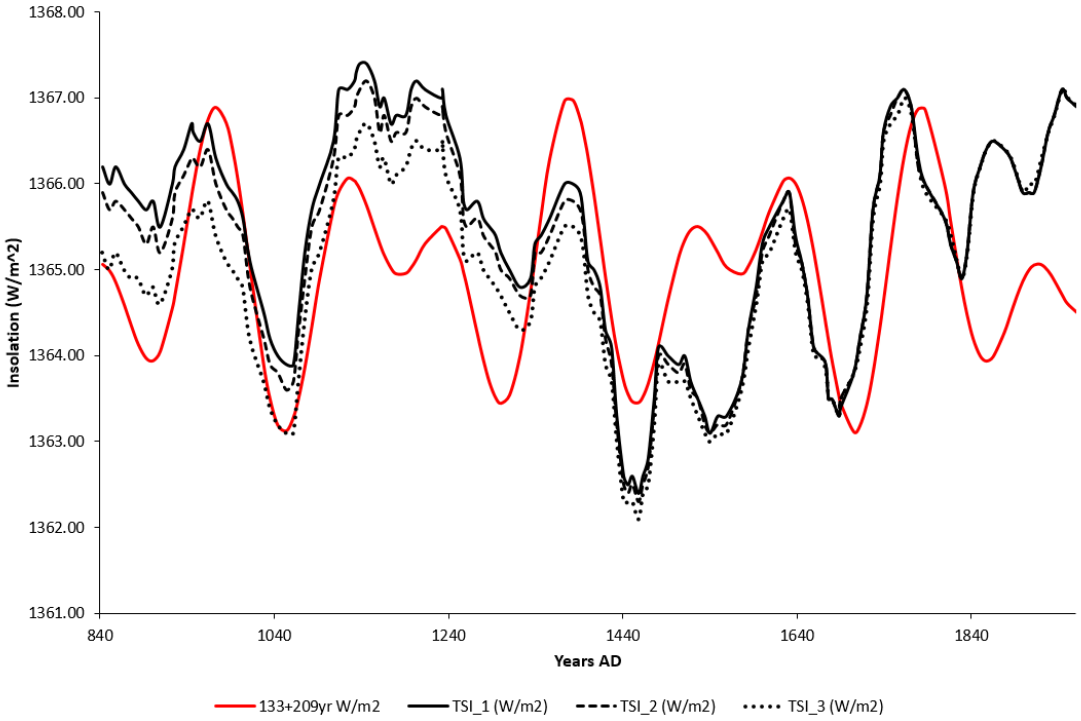

Figure 6.7: The unadjusted, chronologically-anchored normalised model compared to TSI reconstruction from Bard *et al.* (2007). Each of the TSI reconstructions (Section 6.1.1) are shown as indicated in the legend. The red solid line is the model. A strong visual similarity exists between the two.

The statistical results for X^2, r values, and significance (p) appear in Table 6.2. These statistical results can be seen for each of the TSI reconstructions, as well as sections of those reconstructions [Table 6.2]. The X^2 values for the entire length of the model are extremely small (<0.2) and r values show a positive correlation of moderate strength for the entirety of model (r=0.47) and in the two sub-periods (843AD-1481AD and 1481AD-1829AD). The strongest match across all three reconstructions occurs for the period 843AD-1481AD (r=0.64, 0.65, and 0.67 respectively for TSI_1, TSI_2, and TSI_3),

then from 1481AD-1829AD (r=0.51, 0.50, 0.48 respectively for TSI_1, TSI_2, and TSI_3). However, from 1829AD-1961AD, the model shows no correlation (r= -0.1 or -0.06). All results (overall and subperiods) are statistically significant at p=0, except for the third subperiod at p=0.69 (TSI_1 and TSI_2) and p=0.80 (TSI_3).

Table 6.2: Statistical results of X^2, r values, variance (r^2), and significance (p) for unadjusted model.

Stat test/period	TSI_1			TSI_2			TSI_3		
X^2	0.17			0.15			0.14		
Correlation/variance/significance	r	r^2	p	r	r^2	p	r	r^2	p
(entire period)	0.48	0.23	0.00	0.48	0.23	0.00	0.47	0.22	0.00
843AD-1481AD	0.64	0.41	0.00	0.65	0.42	0.00	0.67	0.45	0.00
1481AD-1829AD	0.51	0.26	0.00	0.50	0.25	0.00	0.48	0.23	0.00
1829AD-1961AD	-0.10	0.01	0.69	-0.10	0.01	0.69	-0.06	0.00	0.80

6.2.2.2 Results: model adjusted for precession

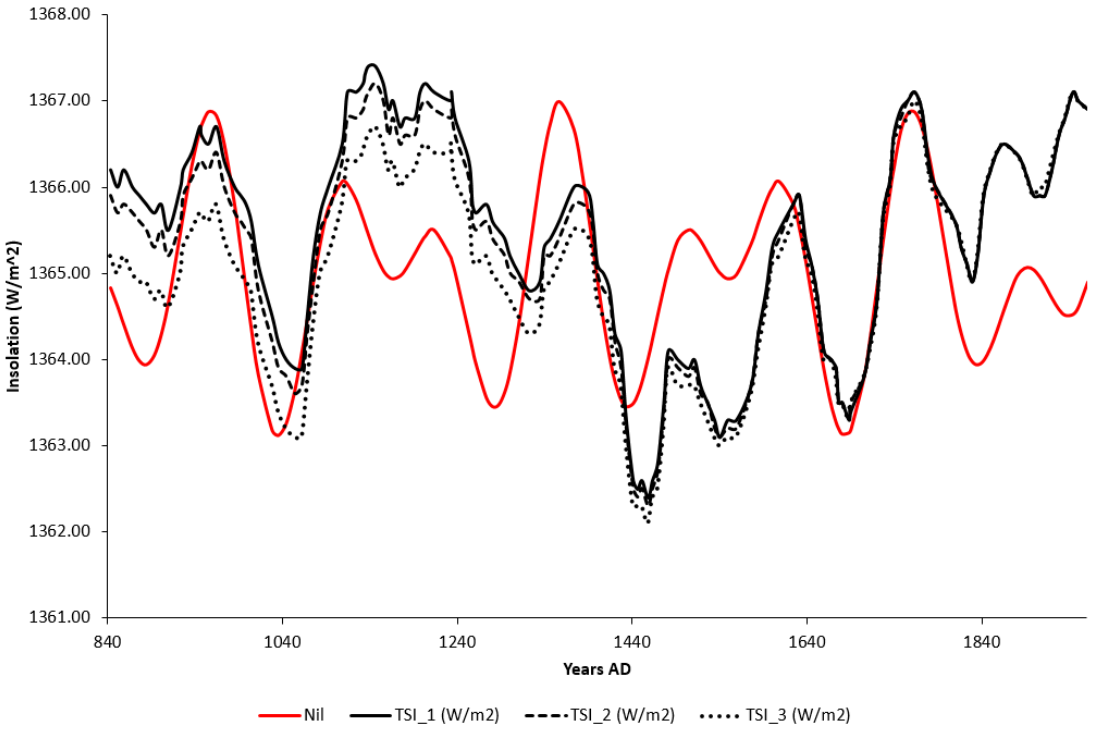

Figure 6.8: The precession-adjusted, chronologically-anchored, normalised model compared to TSI reconstruction from Bard et al. (2007). Each of the TSI reconstructions are shown as indicated in the legend. The red solid line is the model. A good visual match exists between the two and is a vast improvement from the unadjusted model.

The chronologically-anchored model, adjusted for precession, was compared to the TSI reconstruction by Bard *et al*. (2007), with the results graphed in Figure 6.8. The precession-adjusted model scores the same on the X^2 test as the unadjusted model. The statistical results appear in Table 6.3. There is an improvement in overall r values across TSI_1, TSI 2, TSI_3. Of the sub-periods, the largest occurred during the third sub-period (1829AD-1961AD), and then the second sub-period (1481AD-1829AD) as would be expected for precessional adjustment. However, there was a drop across the first sub-period (843AD-1481AD). For the third sub-period, both TSI_1 and TSI_2 jump

from no correlation to a moderately strong, positive correlation, with respective values of r=0.38 and r=0.38, up from r=-0.1. The change in TSI_3 improves from r=-0.06 to r=0.40. Visually, the precession-adjusted model is a better fit [Figure 6.8] than the unadjusted model [Figure 6.7]. The significance values remain unchanged, except for the third subperiod which has considerably improved at p=0.12 (TSI_1 and TSI_2) and p=0.10 (TSI_3).

Table 6.3: Statistical results of X^2, r values, variance (r^2), and significance (p) for precession-adjusted model.

Stat test/period	TSI_1			TSI_2			TSI_3		
X^2	0.17			0.15			0.14		
Correlation/variance/significance	r	r^2	p	r	r^2	p	r	r^2	p
(entire period)	0.50	0.25	0.00	0.50	0.25	0.00	0.48	0.23	0.00
843AD-1481AD	0.55	0.30	0.00	0.56	0.31	0.00	0.57	0.32	0.00
1481AD-1829AD	0.69	0.47	0.00	0.67	0.44	0.00	0.64	0.41	0.00
1829AD-1961AD	0.38	0.14	0.12	0.38	0.14	0.12	0.40	0.16	0.10

6.2.2.3 Results: model adjusted for sunspot activity

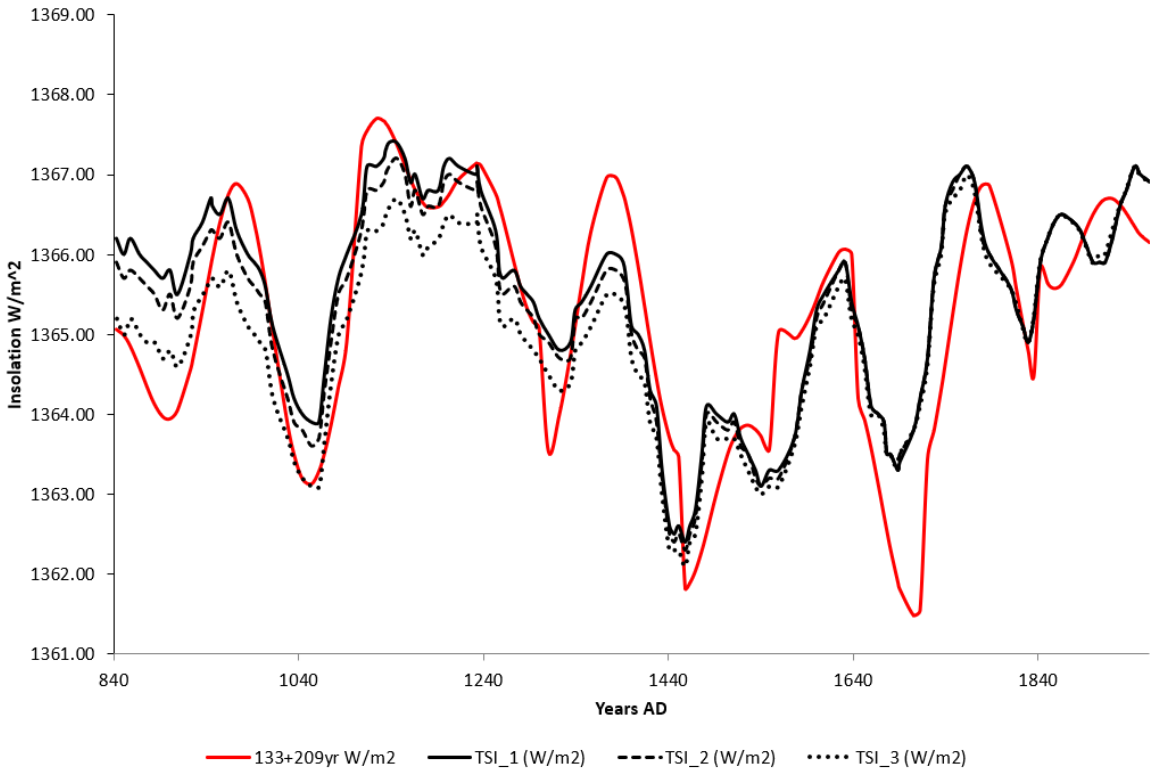

Figure 6.9: The sunspot minima- and maxima- adjusted, chronologically-anchored, normalised model compared to TSI reconstruction from Bard *et al.* (2007). Each of the TSI reconstructions is shown as indicated in the legend. The red solid line is the model. A closer match between the extremes of sunspot minima and maxima can be seen when compared to both Figures 6.6 and 6.7.

The chronologically-anchored model, adjusted for previously specified periods of sunspot activity, was compared to the TSI reconstruction by Bard *et al.* (2007), with the results graphed in Figure 6.9, and associated statistical tests shown in Table 6.4. Once again there is a strong visible similarity

between the TSI reconstructions and the model, but this becomes out-of-step as time progresses because this model has not been precession-corrected. The overall X^2 statistics show an improvement, accompanied by and stronger correlations. This is indicative of a better overall match than either the unadjusted model or precession-adjusted model alone.

Table 6.4: Statistical results of X^2, r values, variance (r^2), and significance (p) for sunspot-adjusted model.

Stat test/period	TSI_1			TSI_2			TSI_3		
X^2	0.08			0.08			0.09		
Correlation/variance/significance	r	r^2	p	r	r^2	p	r	r^2	p
(entire period)	0.83	0.69	0.00	0.83	0.69	0.00	0.81	0.66	0.00
843AD-1481AD	0.85	0.72	0.00	0.86	0.74	0.00	0.88	0.78	0.00
1481AD-1829AD	0.74	0.54	0.00	0.73	0.53	0.00	0.72	0.51	0.00
1829AD-1961AD	0.56	0.32	0.02	0.56	0.32	0.02	0.60	0.36	0.01

Whilst the precession-adjusted model improved on the correlation values for the unadjusted model, there is an even more noteworthy improvement due simply to general adjustments made for sunspot activity during the Medieval Warm Period, Spörer Minimum and Maunder Minimum and after 1835AD. This is also reflected in the overall correlation values for each of the TSI reconstructions (Bard *et al*., 2007), with r=0.83 for TSI_1 and TSI_2, and r=0.81 for TSI_3. The first two sub-periods both show strong positive correlations at r=0.85, 0.86, and 0.88 for TSI_1, TSI_2, and TSI_3 respectively for the first sub-period; and r=0.74, 0.73, and 0.72 for TSI_1, TSI_2, and TSI_3 respectively for the second sub-period. The third sub-period shows a large improvement over the unadjusted model (r-values close to zero) and the precessionally-adjusted model (moderately strong r-values ~0.40), with r=0.56 for TSI_1 and TSI_2, and r=0.6 for TSI_3. All results are statistically significant [Table 6.4].

6.2.2.4 Results: model adjusted for precession and sunspot activity

The normalised, chronologically-anchored model, adjusted for both precession and sunspot activity [Figure 6.10], shows a strong positive correlation compared to the TSI reconstructions from Antarctic ice core data (Bard *et al*., 2007). These adaptations to the model were reflected in an improved X^2 result, better than all previous chronologically-anchored models (Sections 6.3.2.1, 6.3.2.2, 6.3.2.3) with X^2 results of 0.08 for each of TSI_1, TSI_2, TSI_3 [Table 6.5]. For the full range of the model the TSI_1 and TSI_2 scored similarly for correlation, with r=0.84, whilst TSI_3 scored r=0.82. These r values show a strong positive correlation similar to the best results achieved by the Bard reconstruction compared to the dendrochronologically calibrated radiocarbon record (r=0.81) (Section 6.1.1). All three TSI reconstructions showed a strong similarity with the model for the first two sub-periods, with r values between 0.85 and 0.89 (843AD-1481AD) and 0.76 and 0.80 (1481AD-1829AD). For 1829AD-1961AD, the r-values are all moderately strong (0.66 and 0.68), which show large improvements over each of the previous steps. These considerably improved results in the third

sub-period in particular are due to adjustments made for both precession (r=0.38 to 0.40) and sunspot activity (r=0.56 to 0.60). Although all the models are visually very similar, the combined precession and sunspot adjusted model is visually the best match [Figure 6.10]. All results are statistically significant [Table 6.5].

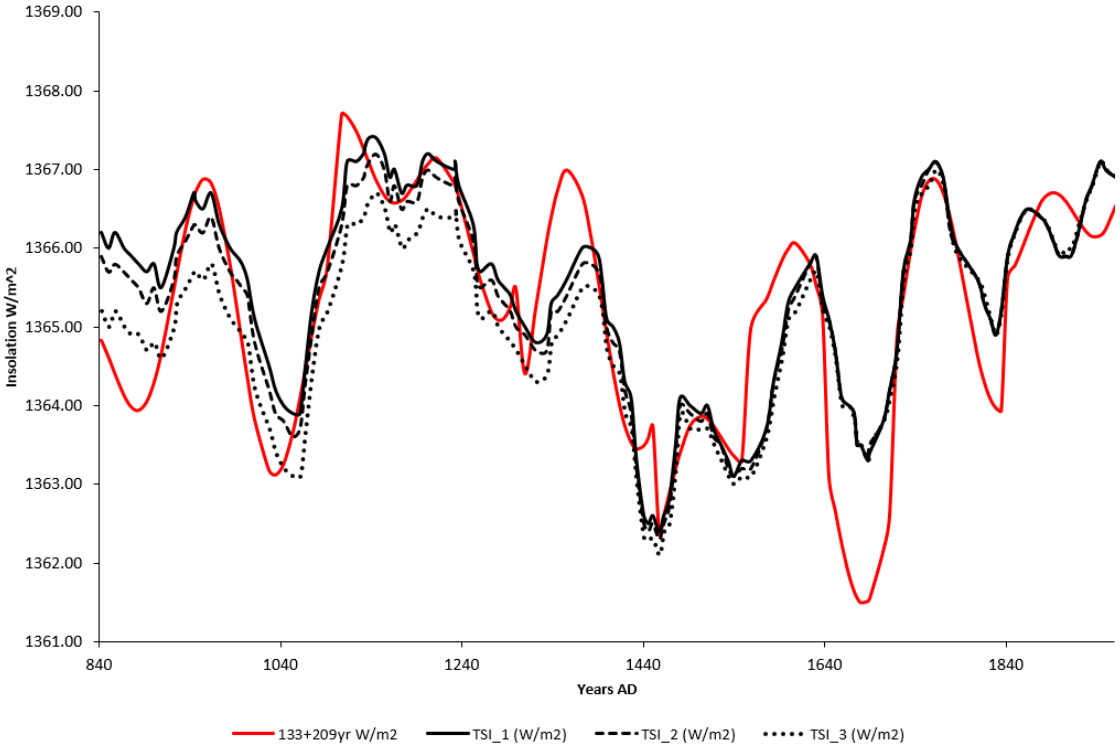

Figure 6.10: The chronologically-anchored, normalised model adjusted for both sunspot minima and maxima and precession compared to TSI reconstruction by Bard *et al.* (2007). Each of the TSI reconstructions is shown as indicated in the legend. The red solid line is the model. A closer match between the model compared to unadjusted and either adjusted model (associated with just sunspot activity or precession) can be seen when compared to Figures 6.6, 6.7, 6.8, and 6.9.

Table 6.5: Statistical results of X^2, r values. variance (r^2), and significance (p) for precession and sunspot-adjusted model.

Stat test/period	TSI_1			TSI_2			TSI_3		
X^2	0.08			0.08			0.08		
Correlation/variance/significance	r	r^2	p	r	r^2	p	r	r^2	p
(entire period)	0.84	0.71	0.00	0.84	0.71	0.00	0.82	0.68	0.00
843AD-1481AD	0.85	0.73	0.00	0.86	0.75	0.01	0.89	0.78	0.00
1481AD-1829AD	0.80	0.63	0.00	0.78	0.61	0.00	0.76	0.58	0.00
1829AD-1961AD	0.66	0.43	0.02	0.66	0.43	0.02	0.68	0.46	0.02

6.2.3 Sensitivity analysis

The TSI at any given time in the year varies due to changes in orbital eccentricity, sunspot cycles, and precession. Reconstruction of TSI values prior to recorded observations are reliant on modelling and proxy data, such as cosmogenic isotopes (Feulner, 2011; Vieira *et al.*, 2012). The early stages of those observations were patchy, with reliable data only extending back ~200 yrs (Eddy, 1976). Consequently, reports on changes in TSI values during the past 300 yrs varies. One study identifies a

difference of 0.2-0.7 W/m^2 at the time of solar minima between the Maunder Minimum and 2008/2009 (Feulner, 2011). Two other studies derive different results, with one suggesting virtually no change, and the other a variation of 5.8 W/m^2 (Shapiro *et al.*, 2011 cited in Feulner, 2011). Calculations of TSI have varied during the past 30 yrs: from 1365.4±1.3 W/m^2 during the 1990s to 1360.8±0.5 W/m^2 during the 2008 solar minimum (Kopp and Lean, 2011).

This picture is complicated by measurements of solar variability, where "rapid solar irradiance variations with larger amplitude are superimposed on the 11-year cycles; decreases on time scales of days to weeks can be as large as 4.6 W m^{-2} (0.34%)" (Kopp and Lean, 2011:1). Time of year must influence the scale of these changes in measurement of TSI, due to the annual variation of TSI associated with orbital eccentricity (cf. Vieira *et al.,* 2012). For example, in late March and early April, and again six months later, the rate of daily change in TSI is at a maximum of 0.81W/m^2 (Tables D.4 to D.6 in Appendix D). Recent irradiance variations were shown to increase on average between solar minima and maxima by 1.6 W/m^2 per month (Kopp and Lean, 2011). "Annually integrated change related to orbital eccentricity variations" were reported to be 1.5 W/m^2, whilst variability due to heliomagnetic activity had a range of 1-8 W/m^2 (Vieira *et al.,* 2012). Recent variations between sunspot minima and maxima were found to be ~1.36 W/m^2 (Vieira *et al.,* 2012). Based on Earth-Sun distances produced by planetarium data and constant solar temperature used in Chapter Five, the maximum variation during the past 5.5 ky was 0.7 W/m^2 [Figure 5.21].

Table 6.6: Statistical results of X^2, r values, variance (r^2), and significance (p) for precession and sunspot-adjusted model using 1 unit of amplitude equal to 0.7 W/m^2.

Stat test/period	TSI_1			TSI_2			TSI_3		
X^2	0.06			0.06			0.06		
Correlation/variance/significance	r	r^2	p	r	r^2	p	r	r^2	p
(entire period)	0.85	0.73	0.00	0.85	0.73	0.00	0.83	0.69	0.00
843AD-1481AD	0.86	0.75	0.00	0.88	0.77	0.00	0.90	0.81	0.00
1481AD-1829AD	0.80	0.64	0.00	0.79	0.62	0.00	0.77	0.60	0.00
1829AD-1961AD	0.68	0.47	0.00	0.68	0.47	0.00	0.71	0.50	0.00

Table 6.7: Statistical results of X^2, r values, variance (r^2), and significance (p) for precession and sunspot-adjusted model using 1 unit of amplitude equal to 0.2 W/m^2.

Stat test/period	TSI_1			TSI_2			TSI_3		
X^2	0.07			0.07			0.07		
Correlation/variance/significance	r	r^2	p	r	r^2	p	r	r^2	p
(entire period)	0.80	0.64	0.00	0.79	0.62	0.00	0.74	0.55	0.00
843AD-1481AD	0.78	0.61	0.00	0.79	0.63	0.00	0.81	0.66	0.00
1481AD-1829AD	0.78	0.61	0.00	0.78	0.60	0.00	0.77	0.59	0.00
1829AD-1961AD	0.71	0.51	0.00	0.71	0.51	0.00	0.73	0.54	0.00

Because the variation in TSI is not constant through time [Figure 5.21], it is difficult to assign a justified value to the amplitude of the model during the normalisation process (Section 6.1.2). In the normalisation of the model, assumptions were made about the amplitude of the model, where 1 unit of amplitude was equal to 1 W/m^2. The sensitivity of the model to assumptions of amplitude (W/m^2) was tested, where amplitude was re-scaled to 0.7 W/m^2 [Figure 6.11], and 0.2 W/m^2 [Figure 6.12] for the final model (precession and sunspot adjusted) (Section 6.2.2.4). In both instances, the X^2 statistic was virtually unchanged and still significantly smaller than the critical X^2 value, indicating retention of the null hypothesis of no difference between expected and observed values [Tables 6.6 and 6.7]. All results are statistically significant at p=0. Regardless, the alternative variations for the scaling of the amplitude (0.7 W/m^2, 0.2W/m^2) produced strong overall correlations for each of the TSI models comparable to the original model of 1 W/m^2 and very similar X^2 results [Tables 6.6 and 6.7]. Regardless of amplitude, the model (at each stage of its development) bears a strong visual resemblance to the TSI reconstructions based on Antarctic ^{10}Be, and the X^2 and regression analysis serve to statistically quantify this relationship. Whilst correlation does not equal causation, this condition is necessary if a cause and effect relationship does exist (Urdan, 2010).

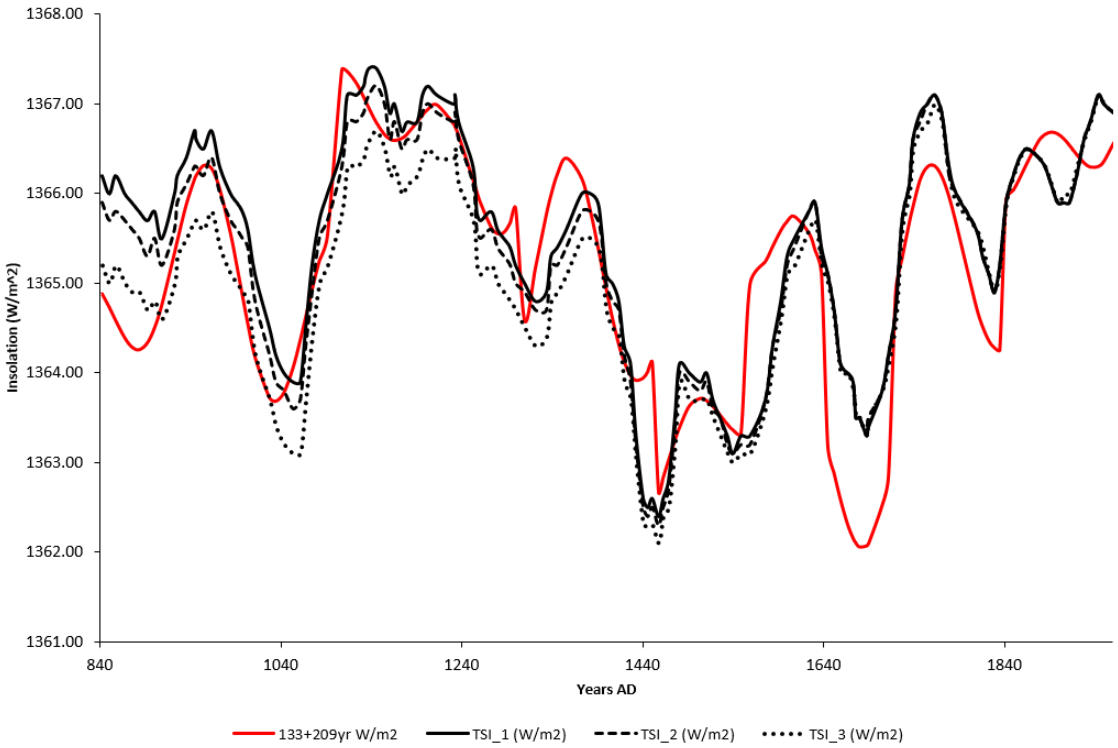

Figure 6.11: The combined sunspot and precession (based on 1 unit of amplitude equals 0.7 W/m^2) compared to TSI reconstruction from Bard *et al.* (2007). These results are visually similar to those used in the original model (1 unit of amplitude equals 1 W/m^2).

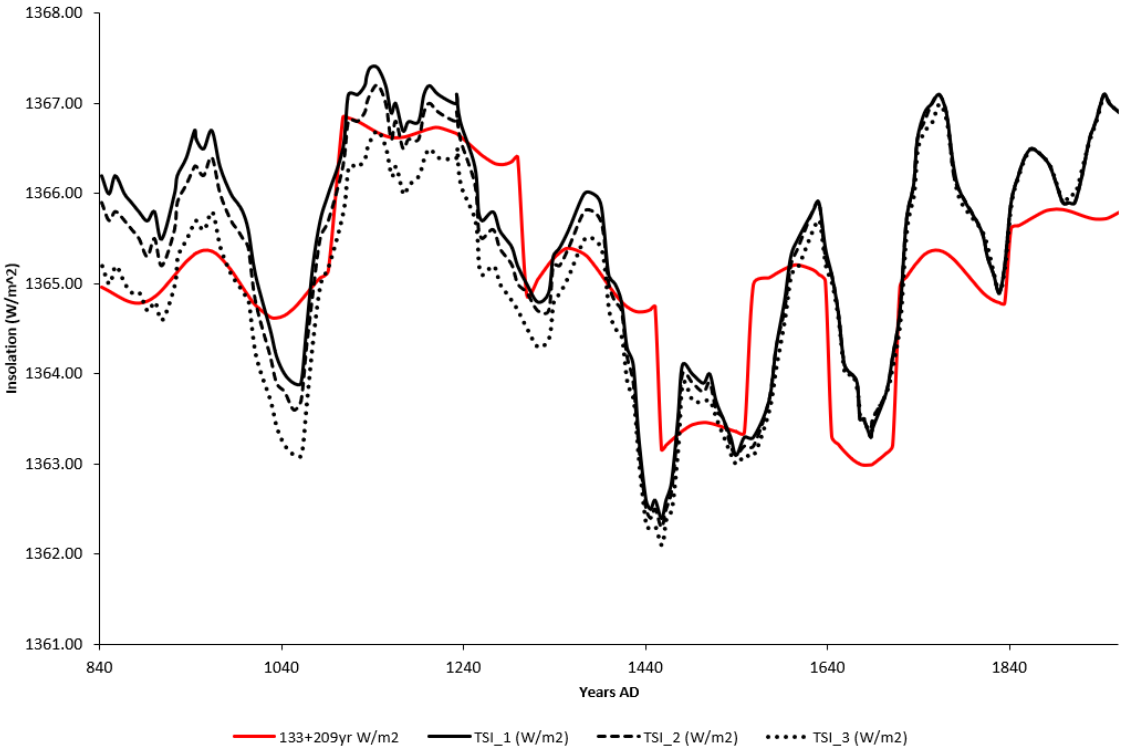

Figure 6.12: The combined sunspot and precession (based on 1 unit of amplitude equals 0.2 W/m^2) compared to TSI reconstruction from Bard et al. (2007). These results are visually dissimilar to those used in the original model (1 unit of amplitude equals 1 W/m^2) and the TSI reconstructions from Bard et al. (2007).

6.3 Chapter summary

The 209-yr and 133-yr periodicities were previously identified as important astronomical cycles in Chapters Four and Five. Their trigonometrically-modelled superposition, through the addition of their sine curves, was found to replicate the controversial ~1470-yr climate signal. The periodicity of this model was 1463 Julian years; when adjusted for precession, the length of the periodicity was ~1474 yrs. This model was chronologically anchored at an important starting point when the Metonic lunation was precisely conjunct the December solstice, which can be seen in Figure 4.9 at 1183BC. The model was then statistically tested against the TSI reconstructions of Bard *et al*., (2007), whose data is used in Intcal calibrations of the radiocarbon curve. This TSI data is based on the smoothed ^{10}Be record derived from Antarctic ice-core data.

These statistical tests X^2 showed that the astronomical model of the interacting 209-yr and 133-yr periodicities could not be dismissed as the cause of the TSI flux in the Bard reconstructions. The regression analysis also showed that all the chronologically-anchored models had a strong positive correlation with the TSI flux models from Bard *et al.* (2007). All models (overall and subperiods) were statistically significant at p=0 except for the third subperiod, which was not statistically significant for the unadjusted model where it showed no correlation. The strongest correlation was with the precession and sunspot adjusted model, with r=0.84 for TSI_1 and TSI_2, and r=0.82 and

p=0 [Table 6.5]. For TSI_1 and TSI_2, r^2=0.71, meaning that the modelled activity accounts for 71% of the variance. The weakest period is the third sub-period (1829AD-1961AD) during times of relatively high sunspot activity (cf. Gray *et al.,* 2010; Kopp and Lean, 2011), but still shows a moderately strong correlation (r=0.66) where none existed in the unadjusted and sunspot models. Adjustments for precession and modern sunspot activity saw substantial improvements in correlation and statistical significance (r=0.66 to r=0.68, p=0.02). In tests for sensitivity, results were very similar. Similar strong correlations were found for alternative adjustments of amplitude to 0.7 W/m^2 and 0.2 W/m^2. In comparison to the model amplitude of 1W/m^2 model, for an amplitude of 0.7 W/m^2 slightly improved statistically-significant (p=0) correlations were obtained for the sunspot and precession adjusted model at r=0.85 for TSI_1 and TSI_2, and r=0.83 for TSI_3.

Chapter 7 – Discussion

This PhD research was driven by questions about millennial-scale climate signals at the sub-Milankovitch scale. Research was primarily focused on a potential astronomical cause of the ~1500-yr quasi-periodicity, which was expressed as a 1490-yr, quasi-periodic signal in the Pacific (Turney *et al.* (2004), and as a mean ~1470-yr signal in Bond IRD data from North Atlantic deep-sea cores (Bond *et al.,* 1997). Both these signals were cross-correlated with Dansgaard-Oeschger signals of oxygen isotopes in the orbitally-tuned GISP2 ice-core. Signals of ~1500 yrs are found across the globe, with one debate focused on whether this climate signal was caused in the North Atlantic or tropical Pacific (e.g., Broecker, 2003; Summerhayes, 2015). Another debate (e.g., Ditlevsen *et al*., 2007) questioned the existence of the ~1500-yr quasi-periodicity and proposed it was little more than stochastic resonance of Earth's internal climate system. Wolff *et al.* (2010) consider this matter unresolved.

Similarities between the length of the ~1500-yr, quasi-periodic climate signal and the Sothic cycle (associated with ancient Egyptian chronometric issues), inspired the proposition that perhaps this climate signal was caused by precession due to the gravitational influence of the Sun and Moon on the Earth. Both the Sun and Moon cause the precession of the equinoxes, which results in the retrograde movement of the equinox along the ecliptic. Throughout history, this problem with equinoctial precession and the imprecise measurement of the tropical year caused disassociation between the Julian calendar and the astronomical system on which it was based (Section 3.2). The Gregorian calendar minimised these problems, but still requires adjustment every ~3.3 ky [Table 7.1]. This table shows the relationships between different cycles, and the Gregorian tropical separation shows the need for adjustment after ~3.3 ky.

Table 7.1: Cyclical relationships between different year types, based on minutes and degrees longitude per annum, and degrees per year. The complete cycle is shown in the final column.

Year type relationship	Minutes p.a.	Deg. long. p.a.	Geographical return (yrs)	Cycle per 360° (yrs)
Anomalistic-tropical	0.42	6.28	57.35	20,645.87
Sidereal-tropical	0.34	5.10	70.62	25,422.04
Julian-tropical	0.19	2.81	128.19	46,148.52
Julian-sidereal	0.15	2.29	157.23	56,603.42
Julian-anomalistic	0.23	3.47	103.78	37,359.90
Anomalistic-sidereal	0.08	1.18	305.25	109,891.45
Gregorian-tropical	0.01	0.11	3,323.36	1,196,410.77
Gregorian-sidereal	0.33	4.99	72.15	25,973.95
Gregorian-anomalistic	0.41	6.17	58.36	21,008.40

The apsides also precess in the opposite direction to the equinoctial precession. The interaction of these two precessions produce the Milankovitch precessional cycle of ~21 ky years (see Table 7.1, which shows the complete cyclical interaction between the tropical and anomalistic years as ~21 ky). Each of the equinoctial and apsidal precessional cycles produces its own contribution to insolation patterns. Figure 7.1 shows the current annual TOA solar irradiance pattern associated with Earth-Sun distances, whilst Figure 7.2 shows daily insolation patterns due to seasonal change, which is dependent upon input from solar irradiance. Additionally, fluctuations in eccentricity vary the TOA solar irradiance levels as shown in Figure 7.1. Consequently, the daily insolation patterns change diachronically. Gravitational force also varies through time based on Earth-Sun and Earth Moon distances.

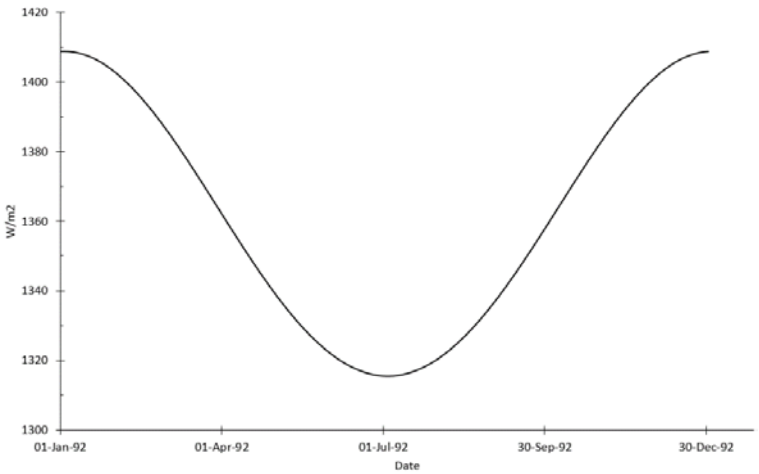

Figure 7.1: Annual fluctuations in TOA irradiance at the current eccentricity. Maximum TOA solar irradiance is reached in January and minimum in July.

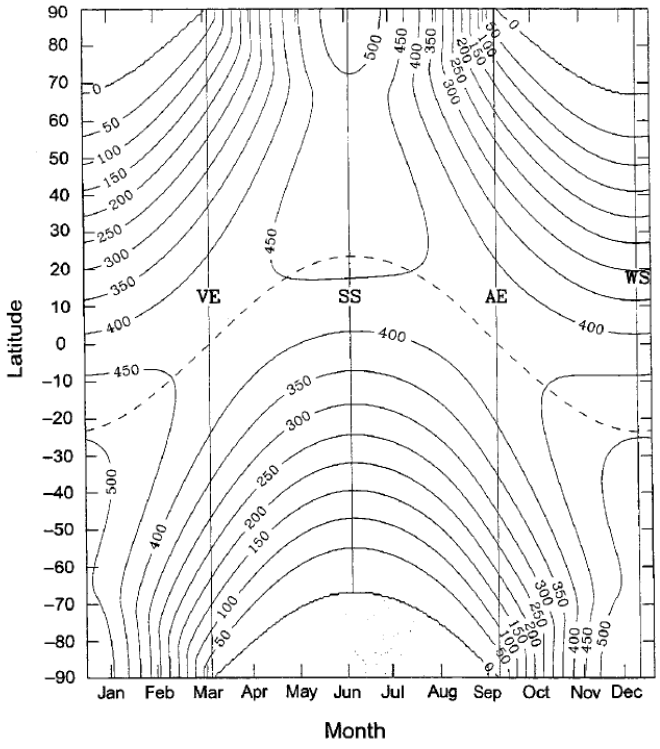

Figure 7.2: Daily solar insolation as a function of latitude and day of year (Liou, 2002:52). These values were calculated on solar constant of 1366 W/m^2 and results are measured in W/m^2. Solid vertical lines mark the March equinox (VE), June solstice (SS), September equinox (AE), and December solstice (WS). The dashed line is solar declination.

In light of the astronomical data, and modelling and statistical results presented over the last three chapters, this chapter takes a new look at the influence of gravitation on insolation and solar irradiance patterns during the last 5.5 ky. The capacity for the Sun-Earth-Moon interaction to cause the ~1500-yr cycle of abrupt climate change is assessed. Connections to established climate cycles are also discussed, as are the mechanisms connecting astrophysical forcing to the various climate cycles associated with the ~1500-yr quasi-periodicity. The evidence here suggests that the ~1500-yr quasi-periodicity associated with millennial-scale ENSO activity in the Pacific and Bond IRD events in the North Atlantic is a real cycle that is neither due to stochastic resonance in Earth's internal climate system (contra Ditlevsen *et al.,* 2005, 2007, 2009) or mathematical averaging (Obrochta *et al.,* 2012). Rather, the results presented here show that this quasi-periodicity is primarily produced from the combination of two main cycles in which lunar influence is strong: 133-yrs and 209-yrs. The 133-yr periodicity is found in the solar declination cycle, and cyclical variations in Earth-Sun and Earth-Moon distances. The 209-yr cycle is the SdV cycle that was first identified in the radiocarbon record (Suess, 1986). Both these cycles are dependent upon the Metonic lunation (Sections 7.2.2 and 7.2.3). These results also show that the ~1500-yr quasi-periodicity is a high-frequency expression of the Milankovitch precessional cycle.

7.1 Gravitation's influential role in climate change

The Sun and Moon imprint their respective stamps on Earth's climate and palaeoclimatic records (Chapter 3). The Sun as the main source of heat and energy in our solar system is the most obvious contributor to Earth's climate. The effects of solar power are felt through Earth-Sun distance, gravitation, solar irradiance, solar flares, sunspot variability, and the solar wind. It is the major driver of Earth's climate and source of heat, and its strength is most strongly felt at perihelion and is weakest at aphelion. The strength of the solar wind, which is associated with sunspot activity, changes the patterning of cosmogenic isotopes in Earth's palaeoclimatic record.

The lunar influence is subtler. The Moon leaves its gravitational imprint on the Earth, having a steadying influence on the Earth by maintaining Earth's axial tilt and seasons (Chapter 3). It acts as a brake to Earth's rotation, without which Earth would be a wind-ravaged planet (Comins and Kaufmann, 2008). Together, the stability of Earth's orbit, rotation, axial tilt, and celestial neighbourhood have allowed the development of life (Chapter 3). The Moon's gravitational influence also determines the timing of the perihelion, and has a greater tidal influence than the Sun on Earth's oceanic tides due to its proximity to Earth. The Moon also contributes two-thirds of the gravitational effect that causes the precessional cycle. By virtue of this contribution to equinoctial precession, which forms part of the Milankovitch precessional cycle, the Moon also influences insolation patterns

through time. The Moon also impacts insolation patterns in other ways such as through obliquity and changes in the length of day associated with seasonal variations.

Just as the individual influences of the Sun and Moon have imprinted on Earth's palaeoclimatic record and climate, their combined forces have maximised their peak influences, such as occur at New and Full Moon, and especially at eclipses and the annual spring tide where gravitational force is maximised (Chapter 3). Bond *et al.* (1997) attributed the ~1500-yr quasi-periodicity potentially to some combination of orbital periodicities and changes in solar output that influenced Earth's coupled ocean-atmosphere system. Given the Moon's role in the patterning of insolation at Milankovitch scales, the potential of the Moon to fulfil such a role in a combination of periodicities at millennial-scale should not be surprising (Section 5.3). On evidence presented here, the Moon is a key player in the SdV cycle and 133-yr cycles (Sections 7.2.2 and 7.2.3). These two cycles interact to shape TOA solar irradiance patterns at the scale of the Bond 'cycle' (Chapter 6 and Section 7.2.5). Additionally, the Moon's gravitational influence and interaction with the perihelion also produce millennial-scale patterns in this range that can account for the occurrence of the Bond 'cycle', which is a climate 'pulse' that underlies Heinrich and Dansgaard-Oeschger events (Section 7.2.5).

Lunar influence was featured in the previous research of Keeling and Whorf (2000) as the potential cause of the 1-2 ky climate signals, but they failed to replicate the ~1500-yr quasi-periodicity (Section 2.2.2.3). Their problems in doing so were attributable to (i) the use of the Saros cycle of eclipses over the Metonic lunation because it was incommensurate with the tropical year, and (ii) overcomplicating the research with the inclusion of the Full Moon. However, criticisms of the Keeling and Whorf model by Munk *et al.* (2002), on the basis of greatest perigean tides occurring currently at the equinoxes, seems to have been misplaced. Perigean-perihelion interaction produces cyclical patterns in astronomical and climate data at sub-Milankovitch scales (Sections 5.3.2 and 5.3.3), and does feature in Bond IRD events (Section 7.2.5). These perigee-perihelion patterns occur as part of a previously unreported Metonic eclipse series (Section 4.4.1). Data and models need to be at the right resolution to be able to see it, and the selection of variables is crucial.

Earth's geography influences how these effects play out through time, because the characteristics of the Earth are not static. Whilst the oceans provide the major storage of Earth's heat and act as the major transporter of heat around the globe (Summerhayes, 2015), the oceans are mutable. Earth's oceans are strongly influenced by the gravitational influence of both the Sun and Moon, creating Earth's tides (Chapter 3). The Moon is particularly influential in this regard because of its proximity to Earth, and its influence on the extremes of tides (both number and size) caused by axial tilt. The strongest of these tides occur respectively at New Moon and Full Moon. The ocean's distribution of heat is influenced by land mass, which continually changes due to plate tectonics (Summerhayes,

2015). Similarly, atmospheric transport of heat and moisture is influenced by solar and lunar tides (Chapter 3; see also Berger *et al.,* 1989b; Davis and Brewer, 2011; Imbrie, 1985; Kohyama and Wallace, 2016), as well as land form.

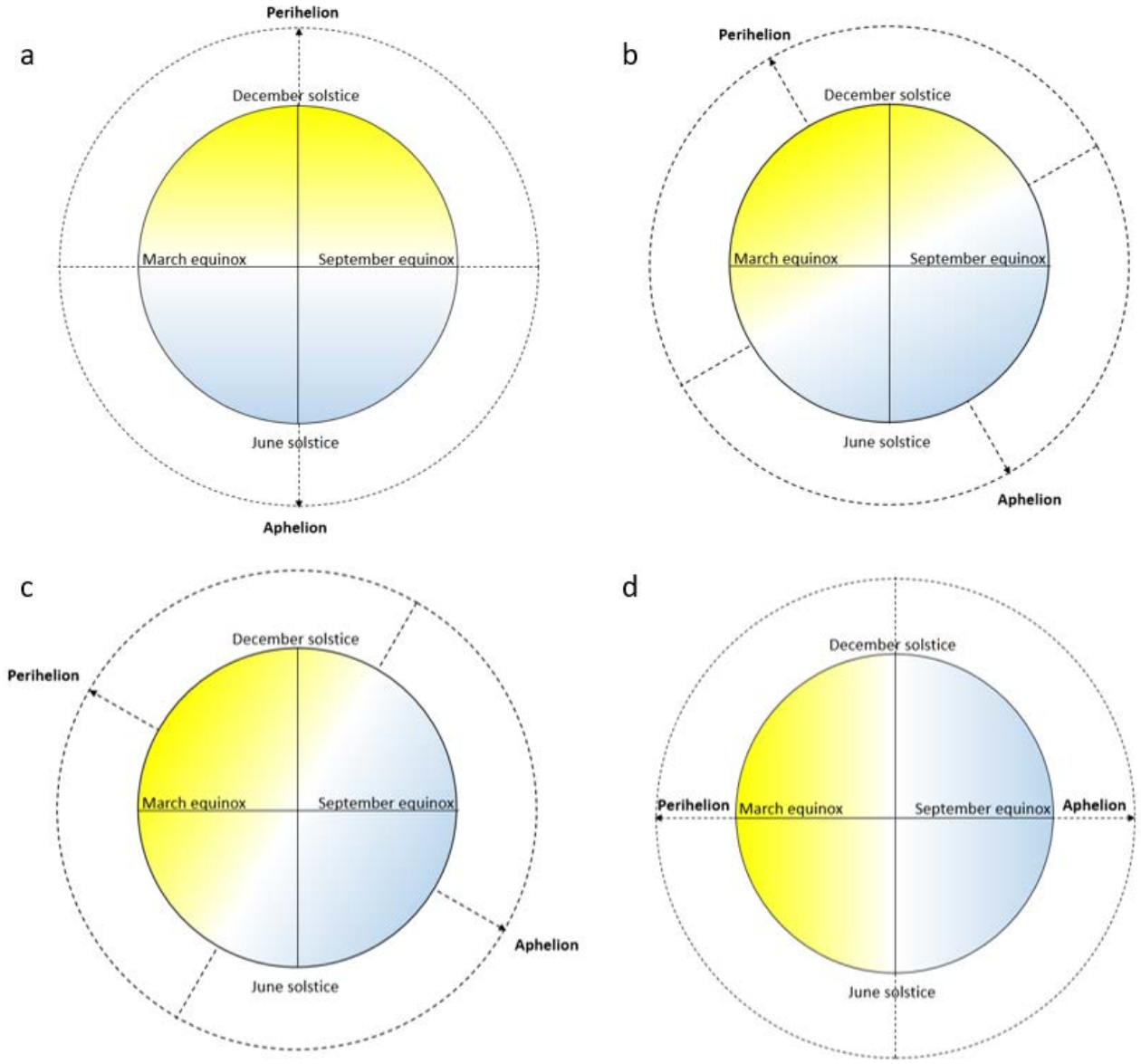

Figure 7.3: Annual solar insolation varies with respect to the seasons as a result of the Milankovitch precessional cycle. Yellow and blue are respectively maximum and minimum annual insolation at Earth's orbit. The panels cover a quarter of the Milankovitch cycle from (a) the position of the perihelion at December solstice around 1308AD through to (d) in ~4.5ky time when the perihelion reaches the March equinox.

The orientation of Earth's axial tilt to the Sun is responsible for the seasons (Chapter 3). However, the relationship of the seasons and Earth's orbit alters through time. This factor causes the Earth's axial tilt to change relative to its position in Earth's orbit. For example, ~700 yrs ago the Earth's south celestial pole was tilted towards the Sun at perihelion, resulting in extra heat input into the Earth's southern hemisphere at the time of the December solstice [Figure 7.3]. However, at ~4.5 ky into the

future, Earth's axis will sit at 90° to that position as the March Equinox will be oriented to the perihelion, resulting in maximum annual heat being directly overhead as the Sun "crosses" the Equator. As pointed out by Hou and Lindzen (2002), heat concentrated on the Equator results in up to a fivefold increase in the intensity of the Hadley circulation. There is also increased intensity of the Hadley circulation where heat is primarily derived from the winter side of the Equator (i.e., when perihelion is either at the June solstice for the southern hemisphere, or December solstice for the northern hemisphere). Ashkenazy *et al.* (2010) showed that the equatorial season behaves differently for modelled behaviour of the timing of the perihelion at the March and September equinoxes. They used a fully coupled oceanic-atmospheric GCM to show that equatorial seasonality is altered by the Milankovitch precessional cycle. Gray *et al.* (2010) reported a number of studies that show changed strength of both the Hadley cells and Walker Circulation at sunspot maxima: both of these are important to the operation of ENSO activity.

The implications of the Hou and Lindzen (2002) work were that small changes in heating distribution produced profound changes in the intensity of the Hadley circulation, as well as in extratropical atmospheric temperature and air pressure. These changes had significant implications for global climate change via the modulation of atmospheric wave transport, as the Hadley circulation is a major convective unit that transfers heat away from the tropics. Both the Hadley and Walker circulations are associated with ENSO's ability to influence global climate via its dynamic ocean-atmosphere activity (see Section 2.2.2.2). In their idealised model, Clement *et al.* (2001) determined that, with the March equinox/perihelion conjunction, increased SSTs occurred in April and October. This event was associated with a strengthening of the equatorial Pacific's seasonal cycle, which is in keeping with Hou and Lindzen (2002). Hou and Lindzen (2002) also found that where the heat is primarily drawn from the winter hemisphere (such as might occur at a winter solstice/perihelion conjunction), an intensification of the Hadley circulation also occurs. Clement *et al.'s* (2001) model showed shutdown of ENSO was expected when the perihelion is at either of the solstices (Clement *et al.,* 2001).

As a consequence of precession, the concentration of maximum annual heat relative to the seasons and equator shifts [Figure 7.3], thereby affecting precipitation and its transport to latitudinal extremes, where it is deposited as snow and contributes to ice formation. As precession brought the perihelion and September equinox into contact ~7.5 kya, sedimentary evidence from Laguna Pallcacocha, Ecuador showed ENSO frequency increased in pulses, reaching a peak ~1.2 ky calBP (Moy *et al.,* 2002) when the Metonic lunation, perihelion, and December solstice conjunction converged [Figures 5.3 and 5.4]. Since that time ENSO frequency has declined towards the modern day (Moy *et al.,*

2002). Through shifting heat patterns associated with precession, it is possible to understand how variations in ENSO intensity at millennial and Milankovitch precessional scales occur.

Marchitto *et al.* (2010) shows millennial-scale patterns of SST that are correlated to TSI reconstructions based on cosmogenic nuclides such as ^{10}Be. In this study, warm El Niño conditions were associated with inferred solar minima. Moy *et al.*'s (2002) data shows this quasi-periodicity, as does Turney *et al.*'s (2004) humification analysis of a peat record from Lynch's Crater in northern Queensland (Section 2.2.2.2). Turney and colleagues linked the 1490-yr cycle in the Pacific to the Dansgaard-Oeschger cycle in the GISP2 ice-core, where millennial-scale events of dryness at Lynch's Crater were correlated with warm phases of the Dansgaard-Oeschger cycle. The Dansgaard-Oeschger cycle in the GISP2 record was also linked to the Bond cycle through cross-correlation (of ice and deep-sea cores). The teleconnections between the extremes of millennial-scale forcing share common links associated with semi-precessional forcing (~11-ky intervals between the perihelion conjunctions with the June and December solstices). Turney *et al.* (2004) see the 1490-yr climatic signal in the Pacific as an amplification of the Milankovitch precessional cycle.

7.1.1 Earth-Sun distance

Results from Chapter Five show Earth-Sun distances decreasing over time as the Metonic lunation series (associated with the tropical year) moves towards a precise conjunction with the perihelion in modern times (cf. Section 5.2). Increased levels in gravitation due to these decreasing distances are also shown, plateauing since the end of the Maunder Minimum and beginning of the Industrial Revolution (Section 5.3). Disruptions in the natural continuity of Earth's radiocarbon have occurred as the result of burning fossil fuels since the Industrial Revolution, diluting it (Libby, 1960). Additionally, atomic bomb explosions in the 20th century reversed this trend (Libby, 1960). What has not been considered are contributions due to solar irradiance fluctuations through time associated with Milankovitch precessional influences, such as are represented by the changing relationship between the perihelion and Metonic lunation (Chapter 5). This precessional influence sees changing Earth-Sun distances with respect to the seasons.

During the term of these data, TOA solar irradiance levels have changed from ~1375 W/m^2 at the Metonic lunation to 1407 W/m^2. These issues are relevant to studies measuring TSI variance over long periods of time, which use a solar constant as a baseline measurement (e.g., Feulner, 2011). Between the Industrial Revolution and 2011, data presented here shows that TOA increased by 0.17 W/m^2 due to this precessional influence [Figure 5.19]. By comparison, differences of 0.2-0.7 W/m^2 in total solar irradiance during the Maunder Minimum and the 2008/2009 year solar minimum have been calculated (Feulner, 2011). Feulner (2011) points out that a number of studies place this difference at a much lower value. Given that reconstruction of total solar irradiance is reliant upon

proxies such as cosmogenic isotopes (i.e., ^{10}Be), it would be necessary to take precessional fluctuations in solar irradiance into account.

The reduction in Earth-Sun distance and corresponding increases in gravitation and TOA solar irradiance during the term of the data generally moves in a step-like manner, with each step of ~133yrs length [Figures 5.5 to 5.9 and 5.18 to 5.20]. This 133-yr periodicity is also seen in solar declination cycles (Section 4.4.2), usually consisting of 57-yr and 76-yr components. These step-like patterns are flattened during the Roman Warm Period (RWP), MWP, and during modern warming [Figures 5.5 to 5.9 and 5.18 to 5.20]. The plateauing of the gravitational curve, bottoming-out of distances, and associated suppression of this step-like movement is associated with the movement towards the perihelion-Metonic lunation conjunction in modern times [Figure 5.2]. Here, peaks in gravitational forcing are evident at 1878AD, 1893AD, 1973AD, 2011AD [Figure 5.19].

The flattening of the 133-yr step-wise sequence in astronomical data during the MWP occurred coincident with the perihelion/December solstice conjunction, which is a once in an ~21-ky event associated with peak insolation. It would be expected that a bottoming out in minimum distance and associated plateau in maximum gravitational force and TOA solar irradiance would result at the perihelion-solstice conjunction, where suppression in variability is exercised in two directions. At the solstice, the apparent latitudinal movement of the Sun is restricted (having reached maximum declination) [Figure 7.1]. At perihelion, Earth is at minimum distance to the Sun [Figure 5.5]. The gravitational influence on the lunar orbital plane would also be influential, as it straightens a little each synodic month as it "faces the Sun" (Gutzwiller, 1998:602). As the lunar orbital plane moves into alignment with the December solstice-perihelion conjunction, it would emphasise this suppression.

Likewise, as the perihelion-Metonic lunation conjuction is reached in the modern era [Figure 5.2], a similar pattern could be expected as depicted in Figure 5.18. There is no obvious cause for the suppressed variability in Earth-Sun distances, gravitation, and insolation patterns during the RWP. However, the start of the RWP pattern occurred when the perihelion was removed one lunar month from its impending conjunction with the December solstice, which may be indicative that it is due to a harmonic relationship between the Metonic lunation series and the perihelion. Additionally, during the RWP, the lunar declination pattern is one full cycle removed (~900 yrs) from those that occur during the MWP [Figure 4.7], emphasising this relationship through the Metonic eclipse series.

7.1.2 Earth-Moon distance

Earth-Moon distances and the resultant gravitational forces showed numerous associations with climatic data (see Sections 5.3.2, 7.2, 7.3, and 7.4). Earth-Moon distances periodically influenced

Earth-Sun distances at ~133-yr intervals at the time of the Metonic lunations [Figure 5.11], when reduced Earth-Moon distances occurred close to a modelled perigee-perihelion return at 125 yrs [Figure 5.15]. The 133-yr cycle (Section 7.2.2) is a time of relative perigee at the New Moon that is coincident with reduced Earth-Sun distances. Gravitational variation due to this influence was ~15% during the range of the data. The similarities in various cyclical patterns in Earth-Moon data appear as spectral peaks in climatic data [Figures 2.15 and 2.16], equivalences in marine reservoir values used in radiocarbon dating (cf. Hua *et al.,* 2015), the timing and variability of Bond IRD events (Section 7.2.5), and equivalences to millennial-scale periods of ENSO events (Section 7.2.5).

Table 7.2: Bond cycle lengths (Bond *et al*., 1999:43).

	Time interval in cal. kyrs	Mean Pacing ±1σ in yrs
Holocene	1.5-12ka	1374±502
Late Glacial	12-32ka	1537±558
Early Glacial	32-75ka	1478±458
~12ky step	13-24ka	1494±624
~12ky step	22-34ka	1631±511
~12ky step	31-43ka	1328±539
~12ky step	43-55ka	1350±302
~12ky step	53-64ka	1443±470
~12ky step	64-79ka	1795±425
Holocene + Glacial	0-79ka	1469±514
Glacial	15-65ka	1476±585

Significantly, the occurrence of Bond events during the period of research, corresponded with times of maximum gravitational forcing at perigee and close to perihelion [Figure 5.13]. These are times of south nodal solar eclipses. Of particular interest are the 1375-yr, 1482-yr, and 1490-yr means of maximum gravitational variance (that occurs at lunar apogee) and a recurring ~1160-yr period (at perigee) in the lunar data [Figure 5.14]. The mean length of the Bond cycle during the Holocene is 1374 yrs, being the same as the 1375-yr mean in Earth-Moon data. Table 7.2 shows the variable lengths of the Bond 'cycle'. The ~1490-yr period was measured in Turney *et al.*'s (2004) peat humification data and is associated with inferred millennial-scale periods of dryness at Lynch's crater. These periods of dryness were found to be correlated with warm Dansgaard-Oeschger events in the GISP2 Greenland ice core. The 1482-yr period corresponds with the Metonic-sunspot return close to an RRA return (indicating peak forcing in gravitation and insolation associated with the perihelion) (Sections 4.4.2 and 4.4.3). This period is close to the mean for the Bond cycle during the Glacial (Section 5.2.3), as well as to ENSO length in the Pacific (Section 2.2.2.2). This 1482-yr period is also

of the same length as the Bond 'cycle' during the Eemian interglacial (MIS 5e), when the mean interval of the cycles occurred at 1480 yrs (Bond *et al.,* 2001).

7.2 Cyclical patterns

7.2.1 A 57-yr cycle

A statistically-significant 57-yr spectral peak appears in radioisotopic data [Figure 2.15] (Stuiver and Braziunas, 1989), whilst a non-stationary 57-yr pattern is found in various climatic data, including: precipitation, SST, sea level peaks, and geomagnetic cycles data (Chambers *et al.,* 2012; Edvardsson *et al.,* 2011; Morner, 2013; Stuiver and Quay, 1980), the length of day (Mazarella, 2008), North Atlantic Oscillation (Mazarella and Scarfetta, 2012), and global air temperature (Mazarella, 2008). Keele (1910) specifically linked a 57-yr precipitation cycle in Australia, Britain and Egypt to southern lunar declinations (Keele, 1910). Additionally, charting of longitudinal movement of the 57-yr cycle [Figure 4.13] shows its non-stationary nature, where it migrates ~70^0 of longitude eastward every 57 yrs and completes a cycle (within 1.5° of precision) at 285-yr intervals.

The 57-yr pattern features in both trigonometric models from Chapter Four. In the first trigonometric model of interacting variables (sunspot, Metonic lunation, and RRA), the sunspot and Metonic cycles interact at 57-yr periods. Variations in the sunspot cycle have been linked to changes in strength of Hadley cells and the Walker circulation in the Pacific (Gray *et al.,* 2010; Marchitto *et al.,* 2010). At 57-yrs, the relationship with the Metonic lunation aligns these solar cycle variations with the tropical year. The sunspot and Metonic cycles also share a numerical relationship at 3.8 yrs and 1482 yrs, both of which are associated with ENSO variability. The 1482-yr period is discussed below (Section 7.2.5) and the 3.8-yr period is found in NINO3.4 data and is the mean length of time between El Niño events (van Buren, 2001).

The second trigonometric model (RRA-RRT separation) also shows a 57-yr pattern, which is essentially a half cycle [Figures 4.22 and 4.23]. RRA and RRT variables are respectively based on the anomalistic and tropical years at the centurial-scale. Additionally, calculations based on NASA (2011) data alone show that the precessional separation rate between the tropical and anomalistic years is one day in 57 yrs [Table 7.1]. From Table 7.1 it can be seen that the 57.35-yr separation rate for the anomalistic and tropical years forms a complete cycle at the mean length of the Milankovitch precessional cycle. The 57-yr cycle therefore links sunspot activity and Metonic lunation relative to the perihelion and precession. This value also appears as a peak in radiocarbon spectral data [Figure 2.16]. Similarly, the separation rate between the Julian and tropical years is known to be one day in 128.19 yrs (Section 3.2.1), and this value can be seen in Table 7.1. The apsidal precessional cycle length is shown as ~110 ky from this table (measured relative to the sidereal year). The Gregorian sidereal year precessional cycle is ~26-ky long, whilst measured relative to the sidereal framework is

~25.6-ky long. These various models show interconnectivity between the short- and long- term astronomical cycles with associated climatic variations, and also emphasises the importance of the 57-yr cycle. From these relationships, it can be seen that as precession separates the solstice and perihelion, associated harmonics are introduced into the solar irradiance signal (Chapter 6).

7.2.2 A 133-yr cycle

The 57-yr cycle also forms a component in the 133-yr solar declination cycle (Section 4.4.1) found in accompanying astronomical data. This 133-yr cycle was also found in Earth-Sun and Earth-Moon distances, and dependent, gravitational, TOA solar irradiance, and insolation data (Chapter 5). The Earth-Sun distance data, and dependent solar irradiance and gravitation data also showed a 57yr component of the 133-yr cycle, which generally moved in a step-like motion of decreasing Earth-Sun distances and increasing solar irradiance and gravitational force. There were variations in these step-like patterns that were suppressed during the RWP and MWP, and at the start of the Industrial Revolution as a plateau was reached [Figures 5.8, 5.9, 5.18 and 5.19].

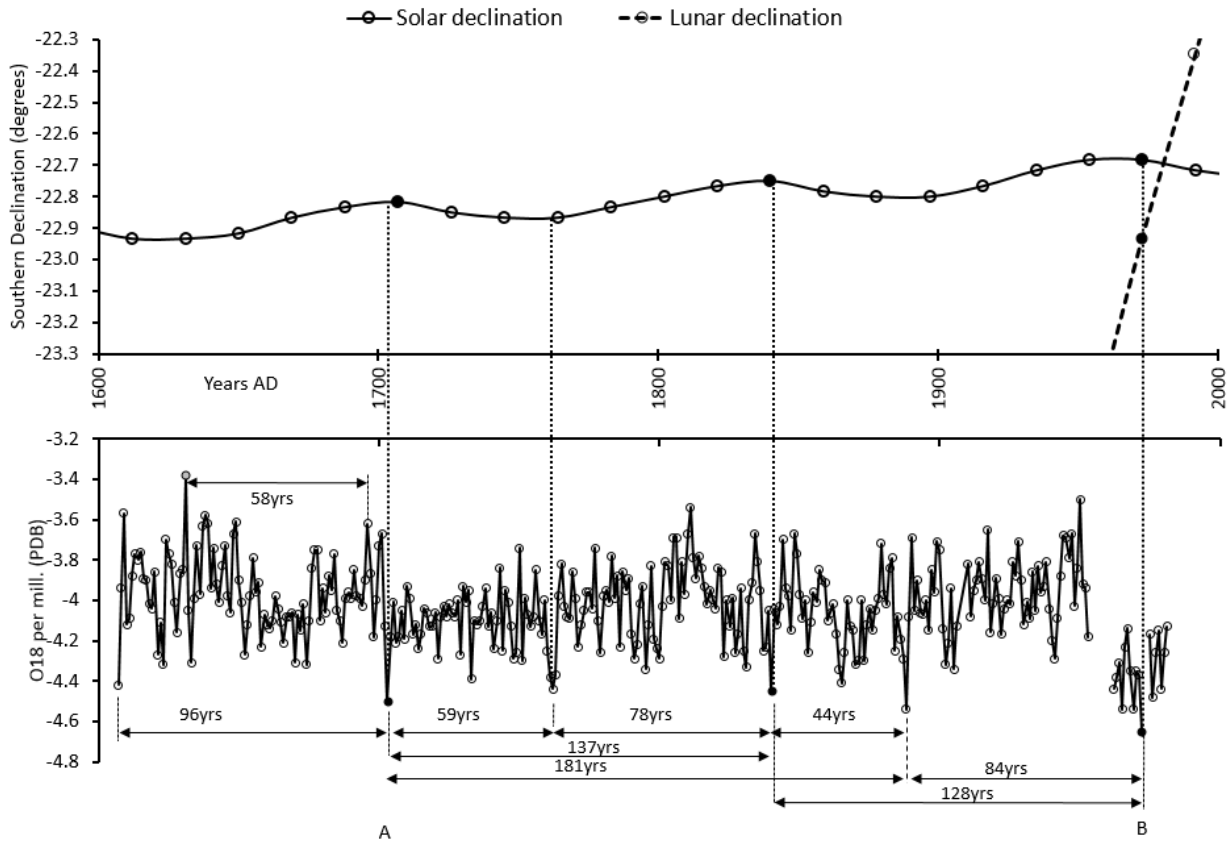

Figure 7.4: Correspondences between solar declination cycle (upper panel) and Galapagos Coral (O-18) data from Dunbar *et al.*, 1994 (lower panel).

However, the solar declination data [Figures 4.5 to 4.10, Appendix B] were suppressed during the 2nd millennium BC and the approach to and departure from this ~1000-ky period were respectively marked by consistently decreasing and increasing amplitudes of generally 133-yr duration [Figure

4.16]. The internal structure of this 133-yr solar declination cycle was more sinusoidal than step-like as in the Earth-Sun distance and associated data, and generally consisted of 76-yr periods of solar northward declination shifts and 57-yr southward declination shifts during the last 2 ky [Figure 4.8] that may be related to the 57-yr precipitation patterns investigated by Keele (1910). This patterning was reversed on the approach to the suppressed solar declination activity [Figure 4.16]. Occasionally, these declination cycles were only 114-yrs in length (twice the 57-yr cycle). Occasionally, the internal structure of these 133-yr periods consisted of 95-yr and 38-yr components. Strengthening an association between the solar declination cycle and climatic influences is a comparison of the 133-yr solar declination cycle with Galapagos oxygen isotope data (Dunbar *et al*., 1994), which shows correspondences between the two [Figure 7.4]. Here, northern-most solar declinations are associated with negative extremes of ^{18}O. Oxygen isotope data is an indicator of ice-volume and SST (Section 2.2.1).

Solar declinations are used in the calculation of the solar zenith angle. Consequently, solar insolation patterns, which are based on the solar zenith angle, also show this 133-yr periodicity [Figures 5.25 to 5.28]. Just as the solar declination pattern is suppressed during the 2nd millennium BC, so too are variations in latitudinally-based insolation graphs (with the exception of the Tropic of Capricorn, where the solar zenith angle is close to zero) [Figure 5.24]. Latitudes with larger solar zenith angles had larger insolation swings and the largest variations in the cycle were at extreme latitudes relative to the solar zenith [Figures 5.25 to 5.28]. At the Arctic Circle, these variations were up to ~1 W/m^2 from the mean. Consequently, these extreme latitudes are the most sensitive to insolation variation, with the capacity to influence regional climate. Milankovitch identified the latitudes of 55°N-65°N as being the "most sensitive to changes in the heat budget" during winter (Imbrie and Imbrie, 1979:106). Whilst the greatest influence of precession has been attributed to equatorial regions and minimal at the poles (Imbrie and Imbrie, 1979), variation in solar insolation patterns caused by precession are significant at the poles [Figures 5.25 to 5.28]. Solar insolation and arctic atmospheric oscillation records record significant solar forcing at ~130-yr periodicity (Darby *et al.,* 2012), and the results of this PhD research suggest that the cause is this 133-yr flux in insolation caused by the solar declination cycle [Figures 4.5 to 4.9]. The variation in solar declination patterns (difference between the solar declination and the ecliptic) is seen in Figure 7.5, where a 133-yr pattern in extremes occurs. There is other evidence of a 133-yr cyclicity in climatic data: tropical Atlantic cyclones, ocean sediments, Nile water levels, auroral records, fire and drought cycles, and Arctic and Antarctic ice core chronologies (Section 2.2.3).

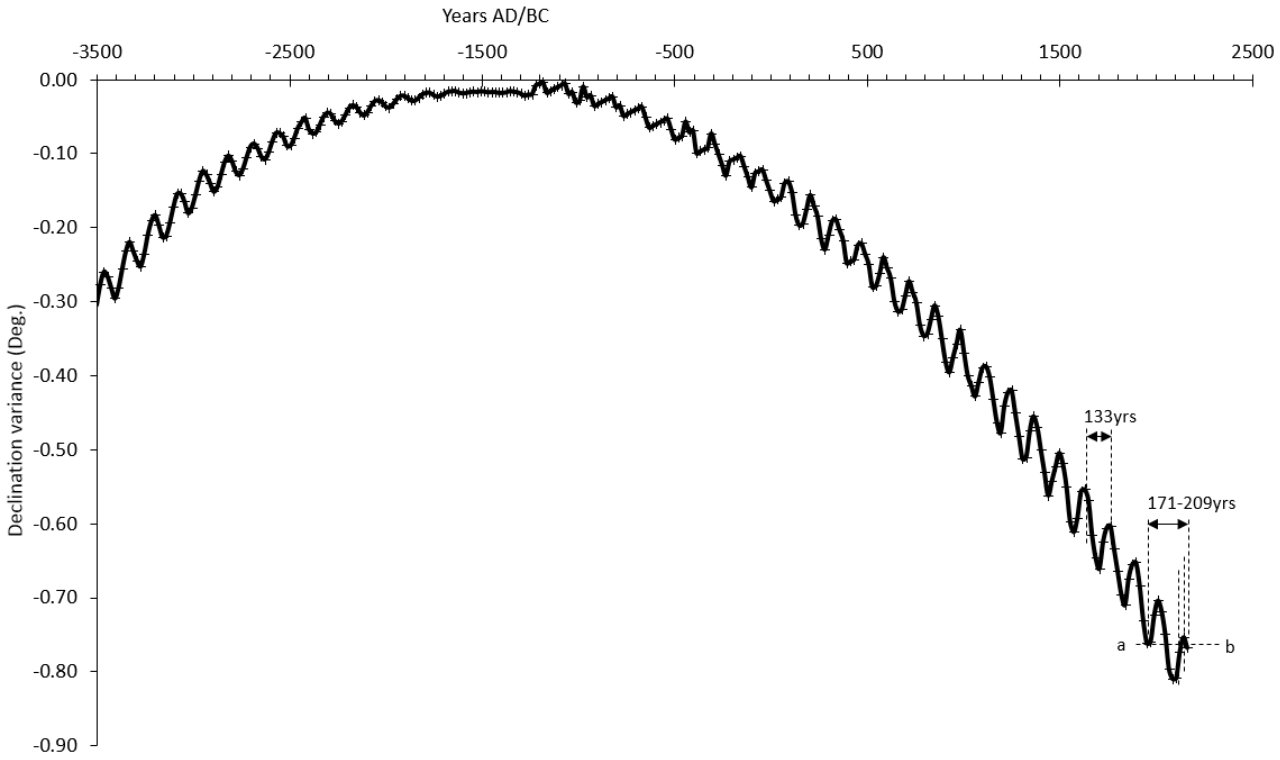

Figure 7.5: Solar declination variation relative to the ecliptic over the past 5.5 ky. Negative values on x-axis are BC. Peaks occur at 133-yr intervals. Along the line ab, the period ranges from 171-209yrs, which is the length of the SdV cycle.

When the perihelion is conjunct the June solstice, insolation swings of the same magnitude would occur at the Antarctic Circle as at the Arctic Circle. The different geographies at these extreme latitudes must affect climatic patterns differently. The Antarctic Circle generally marks the maximum extent of the Antarctic land mass but is predominately ocean [Figure 7.6], whereas the Arctic Circle is predominantly land mass, encircling the Arctic ocean [Figure 7.7]. The Bering Strait, Hudson Bay, Davis and Denmark Straits, and Norwegian Sea delimit the northern continental land masses at the Arctic Circle. The regions linked to the North Atlantic Ocean have been highlighted in previous research for their IRD data associated with Bond and Heinrich events and obviously include all but the Bering Strait, which links the Pacific Ocean to the Arctic Ocean. At the Antarctic Circle are found the Ross, Weddell, Amundsen, and Bellingshausen Seas, of which the first penetrates furthest south. The key areas for cold downwelling of the thermohaline current occur at these extreme northern and southern latitudes. The bipolar theory (Summerhayes, 2015) sees the Arctic warming as the Antarctic cools, and these trends can be seen in insolation data [Figure 5.29]. From the RWP, a gradual increase in insolation for the Arctic Circle and decrease at the Antarctic Circle are evident [Figure 5.29].

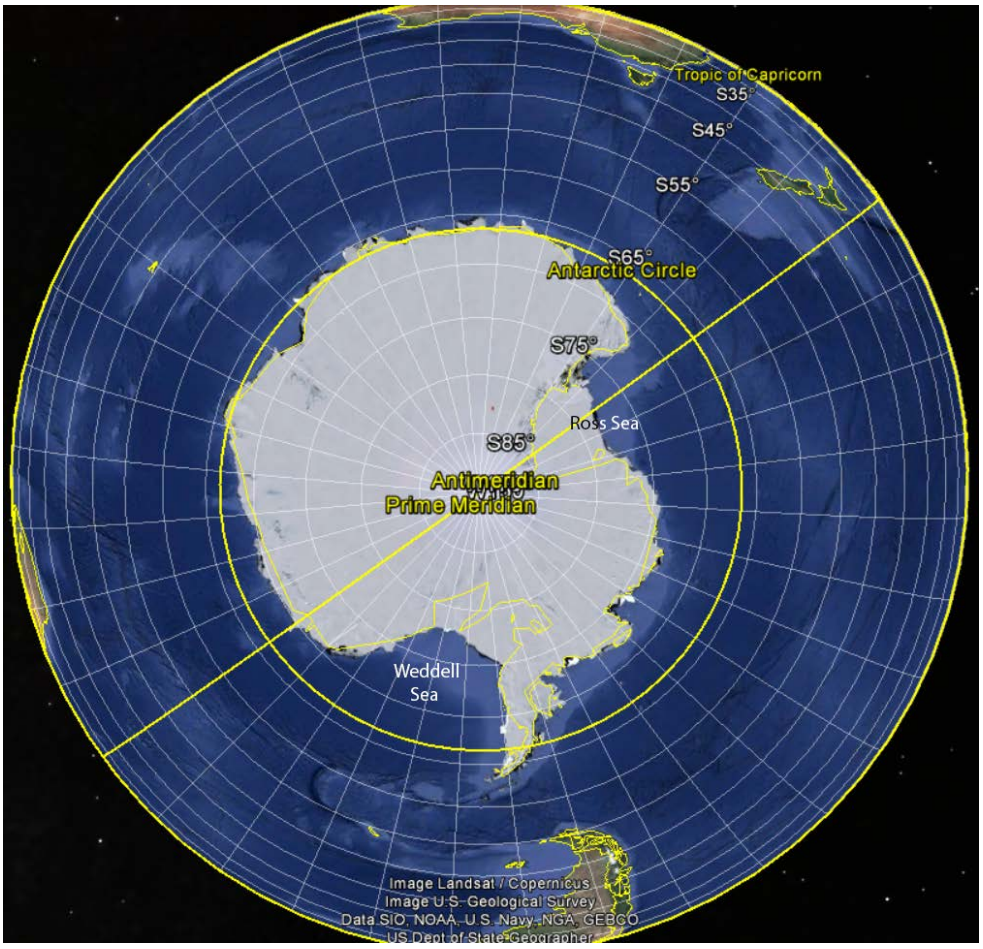

Figure 7.6: Antarctic region, showing Antarctic circle (Google Earth, 2015a). Adapted to label the Ross and Weddell Seas.

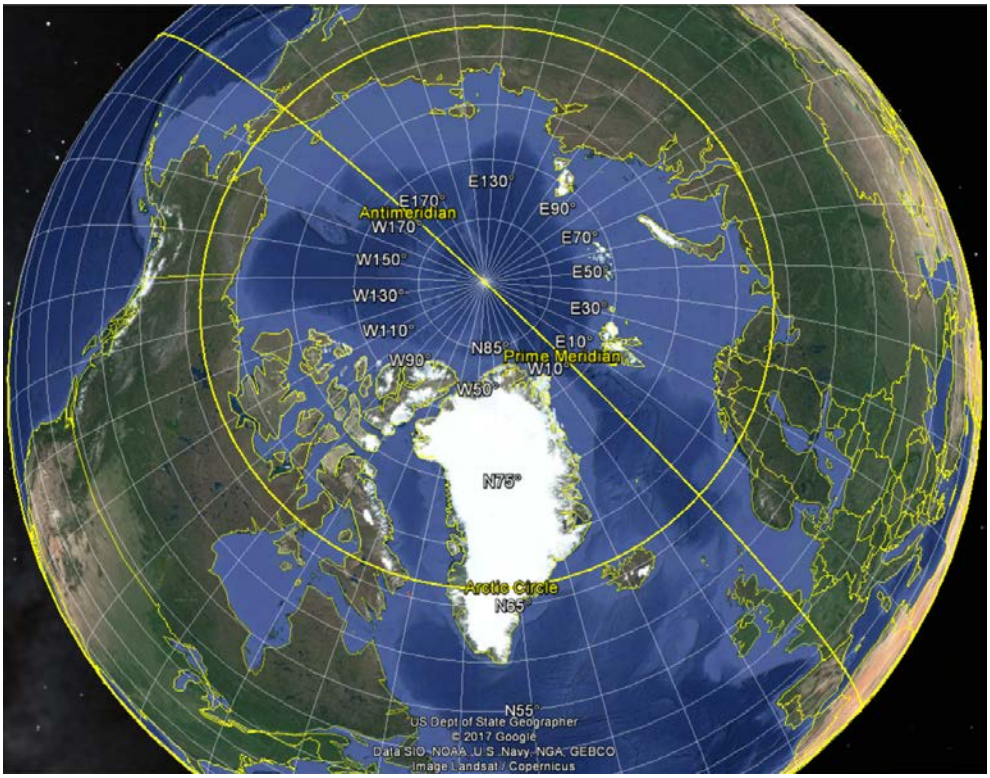

Figure 7.7: Arctic Ocean encircled by land mass (Google Earth, 2015b).

7.2.3 The Suess de Vries and Gleissberg cycles

Both trigonometric modelling and astronomical data from this research project show evidence of a repetitive ~209-yr period similar to the mean length of the SdV cycle, resulting from interaction between the perihelion, Metonic lunation, and the sunspot cycle. Modelling of the interaction of the Metonic lunation individually with the perihelion and then the sunspot cycle each produced a periodicity at the length of the SdV cycle (Section 4.4.4). The Metonic-perihelion interaction produced a periodicity of 209 yrs, with peaks separated alternately by 95-yr and 114-yr periods [Figure 4.14a]. Whilst the Schwabe sunspot (11.4 yr) and Metonic combo resulted in a 57-yr shared harmonic, the Hale sunspot (22.4 yr) and Metonic combination produced a 205-206-yr periodicity [Figure 4.14b]. At the mid-point of the 206-yr and 209-yr variants of the SdV cycle is a cyclical RRA return (within 2°). The Metonic-Hale periodicity produced internal peaks of 91 yrs and 114 yrs [Figure 4.14b]. A 91- to 95- yr cycle has been classed as the Gleissberg cycle, along with a 76-yr periodicity (e.g., Damon and Sonett, 1991; Gray *et al*., 2010). Modelling of perigee-perihelion behaviour also produced a close return at 207-yrs (within ~1.4° of precision) [Figure 5.15]. This is not the first closest return of perigee to perihelion, which occurs later at 289-yrs (within 0.2°).

Whilst trigonometric modelling produced both the SdV and Gleissberg cycle lengths, astronomical data also show evidence of the 209-yr pattern that has persisted throughout the ~50-ky range of radiocarbon data. Lunar declination data shows a complete cycle of either 912 yrs or 893 yrs, consisting respectively of four phases of 228 yrs, or three phases of 228 yrs and one of 209 yrs (Section 4.4.1). Each phase is associated with the movement of the lunar declination between the ecliptic and either extreme northern or southern declination. A complete lunar declination cycle, consisting of these four phases, is the time it takes for the precessional cycle to move to shift the vernal equinox by seven days from its starting location relative to the calendar year.

The solar declination pattern [Figure 7.5] also shows a 171-209yr period along the line a-b. The 171-yr period is the minimum length of the SdV cycle, and 209 yrs is its mean length. Whilst the main feature of the solar declination cycle is a 133-yr periodicity between extremes, a shifting 171-209-yr period sees solar declination returns to the same declination relative to the ecliptic. The start of new period shifts in a step-like pattern [Figure 7.5], separated by a 57-yr interval that is associated with precessional separation between the tropical and anomalistic years (Section 7.2.1). The difference between the mean length of the SdV cycle and the 133-yr cycle is 76 yrs, whilst the difference between the 133-yr cycle and the “mysterious” spectral companion signal of the SdV cycle (228-yrs) (Damon and Peristykh, 2004:243) is 96 yrs. Both the 76-yr and 95-yr cycles fall in the Gleissberg range. The astronomical data and modelling both provide evidence that the 133-yr, Gleissberg, and SdV cycles are closely connected.

Both the 133-yr and ~209-yr declination patterns affect insolation: the first as extremes of insolation patterns, and the second, based around the mean values. These extreme variations were up to 1.6 W/m^2 for the Arctic Circle at the perihelion/December solstice conjunction, with the exception of the Spörer and Dalton minima where the range was ~1.2 W/m^2 [Figure 5.25]. Whilst insolation variation associated with the 133-yr cycle is minimal at the Tropic of Capricorn during the current epoch, the range in insolation patterns at the Tropic of Cancer since the MWP was at least 1.2 W/m^2, increasing to ~1.5 W/m^2 in modern times (except during the Spörer and Dalton minima periods) [Figure 5.27]. By comparison with variations in the solar cycle is associated with variations of ~1 W/m^2 (up to 1.3 W/m^2) (Friis Christensen and Lassen 1991; Kopp and Lean, 2011; Vieira *et al*., 2011; Wang *et al*., 2005), these latitudinal insolation changes are frequently equal to or greater to those that result from solar variability. These latitudinal variations in insolation perhaps offer an explanation for extreme weather events not directly connected with sunspot activity (Section 7.1.1), and an understanding of abrupt climate change that can take place in only a matter of decades (cf. Wolff *et al.,* 2010).

Further support for the SdV cycle being caused by the Moon's interaction with the perihelion can be seen in the solar declination pattern during the 2nd millennium BC, as the amplitude of solar declination is suppressed. This is due to the Metonic lunation being conjunct the December solstice [Figures 5.25 to 5.28]. Similarly, insolation patterns during this time are also suppressed [Figures 5.24 to 5.28] as they are dependent upon the solar zenith angle. In the radiocarbon calibration curve [Figure 3.22], the SdV cycle is similarly dampened during the 2nd millennium BC (Damon and Linick, 1986). Although it was thought that the suppression of these signals was perhaps due to increased heliomagnetic intensity on Earth's geomagnetic dipole (Damon and Linick, 1986), evidence presented here suggests a direct link between solar declination, insolation patterning and the impact on the radionuclides produced by spallation in Earth's atmosphere.

Another feature of SdV wiggles is that they vary diachronically, with strong amplitudes persisting for a millennium before disappearing and later remerging (Abreu *et al.,* 2012). This behaviour could be explained by the influence of precession, where conjunctions between any combination of the solstices, perihelion, and Metonic lunation produce a flattening of the solar declination signal and Earth-Sun distances as they did in the physical data (Chapter 5, Section 7.1). This also is supported by the unanchored model of the interacting 133-yr and 209-yr cycles at 19-yr resolution [Figure 6.3] that showed clear SdV signals at the beginning and end of the millennial-scale signal, but which disappeared in between. This modelling shows that the SdV cycle is strongest at the beginning and end of the millennial-scale cycle with which it is associated.

Although inferences have connected the SdV cycle to the sunspot cycle, the SdV cycle is not found in the sunspot cycle (Hathaway, 2010; also see Section 3.1.3). This inference was made because the

SdV is a multiple of the sunspot cycle as is the Gleissberg cycle (Damon and Sonett, 1991; Suess, 1986; Vieira *et al.,* 2011; also see Chapter 2). Additionally, long-term reconstruction of solar variability relies upon variations in cosmogenic isotopes (i.e., ^{10}Be and ^{14}C) (Feulner, 2011; Vieira *et al.,* 2011). These factors, taken into consideration with the results presented here, may explain why amplitudes of SdV signals are greatest during increased numbers of solar grand minima (cf. Abreu *et al.,* 2012). This aspect of SdV signals could be explained by the superposition of solar minima and maxima on the normal background influence of SdV signal-like behaviour induced by Earth-Sun-Moon interaction [Figures 6.7 to 6.10]. Lending support to this argument of lunar modulation of irradiance patterns is the production of the 1474-yr Bond-cycle by interacting 133-yr and 209-yr cycles [Figures 6.9 and 6.10]. This cycle is strongly correlated with TSI reconstructions and ^{10}Be flux from Antarctica. Adjustments for the extremes of solar minima and maxima showed amplification of these natural trends created by Sun-Moon-Earth interaction, and improved the correlation between the two.

The SdV and Gleissberg cycles, which are cycles of warmer-cooler temperatures, appear to be based on the gravitational impact of Metonic New Moon at perihelion [Figure 4.16a]. At these times, gravitational forces are stronger due to reduced Earth-Sun and Earth-Moon distances in proximity to the perihelion (Section 5.3). The lunar orbital plane, which is inclined at ~5.15° to the ecliptic, vertically straightens up a little at each New Moon (Gutzwiller, 1998) producing a peturbation to the inclination of Earth's axis. Every 133 yrs this influence is maximised by reduced Earth-Sun and Earth-Moon distances. However, the 209-yr lunation cycle is closer to a tighter perihelion return (RRA) than occurs with the 133-yr cycle (4.4° at 130 yrs as opposed to 1.5° at 208 yrs). The Gleissberg cycle separates the 133-yr periodicity from the SdV cycle and its mysterious companion cycle. The first common return point between these two cycles (133 yrs and 209 yrs) occurs at 1463 years (Julian) or 1474 years (tropical) [see Section 7.2.5].

The persistance of the SdV cycle through the last 50-60 ky (Section 3.2.2) is suggestive of persistant astrophysical forcing through rhythmic interaction. This persistance of two regular cycles (the Metonic lunation and anomalistic year) through time is indicative that these two factors have the capacity to fulfill this requirement, and meet the characteristics of the SdV temperature variations found in climatic data. Astronomical data and modelling suggest that the SdV and Gleissberg cycles can be understood in terms of changing gravitational patterns, insolation, and solar irradiance. In particular, modelled interaction between the perihelion and Metonic lunation produce the SdV cycle, with the Gleissberg cycle as an artefact of that interaction.

Although the SdV cycle is not found in sunspot data, the Gleissberg and SdV cycles are multiples of both the sunspot cycle and the Metonic lunation. Individually, the sunspot cycle and the Metonic

lunation cycle have known climatic associations (Section 2.2.3). The sunspot cycle variability has been shown to influence Hadley cell and Walker circulation (Section 7.1). The signature of the Metonic lunation is found in Holocene ice (Yiou *et al.,* 1997); U.S. temperature peaks (Currie, 1993); air pressure and air temperature (O'Brien and Currie, 1993); rainfall data in Australia and South Africa (Vines, 2008); and volcanic eruptions [Figure 2.18] (Hamilton, 1973). Other multiples of the sunspot and Metonic cycles such as the 57-yr and 133-yr cycles are also associated with the Metonic cycle (Sections 7.2.1 and 7.2.2). In particular, the 133-yr solar declination cycle shows direct associations with Galapagos oxygen-isotope data [Figure 7.4]. Whilst the Galapagos data comparison is from a sample for a relatively short time period, it lends support to the theory of lunar precessional influence theorised here. The SdV cycle itself is evident in climate-linked processes such as dendrochronological records, glacier variations, ice core chronologies, monsoon intensity changes, and other climate-linked processes (Breitenmoser *et al.,* 2012; see also Clemens, 2005). The Gleissberg cycle appears in dendrochronological, NINO3.4 SSTs, and Greenland and Antarctic ice-core data (Section 2.2.3).

7.2.4 Metonic eclipse series and Hallstadt cycles

The astronomical data presented here also shows a previously unreported Metonic eclipse series that occurs every 456±38 yrs (Section 4.4.5). At times of eclipses, gravitational force is increased by the alignment of the Sun, Moon, and Earth on the same plane. This magnitude of this force is increased at total solar eclipses when the Earth and Moon are at their closest. Series of these total eclipses occur once every 893 yrs to 912 yrs (lunar declination cycle), and the type of nodal eclipse (north/south lunar node) alternates every eclipse series. Each of the eclipses in the same series spanning 57-76 years is either all north nodal or all south nodal (Section 4.4.1).

Falling within this range of Metonic eclipses is the modelled interaction between the anomalistic year (RRA) and the Metonic lunation, which shows an even more precise conjunction cycle of the Metonic lunation and perihelion than the SdV cycle of 209 yrs. This more precise Metonic-RRA return [Figure 4.19, Table 4.3] occurs at 494 yrs (Section 4.4.5), which is of the same length as the Cartwright tidal sedimentation cycle of 493 yrs (Munk *et al.,* 2002). The RRA occurs at 493-yrs to ≤0.2° from a precise return, compared to the 208-yr RRA return at ~1.5° [Table 4.3]. Close to this cycle is the modelled perihelion-perigean conjunction at 496 yrs (Section 5.3.3), emphasising the importance of the 494-yr Metonic-RRA return in this series of eclipses. Increased gravitational force from the Sun and Moon at perihelion, aided by reduced distances by perigean contact and a solar eclipse, is a reasonable explanation of the 493-yr tidal sedimentation pattern associated with the Cartwright cycle (cf. Munk *et al.*, 2002).

This ~494-yr harmonic is a factor in the 1482-yr sunspot-Metonic cycle identified in Chapter Four (494 x 3 =1482). The 1482-yr periodicity is close to the length of millennial-scale oscillations of ENSO in the Pacific, and the length of Bond IRD 'cycles' (especially during the Eemian). Associated with this 1482-yr sunspot-Metonic conjunction is a very close return of the RRA (~0.59°) to the starting geographical longitude at 1479 yrs [Table 4.3], emphasising a strong influence of the perihelion in terms of gravitation and irradiance. A strong perigean force is also present at this time, with the first double occurrence (within 4 yrs) of a modelled perihelion-perigean conjunction in ~1500 yrs occurring at 1484 yrs and 1488 yrs [Figure 5.17]. These factors ear-mark this period as one of extended gravitational forcing to regionally-sensitive areas, influenced by perihelion, perigee, and Metonic lunation.

7.2.5 Bond events and millennial-scale ENSO cycles

The premise for the PhD research presented here is that gravitational and insolation forcing work together to produce various manifestations of the ~1500-yr quasi-periodicity, through the combination of solar and lunar forcing. A key part in shaping the palaeoclimatic record was postulated to be due to precessional influence, primarily caused by the influence of the Sun and Moon on the Earth. A key focus of interest was the influence of solar forcing through the interaction of the perihelion, Metonic lunation, and sunspot activity, and representation of the separation between tropical and anomalistic years associated with the Milankovitch precessional cycle (Section 4.3.1). A factor considered important to modelling is the ability to account for regional influences (Heinrich, 1988), and this factor was included in the trigonometric models through the geographic longitude at solar zenith. This feature of the model also allowed for the precise modelling of days to years, important in distinguishing between tropical, Julian, and anomalistic years.

Just as extreme latitudes are known to be sensitive to insolation changes at Milankovitch scales (Imbrie and Imbrie, 1979), the Arctic and Antarctic Circles were shown to be sensitive to swings in insolation at the sub-Milankovitch scale where they were magnified [Figures 5.25 and 5.26]. At these extreme latitudes, oceanic tides are more extreme, occurring only daily [Figure 3.20]. Whilst the Antarctic Circle is mostly located in oceanic areas, this is not true for the Arctic Circle. Along the Arctic Circle, Iceland is strategically placed adjacent to the Denmark Strait and Norwegian Sea, which is the main watery body along the Arctic Circle. This area is also the main portal to the Arctic Ocean, followed by the Davis Strait (between Canada and Greenland) and the Bering Strait (separating the Asian and North American continents). Because of the importance of the ocean in the retention and distribution of heat, and the fluid nature of water, these regions are particularly sensitive to the extremes of insolation and gravitation (cf. Mueller *et al.,* 2012; Pritchard *et al.,* 2012). Bond's research into the ~1500-yr quasi-periodicity was located here (Bond *et al.,* 1997), using deep-sea

cores from locations near Iceland, Greenland, and Canada. This area is bounded by the geographical longitudes of ~60°W to ~15°W. Separated by 180° of longitude from the tropical Atlantic is the West Pacific Warm Pool, which is important in the regular functioning of ENSO events (Turney *et al.,* 2004). The deepest penetrations of the Southern Ocean into the Antarctic region occur in the Ross and Weddell Seas [Figure 7.6].

The Ross Sea is linked by longitude to the WPWP, whilst the Weddell Sea shares a longitudinal link to Iceland [Figures 2.11 and 7.6]. The northern-most protrusion of the Antarctic content is located just off the southern tip of South America. Immediately to the west of this region, the Humboldt Current separates from the Antarctic Circumpolar current and begins its northward journey along the west coast of South America to the tropical East Pacific (Lorenzo *et al.,* 2008). Immediately to the east of the Antarctic Peninsula lies the Weddell Sea. Thus, it can be seen that key sensitive geographic regions are closely associated by longitude and the millennial-scale cyclical behaviour of ENSO and North Atlantic IRD events are linked. The geographical overview shows that these climatic responses are linked when considered from a global perspective in conjunction with astronomical forcing. Key sensitive geographical regions associated with ENSO, IRD events, and the thermohaline current are generally clustered 180° apart, likely explaining the teleconnections between them. Peak gravitational forces, tides, and maxima and minima in daily insolation also occur 180° apart.

The poor understanding of the 1500-yr quasi-periodicity has led to debates as to whether it is astronomically- or internally-forced, whether it is a real phenomenon or merely stochastic resonance in Earth's climate system, and whether the quasi-periodicity is caused by millennial-scale ocean-atmosphere interaction or by shutdowns and restart of the thermohaline current, by gravitational forcing or insolation. These limitations do not help with modelling. However, Braun *et al.* (2005) postulated that the cause of the 1470-yr cycle of climate change could be caused by two interacting cycles: the SdV and Gleissberg cycles. Both the Gleissberg and SdV cycles were noted as numerical factors in a 1470-yr periodicity, as both were numerical factors to this cycle length (1470/7=210; 1470/17=86.5). This modelling exercise was based on the inference that both cycles are solar cycles, and involved forcing of the CLIMBER-2 (Version-3) coupled climate system model by these two cycles. CLIMBER-2 is a model of intermediate complexity of low resolution, that was parameterised and tuned to modern climate variables, and shown to emulate modern climate conditions (Petoukhov *et al.*, 2000). This model was previously used to simulate some conditions during the Last Glacial Maximum (~21 kya) and the mid-Holocene (~6 kya) (Petoukhov *et al.*, 2000). Braun *et al.*'s (2005) work focused on the simulation of glacial conditions in the North Atlantic, and the influence on these oscillations on periodic forcing of the thermohaline current by freshwater input without testing

directly against palaeoclimatic data. They concluded that the 1470-yr cycle could be forced by this coupled atmosphere-ocean model.

However, Braun *et al.* (2005) did not show a direct link between the 'solar frequencies' (Gleissberg and SdV cycles) and forced hydrological cycles but assumed they existed. There were two main reasons (Braun et al., 2005:209) for these assumptions and not linking ^{10}Be data directly to the model: (1) "complex and uncertain processes" linking solar forcing and freshwater fluxes could not be achieved for modelling at the millennial scale, and (2) the lack of solar reconstructions of sufficient resolution, dating precision, and reliability during the last glacial. Whilst both the SdV and Gleissberg cycles are multiples of the sunspot cycle, the SdV cycle is not evidenced in sunspot data (Hathaway, 2010). Furthermore, Hathaway (2010) suggests that the Gleissberg cycle consists either of two different components (50-60-yr, 90-100-yr periods) or is changing. Despite no sunspots occurring during the Maunder Minimum, ^{14}C fluctuations still occurred, suggesting that something more complex was going on (Section 3.1.3). Modelling results and astronomical data presented in this PhD thesis have demonstrated that both the SdV and Gleissberg cycles are most likely modulations of solar wind patterns in Earth's climatic data by Sun-Moon-Earth interaction (keeping in mind that the sunspots power the solar wind). This involves the interplay with the Metonic lunation and perihelion, which influences Earth-Sun and Earth-Moon distances, TOA solar irradiance, and gravitational and insolation patterns. This interplay can account for fluctuations during the Maunder Minimum (Chapter 6). The 133-yr cycle is an important component of these interacting cycles (it is also a factor of the ~1470-yr cycle), and is separated in length from the SdV cycle by the length of the Gleissberg cycle.

The modelled interaction of the 133-yr and 209-yr astronomical cycles produced a cycle of 1474-yrs, with the chronologically-anchored model (adjusted for precession and sunspot activity), showing a statistically-significant, strong positive correlation between it and the Bard *et al.* (2007) TSI reconstructions from Antarctic ^{10}Be data (Chapter 6). The Bard data forms part of the radiocarbon calibration dataset (Fairbanks *et al.,* 2005). This modelled activity matches the mean length of the Bond cycle during the entire Glacial and early Glacial [Table 7.2]. Although there was a good match between all the chronologically-anchored models and the TSI reconstructions, the best match occurred between the precessionally-adjusted model (also modified for sunspot activity until the beginning of the Industrial Revolution) and the TSI_1 and TSI_2 reconstruction (latter corrected for geomagnetic modulation of the solar irradiance signal) at r=0.84 and p=0. The climatic effects associated with each of these cycles is discussed above (Sections 7.2.2 and 7.2.3). Not only does this model demonstrate the existence of the 1474-yr climate cycle, it reinforces the work of Braun *et al.*

(2005) that linked the modelled activity of the Gleissberg and SdV cycles to freshwater forcing of the thermohaline current.

The 1470-yr periodicity is also seen in Greenland ice core chronological models (other than GICC05). Of the GISP and GRIP ice-core chronologies, the 1470-yr signal was clearest in the orbitally-tuned GISP2 chronology (Section 2.2.2.4). In the SS09SEA model, the 1470-yr signal was evident but was also accompanied by spectral peaks at 1163 yrs and 1613 yrs (Clemens, 2005). An ~1160-yr period is also found in patterns of solar and lunar gravitational forcing, Earth-Moon and Earth-Sun distances, and perigee-perihelion superposition [Figures 5.12 to 5.15]. Similarly, the 1613-yr spectral peak occurs close to modelled perigee-perihelion forcing at 1609-yrs [Figure 5.16]. The GISP2 record tuned to Hulu-cave speleothem record shows similar spectral peaks to the SS09SEA model at 1190 yrs, 1490 yrs, and 1667 yrs (Clemens, 2005). The first two of these spectral peaks correspond to perigee-perihelion forcing at 1195-yrs and 1484-yrs [Figure 5.16]. No association was found for the 1667-yr signal.

These millennial-scale peaks in the Greenland ice-cores that appear in chronologies based on SS09SEA and the Hulu-cave speleothem record are likely forced by Earth-Sun and Earth-Moon distances, and by associated gravitation and insolation variations that impact on precipitation and tides. Spectral peaks based on modelling of the cyclical interaction between geographic longitude and perihelion (RRA variable in Chapter 4; see Table 4.3) show up as tidal patterns in various climatic cycles. The first four of the most exact cycles in this table matches climatic patterns evidenced in palaeoclimatic data. The first of these tight perihelion returns match an ~1800-yr tidal sedimentation pattern (Petterson, 1930; Keeling and Whorf, 2000) that is also found in Bond IRD data, as is the 1375-yr RRA return that is comparable to the Holocene length of the Bond cycle (1374 yrs) [Table 7.2]. The Cartwright and Hallstadt cycles also appear to be forced by locational sensitivity to the perihelion return [Figure 4.3], being amongst the four tightest perihelion returns.

A 1479-yr perihelion return (to <1°) [Table 4.3] is very close to the mean Bond cycle value for the entire glacial and Holocene period [Table 7.2]. This perihelion return occurs close to the 1482-yr sunspot-Metonic cycle return, which is a multiple of the 493-yr Cartwright cycle (also an RRA cycle) [Figure 4.3]. The 57-yr non-stationary climate cycle that returns to the same geographic longitude at 285-yrs (~1.3° from exactitude) [Table 4.3], is also a factor in the 1482-yr cycle. The SdV cycle is also a factor in this millennial-scale periodicity but is not always associated with a solar eclipse, as the earliest an eclipse can occur in this sequence is 76-yrs distant at 418-yrs (2 x 209). However, the 493-yr Cartwright cycle does occur with an eclipse, but it is not always a total solar eclipse (associated with the south lunar node and perigee): every second Cartwright cycle is a total solar eclipse. Together with the 133-yr and 209-yr cycles, the ~1470-yr cycle is a convergence of multiple shorter cycles

with climatic associations based on interaction between the perihelion, perigee, Metonic lunation, and sunspot cycle. As such, gravitational forcing clearly plays a prominent role in the forcing of the ~1470-yr climate signal along with solar irradiance, with contributions from both Sun and Moon.

The variability of the 1470±500-yr cycle can be explained through the combination of this cycle with the Metonic eclipse series. Patterns of solar irradiance caused by interaction of the 133-yr and 209-yr cycles produce a 1474-yr cycle (Chapter 6). The uniqueness of this cycle is also established in the Metonic eclipse series, as it is the first in the series to be phase aligned with the modelled to the 11.4-yr sunspot cycle [Table 4.3]. At the length of this cycle, there is a repeating pattern of solar irradiance and gravitation associated with the Metonic lunation in conjunction with the perihelion. Whilst three Cartwright cycles (which coincide with a Metonic eclipse) approximate the ~1470-yr cycle (4 x 494 = 1482), the strength of this signal alternates based on whether the solar eclipse is north or south nodal, with south nodal eclipses occurring in association with the Cartwright cycle at 988 yrs (2 x 494).

Distances are minimised, and gravitational forces and TOA solar irradiance are maximised at south nodal solar eclipses when perigee also occurs. Modelled perigee-perihelion interaction at the scale of the lunar declination cycle occurs at 906 and 910 yrs (at between 4-5° of precision) [Figures 5.15 and 5.16]. As a multiple of the south nodal eclipses cycle, there is a modelled perigee-perihelion return at 992-yrs [Figure 5.15]. The combination of the south nodal eclipses with the solar irradiance pattern means that the ~1474-yr cycle is more strongly emphasised once every ~2948-yrs. This value also approximates the average “waiting time” (~2800-yrs) between Dansgaard-Oeschger events indicated in the Ditlevsen *et al*. (2007) statistical study. This study involved the redefinition of Dansgaard-Oeschger events during the period 10-50 kya, using the GICC05 chronology (see Section 2.2.2.4). Under the right conditions as the various contributors to these cycles interact with each other, Bond IRD cycles can be triggered prematurely or delayed. Natural variations in precision of return, length of the sunspot cycle, and the movement of the Metonic lunation though the tropical year from the idealised models presented here would be contributing factors.

Millennial-scale lunar patterns also occur in the SS09SEA chronology and the Hulu speleothem record, as well as in Bond’s data from deep-sea cores. The Moon plays a strong role in shaping these patterns in climatic data, a role that is strongly evident in Figure 5.13. Millennial-scale patterns of peak gravitational forcing are more pronounced in lunar forcing than solar-gravitational forcing (Section 7.1.2). Here, the 133-yr cycle of minimal Earth-Moon distances at New Moon is also strongly featured (Sections 7.1.2 and 7.2.2). During the past 5.5 kya Bond IRD events occurred close to solar eclipses at times of peak gravitational forcing, indicating that the Bond cycle results from a combination of solar and lunar forcing through the effects of both gravitation and insolation. The

1375-yr cycle during the Holocene and early glacial can simply be explained by gravitational forcing [Table 4.3, Figures 4.18, 5.16, and 7.7]. The lunar capacity to imprint on ice-core and deep-sea records is evident, starting with 19-yr patterns found in tidal sedimentation patterns and ice-core chronologies (Section 2.2.3).

Because astronomical variables are influenced by each other, and astronomical cycles are inexact and vary in length based on where they are within the cycle (e.g., Earth's velocity throughout the year which affects the length of day with respect to the seasons and therefore the precessional rate), idealised models can only produce estimates of these cycle lengths. For example, with the 493-yr cycle as the basis of the ~1470-yr Bond cycle a number of series were detected in modelling of the RRA-Metonic lunation and sunspot cycle interaction [Figures 4.18 and 4.19]. These series are relative to a fixed geographic latitude. From this modelling exercise, it can be seen that each of these different series approaches and separates from a return point. At each iteration of the 493-yr cycle, the Metonic lunation moves further away by 1° at each succedent return due to precession (Section 4.4.5). However, there is an adjacent series also moving towards alignment. As ideal conditions align, the cycle can jump-shift to an adjacent series, such as occurs during the Holocene with the 1375-yr signal [Figure 7.8]. This signal is the mean length of the Bond cycle during the Holocene and the beginning of this particular series occurs at 389 yrs [Figure 7.8], which is also a spectral peak in radiocarbon data [Figure 2.16]. Similarly, an 1868-yr signal is also seen, corresponding with tidal forcing and a broad spectral peak in Bond data (Bond *et al.,*1999).

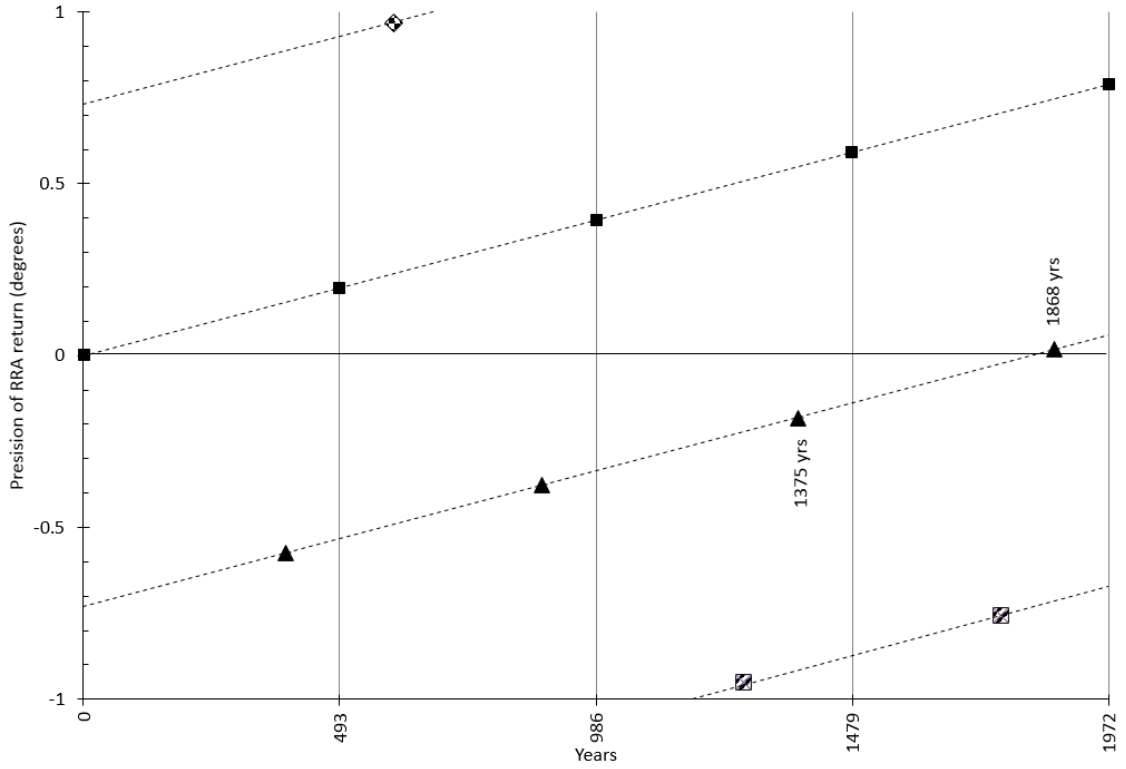

Figure 7.8: Series of 493-yr RRA cycles relative to geographic longitude. Here, four different series can be seen.

Variations on Bond cycle lengths and their variability were detailed in Figure 4.20 and Table 4.4. Discontinuities in this graph associated with RRA returns (perihelion to geographic longitude at the time of the solar zenith), are indicative of close cyclical associations between these two. The longer the peaks in Figure 4.20, the more precise the cyclical return. Periods marked 11-18 in Figure 4.20 are all variations of Bond IRD events for different periods during the last glacial and Holocene. Peaks marked 19-22 are all of Hallstadt cycle length, and peaks 4, 6, 7, 9, 10 are all error margins in radiocarbon dates associated with Bond IRD events. Strong lunar forcing also features here at points 5, 8, associated with the Cartwright sedimentation cycle and Metonic eclipse (point 5) and a complete lunar declination cycle (point 8). The first two points are less exact returns between the RRA and geographic longitude, with the second point also being the length of the Gleissberg cycle. The third point is a solar spectral signal that is at the beginning of the ~500-yr series associated with the Bond-event related cycle of 1375 yrs.

It is also possible for interacting cycles to be activated as they come close to an exact phase alignment as illustrated in the relationship between the perigee and perihelion, where a double occurrence is seen at ~1500 yrs. Figure 5.17 shows the perigee-perihelion conjunction at 1445 yrs and 1484 yrs. The first of these contacts is equal to the Bond 'cycle' length during 53-64 ka [Table 7.2] and the second is close to the mean lengths of the Bond 'cycle' and the millennial-scale ENSO cycle from Lynch's Crater. The 1484-yr return could be triggered off prematurely by the 1474-yr cycle (133-yr/209-yr combo), the 1479-yr RRA return to geographical location, the 1482-yr Metonic-sunspot cycle, or delayed to the 1488-yr perigee-perihelion alignments [Figures 5.15 and 5.16]. Regional weather patterns and variations in such factors as the length of the sunspot cycle and Earth's rotation could alter the precise timing from the idealised model.

Table 7.3: Heinrich event and LIA associations with Milankovitch phases. Turney *et al.* (2004) and Bond *et al.* (1997) are the sources for the time of Heinrich events (H1-H6). The Younger Dryas is H0.

Heinrich event	Milankovitch association	Climatic association
H2, H5, LIA	December solstice/perihelion	H2 Boundary MIS3/2; changes between cold to very cold. H5 in MIS3 Cold LIA follows MWP during Holocene and perihelion/December solstice conjunction
H0	June solstice/perihelion	Boundary MIS1/2; very cold to warm Holocene (Younger Dryas)
H3	September equinox/perihelion	MIS3 Cold
H1, H4, H6	March equinox/perihelion	H1 MIS2 Very Cold H4 MIS3 Cold H6 boundary MIS 4/3; very cold to cold

The Bond ‘cycle’ was found to be closely-coupled to both Dansgaard-Oeschger events and Heinrich events (Bond *et al.,* 1999). However, it has been criticised for its apparent irregular behaviour, weak signals, and inability to conform as desired for statistical tests for which it is not suited (e.g., Ditlevsen *et al.*, 2007). However, if the Bond ‘cycle’ is understood as a convergence of basic, rhythmic solar and lunar cycles that create a background millennial-scale pulse in climate data then the weakness or strength of the signal is of no major consequence. Under the convergence of the right conditions, this pulse is accentuated and gives rise to Bond IRD events, millennial-scale ENSO patterns, Dansgaard-Oeschger and Heinrich events, and Milankovitch cycles. The timing of these events resulting from the combination of these various cycles is non-stationary and non-linear, and is ultimately not suitable for inferential statistics. Essentially, the ~1500 quasi-periodicity is a high-frequency extension expression of the Milankovitch cycles.

Dansgaard-Oeschger events occur at times of rapid warming between stadial and interstadial (Schulz, 2002; cf. Cooper *et al.,* 2015; Wolff *et al.,* 2010), where this warming typically occurs during decades “before plunging back rapidly to a cold baseline” (Wolff *et al.,* 2010:2829). This description certainly fits in with sudden changes in solar declinations [Figure 7.5] and related insolation patterns [Figures 5.24 to 5.28] where, as part of the 133-yr cycle, such a change could occur within 19 yrs. Associated changes in Holocene insolation can be as much as 1.2 W/m^2 during a 19-yr period, with the change in insolation levels occurring at a similar scale to those caused by maxima and minima in sunspot activity. At the extremes of eccentricity, these changes would be larger and more rapid as there is a greater variation in annual TOA solar irradiance, with the maximum insolation greater than current levels and minimum significantly less (Section 5.1). Schultz (2002) and Rahmstorf (2003) reported that Dansgaard-Oeschger cycle deviated by no more than ±20% from multiples of 1470 yrs, *viz* 289 yrs. The 289-yr period is associated with both modelled perigee-perihelion cyclicity [Figure 5.15] and the geographical return of the non-stationary 57-yr period after 285 yrs [Figure 4.13]. The greater the precision of returning cycles (phase alignments between the various contributors), the greater maximisation of potential forcing by gravitation, insolation, and solar irradiance. Heinrich events (Heinrich, 1988) are stronger IRD events than Dansgaard-Oeschger events, requiring significantly stronger forcing. Although during the last 32 ky Heinrich events occurred more frequently, close to perihelion contacts with both the solstices and equinoxes [Table 7.3], they generally operate at the semi-precessional scale (Milankovitch cycle) and are associated with perihelion-solstice conjunctions (June and December) (see also Turney *et al.,* 2004; Bond *et al.,* 1997).

Chapter 8 – Conclusion and Future Research

8.1 Conclusion

This thesis started with the theoretical position that precession, through Sun, Moon, and Earth interaction, produces the ~1500-yr oscillation and sub-harmonics, shaping the gravitational and solar insolation impact on Earth's palaeoclimatic record and climate. The research questions posed were:

1. Is the ~1500-yr quasi-periodicity recorded in palaeoclimatic archives real and explicable by astronomical forcing? Does the interaction of the Sun, Moon, and Earth produce these cycles?
2. How do the following cycles relate to the ~1470-yr quasi-periodicity and do they have an astronomical cause: the Suess de Vries cycle (209 yrs); the Gleissberg cycle (70-100 yrs); radiocarbon signals of 104 yrs and 131 yrs; a 57-yr signal in various climatic datasets.

A strong case has been made for the astronomical forcing of the ~1500-yr quasi-periodicity associated with the Bond 'cycle' and millennial-scale ENSO events in the Pacific (Section 7.2.5). In particular, the lunar modulation of Earth-Sun distance and axial tilt in relative proximity to the perihelion produces patterning in solar irradiance, insolation, and gravitational force that cannot be separated in time despite their very different natures. In terms of insolation and its variation based on latitude, these changes were quite substantial, particularly at extreme latitudes (Section 5.4). In terms of gravitation, it is clear that lunar gravitation causes IRD events, with the size of these events dependent on ice volume, and the magnitude of gravitation (Chapter 5). These events are also accompanied by fluctuations in insolation that cause extreme weather events in sensitive geographic regions, such as the Arctic and Antarctic Circles and the WPWP. These locations are linked by geographic longitude, being either of similar longitude or positioned 180° opposite.

However, insolation variation in the tropical Pacific also occurs at the same time as the gravitational forces producing IRD events at the limits of the polar regions. Earth's climate system is extremely sensitive to the displacement of concentrated heat relative to the equator (Hou and Lindzen, 2002). Factors affecting this are precession (precession/solstice contacts) (e.g., Turney *et al.,* 2004) and solar variability (e.g., Gray *et al.,* 2010). Both these factors affect the Hadley Cell and Walker circulation, enabling ENSO's effects to exercise global impact (Section 2.2.2.2). Both the IRD events of the North Atlantic and millennial-scale ENSO events are symptomatic of astronomical forcing, playing roles in a chain of events that are triggered externally. Teleconnections between the two stem from their common cause. Their natures are different because of the different regional factors influencing their expression.

Variability in the expression of the ~1500-yr quasi-periodicity stems from its composite nature. Both lunar and solar signatures are found in various climate records from around the globe at decadal scales (Chapter 2). The combination of these elements produces shorter climate cycles such as:

- a non-stationary 57-yr cycle linked to precession, Metonic lunation, and sunspot activity
- the Gleissberg cycle as an artefact of interaction between the Metonic lunation, sunspot cycle, and perihelion
- the regional orientation (along a meridian of longitude) to the perihelion at ~104-yrs, which is a spin-orbit coupling (rotation to orbit) associated with the anomalistic year
- a 133-yr cycle of variation in Earth-Sun distance, Earth-Moon distance, solar declination, gravitation, TOA solar irradiance and insolation;
- the 209-yr SdV cycle of perihelion interaction with the Metonic lunation, sunspot cycle, and perigee, and a warm-cool climate cycle
- a previously unreported 456±38-yr cycle of Metonic solar eclipses
- an ~493-yr cycle influenced by perihelion, Metonic solar eclipse, and perigee, which is linked to the ~1500-yr quasi-periodicity, the Hallstadt cycle, and tidal sedimentation patterns.

Of these, the two most important cycles producing the 1474-yr cycle are the 133-yr cycle and 209-yr cycles (Chapter 6, Section 7.2.5). Variation due to the extremes of sunspot activity is superimposed on this pattern to produce extreme variations of the cycle [Figures 6.9 and 6.10]. The importance of the 133-yr cycle is associated with its ability to induce abrupt climate change through dramatic variations in insolation over less than two decades (Section 7.2.2). These variations in climate appear to be related to cycles of precipitation, fire, and tropical cyclonic activity, and its signal is found in ice-cores, ocean sediments, and coral (Section 7.2.2). The 209-yr SdV cycle is expressed in both solar and lunar declination patterns (Sections 4.4.1, 7.2.2, and 7.2.3).

Variability in the ~1500-yr quasi-periodicity depends upon a number of contributing factors, and can result from a combination of perihelion, Metonic lunation or eclipse, and perigee, or individually from the perihelion or Moon (Section 7.2.5). Each of the constituent climate cycles is evident in the palaeoclimatic record (Section 2.2.3 and Chapter 7). The strength of their expression is dependent upon proximity to the maximum gravitational forcing, insolation, and solar irradiance (Chapter 5). For example, the Metonic Moon's interaction with perihelion produces cyclical patterns that are found in ice-cores and deep-sea sediments at the millennial-scale (Section 7.2.5). These varying patterns are found in different glaciological chronologies such as SS09SEA (Section 7.2.5). The timing of relative perigee to the perihelion, close to total solar eclipses, occurs contemporaneously with Bond IRD events. Just as the timing of the perihelion has an impact on the annual spring tide

(Section 3.1.4), its long-term influences are felt at various time intervals (Section 7.2.5). The strongest of these occur at ~1868-yrs and 1375-yrs [Figure 4.3]. The 1375-yr expression of the Bond cycle during the Holocene is clearly sufficient on its own to leave a weak impression on deep-sea records.

Location also influences the length and timing of events. For example, speleothems and ice-cores depend upon precipitation (Section 3.2.3). Whilst these patterns are induced globally by the latitudinal gradient between equator and poles (cf. Davis and Brewer, 2011), precipitation is also very much influenced by regional geographics such as orographic rain, which is caused by moisture-laden air meeting a mountain, forcing it to rise (Arbogast, 2014). In the tropical Pacific, a more immediate and influential response to precessional signals might be expected because of ENSO's sensitivity to heat distribution (Hou and Lindzen, 2002) and tropical response to solar variability (Gray *et al.,* 2010). However, the response of gravitational forcing on oceanic tides and the thermohaline circulation takes longer to implement (cf. Taylor and Bar Yosef, 2014). The thermohaline current is continuously being driven by heat and gravity, and is therefore sensitive to gravitational and solar flux, and local changes in insolation patterns (Section 2.2.1, Chapter 3). Temperature affects the sequestration and release of CO_2 into and from the ocean, especially in key, sensitive regions such as the tropics and Arctic/Antarctic Circles (Lorenzo *et al.*, 2008). In these terms, it can then be understood why ^{14}C deposition lags ^{10}Be deposition (Bard *et al*., 1997), and why Metonic lunation and perihelion cycles are found in the Δr values of marine reservoir figures (see Section 8.2.2). It also assists in understanding the lag between CO_2 patterns and the astronomical events that precipitated them.

Whilst correlation does not equal causation, this research started with a theory from which a testable hypothesis was formed and statistically assessed (Chapter 6). The predicted pattern of insolation based on modelled astronomical cycles associated with the Metonic lunation and perihelion was statistically-significant and strongly correlated with TSI reconstruction from Antarctic ^{10}Be data. A chain of evidence linked this model with astronomical forcing (Chapters 4-6), starting with the justification of astronomical variables, trigonometric modelling of those variables, astronomical data based on the Metonic lunation, and physical models of solar irradiance, insolation and gravitation. These means provided an understanding of the mechanism driving the implementation of astrophysical forces within Earth's climate system, as well as an explanation in physical terms for various component climate signals that are found in palaeoclimatic data (Section 2.2.3 and Chapter 7). These results also support previous theories that some combination of astronomical forcing involving the Sun are responsible for the 1-2-ky climate signals (e.g., Bond *et al.,* 1999; Braun *et al.*, 2005). In the absence of a better theory, this mechanism offers a detailed explanation and understanding where none previously existed. The results presented here suggest that precession causes the ~1500-yr quasi-periodicity through the combined interaction of Earth, Moon, and Sun.

Through astronomical forcing of this millennial-scale signal, the seemingly contradictory characteristics can be understood: the simultaneous forcing of Arctic and Antarctic regions and the bipolar nature of these reactions (Chapter 2).

Essentially, the ~1500-yr quasi-periodicity can be seen as the separation of anomalistic and tropical years, as the perihelion moves relative to the equinoxes and solstices. These patterns are a high-frequency expression of the Milankovitch precessional cycle, created by equinoctial and apsidal precessions. The Moon plays an important role in shaping patterns of insolation and TOA solar irradiance, where inferences previously attributed these patterns solely to the solar wind modulation of cosmic rays. This previously unrealised lunar role has important implications for long-term solar irradiance reconstruction, both in reliance upon cosmogenic isotopes as indicators of sunspot activity, and the precessional influence on chronometry and geochronology. The discovery of the Metonic eclipse series is also an important contribution to knowledge from this research.

8.2 Future Research

Stemming from this PhD project, a number of avenues for future research are apparent. Immediately obvious is research into the effects of precession (Section 8.2.1), radiometric dating, and chronological variability (Section 8.2.2). With links of astronomical forcing to millennial-scale ENSO variability, an obvious avenue of research would be to investigate the roles of the perihelion and Metonic lunation in ENSO activity at interannual and decadal scales. Additionally, the connection between 133-yr cycles of climate variability and the solar declination cycle were shown here to produce substantial variations in latitudinal insolation with the capacity to influence abrupt climate change and extreme climate events. Solar declination is essentially a proxy for the time of year in relation to the seasons. Further research into these associations with different climate datasets of fire patterns, precipitation, SST, and cyclonic activity would assist in better understanding this cycle.

Evidence presented here suggests that the lunar modulation of solar irradiance patterns is the cause of the SdV and Gleissberg cycles. As both are inferred solar cycles, further investigation of these two cycles and the 57-yr cycle of climate change would assist in better understanding radiocarbon chronological and solar variability. Of particular interest is, how does precession affect patterning of cosmogenic data through deep time? Can this throw further light on the 400-ky eccentricity cycle? Are the 11.4-yr cycles associated with precession and the Schwabe sunspot cycle linked and, if so, how? By taking into consideration the impact of precession on solar insolation, how does this affect our understanding of modern climate warming? There is a potential to utilise further palaeoclimatic data as it emerges to test the cycles explored in this thesis, the model, and astronomical data, in particular using high-resolution ITRAX data with strong age control.

The development of planetarium software to aid in the investigation of climate change beyond the Holocene would facilitate the extension of this study of astronomical forcing into the deep past, but could also serve as a predictive tool for future climate change. Such a tool would more readily permit research into Bond, Dansgaard-Oeschger, and Heinrich events, as well as the Milankovitch cycles. It is also feasible that these astronomical cycles could be used in the long-term calibration of ice-cores and deep-sea cores beyond the limits of dendrochronological calibration and fragmented and floating portions of coral records. An external, independent, reference system, such as astronomical markers, would be an invaluable asset in calibration.

8.2.1 Precession and chronometry

The capability of the Moon to modify solar irradiance signals is clearly evident from its roles in the Milankovitch obliquity and precessional cycles. It stabilises Earth's axial tilt, creating the seasons, and produces a slight wobbling of the axis (nutation) (Section 3.1.4). Its cycles are evident in tidal sedimentation patterns and ice-core data at various scales (Chapter 2). From evidence presented here (Chapter 5), the Moon is responsible for extreme swings in insolation patterns at extreme latitudes at the bidecadal, centurial, and millennial-scales, as well as extreme gravitational effects that produce ice-rafting debris events. However, the Moon's connection with the tropical year is not precisely replicated (at 18.9998 Julian years or 19.0002 tropical years), resulting in the movement of the Metonic lunation through the zodiacal belt (seasonal year) over a period of at least 90 ky [Figure 5.3]. The quarterly movement of the Metonic lunation [Figure 5.3] is equivalent to the Milankovitch precessional cycle, where it regularly interacts with the moving perihelion [Figure 5.4]. From Figure 5.4, it can also be seen that the perihelion movement through the entire zodiacal belt is the same as the Milankovitch precessional cycle, which is hardly surprising since it is the interaction of the equinoctial and apsidal precessions, otherwise represented as the separating tropical and anomalistic years from a common starting point. The quarterly movement of the perihelion relative to the zodiacal belt marks the positions where it interacts with each of the solstices and equinoxes in turn.

Table 8.1: Rates of perihelion movement through the tropical year, based on three variants of the Milankovitch cycle length.

Milankovitch cycle variants (ky)	19 ky	21 ky	23 ky
per 30° (30 days)	1583.33 yrs	1750.00 yrs	1916.67 yrs
per day (tropical year)	52.02 yrs	57.50 yrs	62.97 yrs
per 7 days	364.14 yrs	402.5 yrs	440.78 yrs
per synodic month (29.53 days)	1536.15 yrs	1697.98 yrs	1859.50 yrs

The semi-precessional cycle is half of the perihelion movement, whilst quarterly movement occurs at ~5.25 ky. The quarterly movement of the Metonic movement through 30° of the zodiacal belt occurs in the vicinity of ~7.5 ky. Each 30° represents 1/12 of the seasonal year or approximately one calendar month. The 6.1-ky mean periodicity for the occurrence of Heinrich events with a range of ~5-7 ky

(Mayewski *et al.*, 1997) is not strictly periodic (Bond *et al.,* 1999); it's boundaries seem to be related by the relationships of the perihelion and Metonic lunation to each other and the tropical year (Figures 5.4 and 5.4). Similarly, the perihelion's movements through these 30° segments of the zodiacal belt takes between ~1,700 yrs to ~1,864 yrs to complete in a 21-ky cycle [Table 8.1]. This latter timeframe is in the range of the ~1500-yr quasi-periodicity, showing a connection between the Milankovitch precessional cycle and millennial-scale climate patterns that vary through time.

However, the Milankovitch precessional cycle is itself quasi-periodic, with variants of ~19 ky and ~23 ky (Berger, 2009). Consequently, the lengths of time of the moving perihelion through each month varies [Table 8.1], such that the range through the ~19 ky cycle produces millennial scale quasi-periodicities of 1536 yrs (synodic month, from New Moon to New Moon). At the ~23-ky scale the value is ~1860 yrs [Table 8.1]. Taking into consideration variability due to the 209-yr cycle, the lower range of Bond events can occur at 1328 yrs and higher at 2069 yrs [Table 8.1]. In fact, a 1328-yr Bond periodic mean occurred during 31-43 kya [Table 7.2]. The upper range for Bond events (relative to the 23 ky cycle) that occurred during the last 80 ky was during 64-79 kya (with a mean periodicity of 1795 yrs), within 65 yrs of the upper limit for the synodic month. As previously discussed, the rate of precessional movement will vary based upon (i) the interaction between the apsidal and tropical precessions [Figure 3.15], (ii) eccentricity and radius of orbit (Section 3.1.1), and (iii) position of the perihelion within the tropical year (Section 3.1.1).

These patterns provide an overview over a vast period of time into the nature of precession that has been discussed in detail in relation to the 5.5-ky period of astronomical data. They also hint that the lunar progression through the tropical zodiacal belt (~90-ky long) [Figure 5.3] may play an important role in determining cycles of glaciation and deglaciation (see following). It has been suggested that eccentricity does not drive this cycle for a few reasons. Firstly, the capacity of 0.2% variation in insolation due to this cycle was seen as insufficient to do so (Frakes *et al.,* 1992 cited in Summerhayes, 2015). However, TOA solar irradiance varies by 23.2% throughout the year at maximum eccentricity, compared to the current 6.4% annual variation (Berger, 2009), and 2% at minimum eccentricity [Table 5.5]. At current eccentricity, evidence presented here (Sections 5.4, 7.2.2, 7.2.3, and 7.2.4) shows that latitudinal variations in insolation create swings greater than and equivalent to those produced by sunspot activity. The lack of sunspot activity during the LIA has been linked to the extremely cold conditions experienced during that time. As such, this evidence shows that eccentricity has the capacity to produce cycles of glaciation/deglaciation during times (*contra* Frakes *et al.,* 1992) when the annual variance in insolation was greater than now.

However, other factors still create doubt as to the capacity of Earth's 100-ky orbital eccentricity cycle to cause the glaciation/deglaciation cycle. A lack of linear correlation between the glacial cycles and

eccentricity is a problem (cf. Berger, 2009 cited by Summerhayes, 2015). Additionally, the beat of the cycle is not strictly 100 ky, varying between 82 ky to 123 ky (Cronin, 2010 cited in Summerhayes, 2015), with implications that something else is at play, such as precession and obliquity. On the basis of oxygen isotope stratigraphy, Huybers (2007), also concluded that eccentricity did not drive the glacial cycle. Rather, Huybers thought that there was an underlying mechanism driving the cyclicity evidenced in the record (Huybers, 2007 cited in Summerhayes, 2015). Whilst the literature shows that a connection to CO_2 and the oceans plays an important role in glaciation/deglaciation cycles, the exact nature of that relationship is not fully understood (Summerhayes, 2015).

The Metonic lunation movement through the tropical year takes ~90 ky, and plays an influential role in climate and precession. Influencing seasons, tides, and potentially radiocarbon chronological variability and CO_2 processes (Section 7.4), the Moon is a likely candidate for a role in the variable ~100-ky glacial/interglacial cycle. With the Milankovitch precessional cycle shaping eccentricity (Berger 2009), such a candidacy is reinforced. Just as the Milankovitch precessional cycle results from the interacting astronomical forces, ~100-ky eccentricity cycle is likely to result from multiple astronomical contributors (cf. Moss, 1999).

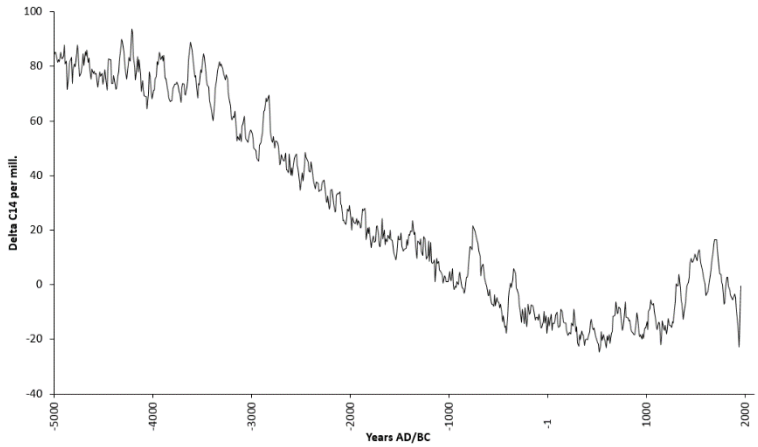

Figure 8.1: Intcal98 radiocarbon calibration curve (Stuiver *et al.*, 1998), showing flattened period of radiocarbon variability coincident with suppressed solar declination. Intcal98 data accessed at UW Quaternary Isotope Laboratory (1999).

Apart from the modulation of climate patterns at Milankovitch scales, evidence presented here shows that the Moon also plays a role in the modulation of insolation at centurial scales. Its role in the Gleissberg and 209-yr SdV cycles has already been discussed (Section 7.2.3), where these cycles have been thought of as purely sunspot cycles despite no evidence of them in sunspot data. The Moon also produces a 133-yr cycle that is closely linked to precession, which is seen in Earth-Sun and Earth-Moon distances and in solar declination patterns (Section 7.2.2). This evidence also shows that patterns in radiometric chronological variability are affected by the Moon and its dominant influence

on precession, namely through repressed SdV activity in the 2nd millennium BC [Figure 3.22] (Stuiver *et al.,* 1998). During this same period, solar declination activity is also repressed, stifling the expression of 133-yr and 209-yr cyclicity [Figure 7.5]. At this time, solar declination changes by <1' of arc. The limited declination movement occurs because the day on which the Metonic lunation falls is the December solstice, where the limit of solar declination is reached [Figures 7.5, 8.1, and 8.2]. As the Metonic lunation moves away from the December solstice, the changes in solar declination are greater [Figure 7.5]. Latitudinal insolation patterns are dependent upon solar declination [Figures 5.24 to 5.28].

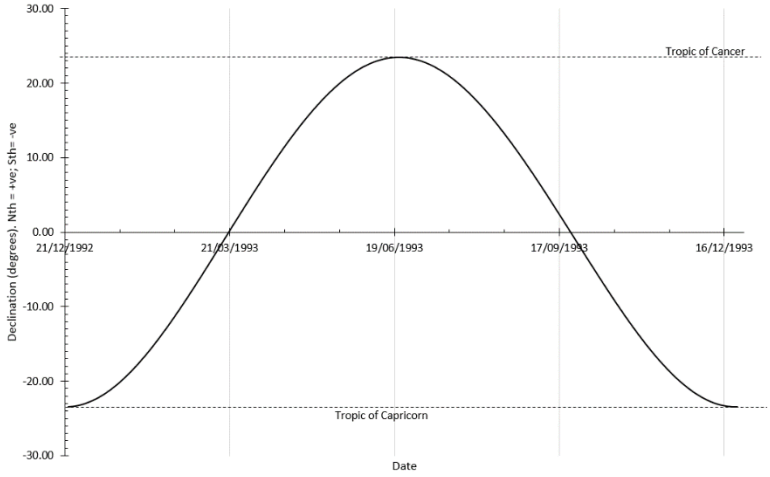

Figure 8.2: Annual pattern of solar declinations during 1993.

These 133-yr and 209-yr cycles, which both show lunar influence, interact to produce the 1474-yr cycle correlated to TOA solar irradiance variations (Chapter 6, Section 7.2.5). There was a precessional adjustment of 11.4 yrs to this combination cycle. This 11.4-yr periodic adjustment is required every 1463-yrs due to the precessional separation of the equinox from the Julian calendar. The question arises about possible connections to the Schwabe sunspot cycle, with a mean periodicity of 11.4 yrs and a range of 9-14 yrs (Wang *et al.,* 2005). Both the sunspot cycle and this precessional separation influence patterning of solar irradiance signals. There may be no connection, or it may simply be that this is an expression of the solar wind influence on Earth's rotation (Morner, 2013), linking the precessional influence and sunspot cycle. All of these questions relating to precession need to be explored through future research.

8.2.2 Radiometric dating and chronological variability

The modelled superposition of the 133-yr and 209-yr cycles replicated patterning in cosmogenic isotopes (^{10}Be) found in Antarctic ice-core data (Bard *et al.*, 2007), with the correlation improved when the model was adjusted for precession. Evidence of lunar influence on the 133-yr, SdV, and Bond cycles was also presented here. Fundamental to these astronomical patterns is the 19-yr Metonic

lunation, as a proxy for the tropical year. Through the Metonic cycle, the monthly lunar cycle and annual solar cycles (and their respective climatic influences) are integrated. The modelled activity links lunar influence to the Bard *et al.* (1997) Antarctic data. Metonic lunation patterns, interacting with the perihelion, can also be seen in Greenland ice core chronology (Section 7.2.5). The Bard *et al.* (2007) reconstruction evidenced matching patterning of ^{14}C and ^{10}Be production, showing a delay of 15-20 yrs between the two isotope deposition patterns [Figure 3.24]. On this basis, it is possible to see how the Metonic lunation cycle can be associated with the 15-20-yr delay in ^{14}C deposition.

Variations in the lengths of the Bond cycles and associated error margins can be linked with solar and lunar astronomical forcing, in which the Moon plays an important role (Section 7.2.5). The 1474-yr cycle produced by these astronomical factors appears to impact solar irradiance and insolation levels [Table 8.2]. In this table, the ±1σ margins in the length of the Bond cycles are compared to potential cyclical relationships with the perihelion, perigee, sunspot, Metonic, Gleissberg, and SdV cycles, but also specifically includes the Metonic eclipse series (the last three columns). The perigee-perihelion conjunction cycle included in this table is the modelled 289-yr cycle depicted in Figure 5.15. Here, it can be seen that the perigean-perihelion conjunction cycle is a major influence in variation of the mean 1476-yr Bond cycle during the last Glacial. All the deviations of the Bond cycle from the mean value can be attributed to combinations of astronomical variables that trigger events. Except in periods shorter than 57-yrs, precessional influences are present in the remaining cycle and therefore show the influence of precession on radiocarbon variation.

Table 8.2: Variations in Bond cycle lengths as factors of various astronomical cycles.

Period		Cycle length (Mean)	Cycle var. ±1σ in years	Cyclical relationships to 1σ var.															
				11.4-yr	18.63-yr	19-yr	22.8-yr	57-yr	76-yr	95-yr	RRA	RRT	133-yr	SdV	228-yr	289-yr	418-yr	456-yr	493-yr
Holocene	1.5-12ka	1374	502	x	x		x					x						x	x
Late Glacial	12-32ka	1537	558	x	x											x			
Early Glacial	32-75ka	1478	458			x	x	x	x						x		x	x	x
12ka steps	13-24ka	1494	624					x			x			x					
	22-34ka	1631	511			x		x				x							x
	31-43ka	1328	539		x				x				x						x
	43-55ka	1350	302			x			x							x			
	53-64ka	1443	470							x					x			x	x
	64-79ka	1795	425								x			x			x	x	
Holo+Glacial	0-79ka	1469	514	x		x		x			x	x							x
Glacial	15-65ka	1476	585													x			

Implications for radiocarbon chronological variability can be found in these astrophysical cycles. Firstly, it is clear that the uncalibrated radiocarbon dates are affected by precession, whilst calibrated dates account for precession. Because the systemic errors in the determination of the ^{14}C half-life are

greater than the error between the lengths of the tropical and Julian years (Section 3.2), it is not possible to produce raw radiocarbon dates that are calibrated. Radiocarbon calibration is achieved through external references to data with annual resolution such as dendrochronological and coral data (Section 3.2). The SdV cycle was first detected in relation to radiocarbon dating through dendrochronological calibration of the radiocarbon signal (Suess, 1986). The 104-yr spectral peak that also appears in dendrochronological data, is half the length of the SdV cycle and was classed as an "overtone" (Damon and Sonett, 1991; Damon and Peristykh, 2004:243). However, this 104-yr period is also the value of the RRA, showing a regional (longitudinal) connection to the perihelion at centurial scales, with the Metonic lunation accentuating this connection at the SdV length (Section 7.2.3) with increased tidal forcing.

It is well-established that the annual spring tide at the time of the perihelion produces peak tides (Chapter 3). These peaks of tidal influence are evident in tidal sedimentation patterns and radiocarbon chronological patterns. For example, the ~1800 tidal pattern (Bond *et al.,* 1999; Keeling and Whorf, 2000; Petterson, 1930) is also associated with the tightest RRA return [Table 4.3], indicating stronger tidal forcing and insolation regionally (along the length of the meridian of longitude). It is a logical step, therefore, to associate a precise return of the RRA at 418 tropical years (which occurs with a solar eclipse) with the general Δr value of the open ocean (420yrs). This 420-yr period forms a significant MEM spectral peak in radiocarbon data [Figure 2.15] (Stuiver and Braziunas, 1989). The Δr value in calibrating dates is to account for the marine reservoir effect on marine samples during the Holocene (cf. Hua *et al.*, 2015).

Table 8.3: Correspondences between Marine Reservoir Δr values and astronomical data. Δr values from Hua *et al*., 2015.

Δr value	Region	Similarities in astronomical data	Comments
920yrs	SE Pacific	Lunar declination cycle of 912yrs [Figure B.9 in Appendix B] at apogee [Figure 5.12] and increased Earth-Sun distance [Figure 5.10]	Occurs at places of strongest upwellings off the Peruvian coast, which is associated with ENSO variability
640yrs	PNG	627-yr interval in Earth-Sun data [Figure 5.10] of changes in gravitational variability	627yrs is a multiple of the SdV cycle. 640yrs could conceivably be a multiple of the SdV cycle (3x213.33)
420yrs	General ocean	Equals 2 SdV cycles based on lunar declination cycle in Metonic lunation data. Within range of 456±38yrs Metonic eclipse cycle.	
410yrs	SW Pacific (Heron Reef and Moreton Bay)	Equals to 2 SdV cycles based on lunar declination data.	
390yrs	SCS	380yr interval in apogee data in association with increased Earth-Sun distances [Figures 5.12 and 5.10].	Values around 400yrs may be variations of the astronomically based 133yr and associated 95yr artefact

Marine reservoir values are used to adjust radiocarbon-dated material derived from marine sources, which are generally older than contemporary terrestrial counterparts (Hua *et al.,* 2015). These values are the difference (Δr) between contemporaneous terrestrial and surface ocean material, and are generally assumed constant for different regions. However, marine Δr used in the adjustment of radiocarbon dates were shown to be variable (Hua *et al.,* 2015). Variations in these reservoir values result from interaction between surface ocean, deeper ocean waters, and the atmosphere. Some of the values for different regions of the Δr in the Pacific Ocean (measured from trough to peak) are shown in Table 8.3. This table also shows associations with astronomical cycles. With warmer conditions and stronger ocean currents there is greater upwelling of old carbon, increasing the age difference and Δr values (Hua *et al.,* 2015). These associations suggest that forcing of oceanic tides by the Sun and Moon contribute to radiocarbon chronological variability. Such matters also require further research to establish this link.

Reference List

ABREU, J. A., BEER, J., FERRIZ-MAS, A., MCCRACKEN, K. G. & STEINHILBER, F. 2012. Is there a planetary influence on solar activity? *Astronomy & Astrophysics,* 548**,** A88.

ADHÉMAR, J. 1842. *Révolution des mers, Déluges périodiques.,* Paris, Privately published.

AGASSIZ, L. 1838. Upon glaciers, moraines, and erratic blocks. *New Philosophical Journal,* 24**,** 364-383.

AGASSIZ, L. 1840. *Etudes sur les Glaciers,* Neuchatel, Privately published.

ALLEY, R. B., ANANDAKRISHNAN, S. & JUNG, P. 2001. Stochastic resonance in the North Atlantic. *Paleoceanography,* 16**,** 190-198.

ANDERSEN, K. K., AZUMA, N., BARNOLA, J. M., BIGLER, M. & NORTH GREENLAND ICE CORE PROJECT, M. 2004. High-resolution record of Northern Hemisphere climate extending into the last interglacial period. *Nature,* 431**,** 147-151.

ANDERSON, A., CHAPPELL, J., GAGAN, M. & GROVE, R. 2006. Prehistoric maritime migration in the Pacific islands: an hypothesis of ENSO forcing. *The Holocene,* 16**,** 1-6.

ARBOGAST, A. 2014. *Discovering Physical Geography, 3rd Edition,* Beaverton, Ringgold Inc.

ARNOLD, J. R. & LIBBY, W. F. 1949. Age determinations by radiocarbon content: checks with samples of known age. *Science,* 110**,** 678-680.

ASHKENAZY, Y., EISENMAN, I., GILDOR, H. & TZIPERMAN, E. 2010. The effect of Milankovitch variations in insolation on equatorial seasonality. *Journal of Climate,* 23**,** 6133-6142.

ATTOLINI, M., CECCHINI, S., GALLI, M. & NANNI, T. 1990. On the persistence of the 22 yr solar cycle. *A Journal for Solar and Solar-Stellar Research and the Study of Solar Terrestrial Physics,* 125**,** 389-398.

B.O.M. n.d.a. *Southern Oscillation Index* [Online]. Available: http://www.bom.gov.au/climate/glossary/soi.shtml [Accessed May 15, 2014].

B.O.M. n.d.b. *The Three Phases of the El Nino-Southern Oscillation Index* [Online]. Available: http://www.bom.gov.au/climate/enso/history/ln-2010-12/three-phases-of-ENSO.shtml [Accessed May 15, 2014].

B.O.M. n.d.c. *About ENSO Outlooks* [Online]. Available: http://www.bom.gov.au/climate/ahead/about-ENSO-outlooks.shtml [Accessed May 15, 2014].

BABCOCK, H. D. 1959. The sun's polar magnetic field. *The Astrophysics Journal,* 130**,** 364-365.

BAKER, R. H. 1959. *Astronomy: A Textbook for University and College Students,* Princeton, New Jersey, D. Van Nostrand Co.

BALTER, M. 2007. Seeking agriculture's ancient roots. *Science,* 316**,** 1830-1835.

BAMBER, J. 2001. *Greenland 5 km DEM, Ice Thickness, and Bedrock Elevation Grids*. Boulder, Colorado USA: NASA DAAC at the National Snow and Ice Data Center.

BANDERAS, R., ALVAREZ-SOLAS, J., ROBINSON, A. & MONTOYA, M. 2015. An interhemispheric mechanism for glacial abrupt climate change. *Climate Dynamics,* 44**,** 2897-2908.

BARD, E., HAMELIN, B., ARNOLD, M., MONTAGGIONI, L., CABIOCH, G., FAURE, G. & ROUGERIE, F. 1996. Deglacial sea-level record from Tahiti corals and the timing of global meltwater discharge. *Nature,* 382**,** 241-244.

BARD, E., HAMELIN, B. & FAIRBANKS, R. G. 1990a. U-Th ages obtained by mass spectrometry in corals from Barbados: sea level during the past 130,000 years. *Nature,* 346**,** 456-458.

BARD, E., HAMELIN, B., FAIRBANKS, R. G. & ZINDLER, A. 1990b. Calibration of the 14C timescale over the past 30,000 years using mass spectrometric U-Th ages from Barbados corals. *Nature,* 345**,** 405-410.

BARD, E., RAISBECK, G., YIOU, F. & JOUZEL, J. 1997. Solar modulation of cosmogenic nuclide production over the last millennium: comparison between 14C and 10Be records. *Earth and Planetary Science Letters,* 150**,** 453-462.

BARD, E., RAISBECK, G., YIOU, F. & JOUZEL, J. 2000. Solar irradiance during the last 1200 years based on cosmogenic nuclides. *Tellus B,* 52**,** 985-992.

BARD, E., RAISBECK, G., YIOU, F. & JOUZEL, J. 2003-2007. Reconstructed Solar Irradiance Data. *In:* BARD, E., RAISBECK, G., YIOU, F. & JOUZEL, J. (eds.). IGBP PAGES/World Data Center for Paleoclimatology, NOAA/NGDC Paleoclimatology Program, Boulder CO, USA. .

BARD, E., RAISBECK, G. M., YIOU, F. & JOUZEL, J. 2007. Comment on "Solar activity during the last 1000 yr inferred from radionuclide records" by Muscheler et al. (2007). *Quaternary Science Reviews,* 26**,** 2301-2304.

BASSINOT, F. C., LABEYRIE, L. D., VINCENT, E., QUIDELLEUR, X., SHACKLETON, N. J. & LANCELOT, Y. 1994. The astronomical theory of climate and the age of the Brunhes-Matuyama magnetic reversal. *Earth and Planetary Science Letters,* 126**,** 91-108.

BATCHELOR, C. R., BRANCH, N. P., ALLISON, E. A., AUSTIN, P. A., BISHOP, B., D. BROWN, A., ELIAS, S. A., GREEN, C. P. & YOUNG, D. S. 2014. The timing and causes of the Neolithic elm decline: New evidence from the Lower Thames Valley (London, UK). *Environmental Archaeology,* 19**,** 263-290.

BAYLISS, A. 2009. Rolling out revolution: using radiocarbon dating in archaeology. *Radiocarbon,* 51**,** 123-147.

BEER, J., ANDREE, M., OESCHGER, H., SIEGENTHALER, U., BONANI, G., HOFMANN, H., MORENZONI, E., NESSI, M., SUTER, M., WÖLFLI, W., FINKEL, R. & LANGWAY, C. 1984. The camp century 10Be record: Implications for long-term variations of the geomagnetic dipole moment. *Nuclear Instruments and Methods in Physics Research Section B: Beam Interactions with Materials and Atoms,* 5**,** 380-384.

BENDER, M., FAIRBANKS, R., TAYLOR, F., MATTHEWS, R., GODDARD, J. & BROECKER, W. 1979. Uranium-series dating of Pleistocene reef tracts of Barbados, West Indies. *Geological Society of America Bulletin,* 90**,** 577-594.

BENGTSON, H. 1968. *The Greeks and the Persians: from the sixth to the fourth centuries,* London, George Weidenfeld and Nicholson Ltd.

BERGER, A. 1977. Support for the astronomical theory of climatic change. *Nature,* 269**,** 44-45.

BERGER, A. 1991. Long-term history of climate ice ages and Milankovitch periodicity. *In:* SONETT, C. G., M., MATTHEWS, M. (ed.) *The Sun in Time.* Tucson: University of Arizona.

BERGER, A. 2009. Astronomical Theory of Climate Change. *In:* GORNITZ, V. (ed.) *Encyclopedia of Paleoclimatology and Ancient Environments.* Dordrecht: Springer Netherlands.

BERGER, A., LOUTRE, M. F. & DEHANT, V. 1989a. Astronomical frequencies for pre-Quaternary palaeoclimate studies. *Terra Nova,* 1**,** 474-479.

BERGER, A., LOUTRE, M. F. & DEHANT, V. 1989b. Influence of the changing lunar orbit on the astronomical frequencies of pre-Quaternary insolation patterns. *Paleoceanography,* 4**,** 555-564.

BERGER, A., LOUTRE, M. F. & MÉLICE, J. L. 2006. Equatorial insolation: from precession harmonics to eccentricity frequencies. *Climate of the Past,* 2**,** 131-136.

BERGER, W. H. & WEFER, G. 2013. On the Dynamics of The Ice Ages: Stage-11 Paradox, Mid-Brunhes Climate Shift, and 100-Ky Cycle. *Earth's Climate and Orbital Eccentricity: The Marine Isotope Stage 11 Question.* American Geophysical Union.

BERGLUND, B. E. 2003. Human impact and climate changes—synchronous events and a causal link? *Quaternary International,* 105**,** 7-12.

BIAGIONI, S., KRASHEVSKA, V., ACHNOPHA, Y., SAAD, A., SABIHAM, S. & BEHLING, H. 2015. 8000 years of vegetation dynamics and environmental changes of a unique inland peat ecosystem of the Jambi Province in Central Sumatra, Indonesia. *Palaeogeography, Palaeoclimatology, Palaeoecology,* 440**,** 813-829.

BLAAUW, M. 2012. Out of tune: the dangers of aligning proxy archives. *Quaternary Science Reviews,* 36**,** 38-49.

BLAAUW, M., HEUVELINK, G. B. M., MAUQUOY, D., VAN DER PLICHT, J. & VAN GEEL, B. 2003. A numerical approach to 14C wiggle-match dating of organic deposits: best fits and confidence intervals. *Quaternary Science Reviews,* 22**,** 1485-1500.

BLAAUW, M., VAN GEEL, B. & VAN DER PLICHT, J. 2004. Solar forcing of climatic change during the mid-Holocene: indications from raised bogs in The Netherlands. *The Holocene,* 14**,** 35-44.

BLACKFORD, J. & CHAMBERS, F. 1991. Proxy records of climate from blanket mires: evidence for a Dark Age (1400BP) climatic deterioration in the British Isles. *The Holocene,* 1**,** 63-67.

BLACKMAN, A., S., BOTTLE, S. S., MOCERINO, M., WILLE, U., BRADY, J., SENESE, F., BROWN, W., POON, T., OLMSTED III, J. & WILLIAMS, G. 2008. *Chemistry,* Brisbane, John Wiley and Sons Australia Ltd.

BLACKWELL, P. & BUCK, C. 2008. Estimating radiocarbon calibration curves. *Bayesian Analysis,* 3**,** 225-248.

BLOIS, J. L., ZARNETSKE, P. L., FITZPATRICK, M. C. & FINNEGAN, S. 2013. Climate change and the past, present, and future of biotic interactions. *Science,* 341**,** 499.

BLUNIER, T. & BROOK, E. J. 2001. Timing of Millennial- Scale Climate Change in Antarctica and Greenland During the Last Glacial Period.(Statistical Data Included). *Science,* 291**,** 109.

BOND, G., KROMER, B., BEER, J., MUSCHELER, R., EVANS, M. N., SHOWERS, W., HOFFMANN, S., LOTTI-BOND, R., HAJDAS, I. & BONANI, G. 2001. Persistent solar influence on North Atlantic climated during the Holocene. *Science,* 294**,** 2130-2136.

BOND, G., SHOWERS, W., CHESEBY, M., LOTTI, R., ALMASI, P., DEMENOCAL, P., PRIORE, P., CULLEN, H., HAJDAS, I. & BONANI, G. 1997. A pervasive millennial-scale cycle in North Atlantic Holocene and Glacial climates. *Science,* 278**,** 1257-1266.

BOND, G. C., SHOWERS, W., ELLIOT, M., EVANS, M., LOTTI, R., HAJDAS, I., BONANI, G. & JOHNSON, S. 1999. The North Atlantic's 1-2 Kyr Climate Rhythm: Relation to Heinrich Events, Dansgaard/Oeschger Cycles and the Little Ice Age. *Mechanisms of Global Climate Change at Millennial Time Scales.* American Geophysical Union.

BOWEN, A. 2013. Kallippos, astronomer. *In:* BAGNALL, R. S., BRODERSEN, K., CHAMPION, C. B., ERSKINE, A. & HUEBNER, S. R. (eds.) *The Encyclopedia of Ancient History.* 1st Edition ed.: Blackwell Publishing Ltd.

BOWLER, S. 2009. Archaeology and astronomy. *Astronomy and Geophysics,* 50.

BOWMAN, S. 1990. *Interpreting the Past: Radiocarbon Dating,* Berkeley, University of California Press.

BRANCH, N., CANTI, M., CLARK, P. & TURNEY, C. 2005. *Environmental Archaeology: Theoretical and Practical Approaches,* London; New York, London: Hodder Arnold; New York: Distributed in the United States by Oxford University Press.

BRAUN, H., CHRISTL, M., RAHMSTORF, S., GANOPOLSKI, A., MANGINI, A., KUBATZKI, C., ROTH, K. & KROMER, B. 2005. Possible solar origin of the 1,470-year glacial climate cycle demonstrated in a coupled model. *Nature,* 438**,** 208-211.

BREITENMOSER, P., BEER, J., BRONNIMANN, S., FRANK, D., STEINHILBER, F. & WANNER, H. 2012. Solar and volcanic fingerprints in tree-ring chronologies over the past 2000 years. *Palaeogeography, Palaeoclimatology, Palaeoecology,* 313-314**,** 127.

BROECKER, W. 2009. The mysterious 14C decline. *Radiocarbon,* 51**,** 109-119.

BROECKER, W. S. 1998. Paleocean circulation during the Last Deglaciation: A bipolar seesaw? *Paleoceanography,* 13**,** 119-121.

BROECKER, W. S. 2003. Does the trigger for abrupt climate change reside in the ocean or in the atmosphere? *Science,* 300**,** 1519-1522.

BROECKER, W. S. & HENDERSON, G. M. 1998. The sequence of events surrounding Termination II and their implications for the cause of glacial-interglacial CO2 changes. *Paleoceanography,* 13**,** 352-364.

BROECKER, W. S. & THURBER, D. L. 1965. Uranium-series dating of corals and oolites from Bahaman and Florida Key limestones. *Science,* 149**,** 58-60.

BROECKER, W. S., THURBER, D. L., GODDARD, J., KU, T.-L., MATTHEWS, R. K. & MESOLELLA, K. J. 1968. Milankovitch hypothesis supported by precise dating of coral reefs and deep-sea sediments. *Science,* 159**,** 297-300.

BROECKER, W. S. & VAN DONK, J. 1970. Insolation changes, ice volumes, and the O18 record in deep-sea cores. *Reviews of Geophysics,* 8**,** 169-198.

BUTT, Y. 2009. Beyond the myth of the supernova-remnant origin of cosmic rays. *Nature,* 460**,** 701-704.

CALLAWAY, E. 2012. Core sample sends carbon clock farther back in time. *Nature News*.

CAPRON, E., LANDAIS, A., CHAPPELLAZ, J., SCHILT, A., BUIRON, D., DAHL-JENSEN, D., JOHNSEN, S. J., JOUZEL, J., LEMIEUX-DUDON, B., LOULERGUE, L., LEUENBERGER, M., MASSON-DELMOTTE, V., MEYER, H., OERTER, H. & STENNI, B. 2010. Millennial and sub-millennial scale climatic variations recorded in polar ice cores over the last glacial period. *Climate of the Past,* 6**,** 345-365.

CARTWRIGHT, D. E. 1974. Years of peak astronomical tides. *Nature,* 248**,** 656-657.

CHAMBERS, D. P., MERRIFIELD, M. A. & NEREM, R. S. 2012. Is there a 60-year oscillation in global mean sea level? *Geophysical Research Letters,* 39**,** 1-6.

CHAPPELL, J. 1973. Astronomical theory of climatic change: status and problem. *Quaternary Research,* 3**,** 221-236.

CHAPPELL, J. 1974. Geology of coral terraces, Huon Peninsula, New Guinea: a study of Quaternary tectonic vovements and sea-level changes. *The Geological Society of America Bulletin,* 85**,** 553-570.

CHARBONNEAU, P. 2005. Dynamo models of the solar cycle. *Living Reviews in Solar Physics,* 2.

CHARBONNEAU, P. 2013. Solar physics: the planetary hypothesis revived. *Nature,* 493**,** 613-614.

CHIU, T.-C., FAIRBANKS, R. G., CAO, L. & MORTLOCK, R. A. 2007. Analysis of the atmospheric 14C record spanning the past 50,000 years derived from high-precision 230Th/234U/238U, 231Pa/235U and 14C dates on fossil corals. *Quaternary Science Reviews,* 26**,** 18-36.

CLEMENS, S. C. 2005. Millennial-band climate spectrum resolved and linked to centennial-scale solar cycles. *Quaternary Science Reviews,* 24**,** 521-531.

CLEMENT, A. C. & CANE, M. A. 1999. A role for the tropical Pacific coupled ocean-atmosphere system on Milankovitch and millennial timescales. Part 1: a modeling study of tropical Pacific variability. *In:* CLARK, P. U., WEBB, R. S. & KEIGWIN, L. D. (eds.) *Mechanisms of Global Climate Change.* Washington, D. C.: AGU.

CLEMENT, A. C., CANE, M. A. & SEAGER, R. 2001. An orbitally driven tropical source for abrupt climate change. *Journal of Climate,* 14**,** 2369-2375.

CLEMENT, A. C. & PETERSON, L. C. 2008. Mechanisms of abrupt climate change of the last glacial period. *Reviews of Geophysics,* 46**,** RG4002.

COBB, K., COLE, J., LOUGH, J. & TUDHOPE, S. 2008. Annually-banded corals as climate proxies: 'White paper' for Trieste meeting 9-11 June 2008.

COHEN, T. J. & SWEETSER, E. I. 1975. The `spectra' of the solar cycle and of data for Atlantic tropical cyclones. *Nature,* 256**,** 295-296.

COMINS, N. & KAUFMANN, W. 2008. *Discovering the Universe,* New York, W.H. Freeman and Company.

COOPER, A., TURNEY, C., HUGHEN, K. A., BROOK, B. W., MCDONALD, H. G. & COREY, J. A. B. 2015. Abrupt warming events drove Late Pleistocene Holarctic megafaunal turnover. *Science,* 349**,** 602-606.

CROLL, J. 1864. XIII. On the physical cause of the change of climate during geological epochs. *Philosophical Magazine Series 4,* 28**,** 121-137.

CROLL, J. 1875. *Climate and Time in their Geological Relations,* London, NY., Appleton.

CRONIN, T. M. 2010. *Paleoclimates: Understanding Climate Change, Past and Present,* New York, New York : Columbia University Press.

CURRIE, R. G. 1993. Luni-solar 18.6- and solar cycle 10–11-year signals in USA air temperature records. *International Journal of Climatology,* 13**,** 31-50.

DAMON, P. & LINICK, T. W. 1986. Geomagnetic-heliomagnetic modulation of atmospheric radiocarbon production. *Radiocarbon,* 28**,** 266-278.

DAMON, P. & SONETT, C. 1991. Solar and atmospheric components of the atmospheric 14C variation spectrum. *In:* SONETT, C., GIAMPAPA, M. & MATTHEWS, M. (eds.) *The Sun in Time.* Tucson: University of Arizona.

DAMON, P. E. & PERISTYKH, A. N. 2013. Solar and Climatic Implications of the Centennial and Millennial Periodicities in Atmospheric Δ14C Variations. *Solar Variability and Its Effects on Climate.* American Geophysical Union.

DANA, J. D. 1894. *Manual of Geology,* New York, American Book Co.

DANSGAARD, W., CLAUSEN, H. B., GUNDESTRUP, N., JOHNSEN, S. J. & RYGNER, C. 1985. Dating and Climatic Interpretation of Two Deep Greenland Ice Cores. *Greenland Ice Core: Geophysics, Geochemistry, and the Environment.* American Geophysical Union.

DANSGAARD, W., JOHNSEN, S. J., CLAUSEN, H. B., DAHL-JENSEN, D., GUNDESTRUP, N. S., HAMMER, C. U., HVIDBERG, C. S., STEFFENSEN, J. P., SVEINBJORNSDOTTIR, A. E., JOUZEL, J. & BOND, G. 1993. Evidence for general instability of past climate from a 250-kyr ice-core record. *Nature,* 364**,** 218-220.

DARBY, D. A., ORTIZ, J. D., GROSCH, C. E. & LUND, S. P. 2012. 1,500-year cycle in the Arctic Oscillation identified in Holocene Arctic sea-ice drift. *Nature Geoscience,* 5**,** 897-900.

DAVIS, B. A. S. & BREWER, S. 2011. A unified approach to orbital, solar, and lunar forcing based on the Earth's latitudinal insolation/temperature gradient. *Quaternary Science Reviews,* 30**,** 1861-1874.

DE JONG, T. 2006. The heliacal rising of Sirius. *In:* HORNUNG, E., KRAUSS, R. & WARBURTON, D. (eds.) *Ancient Egyptian Chronology.* Leiden, NL: Brill Academic Publishers.

DE VRIES, H. 1958. *Variation in Concentration of Radiocarbon with Time and Location on Earth*, Akademie Van Wet.

DEBENEDICTIS, T. 1993-2004. SkyChart III. San Francisco, CA.: Southern Stars Group.

DEMENOCAL, P., ORTIZ, J., GUILDERSON, T. & SARNTHEIN, M. 2000. Coherent high- and low-latitude climate variability during the Holocene warm period. *Science,* 288**,** 2198-2202.

DENTON, G. H. & KARLÉN, W. 1973. Holocene climatic variations—Their pattern and possible cause. *Quaternary Research,* 3**,** 155-205.

DERRICOURT, R. M. 1971. Radiocarbon chronology for Egypt and North Africa. *Journal of Near Eastern Studies,* 30**,** 271-292.

DIAMOND, J. M. 2005. *Collapse: How Societies Choose to Fail or Succeed,* Camberwell, Vic., Camberwell, Vic. : Penguin Group.

DINCAUZE, D. F. 2000. *Environmental Archaeology: Principles and Practice,* Cambridge, UK; New York, Cambridge University Press.

DITLEVSEN, P. D., ANDERSEN, K. K. & SVENSSON, A. 2007. The DO-climate events are probably noise induced: statistical investigation of the claimed 1470 years cycle. *Climate of the Past,* 3**,** 129-134.

DITLEVSEN, P. D. & DITLEVSEN, O. D. 2009. On the stochastic nature of the rapid climate shifts during the last Ice Age. *Journal of Climate,* 22**,** 446-457.

DITLEVSEN, P. D., KRISTENSEN, M. S. & ANDERSEN, K. K. 2005. The recurrence time of Dansgaard-Oeschger events and limits on the possible periodic component. *Journal of Climate,* 18**,** 2594-2603.

DONDERS, T. H., WAGNER, F. & VISSCHER, H. 2006. Late Pleistocene and Holocene subtropical vegetation dynamics recorded in perched lake deposits on Fraser Island, Queensland, Australia. *Palaeogeography, Palaeoclimatology, Palaeoecology,* 241**,** 417-439.

DONNE, J. 1624. No Man is an Island. *Meditation XVII.*

DUNBAR, R. B., WELLINGTON, G. M., COLGAN, M. W. & GLYNN, P. W. 1994. Eastern Pacific sea surface temperature since 1600 A.D.: The δ18O record of climate variability in Galápagos Corals. *Paleoceanography,* 9**,** 291-315.

EARTH. 2015a. *Antarctica*. Google Earth.

EARTH. 2015b. *Arctic Ocean*. Google Earth.

EDDY, J. A. 1976. The Maunder Minimum. *Science,* 192**,** 1189-1202.

EDMUNDS, M. G. & MORGAN, P. 2000. The Antikythera Mechanism: still a mystery of Greek astronomy? *Astronomy & Geophysics,* 41**,** 6.10-6.17.

EDVARDSSON, J., LINDERHOLM, H. W. & HAMMARLUND, D. 2011. Enigmatic cycles detected in subfossil and modern bog-pine chronologies from southern Sweden. *TRACE,* 9**,** 173-180.

EMILIANI, C. 1955. Pleistocene Temperatures. *The Journal of Geology,* 63**,** 538-578.

EPICA COMMUNITY MEMBERS. 2006. One-to-one coupling of glacial climate variability in Greenland and Antarctica. *Nature,* 444**,** 195-198.

ERICKSON, D. J., MERRILL, J. T. & DUCE, R. A. 1986. Seasonal estimates of global atmospheric sea-salt distributions. *Journal of Geophysical Research,* 91**,** 1067-1072.

ERICSON, D., EWING, M., WOLLIN, G. & HEEZEN, B. 1961. Atlantic deep-sea sediment cores. *Bulletin of the Geological Society of America,* 72**,** 193-286.

ESPENAK, F. 2012a. *Eclipses and the Saros* [Online]. NASA. Available: http://eclipse.gsfc.nasa.gov/SEsaros/SEsaros.html [Accessed August 26, 2013].

ESPENAK, F. 2012b. *Periodicity of Solar Eclipses* [Online]. NASA. Available: http://eclipse.gsfc.nasa.gov/SEsaros/SEperiodicity.html [Accessed August 26, 2013].

FAIRBANKS, R. G., CHIU, T.-C., CAO, L., MORTLOCK, R. A. & KAPLAN, A. 2006. Rigorous quality control criteria for screening coral samples and radiocarbon calibration data based on 14C, 230Th/234U/238U and 231Pa/235U dated corals—A reply to the comment by Yusuke Yokoyama and Tezer M. Esat on "Extending the radiocarbon calibration beyond 26,000 years before present using fossil corals" by T.-C. Chiu, R.G. Fairbanks, R.A. Mortlock, A.L. Bloom (Quaternary Science Reviews 24 (2005) 1797–1808). *Quaternary Science Reviews,* 25**,** 3084-3087.

FAIRBANKS, T. W., FAIRBANKS, R. G., MORTLOCK, R. A., CHIU, T.-C., CAO, L., KAPLAN, A., GUILDERSON, T. P., BLOOM, A. L., GROOTES, P. M. & NADEAU, M.-J. 2005. Radiocarbon calibration curve spanning 0 to 50,000 years BP based on paired 230Th/ 234U/ 238U and 14C dates on pristine corals. *Quaternary Science Reviews,* 24**,** 1781-1796.

FAIRFAX, R., ROWLAND, J., RYAN, T. & DRIMER, J. 2011. A Preliminary Investigtion into 'Patterned Fens' of the Great Sandy Region. Unpublished report to Commonwealth Department of Sustainability, Environment, Water, Population and Communities, Queensland Herbarium, Queensland Department of Environment and Resource Management, Brisbane.

FEULNER, G. 2011. Are the most recent estimates for Maunder Minimum solar irradiance in agreement with temperature reconstructions? *Geophysical Research Letters,* 38.

FEYNMAN, J. & RUZMAIKIN, A. 2007. Climate stability and the development of agricultural societies. *Climatic Change,* 84**,** 295-311.

FRAKES, L. A., FRANCIS, J. E. & SYKTUS, J. I. 1992. *Climate modes of the phanerozoi : the history of the Earth's climate over the past 600 million years,* New York, N.Y., Cambridge University Press.

FRIIS-CHRISTENSEN, E. & LASSEN, K. 1991. Length of the solar cycle: an indicator of solar activity closely associated with climate. *Science,* 254**,** 698-700.

GAGAN, M. K., HENDY, E. J., HABERLE, S. G. & HANTORO, W. S. 2004. Post-glacial evolution of the Indo-Pacific Warm Pool and El Niño-Southern oscillation. *Quaternary International,* 118**,** 127-143.

GANOPOLSKI, A. & RAHMSTORF, S. 2001. Rapid changes of glacial climate simulated in a coupled climate model. *Nature,* 409**,** 153.

GOLDSTEIN, B. R. & BOWEN, A. C. 1989. On early Hellenistic astronomy: Timocharis and the first Callippic calendar. *Centaurus,* 32**,** 272-293.

GOSLAR, T., ARNOLD, M., BARD, E., KUC, T., PAZDUR, M. F., RALSKA-JASIEWICZOWA, M., ROZANSKI, K., TISNERAT, N., WALANUS, A., WICIK, B. & WIEQKOWSKI, K. 1995. High concentration of atmospheric 14C during the Younger Dryas cold episode. *Nature,* 377**,** 414-417.

GOSSEN, C. 2011. Deforestation, drought and humans: new discoveries of the Late Quaternary paleoenvironment of Rapa Nui (Easter Island). *In:* KHALIL, M. A. K., ATKINSON, D., DUNBAR, R., JOHNSON, D., LATZ, G. & SCHOONMAKER, P. (eds.). ProQuest Dissertations Publishing.

GRAY, L. J., BEER, J., GELLER, M., HAIGH, J. D., LOCKWOOD, M., MATTHES, K., CUBASCH, U., FLEITMANN, D., HARRISON, G., HOOD, L., LUTERBACHER, J., MEEHL, G. A., SHINDELL, D., VAN GEEL, B. & WHITE, W. 2010. Solar influences on climate. *Reviews of Geophysics* [Online], 48. Available: http://dx.doi.org/10.1029/2009RG000282 [Accessed February 16, 2017].

GREENBERG, R. 1981. Apsidal precession of orbits about an oblate planet. *The Astronomical Journal,* 86**,** 912-914.

GROOTES, P. M. & STUIVER, M. 1997. Oxygen 18/16 variability in Greenland snow and ice with 10^-3 to 10^5 - year time resolution. *Journal of Geophysical Research,* 102**,** 26455-26470.

GROOTES, P. M., STUIVER, M., WHITE, J. W. C., JOHNSEN, S. & JOUZEL, J. 1993. Comparison of oxygen isotope records from the GISP2 and GRIP. *Nature,* 366 552-554.

GUBBINS, D., JONES, A. L. & FINLAY, C. C. 2006. Fall in Earth's magnetic field is erratic. *Science,* 312**,** 900-902.

GUTZWILLER, M. C. 1998. Moon-Earth-Sun: the oldest three-body problem. *Reviews of Modern Physics,* 70**,** 589-639.

HAGELBERG, T. K., BOND, G. & DEMENOCAL, P. B. 1994. Milankovitch band forcing of sub-Milankovitch climate variability during the Pleistocene. *Paleoceanography,* 9**,** 545-558.

HAJDAS, I., IVY, S. D., BEER, J., BONANI, G., IMBODEN, D., LOTTED, A. F., STURM, M. & SUTER, M. 1993. AMS radiocarbon dating and varve chronology of Lake Soppensee: 6000 to 12000 14C years BP. *Climate Dynamics,* 9**,** 107-116.

HAMILTON, W. L. 1973. Tidal cycles of volcanic eruptions: fortnightly to 19 yearly periods. *Journal of Geophysical Research,* 78**,** 3363-3375.

HAMMER, C., MAYEWSKI, P. A., PEEL, D. & STUIVER, M. 1997. Preface [to special section on Greenland Summit Ice Cores]. *Journal of Geophysical Research: Oceans,* 102**,** 26315-26316.

HAND, E. 2010. Cosmic-ray theory unravels. *Nature,* 463**,** 1011-1011.

HAND, R. 1989-1994. NOVA 2.13. Brewster, MA: Astrolabe Inc.

HATHAWAY, D. H. 2010. The solar cycle. *Living Reviews in Solar Physics,* 7**,** 1.

HATHAWAY, D. H. 2015. *The Sunspot Cycle* [Online]. Available: https://solarscience.msfc.nasa.gov/SunspotCycle.shtml [Accessed August 22, 2016].

HAYS, J. D., IMBRIE, J. & SHACKLETON, N. J. 1976. Variations in the Earth's orbit: pacemaker of the Ice Ages. *Science,* 194**,** 1121-1132.

HEINRICH, H. 1988. Origin and consequences of cyclic ice rafting in the Northeast Atlantic Ocean during the past 130,000 years. *Quaternary Research,* 29**,** 142-152.

HENRY, A. J. 1927. The Bruckner cycle of climatic oscillations in the United States. *Annals of the Association of American Geographers,* 17**,** 60-71.

HENSHILWOOD, CHRISTOPHER S. & MAREAN, CURTIS W. 2003. The origin of modern human behavior: critique of the models and their test implications. *Current Anthropology,* 44**,** 627-651.

HERSCHEL, W. 1832. On the astronomical causes which may influence geological phenomena. *Transactions of the Geological Society,* III**,** 293-299.

HERTZ, J. H. 1981. *The Pentateuch and Haftorahs,* London, Soncino Press.

HERTZBERG, J. E., BLACK, D. E., PETERSON, L. C., THUNELL, R. C. & HAUG, G. H. 2012. Decadal- to centennial-scale tropical Atlantic climate variability across a Dansgaard-Oeschger cycle. *Paleoceanography* [Online], 27. Available: http://dx.doi.org/10.1029/2011PA002251 [Accessed February 25, 2017].

HOGG, A. G., HUA, Q., BLACKWELL, P. G., NIU, M., BUCK, C. E., GUILDERSON, T. P., HEATON, T. J., PALMER, J. G., REIMER, P. J., REIMER, R. W., TURNEY, C. S. M. & ZIMMERMAN, S. R. H. 2013. SHCal13 Southern Hemisphere Calibration, 0–50,000 Years cal BP. *Radiocarbon,* 55**,** 1889-1903.

HOLDAWAY, S. 2006. Absolute dating. *In:* BALME, J. & PATERSON, A. (eds.) *Archaeology in Practice : A Student Guide to Archaeological Analyses.* Malden, MA: Blackwell.

HORNUNG, E. 2006. Introduction. *In:* HORNUNG, E., KRAUSS, R. & WARBURTON, D. (eds.) *Ancient Egyptian Chronology.* Leiden, NL: Brill Academic Publishers.

HOU, A. Y. & LINDZEN, R. S. 1992. The influence of concentrated heating on the Hadley Circulation. *Journal of the Atmospheric Sciences,* 49**,** 1233-1241.

HUA, Q., WEBB, G. E., ZHAO, J.-X., NOTHDURFT, L. D., LYBOLT, M., PRICE, G. J. & OPDYKE, B. N. 2015. Large variations in the Holocene marine radiocarbon reservoir effect reflect ocean circulation and climatic changes. *Earth and Planetary Science Letters,* 422**,** 33-44.

HUGHEN, K., LEHMAN, S., SOUTHON, J., OVERPECK, J., MARCHAL, O., HERRING, C. & TURNBULL, J. 2004. 14C activity and global carbon cycle changes over the past 50,000 years. *Science,* 303**,** 202-207.

HUGHEN, K. A., OVERPECK, J. T., LEHMAN, S. J., KASHGARIAN, M., SOUTHON, J., PETERSON, L. C., ALLEY, R. & SIGMAN, D. M. 1998. Deglacial changes in ocean circulation from an extended radiocarbon calibration. *Nature,* 391**,** 65-68.

HUNTEN, D. M., GERARD, J.-C. & FRANCOIS, L. M. 1993. The atmosphere's response to solar radiation. *In:* SONETT, C., GIAMPAPA, M. & MATTHEWS, M. (eds.) *The Sun in Time.* Milwaukee: Kalmbach Publishing Company.

HUYBERS, P. 2007. Glacial variability over the last two million years: an extended depth-derived agemodel, continuous obliquity pacing, and the Pleistocene progression. *Quaternary Science Reviews,* 26**,** 37-55.

HUYBERS, P. & DENTON, G. 2008. Antarctic temperature at orbital timescales controlled by local summer duration. *Nature Geoscience,* 1**,** 787-792.

HUYBERS, P. & LANGMUIR, C. 2009. Feedback between deglaciation, volcanism, and atmospheric CO2. *Earth and Planetary Science Letters,* 286**,** 479-491.

IMBRIE, I. & IMBRIE, K. 1979. *Ice Ages: Solving the Mystery,* New Jersey, Enslow Publishers.

IMBRIE, J. 1985. A theoretical framework for the Pleistocene ice ages: William Smith Lecture. *Journal of the Geological Society,* 142**,** 417-432.

IMBRIE, J., BERGER, A., BOYLE, E. A., CLEMENS, S. C., DUFFY, A., HOWARD, W. R., KUKLA, G., KUTZBACH, J., MARTINSON, D. G., MCINTYRE, A., MIX, A. C., MOLFINO, B., MORLEY, J. J., PETERSON, L. C., PISIAS, N. G., PRELL, W. L., RAYMO, M. E., SHACKLETON, N. J. & TOGGWEILER, J. R. 1993. On the structure and origin of major glaciation cycles 2. The 100,000-year cycle. *Paleoceanography,* 8**,** 699-735.

IMBRIE, J., HAYS, J. D., MARTINSON, D., MCINTYRE, A., MIX, A., MORLEY, J., PISIAS, N., PRELL, W. & SHACKLETON, N. J. 1984. The Orbital Theory of Pleistocene climate: support from a revised chronology of the marine δ18O record. *In:* BERGER, A., IMBRIE, J., HAYS, J. D., KUKLA, G. & SALTZMAN, B. (eds.). Dordrecht: Reidel Publishing Co.

JESPERSEN, J. & FITZ-RANDOLPH, J. 1999. *From Sundials to Atomic Clocks: Understanding Time and Frequency*. US Department of Commerce Technology Administration, National Institute of Standards and Technology. Monograph 155.

JOHNSEN, S. J., CLAUSEN, H. B., DANSGAARD, W., FUHRER, K., GUNDESTRUP, N., HAMMER, C. U., IVERSEN, P., JOUZEL, J., STAUFFER, B. & STEFFENSEN, J. P. 1992. Irregular glacial interstadials recorded in a new Greenland ice core. *Nature,* 359**,** 311-313.

JOHNSEN, S. J., DAHL-JENSEN, D., GUNDESTRUP, N., STEFFENSEN, J. P., CLAUSEN, H. B., MILLER, H., MASSON-DELMOTTE, V., SVEINBJÖRNSDOTTIR, A. E. & WHITE, J. 2001. Oxygen isotope and palaeotemperature records from six Greenland ice-core stations: Camp Century, Dye-3, GRIP, GISP2, Renland and NorthGRIP. *Journal of Quaternary Science,* 16**,** 299-307.

JORDANOVA, V. K. 2016. Global Modeling of Wave Generation Processes in the Inner Magnetosphere. *Magnetosphere-Ionosphere Coupling in the Solar System.* John Wiley & Sons, Inc.

JUNK, C. & CLAUSSEN, M. 2011. Simulated climate variability in the region of Rapa Nui during the last millennium. *Climate of the Past,* 7**,** 579-586.

KEELE, T. W. 1910. The great weather cycle. *Journal and Proceedings of the Royal Society of NSW,* 44**,** 25-76.

KEELING, C. D. & WHORF, T. P. 2000. The 1,800-year oceanic tidal cycle: a possible cause of rapid climate change. *Proceedings of the National Academy of Sciences of the United States of America,* 97**,** 3814-3819.

KELLY, P. M. 1977. Solar influence on North Atlantic mean sea level pressure. *Nature,* 269**,** 320-322.

KELSEY, A. M., MENK, F. W. & MOSS, P. T. 2015. An astronomical correspondence to the 1470 year cycle of abrupt climate change. *Climate of the Past Discussions,* 2015**,** 4895-4915.

KINTISCH, E. 2016. THE LOST NORSE. *Science,* 354**,** 696-701.

KITCHEN, K. A. 1991. The chronology of ancient Egypt. *World Archaeology,* 23**,** 201-208.

KOHYAMA, T. & WALLACE, J. M. 2016. Rainfall variations induced by the lunar gravitational atmospheric tide and their implications for the relationship between tropical rainfall and humidity. *Geophysical Research Letters,* 43**,** 918-923.

KOPP, G. & LEAN, J. L. 2011. A new, lower value of total solar irradiance: Evidence and climate significance. *Geophysical Research Letters* [Online], 38. [Accessed December 7, 2014].

KÖPPEN, W. P. & WEGENER, A. 1924. *Die klimate der geologischen vorzeit*, Gebrüder Borntraeger.

KORTE, M. & CONSTABLE, C. G. 2005. Continuous geomagnetic field models for the past 7 millennia: 2. CALS7K. *Geochemistry, Geophysics, Geosystems* [Online], 6. Available: http://dx.doi.org/10.1029/2004GC000801 [Accessed November 30, 2015].

KRAUSS, R. 2006. Egyptian Sirius/Sothic dates, and the question of the Sothis-based lunar calendar. *In:* HORNUNG, E., KRAUSS, R. & WARBURTON, D. (eds.) *Ancient Egyptian Chronology.* Leiden, NL: Brill Academic Publishers.

KUKLA, G. J. & KOČÍ, A. 1972. End of the Last Interglacial in the Loess Record. *Quaternary Research,* 2**,** 374-383.

LABITZKE, K. & LOON, H. V. 1988. Associations between the 11-year solar cycle, the QBO and the atmosphere. Part I: the troposphere and stratosphere in the northern hemisphere in winter. *Journal of Atmospheric and Terrestrial Physics,* 50**,** 197-206.

LAING, A. & EVANS, J.-L. 2011. Introduction to Tropical Meteorology. 2nd edition ed.

LAL, D. & LINGENFELTER, R. 1993. History of the sun during the past 4.5gyr as revealed by studies of energetic solar particles recorded as extraterrestrial and terrestrial samples. *In:* SONETT, C. P., GIAMPAPA, M. S. & MATTHEWS, M. S. (eds.) *The Sun in Time.* Tucson: University of Arizona.

LAMB, H. H. 1977. *Climate History and the Future,* Princeton, Princeton University Press.

LANGGUT, D., FINKELSTEIN, I. & LITT, T. 2013. Climate and the late Bronze collapse: new evidence from the Southern Levant. *Tel Aviv,* 40**,** 149-175.

LAUT, P. 2003. Solar activity and terrestrial climate: an analysis of some purported correlations. *Journal of Atmospheric and Solar-Terrestrial Physics,* 65**,** 801-812.

LAWRENCE EDWARDS, R., CHEN, J. H. & WASSERBURG, G. J. 1987. 238U-234U-230Th-232Th systematics and the precise measurement of time over the past 500,000 years. *Earth and Planetary Science Letters,* 81**,** 175-192.

LEMIEUX-DUDON, B., BLAYO, E., PETIT, J.-R., WAELBROECK, C., SVENSSON, A., RITZ, C., BARNOLA, J.-M., NARCISI, B. M. & PARRENIN, F. 2010. Consistent dating for Antarctic and Greenland ice cores. *Quaternary Science Reviews,* 29**,** 8-20.

LIBBY, W. F. 1960. *Radiocarbon Dating* [Online]. Nobel Media AB. Available: http://www.nobelprize.org/nobel_prizes/chemistry/laureates/1960/libby-lecture.pdf [Accessed October 23, 2012].

LIBBY, W. F. 1980. Archaeology and radiocarbon dating. *Radiocarbon,* 22**,** 1017-1020.

LINICK, T. W., DAMON, P. E., DONAHUE, D. J. & JULL, A. J. T. 1989. Accelerator mass spectrometry: the new revolution in radiocarbon dating. *Quaternary International,* 1**,** 1-6.

LIOU, K.-N. 2002. *An introduction to atmospheric radiation,* Boston, Academic Press.

LOCKYER, S. N. 1964. *The Dawn of Astronomy,* Cambridge, The MIT Press.

LOISEL, J. & GARNEAU, M. 2010. Late Holocene paleoecohydrology and carbon accumulation estimates from two boreal peat bogs in eastern Canada: Potential and limits of multi-proxy archives. *Palaeogeography, Palaeoclimatology, Palaeoecology,* 291**,** 493-533.

LONGLEY, P. M., GOODCHILD, D., MAGUIRE , D. & RIND, D. 2011. *Geographic information systems & science,* Hoboken, NJ, Wiley.

LORENZO, M. N., TABOADA, J. J., IGLESIAS, I. & ÁLVAREZ, I. 2008. The role of stochastic forcing on the behavior of thermohaline circulation. *Annals of the New York Academy of Sciences,* 1146**,** 60-86.

LOUTRE, M.-F., PAILLARD, D., VIMEUX, F. & CORTIJO, E. 2004. Does mean annual insolation have the potential to change the climate? *Earth and Planetary Science Letters,* 221**,** 1-14.

LOWE, J. & WALKER, M. 1997. *Reconstructing Quaternary Environments,* Harlow, Pearson Education.

LOWRIE, W. 2007. *Fundamentals of Geophysics,* Cambridge, Cambridge University Press.

LYELL, C. 1830. *Principles of Geology,* London, John Murray.

MANZANILLA, L. 1997. The impact of climatic change on past civilizations. A revisionist agenda for further investigation. *Quaternary International,* 43**,** 153-159.

MARCHITTO, T. M., MUSCHELER, R., ORTIZ, J. D., CARRIQUIRY, J. D. & VAN GEEN, A. 2010. Dynamical response of the tropical Pacific Ocean to solar forcing during the early Holocene. *Science,* 330**,** 1378-1381.

MARTINSON, D. G., PISIAS, N. G., HAYS, J. D., IMBRIE, J., MOORE, T. C. & SHACKLETON, N. J. 1987. Age dating and the orbital theory of the ice ages: development of a high-resolution 0 to 300,000-year chronostratigraphy. *Quaternary Research,* 27**,** 1-29.

MARTRAT, B., GRIMALT, J. O., SHACKLETON, N. J., DE ABREU, L., HUTTERLI, M. A. & STOCKER, T. F. 2007. Four climate cycles of recurring deep and surface water destabilizations on the Iberian margin. *Science,* 317**,** 502-507.

MAUQUOY, D., VAN GEEL, B., BLAAUW, M., SPERANZA, A., VAN DER PLICHT, J., PALEOBIOLOGI, UPPSALA, U., GEOVETENSKAPLIGA, S., TEKNISK-NATURVETENSKAPLIGA, V. & INSTITUTIONEN FÖR, G. 2004. Changes in solar activity and Holocene climatic shifts derived from 14C wiggle-match dated peat deposits. *The Holocene,* 14**,** 45-52.

MAYEWSKI, P. A., MEEKER, L. D., TWICKLER, M. S., WHITLOW, S., YANG, Q., LYONS, W. B. & PRENTICE, M. 1997. Major features and forcing of high-latitude northern hemisphere atmospheric circulation using a 110,000-year-long glaciochemical series. *Journal of Geophysical Research: Oceans,* 102**,** 26345-26366.

MAZARELLA, A. 2008. Solar forcing of changes in atmospheric circulation, Earth's rotation and climate. 2**,** 181-184.

MAZZARELLA, A. & SCAFETTA, N. 2012. Evidences for a quasi 60-year North Atlantic Oscillation since 1700 and its meaning for global climate change. *Theoretical and Applied Climatology,* 107**,** 599-609.

MCGEE, W. J. 1892. Comparative chronology. *American Anthropologist,* 5**,** 327-344.

MCMICHAEL, A. 2017. *Climate Change and the Health of Nations: Famines, Fevers, and the Fate of Populations,* Oxford U.S., Oxford University Press.

MEESE, D. A., GOW, A. J., ALLEY, R. B., ZIELINSKI, G. A., GROOTES, P. M., RAM, M., TAYLOR, K. C., MAYEWSKI, P. A. & BOLZAN, J. F. 1997. The Greenland Ice Sheet Project 2 depth-age scale: methods and results. *Journal of Geophysical Research: Oceans,* 102**,** 26411-26423.

MELLARS, P. 2006. A new radiocarbon revolution and the dispersal of modern humans in Eurasia. *Nature,* 439**,** 931-935.

MILANKOVITCH, M. 1941. Kanon der Erdbestrahlung und seine Andwendung auf das Eiszeitenproblem. Belgrade: Royal Serbian Academy special publications.

MITCHELL, A. 1999. *The ESRI guide to GIS analysis,* Redlands, Calif, ESRI Press.

MÖRNER, N.-A. 2013. Solar wind, Earth's rotation and changes in terrestrial climate. *Physical Review & Research International,* 3**,** 117-136.

MOSS, P., PETHERICK, L. & NEIL, D. 2011. Environmental change at Myora Springs, North Stradbroke island over the last millennium. *The Proceedings of the Royal Society of Queensland,* 117**,** 113-140.

MOSS, P. T. 1999. *Late Quaternary environments of the humid tropics of northeastern Australia.* . PhD, Monash University, Melbourne.

MOSS, P. T., SMITH, R. Y. & GREENWOOD, D. R. 2016. A window into mid-latitudinal Early Eocene environmental variability: a high-resolution palynological analysis of the Falkland site, Okanagan Highlands, British Columbia, Canada. *Canadian Journal of Earth Sciences,* 53**,** 605-613.

MOSS, P. T., TIBBY, J., PETHERICK, L., MCGOWAN, H. & BARR, C. 2013. Late Quaternary vegetation history of North Stradbroke Island, Queensland, eastern Australia. *Quaternary Science Reviews,* 74**,** 257-272.

MOY, C., M., SELTZER, G., O. , RODBELL, D., T. & ANDERSON, D., M. 2002. Variability of El Niño/ Southern Oscillation activity at millennial timescales during the Holocene epoch. *Nature,* 420**,** 162.

MUELLER, R. D., PADMAN, L., DINNIMAN, M. S., EROFEEVA, S. Y., FRICKER, H. A. & KING, M. A. 2012. Impact of tide-topography interactions on basal melting of Larsen C Ice Shelf, Antarctica. *Journal of Geophysical Research,* 117.

MUNK, W., DZIECIUCH, M. & JAYNE, S. 2002. Millennial climate variability: is there a tidal connection? *Journal of Climate,* 15**,** 370-385.

MUNK, W. H. & CARTWRIGHT, D. E. 1966. Tidal spectroscopy and prediction. *Philosophical Transactions of the Royal Society of London.Series A, Mathematical and Physical Sciences,* 259**,** 533-581.

MUSCHELER, R., JOOS, F., BEER, J., MÜLLER, S. A., VONMOOS, M. & SNOWBALL, I. 2007. Reply to the comment by Bard et al. on "Solar activity during the last 1000 yr inferred from radionuclide records". *Quaternary Science Reviews,* 26**,** 2304-2308.

NASA. 2011. *Dictionary of Technical Terms for Aerospace Use* [Online]. Available: http://er.jsc.nasa.gov/seh/menu.html [Accessed November, 25 2013].

NASA. 2016. *Constellations and the Calendar* [Online]. Available: https://spaceplace.nasa.gov/starfinder2/en/ [Accessed February 6, 2017].

NASA. n.d. *Astronomical Unit* [Online]. Available: https://cneos.jpl.nasa.gov/glossary/au.html [Accessed January 8, 2017].

NASA, ADLER, CHICAGO, U. O., WESLEYAN & JPL-CALTECH. 2012. *Milky Way and Our Location* [Online]. Available: https://www.nasa.gov/mission_pages/sunearth/news/gallery/galaxy-location.html [Accessed August 28, 2016].

NASA ASTROPHYSICS. 2013. Fermi Proves Supernova Remnants Produce Cosmic Rays. Goddard Space Centre.

NASA/JPL. 2010. Thermohaline circulation [image]. Available: http://www.jpl.nasa.gov/images/earth/20100325/atlantic20100325-full.jpg [Accessed August 22, 2016].

NUNN, P. D. & BRITTON, J. M. R. 2001. Human-Environment Relationships in the Pacific Islands around A.D. 1300. *Environment and History,* 7**,** 3-22.

O'BRIEN, D. P. & CURRIE, R. G. 1993. Observations of the 18.6-year cycle of air pressure and a theoretical model to explain certain aspects of this signal. *Climate Dynamics,* 8.

O'BRIEN, S. R., MAYEWSKI, P. A., MEEKER, L. D., MEESE, D. A., TWICKLER, M. S. & WHITLOW, S. I. 1995. Complexity of Holocene climate as reconstructed from a Greenland ice core. *Science,* 270**,** 1962-1964.

O'CONNELL, J. F. & ALLEN, J. 2004. Dating the colonization of Sahul (Pleistocene Australia–New Guinea): a review of recent research. *Journal of Archaeological Science,* 31**,** 835-853.

O'NEIL, W. M. 1975. *Time and the Calendars,* Sydney, Sydney University Press.

OLSSON, I. U., UPPSALA, U., INSTITUTIONEN FÖR FYSIK OCH, M., FYSISKA, S. & TEKNISK-NATURVETENSKAPLIGA, V. 2009. Radiocarbon dating history: early days, questions, and problems met. *Radiocarbon,* 51**,** 1.

OOST, A. P., DE HAAS, H., IJNSEN, F., VAN DEN BOOGERT, J. M. & DE BOER, P. L. 1993. The 18.6 yr nodal cycle and its impact on tidal sedimentation. *Sedimentary Geology,* 87**,** 1-11.

PAILLARD, D. 2010. Climate and the orbital parameters of the Earth. *Comptes Rendus Geoscience,* 342**,** 273-285.

PAILLARD, D. & LABEYRIET, L. 1994. Role of the thermohaline circulation in the abrupt warming after Heinrich events. *Nature,* 372**,** 162-164.

PALLÉ, E., BUTLER, C. J. & O'BRIEN, K. 2004. The possible connection between ionization in the atmosphere by cosmic rays and low level clouds. *Journal of Atmospheric and Solar-Terrestrial Physics,* 66**,** 1779-1790.

PARKER, A., GOUDIE, A., ANDERSON, D., ROBINSON, M. & BONSALL, C. 2002. A review of the mid-Holocene elm decline in the British Isles. *Progress in Physical Geography,* 26**,** 1-45.

PARRENIN, F., BARNOLA, J. M., BEER, J., BLUNIER, T., CASTELLANO, E., CHAPPELLAZ, J., DREYFUS, G., FISCHER, H., FUJITA, S., JOUZEL, J., KAWAMURA, K., LEMIEUX-DUDON, B., LOULERGUE, L., MASSON-DELMOTTE, V., NARCISI, B., PETIT, J. R., RAISBECK, G., RAYNAUD, D., RUTH, U., SCHWANDER, J., SEVERI, M., SPAHNI, R., STEFFENSEN, J. P., SVENSSON, A., UDISTI, R., WAELBROECK, C. & WOLFF, E. 2007. The EDC3 chronology for the EPICA Dome C ice core. *Climate of the Past,* 3**,** 485-497.

PEARSON, G. 1986. Precise calendrical dating of known growth period samples using a 'curve fitting' technique. *Radiocarbon,* 28**,** 292-299.

PEDRO, J. B., RASMUSSEN, S. O. & VAN OMMEN, T. D. 2012. Tightened constraints on the time-lag between Antarctic temperature and CO2 during the last deglaciation. *Climate of the Past,* 8**,** 1213-1221.

PENCK, A. & BRÜCKNER, E. 1909. *Die Alpen im Eiszeitalter,* Leipzig, Tauchnitz.

PETIT, J. R., JOUZEL, J., RAYNAUD, D., BARKOV, N. I., BARNOLA, J. M., BASILE, I., BENDER, M., CHAPPELLAZ, J., DAVIS, M., DELAYGUE, G., DELMOTTE, M., KOTLYAKOV, V. M., LEGRAND, M., LIPENKOV, V. Y., LORIUS, C., PEPIN, L., RITZ, C., SALTZMAN, E. & STIEVENARD, M. 1999. Climate and atmospheric history of the past 420,000 years from the Vostok ice core, Antarctica. *Nature,* 399**,** 429-436.

PETOUKHOV, V., GANOPOLSKI, A., BROVKIN, V., CLAUSSEN, M., ELISEEV, A., KUBATZKI, C. & RAHMSTORF, S. 2000. CLIMBER-2: a climate system model of intermediate complexity. Part I: model description and performance for present climate. *Climate Dynamics,* 16**,** 1-17.

PETTERSSON, O. 1929. Changes in the Oceanic Circulation and Their Climatic Consequences. *Geographical Review,* 19**,** 121-131.

PETTERSSON, O. 1930. The Tidal Force, u. *Geografiska Annaler,* 12**,** 261.

PICKETT, J. W., KU, T. L., THOMPSON, C. H., ROMAN, D., KELLEY, R. A. & HUANG, Y. P. 1989. A review of age determinations on Pleistocene corals in eastern Australia. *Quaternary Research,* 31**,** 392-395.

POPPER, K. S. 1972. *Objective Knowledge: An Evolutionary Approach,* Oxford, Clarendon Press.

POSSEHL, G. 1993. Climate, collapse, and civilisation in the Greater Indus region. *57th Annual Meeting of the Society of American Archaeology.* St. Louis.

PRITCHARD, H. D., LIGTENBERG, S. R. M., FRICKER, H. A., VAUGHAN, D. G., BROEKE, M. R. V. D. & PADMAN, L. 2012. Antarctic ice-sheet loss driven by basal melting of ice shelves. *Nature,* 484**,** 502-505.

PRITCHARD, J. B. 1971. *The Ancient Near East: An Anthology of Texts and Pictures,* London, Oxford University Press.

PRITCHETT, W. K. & NEUGEBAUER, O. 1947. *The Calendars of Athens,* Cambridge, Harvard University Press.

QUINN, W., NEAL, V. & QUINN, W. 1987. El Niño occurrences over the past four and a half centuries. *Journal of Geophysical Research: Oceans,* 92**,** 14449-14461.

RAHMSTORF, S. 2003. Timing of abrupt climate change: A precise clock. *Geophysical Research Letters,* 30**,** 17-1.

RASPOPOV, O., SHUMILOV, O., KASATKINA, E., TURURNEN, E. & LINDHOLM, M. 2000. 35-year climatic Bruckner cycle – solar control of climate variability? *Proceedings of the First Solar Weather Euroconference, 'The Solar Cycle and Terrestrial Climate'.* Santa Cruz de Tenerife, Tenerife, Spain.

RASPOPOV, O. M., DERGACHEV, V. A., OGURTSOV, M. G., KOLSTRÖM, T., JUNGNER, H. & DMITRIEV, P. B. 2011. Variations in climate parameters at time intervals from hundreds to tens of millions of years in the past and its relation to solar activity. *Journal of Atmospheric and Solar-Terrestrial Physics,* 73**,** 388-399.

REID, G. C. 1987. Influence of solar variability on global sea surface temperatures. *Nature,* 329**,** 142-143.

ROSEN, A. M. 2007. From hunter-gatherers to village farmers: the role of climate change in the origins of agriculture. *In:* ROSEN, A. M. (ed.) *Civilising Climate.* Plymouth: Altamira.

ROTH, R. & JOOS, F. 2013. A reconstruction of radiocarbon production and total solar irradiance from the Holocene 14C and CO2 records: implications of data and model uncertainties. *Climate of the Past Discussions,* 9**,** 1165-1235.

RUDDIMAN, W. F. 2003. Orbital insolation, ice volume, and greenhouse gases. *Quaternary Science Reviews,* 22**,** 1597-1629.

RUDDIMAN, W. F. 2004. The role of greenhouse gases in orbital-scale climatic changes. *Eos, Transactions American Geophysical Union,* 85**,** 1-7.

RUDDIMAN, W. F. & MCINTYRE, A. 1981. Oceanic mechanisms for amplification of the 23,000-year ice-volume cycle. *Science,* 212**,** 617-627.

RUSTIC, G. T., KOUTAVAS, A., MARCHITTO, T. M. & LINSLEY, B. K. 2015. Dynamical excitation of the tropical Pacific Ocean and ENSO variability by Little Ice Age cooling. *Science,* 350**,** 1537-1541.

SCHULZ, M. 2002. On the 1470-year pacing of Dansgaard-Oeschger warm events. *Paleoceanography,* 17**,** 1014.

SCHWARCZ, H. P. 1989. Uranium series dating of Quaternary deposits. *Quaternary International*, 7-17.

SERENO, P. C., GARCEA, E. A. A., JOUSSE, H., STOJANOWSKI, C. M., SALIÈGE, J.-F., MAGA, A., IDE, O. A., KNUDSON, K. J., MERCURI, A. M., STAFFORD, T. W., KAYE, T. G., GIRAUDI, C., N'SIALA, I. M., COCCA, E., MOOTS, H. M., DUTHEIL, D. B., STIVERS, J. P. & HARPENDING, H. 2008. Lakeside Cemeteries in the Sahara: 5000 Years of Holocene Population and Environmental Change. *PLoS ONE,* 3.

SHACKLETON, N. J. 1969. The Last Interglacial in the Marine and Terrestrial Records. *Proceedings of the Royal Society of London. Series B. Biological Sciences,* 174, 135-154.

SHACKLETON, N. J. 2000. The 100,000-Year Ice-Age Cycle Identified and Found to Lag Temperature, Carbon Dioxide, and Orbital Eccentricity. *Science,* 289, 1897-1902.

SHACKLETON, N. J., FAIRBANKS, R. G., CHIU, T.-C. & PARRENIN, F. 2004. Absolute calibration of the Greenland time scale: implications for Antarctic time scales and for Δ14C. *Quaternary Science Reviews,* 23, 1513-1522.

SHACKLETON, N. J. & OPDYKE, N. D. 1973. Oxygen isotope and palaeomagnetic stratigraphy of equatorial Pacific core V28-238: Oxygen isotope temperatures and ice volumes on a 105 year and 106 year scale. *Quaternary Research,* 3, 39-55.

SHAPIRO, A. I., SCHMUTZ, W., ROZANOV, E., SCHOELL, M., HABERREITER, M., SHAPIRO, A. V. & NYEKI, S. 2011. A new approach to the long-term reconstruction of the solar irradiance leads to large historical solar forcing. *Astronomy &Astrophysics,* 529, A67.

SHULMEISTER, J. 1999. Australasian evidence for mid-holocene climate change implies precessional control of Walker Circulation in the Pacific. *Quaternary International,* 57, 81-91.

SHULMEISTER, J. & LEES, B. G. 1995. Pollen evidence from tropical Australia for the onset of an ENSO-dominated climate at c. 4000 BP. *The Holocene,* 5, 10-18.

SISCOE, G. L. 1980. Evidence in the auroral record for secular solar variability. *Reviews of Geophysics,* 18, 647-658.

SKINNER, L. C. 2008. Revisiting the absolute calibration of the Greenland ice-core age-scales. *Climate of the Past,* 4, 295-302.

SMART, P. L. 1991. Uranium series dating. *In:* SMART, P. L. & FRANCES, P. D. (eds.) *Quaternary Dating Methods - A User's Guide.* Cambridge, England: Quaternary Research Association.

SOMMERVILLE, W. 2000. When the calendar started. *Astronomy and Geophysics,* 4**,** 4.9.

SONETT, C. P. & SUESS, H. E. 1984. Correlation of bristlecone pine ring widths with atmospheric 14C variations: a climate-Sun relation. *Nature,* 307**,** 141-143.

SOUTHON, J. 2002. A first step to reconciling the GRIP and GISP2 ice-core chronologies, 0–14,500 yr B.P. *Quaternary Research,* 57**,** 32-37.

STEINHILBER, F., ABREU, J. A., BEER, J., BRUNNER, I., CHRISTL, M., FISCHER, H., HEIKKILÄ, U., KUBIK, P. W., MANN, M., MCCRACKEN, K. G., MILLER, H., MIYAHARA, H., OERTER, H. & WILHELMS, F. 2012. 9,400 years of cosmic radiation and solar activity from ice cores and tree rings. *Proceedings of the National Academy of Sciences of the United States of America,* 109**,** 5967-5971.

STEINHILBER, F. & BEER, J. 2013. Prediction of solar activity for the next 500 years. *Journal of Geophysical Research. Space Physics,* 118**,** 1861.

STERNBERG, R. S. & DAMON, P. E. 1983. Atmospheric Radiocarbon: Implications for the Geomagnetic Dipole Moment. *Radiocarbon,* 25**,** 239-248.

STEVENS, B. & BONY, S. 2013. What are climate models missing? *Science,* 340**,** 1053-1054.

STOTT, L., POULSEN, C., LUND, S. & THUNELL, R. 2002. Super ENSO and global climate oscillations at millennial time scales. *Science,* 297**,** 222-226.

STUIVER, M. 1961. Variations in radiocarbon concentration and sunspot activity. *Journal of Geophysical Research,* 66**,** 273.

STUIVER, M. 1965. Carbon-14 content of 18th- and 19th-century wood: variations correlated with sunspot activity. *Science,* 149**,** 533-535.

STUIVER, M. & BRAZIUNAS, T. F. 1989. Atmospheric 14C and century-scale solar oscillations. *Nature,* 338**,** 405-408.

STUIVER, M. & BRAZIUNAS, T. F. 1998. Anthropogenic and solar components of hemispheric 14C. *Geophysical Research Letters,* 25**,** 329-332.

STUIVER, M., BRAZIUNAS, T. F., BECKER, B. & KROMER, B. 1991. Climatic, solar, oceanic, and geomagnetic influences on late-glacial and holocene atmospheric 14 C 12 C change. *Quaternary Research,* 35**,** 1-24.

STUIVER, M., GROOTES, P. M. & BRAZIUNAS, T. F. 1995. The GISP2 δ18O climate record of the past 16,500 years and the role of the Sun, ocean, and volcanoes. *Quaternary Research,* 44**,** 341-354.

STUIVER, M. & QUAY, P. D. 1980. Changes in atmospheric carbon-14 attributed to a variable sun. *Science,* 207**,** 11-19.

STUIVER, M., REIMER, J., BARD, E., WARREN BECK, J., BURR, G., HUGHEN, K., KROMER, B., MCCORMAC, G., VAN DER PLICHT, J. & SPURK, M. 1998. Intcal98 radiocarbon age calibration, 24,000-0 cal BP. *Radiocarbon,* 40**,** 1041-1083.

SUESS, H. E. Natural radiocarbon and the rate of exchange of carbon dioxide between the atmosphere and the sea. Williams Bay Conference on Nuclear Settings, 1953. 52-56.

SUESS, H. E. 1955. Radiocarbon Concentration in Modern Wood. *Science,* 122**,** 415-417.

SUESS, H. E. The three causes of secular C14 fluctuations, their amplitudes and time constants. *In:* OLSSON, I. U., ed. Radiocarbon variations and absolute chronology: 12th Nobel Symposium, 1969 Uppsala University. New York: Wiley Interscience Division.

SUESS, H. E. 1986. Secular variations of cosmogenic 14C on Earth: their discovery and interpretation. *Radiocarbon,* 2A**,** 259-265.

SUMMERHAYES, C. P. 2015. Earth's Climate Evolution. http://onlinelibrary.wiley.com: Wiley Online Library.

SVENSMARK, H. & FRIIS-CHRISTENSEN, E. 1997. Variation of cosmic ray flux and global cloud coverage—a missing link in solar-climate relationships. *Journal of Atmospheric and Solar-Terrestrial Physics,* 59**,** 1225-1232.

SVENSMARK, H., ENGHOFF, M. B., SHAVIV, N. J. & SVENSMARK, J. 2017. Increased ionization supports growth of aerosols into cloud condensation nuclei. *Nature Communications,* 8**,** 2199.

SVENSSON, A., ANDERSEN, K. K., BIGLER, M., CLAUSEN, H. B., DAHL-JENSEN, D., DAVIES, S. M., JOHNSEN, S. J., MUSCHELER, R., PARRENIN, F., RASMUSSEN, S. O., RÖTHLISBERGER, R., SEIERSTAD, I., STEFFENSEN, J. P., VINTHER, B. M., NATURVETENSKAP, KVARTÄRGEOLOGI, SCIENCE, GEOCENTRUM, II, DEPARTMENT OF, G., QUATERNARY, S., LUNDS, U., GEOCENTRE, II, GEOLOGISKA, I., LUND, U., BIOLOGISK-GEOVETENSKAPLIGA, V., SECTION OF, B. & EARTH, S. 2008. A 60,000 year Greenland stratigraphic ice core chronology. *Climate of the Past,* 4**,** 47-57.

SVENSSON, A., ANDERSEN, K. K., BIGLER, M., CLAUSEN, H., DAHL-JENSEN, D., JOHNSEN, S., RASMUSSEN, S. O., RÖTHLISBERGER, R., STEFFENSEN, J. P. & VINTHER, B. 2007. A new 60,000 year Greenland stratigraphic ice corechronology. *4th EGU General Assembly.* Vienna, Austria.

SVENSSON, A., ANDERSEN, K. K., BIGLER, M., CLAUSEN, H. B., DAHL-JENSEN, D., DAVIES, S. M., JOHNSEN, S. J., MUSCHELER, R., RASMUSSEN, S. O., RÖTHLISBERGER, R., PEDER STEFFENSEN, J. & VINTHER, B. M. 2006. The Greenland Ice Core Chronology 2005, 15–42ka. Part 2: comparison to other records. *Quaternary Science Reviews,* 25**,** 3258-3267.

TAYLOR, R. E., BAR-YOSEF, O. & RENFREW, C. 2014. *Radiocarbon Dating: an archaeological perspective,* Walnut Creek, California, Left Coast Press, Inc.

THOMSON, D. J. 1997. Dependence of global temperatures on atmospheric CO2 and solar irradiance. *Proceedings of the National Academy of Sciences,* 94**,** 8370-8377.

TINSLEY, B. A. 1994. Solar wind mechanism suggested for weather and climate change. *Eos, Transactions American Geophysical Union,* 75**,** 369.

TIWARI, R. & RAO, K. 1998. Correlated variations and periodicity of global CO2, biological mass extinctions and extra-terrestrial bolide impacts over the past 250 million years and possible geodynamical implications. *Geofizika,* 15**,** 103-117.

TOGGWEILER, J. R. & KEY, R. M. 2001. Ocean circulation: Thermohaline circulation. *In:* HOLTON, J., PYLE, J., CURRY, J. (ed.) *Encyclopedia of Atmospheric Sciences.* London: Academic Press.

TOMPKINS, P. 1978. *Secrets of the Great Pyramid,* New York, Harper Row.

TRENBERTH, K. E. 1997. The definition of El Nino. *Bulletin of the American Meteorological Society,* 78**,** 2771-2777.

TURNEY, C. 2006. *Bones, Rocks and Stars: The Science of When Things Happened,* Basingstoke, GB, Macmillan Science.

TURNEY, C. 2008. *Ice, Mud and Blood: Lessons from Climates Past,* Basingstoke, Palgrave Macmillan.

TURNEY, C. S. M. & HOBBS, D. 2006. ENSO influence on Holocene Aboriginal populations in Queensland, Australia. *Journal of Archaeological Science,* 33**,** 1744-1748.

TURNEY, C. S. M., KERSHAW, A. P., CLEMENS, S. C., BRANCH, N., MOSS, P. T. & KEITH FIFIELD, L. 2004. Millennial and orbital variations of El Nino/Southern Oscillation and high-latitude climate in the last glacial period. *Nature,* 428**,** 306-310.

TURNEY, C. S. M. & PALMER, J. G. 2007. Does the El Niño–Southern Oscillation control the interhemispheric radiocarbon offset? *Quaternary Research,* 67**,** 174-180.

TWISS, K. C. 2007. The Neolithic of the Southern Levant. *Evolutionary Anthropology,* 16**,** 24-35.

URDAN, T. C. 2010. *Statistics in Plain English,* Hoboken, Taylor & Francis.

USGS. 2013. *The Sun and Climate* [Online]. USGS. Available: http://pubs.usgs.gov/fs/fs-0095-00/fs-0095-00.pdf [Accessed July 19, 2013].

USOSKIN, I. G., SOLANKI, S. K. & KOVALTSOV, G. A. 2007. Grand minima and maxima of solar activity: new observational constraints. *Astronomy and Astrophysics,* 471**,** 301-309.

UW QUATERNARY ISOTOPE LABORATORY 1999. *1998 International 14C atmospheric decadal data set (24,000 to 0 BP)* [Online]. Available: http://depts.washington.edu/qil/datasets/ [Accessed April 24, 2015].

VAN BUREN, M. 2001. The archaeology of El Niño events and other "natural" disasters. *Journal of Archaeological Method and Theory,* 8**,** 129-149.

VAN GEEL, B., HEIJNIS, H., CHARMAN, D. J., THOMPSON, G. & ENGELS, S. 2014. Bog burst in the eastern Netherlands triggered by the 2.8 kyr BP climate event. *The Holocene,* 24**,** 1465-1477.

VASILIEV, S. S. & DERGACHEV, V. A. 2002. The ~ 2400-year cycle in atmospheric radiocarbon concentration: bispectrum of 14C data over the last 8000 years. *Annales Geophysicae,* 20**,** 115-120.

VAUTRAVERS, M. J. & SHACKLETON, N. J. 2006. Centennial-scale surface hydrology off Portugal during marine isotope stage 3: Insights from planktonic foraminiferal fauna variability. *Paleoceanography* [Online], 21. Available: http://dx.doi.org/10.1029/2005PA001144 [Accessed May 27, 2017].

VÁZQUEZ, A., CLIMENT, J. M., CASAIS, L. & QUINTANA, J. R. 2015. Current and future estimates for the fire frequency and the fire rotation period in the main woodland types of peninsular Spain: a case-study approach. *Forest Systems,* 24**,** e031-e031.

VERES, D., BAZIN, L., LANDAIS, A., TOYÉ MAHAMADOU KELE, H., LEMIEUX-DUDON, B., PARRENIN, F., MARTINERIE, P., BLAYO, E., BLUNIER, T., CAPRON, E.,

CHAPPELLAZ, J., RASMUSSEN, S. O., SEVERI, M., SVENSSON, A., VINTHER, B. & WOLFF, E. W. 2013. The Antarctic ice core chronology (AICC2012): an optimized multi-parameter and multi-site dating approach for the last 120 thousand years. *Climate of the Past,* 9**,** 1733-1748.

VIEIRA, L. E. A. & DA SILVA, L. A. 2006. Geomagnetic modulation of clouds effects in the Southern Hemisphere Magnetic Anomaly through lower atmosphere cosmic ray effects. *Geophysical Research Letters* [Online], 33.

VIEIRA, L. E. A., NORTON, A., DUDOK DE WIT, T., KRETZSCHMAR, M., SCHMIDT, G. A. & CHEUNG, M. C. M. 2012. How the inclination of Earth's orbit affects incoming solar irradiance. *Geophysical Research Letters* [Online], 39. Available: http://dx.doi.org/10.1029/2012GL052950.

VIEIRA, L. E. A., SOLANKI, S. K., KRIVOVA, N. A. & USOSKIN, I. 2011. Evolution of the solar irradiance during the Holocene. *Astronomy & Astrophysics* [Online], 531. Available: http://www.aanda.org/articles/aa/pdf/2011/07/aa15843-10.pdf [Accessed May 3, 2014].

VINES, R. G. 2008. Australian rainfall patterns and the southern oscillation. 2. A regional perspective in relation to Luni-solar (Mn) and Solar-cycle (Sc) signals. *The Rangeland Journal,* 30**,** 349.

VOLK, T. & LIU, Z. 1988. Controls of CO2 sources and sinks in the Earth scale surface ocean: temperature and nutrients. *Global Biogeochemical Cycles,* 2**,** 73-89.

WANG, B., LIU, J., KIM, H.-J., WEBSTER, P. J., YIM, S.-Y. & XIANG, B. 2013. Northern Hemisphere summer monsoon intensified by mega-El Niño/southern oscillation and Atlantic multidecadal oscillation. *Proceedings of the National Academy of Sciences,* 110**,** 5347-5352.

WANG, P., CLEMENS, S., BEAUFORT, L., BRACONNOT, P., GANSSEN, G., JIAN, Z., KERSHAW, P. & SARNTHEIN, M. 2005. Evolution and variability of the Asian monsoon system: state of the art and outstanding issues. *Quaternary Science Reviews,* 24**,** 595-629.

Clockwork and Creation, 2012. Documentary. Directed by WARD, A. Netflix.

WEIRAUCH, D., BILLUPS, K. & MARTIN, P. 2008. Evolution of millennial-scale climate variability during the mid-Pleistocene. *Paleoceanography* [Online], 23. [Accessed May 26, 2017].

WIEDER, R. K., VILE, M. & SCOTT, K. 2010. Cosmogenic 10Be as a potential dating tool in peat. *Biogeochemistry,* 101**,** 177-182.

WEIS DIVIDE COMMUNITY MEMBERS. 2013. Onset of deglacial warming in West Antarctica driven by local orbital forcing. *Nature,* 500**,** 440-444.

WILLIAMS, R. 2013. *Sun Fact Sheet* [Online]. NASA. Available: http://nssdc.gsfc.nasa.gov/planetary/factsheet/sunfact.html [Accessed August 25, 2013].

WOHLFARTH, B. 1996. The chronology of the last termination: a review of radiocarbon-dated, high-resolution terrestrial stratigraphies. *Quaternary Science Reviews,* 15**,** 267-284.

WOLFF, E. W., CHAPPELLAZ, J., BLUNIER, T., RASMUSSEN, S. O. & SVENSSON, A. 2010. Millennial-scale variability during the last glacial: the ice core record. *Quaternary Science Reviews,* 29**,** 2828-2838.

WUNSCH, C. 2010. Towards understanding the Paleocean. *Quaternary Science Reviews,* 29**,** 1960-1967.

XAPSOS, M. A. & BURKE, E. A. 2009. Evidence of 6 000-year periodicity in reconstructed sunspot numbers. *Solar Physics,* 257**,** 363-369.

XUE, J., ZHONG, W., ZHAO, Y. & PENG, X. 2008. Holocene abrupt climate shifts and mid-Holocene drought intervals recorded in Barkol Lake of Northern Xinjiang of China. *Chinese Geographical Science,* 18**,** 54-61.

YANG, S., ODAH, H. & SHAW, J. 2000. Variations in the geomagnetic dipole moment over the last 12 000 years. *Geophysical Journal International,* 140**,** 158-162.

YIOU, F., RAISBECK, G. M., BAUMGARTNER, S., BEER, J., HAMMER, C., JOHNSEN, S., JOUZEL, J., KUBIK, P. W., LESTRINGUEZ, J., STIÉVENARD, M., SUTER, M. & YIOU, P. 1997. Beryllium 10 in the Greenland Ice Core Project ice core at Summit, Greenland. *Journal of Geophysical Research,* 102**,** 26783-26794.

YOUSEF, S. M. 2000. The solar Wolf-Gleissberg cycle and its influence on the Earth. *International Conference for Environmental Hazard.* Cairo: Cairo University.

ZHOU, L. P. & SHACKLETON, N. J. 1999. Misleading positions of geomagnetic reversal boundaries in Eurasian loess and implications for correlation between continental and marine sedimentary sequences. *Earth and Planetary Science Letters,* 168**,** 117-130.

ZHU, Y. & NEWELL, R. E. 1994. Atmospheric rivers and bombs. *Geophysical Research Letters,* 21**,** 1999.

Appendix A

Table A.1: Extract of modelled cycles for the first 104 yrs (Part A). RRA, RRS, RRT rotation variables (as part of a full cycle (360°) of geographical longitude were calculated by annual angular advancement. The sunspot (Schwabe and Hale), Metonic, and lunar nodal cycles were also modelled. These latter variables are expressed here as frequencies (F) and associated sine value.

Cycle No.	Rotation variables (degrees)			Schwabe		Hale		Metonic		Lunar node	
(yrs)	RRS	RRT	RRA	F	sin()	F	sin()	F	sin()	F	Sin ()
0	0.00	0.00	0.00	0.00	0.00	0.00	0.00	0.00	0.00	0.00	0.00
1	92.29	87.19	93.47	0.09	0.52	0.04	0.27	0.05	0.32	0.05	0.33
2	184.58	174.38	186.94	0.18	0.89	0.09	0.52	0.11	0.61	0.11	0.62
3	276.87	261.58	280.41	0.26	1.00	0.13	0.74	0.16	0.84	0.16	0.85
4	9.16	348.77	13.88	0.35	0.81	0.18	0.89	0.21	0.97	0.21	0.98
5	101.45	75.96	107.34	0.44	0.38	0.22	0.98	0.26	1.00	0.27	0.99
6	193.74	163.15	200.81	0.53	-0.16	0.26	1.00	0.32	0.92	0.32	0.90
7	286.03	250.34	294.28	0.61	-0.66	0.31	0.94	0.37	0.74	0.38	0.70
8	18.32	337.53	27.75	0.70	-0.95	0.35	0.81	0.42	0.48	0.43	0.43
9	110.61	64.73	121.22	0.79	-0.97	0.39	0.61	0.47	0.16	0.48	0.11
10	202.90	151.92	214.69	0.88	-0.70	0.44	0.38	0.53	-0.16	0.54	-0.23
11	295.19	239.11	308.16	0.96	-0.22	0.48	0.11	0.58	-0.48	0.59	-0.54
12	27.48	326.30	41.63	1.05	0.32	0.53	-0.16	0.63	-0.74	0.64	-0.79
13	119.76	53.49	135.10	1.14	0.77	0.57	-0.43	0.68	-0.92	0.70	-0.95
14	212.05	140.68	228.57	1.23	0.99	0.61	-0.66	0.74	-1.00	0.75	-1.00
15	304.34	227.88	322.03	1.32	0.92	0.66	-0.84	0.79	-0.97	0.81	-0.94
16	36.63	315.07	55.50	1.40	0.57	0.70	-0.95	0.84	-0.84	0.86	-0.78
17	128.92	42.26	148.97	1.49	0.06	0.75	-1.00	0.89	-0.61	0.91	-0.52
18	221.21	129.45	242.44	1.58	-0.48	0.79	-0.97	0.95	-0.32	0.97	-0.21
19	313.50	216.64	335.91	1.67	-0.87	0.83	-0.87	1.00	0.00	1.02	0.12
20	45.79	303.83	69.38	1.75	-1.00	0.88	-0.70	1.05	0.32	1.07	0.45
21	138.08	31.03	162.85	1.84	-0.84	0.92	-0.48	1.11	0.61	1.13	0.72
22	230.37	118.22	256.32	1.93	-0.43	0.96	-0.22	1.16	0.84	1.18	0.91
23	322.66	205.41	349.79	2.02	0.11	1.01	0.06	1.21	0.97	1.23	1.00
24	54.95	292.60	83.26	2.11	0.61	1.05	0.32	1.26	1.00	1.29	0.97
25	147.24	19.79	176.72	2.19	0.94	1.10	0.57	1.32	0.92	1.34	0.84
26	239.53	106.98	270.19	2.28	0.98	1.14	0.77	1.37	0.74	1.40	0.61
27	331.82	194.18	3.66	2.37	0.74	1.18	0.92	1.42	0.48	1.45	0.31
28	64.11	281.37	97.13	2.46	0.27	1.23	0.99	1.47	0.16	1.50	-0.02
29	156.40	8.56	190.60	2.54	-0.27	1.27	0.99	1.53	-0.16	1.56	-0.35
30	248.69	95.75	284.07	2.63	-0.74	1.32	0.92	1.58	-0.48	1.61	-0.64
31	340.98	182.94	17.54	2.72	-0.98	1.36	0.77	1.63	-0.74	1.66	-0.86
32	73.27	270.13	111.01	2.81	-0.94	1.40	0.57	1.68	-0.92	1.72	-0.98
33	165.56	357.33	204.48	2.89	-0.61	1.45	0.32	1.74	-1.00	1.77	-0.99
34	257.85	84.52	297.94	2.98	-0.11	1.49	0.06	1.79	-0.97	1.83	-0.89
35	350.14	171.71	31.41	3.07	0.43	1.54	-0.22	1.84	-0.84	1.88	-0.69
36	82.43	258.90	124.88	3.16	0.84	1.58	-0.48	1.89	-0.61	1.93	-0.41
37	174.72	346.09	218.35	3.25	1.00	1.62	-0.70	1.95	-0.32	1.99	-0.09
38	267.01	73.28	311.82	3.33	0.87	1.67	-0.87	2.00	0.00	2.04	0.25
39	359.29	160.48	45.29	3.42	0.48	1.71	-0.97	2.05	0.32	2.09	0.55
40	91.58	247.67	138.76	3.51	-0.06	1.75	-1.00	2.11	0.61	2.15	0.80
41	183.87	334.86	232.23	3.60	-0.57	1.80	-0.95	2.16	0.84	2.20	0.95
42	276.16	62.05	325.70	3.68	-0.92	1.84	-0.84	2.21	0.97	2.25	1.00
43	8.45	149.24	59.17	3.77	-0.99	1.89	-0.66	2.26	1.00	2.31	0.93
44	100.74	236.43	152.63	3.86	-0.77	1.93	-0.43	2.32	0.92	2.36	0.76
45	193.03	323.63	246.10	3.95	-0.32	1.97	-0.16	2.37	0.74	2.42	0.51
46	285.32	50.82	339.57	4.04	0.22	2.02	0.11	2.42	0.48	2.47	0.19
47	17.61	138.01	73.04	4.12	0.70	2.06	0.38	2.47	0.16	2.52	-0.14
48	109.90	225.20	166.51	4.21	0.97	2.11	0.61	2.53	-0.16	2.58	-0.46
49	202.19	312.39	259.98	4.30	0.95	2.15	0.81	2.58	-0.48	2.63	-0.73
50	294.48	39.58	353.45	4.39	0.66	2.19	0.94	2.63	-0.74	2.68	-0.91
51	26.77	126.78	86.92	4.47	0.16	2.24	1.00	2.68	-0.92	2.74	-1.00
52	119.06	213.97	180.39	4.56	-0.38	2.28	0.98	2.74	-1.00	2.79	-0.97

Table A.2: Extract of modelled cycles for the first 104 yrs (Part B). RRA, RRS, RRT rotation variables (as part of a full cycle (360°) of geographical longitude were calculated by annual angular advancement. The sunspot (Schwabe and Hale), Metonic, and lunar nodal cycles were also modelled. These latter variables are expressed here as frequencies (F) and associated sine value.

Cycle No.	Rotation variables (degrees)			Schwabe		Hale		Metonic		Lunar node	
(yrs)	RRS	RRT	RRA	F	sin()	F	sin()	F	sin()	F	Sin ()
53	211.35	301.16	273.85	4.65	-0.81	2.32	0.89	2.79	-0.97	2.84	-0.83
54	303.64	28.35	7.32	4.74	-1.00	2.37	0.74	2.84	-0.84	2.90	-0.60
55	35.93	115.54	100.79	4.82	-0.89	2.41	0.52	2.89	-0.61	2.95	-0.30
56	128.22	202.73	194.26	4.91	-0.52	2.46	0.27	2.95	-0.32	3.01	0.04
57	220.51	289.93	287.73	5.00	0.00	2.50	0.00	3.00	0.00	3.06	0.37
58	312.80	17.12	21.20	5.09	0.52	2.54	-0.27	3.05	0.32	3.11	0.65
59	45.09	104.31	114.67	5.18	0.89	2.59	-0.52	3.11	0.61	3.17	0.87
60	137.38	191.50	208.14	5.26	1.00	2.63	-0.74	3.16	0.84	3.22	0.98
61	229.67	278.69	301.61	5.35	0.81	2.68	-0.89	3.21	0.97	3.27	0.99
62	321.96	5.88	35.08	5.44	0.38	2.72	-0.98	3.26	1.00	3.33	0.88
63	54.25	93.08	128.54	5.53	-0.16	2.76	-1.00	3.32	0.92	3.38	0.68
64	146.54	180.27	222.01	5.61	-0.66	2.81	-0.94	3.37	0.74	3.44	0.40
65	238.82	267.46	315.48	5.70	-0.95	2.85	-0.81	3.42	0.48	3.49	0.07
66	331.11	354.65	48.95	5.79	-0.97	2.89	-0.61	3.47	0.16	3.54	-0.26
67	63.40	81.84	142.42	5.88	-0.70	2.94	-0.38	3.53	-0.16	3.60	-0.57
68	155.69	169.03	235.89	5.96	-0.22	2.98	-0.11	3.58	-0.48	3.65	-0.81
69	247.98	256.23	329.36	6.05	0.32	3.03	0.16	3.63	-0.74	3.70	-0.96
70	340.27	343.42	62.83	6.14	0.77	3.07	0.43	3.68	-0.92	3.76	-1.00
71	72.56	70.61	156.30	6.23	0.99	3.11	0.66	3.74	-1.00	3.81	-0.93
72	164.85	157.80	249.77	6.32	0.92	3.16	0.84	3.79	-0.97	3.86	-0.75
73	257.14	244.99	343.23	6.40	0.57	3.20	0.95	3.84	-0.84	3.92	-0.49
74	349.43	332.18	76.70	6.49	0.06	3.25	1.00	3.89	-0.61	3.97	-0.17
75	81.72	59.38	170.17	6.58	-0.48	3.29	0.97	3.95	-0.32	4.03	0.16
76	174.01	146.57	263.64	6.67	-0.87	3.33	0.87	4.00	0.00	4.08	0.48
77	266.30	233.76	357.11	6.75	-1.00	3.38	0.70	4.05	0.32	4.13	0.74
78	358.59	320.95	90.58	6.84	-0.84	3.42	0.48	4.11	0.61	4.19	0.92
79	90.88	48.14	184.05	6.93	-0.43	3.46	0.22	4.16	0.84	4.24	1.00
80	183.17	135.33	277.52	7.02	0.11	3.51	-0.06	4.21	0.97	4.29	0.96
81	275.46	222.53	10.99	7.11	0.61	3.55	-0.32	4.26	1.00	4.35	0.82
82	7.75	309.72	104.45	7.19	0.94	3.60	-0.57	4.32	0.92	4.40	0.58
83	100.04	36.91	197.92	7.28	0.98	3.64	-0.77	4.37	0.74	4.46	0.28
84	192.33	124.10	291.39	7.37	0.74	3.68	-0.92	4.42	0.48	4.51	-0.06
85	284.62	211.29	24.86	7.46	0.27	3.73	-0.99	4.47	0.16	4.56	-0.38
86	16.91	298.48	118.33	7.54	-0.27	3.77	-0.99	4.53	-0.16	4.62	-0.67
87	109.20	25.68	211.80	7.63	-0.74	3.82	-0.92	4.58	-0.48	4.67	-0.88
88	201.49	112.87	305.27	7.72	-0.98	3.86	-0.77	4.63	-0.74	4.72	-0.99
89	293.78	200.06	38.74	7.81	-0.94	3.90	-0.57	4.68	-0.92	4.78	-0.99
90	26.07	287.25	132.21	7.89	-0.61	3.95	-0.32	4.74	-1.00	4.83	-0.87
91	118.35	14.44	225.68	7.98	-0.11	3.99	-0.06	4.79	-0.97	4.88	-0.66
92	210.64	101.63	319.14	8.07	0.43	4.04	0.22	4.84	-0.84	4.94	-0.38
93	302.93	188.83	52.61	8.16	0.84	4.08	0.48	4.89	-0.61	4.99	-0.05
94	35.22	276.02	146.08	8.25	1.00	4.12	0.70	4.95	-0.32	5.05	0.28
95	127.51	3.21	239.55	8.33	0.87	4.17	0.87	5.00	0.00	5.10	0.58
96	219.80	90.40	333.02	8.42	0.48	4.21	0.97	5.05	0.32	5.15	0.82
97	312.09	177.59	66.49	8.51	-0.06	4.25	1.00	5.11	0.61	5.21	0.96
98	44.38	264.78	159.96	8.60	-0.57	4.30	0.95	5.16	0.84	5.26	1.00
99	136.67	351.98	253.43	8.68	-0.92	4.34	0.84	5.21	0.97	5.31	0.92
100	228.96	79.17	346.90	8.77	-0.99	4.39	0.66	5.26	1.00	5.37	0.74
101	321.25	166.36	80.36	8.86	-0.77	4.43	0.43	5.32	0.92	5.42	0.47
102	53.54	253.55	173.83	8.95	-0.32	4.47	0.16	5.37	0.74	5.48	0.16
103	145.83	340.74	267.30	9.04	0.22	4.52	-0.11	5.42	0.48	5.53	-0.18
104	238.12	67.93	0.77	9.12	0.70	4.56	-0.38	5.47	0.16	5.58	-0.49

Table A.3: Extract of modelled cycles for years (from 1459 to 1491). RRA, RRS, RRT rotation variables (as part of a full cycle (360°) of geographical longitude were calculated by annual angular advancement. The sunspot (Schwabe and Hale), Metonic, and lunar nodal cycles were also modelled. These latter variables are expressed here as frequencies (F) and associated sine value.

Cycle No.	Rotation variables (degrees)			Schwabe		Hale		Metonic		Lunar node	
(yrs)	RRS	RRT	RRA	F	sin()	F	sin()	F	sin()	F	Sin ()
1459	10.55	132.66	291.21	127.98	-0.11	63.99	-0.06	76.79	-0.97	78.31	0.92
1460	102.84	219.85	24.68	128.07	0.43	64.04	0.22	76.84	-0.84	78.37	0.74
1461	195.13	307.04	118.15	128.16	0.84	64.08	0.48	76.89	-0.61	78.42	0.47
1462	287.42	34.23	211.62	128.25	1.00	64.12	0.70	76.95	-0.32	78.48	0.15
1463	19.71	121.42	305.09	128.33	0.87	64.17	0.87	77.00	0.00	78.53	-0.18
1464	111.99	208.61	38.56	128.42	0.48	64.21	0.97	77.05	0.32	78.58	-0.50
1465	204.28	295.81	132.03	128.51	-0.06	64.25	1.00	77.11	0.61	78.64	-0.76
1466	296.57	23.00	225.50	128.60	-0.57	64.30	0.95	77.16	0.84	78.69	-0.93
1467	28.86	110.19	318.96	128.68	-0.92	64.34	0.84	77.21	0.97	78.74	-1.00
1468	121.15	197.38	52.43	128.77	-0.99	64.39	0.66	77.26	1.00	78.80	-0.96
1469	213.44	284.57	145.90	128.86	-0.77	64.43	0.43	77.32	0.92	78.85	-0.80
1470	305.73	11.76	239.37	128.95	-0.32	64.47	0.16	77.37	0.74	78.90	-0.56
1471	38.02	98.96	332.84	129.04	0.22	64.52	-0.11	77.42	0.48	78.96	-0.26
1472	130.31	186.15	66.31	129.12	0.70	64.56	-0.38	77.47	0.16	**79.01**	0.08
1473	222.60	273.34	159.78	129.21	0.97	64.61	-0.61	77.53	-0.16	79.07	0.40
1474	314.89	**0.53**	253.25	129.30	0.95	64.65	-0.81	77.58	-0.48	79.12	0.68
1475	47.18	87.72	346.72	129.39	0.66	64.69	-0.94	77.63	-0.74	79.17	0.89
1476	139.47	174.91	80.18	129.47	0.16	64.74	-1.00	77.68	-0.92	79.23	0.99
1477	231.76	262.11	173.65	129.56	-0.38	64.78	-0.98	77.74	-1.00	79.28	0.98
1478	324.05	349.30	267.12	129.65	-0.81	64.82	-0.89	77.79	-0.97	79.33	0.86
1479	56.34	76.49	**0.59**	129.74	-1.00	64.87	-0.74	77.84	-0.84	79.39	0.65
1480	148.63	163.68	94.06	129.82	-0.89	64.91	-0.52	77.89	-0.61	79.44	0.36
1481	240.92	250.87	187.53	129.91	-0.52	64.96	-0.27	77.95	-0.32	79.50	0.03
1482	333.21	338.06	281.00	**130.00**	0.00	**65.00**	0.00	**78.00**	0.00	79.55	-0.30
1483	65.50	65.26	14.47	130.09	0.52	65.04	0.27	78.05	0.32	79.60	-0.60
1484	157.79	152.45	107.94	130.18	0.89	65.09	0.52	78.11	0.61	79.66	-0.83
1485	250.08	239.64	201.41	130.26	1.00	65.13	0.74	78.16	0.84	79.71	-0.97
1486	342.37	326.83	294.87	130.35	0.81	65.18	0.89	78.21	0.97	79.76	-1.00
1487	74.66	54.02	28.34	130.44	0.38	65.22	0.98	78.26	1.00	79.82	-0.91
1488	166.95	141.21	121.81	130.53	-0.16	65.26	1.00	78.32	0.92	79.87	-0.72
1489	259.24	228.41	215.28	130.61	-0.66	65.31	0.94	78.37	0.74	79.92	-0.45
1490	351.52	315.60	308.75	130.70	-0.95	65.35	0.81	78.42	0.48	**79.98**	-0.13
1491	83.81	42.79	42.22	130.79	-0.97	65.39	0.61	78.47	0.16	**80.03**	0.20

Table A.4: Table showing the interaction of different calendar and yearly cycles. For example, at 57 yrs there is an alignment of the anomalistic and tropical years occurs which is displaced ~72º of longitude eastwards (refer Table B.1). At 20,646 yrs a complete cycle occurs with a return to the starting geographic longitude (this is the mean length of the Milankovitch cycle). The base signal (~128 yrs) of the Julian-tropical cycle is the rate of separation between the tropical year and Julian year. Similarly, the base signal of the anomalistic and tropical year interaction is the separation rate between the tropical and anomalistic years.

Interactive Cycle Years/Calendars	Annual rate of separation		Base signal	Total cycle length
	(minutes)	(º. Longitude)	(years)	(years)
Anomalistic-tropical	0.42	6.28	57.35	20,645.87
Sidereal-tropical	0.34	5.10	70.62	25,422.04
Julian-tropical	0.19	2.81	128.19	46,148.52
Julian-sidereal	0.15	2.29	157.23	56,603.42
Julian-anomalistic	0.23	3.47	103.78	37,359.90
Anomalistic-sidereal	0.08	1.18	305.25	109,891.45
Gregorian-tropical	0.01	0.11	3,323.36	1,196,410.77
Gregorian-sidereal	0.33	4.99	72.15	25,973.95
Gregorian-anomalistic	0.41	6.17	58.36	21,008.40

Appendix B

Table B.1: Extract of Metonic lunation data (from 1364AD to 2163AD). Note the implementation of Gregorian calendar in 1582 and the loss of days from the Julian calendar (Section 3.2.1).

Year	Lunation	Lunation	Lunation	Declinations		Right Ascension (deg.)		
BC/AD	Date (Gregorian)	Date (Julian)	Lunation type	Sun	Moon	Sun RA	Moon RA	Obliquity
2163	4 January 2163	4 January 2163	New Moon	-22.65	-17.90	285.60	285.07	-23.42
2144	5 January 2144	5 January 2144	New Moon	-22.67	-18.18	285.38	284.88	-23.42
2125	4 January 2125	4 January 2125	New Moon	-22.65	-18.48	285.55	285.08	-23.42
2106	5 January 2106	5 January 2106	New Moon	-22.62	-18.82	285.88	285.45	-23.43
2087	4 January 2087	4 January 2087	New Moon	-22.62	-19.23	286.03	285.63	-23.43
2068	5 January 2068	5 January 2068	New Moon	-22.63	-19.78	285.80	285.48	-23.43
2049	4 January 2049	4 January 2049	New Moon	-22.68	-20.42	285.37	285.12	-23.43
2030	4 January 2030	4 January 2030	New Moon	-22.72	-21.08	284.97	284.78	-23.44
2011	4 January 2011	4 January 2011	Partial eclipse	-22.73	-21.75	284.82	284.72	-23.44
1992	4 January 1992	4 January 1992	Annular eclipse	-22.72	-22.35	285.05	285.00	-23.44
1973	4 January 1973	4 January 1973	Annular eclipse	-22.68	-22.93	285.38	285.40	-23.44
1954	5 January 1954	5 January 1954	Annular eclipse	-22.68	-23.58	285.43	285.55	-23.45
1935	5 January 1935	5 January 1935	Partial eclipse	-22.72	-24.27	285.15	285.33	-23.45
1916	5 January 1916	5 January 1916	New Moon	-22.77	-24.95	284.70	284.93	-23.45
1897	3 January 1897	3 January 1897	New Moon	-22.80	-25.58	284.33	284.63	-23.45
1878	3 January 1878	3 January 1878	New Moon	-22.80	-26.10	284.27	284.63	-23.46
1859	4 January 1859	4 January 1859	New Moon	-22.78	-26.50	284.55	284.97	-23.46
1840	4 January 1840	4 January 1840	New Moon	-22.75	-26.87	284.85	285.33	-23.46
1821	4 January 1821	4 January 1821	New Moon	-22.77	-27.22	284.83	285.35	-23.46
1802	4 January 1802	4 January 1802	New Moon	-22.80	-27.50	284.50	285.03	-23.47
1783	3 January 1783	3 January 1783	New Moon	-22.83	-27.72	284.05	284.58	-23.47
1764	3 January 1764	3 January 1764	New Moon	-22.87	-27.83	283.73	284.27	-23.47
1745	2 January 1745	2 January 1745	New Moon	-22.87	-27.82	283.77	284.30	-23.47
1726	3 January 1726	3 January 1726	New Moon	-22.85	-27.70	284.08	284.62	-23.48
1707	4 January 1707	4 January 1707	New Moon	-22.82	-27.53	284.33	284.87	-23.48
1688	3 January 1688	3 January 1688	New Moon	-22.83	-27.30	284.25	284.73	-23.48
1669	2 January 1669	2 January 1669	New Moon	-22.87	-26.98	283.87	284.30	-23.48
1650	2 January 1650	2 January 1650	New Moon	-22.92	-26.62	283.43	283.82	-23.48
1631	2 January 1631	2 January 1631	New Moon	-22.93	-26.17	283.17	283.48	-23.49
1612	3 January 1612	3 January 1612	New Moon	-22.93	-25.63	283.27	283.53	-23.49
1593	2 January 1593	23 December 1592	New Moon	-22.90	-25.07	282.38	283.83	-23.49
1574	3 January 1574	24 December 1573	New Moon	-22.88	-24.47	283.80	283.97	-23.49
1555	3 January 1555	24 December 1554	Total eclipse	-22.90	-23.83	283.63	283.72	-23.50
1536	3 January 1536	24 December 1535	Total eclipse	-22.95	-23.20	283.20	283.22	-23.50
1517	2 January 1517	23 December 1516	Total eclipse	-22.98	-22.57	282.77	282.73	-23.50
1498	1 January 1498	23 December 1497	Partial eclipse	-23.00	-21.90	282.58	282.48	-23.50
1479	2 January 1479	24 December 1478	New Moon	-22.98	-21.28	282.77	282.60	-23.51
1460	3 January 1460	25 December 1459	New Moon	-22.97	-20.70	283.10	282.88	-23.51
1441	2 January 1441	24 December 1440	New Moon	-22.95	-20.13	283.22	282.95	-23.51
1422	2 January 1422	24 December 1421	New Moon	-22.98	-19.62	282.98	282.65	-23.51
1403	2 January 1403	24 December 1402	New Moon	-23.02	-19.20	282.55	282.18	-23.52
1384	1 January 1384	24 December 1383	New Moon	-23.05	-18.82	282.15	281.77	-23.52
1364	31 December 1364	23 December 1364	New Moon	-23.07	-18.52	282.03	281.65	-23.52
1346	1 January 1346	24 December 1345	New Moon	-23.05	-18.30	282.28	281.85	-23.52
1327	2 January 1327	25 December 1326	New Moon	-23.02	-18.12	282.62	282.17	-23.53
1308	2 January 1308	25 December 1307	New Moon	-23.02	-18.03	282.67	282.20	-23.53
1289	31 December 1288	24 December 1288	New Moon	-23.05	-18.08	282.37	281.92	-23.53
1270	31 December 1269	24 December 1269	New Moon	-23.08	-18.22	281.92	281.5	-23.53
1251	31 December 1250	24 December 1250	New Moon	-23.12	-18.45	281.57	281.17	-23.54
1232	1 January 1232	25 December 1231	New Moon	-23.12	-18.73	281.53	281.17	-23.54

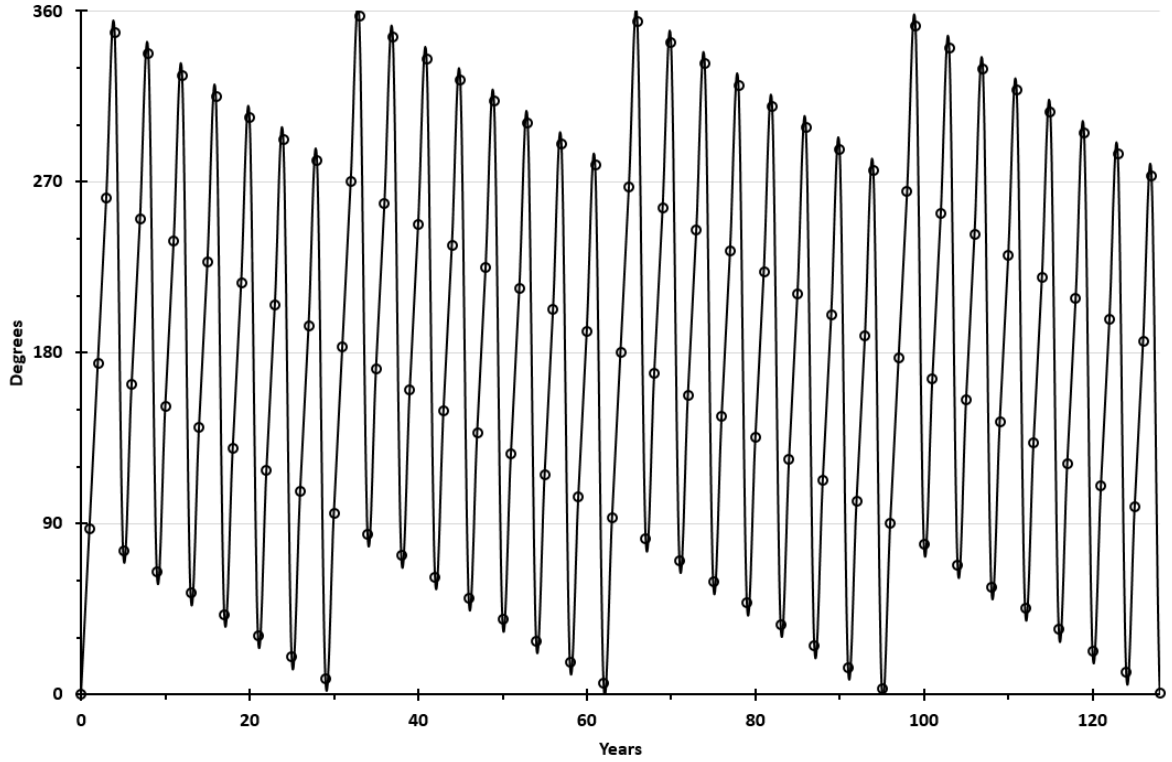

Figure B.1: Earth's rotation-revolution relative to the March equinox in geographic context (associated with RRT). The starting point is 0°. A close return (<3º) occurs at 33yrs, which is the Bruckner cycle found in dendrochronological records. The closest return (<1º) occurs at 128 yrs, which is also the rate of equinoctial precessional movement relative to the Julian year.

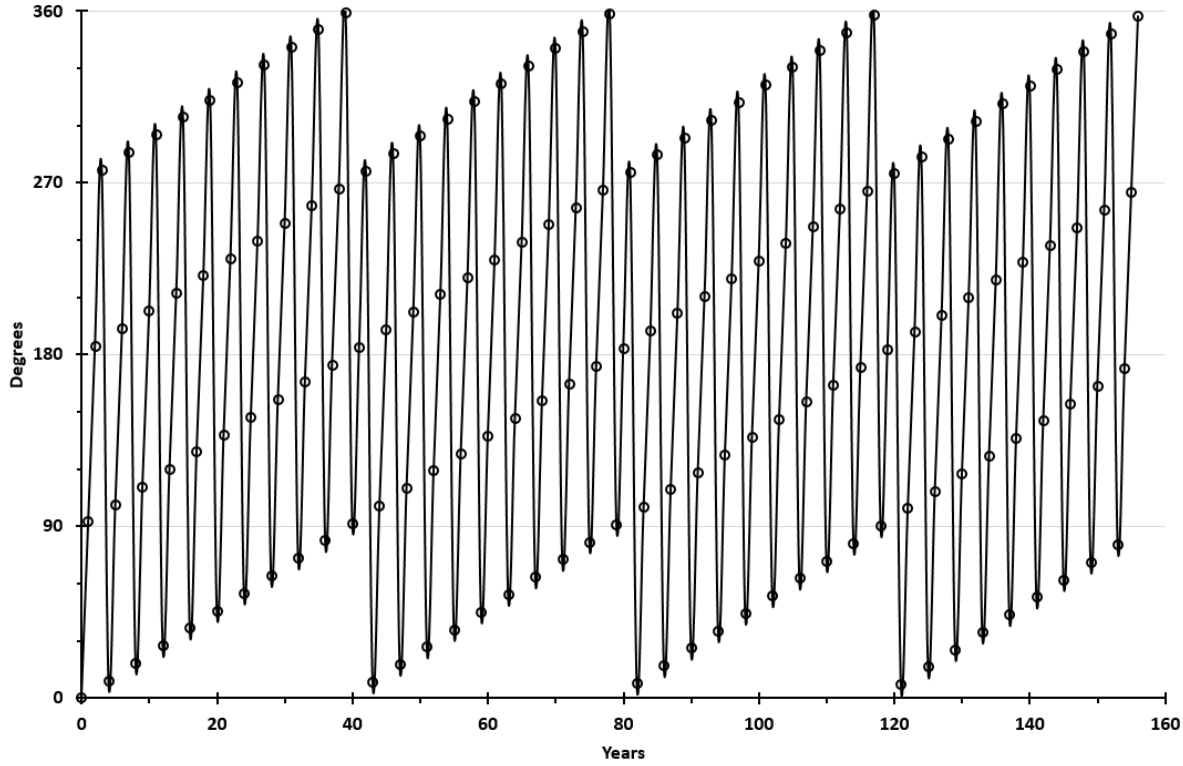

Figure B.2: Earth's rotation-revolution relative to the sidereal year in geographic context (associated with RRS). The starting point is 0°. The closest close return (<1º) occurs at 39 yrs. Other early close returns occur at 78 yrs, 117 yrs and 156 yrs.

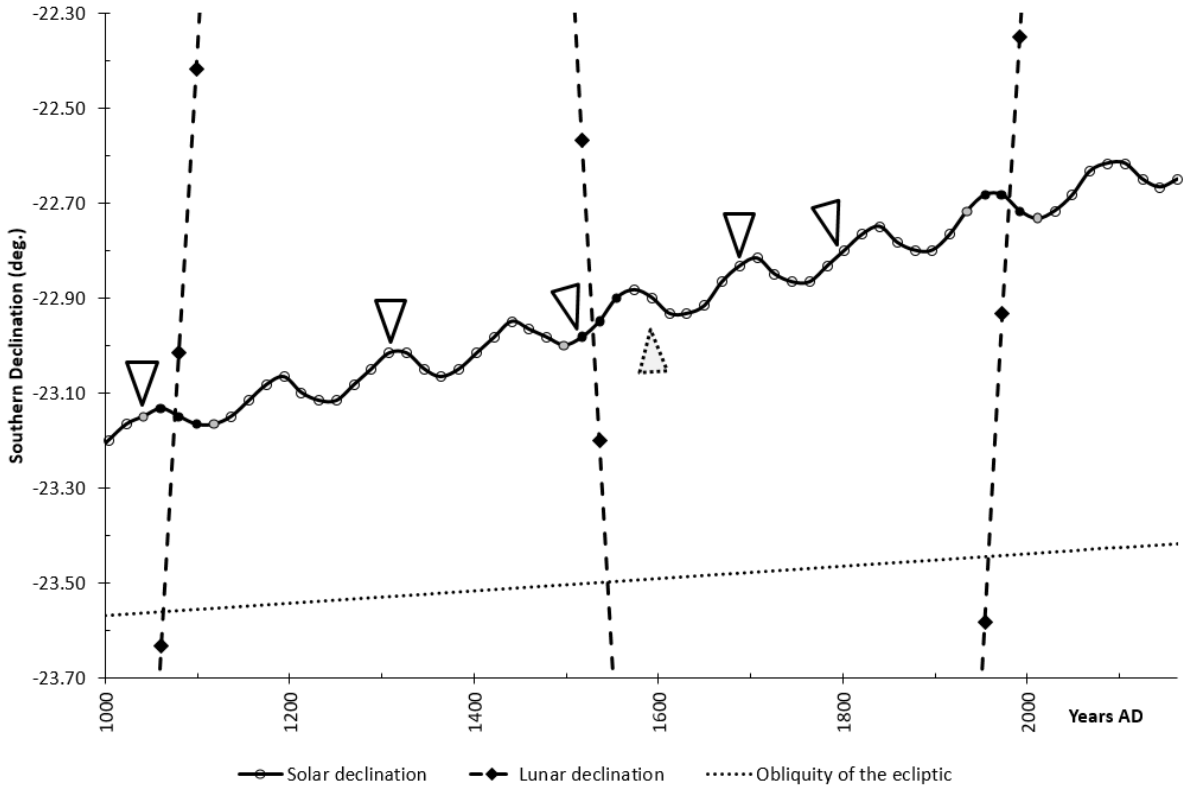

Figure B.3: Zoom of solar declination cycle since 1000AD. Black-filled markers are total or annular eclipses; grey-filled markers are partial eclipses; grey-filled arrow is approximate location of Bond event. Clear arrows in order from left to right show the Oort minimum, Wolf Minimum, Spörer Minimum, Maunder Minimum, Dalton Minimum. All these minima occur close to the northern peaks of the solar declination movement, with the exception of the Spörer Minimum (which is a split peak incorporating a Gleissberg cycle).

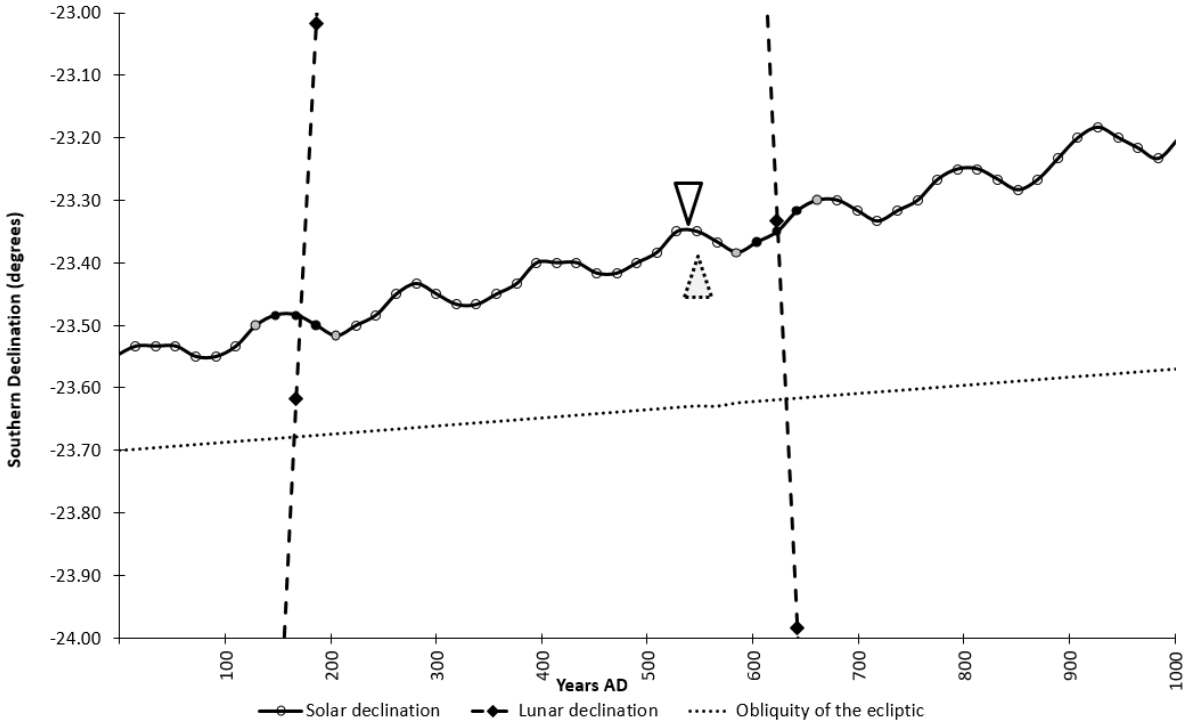

Figure B.4: Zoom of solar declination cycle between 1BC and 1000AD. Black-filled markers are total or annular eclipses; grey-filled markers are partial eclipses. Grey-filled arrow approximates to IRD event (Bond *et al.*, 1997). White arrow= sudden Dark Age Cooling event. Bump in obliquity due to change of month from December 31 to January 1. Zero value on x-axis is 1BC.

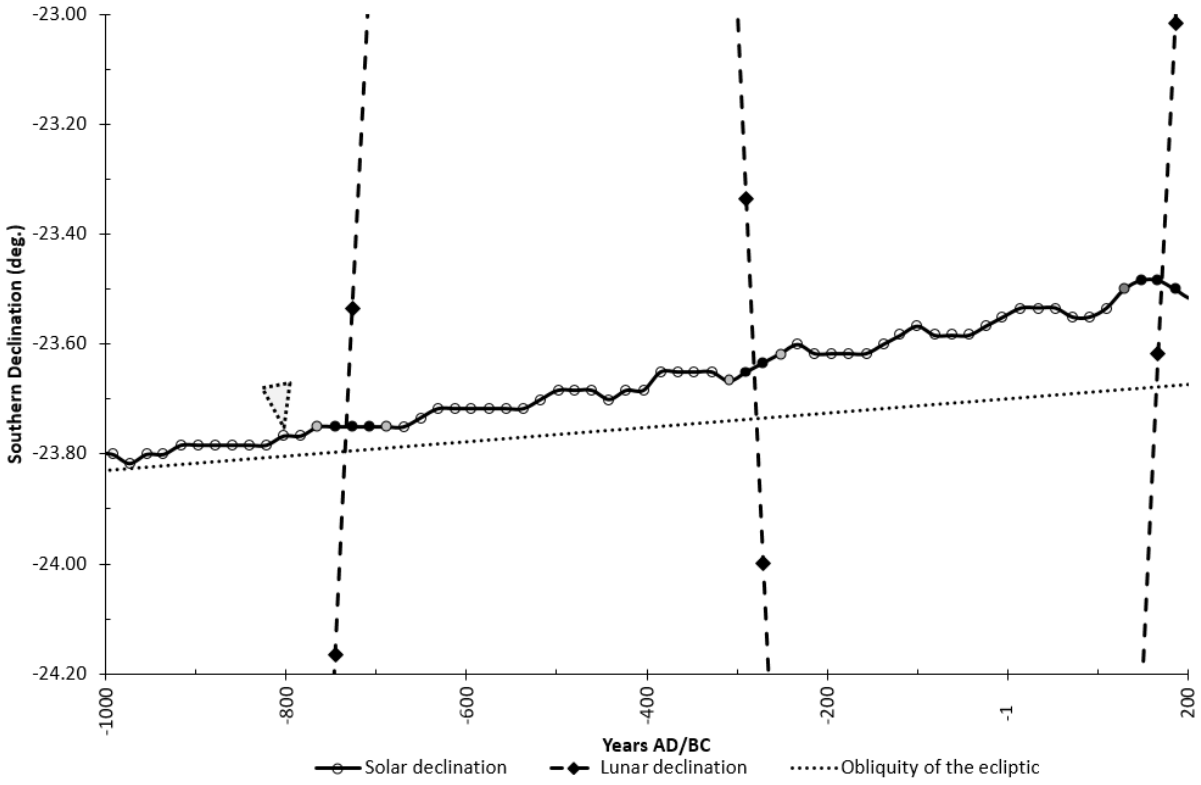

Figure B.5: Zoom of solar declination cycle between 1000BC and 200AD. Black-filled markers are total or annular eclipses; grey-filled markers are partial eclipses. Grey-filled arrow approximate location of Bond event (which occurs 76 yrs (Gleissberg cycle) ahead of eclipse).

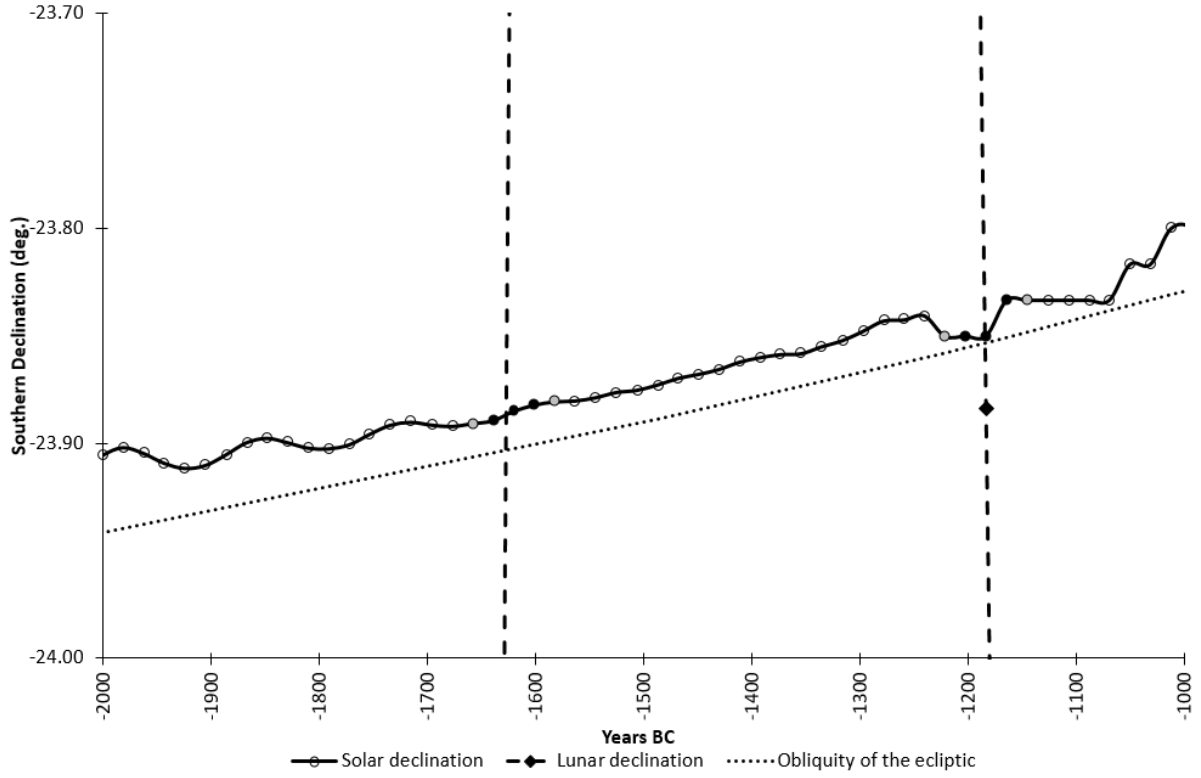

Figure B.6: Zoom of solar declination cycle between 2000BC and 1000BC. A period of flattened 133yr cycles is evidenced, corresponding with flattened SdV cycles in C14. The December solstice in 1183BC falls on the line indicated by the obliquity of the ecliptic. Negative values on the axis are BC.

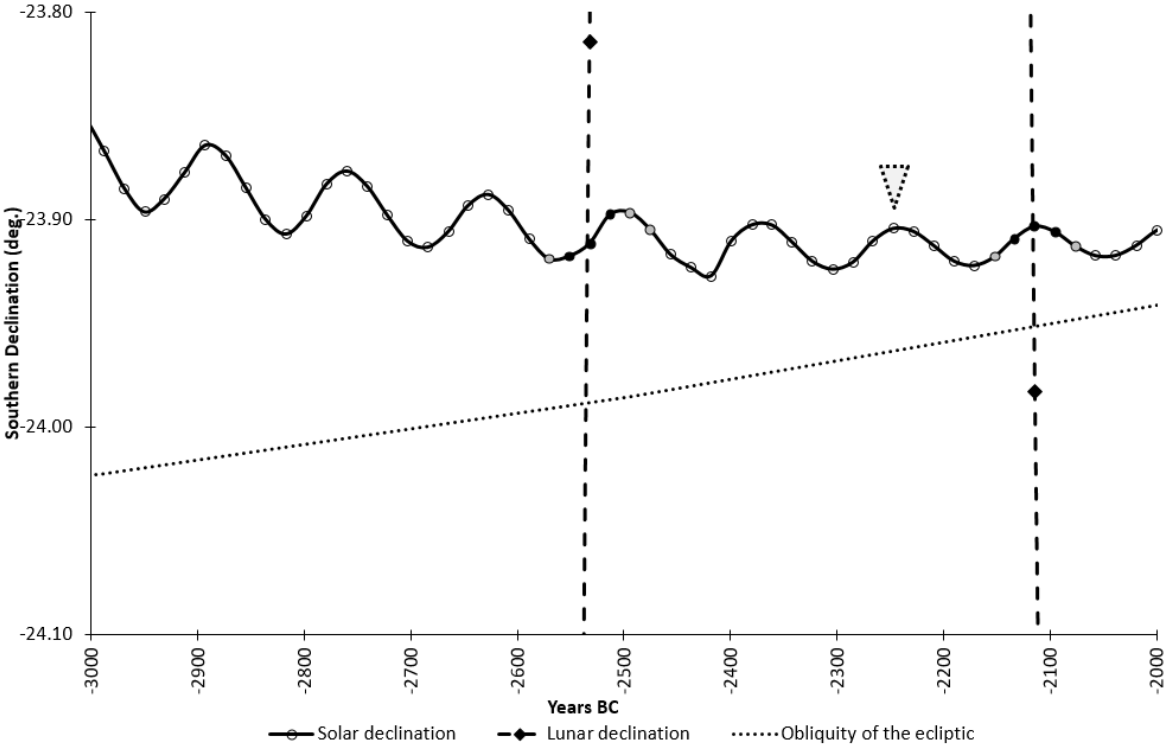

Figure B.7: Zoom of solar declination cycle between 3000BC and 2000BC. Black-filled markers are total or annular eclipses; grey-filled markers are partial eclipses. Grey- filled arrow approximate location of IRD event (Bond *et al.*, 1999), which occurs 95 yrs (Gleissberg cycle) ahead of eclipse.

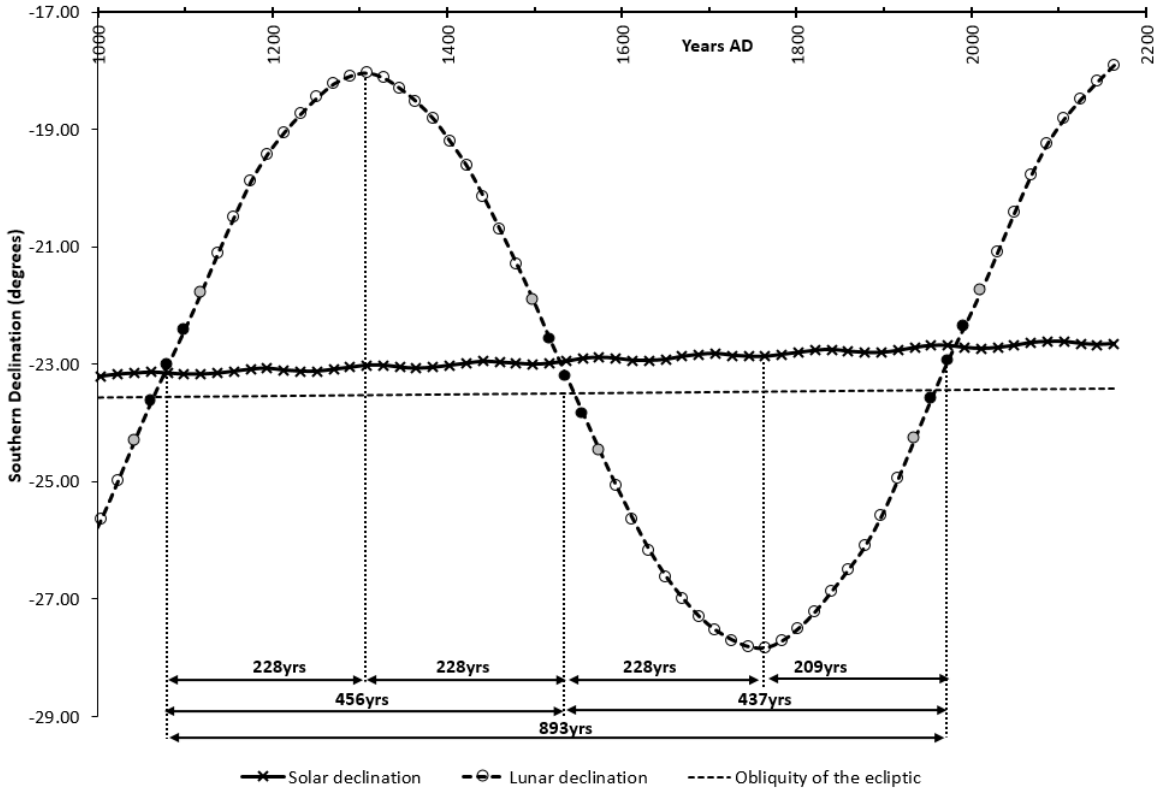

Figure B.8: Zoom of lunar declination cycle since 1000AD, showing Metonic eclipse series, period and phases of the lunar declination cycle. Black-filled markers are total or annular eclipses; grey-filled markers are partial eclipses.

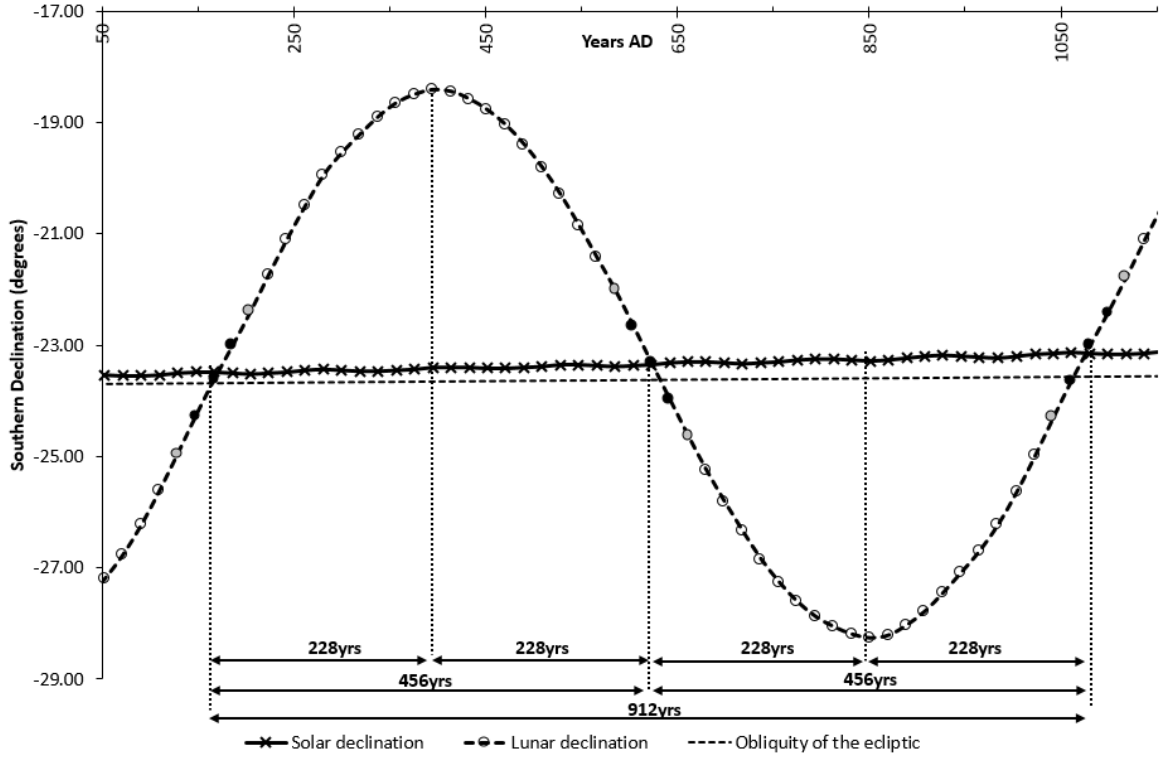

Figure B.9: Zoom of lunar declination cycle from 50AD to 1150AD, showing Metonic eclipse series, period and phases of the lunar declination cycle. Black-filled markers are total or annular eclipses; grey-filled markers are partial eclipses.

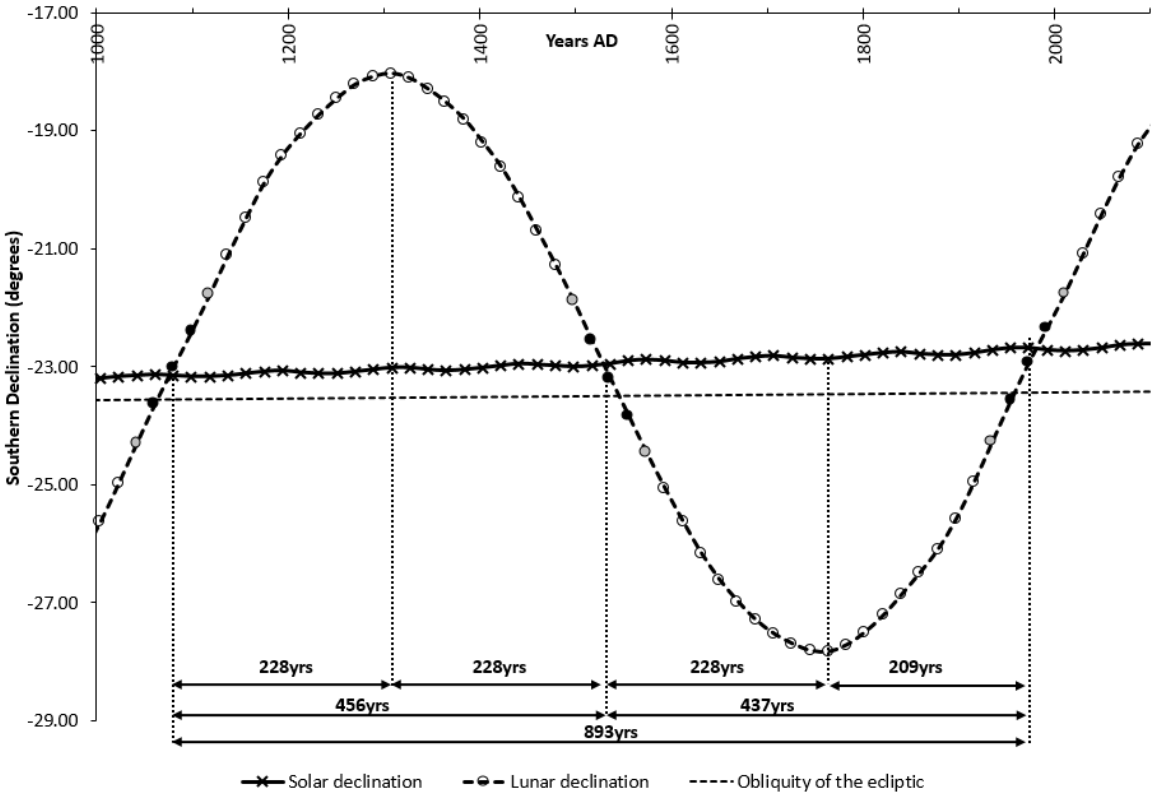

Figure B.10: Zoom of lunar declination cycle from 850BC to 200AD, showing Metonic eclipse series, period and phases of the lunar declination cycle. Black-filled markers are total or annular eclipses; grey-filled markers are partial eclipses. Negative values on x-axis are BC.

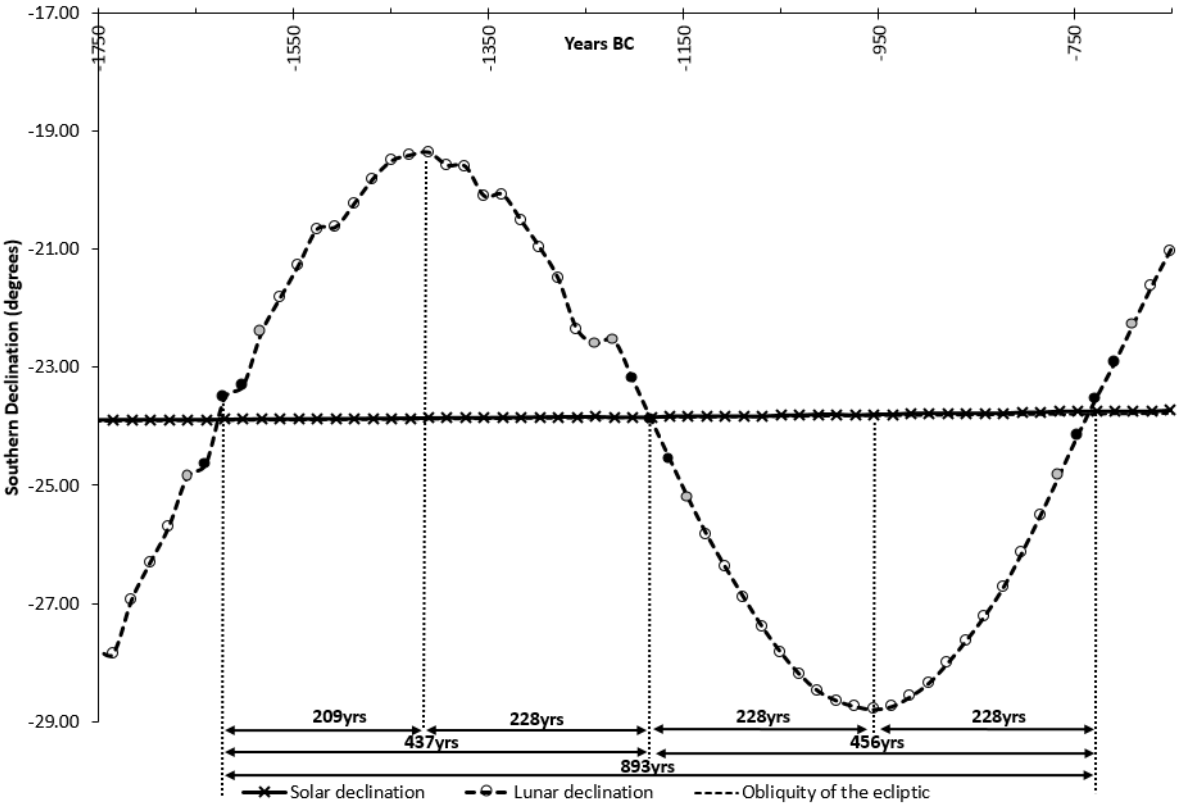

Figure B.11: Zoom of lunar declination cycle from 1750-650BC, showing Metonic eclipse series, period and phases of the lunar declination cycle. Black-filled markers are total or annular eclipses; grey-filled markers are partial eclipses. Note change of planetarium software at 1240BC. December solstice and Metonic lunation exact at 1183BC.

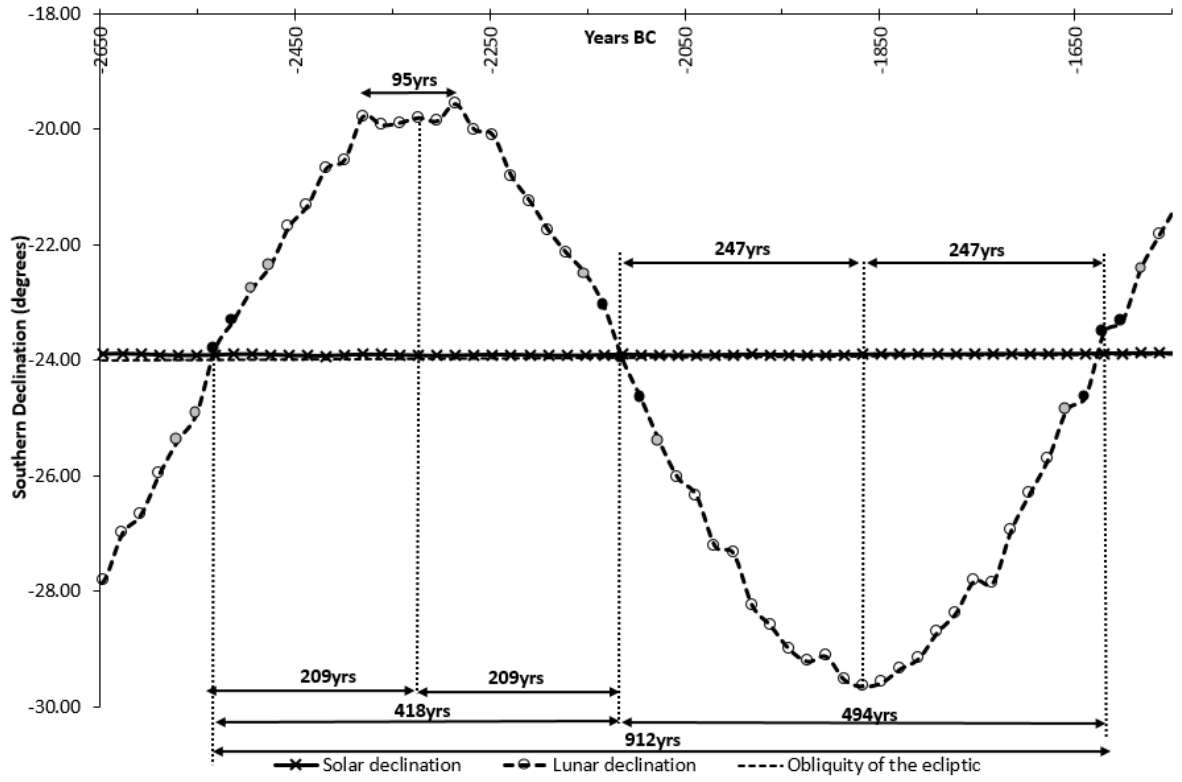

Figure B.12: Zoom of lunar declination cycle from 2650BC-1550BC, showing Metonic eclipse series, period and phases of the lunar declination cycle. Black-filled markers are total or annular eclipses; grey-filled markers are partial eclipses.

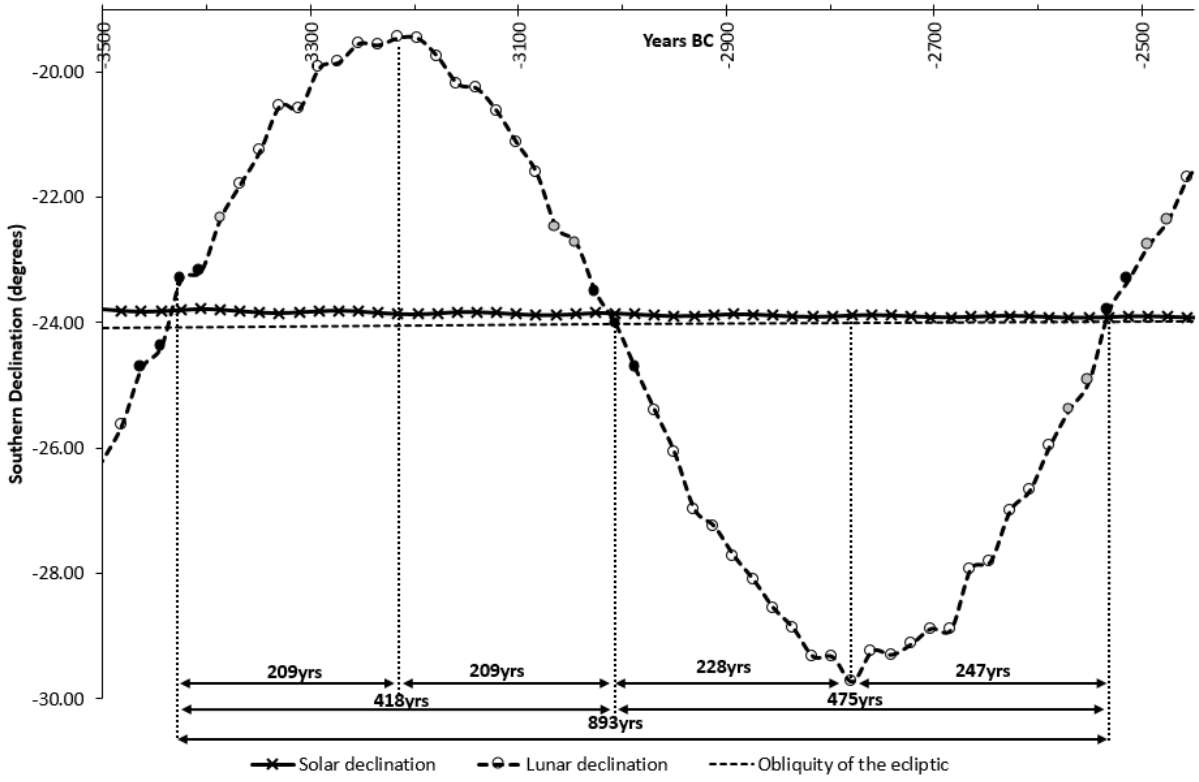

Figure B.13: Zoom of lunar declination cycle from 3550BC-2450BC, showing Metonic eclipse series, period and phases of the lunar declination cycle. Black-filled markers are total or annular eclipses; grey-filled markers are partial eclipses.

Appendix C

Table C.1: Excerpt from gravitational model. This table shows lunation date, Gregorian calendar date, and gravitational calculations based on Earth-Moon and Earth-Sun distances at the time of the Metonic lunation.

Year BC/AD	Lunation date (Gregorian)	Earth-Moon distance (m)	Gravitation (N) Earth-Moon	Gravitation var (N) Earth-Moon	Earth-Sun distance (r) (AU)	Earth-Sun distance at Metonic lunation (m)	Earth-Sun gravitation (N) at Metonic lunation	Earth-Sun gravitation (N) var
2163	4 January 2163	3.70E+08	2.14E+20		0.98329	1.47E+11	3.67E+25	-7.46E+20
2144	5 January 2144	3.89E+08	1.93E+20	-2.05E+19	0.98328	1.47E+11	3.67E+25	-1.49E+21
2125	4 January 2125	4.05E+08	1.79E+20	-1.47E+19	0.98326	1.47E+11	3.67E+25	-1.49E+21
2106	5 January 2106	4.02E+08	1.81E+20	2.41E+18	0.98324	1.47E+11	3.67E+25	2.98E+21
2087	4 January 2087	3.90E+08	1.93E+20	1.17E+19	0.98328	1.47E+11	3.67E+25	0.00E+00
2068	5 January 2068	3.69E+08	2.16E+20	2.28E+19	0.98328	1.47E+11	3.67E+25	0.00E+00
2049	4 January 2049	3.62E+08	2.24E+20	8.21E+18	0.98328	1.47E+11	3.67E+25	0.00E+00
2030	4 January 2030	3.73E+08	2.10E+20	-1.34E+19	0.98328	1.47E+11	3.67E+25	-2.24E+21
2011	4 January 2011	3.90E+08	1.93E+20	-1.77E+19	0.98325	1.47E+11	3.67E+25	2.98E+21
1992	4 January 1992	4.11E+08	1.73E+20	-1.95E+19	0.98329	1.47E+11	3.67E+25	-2.24E+21
1973	4 January 1973	4.01E+08	1.83E+20	9.36E+18	0.98326	1.47E+11	3.67E+25	2.24E+21
1954	5 January 1954	3.85E+08	1.98E+20	1.50E+19	0.98329	1.47E+11	3.67E+25	-7.46E+20
1935	5 January 1935	3.64E+08	2.21E+20	2.36E+19	0.98328	1.47E+11	3.67E+25	0.00E+00
1916	5 January 1916	3.61E+08	2.24E+20	3.25E+18	0.98328	1.47E+11	3.67E+25	-7.46E+20
1897	3 January 1897	3.75E+08	2.08E+20	-1.60E+19	0.98327	1.47E+11	3.67E+25	-1.49E+21
1878	3 January 1878	3.94E+08	1.89E+20	-1.96E+19	0.98325	1.47E+11	3.67E+25	2.98E+21
1859	4 January 1859	4.10E+08	1.75E+20	-1.42E+19	0.98329	1.47E+11	3.67E+25	1.49E+21
1840	4 January 1840	4.02E+08	1.81E+20	6.62E+18	0.98331	1.47E+11	3.67E+25	-7.46E+20
1821	4 January 1821	3.78E+08	2.05E+20	2.43E+19	0.98330	1.47E+11	3.67E+25	0.00E+00
1802	4 January 1802	3.59E+08	2.27E+20	2.14E+19	0.98330	1.47E+11	3.67E+25	-7.46E+20
1783	3 January 1783	3.61E+08	2.25E+20	-1.61E+18	0.98329	1.47E+11	3.67E+25	-7.46E+20
1764	3 January 1764	3.77E+08	2.06E+20	-1.88E+19	0.98328	1.47E+11	3.67E+25	2.24E+21
1745	2 January 1745	4.03E+08	1.81E+20	-2.59E+19	0.98331	1.47E+11	3.67E+25	-1.49E+21
1726	3 January 1726	4.05E+08	1.78E+20	-2.22E+18	0.98329	1.47E+11	3.67E+25	4.47E+21
1707	4 January 1707	3.98E+08	1.85E+20	6.63E+18	0.98335	1.47E+11	3.67E+25	-2.24E+21
1688	3 January 1688	3.70E+08	2.14E+20	2.92E+19	0.98332	1.47E+11	3.67E+25	-7.46E+20
1669	2 January 1669	3.56E+08	2.31E+20	1.69E+19	0.98331	1.47E+11	3.67E+25	0.00E+00
1650	2 January 1650	3.61E+08	2.24E+20	-6.54E+18	0.98331	1.47E+11	3.67E+25	7.46E+20
1631	2 January 1631	3.81E+08	2.01E+20	-2.32E+19	0.98332	1.47E+11	3.67E+25	3.73E+21
1612	3 January 1612	4.08E+08	1.76E+20	-2.49E+19	0.98337	1.47E+11	3.67E+25	0.00E+00
1593	2 January 1593	4.08E+08	1.76E+20	2.25E+16	0.98337	1.47E+11	3.67E+25	0.00E+00
1574	3 January 1574	3.89E+08	1.94E+20	1.75E+19	0.98337	1.47E+11	3.67E+25	0.00E+00
1555	3 January 1555	3.65E+08	2.20E+20	2.57E+19	0.98337	1.47E+11	3.67E+25	0.00E+00
1536	3 January 1536	3.55E+08	2.32E+20	1.24E+19	0.98337	1.47E+11	3.67E+25	-7.46E+20
1517	2 January 1517	3.64E+08	2.21E+20	-1.09E+19	0.98336	1.47E+11	3.67E+25	2.24E+21
1498	1 January 1498	3.89E+08	1.93E+20	-2.77E+19	0.98339	1.47E+11	3.67E+25	7.45E+20
1479	2 January 1479	4.05E+08	1.79E+20	-1.48E+19	0.98340	1.47E+11	3.67E+25	4.47E+21
1460	3 January 1460	4.08E+08	1.76E+20	-3.00E+18	0.98346	1.47E+11	3.67E+25	-2.24E+21
1441	2 January 1441	3.82E+08	2.01E+20	2.55E+19	0.98343	1.47E+11	3.67E+25	1.49E+21
1422	2 January 1422	3.63E+08	2.22E+20	2.12E+19	0.98345	1.47E+11	3.67E+25	-7.45E+20
1403	2 January 1403	3.56E+08	2.31E+20	8.23E+18	0.98344	1.47E+11	3.67E+25	0.00E+00
1384	1 January 1384	3.69E+08	2.15E+20	-1.59E+19	0.98344	1.47E+11	3.67E+25	3.73E+21
1364	31 December 1364	3.97E+08	1.86E+20	-2.87E+19	0.98349	1.47E+11	3.66E+25	-1.49E+21
1346	1 January 1346	4.04E+08	1.79E+20	-6.76E+18	0.98347	1.47E+11	3.66E+25	3.73E+21
1327	2 January 1327	4.01E+08	1.82E+20	2.75E+18	0.98352	1.47E+11	3.66E+25	7.45E+20
1308	2 January 1308	3.79E+08	2.04E+20	2.23E+19	0.98353	1.47E+11	3.66E+25	1.49E+21
1289	31 December 1288	3.63E+08	2.22E+20	1.82E+19	0.98355	1.47E+11	3.66E+25	-7.45E+20
1270	31 December 1269	3.60E+08	2.26E+20	3.12E+18	0.98354	1.47E+11	3.66E+25	0.00E+00
1251	31 December 1250	3.78E+08	2.05E+20	-2.02E+19	0.98354	1.47E+11	3.66E+25	1.49E+21
1232	1 January 1232	3.99E+08	1.84E+20	-2.13E+19	0.98356	1.47E+11	3.66E+25	2.98E+21
1213	31 December 1212	4.11E+08	1.74E+20	-1.04E+19	0.98360	1.47E+11	3.66E+25	-7.45E+20
1194	1 January 1194	3.94E+08	1.89E+20	1.51E+19	0.98359	1.47E+11	3.66E+25	4.47E+21
1175	1 January 1175	3.78E+08	2.05E+20	1.64E+19	0.98365	1.47E+11	3.66E+25	7.45E+20

Table C.2: Perigee-perihelion relationships. This table shows the proximity of the perigean conjunction (degrees), which is calculated annually with the occurrence of perihelion.

Cycle (Yr)	Tropical year	Residual (tropical)	Anomalistic year	Residual (anomalistic)	Perigee-Perihelion conjunction
0	0.00	0.00	0.00	0.00	0.00
1	13.26	0.26	13.26	0.26	92.18
2	26.51	0.51	26.51	0.51	184.36
3	39.77	0.77	39.77	0.77	276.54
4	53.02	0.02	53.02	0.02	8.72
5	66.28	0.28	66.28	0.28	100.90
6	79.53	0.53	79.54	0.54	193.08
7	92.79	0.79	92.79	0.79	285.26
8	106.04	0.04	106.05	0.05	17.44
9	119.30	0.30	119.30	0.30	109.62
10	132.55	0.55	132.56	0.56	201.80
11	145.81	0.81	145.82	0.82	293.99
12	159.07	0.07	159.07	0.07	26.17
13	172.32	0.32	172.33	0.33	118.35
14	185.58	0.58	185.58	0.58	210.53
15	198.83	0.83	198.84	0.84	302.71
16	212.09	0.09	212.10	0.10	34.89
17	225.34	0.34	225.35	0.35	127.07
18	238.60	0.60	238.61	0.61	219.25
19	251.85	0.85	251.87	0.87	311.43
20	265.11	0.11	265.12	0.12	43.61
21	278.36	0.36	278.38	0.38	135.79
22	291.62	0.62	291.63	0.63	227.97
23	304.87	0.87	304.89	0.89	320.15
24	318.13	0.13	318.15	0.15	52.33
25	331.39	0.39	331.40	0.40	144.51
26	344.64	0.64	344.66	0.66	236.69
27	357.90	0.90	357.91	0.91	328.87
28	371.15	0.15	371.17	0.17	61.05
29	384.41	0.41	384.43	0.43	153.23
30	397.66	0.66	397.68	0.68	245.41
31	410.92	0.92	410.94	0.94	337.59
32	424.17	0.17	424.19	0.19	69.78
33	437.43	0.43	437.45	0.45	161.96
34	450.68	0.68	450.71	0.71	254.14
35	463.94	0.94	463.96	0.96	346.32
36	477.20	0.20	477.22	0.22	78.50
37	490.45	0.45	490.47	0.47	170.68
38	503.71	0.71	503.73	0.73	262.86
39	516.96	0.96	516.99	0.99	355.04
40	530.22	0.22	530.24	0.24	87.22
41	543.47	0.47	543.50	0.50	179.40
42	556.73	0.73	556.75	0.75	271.58
43	569.98	0.98	570.01	0.01	3.76
44	583.24	0.24	583.27	0.27	95.94
45	596.49	0.49	596.52	0.52	188.12
46	609.75	0.75	609.78	0.78	280.30
47	623.00	0.00	623.03	0.03	12.48
48	636.26	0.26	636.29	0.29	104.66
49	649.52	0.52	649.55	0.55	196.84
50	662.77	0.77	662.80	0.80	289.02
51	676.03	0.03	676.06	0.06	21.20
52	689.28	0.28	689.31	0.31	113.38
53	702.54	0.54	702.57	0.57	205.56
54	715.79	0.79	715.83	0.83	297.75
55	729.05	0.05	729.08	0.08	29.93
56	742.30	0.30	742.34	0.34	122.11
57	755.56	0.56	755.60	0.60	214.29

Table C.3: Excerpt from solar irradiance and insolation model. Shown are solar declination data, Gregorian calendar date, solar zenith angles (in radians), Earth-Sun distance, TOA solar irradiance at the date of the Metonic lunation, and insolation for selected latitudes.

Metonic lunation data			Solar zenith angles (radians)							Solar insolation for:				
Year BC/AD	Lunation date (Gregorian)	Solar declination (degrees)	Tropic of Capricorn	Tropic of Cancer	Equator	Antarctic Circle	Arctic Circle	Earth-Sun distance at Metonic lunation (r) (m)	Solar irradiance (TOA) at Metonic lunation) W/m^2)	Tropic of Capricorn	Tropic of Cancer	Equator	Antarctic circle	Arctic circle
2163	4 January 2163	-22.65	0.01	0.80	0.40	0.77	1.56	1.47E+11	1407.09	1407.52	976.24	1299.08	1013.43	18.43
2144	5 January 2144	-22.67	0.01	0.80	0.40	0.77	1.56	1.47E+11	1407.12	1407.55	975.97	1298.95	1013.74	18.02
2125	4 January 2125	-22.65	0.01	0.80	0.40	0.77	1.56	1.47E+11	1407.17	1407.60	976.30	1299.16	1013.49	18.43
2106	5 January 2106	-22.62	0.01	0.80	0.39	0.77	1.56	1.47E+11	1407.23	1407.65	976.93	1299.53	1012.97	19.25
2087	4 January 2087	-22.62	0.01	0.80	0.39	0.77	1.56	1.47E+11	1407.12	1407.53	976.85	1299.43	1012.88	19.24
2068	5 January 2068	-22.63	0.01	0.80	0.40	0.77	1.56	1.47E+11	1407.12	1407.54	976.56	1299.27	1013.17	18.84
2049	4 January 2049	-22.68	0.01	0.81	0.40	0.77	1.56	1.47E+11	1407.12	1407.56	975.67	1298.80	1014.02	17.61
2030	4 January 2030	-22.72	0.01	0.81	0.40	0.77	1.56	1.47E+11	1407.12	1407.57	975.08	1298.48	1014.59	16.79
2011	4 January 2011	-22.73	0.01	0.81	0.40	0.77	1.56	1.47E+11	1407.20	1407.66	974.85	1298.40	1014.93	16.38
1992	4 January 1992	-22.72	0.01	0.81	0.40	0.77	1.56	1.47E+11	1407.09	1407.54	975.06	1298.45	1014.57	16.79
1973	4 January 1973	-22.68	0.01	0.81	0.40	0.77	1.56	1.47E+11	1407.17	1407.61	975.71	1298.85	1014.06	17.61
1954	5 January 1954	-22.68	0.01	0.81	0.40	0.77	1.56	1.47E+11	1407.09	1407.53	975.65	1298.77	1014.00	17.61
1935	5 January 1935	-22.72	0.01	0.81	0.40	0.77	1.56	1.47E+11	1407.12	1407.57	975.08	1298.48	1014.59	16.79
1916	5 January 1916	-22.77	0.01	0.81	0.40	0.77	1.56	1.47E+11	1407.12	1407.58	974.20	1298.00	1015.44	15.56
1897	3 January 1897	-22.80	0.01	0.81	0.40	0.76	1.56	1.47E+11	1407.15	1407.62	973.63	1297.71	1016.03	14.74
1878	3 January 1878	-22.80	0.01	0.81	0.40	0.76	1.56	1.47E+11	1407.20	1407.68	973.67	1297.77	1016.07	14.74
1859	4 January 1859	-22.78	0.01	0.81	0.40	0.76	1.56	1.47E+11	1407.09	1407.56	973.88	1297.82	1015.70	15.15
1840	4 January 1840	-22.75	0.01	0.81	0.40	0.77	1.56	1.47E+11	1407.03	1407.49	974.43	1298.08	1015.09	15.97
1821	4 January 1821	-22.77	0.01	0.81	0.40	0.77	1.56	1.47E+11	1407.06	1407.52	974.16	1297.95	1015.40	15.56
1802	4 January 1802	-22.80	0.01	0.81	0.40	0.76	1.56	1.47E+11	1407.06	1407.53	973.57	1297.63	1015.97	14.74
1783	3 January 1783	-22.83	0.01	0.81	0.40	0.76	1.56	1.47E+11	1407.09	1407.57	972.99	1297.34	1016.55	13.92
1764	3 January 1764	-22.87	0.01	0.81	0.40	0.76	1.56	1.47E+11	1407.12	1407.61	972.42	1297.05	1017.14	13.10
1745	2 January 1745	-22.87	0.01	0.81	0.40	0.76	1.56	1.47E+11	1407.03	1407.52	972.36	1296.97	1017.08	13.10
1726	3 January 1726	-22.85	0.01	0.81	0.40	0.76	1.56	1.47E+11	1407.09	1407.58	972.70	1297.18	1016.84	13.51
1707	4 January 1707	-22.82	0.01	0.81	0.40	0.76	1.56	1.47E+11	1406.92	1407.40	973.17	1297.34	1016.15	14.33
1688	3 January 1688	-22.83	0.01	0.81	0.40	0.76	1.56	1.47E+11	1407.00	1407.49	972.94	1297.26	1016.49	13.92
1669	2 January 1669	-22.87	0.01	0.81	0.40	0.76	1.56	1.47E+11	1407.03	1407.52	972.36	1296.97	1017.08	13.10
1650	2 January 1650	-22.92	0.01	0.81	0.40	0.76	1.56	1.47E+11	1407.03	1407.53	971.47	1296.50	1017.93	11.87
1631	2 January 1631	-22.93	0.01	0.81	0.40	0.76	1.56	1.47E+11	1407.00	1407.51	971.16	1296.31	1018.19	11.46
1612	3 January 1612	-22.93	0.01	0.81	0.40	0.76	1.56	1.47E+11	1406.86	1407.37	971.06	1296.18	1018.09	11.46
1593	2 January 1593	-22.90	0.01	0.81	0.40	0.76	1.56	1.47E+11	1406.86	1407.36	971.65	1296.50	1017.52	12.28
1574	3 January 1574	-22.88	0.01	0.81	0.40	0.76	1.56	1.47E+11	1406.86	1407.36	971.95	1296.66	1017.24	12.69
1555	3 January 1555	-22.90	0.01	0.81	0.40	0.76	1.56	1.47E+11	1406.86	1407.36	971.65	1296.50	1017.52	12.28
1536	3 January 1536	-22.95	0.01	0.81	0.40	0.76	1.56	1.47E+11	1406.86	1407.37	970.76	1296.02	1018.37	11.05
1517	2 January 1517	-22.98	0.01	0.81	0.40	0.76	1.56	1.47E+11	1406.89	1407.41	970.19	1295.72	1018.95	10.24
1498	1 January 1498	-23.00	0.01	0.81	0.40	0.76	1.56	1.47E+11	1406.80	1407.32	969.83	1295.49	1019.17	9.83
1479	2 January 1479	-22.98	0.01	0.81	0.40	0.76	1.56	1.47E+11	1406.77	1407.29	970.11	1295.62	1018.87	10.23
1460	3 January 1460	-22.97	0.01	0.81	0.40	0.76	1.56	1.47E+11	1406.60	1407.12	970.29	1295.62	1018.46	10.64
1441	2 January 1441	-22.95	0.01	0.81	0.40	0.76	1.56	1.47E+11	1406.69	1407.20	970.64	1295.86	1018.24	11.05
1422	2 January 1422	-22.98	0.01	0.81	0.40	0.76	1.56	1.47E+11	1406.63	1407.15	970.01	1295.49	1018.77	10.23
1403	2 January 1403	-23.02	0.01	0.81	0.40	0.76	1.56	1.47E+11	1406.66	1407.18	969.44	1295.19	1019.35	9.41
1384	1 January 1384	-23.05	0.01	0.81	0.40	0.76	1.56	1.47E+11	1406.66	1407.19	968.85	1294.87	1019.92	8.60
1364	31 December 1364	-23.07	0.01	0.81	0.40	0.76	1.56	1.47E+11	1406.52	1407.05	968.45	1294.58	1020.09	8.19
1346	1 January 1346	-23.05	0.01	0.81	0.40	0.76	1.56	1.47E+11	1406.57	1407.10	968.79	1294.79	1019.85	8.60
1327	2 January 1327	-23.02	0.01	0.81	0.40	0.76	1.56	1.47E+11	1406.43	1406.95	969.28	1294.98	1019.19	9.41
1308	2 January 1308	-23.02	0.01	0.81	0.40	0.76	1.56	1.47E+11	1406.40	1406.93	969.26	1294.96	1019.17	9.41
1289	31 December 1288	-23.05	0.01	0.81	0.40	0.76	1.56	1.47E+11	1406.34	1406.87	968.63	1294.58	1019.69	8.59
1270	31 December 1269	-23.08	0.01	0.81	0.40	0.76	1.57	1.47E+11	1406.37	1406.91	968.05	1294.29	1020.27	7.78
1251	31 December 1250	-23.12	0.01	0.81	0.40	0.76	1.57	1.47E+11	1406.37	1406.91	967.46	1293.97	1020.84	6.96
1232	1 January 1232	-23.12	0.01	0.81	0.40	0.76	1.57	1.47E+11	1406.32	1406.86	967.42	1293.92	1020.79	6.96
1213	31 December 1212	-23.10	0.01	0.81	0.40	0.76	1.57	1.47E+11	1406.20	1406.74	967.64	1293.97	1020.43	7.37
1194	1 January 1194	-23.07	0.01	0.81	0.40	0.76	1.56	1.47E+11	1406.23	1406.76	968.25	1294.32	1019.89	8.18
1175	1 January 1175	-23.08	0.01	0.81	0.40	0.76	1.57	1.47E+11	1406.06	1406.59	967.84	1294.00	1020.04	7.77
1156	1 January 1156	-23.12	0.01	0.81	0.40	0.76	1.57	1.47E+11	1406.03	1406.57	967.22	1293.65	1020.59	6.96
1137	31 December 1136	-23.15	0.01	0.81	0.40	0.76	1.57	1.47E+11	1406.06	1406.60	966.65	1293.36	1021.17	6.14
1118	1 January 1118	-23.17	0.00	0.81	0.40	0.76	1.57	1.47E+11	1406.03	1406.58	966.33	1293.17	1021.43	5.73
1099	31 December 1098	-23.17	0.00	0.81	0.40	0.76	1.57	1.47E+11	1406.12	1406.66	966.39	1293.25	1021.49	5.73

Appendix D

Tables D.1, D.2, and D.3 show excerpts from the model of superpositioned 133-yr and 209-yr cycles. Total solar irradiance (W/m2) are shown for both the normalised model and Bard TSI reconstructions. The normalised model was developed in stages showing TSI for no adjustments, and subsequent adjustments for sunspot activity (S), precession (P), and both sunspot and precessional. Trigonometric values and frequencies for both contributing cycles are shown. These trigonometric values are calculated on the interval since 1183BC for unadjusted model when precession was not considered, and on the precession adjusted interval otherwise.

Table D.1: Excerpt from the model of superpositioned 133-yr and 209-yr cycles (843AD-1134AD).

	Unadjusted	Adjusted for	133yr cycle		209yr cycle		Normalised model and adjustments				Bard *et al.* (2007) data		
Yr (AD)		precession	F	Sin()	F	Sin()	Nil	S	P	S and P	TSI_1	TSI_2	TSI_3
843	2025	2041	15.35	0.82	9.77	-1.00	1365.06	1365.06	1364.83	1364.83	1366.2	1365.9	1365.2
851	2033	2049	15.41	0.56	9.80	-0.94	1364.99	1364.99	1364.61	1364.61	1366.0	1365.7	1365.0
858	2040	2056	15.46	0.26	9.84	-0.85	1364.85	1364.85	1364.40	1364.40	1366.2	1365.8	1365.2
868	2050	2066	15.53	-0.21	9.89	-0.66	1364.58	1364.58	1364.13	1364.13	1366.0	1365.7	1365.0
876	2058	2074	15.59	-0.56	9.92	-0.46	1364.34	1364.34	1363.98	1363.98	1365.9	1365.6	1364.9
884	2066	2082	15.65	-0.82	9.96	-0.24	1364.13	1364.13	1363.94	1363.94	1365.8	1365.5	1364.9
893	2075	2091	15.72	-0.98	10.00	0.03	1363.97	1363.97	1364.05	1364.05	1365.7	1365.3	1364.7
901	2083	2099	15.78	-0.98	10.04	0.27	1363.94	1363.94	1364.29	1364.29	1365.8	1365.5	1364.8
909	2091	2107	15.84	-0.84	10.08	0.49	1364.05	1364.05	1364.65	1364.65	1365.5	1365.2	1364.6
923	2105	2121	15.95	-0.32	10.15	0.80	1364.55	1364.55	1365.48	1365.48	1366.0	1365.6	1365.0
926	2108	2124	15.97	-0.19	10.16	0.85	1364.70	1364.70	1365.67	1365.67	1366.2	1365.9	1365.3
936	2118	2134	16.05	0.28	10.21	0.97	1365.29	1365.29	1366.25	1366.25	1366.4	1366.1	1365.5
945	2127	2143	16.11	0.65	10.25	1.00	1365.85	1365.85	1366.65	1366.65	1366.7	1366.3	1365.7
947	2129	2145	16.13	0.72	10.26	1.00	1365.97	1365.97	1366.72	1366.72	1366.6	1366.3	1365.7
955	2137	2153	16.19	0.93	10.30	0.95	1366.40	1366.40	1366.87	1366.87	1366.5	1366.2	1365.6
964	2146	2162	16.26	1.00	10.34	0.83	1366.75	1366.75	1366.83	1366.83	1366.7	1366.4	1365.8
973	2155	2172	16.33	0.87	10.39	0.63	1366.88	1366.88	1366.50	1366.50	1366.3	1366.0	1365.4
985	2167	2184	16.42	0.48	10.45	0.31	1366.70	1366.70	1365.79	1365.79	1366.0	1365.7	1365.1
992	2174	2191	16.47	0.16	10.48	0.11	1366.40	1366.40	1365.27	1365.27	1365.9	1365.6	1365.0
998	2180	2197	16.52	-0.12	10.51	-0.08	1366.05	1366.05	1364.81	1364.81	1365.8	1365.5	1364.9
1004	2186	2203	16.56	-0.39	10.54	-0.25	1365.64	1365.64	1364.36	1364.36	1365.6	1365.4	1364.8
1012	2194	2211	16.62	-0.70	10.58	-0.48	1365.04	1365.04	1363.82	1363.82	1365.1	1364.8	1364.2
1028	2210	2227	16.74	-1.00	10.66	-0.83	1363.88	1363.88	1363.17	1363.17	1364.5	1364.2	1363.7
1035	2217	2234	16.80	-0.96	10.69	-0.93	1363.50	1363.50	1363.12	1363.12	1364.2	1363.9	1363.4
1044	2226	2243	16.86	-0.75	10.73	-0.99	1363.19	1363.19	1363.25	1363.25	1364.0	1363.8	1363.2
1054	2236	2253	16.94	-0.37	10.78	-0.98	1363.13	1363.13	1363.65	1363.65	1363.9	1363.6	1363.1
1062	2244	2261	17.00	0.00	10.82	-0.91	1363.28	1363.28	1364.09	1364.09	1363.9	1363.7	1363.1
1068	2250	2267	17.05	0.28	10.85	-0.82	1363.51	1363.51	1364.46	1364.46	1364.5	1364.3	1363.7
1075	2257	2274	17.10	0.58	10.88	-0.68	1363.86	1363.86	1364.89	1364.89	1365.2	1364.9	1364.4
1083	2265	2282	17.16	0.84	10.92	-0.49	1364.33	1364.33	1365.35	1365.35	1365.7	1365.5	1365.0
1092	2274	2291	17.23	0.99	10.96	-0.24	1364.89	1364.89	1365.75	1365.75	1366.0	1365.7	1365.2
1108	2290	2308	17.35	0.80	11.04	0.27	1365.71	1367.35	1366.06	1367.70	1366.5	1366.3	1365.8
1114	2296	2314	17.40	0.60	11.07	0.44	1365.91	1367.55	1366.03	1367.67	1367.1	1366.8	1366.3
1124	2306	2324	17.47	0.16	11.12	0.68	1366.06	1367.70	1365.85	1367.49	1367.1	1366.8	1366.3
1132	2314	2332	17.53	-0.21	11.16	0.84	1366.03	1367.67	1365.63	1367.26	1367.2	1366.9	1366.4
1134	2316	2334	17.55	-0.30	11.17	0.87	1366.01	1367.65	1365.57	1367.20	1367.3	1367.0	1366.5

Table D.2: Excerpt from the model of superpositioned 133-yr and 209-yr cycles (1138AD-1540AD).

Yr (AD)	Unadjusted	Adjusted for precession	133yr cycle F	133yr cycle Sin()	209yr cycle F	209yr cycle Sin()	Normalised model and adjustments Nil	S	P	S and P	Bard *et al.* (2007) data TSI_1	TSI_2	TSI_3
1138	2320	2338	17.58	-0.48	11.19	0.92	1365.94	1367.58	1365.45	1367.08	1367.4	1367.1	1366.6
1146	2328	2346	17.64	-0.77	11.22	0.99	1365.74	1367.38	1365.22	1366.86	1367.4	1367.2	1366.7
1155	2337	2355	17.71	-0.96	11.27	0.99	1365.48	1367.11	1365.03	1366.67	1367.2	1367.0	1366.5
1161	2343	2361	17.75	-1.00	11.30	0.96	1365.30	1366.94	1364.96	1366.60	1366.9	1366.6	1366.2
1166	2348	2366	17.79	-0.97	11.32	0.90	1365.17	1366.81	1364.93	1366.57	1367.0	1366.8	1366.3
1174	2356	2374	17.85	-0.81	11.36	0.78	1365.01	1366.65	1364.96	1366.60	1366.7	1366.5	1366.0
1180	2362	2380	17.89	-0.61	11.39	0.65	1364.95	1366.59	1365.03	1366.67	1366.8	1366.6	1366.1
1191	2373	2391	17.98	-0.14	11.44	0.37	1364.96	1366.59	1365.23	1366.86	1366.8	1366.6	1366.2
1197	2379	2397	18.02	0.14	11.47	0.19	1365.02	1366.66	1365.34	1366.97	1367.1	1366.9	1366.4
1203	2385	2403	18.07	0.41	11.50	0.02	1365.12	1366.75	1365.43	1367.07	1367.2	1367.0	1366.5
1213	2395	2413	18.14	0.78	11.55	-0.28	1365.30	1366.94	1365.50	1367.14	1367.1	1366.9	1366.4
1232	2414	2433	18.29	0.96	11.64	-0.78	1365.50	1367.14	1365.19	1366.83	1367.0	1366.8	1366.4
1233	2415	2434	18.30	0.95	11.65	-0.79	1365.50	1367.14	1365.16	1366.79	1367.1	1366.9	1366.5
1237	2419	2438	18.33	0.87	11.67	-0.86	1365.48	1367.11	1365.01	1366.65	1366.8	1366.6	1366.1
1253	2435	2454	18.45	0.30	11.74	-1.00	1365.12	1366.76	1364.30	1365.94	1366.3	1366.1	1365.7
1257	2439	2458	18.48	0.12	11.76	-1.00	1364.97	1366.61	1364.12	1365.76	1365.8	1365.6	1365.2
1261	2443	2462	18.51	-0.07	11.78	-0.98	1364.81	1366.45	1363.95	1365.58	1365.7	1365.5	1365.1
1273	2455	2474	18.60	-0.60	11.84	-0.85	1364.26	1365.89	1363.55	1365.19	1365.8	1365.6	1365.2
1280	2462	2481	18.65	-0.82	11.87	-0.73	1363.95	1365.58	1363.45	1365.09	1365.6	1365.4	1365.0
1287	2469	2488	18.71	-0.96	11.90	-0.57	1363.69	1365.32	1363.47	1365.11	1365.5	1365.3	1364.9
1294	2476	2495	18.76	-1.00	11.94	-0.38	1363.51	1365.15	1363.62	1365.26	1365.4	1365.2	1364.8
1300	2482	2501	18.80	-0.94	11.97	-0.21	1363.45	1365.08	1363.85	1365.49	1365.2	1365.0	1364.7
1310	2492	2511	18.88	-0.69	12.01	0.09	1363.54	1363.54	1364.40	1364.40	1365.0	1364.9	1364.5
1322	2504	2523	18.97	-0.19	12.07	0.44	1364.00	1364.00	1365.25	1365.25	1364.8	1364.7	1364.3
1334	2516	2535	19.06	0.37	12.13	0.73	1364.74	1364.74	1366.09	1366.09	1364.9	1364.7	1364.4
1339	2521	2540	19.10	0.58	12.15	0.82	1365.10	1365.10	1366.40	1366.40	1365.3	1365.2	1364.8
1346	2528	2547	19.15	0.81	12.19	0.92	1365.61	1365.61	1366.73	1366.73	1365.4	1365.2	1364.9
1356	2538	2558	19.23	0.99	12.24	1.00	1366.28	1366.28	1366.99	1366.99	1365.6	1365.4	1365.1
1373	2555	2575	19.36	0.77	12.32	0.90	1366.96	1366.96	1366.67	1366.67	1366.0	1365.8	1365.5
1383	2565	2585	19.44	0.39	12.37	0.74	1366.96	1366.96	1366.13	1366.13	1366.0	1365.8	1365.5
1391	2573	2593	19.50	0.02	12.41	0.55	1366.75	1366.75	1365.58	1365.58	1365.9	1365.7	1365.4
1395	2577	2597	19.53	-0.16	12.43	0.45	1366.58	1366.58	1365.28	1365.28	1365.6	1365.5	1365.2
1400	2582	2602	19.56	-0.39	12.45	0.31	1366.31	1366.31	1364.92	1364.92	1365.1	1365.0	1364.7
1407	2589	2609	19.62	-0.67	12.48	0.11	1365.86	1365.86	1364.44	1364.44	1365.0	1364.8	1364.5
1414	2596	2616	19.67	-0.87	12.52	-0.11	1365.36	1365.36	1364.02	1364.02	1364.8	1364.7	1364.4
1420	2602	2622	19.71	-0.97	12.55	-0.28	1364.92	1364.92	1363.74	1363.74	1364.3	1364.2	1363.9
1427	2609	2629	19.77	-0.99	12.58	-0.48	1364.44	1364.44	1363.53	1363.53	1364.1	1363.9	1363.7
1433	2615	2635	19.81	-0.93	12.61	-0.63	1364.08	1364.08	1363.45	1363.45	1363.3	1363.2	1363.0
1441	2623	2643	19.87	-0.72	12.65	-0.79	1363.71	1363.71	1363.49	1363.49	1362.6	1362.5	1362.3
1446	2628	2648	19.91	-0.54	12.67	-0.88	1363.55	1363.55	1363.59	1363.59	1362.5	1362.4	1362.3
1451	2633	2653	19.95	-0.32	12.69	-0.94	1363.47	1363.47	1363.74	1363.74	1362.6	1362.5	1362.3
1458	2640	2660	20.00	0.00	12.73	-0.99	1363.45	1361.82	1364.01	1362.37	1362.4	1362.3	1362.1
1463	2645	2665	20.04	0.23	12.75	-1.00	1363.52	1361.88	1364.23	1362.60	1362.6	1362.5	1362.4
1469	2651	2671	20.08	0.50	12.78	-0.98	1363.67	1362.04	1364.51	1362.88	1362.8	1362.7	1362.5
1476	2658	2678	20.14	0.75	12.81	-0.92	1363.93	1362.29	1364.83	1363.19	1363.5	1363.4	1363.2
1481	2663	2683	20.17	0.89	12.84	-0.85	1364.14	1362.51	1365.03	1363.39	1364.1	1364.0	1363.9
1492	2674	2695	20.26	1.00	12.89	-0.61	1364.65	1363.02	1365.38	1363.74	1364.0	1363.9	1363.7
1504	2686	2707	20.35	0.80	12.95	-0.30	1365.14	1363.50	1365.50	1363.86	1363.9	1363.8	1363.7
1511	2693	2714	20.41	0.56	12.99	-0.09	1365.34	1363.70	1365.47	1363.83	1364.0	1363.9	1363.7
1518	2700	2721	20.46	0.26	13.02	0.12	1365.46	1363.82	1365.38	1363.74	1363.7	1363.6	1363.5
1526	2708	2729	20.52	-0.12	13.06	0.35	1365.50	1363.86	1365.24	1363.60	1363.5	1363.5	1363.3
1534	2716	2737	20.58	-0.48	13.10	0.57	1365.45	1363.81	1365.09	1363.45	1363.3	1363.2	1363.1
1540	2722	2743	20.62	-0.70	13.12	0.70	1365.36	1363.72	1365.00	1363.36	1363.1	1363.1	1363.0

Table D.3: Excerpt from the model of superpositioned 133-yr and 209-yr cycles (1549AD-1961AD).

Yr (AD)	Unadjusted	Adjusted for precession	133yr cycle F	133yr cycle Sin()	209yr cycle F	209yr cycle Sin()	Normalised model and adjustments Nil	S	P	S and P	Bard *et al.* (2007) data TSI 1	TSI 2	TSI 3
1549	2731	2752	20.69	-0.93	13.17	0.87	1365.20	1363.56	1364.93	1363.30	1363.3	1363.2	1363.1
1559	2741	2762	20.77	-0.99	13.22	0.98	1365.03	1365.03	1364.98	1364.98	1363.3	1363.2	1363.1
1576	2758	2779	20.89	-0.61	13.30	0.96	1364.95	1364.95	1365.34	1365.34	1363.7	1363.7	1363.6
1584	2766	2787	20.95	-0.28	13.33	0.86	1365.04	1365.04	1365.58	1365.58	1364.3	1364.3	1364.1
1593	2775	2796	21.02	0.14	13.38	0.69	1365.23	1365.23	1365.83	1365.83	1364.8	1364.7	1364.6
1600	2782	2803	21.08	0.46	13.41	0.53	1365.43	1365.43	1365.98	1365.98	1365.3	1365.2	1365.1
1608	2790	2811	21.14	0.75	13.45	0.31	1365.67	1365.67	1366.06	1366.06	1365.5	1365.4	1365.2
1624	2806	2828	21.26	1.00	13.53	-0.19	1366.03	1366.03	1365.80	1365.80	1365.8	1365.8	1365.6
1631	2813	2835	21.32	0.92	13.56	-0.39	1366.06	1366.06	1365.52	1365.52	1365.9	1365.9	1365.7
1638	2820	2842	21.37	0.74	13.60	-0.58	1366.00	1366.00	1365.16	1365.16	1365.4	1365.3	1365.2
1645	2827	2849	21.42	0.48	13.63	-0.74	1365.83	1364.20	1364.74	1363.10	1365.1	1365.1	1365.0
1652	2834	2856	21.47	0.16	13.67	-0.86	1365.57	1363.93	1364.30	1362.67	1364.7	1364.7	1364.6
1659	2841	2863	21.53	-0.16	13.70	-0.95	1365.21	1363.58	1363.89	1362.25	1364.1	1364.1	1364.0
1667	2849	2871	21.59	-0.52	13.74	-1.00	1364.74	1363.10	1363.49	1361.85	1364.0	1364.0	1364.0
1673	2855	2877	21.63	-0.74	13.77	-1.00	1364.37	1362.73	1363.27	1361.63	1363.9	1363.9	1363.8
1676	2858	2880	21.65	-0.82	13.78	-0.98	1364.18	1362.54	1363.19	1361.56	1363.5	1363.5	1363.5
1680	2862	2884	21.68	-0.92	13.80	-0.95	1363.94	1362.31	1363.13	1361.50	1363.5	1363.5	1363.5
1688	2870	2892	21.74	-1.00	13.84	-0.85	1363.53	1361.89	1363.15	1361.51	1363.3	1363.3	1363.3
1690	2872	2894	21.76	-1.00	13.85	-0.82	1363.44	1361.81	1363.18	1361.55	1363.4	1363.5	1363.5
1705	2887	2909	21.87	-0.72	13.92	-0.49	1363.11	1361.48	1363.79	1362.15	1363.8	1363.8	1363.8
1712	2894	2916	21.92	-0.46	13.95	-0.30	1363.18	1361.55	1364.25	1362.61	1364.2	1364.2	1364.1
1720	2902	2924	21.98	-0.09	13.99	-0.06	1363.43	1363.43	1364.85	1364.85	1364.7	1364.7	1364.6
1727	2909	2931	22.04	0.23	14.02	0.15	1363.79	1363.79	1365.38	1365.38	1365.7	1365.7	1365.6
1735	2917	2939	22.10	0.58	14.06	0.38	1364.32	1364.32	1365.96	1365.96	1366.1	1366.1	1366.0
1739	2921	2943	22.13	0.72	14.08	0.49	1364.62	1364.62	1366.21	1366.21	1366.6	1366.6	1366.5
1747	2929	2952	22.20	0.94	14.12	0.70	1365.23	1365.23	1366.65	1366.65	1366.9	1366.8	1366.7
1755	2937	2960	22.26	1.00	14.16	0.85	1365.82	1365.82	1366.85	1366.85	1367.0	1367.0	1366.8
1763	2945	2968	22.32	0.92	14.20	0.95	1366.32	1366.32	1366.87	1366.87	1367.1	1367.1	1367.0
1771	2953	2976	22.38	0.70	14.24	1.00	1366.68	1366.68	1366.70	1366.70	1366.9	1366.9	1366.8
1779	2961	2984	22.44	0.39	14.28	0.99	1366.87	1366.87	1366.38	1366.38	1366.3	1366.2	1366.2
1787	2969	2992	22.50	0.02	14.32	0.92	1366.86	1366.86	1365.94	1365.94	1366.0	1366.0	1365.9
1809	2991	3014	22.66	-0.85	14.42	0.48	1366.00	1366.00	1364.63	1364.63	1365.6	1365.6	1365.6
1816	2998	3021	22.71	-0.97	14.45	0.28	1365.57	1365.57	1364.31	1364.31	1365.3	1365.3	1365.4
1823	3005	3028	22.77	-0.99	14.49	0.08	1365.14	1365.14	1364.08	1364.08	1365.1	1365.1	1365.1
1829	3011	3034	22.81	-0.93	14.52	-0.11	1364.79	1364.79	1363.97	1363.97	1364.9	1364.9	1364.9
1835	3017	3040	22.86	-0.78	14.55	-0.28	1364.48	1364.48	1363.94	1363.94	1365.2	1365.2	1365.2
1842	3024	3047	22.91	-0.54	14.58	-0.48	1364.20	1365.83	1363.99	1365.62	1365.9	1365.9	1365.9
1850	3032	3055	22.97	-0.19	14.62	-0.67	1364.00	1365.63	1364.14	1365.78	1366.2	1366.2	1366.2
1857	3039	3062	23.02	0.14	14.65	-0.81	1363.94	1365.57	1364.33	1365.97	1366.4	1366.4	1366.4
1865	3047	3070	23.08	0.50	14.69	-0.93	1363.99	1365.62	1364.57	1366.21	1366.5	1366.5	1366.5
1878	3060	3084	23.19	0.92	14.76	-1.00	1364.27	1365.91	1364.93	1366.56	1366.4	1366.4	1366.4
1885	3067	3091	23.24	1.00	14.79	-0.97	1364.48	1366.12	1365.03	1366.67	1366.3	1366.3	1366.3
1892	3074	3098	23.29	0.96	14.82	-0.90	1364.69	1366.32	1365.07	1366.70	1366.1	1366.1	1366.1
1899	3081	3105	23.35	0.82	14.86	-0.78	1364.86	1366.50	1365.04	1366.68	1365.9	1365.9	1365.9
1906	3088	3112	23.40	0.60	14.89	-0.64	1364.99	1366.63	1364.96	1366.60	1365.9	1365.9	1366.0
1912	3094	3118	23.44	0.35	14.92	-0.49	1365.05	1366.69	1364.86	1366.50	1365.9	1365.9	1366.0
1920	3102	3126	23.50	-0.02	14.96	-0.27	1365.06	1366.70	1364.71	1366.35	1366.2	1366.2	1366.3
1928	3110	3134	23.56	-0.39	15.00	-0.03	1364.99	1366.62	1364.58	1366.22	1366.6	1366.6	1366.6
1935	3117	3141	23.62	-0.67	15.03	0.18	1364.88	1366.51	1364.51	1366.15	1366.8	1366.8	1366.8
1944	3126	3150	23.68	-0.92	15.07	0.44	1364.71	1366.35	1364.52	1366.16	1367.1	1367.1	1367.1
1950	3132	3156	23.73	-0.99	15.10	0.59	1364.61	1366.25	1364.60	1366.24	1367.0	1367.0	1367.0
1961	3143	3167	23.81	-0.93	15.15	0.82	1364.50	1366.14	1364.90	1366.53	1366.9	1366.9	1366.9

Table D.4: Daily approximation of TSI values (W/m2) and daily rate of change (TSI Var) during 1992 (January to April inclusive). Calculations for TSU values are based on the Julian Day (JD) and associated sine value, where (i) y=sin(2π x ((JD-277)/366)), and (ii) TSI =1361+(y*46.9).

Date	JD	Sine value	TSI W/m2	TSI Var W/m2	Date	JD	Sine value	TSI W/m2	TSI Var W/m2	Date	JD	Sine value	TSI W/m2	TSI Var W/m2	Date	JD	Sine value	TSI W/m2	TSI Var W/m2
01-Jan-92	0	0.9991	1407.86		01-Feb-92	31	0.8827	1402.40	-0.37	01-Mar-92	60	0.5511	1386.85	-0.67	01-Apr-92	91	0.0515	1363.41	-0.81
02-Jan-92	1	0.9997	1407.88	0.03	02-Feb-92	32	0.8745	1402.01	-0.38	02-Mar-92	61	0.5367	1386.17	-0.67	02-Apr-92	92	0.0343	1362.61	-0.81
03-Jan-92	2	1.0000	1407.90	0.01	03-Feb-92	33	0.8660	1401.62	-0.40	03-Mar-92	62	0.5221	1385.49	-0.68	03-Apr-92	93	0.0172	1361.81	-0.81
04-Jan-92	3	1.0000	1407.90	0.00	04-Feb-92	34	0.8573	1401.21	-0.41	04-Mar-92	63	0.5074	1384.80	-0.69	04-Apr-92	94	0.0000	1361.00	-0.81
05-Jan-92	4	0.9997	1407.88	-0.01	05-Feb-92	35	0.8484	1400.79	-0.42	05-Mar-92	64	0.4925	1384.10	-0.70	05-Apr-92	95	-0.0172	1360.19	-0.81
06-Jan-92	5	0.9991	1407.86	-0.03	06-Feb-92	36	0.8391	1400.36	-0.43	06-Mar-92	65	0.4775	1383.40	-0.70	06-Apr-92	96	-0.0343	1359.39	-0.81
07-Jan-92	6	0.9982	1407.82	-0.04	07-Feb-92	37	0.8297	1399.91	-0.44	07-Mar-92	66	0.4624	1382.69	-0.71	07-Apr-92	97	-0.0515	1358.59	-0.81
08-Jan-92	7	0.9970	1407.76	-0.06	08-Feb-92	38	0.8200	1399.46	-0.46	08-Mar-92	67	0.4471	1381.97	-0.72	08-Apr-92	98	-0.0686	1357.78	-0.81
09-Jan-92	8	0.9955	1407.69	-0.07	09-Feb-92	39	0.8100	1398.99	-0.47	09-Mar-92	68	0.4317	1381.25	-0.72	09-Apr-92	99	-0.0857	1356.98	-0.81
10-Jan-92	9	0.9938	1407.61	-0.08	10-Feb-92	40	0.7998	1398.51	-0.48	10-Mar-92	69	0.4161	1380.52	-0.73	10-Apr-92	100	-0.1028	1356.18	-0.80
11-Jan-92	10	0.9917	1407.51	-0.10	11-Feb-92	41	0.7894	1398.02	-0.49	11-Mar-92	70	0.4005	1379.78	-0.73	11-Apr-92	101	-0.1199	1355.38	-0.80
12-Jan-92	11	0.9894	1407.40	-0.11	12-Feb-92	42	0.7788	1397.52	-0.50	12-Mar-92	71	0.3847	1379.04	-0.74	12-Apr-92	102	-0.1369	1354.58	-0.80
13-Jan-92	12	0.9867	1407.28	-0.12	13-Feb-92	43	0.7679	1397.01	-0.51	13-Mar-92	72	0.3688	1378.29	-0.74	13-Apr-92	103	-0.1539	1353.78	-0.80
14-Jan-92	13	0.9838	1407.14	-0.14	14-Feb-92	44	0.7568	1396.49	-0.52	14-Mar-92	73	0.3528	1377.54	-0.75	14-Apr-92	104	-0.1708	1352.99	-0.80
15-Jan-92	14	0.9806	1406.99	-0.15	15-Feb-92	45	0.7454	1395.96	-0.53	15-Mar-92	74	0.3366	1376.79	-0.76	15-Apr-92	105	-0.1877	1352.20	-0.80
16-Jan-92	15	0.9771	1406.82	-0.16	16-Feb-92	46	0.7339	1395.42	-0.54	16-Mar-92	75	0.3204	1376.03	-0.76	16-Apr-92	106	-0.2046	1351.41	-0.79
17-Jan-92	16	0.9733	1406.65	-0.18	17-Feb-92	47	0.7221	1394.87	-0.55	17-Mar-92	76	0.3041	1375.26	-0.76	17-Apr-92	107	-0.2213	1350.62	-0.79
18-Jan-92	17	0.9692	1406.45	-0.19	18-Feb-92	48	0.7101	1394.31	-0.56	18-Mar-92	77	0.2877	1374.49	-0.77	18-Apr-92	108	-0.2380	1349.84	-0.79
19-Jan-92	18	0.9648	1406.25	-0.21	19-Feb-92	49	0.6979	1393.73	-0.57	19-Mar-92	78	0.2712	1373.72	-0.77	19-Apr-92	109	-0.2547	1349.06	-0.78
20-Jan-92	19	0.9601	1406.03	-0.22	20-Feb-92	50	0.6855	1393.15	-0.58	20-Mar-92	79	0.2547	1372.94	-0.78	20-Apr-92	110	-0.2712	1348.28	-0.78
21-Jan-92	20	0.9552	1405.80	-0.23	21-Feb-92	51	0.6729	1392.56	-0.59	21-Mar-92	80	0.2380	1372.16	-0.78	21-Apr-92	111	-0.2877	1347.51	-0.78
22-Jan-92	21	0.9500	1405.55	-0.24	22-Feb-92	52	0.6602	1391.96	-0.60	22-Mar-92	81	0.2213	1371.38	-0.78	22-Apr-92	112	-0.3041	1346.74	-0.77
23-Jan-92	22	0.9445	1405.30	-0.26	23-Feb-92	53	0.6472	1391.35	-0.61	23-Mar-92	82	0.2046	1370.59	-0.79	23-Apr-92	113	-0.3204	1345.97	-0.77
24-Jan-92	23	0.9387	1405.03	-0.27	24-Feb-92	54	0.6340	1390.73	-0.62	24-Mar-92	83	0.1877	1369.80	-0.79	24-Apr-92	114	-0.3366	1345.21	-0.76
25-Jan-92	24	0.9327	1404.74	-0.28	25-Feb-92	55	0.6206	1390.11	-0.63	25-Mar-92	84	0.1708	1369.01	-0.79	25-Apr-92	115	-0.3528	1344.46	-0.76
26-Jan-92	25	0.9263	1404.44	-0.30	26-Feb-92	56	0.6071	1389.47	-0.64	26-Mar-92	85	0.1539	1368.22	-0.80	26-Apr-92	116	-0.3688	1343.71	-0.76
27-Jan-92	26	0.9197	1404.13	-0.31	27-Feb-92	57	0.5933	1388.83	-0.64	27-Mar-92	86	0.1369	1367.42	-0.80	27-Apr-92	117	-0.3847	1342.96	-0.75
28-Jan-92	27	0.9128	1403.81	-0.32	28-Feb-92	58	0.5794	1388.17	-0.65	28-Mar-92	87	0.1199	1366.62	-0.80	28-Apr-92	118	-0.4005	1342.22	-0.74
29-Jan-92	28	0.9057	1403.48	-0.34	29-Feb-92	59	0.5653	1387.51	-0.66	29-Mar-92	88	0.1028	1365.82	-0.80	29-Apr-92	119	-0.4161	1341.48	-0.74
30-Jan-92	29	0.8983	1403.13	-0.35						30-Mar-92	89	0.0857	1365.02	-0.80	30-Apr-92	120	-0.4317	1340.75	-0.73
31-Jan-92	30	0.8906	1402.77	-0.36						31-Mar-92	90	0.0686	1364.22	-0.80					

Table D.5: Daily approximation of TSI values (W/m2) and daily rate of change (TSI Var) during 1992 (May to August inclusive). Calculations for TSU values are based on the Julian Day (JD) and associated sine value, where (i) y=sin(2π x ((JD-277)/366)), and (ii) TSI =1361+(y*46.9).

Date	JD	Sine value	TSI W/m2	TSI Var W/m2	Date	JD	Sine value	TSI W/m2	TSI Var W/m2	Date	JD	Sine value	TSI W/m2	TSI Var W/m2	Date	JD	Sine value	TSI W/m2	TSI Var W/m2
01-May-92	121	-0.4471	1340.03	-0.72	01-Jun-92	152	-0.8391	1321.64	-0.44	01-Jul-92	182	-0.9982	1314.20	-0.04	01-Aug-92	213	-0.8906	1319.23	0.42
02-May-92	122	-0.4624	1339.31	-0.72	02-Jun-92	153	-0.8484	1321.21	-0.43	02-Jul-92	183	-0.9991	1314.15	-0.05	02-Aug-92	214	-0.8827	1319.60	0.37
03-May-92	123	-0.4775	1338.60	-0.71	03-Jun-92	154	-0.8573	1320.79	-0.42	03-Jul-92	184	-0.9997	1314.12	-0.03	03-Aug-92	215	-0.8745	1319.99	0.38
04-May-92	124	-0.4925	1337.90	-0.70	04-Jun-92	155	-0.8660	1320.38	-0.41	04-Jul-92	185	-1.0000	1314.10	-0.02	04-Aug-92	216	-0.8660	1320.38	0.40
05-May-92	125	-0.5074	1337.20	-0.70	05-Jun-92	156	-0.8745	1319.99	-0.40	05-Jul-92	186	-1.0000	1314.10	0.00	05-Aug-92	217	-0.8573	1320.79	0.41
06-May-92	126	-0.5221	1336.51	-0.69	06-Jun-92	157	-0.8827	1319.60	-0.38	06-Jul-92	187	-0.9997	1314.11	0.01	06-Aug-92	218	-0.8484	1321.21	0.42
07-May-92	127	-0.5367	1335.83	-0.68	07-Jun-92	158	-0.8906	1319.23	-0.37	07-Jul-92	188	-0.9991	1314.14	0.02	07-Aug-92	219	-0.8391	1321.64	0.43
08-May-92	128	-0.5511	1335.15	-0.68	08-Jun-92	159	-0.8983	1318.87	-0.36	08-Jul-92	189	-0.9982	1314.17	0.04	08-Aug-92	220	-0.8297	1322.09	0.44
09-May-92	129	-0.5653	1334.49	-0.67	09-Jun-92	160	-0.9057	1318.52	-0.35	09-Jul-92	190	-0.9970	1314.23	0.05	09-Aug-92	221	-0.8200	1322.54	0.46
10-May-92	130	-0.5794	1333.83	-0.66	10-Jun-92	161	-0.9128	1318.19	-0.34	10-Jul-92	191	-0.9955	1314.29	0.07	10-Aug-92	222	-0.8100	1323.01	0.47
11-May-92	131	-0.5933	1333.17	-0.65	11-Jun-92	162	-0.9197	1317.87	-0.32	11-Jul-92	192	-0.9938	1314.37	0.08	11-Aug-92	223	-0.7998	1323.49	0.48
12-May-92	132	-0.6071	1332.53	-0.64	12-Jun-92	163	-0.9263	1317.56	-0.31	12-Jul-92	193	-0.9917	1314.46	0.09	12-Aug-92	224	-0.7894	1323.98	0.49
13-May-92	133	-0.6206	1331.89	-0.64	13-Jun-92	164	-0.9327	1317.26	-0.30	13-Jul-92	194	-0.9894	1314.57	0.11	13-Aug-92	225	-0.7788	1324.48	0.50
14-May-92	134	-0.6340	1331.27	-0.63	14-Jun-92	165	-0.9387	1316.97	-0.28	14-Jul-92	195	-0.9867	1314.69	0.12	14-Aug-92	226	-0.7679	1324.99	0.51
15-May-92	135	-0.6472	1330.65	-0.62	15-Jun-92	166	-0.9445	1316.70	-0.27	15-Jul-92	196	-0.9838	1314.83	0.13	15-Aug-92	227	-0.7568	1325.51	0.52
16-May-92	136	-0.6602	1330.04	-0.61	16-Jun-92	167	-0.9500	1316.45	-0.26	16-Jul-92	197	-0.9806	1314.98	0.15	16-Aug-92	228	-0.7454	1326.04	0.53
17-May-92	137	-0.6729	1329.44	-0.60	17-Jun-92	168	-0.9552	1316.20	-0.24	17-Jul-92	198	-0.9771	1315.14	0.16	17-Aug-92	229	-0.7339	1326.58	0.54
18-May-92	138	-0.6855	1328.85	-0.59	18-Jun-92	169	-0.9601	1315.97	-0.23	18-Jul-92	199	-0.9733	1315.31	0.18	18-Aug-92	230	-0.7221	1327.13	0.55
19-May-92	139	-0.6979	1328.27	-0.58	19-Jun-92	170	-0.9648	1315.75	-0.22	19-Jul-92	200	-0.9692	1315.50	0.19	19-Aug-92	231	-0.7101	1327.69	0.56
20-May-92	140	-0.7101	1327.69	-0.57	20-Jun-92	171	-0.9692	1315.55	-0.21	20-Jul-92	201	-0.9648	1315.71	0.20	20-Aug-92	232	-0.6979	1328.27	0.57
21-May-92	141	-0.7221	1327.13	-0.56	21-Jun-92	172	-0.9733	1315.35	-0.19	21-Jul-92	202	-0.9601	1315.92	0.22	21-Aug-92	233	-0.6855	1328.85	0.58
22-May-92	142	-0.7339	1326.58	-0.55	22-Jun-92	173	-0.9771	1315.18	-0.18	22-Jul-92	203	-0.9552	1316.15	0.23	22-Aug-92	234	-0.6729	1329.44	0.59
23-May-92	143	-0.7454	1326.04	-0.54	23-Jun-92	174	-0.9806	1315.01	-0.16	23-Jul-92	204	-0.9500	1316.40	0.24	23-Aug-92	235	-0.6602	1330.04	0.60
24-May-92	144	-0.7568	1325.51	-0.53	24-Jun-92	175	-0.9838	1314.86	-0.15	24-Jul-92	205	-0.9445	1316.65	0.26	24-Aug-92	236	-0.6472	1330.65	0.61
25-May-92	145	-0.7679	1324.99	-0.52	25-Jun-92	176	-0.9867	1314.72	-0.14	25-Jul-92	206	-0.9387	1316.92	0.27	25-Aug-92	237	-0.6340	1331.27	0.62
26-May-92	146	-0.7788	1324.48	-0.51	26-Jun-92	177	-0.9894	1314.60	-0.12	26-Jul-92	207	-0.9327	1317.20	0.28	26-Aug-92	238	-0.6206	1331.89	0.63
27-May-92	147	-0.7894	1323.98	-0.50	27-Jun-92	178	-0.9917	1314.49	-0.11	27-Jul-92	208	-0.9263	1317.50	0.30	27-Aug-92	239	-0.6071	1332.53	0.64
28-May-92	148	-0.7998	1323.49	-0.49	28-Jun-92	179	-0.9938	1314.39	-0.10	28-Jul-92	209	-0.9197	1317.81	0.31	28-Aug-92	240	-0.5933	1333.17	0.64
29-May-92	149	-0.8100	1323.01	-0.48	29-Jun-92	180	-0.9955	1314.31	-0.08	29-Jul-92	210	-0.9128	1318.13	0.32	29-Aug-92	241	-0.5794	1333.83	0.65
30-May-92	150	-0.8200	1322.54	-0.47	30-Jun-92	181	-0.9970	1314.24	-0.07	30-Jul-92	211	-0.9057	1318.46	0.33	30-Aug-92	242	-0.5653	1334.49	0.66
31-May-92	151	-0.8297	1322.09	-0.46						31-Jul-92	212	-0.8983	1318.81	0.35	31-Aug-92	243	-0.5511	1335.15	0.67

Table D.6: Daily approximation of TSI values (W/m2) and daily rate of change (TSI Var) during 1992 (September to December inclusive). Calculations for TSU values are based on the Julian Day (JD) and associated sine value, where (i) y=sin(2π x ((JD-277)/366)), and (ii) TSI =1361+(y*46.9).

Date	JD	value	W/m2	W/m2	Date	JD	value	TSI W/m2	W/m2	Date	JD	value	TSI W/m2	W/m2	Date	JD	Sine value	TSI W/m2	W/m2
01-Sep-92	244	-0.5367	1335.83	0.68	01-Oct-92	274	-0.0515	1358.59	0.80	01-Nov-92	305	0.4624	1382.69	0.72	01-Dec-92	335	0.8391	1400.36	0.44
02-Sep-92	245	-0.5221	1336.51	0.68	02-Oct-92	275	-0.0343	1359.39	0.80	02-Nov-92	306	0.4775	1383.40	0.71	02-Dec-92	336	0.8484	1400.79	0.43
03-Sep-92	246	-0.5074	1337.20	0.69	03-Oct-92	276	-0.0172	1360.19	0.80	03-Nov-92	307	0.4925	1384.10	0.70	03-Dec-92	337	0.8573	1401.21	0.42
04-Sep-92	247	-0.4925	1337.90	0.70	04-Oct-92	277	0.0000	1361.00	0.81	04-Nov-92	308	0.5074	1384.80	0.70	04-Dec-92	338	0.8660	1401.62	0.41
05-Sep-92	248	-0.4775	1338.60	0.70	05-Oct-92	278	0.0172	1361.81	0.81	05-Nov-92	309	0.5221	1385.49	0.69	05-Dec-92	339	0.8745	1402.01	0.40
06-Sep-92	249	-0.4624	1339.31	0.71	06-Oct-92	279	0.0343	1362.61	0.80	06-Nov-92	310	0.5367	1386.17	0.68	06-Dec-92	340	0.8827	1402.40	0.38
07-Sep-92	250	-0.4471	1340.03	0.72	07-Oct-92	280	0.0515	1363.41	0.80	07-Nov-92	311	0.5511	1386.85	0.68	07-Dec-92	341	0.8906	1402.77	0.37
08-Sep-92	251	-0.4317	1340.75	0.72	08-Oct-92	281	0.0686	1364.22	0.80	08-Nov-92	312	0.5653	1387.51	0.67	08-Dec-92	342	0.8983	1403.13	0.36
09-Sep-92	252	-0.4161	1341.48	0.73	09-Oct-92	282	0.0857	1365.02	0.80	09-Nov-92	313	0.5794	1388.17	0.66	09-Dec-92	343	0.9057	1403.48	0.35
10-Sep-92	253	-0.4005	1342.22	0.73	10-Oct-92	283	0.1028	1365.82	0.80	10-Nov-92	314	0.5933	1388.83	0.65	10-Dec-92	344	0.9128	1403.81	0.34
11-Sep-92	254	-0.3847	1342.96	0.74	11-Oct-92	284	0.1199	1366.62	0.80	11-Nov-92	315	0.6071	1389.47	0.64	11-Dec-92	345	0.9197	1404.13	0.32
12-Sep-92	255	-0.3688	1343.71	0.75	12-Oct-92	285	0.1369	1367.42	0.80	12-Nov-92	316	0.6206	1390.11	0.64	12-Dec-92	346	0.9263	1404.44	0.31
13-Sep-92	256	-0.3528	1344.46	0.75	13-Oct-92	286	0.1539	1368.22	0.80	13-Nov-92	317	0.6340	1390.73	0.63	13-Dec-92	347	0.9327	1404.74	0.30
14-Sep-92	257	-0.3366	1345.21	0.76	14-Oct-92	287	0.1708	1369.01	0.79	14-Nov-92	318	0.6472	1391.35	0.62	14-Dec-92	348	0.9387	1405.03	0.28
15-Sep-92	258	-0.3204	1345.97	0.76	15-Oct-92	288	0.1877	1369.80	0.79	15-Nov-92	319	0.6602	1391.96	0.61	15-Dec-92	349	0.9445	1405.30	0.27
16-Sep-92	259	-0.3041	1346.74	0.76	16-Oct-92	289	0.2046	1370.59	0.79	16-Nov-92	320	0.6729	1392.56	0.60	16-Dec-92	350	0.9500	1405.55	0.26
17-Sep-92	260	-0.2877	1347.51	0.77	17-Oct-92	290	0.2213	1371.38	0.79	17-Nov-92	321	0.6855	1393.15	0.59	17-Dec-92	351	0.9552	1405.80	0.24
18-Sep-92	261	-0.2712	1348.28	0.77	18-Oct-92	291	0.2380	1372.16	0.78	18-Nov-92	322	0.6979	1393.73	0.58	18-Dec-92	352	0.9601	1406.03	0.23
19-Sep-92	262	-0.2547	1349.06	0.78	19-Oct-92	292	0.2547	1372.94	0.78	19-Nov-92	323	0.7101	1394.31	0.57	19-Dec-92	353	0.9648	1406.25	0.22
20-Sep-92	263	-0.2380	1349.84	0.78	20-Oct-92	293	0.2712	1373.72	0.78	20-Nov-92	324	0.7221	1394.87	0.56	20-Dec-92	354	0.9692	1406.45	0.21
21-Sep-92	264	-0.2213	1350.62	0.78	21-Oct-92	294	0.2877	1374.49	0.77	21-Nov-92	325	0.7339	1395.42	0.55	21-Dec-92	355	0.9733	1406.65	0.19
22-Sep-92	265	-0.2046	1351.41	0.79	22-Oct-92	295	0.3041	1375.26	0.77	22-Nov-92	326	0.7454	1395.96	0.54	22-Dec-92	356	0.9771	1406.82	0.18
23-Sep-92	266	-0.1877	1352.20	0.79	23-Oct-92	296	0.3204	1376.03	0.76	23-Nov-92	327	0.7568	1396.49	0.53	23-Dec-92	357	0.9806	1406.99	0.16
24-Sep-92	267	-0.1708	1352.99	0.79	24-Oct-92	297	0.3366	1376.79	0.76	24-Nov-92	328	0.7679	1397.01	0.52	24-Dec-92	358	0.9838	1407.14	0.15
25-Sep-92	268	-0.1539	1353.78	0.79	25-Oct-92	298	0.3528	1377.54	0.76	25-Nov-92	329	0.7788	1397.52	0.51	25-Dec-92	359	0.9867	1407.28	0.14
26-Sep-92	269	-0.1369	1354.58	0.80	26-Oct-92	299	0.3688	1378.29	0.75	26-Nov-92	330	0.7894	1398.02	0.50	26-Dec-92	360	0.9894	1407.40	0.12
27-Sep-92	270	-0.1199	1355.38	0.80	27-Oct-92	300	0.3847	1379.04	0.75	27-Nov-92	331	0.7998	1398.51	0.49	27-Dec-92	361	0.9917	1407.51	0.11
28-Sep-92	271	-0.1028	1356.18	0.80	28-Oct-92	301	0.4005	1379.78	0.74	28-Nov-92	332	0.8100	1398.99	0.48	28-Dec-92	362	0.9938	1407.61	0.10
29-Sep-92	272	-0.0857	1356.98	0.80	29-Oct-92	302	0.4161	1380.52	0.73	29-Nov-92	333	0.8200	1399.46	0.47	29-Dec-92	363	0.9955	1407.69	0.08
30-Sep-92	273	-0.0686	1357.78	0.80	30-Oct-92	303	0.4317	1381.25	0.73	30-Nov-92	334	0.8297	1399.91	0.46	30-Dec-92	364	0.9970	1407.76	0.07
					31-Oct-92	304	0.4471	1381.97	0.72						31-Dec-92	365	0.9982	1407.82	0.06